Harnessing light beyond equilibrium: from molecular photoswitches to out-of-equilibrium supramolecular assemblies

Dissertation

zur

Erlangung des Doktorgrades (Dr. rer. nat.)

der

Mathematisch-Naturwissenschaftlichen Fakultät

der

Rheinischen Friedrich-Wilhelms-Universität Bonn

vorgelegt von

Lidón Pruñonosa Lara

aus

Benicasim, Spanien

Bonn 2025

Angefertigt mit der Genehmigung der Mathematisch-Naturwissenschaftlichen Fakultät
der Rheinischen Friedrich-Wilhelms-Universität Bonn

Gutachter/Betreuer: Dr. Larissa K.S. von Krbek
Gutachter: Priv. Doz. Dr. Marianne Engeser
Tag der Promotion: 19.12.2025
Erscheinungsjahr: 2026

Die vorliegende Arbeit wurde in der Zeit von Oktober 2021 bis Oktober 2025 am Kekulé-Institut für Organische Chemie und Biochemie der Rheinischen Friedrich-Wilhelms-Universität Bonn unter Anleitung von Dr. Larissa K.S. von Krbek angefertigt.

Acknowledgements

First and foremost, I would like to express my deepest gratitude to my supervisor, **Larissa K.S. von Krbek**, for believing in me since that first video call interview in February 2021. Thank you for continuously encouraging me to grow, both professionally and personally, and for challenging me to become the best version of myself. I am especially grateful for the freedom you gave me to design and present my own project ideas, and for the invaluable opportunities to share them in international settings.

I would also like to sincerely thank **Marianne Engeser**, not only for co-examining this thesis but for your insightful guidance during our weekly group seminars. Your thoughtful questions encouraged me to strengthen my work. Thank you for always keeping an open door and for your patience when working with my delicate cage complex samples, even when they were in DMSO.

To our collaborators: **Oliver Thorn-Seshold**, thank you for conceiving the original *azoplatin* project. Even though it did not unfold as expected, I truly enjoyed our discussions and appreciated being entrusted with trying to bring the idea to life. **Mike Ward and Max Tipping**, thank you for letting me be part of such complex yet exciting project, and for bring together such a beautifully publication. **Benedikt Bädorf and Stefan Grimme**, I am incredibly grateful for your time and effort spent optimising the intricate structures I designed.

To everyone in the **administration**, **ZVE**, and the **electronic**, **mechanical**, and **glassblowing workshops** – thank you for keeping everything running smoothly. To the **NMR**, **Mass Spectrometry**, and **Elemental Analysis** departments – thank you for your dedication and countless hours analysing my samples. Special thanks to **Karin Peters-Pflaumbaum** for your help with “ex-situ” mass spectrometry, and to **Senada Nozinovic** for your enthusiasm and assistance with ROESY NMR measurements. A heartfelt thank you to **Ulrike Weynand** for your endless kindness and for understanding me beyond words, even when my German was not quite there yet.

Arne Lützen and all members of his group, thank you for the exciting discussions and thoughtful input during our weekly meetings (especially to my *amiga* **Hannah Wessely**).

To my Bachelor students – **Evelin Schulz**, **Fabian Herpell**, and **Gianluca Jung** – I know the projects did not always go to plan, but thank you for pushing through and always giving your best.

To all past and new members of the Krbek group, but in particular to: **Max Notheis**, more than just a lab partner, you have been a true friend and constant supporter. Thank you for everything, from surviving the "glowy fingers" summer to all the moments that turned chaos into laughter (including the bike-police incident). **Anne Müller-Feyen**, my partner in crime, your positive energy kept me going. I loved how we always knew exactly what the other was thinking. I could not have asked for a better woman to surf the chaotic sea of men in the lab. **Justin Konen**, you were far more than just a Master's student – you were my singing partner, fumehoodie, and my *brüderchen*. Thank you for your kindness and unwavering support. **Parveen Kumar**, though you joined towards the end of my PhD journey, your steadfast belief in me and genuine care meant the world. **Vigan Sahiti**, thank you for always lifting the mood with your humour, for enduring my "emo pop" music, and for your much needed help with quantum chemistry. **Johannes Volk**, your constant willingness to help, whether with IT emergencies or colour layouts on posters, never went unnoticed – thank you. **Ruben Falkenburg**, thank you for your support during fashion emergencies and German oral exams, and for meeting me at the airport on my very first day in Bonn – it meant a great deal.

To all past and present members of the **Menche group**, thank you for welcoming me as one of your own. To me, we have always been one big group. A special thanks to my girlies **Vivi** and **Tragi**, and fitness team.

To my German *mama*, **Christina**, I honestly do not think I could have physically nor emotionally survived living in Germany without you. Thank you for always looking out for me. I could not have been luckier.

To all those who made Bonn feel like home (**Matteo**, **Franzi**, and my **Tierheim family** – especially **Janina**) and to those who were rooting for me from afar (**Abi**, **Elizabeth**, **Pranita**, **Pau**, ***mis patatas***).

To my role model, **Rhiannon**, thank you for being a constant source of inspiration and for always picking up the phone no matter the hour.

To **Nora**, **Ellie**, **Homie**, and **Valentin**, many may think I saved your lives, but the truth is: you saved mine.

To my soul sister, **Sachi**, I could not have done this without you. Thank you for crying with me, listening to endless monologues, for never giving up on me, and for always being my greatest cheerleader. Thank you for being you.

To my partner in life, **Callum**, thank you for standing by me through thick and thin. Your support has meant everything, even when it meant living in different countries (or continents) for years. Thank you for your patience, kindness, and most of all, for never giving up on us.

Lastly but definitely not least, to the ones who gave me roots to grow from and wings to fly with, **Mum**, **Dad**, thank you for your unconditional love and support. *Por último, pero definitivamente no menos importante, a los que me dieron raíces con las que crecer y alas con las que volar,* ***Mamá****,* ***Papá****, gracias por vuestro cariño y apoyo incondicional.*

Table of Contents

Abbreviations

CPL	Circular Polarised Light
DFT	Density Functional Theory
DMF	Dimethylformamide
DMSO	Dimethyl sulfoxide
DPPP	1,3-Bis(diphenylphosphino)propane
DTEs	Dithienylethenes
EDG	Electron-donating group
ESI MS	Electrospray Ionisation Mass Spectrometry
EtOAc	Ethyl acetate
GFN-xTB	Geometry, Frequency, Noncovalent interactions - extended Tight Binding
HPLC	High-Performance Liquid Chromatography
L	Ligand
M	Metal
MeCN	Acetonitrile
MM2	Molecular Mechanics II
NMR	Nuclear Magnetic Resonance
n.d.	Not detected by NMR and mass spectrometry
PSS	Photostationary state
r.t.	Room temperature
S_N	Nucleophilic substitution
UV-vis	Ultraviolet-visible
$\tau_{½}$	Half life
ε	Molar attenuation coefficient
Φ	Quantum yield
λ	Wavelength

Abstract

Supramolecular chemistry enables dynamic, functional architectures to be constructed through reversible, non-covalent interactions. Metal-organic cages, in particular, offer a versatile platform for exploring light-responsive behaviour, owing to their defined geometry, internal cavities, and capacity for structural reconfiguration. This thesis explores how light can be harnessed to control and drive the behaviour of these assemblies, progressing from reversible molecular photoswitching to out-of-equilibrium transformations sustained by continuous irradiation.

Three interconnected projects examine how metal coordination, ligand geometry, and continuous light input influence the switching behaviour and structural dynamics of self-assembled cages. The first project explores the influence of metal coordination on the photochemical properties of azobenzene derivatives. A tridentate azobenzene-based ligand was designed to form a mononuclear Pd(II) complex, enabling the systematic investigation of the effects of coordination on isomerisation efficiency, thermal relaxation, and reversibility. These studies provide a foundation for understanding how proximity to metal centres modulates switching behaviour.

The second project investigates how variations in coordination vectors, resulting from ligand connectivity and *E/Z* isomerisation, influence the geometry and responsiveness of metal-organic cages. Comparative studies of *para*- and *meta*-substituted photoswitchable azobenzene ligands revealed that subtle structural changes can have a significant impact on the extent and reversibility of light-induced reconfiguration in Co(II)-based assemblies. The conditions under which concerted, reversible switching can be achieved were also examined in this work.

The final project applies these principles to out-of-equilibrium systems, demonstrating how continuous light input can drive a metallo-supramolecular assembly away from equilibrium via a molecular ratchet mechanism. Pd(II)-based structures incorporating azobispyrazole ligands were designed to undergo directional transformations between discrete assemblies under sustained irradiation. As both the *E* and *Z* states absorb visible light, the system remains responsive under constant white-light and sunlight exposure, operating autonomously and temporarily storing light energy as chemical energy.

Together, these studies advance our understanding of how molecular photoswitching translates into controllable supramolecular behaviour, and how light can be harnessed to not only modulate structure, but also drive directional, energy-fuelled transformations. By establishing design principles that preserve switching function, elucidating how ligand geometry governs responsiveness, and demonstrating autonomous operation under continuous irradiation, this work bridges the gap between molecular photoswitches and functional, light-powered supramolecular machines. These insights pave the way for future designs that couple structural adaptability with energy-driven functionality, providing a blueprint for artificial molecular devices capable of converting light into stored chemical energy.

1. Introduction

Supramolecular chemistry explores how molecules interact beyond covalent bonds to form larger, functional architectures.[1] These systems exhibit organisation and adaptability reminiscent of biological structures through reversible, directional, and selective non-covalent interactions.[2] Nature's intricate assemblies, ranging from lipid bilayer formation to enzyme-substrate recognition, provide an ongoing source of inspiration, showcasing how functionality can arise from the controlled interplay of weak interactions.[3,4] By mimicking these processes in synthetic systems, chemists can design dynamic materials that are capable of reversible organisation, environmental responsiveness, and adaptive behaviour.[5]

At the heart of supramolecular chemistry lies the concept of self-assembly, whereby molecular building blocks spontaneously organise into ordered structures under thermodynamic control.[6] The resulting architecture represents the lowest free-energy configuration compatible with the system's constraints.[7] This principle has enabled the construction of a vast range of discrete and extended structures, including metal-organic cages, which are the focus of this thesis. These hollow architectures, commonly referred to as capsules, are formed through the self-assembly of metal centres with multitopic ligands.[8] However, given that even slight variations in molecular design or environmental conditions can result in significant differences in the structure and behaviour of the resulting assemblies, understanding how to guide and manipulate metal-ligand coordination processes to achieve specific functions remains a primary objective.[9]

Structural control in supramolecular systems can be achieved by exploiting external stimuli that trigger specific molecular responses within the building blocks. These stimuli may be chemical,[10] electrochemical,[11] or photochemical.[12] Amongst these, light is exceptionally versatile for *in-situ* manipulation: it can be applied remotely with high spatial and temporal precision without introducing further chemicals.[13] Furthermore, its reversibility allows for repeated, non-invasive modulation of structure and function. The ability to convert light energy into precise molecular reconfiguration establishes light as a cornerstone in the design of responsive supramolecular systems. Consequently, this thesis will focus exclusively on light-responsive assemblies.

To make a supramolecular structure light-responsive, molecular photoswitches are typically incorporated into the building blocks.[14] Molecular photoswitches undergo reversible structural and electronic changes upon exposure to light, interconverting between two or more isomeric states.[15] These states typically differ in geometry, polarity, or coordination properties, enabling the photoswitch to exert control over a larger assembly. Azobenzenes are one of the most widely used classes of photoswitches, interconverting between planar *E*- and bent *Z*-isomers under light or thermal stimuli via the N=N azo group.[16] While azobenzenes are well established, this thesis also explores the incorporation of other, less commonly studied, photoswitches into the building blocks. Azobispyrazoles photoswitches, which are also N=N based, have been scarcely investigated in supramolecular systems and, to our knowledge, have not previously been incorporated into metal-organic cages.[17]

Combining metal ions with photoswitches significantly broadens the design space for light-responsive materials.[18] Metal ions offer defined coordination preferences and geometries that complement and extend those of purely organic switches.[19] Integrating photoswitches into metal-organic coordination cages opens new possibilities for the development of assemblies whose geometry and stability can be reversibly tuned by light. However, the intrinsic photoresponsive properties of photoswitches are not always preserved upon coordination to metal centres.[20] Metal binding can perturb the electronic environment around the switching unit, i.e. the N=N bond in azo systems, thereby altering or even inhibiting its switching behaviour.[21] Therefore, understanding how metal coordination affects photoswitching is a fundamental step towards the rational design of light-responsive supramolecular architectures.

Metal-organic cages can serve as model systems for studying light-responsive supramolecular behaviour. These discrete assemblies, formed through metal-ligand coordination, possess well-defined internal cavities capable of encapsulating guest molecules or mediating confined chemical reactivity.[22] By incorporating photoswitchable ligands, it becomes possible to reversibly alter the cavity volume and shape in response to light, thereby enabling reversible control over molecular recognition and reactivity.[12] However, even subtle changes in ligand design – such as variations in substitution patterns or connectivity – can significantly influence coordination geometry and consequently the assembly's overall structure.[9] These effects become even more

pronounced when combined with light-induced configurational changes, making it difficult to predict how molecular-level photoisomerisation will translate into well-defined structural outcomes at the supramolecular level. Moreover, achieving cooperative switching, where all the ligands within a cage respond in simultaneously to light by switching to the same isomer, is challenging.[23]

Although many supramolecular assemblies operate under thermodynamic control, whereby the system relaxes to the lowest free-energy state, nature's most sophisticated molecular systems function far from equilibrium.[24] In equilibrium systems, once the most stable structure is reached, the assembly remains static unless the energy landscape is perturbed. In contrast, out-of-equilibrium systems rely on continuous energy input to maintain metastable states, which enables transient access to structures and functions that would otherwise be thermodynamically unfavourable.[25] When the energy supply ceases (e.g. light), these systems relax back to equilibrium.[26]

Light offers a particularly powerful means of driving systems away from equilibrium.[27] Its spatial and temporal precision, reversibility, and non-invasive nature enable it to fuel complex reaction networks without generating chemical waste. When coupled to reaction cycles that selectively link energy-releasing and energy-consuming steps, light can bias molecular transformations and sustain non-equilibrium behaviour.[28] This concept underpins molecular ratchets: chemical reaction cycles in which components react preferentially in one direction. While molecular ratchets have been demonstrated in supramolecular systems, their integration into metal-organic cages remains limited.[29] Additionally, achieving autonomous, light-driven ratcheting in these assemblies represents a critical step towards mimicking the operation of natural molecular machines.

The work in this thesis explores how light can be harnessed to control and, ultimately, drive supramolecular assemblies beyond equilibrium. First, it examines how metal coordination influences the photochemical properties of azobenzene ligands, revealing the interplay between the coordination environment and photoswitching behaviour. Transitioning from mononuclear systems to three-dimensional, discrete cages, the thesis then investigates how subtle ligand modifications dictate their geometry and light responsiveness. Finally, it demonstrates how continuous light input can sustain a non-

equilibrium state in a metallo-supramolecular assembly, enabling autonomous, directional molecular ratcheting. Together, these studies advance our fundamental understanding of light-controlled supramolecular systems and pay the way for future designs that couple structural adaptability with energy-driven functionality.

2. Theoretical background

2.1 Photoswitches

A central strategy in designing responsive chemical systems is to control the molecular structure and function with external stimuli. Various triggers, such as temperature,[30] pH,[10] redox conditions,[11] or light,[12,14] can be used to induce specific molecular changes. Light is a particularly versatile stimulus for *in-situ* manipulation, as it can be spatiotemporally controlled, its wavelength and intensity can be precisely regulated, it is waste-free, and it avoids introducing further chemicals.[13,31] These advantages have driven the development of photoresponsive compounds, known as photoswitches, which can undergo reversible structural and electronic changes when exposed to light.[32–35]

A photoswitch is a compound that can be reversibly interconverted between two or more isomeric states upon irradiation with light (Figure 1a).[15] This photochemical isomerisation process is accompanied by changes in molecular geometry and electronic distribution, which often produce distinct UV-vis absorption spectra for the different isomers.[36,37] UV-vis spectroscopy is therefore a widely used method for characterising photoswitches, as it allows isomers to be distinguished and their interconversion kinetics to be monitored over time.[38] The shapes of the absorption bands, as well as the differences in the absorption maxima between the isomers, can be exploited to drive switching by selecting an appropriate wavelength for irradiation.[39]

In a typical isomerisation process (Figure 1b), the thermodynamically stable isomer absorbs a photon and is promoted to an electronically excited state.[40] After rapid vibrational relaxation, the molecule returns to the ground state via a pathway that can lead either back to the original isomer or to a different isomeric form.[40] The newly generated photoisomer has a higher free energy than the original one and is, therefore, referred to as the metastable isomer. This metastable isomer can thermally relax back to the stable form; this process is described by its half-life ($\tau_{½}$), the time required for 50% of the metastable population to relax back to the stable form.[15]

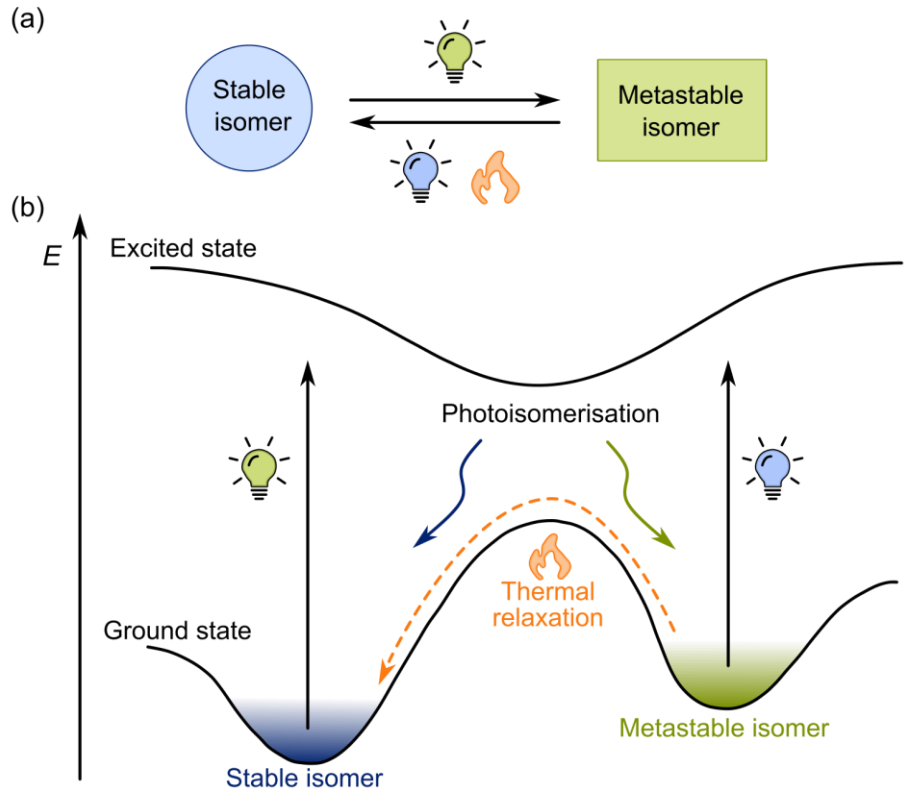

Figure 1. (a) General photoswitch isomerisation upon light irradiation, interconverting between stable and metastable forms. (b) A simplified representation of the potential energy surfaces involved in the isomerisation of a photoswitch.

Photoswitching is generally a reversible and non-destructive process. However, in some systems, repeated cycling can lead to a gradual loss of performance due to side reactions such as photodegradation, irreversible cyclisation, or dimerisation.[41] The extent of isomerisation can be described by the photostationary state (PSS), defined as the steady state between isomers that is established under continuous irradiation with light of a given wavelength.[42] At the PSS, the ratio of isomers is determined by: how strongly each one absorbs light at the wavelength used for irradiation (its molar attenuation coefficient, ε), how efficiently the absorbed light drives isomerisation (its quantum yield, Φ), and how much their absorption bands overlap in the UV-vis spectrum.[42] This spectral overlap also forms the basis for bidirectional switching using different irradiation wavelengths. When the absorption spectra of the two isomers overlap significantly, both forward and backward photoisomerisations occur simultaneously, which limits the maximum enrichment of either isomer and reduces the efficiency of switching. A large spectral separation between the absorption bands therefore enables higher PSS values and more selective photoswitching.[40]

If the thermal barrier for relaxation from the metastable to the stable form is relatively low, back-isomerisation occurs readily under ambient conditions, and the photoswitch is classified as a T-type. Conversely, when this barrier is high, both isomers are kinetically stable and interconversion takes place almost exclusively via light irradiation; such systems are referred to as P-type photoswitches.[43]

These kinetic behaviours are found in different photoswitch families. The following subsections introduce four relevant classes: azobenzenes, azobispyrazoles, diazocines, and dithienylethenes (DTEs).

2.1.1 Azobenzenes

Azobenzene is amongst the most widely studied molecular photoswitches, characterised by a diaryl-diazene (Ar-N=N-Ar) core that can adopt two distinct geometric configurations: the thermodynamically favoured *E*-isomer and the higher-energy, metastable *Z*-isomer (Scheme 1).[44] Where *Z*-azobenzene is reported to be 42-55 kJ/mol less stable than *E*-azobenzene.[45]

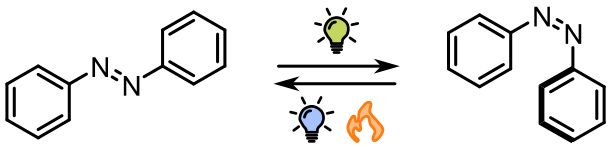

E-azobenzene *Z*-azobenzene

Scheme 1. Structure of azobenzene in its ground state (*E*-azobenzene) and its metastable state (*Z*-azobenzene).

Despite having the same chemical composition, the different configurations of these isomers significantly impact their molecular geometry and physicochemical properties. The planar *E*-isomer has no dipole moment, whereas the bent *Z*-isomer has a dipole moment of almost 3 D.[46] Structurally, the distance between the *para*-carbons decreases from approximately 9 Å in *E*-azobenzene to 5.5 Å in the *Z*-form.[44] These geometric differences produce a noticeable anisotropic effect in the ^{1}H NMR spectra, with *Z*-azobenzene signals shifting upfield relative to the *E*-form.[44] Additionally, as the *Z*-isomer's ring orientation increases its polarity, the stability of *Z*-azobenzene is enhanced

in polar solvents.[45] Consequently, the PSS of both isomers is strongly influenced by the polarity of the solvent.

The interconversion between these isomers can be triggered by light or heat. Typically, *E*→*Z* photoisomerisation occurs upon irradiation with UV light (commonly 320-360 nm), whereas *Z*→*E* switching is promoted either photochemically via irradiation with visible light (400-450 nm) or thermally.[47] The half-lives of the *Z*→*E* thermal isomerisation range from milliseconds to days, depending on the substituents, the solvent polarity, and the temperature.[48–51]

UV-vis spectroscopy is the primary analytical method used to monitor azobenzene switching. Most azobenzene derivatives display two characteristic absorption bands: a high-intensity π→π* transition at shorter wavelengths, and a weaker n→π* transition at longer wavelengths, which arises from non-bonding electron pairs on the nitrogen (Figure 2).[46,52,53] In unsubstituted *E*-azobenzene, the n→π* transition is symmetry-forbidden and thus, minimally observable.[54] However, this transition becomes more pronounced upon functionalisation and in the *Z*-form.[45] Selective irradiation of these bands enables the controlled enrichment of either isomer, with the PSS composition depending on the wavelength, the substituents, and the solvent used.[53] Reported photoconversion values for unsubstituted azobenzene therefore vary; however, efficiencies of up to ~90% have been observed, with slightly lower values for the reverse process.[55]

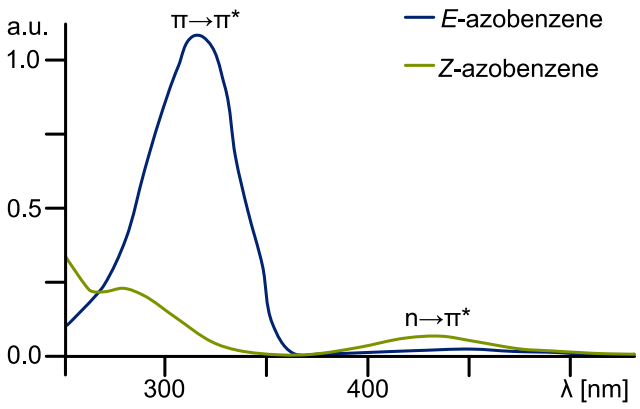

Figure 2. UV-vis absorption spectra of *E* and *Z* azobenzene in acetonitrile. Spectra plotted from data reported by Kovalenko and co-workers.[52]

The photoisomerisation pathway remains an ongoing area of research. Two mechanisms are commonly proposed: (i) inversion at one nitrogen atom and (ii) rotation involving torsion about the N=N double bond (Scheme 2).[15,44,53,56,57] While both mechanisms are supported by computational studies, there is still a lack of experimental evidence.[58]

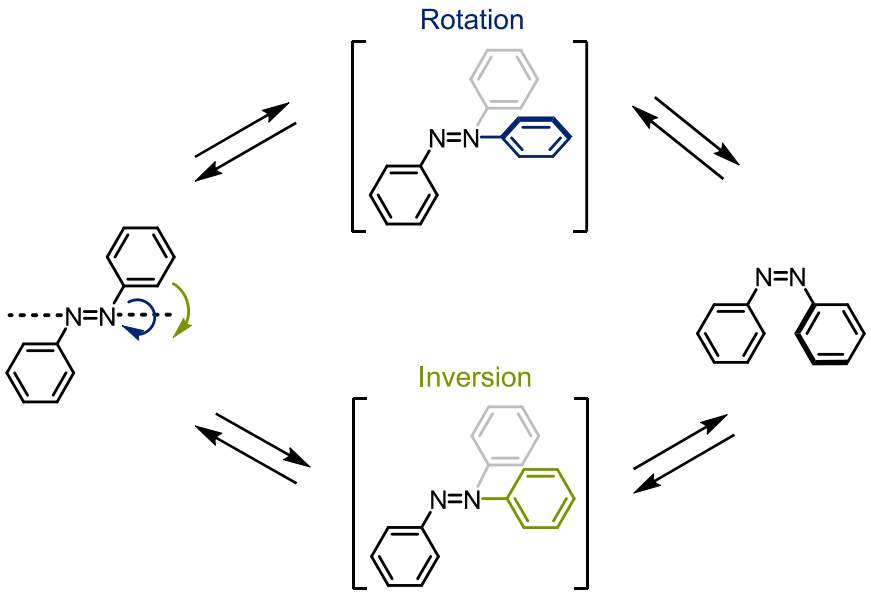

Scheme 2. Proposed mechanisms for the isomerisation of azobenzene.

The substitution pattern on the aromatic rings has a significant impact on the absorption maxima, quantum yield, and thermal stability of azobenzenes. A 2022 study by Hans-Dieter Arndt and co-workers demonstrated that electron-donating groups (EDGs) in the *para* position can increase the PSS of the *Z*-isomer, whereas *ortho* or *meta* substituents may accelerate thermal relaxation (Figure 3).[59] On the other hand, bulky *ortho* substituents can sterically hinder back-rotation, thereby slowing relaxation and extending half-lives from milliseconds to days.[59] In 2012, Hecht and co-workers observed that electron-withdrawing groups, such as fluorine, can shift the absorption spectrum into the visible region and enhance the stability of the *Z*-isomer.[60] Despite decades of azobenzene studies, a universal predictive trend for substituent effects remains elusive, and achieving detailed tuning of photophysical properties usually requires empirical optimisation.[61–65]

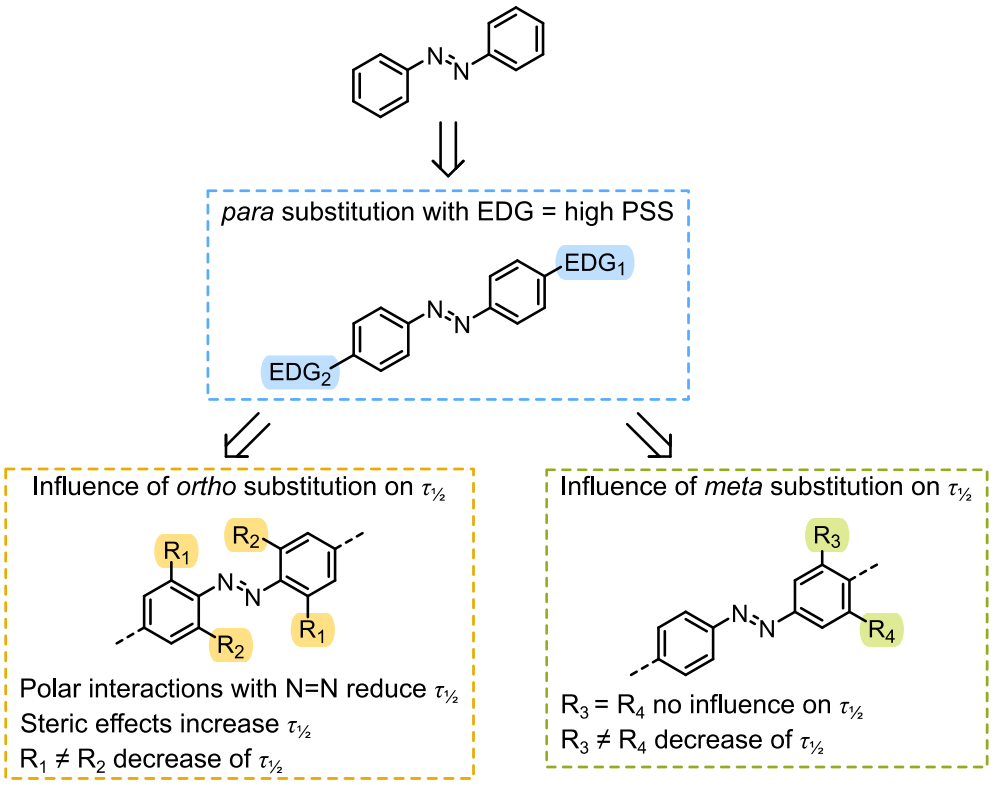

Figure 3. General influence of azobenzene substitution patterns studied by Hans-Dieter Arndt and co-workers.[59]

In recent years, azobispyrazoles, another class of azo (N=N) photoswitches, have been studied to address some of the limitations of classical azobenzenes, i.e., low PSS conversion. These compounds have been incorporated into supramolecular systems and are becoming increasingly relevant in light-controlled molecular applications, including those explored in this thesis.[66,67]

2.1.2 Azobispyrazoles

Azobispyrazoles are a family of bis-heteroaryl azo switches (Het-N=N-Het) that offer near-quantitative, bidirectional photoisomerisation alongside widely tuneable *Z*-isomer thermal half-lives, ranging from hours to years (Scheme 3).[17] Similar to azobenzenes, the *E*-configurations is the thermodynamically stable state and the *Z*-isomer is metastable. Isomerisation from *E* to *Z* is typically triggered by irradiation with UV light, while the reverse *Z*→*E* process can be achieved either photochemically using white light or thermally in the dark.[17] Whilst both mono- and bis-heteroaryl azo compounds have been explored, this thesis focuses specifically on bis-pyrazolyl systems.

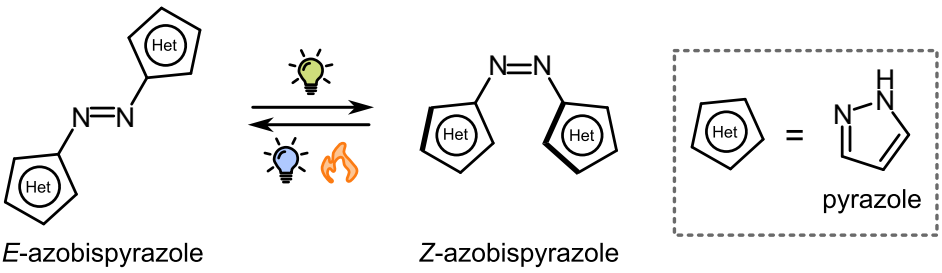

Scheme 3. Structure of azobispyrazole in its ground state (*E*-azobispyrazole) and its metastable state (*Z*-azobispyrazole).

Structurally, replacing the phenyl rings of azobenzenes with pyrazoles alters the electronic structure and geometry of the azo unit, resulting in unique switching characteristics.[68] A defining feature is the geometry of the *Z*-azobispyrazole isomer, which adopts a twisted conformation that makes efficient *Z*→*E* photoisomerisation possible.[17] However, the thermal half-life of the *Z*-isomer is not solely determined by this geometry. Instead, it can be tuned across several orders of magnitude by changing how the azo group is connected to the pyrazole rings (whether through carbon or nitrogen).[17] Thereby, modulating conjugation and electronic delocalisation. This structural flexibility allows for both high photoconversion and controllable thermal stability within the same molecular family, although no general trend has yet been established.

Another important feature of azobispyrazoles is the clear separation of their absorption bands, as can be seen in the UV-vis spectrum (Figure 4).[17] The π→π* and n→π* transitions in these heteroaryl systems are distinctly resolved, enabling very efficient bidirectional switching and, as a result, achieving favourable PSS compositions.[17]

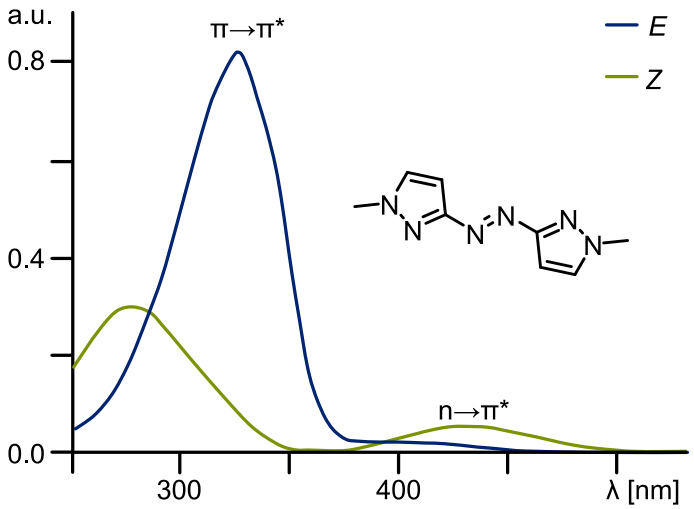

Figure 4. UV-vis absorption spectra of *E* and *Z* 1,2-bis(1-methyl-1H-pyrazol-3-yl)diazene in acetonitrile. Spectra plotted from data reported by Tao Li co-workers.[17]

The importance of this new family of photoswitches was demonstrated in 2021, when Tao Li and co-workers reported a detailed study of azobispyrazole switches.[17] They synthesised a series of C-linked azobispyrazole compounds, where the position of the linkage was varied (Figure 5a). All of the switches exhibited excellent bidirectional photoconversion efficiencies, and by altering the linkage, the half-life of the *Z*-isomer could be tuned from hours to years while maintaining nearly quantitative switching in both directions (Figure 5a).

Subsequent work by Fuchter, Han, and co-workers further broadened the scope of application of azobispyrazoles.[69] The introduction of *ortho*-methyl substituents, at carbon positions adjacent to the azo linkage within the pyrazole rings (Figure 5b), improved fatigue resistance and slightly increased the *Z*-isomer content at the PSS. These modifications were reported to make azobispyrazoles suitable for use in photocontrolled energy storage applications.[69]

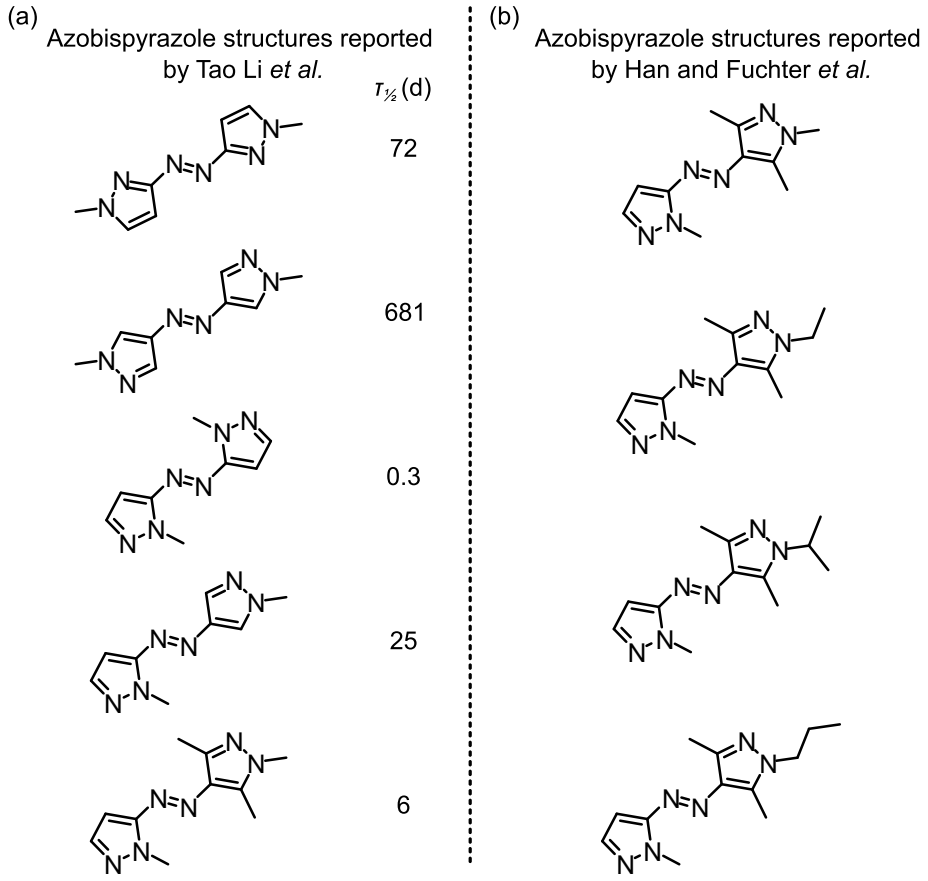

Figure 5. (a) Azobispyrazole structures and *Z*-isomer half-lives reported by Tao Li and co-workers.[17] (b) Azobispyrazole structures reported by Han, Fuchter, and co-workers.[69]

Taken together, these results establish azobispyrazoles as a next generation of azo photoswitches. They combine: (i) well-separated absorption bands for high PSS conversion, (ii) near-quantitative bidirectional photoisomerisation, and (iii) thermally tuneable *Z*-isomer half-lives. While the full potential of azobispyrazoles-based architectures remains far from fully explored, their future prospects are highly promising.

Although the two photoswitches discussed so far, azobenzenes and azobispyrazoles, favour the *E*-isomer as their most stable configuration, this is not true of all photoswitches. Diazocines, another class of azo switches, will be introduced next.

2.1.3 Diazocines

Diazocines are a class of bridged azobenzene derivatives (see Section 2.1.1), where the two aryl rings are covalently connected by a short linker, most commonly by a CH_2-CH_2 unit, to form an eight-membered cyclic structure (Scheme 4).[70] Variants in which the bridge contains heteroatoms, such as O, S, or NR (e.g., NH, NMe, Net or NAc), are generally referred to as diazocine derivatives since they have the same core architecture, but differ in the bridge composition.[15] In this thesis, the term 'diazocine' primarily refers to the parent CH_2-CH_2 bridged system, while the heteroatom-containing analogues are treated as derivatives.

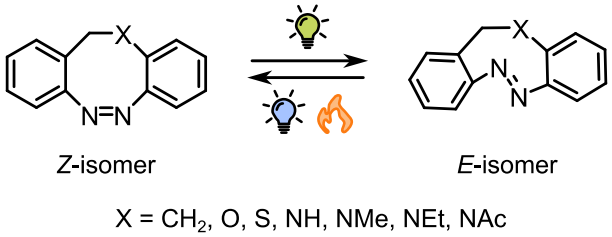

Scheme 4. Structure of diazocine in its ground state (*Z*) and metastable state (*E*) with different substituents X in the bridging unit.

The conformational constraint introduced by the bridge reduces the system's flexibility, resulting in a more rigid tricyclic framework than that of unbridged azobenzenes.[70] Notably, this ring strain inverts the relative stability of the photoisomers: unlike azobenzenes, the U-shaped *Z*-isomer of diazocine is thermodynamically favoured, while the planar *E*-isomer is metastable.[71]

The photochemical behaviour of diazocines is characterised by well-resolved UV-vis absorption bands corresponding to the $n\rightarrow\pi^*$ transition of the *Z*-isomer and the $\pi\rightarrow\pi^*$ transition of the *E*-isomer, which facilitate selective excitation (Figure 6).[9,70] Typically, $Z\rightarrow E$ isomerisation is induced by near-UV light, whereas the reverse $E\rightarrow Z$ switching proceeds quantitatively under green light.[72] In some derivatives, even far-red or near-infrared light can promote switching, highlighting the versatility of these systems and their potential use for *in vivo* medical applications.[70]

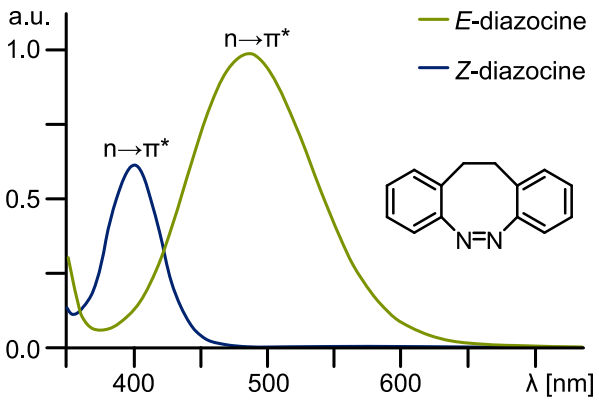

Figure 6. UV-vis absorption spectra of *Z* and *E* diazocine in acetonitrile. Spectra plotted from data reported by Herges and co-workers.[70]

Beyond their inverted thermodynamic preference relative to azobenzenes, the rigid cyclic structure of diazocines also improves the photoisomerisation quantum yields.[73] The metastable *E*-isomer is typically thermally stable for several hours at room temperature, though exact values depend on the solvent and substituents present.[74] Diazocines also exhibit remarkable photostability, showing no signs of photodegradation even after repeated alternating irradiation cycles.[75] Together with their stable *Z* ground state, tuneable *E* lifetime, efficient bidirectional switching, and favourable PSS, these features make diazocines a particularly valuable class of photoswitches, offering high efficiency, precise control, and robust switching behaviour.[76]

The photoswitches discussed so far (azobenzenes, azobispyrazoles, and diazocines) operate via light-driven interconversions between *E* and *Z*-isomers of an azo unit. However, not all molecular photoswitches are based on an N=N double bond. An important and widely studied class of non-azo photoswitches are dithienylethenes (DTEs), which interconvert between open- and closed-ring isomers. This photoswitch type will be discussed in the following section.

2.1.4 Dithienylethenes (DTEs)

Dithienylethenes (DTEs) are characterised by a central ethene (C=C) bridge that is substituted with two thiophene rings which undergo reversible photochemical electrocyclisation (Scheme 5).[15] These reactions interconvert between an open-ring (*o*) and closed-ring (*c*) form via photocyclisation (*o*→*c*) and cycloreversion (*c*→*o*).[77] Ring closure is typically induced by UV light irradiation, whereas the ring-opening reaction is driven by visible light.[78] The *o*-form is usually the thermodynamically stable state, whereas the *c*-form is a higher-energy, photoinduced, kinetically trapped state.[79]

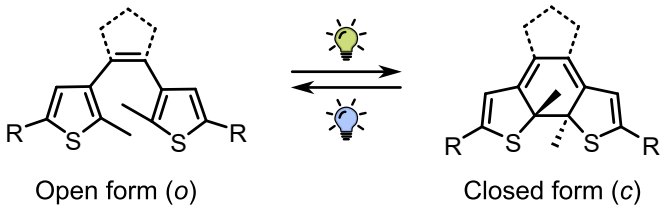

Scheme 5. Photochromic inversion of a dithienylethene (DTE) scaffold between its open (*o*) and closed (*c*) form.

The structural change between isomers is accompanied by significant differences in conjugation. In the *o*-form, the π-systems of the thiophene units are electronically decoupled due to a non-planar geometry that disrupts π-overlap and conjugation.[77,80] In contrast, in the *c*-form, extended conjugation across the ethene bridge establishes the continuous delocalisation of π-electrons.[15,77] This electronic reorganisation results in distinct optical properties that can be observed by UV-vis absorption spectroscopy (Figure 7): the *o*-form primarily absorbs in the UV region, while the *c*-form displays new, red-shifted absorption bands in the visible region.[78]

A defining feature of DTE photoswitches is their excellent thermal stability. Under ambient conditions, both isomers are thermally irreversible; interconversion occurs only upon photoexcitation, classifying them as P-type molecules (see Section 2.1).[81] This contrasts with azobenzenes and related azo switches, where the metastable isomer undergoes thermal relaxation in the dark (see Sections 2.1.1-2.1.3). The bistability of DTEs, together with their typically high photoisomerisation quantum yields, and their ability to achieve photostationary states approaching quantitative conversion (>95%), makes them highly reliable photoswitches.[77,82] Additionally, DTEs exhibit excellent

fatigue resistance, with repeated irradiation cycles proceeding without appreciable photodegradation.[81,83]

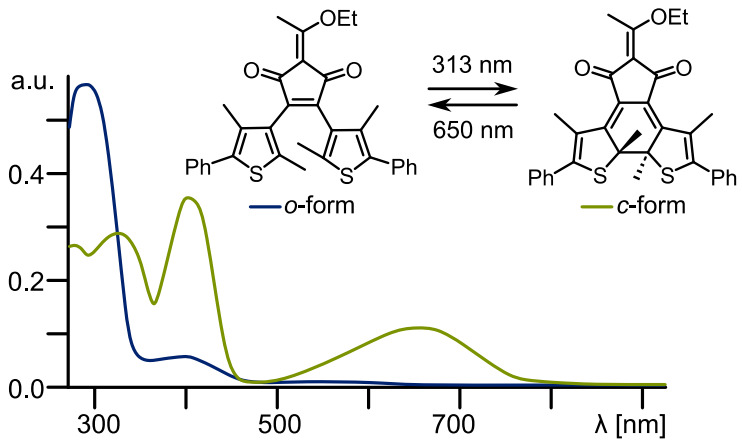

Figure 7. UV-vis absorption spectra of a dithienylethene (DTE) scaffold in its open (*o*) and closed (*c*) form in acetonitrile. Spectra plotted from data reported by You and co-workers.[79]

Despite the described advantages, some challenges remain. For most DTE derivatives, the *o*→*c* photocyclisation requires high-energy UV light, which can promote side reactions that limit practical applications.[78] To address this, extensive synthetic strategies have focused on red-shifting the excitation wavelengths into the visible region by extending conjugation on the thiophene rings, modifying the central ethene bridge, or introducing electron-donating or withdrawing substituents.[84,85] While such structural modifications can enable visible-light responsiveness, they may also reduce quantum yields or compromise switching behaviour if the electronic balance of the switching core is perturbed.[82] Thus, developing DTEs that combine reliable bistability with efficient, fully visible-light responsiveness remains an important and active area of research.

2.2 Light responsive complexes

Molecular systems capable of undergoing light-induced structural transformations have attracted considerable research interest due to their wide range of applications, from smart materials[86,87] to photopharmacology.[88,89] Coupling photoswitches, such as those introduced in Section 2.1, to metal ions provides a means of developing such light-responsive molecular systems.[18] This section focuses, in particular, on mononuclear metal complexes bearing photochromic ligands that switch between two states under light irradiation, although the reversibility of this process varies between systems.

Incorporating a metal centre into the molecular framework of light-responsive systems significantly broadens the design space.[90] Metal ions bring defined coordination preferences and geometries that complement and extend those of purely organic switches. Factors such as the preferred coordination number, ligand denticity, and the geometric constraints imposed by chelating ligands (e.g., bite angle) provide versatile design parameters for tailoring molecular architecture and light-responsive behaviour.[19] Furthermore, metal ions can influence the electronic properties of coordinated ligands, often affecting their absorption characteristics and switching behaviour.[91,92]

Nonetheless, the intrinsic photoresponsive properties of the ligands are not always preserved upon coordination. Metal binding can perturb the electronic environment around the switching unit, i.e. the N=N bond in azo systems, leading to altered UV-vis absorption profiles, shifts in the relative stability of isomeric states, and changes in thermal relaxation kinetics.[20] In some cases, coordination can even inhibit switching altogether.[21] A clear understanding of these effects is essential for designing metal-photoswitch systems that retain functional responsiveness and enable reliable light-induced control within molecular architectures.

In 2021, Bogliotti and co-workers reported the synthesis of arene Ru(II) complexes based on 2,2′-azobispyridine (Scheme 6), a photochromic ligand structurally related to azobenzene (Section 2.1.1).[93] As with azobenzene, the free ligand can adopt either the thermodynamically stable *E* or the metastable *Z*-configuration and undergo reversible *E/Z* isomerisation upon UV light irradiation. Using column chromatography, the authors were able to separate both ligand isomers, obtaining 60% of the *E*-form and 40% of the *Z*-form, the latter of which was remarkably stable in the dark for several months when stored below 4 °C.

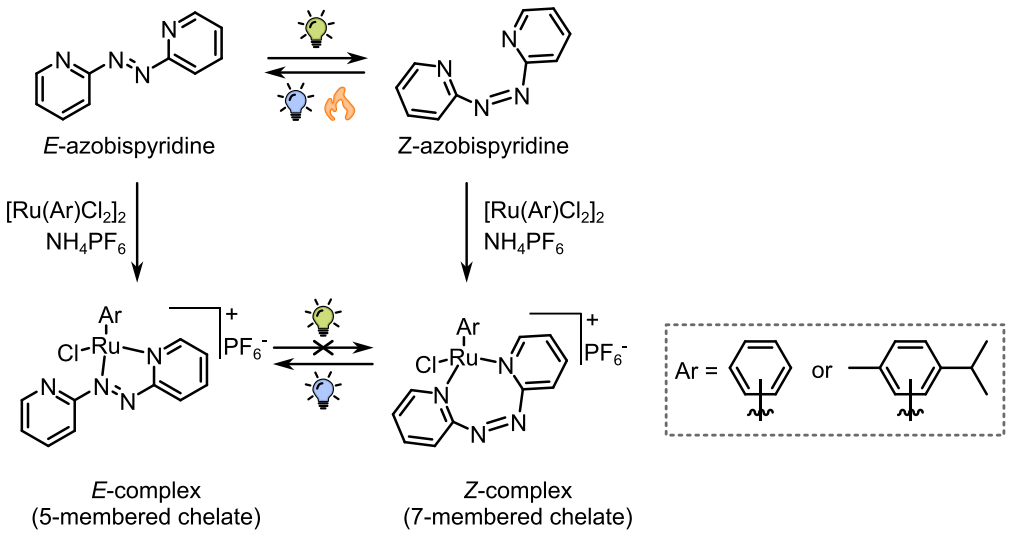

Scheme 6. Top: structure of 2,2′-azobispyridine in its ground state (*E*-azobispyridine) and its metastable state (*Z*-azobispyridine). Bottom: irreversible light induced isomerisation of *Z*-configured 7-membered chelate Ru(II) complexes into *E*-configured 5-membered chelate complexes.[93]

Complexation was achieved by reacting the isolated ligand isomers in methanol with the Ru(II) dimer precursors $[Ru(Ar)Cl_2]_2$ (Ar = benzene or *para*-cymene), followed by counterion exchange with NH_4PF_6. Crucially, the isomeric state of the ligand was preserved during complex formation: *E*-azobispyridine produced the *E*-complex, while *Z*-azobispyridine yielded the *Z*-complex (Scheme 6). Structural analysis revealed that the *E*-complex forms a five-membered chelate ring in which one nitrogen atom from the azo bridge coordinates to the Ru(II) metal centre. In contrast, the *Z*-complex forms an unprecedented seven-membered chelate ring in which the azo bridge is not involved in coordination.

The light response of these complexes, however, differed from that of the free ligand. UV light irradiation of the *Z*-complex induced irreversible *Z*→*E* isomerisation, accompanied by reorganisation of the coordination mode to generate the thermodynamically favoured five-membered chelate ring (Scheme 6). In contrast, irradiation of the *E*-complex produced no detectable *E*→*Z* conversion. Thus, both complex isomers could be accessed synthetically, but light only enabled a one-way *Z*→*E* transformation. Furthermore, thermal studies of the *Z*-complex at room temperature and in the dark showed that no isomerisation occurred over several weeks. Similarly, heating the *Z*-complex to 60 °C for 24 h did not induce any detectable isomerisation, demonstrating that thermal *Z*→*E* relaxation does not occur under the conditions tested. Consequently, the authors defined the *Z*-complex as being kinetically trapped under thermal conditions.

Together, these findings emphasise the crucial impact of metal coordination on the photoswitching behaviour. While the free 2,2′-azobispyridine ligand undergoes reversible photoisomerisation, binding to Ru(II) fundamentally alters this process, enforcing a one-way, irreversible *Z*→*E* transformation. This example demonstrates how coordination to a metal can prevent the usual bidirectional switching and instead impose unidirectional switching behaviour.

The above case study illustrates how metal coordination can strongly affect switching, however; the ligand framework itself can also play a decisive role in shaping the photoresponse of the resulting complexes. In 2023, Bogliotti and co-workers reported a series of sulfonamide azobenzene ligands bearing alkyl substituents of increasing steric bulk at the *ortho* position of the N=N bond, and their corresponding Ru(II) complexes (Scheme 7).[94] This study revealed how subtle variations in ligand substitution can strongly influence the photoisomerisation behaviour and stability of the resulting complexes.

Complexation of the monosubstituted ligands afforded Ru(II) complexes in the *E*-configuration, in which the azo bond adopted an exocyclic arrangement (Scheme 7). These complexes underwent *E*→*Z* isomerisation under visible light irradiation, followed by *Z*→*E* thermal relaxation in the dark at room temperature. Notably, the half-lives of the Ru(II) *Z*-complexes were significantly shorter, ranging from 22 to 63 min, than those of the corresponding free *Z*-ligands (between 4.1 and 59 h) in dichloromethane.

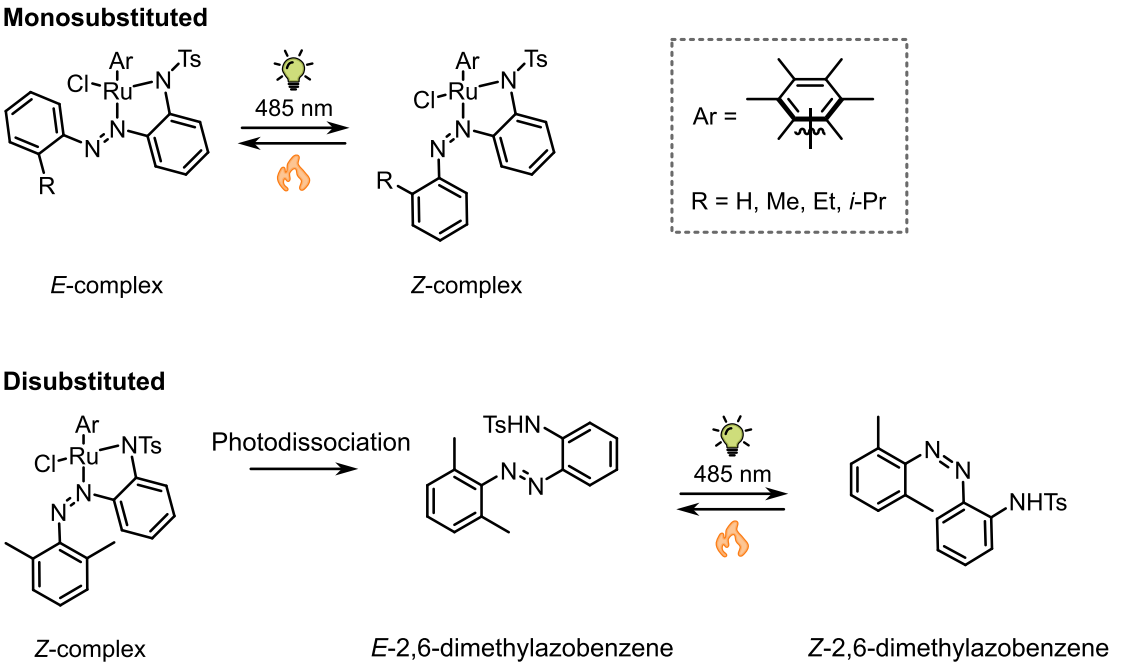

Scheme 7. Structure overview and photoisomerisation behaviour of the monosubstituted and disubstituted azobenzene Ru(II) complexes studied by Bogliotti and co-workers.[94] The disubstituted *Z*-complex undergoes photodissociation under 485 nm light irradiation.

Building on the monosubstituted system, the authors also examined a disubstituted ligand, namely 2,6-dimethylazobenzene, to assess the impact of enhanced steric bulk at both *ortho* positions (Scheme 7). Its Ru(II) complex was crystallographically characterised in the *Z*-configuration, despite its free ligand favouring the *E*-isomer in solution. Upon visible-light irradiation, the *Z*-complex did not undergo *Z*→*E* isomerisation, but instead underwent irreversible dissociation of the coordinated azobenzene ligand, observed in the *E*-configuration (Scheme 7).

The dissociation process of the disubstituted 2,6-dimethylazobenzene Ru(II) complex was found to be solvent-dependent. Under visible-light irradiation in acetonitrile, dichloromethane, or chloroform, the complex underwent irreversible photodissociation of the azobenzene ligand. On the other hand, in toluene, a non-polar solvent, the 2,6-dimethylazobenzene Ru(II) complex showed no photodissociation under visible-light irradiation and retained the *Z*-configuration. Unfortunately, the thermal relaxation of this *Z*-complex was not investigated.

These results demonstrate that the presence of substituents *ortho* to the N=N bond, together with the solvent environment, significantly impacts the photoresponse and stability of Ru(II)-photoswitch complexes. Monosubstituted azobenzene complexes underwent light-induced *E*→*Z* isomerisation, followed by thermal *Z*→*E* relaxation. In contrast, introducing steric hindrance at both *ortho* positions enforced a *Z*-configured complex that only underwent irreversible ligand dissociation in polar solvents.

Although the above examples focus on Ru(II) complexes, light-responsive behaviour is not limited to this metal centre. For example, Pd(II) can also form photoswitchable complexes with azo-based ligands.[21] Furthermore, not all systems yield exclusively *E*- or *Z*-configured complexes; in some cases, distinct *E*- and *Z*-complexes can coexist in solution. In these systems, the *E/Z* ratio can be tuned photochemically, with the PSS depending on the irradiation wavelength used.[95]

In 2010, Han and co-workers reported a mononuclear Pd(II) complex with *ortho*-diethylated azobenzene ligands (Scheme 8).[95] In the solid state, X-ray diffraction confirmed a square-planar Pd(II) centre coordinated to two chloride ligands and two monodentate *E* azobenzene-based ligands, each binding through one azo nitrogen atom. In solution, however, both *E*- and *Z*-configured complexes were present, with their relative abundances dependent on the irradiation wavelength. Irradiation with UV light (365 nm) yielded a PSS of approximately 40:60 (*E*:*Z*), while visible light (436 nm) reversed the distribution to 60:40 (*E*:*Z*). Importantly, no photodegradation was detected over five consecutive switching cycles.

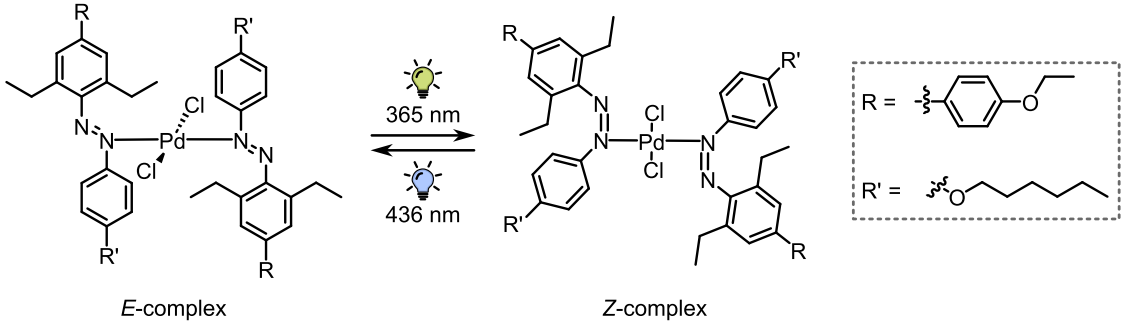

Scheme 8. Structure overview and photoisomerisation behaviour of the Pd(II) complexes studied by Han and co-workers.[95] Irradiation with 365 nm induces *Z*→*E* isomerisation yielding 60% of the *Z*-complex. Irradiation with 436 nm induces *E*→*Z* isomerisation affording 60% of the *E*-complex.

The thermal back-isomerisation ($Z \rightarrow E$) of the UV-exposed Pd(II) complex was monitored by ^{1}H NMR spectroscopy in the dark at ambient temperature. However, gradual dissociation of the Pd(II) complex released free azobenzene ligand, detected already after one day and increasing to 67% after 32 days.

This system illustrates two key properties of photoswitchable metal complexes. Firstly, it exemplifies that both *E*- and *Z*-complexes can coexist in solution, with their ratios precisely and reversibly regulated through wavelength-dependent irradiation. Secondly, it reveals that while such systems offer reversible switching, their long-term stability may be limited by ligand dissociation, highlighting a potential constraint in the design of durable photoswitchable systems.

Altogether, these examples of mononuclear photoswitchable complexes illustrate how metal coordination can dictate not only the isomerisation pathway, whether reversible or unidirectional, but also the stabilised isomeric form of the resulting complex. The ligand substitution pattern and the solvent environment can also influence the photoresponse, demonstrating that the photoswitch plays a direct role in modulating the light-induced switching behaviour of the metal complex. These principles can be extended beyond discrete mononuclear complexes to multinuclear architectures, in which various ligands and metals are combined to form more complex, light-responsive systems. How such assemblies are formed will be the focus of the next chapter.

2.3 Self-assembly

The ability to construct large, topologically complex molecular architectures is essential for advancing the design of adaptive, stimuli-responsive molecular systems. Accessing these architectures via conventional covalent synthesis is often challenging and usually involves multistep routes, protection and deprotection strategies, and precise control of functional group compatibility. On the contrary, self-assembly is a complementary strategy: instead of building architectures step by step, simple building blocks can spontaneously organise to form ordered structures (Scheme 9).[6]

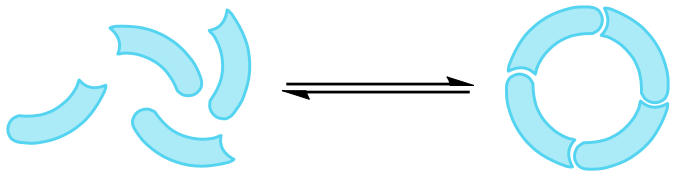

Scheme 9. Representation of a self-assembly process wherein curved building blocks bearing complementary recognition sites organise into a discrete macrocyclic architecture.

Self-assembly refers to the spontaneous organisation of molecular subunits into larger, well-defined architectures through reversible, non-covalent interactions, which are often complemented by metal-ligand coordination.[2] In supramolecular chemistry, self-assembly specifically describes the formation of structures in which molecules or ions are held together by forces such as hydrogen bonding, π-π stacking, electrostatic interactions, halogen bonding, and coordination bonds.[96] While these interactions are individually much weaker than covalent bonds, their cooperative effects provide sufficient stability to generate discrete, highly ordered structures.[97] The geometric complementarity of the building blocks, together with the binding preferences of their functional groups, guides the components towards specific architectures rather than forming ill-defined aggregates.[98]

A defining feature of self-assembly is its reversibility. During the assembly process, dynamic bond exchange allows misbound components to dissociate and re-coordinate into lower-energy configurations.[7] Defects are thus corrected, allowing the ensemble to relax towards the most stable structure available under the given conditions. This intrinsic capacity for error correction is one of the main reasons why self-assembly is such a

powerful strategy for constructing elaborate architectures with comparatively little synthetic effort. Not only is reversibility essential for error correction, it is also crucial for guiding the system towards its thermodynamically most stable state.[6]

The driving force for self-assembly is described by the free energy relation $\Delta G = \Delta H - T\Delta S$, which relates the change in Gibbs free energy (ΔG) to the change in enthalpy (ΔH), temperature (T), and the change in entropy (ΔS).[6] Enthalpic contributions arise from the formation of multiple non-covalent and coordination interactions, which together stabilise the final assembly.[99] An additional enthalpy gain arises from the chelate effect, whereby multidentate ligands increase the stability of the complexes formed.[100] By contrast, entropy is often unfavourable, since combining several free components into one assembly reduces their overall translational and rotational freedom.[101] Nevertheless, entropy can sometimes favour self-assembly – for example, when solvent molecules or counterions are released upon ligand coordination to metals.[102] Other effects can also promote assembly. For instance, the hydrophobic effect drives nonpolar groups to cluster in aqueous media, reducing the number of ordered water molecules and thereby increasing the entropy of the system.[103,104]

The resulting supramolecular structures are strongly influenced by the experimental conditions, particularly the polarity of the solvent used. Polar solvents, such as water or methanol, compete with the building blocks for hydrogen bonding sites, thereby disrupting the non-covalent interactions. In contrast, non-polar solvents, such as hexane, do not interfere with hydrogen bonding, allowing these interactions to persist and form stable assemblies.[105]

Beyond solvent effects, other experimental parameters can also critically shape the outcome of the self-assembly. Temperature modulates the delicate balance between enthalpy and entropy, as described by the Gibbs free energy equation ($\Delta G = \Delta H - T\Delta S$).[106] At low temperatures, enthalpic interactions dominate, favouring the formation of ordered structures that are thermodynamically stable under those conditions. Whereas at elevated temperatures, the entropic contribution becomes more significant,[107] and depending on the system, this can either disrupt existing assemblies or promote reorganisation into less ordered, entropically favoured structures by overcoming kinetic barriers.[108]

Concentration also plays a crucial role, influencing both the rate of formation and the thermodynamic favourability of assembly.[109] From a kinetic perspective, higher concentrations statistically increase the likelihood of building blocks colliding and assembling, thereby accelerating the rate at which discrete components associate into larger, organised architectures. Thermodynamically, concentration influences the entropy term (ΔS). At low concentrations, below the critical self-assembly concentration (defined as the minimum concentration required for spontaneous assembly), the entropic cost of organisation is less easily compensated by enthalpic gains. This often favours smaller, discrete assemblies or can even prevent formation altogether.[110]

Amongst the various classes of supramolecular self-assembly, coordination-driven self-assembly is of particular relevance to this thesis. In such systems, metal ions and organic ligands spontaneously organise into well-defined supramolecular architectures through directional metal-ligand coordination bonds.[111,112] These resulting assemblies combine the structural rigidity of the metal's preferred coordination geometry and the geometric constraints of the ligand framework, while retaining the dynamic reversibility of ligand-exchange processes at the metal centre.[113] In addition to the solvent, temperature, and concentration effects outlined above, the equilibrium distribution between possible coordination-driven architectures is also strongly influenced by stoichiometry, the nature of the counter-ion, and the use of pre-organised templates.[114,115] These parameters can bias the assembly pathway by stabilising particular intermediates or preferentially lowering the free energy of certain products, thereby directing the system towards selected target topologies even when alternative structures are thermodynamically accessible.[116,117] Coordination-driven self-assembly thus provides a versatile platform for constructing structurally complex supramolecular architectures with high precision and tuneability.

As a whole, self-assembly is a versatile approach to building complex architectures. It offers rapid access to large structures from relatively simple components, and allows access to related assemblies through variation of the building blocks. Functionalisation of the building blocks enables responsiveness to external stimuli, such as light. The following chapter explores examples of coordination-driven self-assembly in the context of photoswitchable supramolecular cages.

2.4 Self-assembled photoswitchable metal-organic cages

Metal-organic cages are discrete, hollow architectures formed through the self-assembly of metal centres with multitopic ligands.[8] These structures, sometimes referred to as capsules, feature well-defined internal cavities capable of hosting and stabilising guest molecules.[22] Such host-guest interactions have enabled a wide range of applications including catalysis,[118,119] drug delivery,[120,121] and selective molecular separation.[122,123] Beyond their encapsulation capabilities, metal-organic cages are increasingly recognised as dynamic molecular platforms that can support mechanical motion,[108] modulate chemical behaviour,[124] and serve as modular building blocks for extended functional materials.[125]

To harness the full potential of these systems, introducing external stimuli — chemical,[10] electrochemical,[11] or photochemical[12,20] — offers an effective means of controlling their behaviour. As discussed in Section 2.1, light is a particularly versatile stimulus for *in-situ* manipulation.[13] When photoswitches, such as those introduced in Section 2.1, are incorporated into the ligands of metal-organic cages, light can regulate the ingress and egress of guest molecules, drive transformations between distinct cage architectures, and sustain assemblies away from equilibrium.[12,14,29] This section will therefore focus on light-responsive metal-organic cages.

In 2013, Clever and co-workers reported one of the emerging examples of light-reversible regulation of host-guest interactions in a cage system.[126] They synthesised a bis-monodentate pyridyl ligand (**L^1**) bearing a DTE photoswitch (introduced in Section 2.1.4) which can be reversibly interconverted between its flexible open form (*o*-**L^1**) and its rigid closed-ring isomer (*c*-**L^1**) upon irradiation with UV and white light, respectively. Self-assembly of *o*-**L^1** with Pd(II) afforded the open-form cage $[Pd_2(o\text{-}\mathbf{L^1})_4](BF_4)_4$ (*o*-**C**), while *c*-**L^1** yielded the closed-form cage $[Pd_2(c\text{-}\mathbf{L^1})_4](BF_4)_4$ (*c*-**C**) (Scheme 10). Irradiation with UV and white light also enables reversible interconversion between the two cage isomers, thereby directly transferring the photoresponsiveness of the ligand framework into the supramolecular assembly.

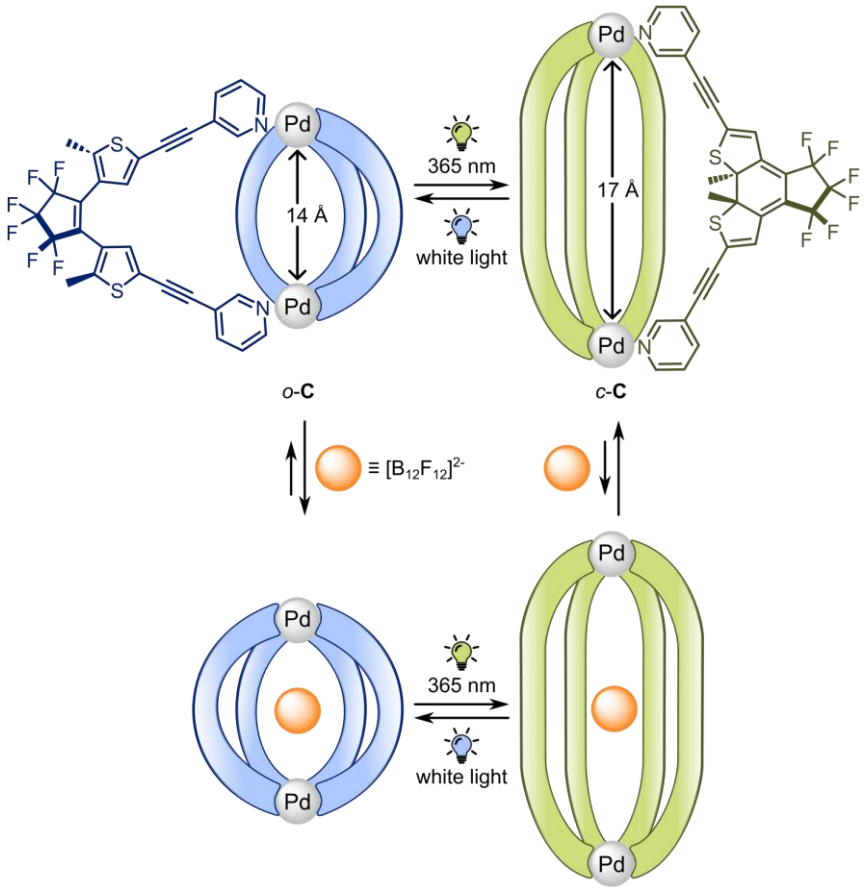

Scheme 10. Structure and photoisomerisation behaviour of the Pd(II) cages studied by Clever and co-workers.[126] Irradiation with 365 nm converts the open-form cage (*o*-**C**) to the closed-form cage (*c*-**C**); white light reverses the process, regardless of guest encapsulation.

Diffusion-ordered NMR spectroscopy (DOSY) confirmed that, although both *o*-$\mathbf{L^1}$ and *c*-$\mathbf{L^1}$ adopt an M_2L_4 composition, they differ in size due to the ring closure of the DTE units, with *o*-**C** being smaller than *c*-**C** (Scheme 10). This difference in cavity size prompted a study of their anion-binding behaviour. The dodecafluorododecaborate anion ($[B_{12}F_{12}]^{2-}$) was chosen as the guest molecule, and it was found that both cage isomers encapsulated this spherical anion, forming a 1:1 host-guest complex. However, titration experiments revealed that *o*-**C** binds the anion approximately two orders of magnitude more strongly than *c*-**C**. Nonetheless, photoswitching between the two cage isomers was not affected by the encapsulated guest (Scheme 10).

This study laid the foundation for light-responsive cages by showing that irradiation can be used to not only interconvert cage architectures, but also to modulate their binding properties. This is an essential step towards designing artificial host systems with programmable, light-driven functions.

Stimuli responsive metal-organic cages can not only interconvert between architectures of the same overall composition, but can also undergo substantial structural changes upon photoswitching. In 2022, Beves and co-workers reported a bis-monodentate quinoline ligand (**L²**) incorporating an *ortho*-tetrafluoroazobenzene photoswitch (introduced in Section 2.1.1).[127] This ligand undergoes reversible *E/Z* isomerisation under visible-light irradiation; however, complete conversion to a single isomer cannot be achieved in solution (405 nm = 80% *E*-**L²** and 617 nm = 90% *Z*-**L²**). In the *E*-configuration, the coordination vectors are almost parallel, while in the *Z* state they diverge to form an angle approaching 180º, which significantly influences the type of assembly formed (Scheme 11).

Upon coordination of predominantly *E*-**L²** with Pd(II), a single isomeric cage was obtained: Pd_2(*E*-**L²**)$_4$. Metal coordination therefore imposed a strong structural preference, stabilising the lantern-shaped M_2L_4 assembly. Nonetheless, coordination did not suppress photoswitching. Irradiation of Pd_2(*E*-**L²**)$_4$ with green light induced *E*→*Z* isomerisation, yielding a mononuclear Pd(II) complex: Pd(*Z*-**L²**)$_2$ (Scheme 11). This example illustrates how a change in ligand geometry upon isomerisation can transform a defined cage into discrete mononuclear complexes.

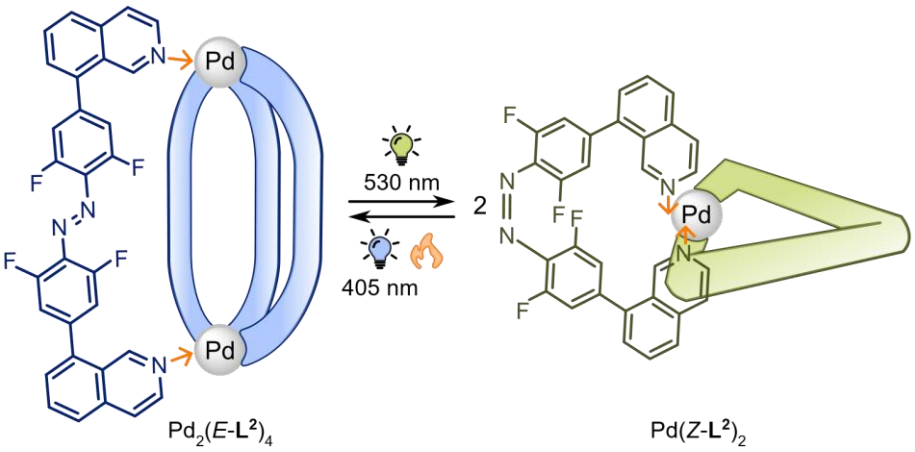

Scheme 11. Structure and photoisomerisation behaviour of the Pd(II) assemblies studied by Beves and co-workers.[127] Irradiation with 530 nm light induces *E*→*Z* isomerisation; 405 nm light or thermal relaxation reverses the process. The arrows highlight the ligand's bite angle which dictates whether a lantern-shaped cage or mononuclear complex is formed.

A further notable feature of this system is the enhanced thermal stability of the metastable *Z*-isomer upon coordination. Whereas the free *Z*-**L²** undergoes thermal *Z*→*E* isomerisation with a half-life of 40 days at room temperature, the corresponding Pd(*Z*-**L²**)$_2$ complex has a thermal half-life of 850 days. This shows that, in this case, metal coordination improves both the PSS distribution and the stability of the metastable isomer, rather than limiting its photoresponsiveness.

Interconverting between two discrete architectures upon light exposure, as shown in the previous examples, is not always possible. In some systems, irradiation instead enables the reversible transformation of ill-defined species into a single defined cage. In 2022, Clever, Herges, and co-workers reported the first coordination-driven cage embedding a diazocine photoswitch (introduced in Section 2.1.3).[128] They synthesised a bis-pyridyl diazocine-based ligand (**L³**) that adopts a thermodynamically stable *Z*-configuration (*Z*-**L³**), which can be switched to the metastable *E*-form (*E*-**L³**) under UV light irradiation (385 nm). Exposure to green light (530 nm) or thermal relaxation induces the reverse *E*→*Z* isomerisation.

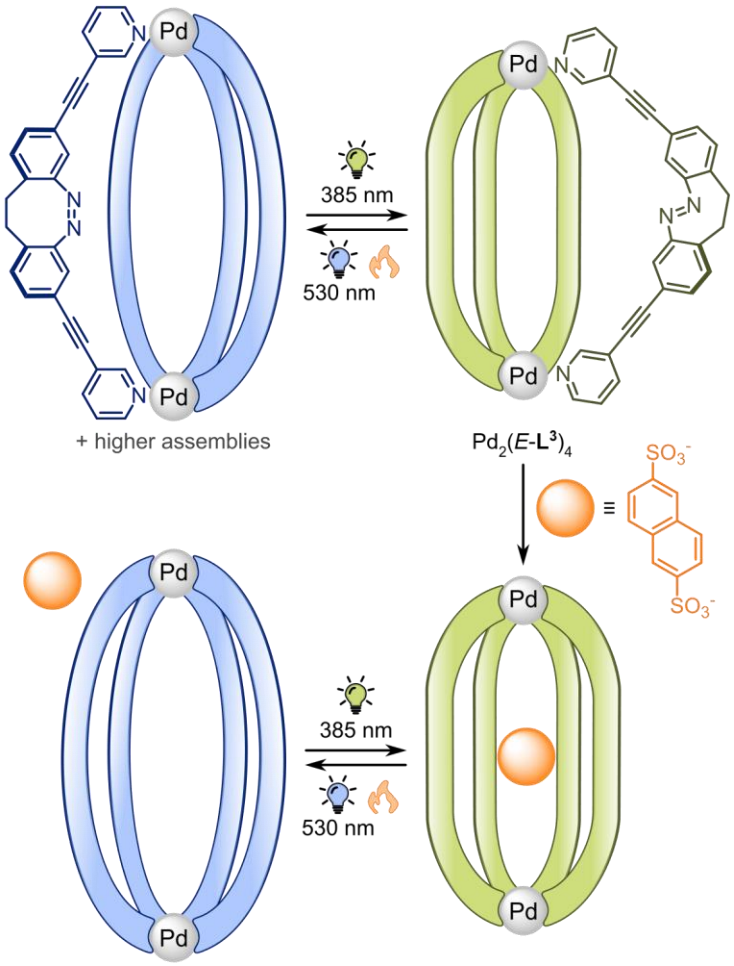

Scheme 12. Structure and photoisomerisation behaviour of the Pd(II) cages studied by Clever, Herges, and co-workers.[128] Irradiation with 385 nm light induces *Z*→*E* isomerisation; 530 nm light or thermal relaxation reverses the process. Guest uptake and release was controlled by light irradiation and thermal relaxation.

The self-assembly of *Z*-**L**^{3} with Pd(II) produced a mixture of species of varying nuclearity, formulated as $Pd_n(Z\text{-}\mathbf{L}^3)_{2n}$ (n = 2,3, …). Structural strain within the ligand framework hinders the exclusive formation of a single, well-defined architecture, resulting instead in a distribution of assemblies. By contrast, the coordination of the metastable *E*-**L**^{3} yielded a single lantern-shaped cage, $Pd_2(E\text{-}\mathbf{L}^3)_4$ (Scheme 12). Nonetheless, this discrete assembly only persists under continuous UV irradiation; upon removal of the stimulus, thermal relaxation ($\tau_{½}$ = 6.1 h, 298 K) or irradiation with 530 nm light regenerates the ill-defined mixture. The system can be cycled reversibly over twenty times without any detectable photodegradation, which highlights the robustness of the diazocine motif within a self-assembled structure. Moreover, free *E*-**L**^{3} and the $Pd_2(E\text{-}\mathbf{L}^3)_4$ cage exhibit similar thermal half-lives, suggesting that the switching behaviour of *E*-**L**^{3} is largely retained upon coordination.

A further feature of this system was revealed through host-guest studies. The lantern cage $Pd_2(E\text{-}\mathbf{L^3})_4$ was shown to encapsulate one bis-anionic 2,6-naphthalene bissulfonate guest molecule in a 1:1 complex, whereas the *Z*-assemblies do not support encapsulation. Therefore, guest uptake is restricted to the *E*-cage, with light-driven interconversion providing reversible control over the ingress and egress of the guest molecule. Similarly, thermal relaxation results in guest release, underscoring the direct link between photoswitching and the cage's guest binding behaviour.

This study demonstrated that photoswitching can be harnessed to not only switch between distinct, well-defined cages, but also to interconvert between an ill-defined mixture and a single discrete architecture. Furthermore, the diazocine moiety preserves its full photoswitching properties upon coordination, showing that photoswitches can retain their intrinsic function within self-assembled architectures.

All of the systems discussed so far were based on Pd(II); however, light-responsive assemblies can also be constructed using other metals. Additionally, while different types of photoswitches have been employed to induce substantial changes in assembly outcome, alterations in ligand substitution pattern can be equally decisive. In 2023, McConnell, Herges, and co-workers reported two regioisomeric bis-bidentate ligands ($\mathbf{L^4}$ and $\mathbf{L^5}$) embedding a diazocine photoswitch.[9] Each ligand contains two 2-pyridyl-triazole coordination sites linked by a diazocine backbone, however, they differ in their point of attachment. In $\mathbf{L^4}$, the triazole-pyridyl units are connected at the *para* position relative to the N=N azo bridge, whereas in $\mathbf{L^5}$ they are attached at the *meta* position. As expected for diazocines, both ligands undergo reversible *Z/E* isomerisation: the thermodynamically stable *Z*-isomer converts to the metastable *E*-form upon irradiation with UV light (385 nm), and the reverse process occurs under green light (520 nm) or upon thermal relaxation.

The self-assembly behaviour with Co(II) depends on both the substitution pattern and the photoisomeric state. In the *Z*-configuration, only $\mathbf{L^4}$ formed a well-defined M_2L_3 helicate, $Co_2(Z\text{-}\mathbf{L^4})_3$, whereas $Z\text{-}\mathbf{L^5}$ afforded ill-defined species. Upon $Z \rightarrow E$ photoisomerisation, however, the situation is reversed: $E\text{-}\mathbf{L^5}$ assembled into the corresponding helicate $Co_2(E\text{-}\mathbf{L^5})_3$, while $E\text{-}\mathbf{L^4}$ produced a mixture of undefined assemblies. The *E*-helicate is only metastable and reverts back upon thermal relaxation, whereas $Co_2(Z\text{-}\mathbf{L^4})_3$ remains

thermodynamically stable. Photoswitching between the helicate and the ill-defined mixtures is fully reversible for both ligands and occurs without photodegradation over twenty cycles.

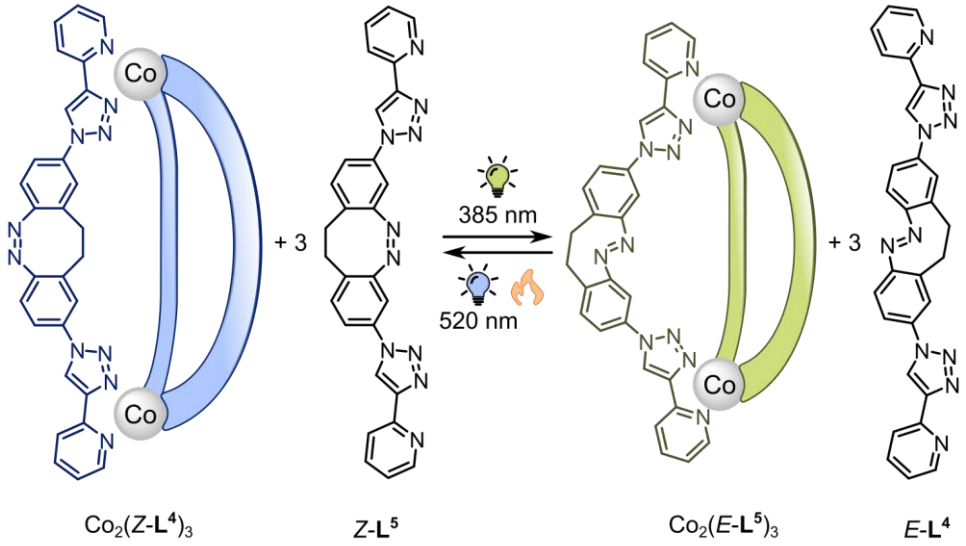

Scheme 13. Structure and photoisomerisation behaviour of the Co(II) cages studied by McConnell, Herges, and co-workers.[9] The $Co_2(Z\text{-}\mathbf{L^4})_2$ helicate disassembles under UV light while $Co_2(E\text{-}\mathbf{L^5})_2$ is formed; green light and thermal relaxation reverse the process.

When both regioisomers were present in solution, light irradiation selectively determined which ligand participated in the helicate formation. Under green light, the stable *Z*-isomer predominated, leading to $Co_2(Z\text{-}\mathbf{L^4})_3$ formation alongside uncoordinated *Z*-$\mathbf{L^5}$. Upon UV light irradiation, *Z*→*E* isomerisation triggered the formation of $Co_2(E\text{-}\mathbf{L^5})_3$, with *E*-$\mathbf{L^4}$ remaining uncoordinated (Scheme 13). Thus, light enables the selective and reversible exchange of helicates derived from the two regioisomers.

This study emphasises the pivotal role of substitution patterns in determining the coordination vectors of diazocine-based ligands and consequently, the supramolecular architectures formed. Both *para* and *meta* substitution lead to orthogonal assembly preferences, enabling light to switch between not only assembled and non-assembled states, but also between helicates derived from different regioisomers.

2.5 From equilibrium to out-of-equilibrium systems

Most of the supramolecular assemblies described so far operate under thermodynamic control, where the system explores possible configurations and ultimately adopts the most stable, lowest free-energy structure.[24] These systems are referred to as equilibrium systems, in which the final assembly corresponds to the thermodynamic minimum under the given conditions. Once formed, the assembly remains stable unless the free energy landscape is perturbed; for instance, changes in temperature can alter the preferred assembly outcome (see Section 2.3).[129] Thermodynamic assembly under equilibrium conditions has thereby enabled the construction of many well-defined supramolecular architectures, including some examples described in Section 2.4 by Beves and Clever.[126,127]

In contrast, out-of-equilibrium systems do not reside at the global free-energy minimum but instead rely on continuous energy input to maintain a dynamic state.[25] If this energy supply is removed, the system returns to equilibrium.[26] Operating away from equilibrium introduces additional complexity, allowing new behaviours to emerge that cannot be achieved under equilibrium conditions, i.e. directional motion.[130]

Driving a system out of equilibrium requires a continuous supply of energy, which can be provided by external stimuli.[131] As discussed in Section 2.1, light is a particularly advantageous stimulus that can be applied with high spatial and temporal precision. In some cases, light irradiation can drive a system away from equilibrium and prevent it from returning to the thermodynamic minimum, thereby enabling new structural transformations and functional responses.[27] While various classes of out-of-equilibrium supramolecular systems have been studied, the following section focuses on an important concept in this thesis: the molecular ratchet, a system capable of biasing molecular motion to achieve directed, non-equilibrium behaviour.[28,132]

2.6 Molecular ratchets

Building on the principles of energy-driven assembly, see Section 2.5, molecular ratchets represent a class of out-of-equilibrium systems that achieve meta-stable states by coupling energy-releasing and energy-consuming reactions.[28] At the heart of this mechanism lies a fundamental distinction: exergonic reactions, which release free energy and proceed spontaneously, and endergonic reactions, which require energy input and are non-spontaneous.[132] When these reactions are embedded within the same chemical network, the energy liberated by the exergonic step can be channelled into driving the endergonic one, enabling the system to perform work and sustain non-equilibrium behaviour.[133]

Molecular ratchets exploit this coupling by integrating exergonic and endergonic steps within a single, unified reaction network. Crucially, these processes are chemically linked so that the energy dissipated during the driving step can be harnessed to promote the otherwise unfavourable driven step.[133] Through this coupling, molecular ratchets can access reaction pathways and structural outcomes that would otherwise remain thermodynamically inaccessible under equilibrium conditions.[134]

This ratcheting mechanism can be illustrated (Scheme 14) by considering two states: A, a low-energy state, and B, a high-energy state. The direct A→B conversion is endergonic and therefore does not occur spontaneously. However, if the reaction network provides an alternative pathway from A to B that includes an exergonic driving step, the overall transformation can proceed. This constitutes a chemical reaction cycle incorporating both the driving and the driven processes. When such a cycle exhibits a directional bias, progressing preferentially in one direction rather than shifting randomly, it defines a ratchet mechanism. It is this directional bias that enables molecular ratchets to maintain non-equilibrium behaviour and, in some cases, perform work.[132]

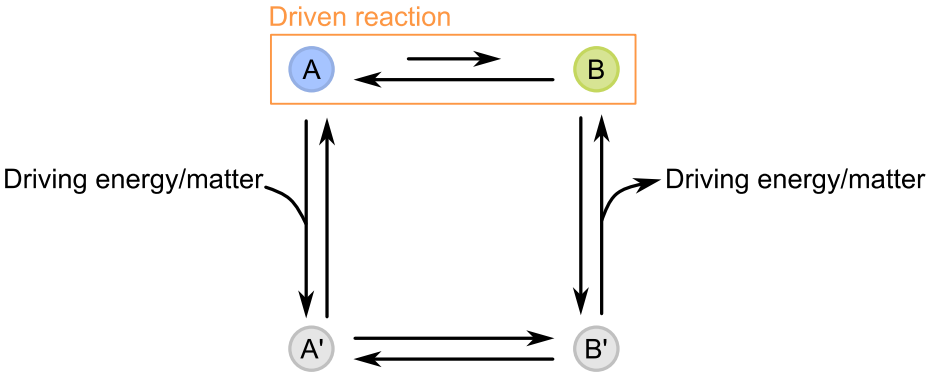

Scheme 14. Illustration of a chemical reaction cycle in which a lower-energy species (A) is converted into a higher-energy form (B), maintaining the system in a non-equilibrium state through continuous energy input. Vertical arrows denote generic fluxes of energy and matter entering or leaving the system. This cycle is intended as a general representation of a chemical reaction network and does not specifically depict and energy ratchet or information ratchet.

Molecular ratchets can be powered by various energy sources, including chemical fuels,[135] redox reactions,[136] and light.[28,29] This thesis will focus on light-driven ratchets, which harness light to drive structural changes that push the system away from equilibrium. As introduced in Sections 2.1, 2.2, and 2.4, photoswitches and photoswitchable cages provide versatile platforms to exploit light-induced isomerisation processes. Upon absorption of photons, photoswitches undergo conformational changes that temporarily shift the system from its equilibrium state. The energy involved in these photoinduced transformations can be coupled to other reactions within the network, allowing light-driven molecular ratchets to channel light energy into driving directional ratchets and sustaining non-equilibrium behaviour.[132] Irrespective of the energy source, two main classes of ratchet mechanisms are commonly distinguished: energy ratchets and information ratchets.

2.6.1 Energy ratchets

Energy ratchets represent one of the two principal mechanisms by which directional bias within a reaction cycle can be achieved. They operate by exploiting changes in external conditions, such as light, to temporarily alter the population distribution between existing states (e.g. A and B; see Scheme 15), without affecting the underlying equilibrium between them (i.e. A⇌B remains unchanged).[29] These external changes enable access to an alternative pathway (e.g. A'⇌B'; see Scheme 15), where the forward and reverse

reaction from the alternative pathway (A'⇌B') is different, creating conditions under which the system is more likely to proceed in one direction rather than fluctuate randomly. After an initial energy input alters the reaction landscape, the energy ratchet guides the system through a sequence of thermodynamically downhill steps.[28] For a successful energy ratchet, where a metastable state can actually be observed, the reverse reaction B→A must be slower than the forward sequence A→A'→B'→B. This results in a biased cycle that accumulates metastable states.

In 2022, Feringa, Kathan, and co-workers reported a light-driven system exemplifying this principle.[137] Azobenzene dialdehydes were combined with triamines to form a triply-stranded dynamic covalent cage via reversible imine condensation (Scheme 15). With the azobenzene unit in its *E*-configuration, the cage is highly stable and is referred to as the *E*-cage. Upon irradiation with UV light, the azobenzene units undergo *E*→*Z* isomerisation, introducing strain to the cage and thus forming the less stable *Z*-cage. To relieve this strain, the *Z*-cage undergoes imine exchange with added monoamines, opening the structure. Subsequent visible light irradiation of the open *Z*-cage switches the azobenzene units back to the *E*-form, yielding a high-energy open *E*-cage. Over time, this kinetically trapped open *E*-cage relaxes to its thermodynamic minimum, displacing the monoamine and regenerating the stable *E*-cage.

This sequence of light-induced switching, exchange, and thermal relaxation constitutes a full cycle, whereby light energy is converted into chemical energy. The system repeatedly departs from equilibrium, accumulating metastable intermediates that would not form under thermodynamic control alone. In this context, the cage functions as an energy ratchet, with directionality arising from stepwise irradiation with different wavelengths, rather than from the network's inherent structure. The cycle harnesses the A' to B' (Scheme 15) directionality maintaining the system in a non-equilibrium regime and enabling controlled, directional transformation.

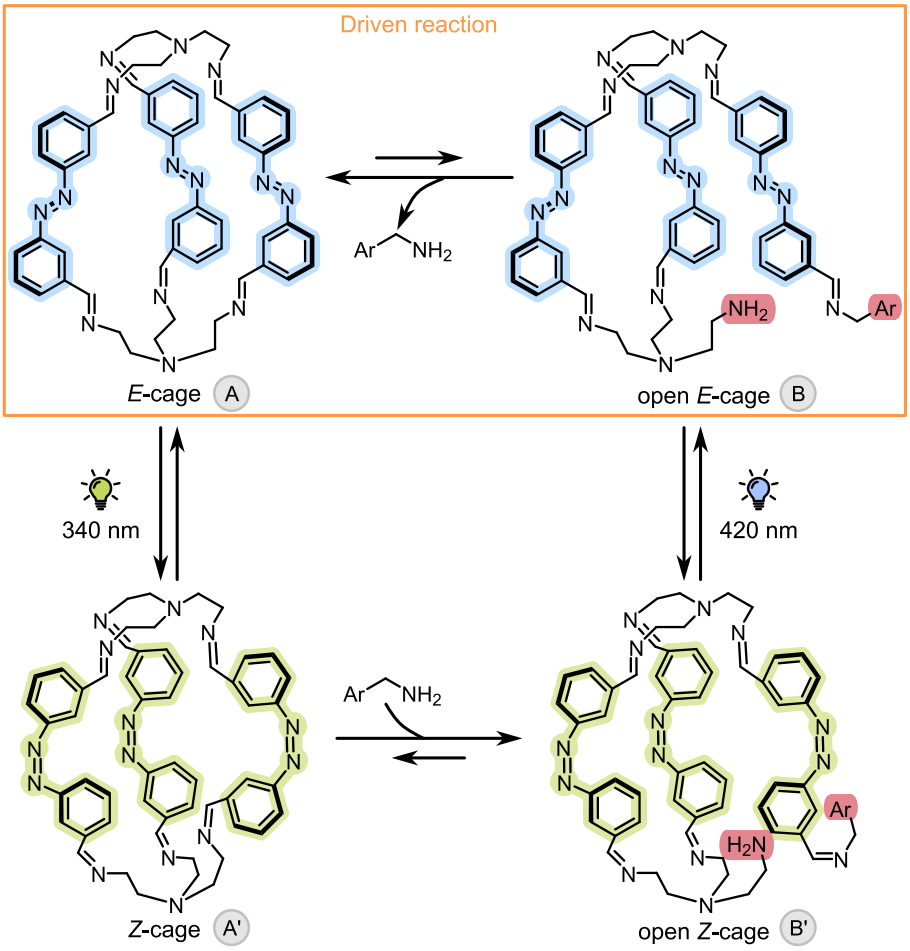

Scheme 15. Feringa's light-driven energy ratchet reaction network illustrates the interconversion between *E*- and *Z*-configured cages and their open forms.[137] The highlighted driven step represents where light energy directs the system away from equilibrium via azobenzene isomerisation coupled with imine exchange.

2.6.2 Information ratchets

Information ratchets represent another principial mechanism by which directional bias within a reaction cycle can be achieved. Unlike energy ratchets, where directionality is typically governed by the thermodynamics of the A'→B' transformation (Scheme 15), information ratchets operate under steady-state conditions, with directionality arising from kinetic control.[130] Their bias stems from kinetic asymmetry – where the forward (A→A') and backward (B→B') steps in a reaction cycle proceed at different rates – favouring moment in one direction (Scheme 16). This built-in preference allows the system to move directionally through a repeating sequence of molecular transformations without requiring changes to the external conditions.[138]

In 2006 Tamaoki and co-workers reported an illustrative example of an information ratchet based on a photoactive bicyclic azobenzene system.[139] The molecule incorporates two azobenzene switches (see Section 2.1.1) arranged within a chiral framework (Scheme 16). In the *E*-configuration, the structure is rigid and enantiomerisation between its *R* and *S* forms is negligible. However, when both azobenzene units adopt the *Z*-configuration, conformational flexibility increases and racemisation becomes possible, creating a dynamic network that interconverts the two enantiomers.

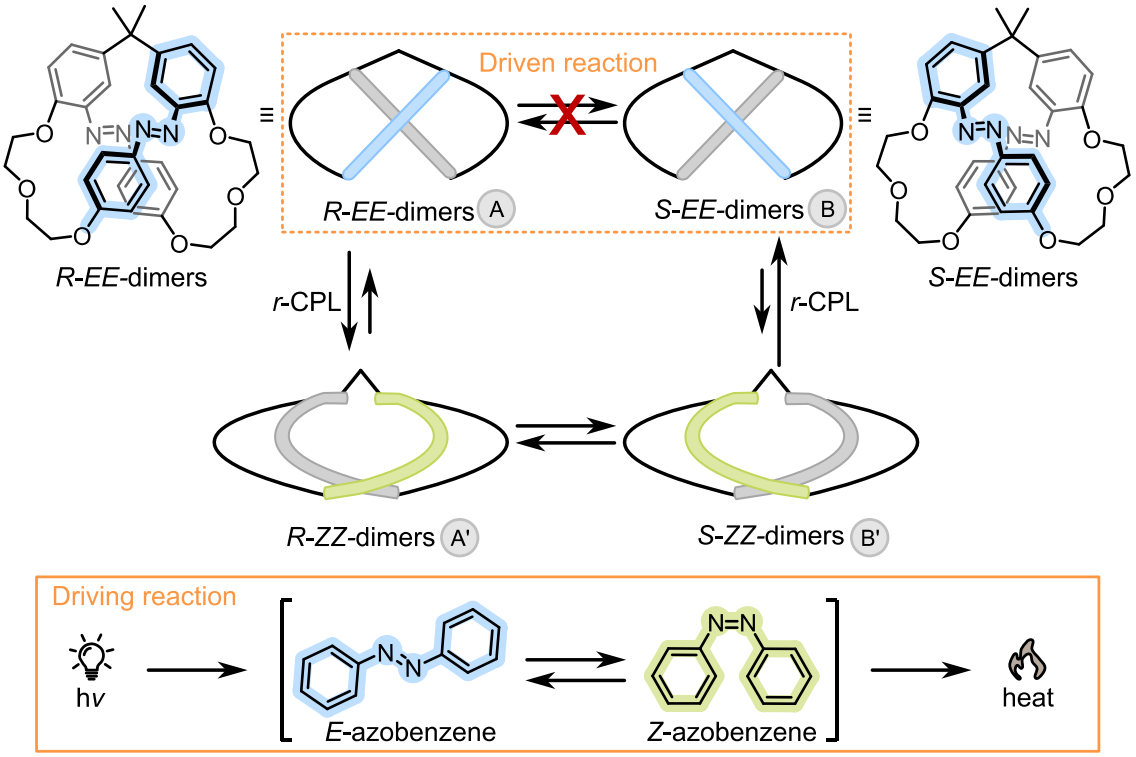

Scheme 16. CPL-driven information ratchet of a bicyclic azobenzene system where *Z*-isomerisation enables enantiomerisation.[139] CPL introduces kinetic asymmetry, favouring one enantiomeric pathway and causing enantioenrichment under steady irradiation: right-CPL favours the *S*-*EE*-dimer, while left-CPL favours the *R*-*EE*-dimer.

The crucial element of the ratchet arises under circularly polarised light (CPL), which introduces kinetic asymmetry because left- and right-handed CPL interact differently with the chiral environment, causing the rates of photochemical reactions leading to each enantiomer to differ. This kinetic asymmetry results in the preferential accumulation of one enantiomer over another. For instance, irradiation with right-CPL favours the formation of the *S* enantiomer (Scheme 16), whereas left-CPL favours the *R* form. Over

continuous irradiation, a small but measurable enantiomeric excess (around 1.1%) accumulates. In this context, the system functions as an information ratchet: directionality arises from kinetic asymmetry induced by CPL, rather than from external modulation of the reaction landscape.

3. Aims and objectives

Building on the concepts introduced in Sections 1 and 2, this thesis aims to elucidate how light can be harnessed to control, and ultimately drive, the behaviour of supramolecular assemblies. The overarching goal is to understand how photoisomerisation at the molecular level translates into well-defined, controllable changes in supramolecular assemblies, and how continuous energy input can push such systems out of equilibrium. To this end, the research addresses three central questions:

(i) How does metal coordination influence the photochemical properties of azobenzene ligands?

(ii) How do variations in coordination vectors determine the geometry, responsiveness, and potential for concerted switching in photoswitchable metal-organic cages?

(iii) Can continuous light input drive a metallo-supramolecular system out of equilibrium, enabling autonomous, directional transformations via a molecular ratchet mechanism that converts light into stored chemical energy?

Each of these questions will be explored through a dedicated project, progressing from fundamental molecular insights to increasingly complex supramolecular functions.

The first project (i) investigates how coordination to metal centres affects the intrinsic photoresponsive properties of azobenzene-based ligands. Although azobenzenes are well-established photoswitches (Section 2.1.1), their isomerisation efficiency and thermal stability are often affected upon metal binding due to changes in the electronic environment around the N=N azo group (Section 2.2). To probe this relationship, a tridentate azobenzene-based ligand was designed to coordinate in its *E*-form to Pd(II), forming a mononuclear ML_1 complex that serves as a minimal model system (Scheme 17). Upon irradiation, $E \rightarrow Z$ isomerisation is expected to induce a change in denticity, converting the tridentate *E* ligand into a bidentate *Z*-ligand. This transformation enables the investigation of how metal coordination influences switching efficiency, thermal relaxation, and reversibility – including the possibility of isomerisation inhibition. These insights will provide a foundation for understanding how proximity to metal centers affects switching behaviour, guiding the design of more complex supramolecular assemblies explored in later projects.

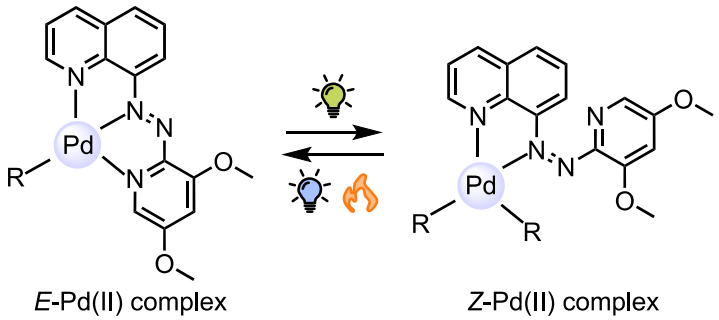

Scheme 17. Design of a Pd(II) complex to investigate how metal coordination affects the photoswitching behaviour of azobenzene-based ligands. The shown structures reflect the intended coordination mode and switching behaviour. R = solvent molecule or counter anion.

The second project (ii) addresses how subtle differences in coordination vectors, arising from ligand connectivity and *E/Z* isomerisation, influence the geometry and responsiveness of self-assembled metal-organic cages. Incorporating azobenzene photoswitches into ditopic bridging ligands enables the coordination angles to be modulated using light, allowing structural reconfiguration of the resulting assemblies. Two regioisomeric ligands, differing in *meta* and *para* connectivity (Scheme 18), will be synthesised to investigate the effect of these variations on the structure of Co(II)-based cages (Scheme 19). The project will also explore how photoinduced configurational changes (*E/Z*) influence the overall assembly, and the conditions under which concerted, reversible switching can be achieved (Scheme 19). Together, these studies aim to deepen our understanding of how ligand geometry and switching behaviour shape the emergent properties of light-responsive metal-organic cages.

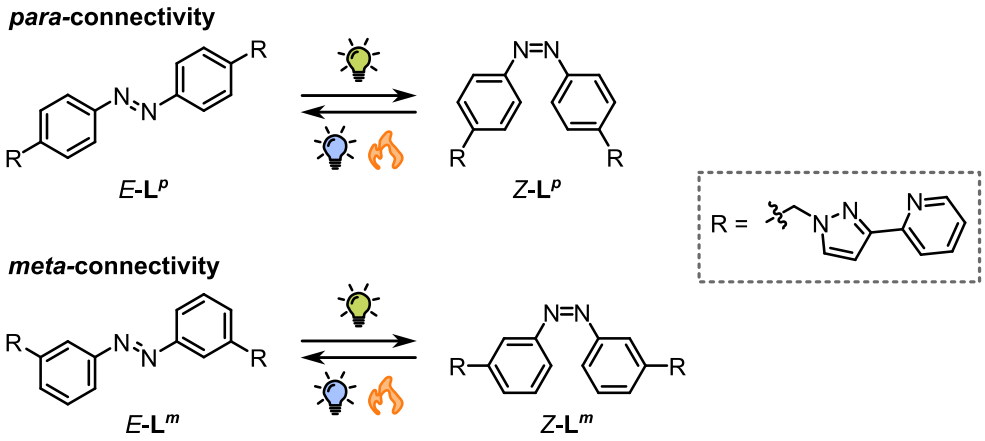

Scheme 18. Light induced isomerisation of *para*- (**L**^{p}) and *meta*-connected (**L**^{m}) azobenzene ligands used to probe how changes in coordination vectors influence the geometry of metal-organic cages.

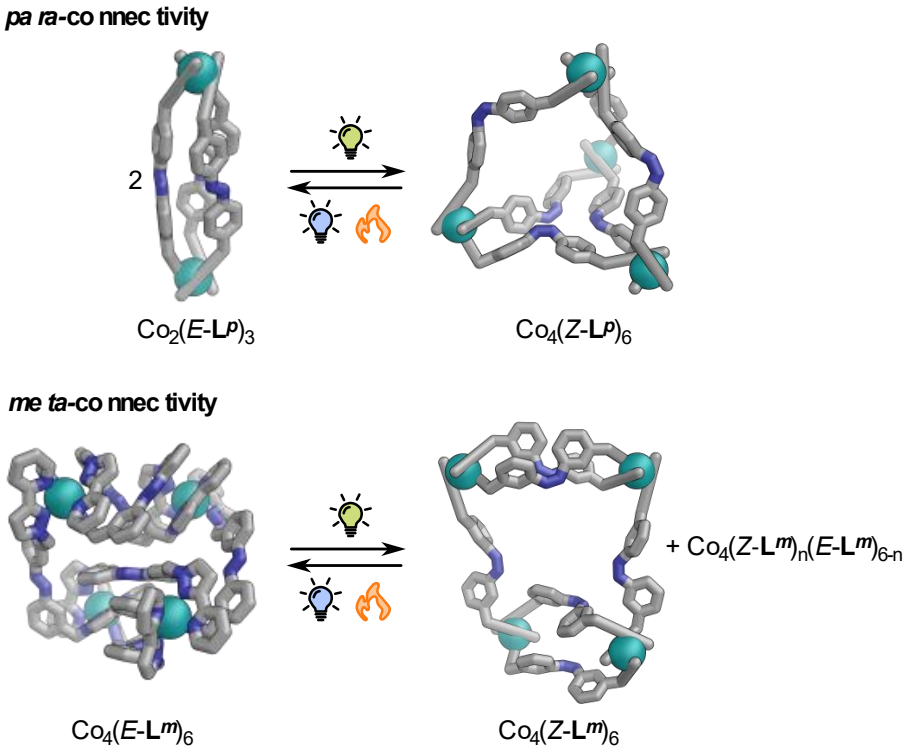

Scheme 19. Co(II)-based cages formed from *para*- and *meta*-substituted azobenzene ligands in their *E*- and *Z*-configurations. Adapted from Tipping et al.[23]

The third project (iii) finally investigates whether sustained light input can drive a metallo-supramolecular system out of equilibrium, enabling autonomous, directional transformations via a molecular ratchet mechanism that converts light into stored chemical energy. To achieve this, a Pd(II)-based assembly will be designed that incorporates a photoswitchable azobispyrazole ligand capable of undergoing reversible *E/Z* isomerisation and conformational change. The system will be constructed to undergo directional switching between discrete cage structures under sustained irradiation (Scheme 20). By mimicking nature's strategy of coupling exergonic and endergonic processes, this project aims to develop a functional supramolecular system that can translate light energy (i.e. sunlight) into controlled, directional motion, and temporarily store it as chemical energy within an out-of-equilibrium structure.

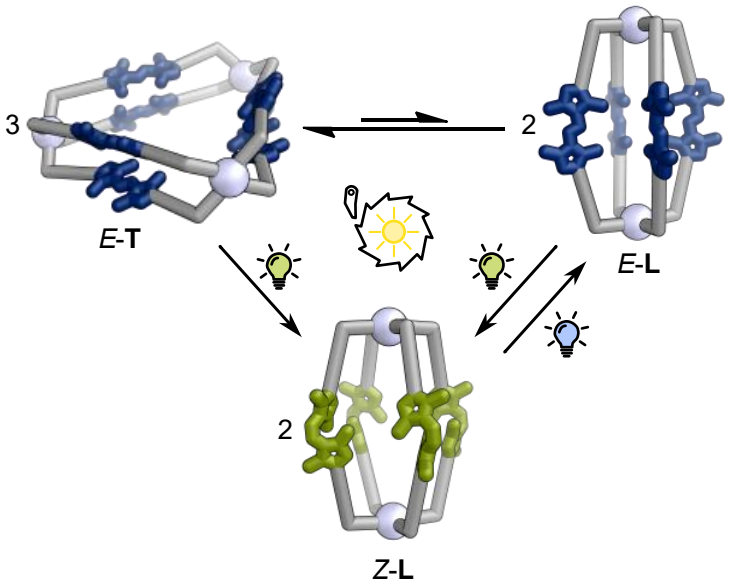

Scheme 20. Schematic representation of the autonomous, light-powered molecular ratchet designed to investigate how continuous irradiation (sunlight) can drive a Pd(II) cage out of equilibrium. Adapted from Pruñonosa Lara et al.[140]

4. Influence of metal coordination on the photoswitching properties of azobenzene derivatives

As introduced in Section 2.1, photoswitches, such as azobenzenes, are key components in the development of light-responsive metal–ligand (M–L) architectures, including dynamic coordination cages capable of controlling guest binding and release (e.g., for drug delivery).[141] However, the intrinsic photoresponsive properties of these ligands are not always preserved upon coordination to metal centres. In some cases, metal binding can significantly alter,[142,143] or even inhibit,[144,145] the switching behaviour by perturbing the electronic environment around the azo bridge (N=N), see Section 2.2. Therefore, a thorough understanding of how coordination to a metal ion affects azobenzene-based ligands at the molecular level is essential before progressing towards more complex supramolecular assemblies.

The first project of my PhD served a dual purpose. Scientifically, it was designed to investigate how metal coordination influences the photoswitching properties of azobenzene derivatives, with mononuclear ML_1 complexes acting as model systems. Practically, it established the experimental foundation for the remainder of my PhD journey, equipping me with the practical skills and conceptual understanding needed to work with light-responsive molecular systems.

The main research objectives were:

- To understand how to characterise azobenzene-based photoswitches in solution.
- To identify how metal coordination affects the switching efficiency and thermal stability of these photoswitches.
- To investigate whether metal coordination inhibits photoswitching, and if so, whether this depends on direct coordination to the azo core.
- To determine which experimental techniques and instrumentation are required to study such effects.
- To establish a basis for assessing structure-property relationships between ligand design, metal binding, and switching behaviour.

To address these questions, an azobenzene-based ligand (**1**) was designed, featuring a central N=N azo bridge bonded to a quinoline and a pyridine group (Scheme 21). To the best of our knowledge, this particular ligand architecture had not been reported before.

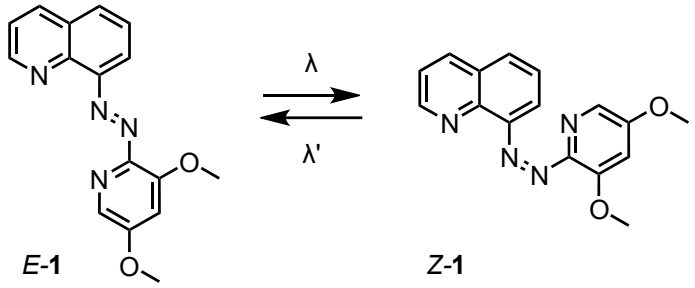

Scheme 21. Structures of the *E*- and *Z*-isomers of the azobenzene-based ligand **1** designed for this study.

The *E*-isomer of **1** (*E*-**1**) was intentionally constructed to function as a tridentate ligand upon coordination to Pd(II). Where such metal centre would be expected to bind to three nitrogen (N) atoms: the N-quinoline, one of the azo N=N nitrogens, and the N-pyridine. This specific design would enable the formation of a mononuclear ML_1 complex (Scheme 22). The photoswitchable nature of **1** raises a key question for this study: can light irradiation induce *E*→*Z* isomerisation while **1** remains metal-bound? Based on the intended design, photoisomerisation of the azo unit would convert **1** from a tridentate to a bidentate coordination mode. Scheme 22 illustrates this proposed behaviour, showing the expected structural change upon irradiation and highlighting the targeted *E*/*Z* switching of the bound ligand. Allowing us to probe how metal coordination influences photoswitching properties.

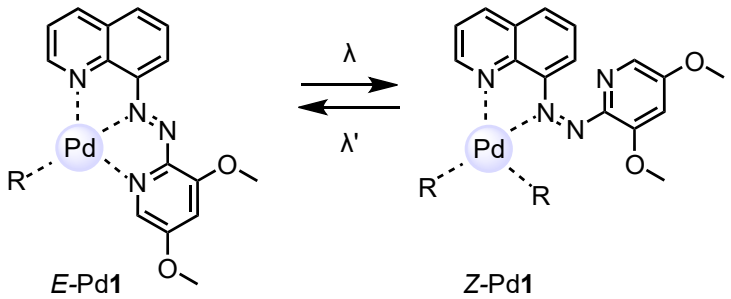

R = solvent molecule or counter anion

Scheme 22. Proposed formation of the Pd(II) complex with ligand **1** and its expected light-induced isomerisation behaviour. Shown structures reflect the intended coordination mode and targeted *E/Z* switching under light irradiation.

Pd(II) was selected as the metal centre for two main reasons, the first being its strong preference for a square planar geometry with four coordination sites.[146,147] In this arrangement, the coordination of a tridentate ligand leaves only one remaining site (occupied by a solvent molecule or anion), thereby favouring the exclusive formation of a ML_1 complex. In contrast, octahedral metals such as Fe(II) or Co(II) can bind two tridentate ligands, forming ML_2 species with added stereochemical intricacy: the octahedral coordination environment introduces metal-centred chirality (Δ/Λ) in addition to the *E/Z* photoisomerism of the ligands, substantially complicating structural analysis. Secondly, Pd(II) was preferred over other square-planar metals, such as Pt(II), due to its higher ligand-exchange lability. Making, in theory, any Pd–L bonds easier to break and re-form under light irradiation.

To investigate how metal coordination affects the fundamental photoswitching properties of the azobenzene core, the free ligand will be directly compared with its Pd(II) complex. The analysis will include optimal irradiation wavelengths, photostationary states, resistance to photobleaching, and thermal half-life.

This project was also shaped by the unique context of our research group at the time. As the second PhD student to join the group, much of the early work involved learning from the ground up how to handle, study, and interpret the behaviour of photoswitches. Together with other group members, I took part in establishing the experimental strategies and characterisation methods that later become routine in our laboratory for studying light-responsive systems.

By focusing on the fundamental relationship between coordination chemistry and the photoswitching behaviour of azobenzene-based ligands, this chapter highlights the importance of understanding how metal binding influences photoresponsiveness. In doing so, it lays the groundwork for the more complex light-sensitive supramolecular assemblies presented later in this thesis.

4.1 Synthesis and photoswitching properties of **1**

Ligand **1** was synthesised following an azo coupling between quinolin-8-amine and pyridine-3,5-diol, proceeding through *in-situ* diazotisation, to give precursor $\mathbf{1^{OH}}$ (23-48% yield). Subsequent O,O-dimethylation of $\mathbf{1^{OH}}$ with dimethyl sulfate via an S_N2 reaction produced ligand **1** (0-15% yield) (Scheme 23).

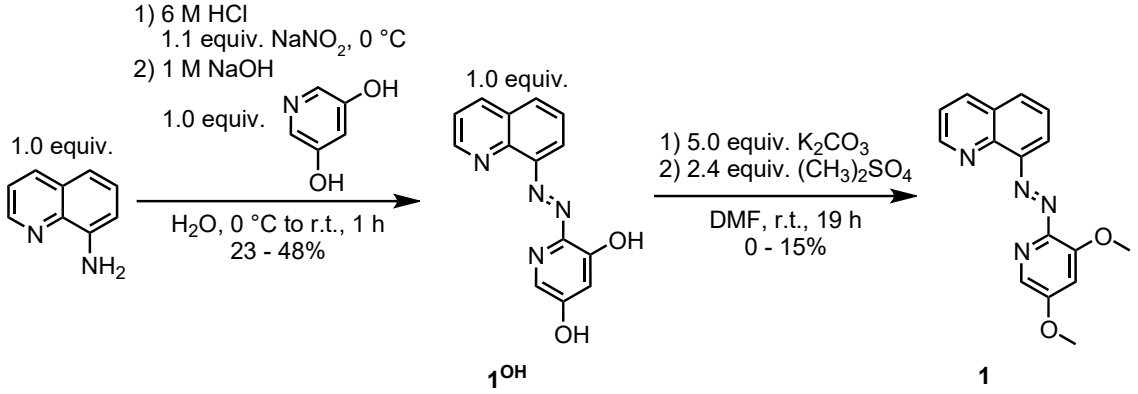

Scheme 23. Two step synthesis of ligand **1** via an azo coupling and subsequent methylation of $\mathbf{1^{OH}}$.

Despite successfully synthesising ligand **1**, the low yields of $\mathbf{1^{OH}}$, coupled with the limited reproducibility of the subsequent methylation step, made obtaining sufficient quantities of **1** challenging. Thereby, efforts were made to develop a one-step synthesis of **1** that bypassed the preparation of $\mathbf{1^{OH}}$ (Scheme 24).

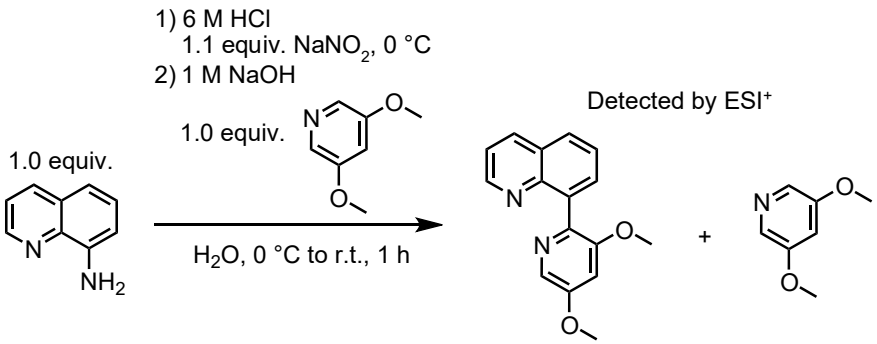

Scheme 24. Attempted synthesis of ligand **1** from 3,5-dimethoxypyridine. Unreacted starting material and 8-(3,5-dimethoxypyridin-2-yl)quinoline were detected by ESI^+; no isolable products were obtained.

Performing the azo coupling under the same reaction conditions as previously described (Scheme 23), this time using 3,5-dimethoxypyridine in place of pyridine-3,5-diol, did not yield the desired ligand **1**. Traces of unreacted 3,5-dimethoxypyridine and the undesired 8-(3,5-dimethoxypyridin-2-yl)quinoline were detected by ESI^+, although neither was

isolated (Scheme 24). These results, together with examples from the literature, suggest that the presence of hydroxyl groups in the nucleophilic coupling compound may facilitate azo bond formation under the conditions used.[148,149] Consequently, the two-step reaction sequence, azo coupling followed by methylation, remains the only viable route to access ligand **1**.

Methylating $\mathbf{1^{OH}}$ prior to photochemical studies was necessary to address the potential hindrance of photoswitching. In literature, hydroxy-substituted azobenzenes are often further functionalised to alkoxy derivatives prior to photochemical studies to improve their photoswitching properties by modifying electronic effects and preventing undesired intramolecular interactions.[150] In particular, hydroxyl groups proximal to the azo (N=N) bridge are known to engage in intramolecular hydrogen bonding, which can restrict or inhibit efficient photoisomerisation.[64,151]

Consistent with this, compound $\mathbf{1^{OH}}$ showed no detectable photoresponse in acetonitrile at 25 °C upon *in-situ* irradiation across a broad range of wavelengths (310-655 nm), as evidenced by unchanged UV-vis absorbance spectra (Figure 8). This lack of photoswitching is in line with hydrogen bonding effects hindering the isomerisation process, thereby motivating the methylation of $\mathbf{1^{OH}}$ to the dimethoxy-substituted ligand **1**. Despite the limited reproducibility of the methylation step (Scheme 23), converting the free hydroxyl groups to methoxy substituents was essential to enable photoswitching.

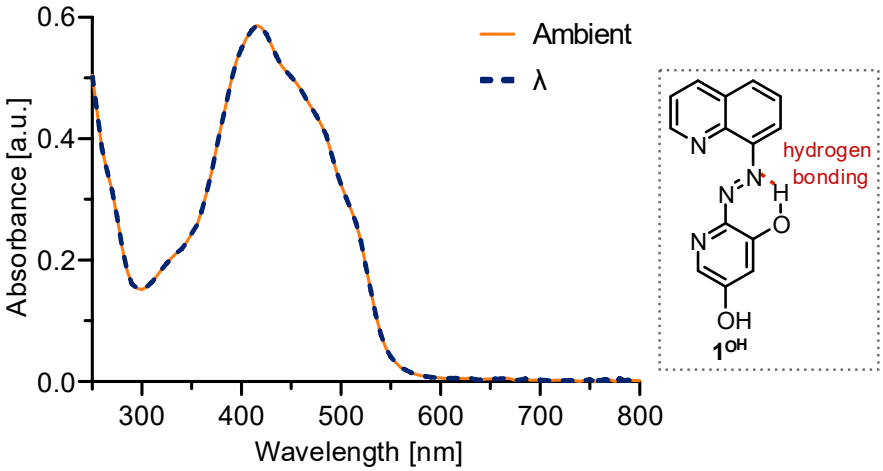

Figure 8. UV-vis spectrum of $\mathbf{1^{OH}}$ (74 µM, CH_3CN, 25 °C) when exposed to different wavelengths of light (λ = 310, 325, 365, 390, 405, 430, 450, 500, 550, 590, 655 nm) and its proposed structure with hydrogen bonding.

The photoswitching behaviour of ligand **1**, summarised in Scheme 25, was investigated in acetonitrile at 25 °C by UV-vis and ^{1}H NMR spectroscopy. The optimal wavelengths for bidirectional switching were identified as 390 nm (*E*→*Z*) and 310 nm (*Z*→*E*) via *in-situ* UV-vis measurements, as these produced the largest changes in the absorbance spectrum (Figure 9). The UV-vis spectrum of the *E*-isomer (*E*-**1**) displayed a strong π→π* absorption band centred at 365 nm (Figure 10a). Upon irradiation with 390 nm light, the band intensity decreases, indicating conversion to the *Z*-isomer (*Z*-**1**), which exhibits a blue-shifted π→π* absorption at 305 nm (Figure 10a). The switching process was fully reversible over at least ten irradiation cycles with no detectable photobleaching (Figure 10b), indicating good fatigue resistance.

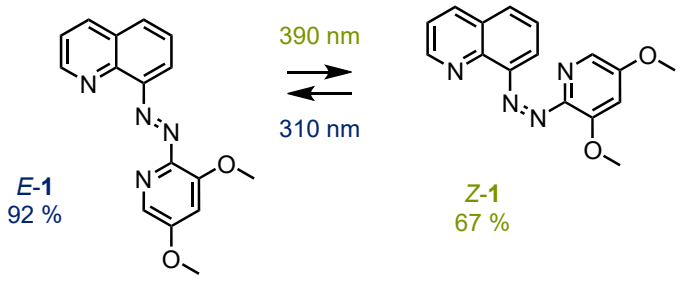

Scheme 25. *E*- and *Z*-isomer structures of ligand **1** upon irradiation with 390 nm light (*E*→*Z*, PSS 67% *Z*-**1**) and 310 nm light (*Z*→*E*, PSS 92% *E*-**1**).

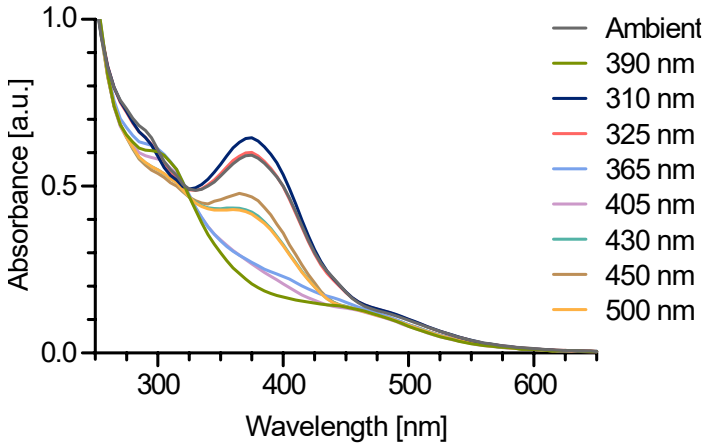

Figure 9. UV-vis spectra of ligand **1** (76 μM, CH_3CN, 25 °C) before and after irradiation with different wavelengths of light for 1 min each.

Notably, no clear isosbestic point was observed during the *in-situ* UV-vis measurements (Figure 9), suggesting that the *E/Z* photoisomerisation may not have occurred exclusively between *E*-**1** and *Z*-**1**. This could be attributed to sample impurities present during early-

stage measurements.[152] In contrast, the thermal relaxation spectra (Figure 11a), recorded at a later stage with a purer sample, display distinct isosbestic points that are consistent with clean *Z*→*E* isomerisation of ligand **1**.

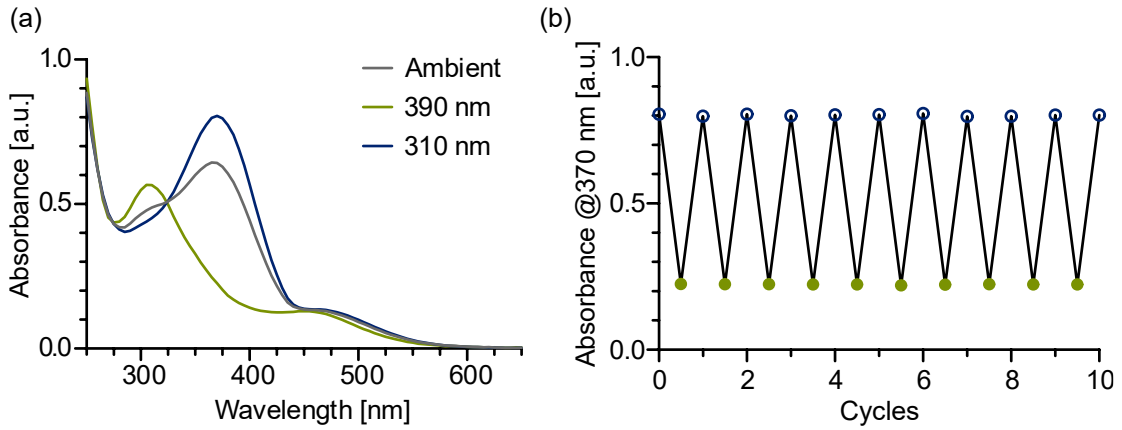

Figure 10. (a) UV-vis spectra of ligand **1** (85 μM, CH_3CN, 25 °C) under ambient light and after irradiation with 390 nm and 310 nm light for 1 min, respectively. (b) UV-vis switching reversibility experiment of **1** (85 μM, CH_3CN, 25 °C) showing absorbance at 370 nm after alternating light irradiation with 390 nm (1 min) and 310 nm (1 min), respectively. No apparent photodegradation was observed over 10 switching cycles.

The thermal relaxation of *Z*-**1** in the dark at 25 °C was monitored over 14 h by UV-vis spectroscopy (Figure 11), revealing a thermal half-life of 3.7 h for the *Z*→*E* isomerisation; which falls within the typical range observed for alkoxy-substituted azobenzenes.[53] This thermal stability is sufficient to allow controlled photoswitching experiments and ensures that the *Z*-isomer remains stable for NMR analysis within a few minutes after irradiation.

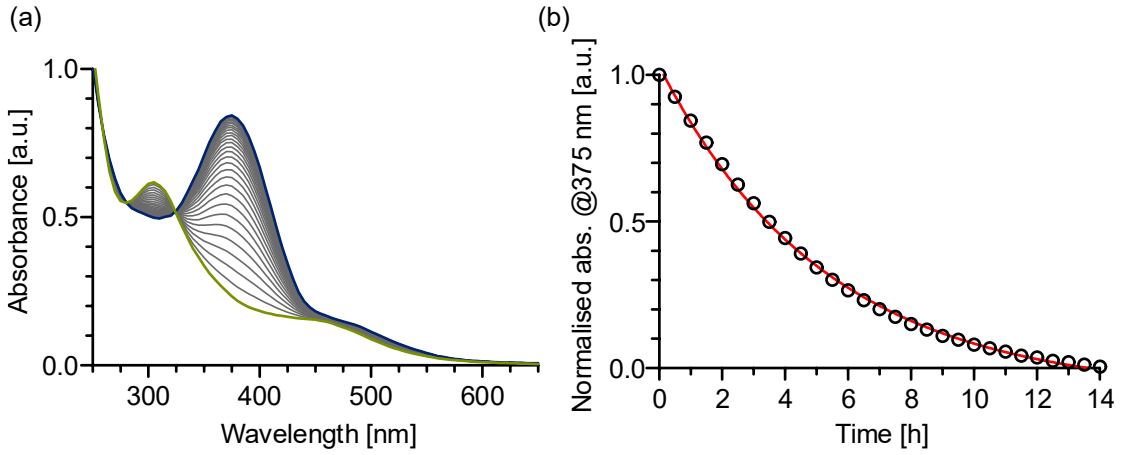

Figure 11. Thermal relaxation of ligand **1** (85 μM, CH_3CN, 25 °C). (a) UV-vis spectra of **1** measured every 30 min in the dark after irradiating with 390 nm light. (b) Change in absorption $(A_t - A_\infty) \cdot (A_0 - A_\infty)^{-1}$ plotted over time *t* following thermal relaxation of **1** to provide its half-life, $\tau_{½}$ = 3.7 h.

Determined by ^{1}H NMR analysis, upon irradiation with 390 nm light for 20 min *E*-**1** was converted to *Z*-**1**, achieving a PSS comprising of 67% *Z*-**1** (Figure 12). Back-isomerisation of *Z*-**1** to *E*-**1** was accomplished by irradiation with 310 nm light overnight, yielding a PSS with 92% *E*-**1** (Figure 12).

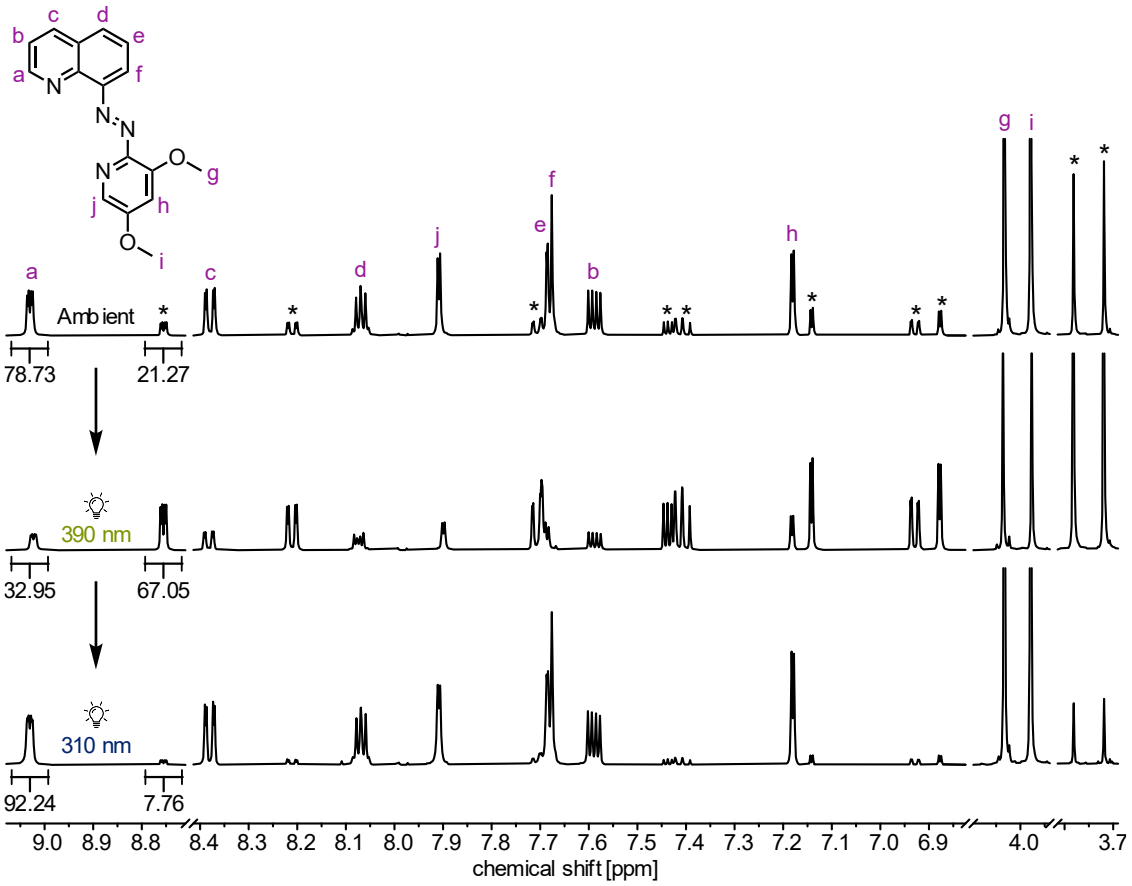

Figure 12. ^{1}H NMR spectra (500 MHz, CD_3CN, 298 K) of ligand **1** under ambient light, after irradiation with 390 nm light (20 min, PSS 67% *Z*-**1**), and after irradiation with 310 nm light (17 h, PSS 92% *E*-**1**). Signals marked with an asterisk correspond to *Z*-**1**.

These spectroscopic studies confirm that the dimethoxy-substituted ligand **1** undergoes efficient, reversible photoswitching between its *E*- and *Z*-isomers upon UV irradiation. In comparison to classical azobenzenes, which often exhibit higher *Z*-isomer photostationary states (commonly >80–90%)[46], ligand **1** shows a low PSS for *Z*-**1** of 67% under irradiation with 390 nm light.

The substitution pattern in ligand **1** provides one possible explanation for this behaviour. Electron-donating methoxy groups are known to modulate the absorption properties and isomerisation behaviour of azobenzenes by red-shifting the π–π* and n–π* transitions,[153] thereby altering the wavelengths at which photoisomerisation is most effective. Moreover, the PSS of the *Z*-isomer depends strongly on the position of substitution and the electronic nature of the azo framework.[154] In systems with both *ortho*- and *para*-methoxy groups, as in ligand **1**, competing electronic and steric effects may influence the PSS alongside the intrinsic properties of the quinoline–pyridine azo scaffold. Comparative studies with an unsubstituted analogue **1** would help to determine whether the observed switching behaviour is dominated by the methoxy substituents or by the quinoline–pyridine azo framework itself.

4.2 Synthesis and photoswitching properties of Pd**1**

Having established the photoswitching behaviour of ligand **1**, its coordination to Pd(II) was next investigated to assess the effect of metal complexation on its photoswitching properties.

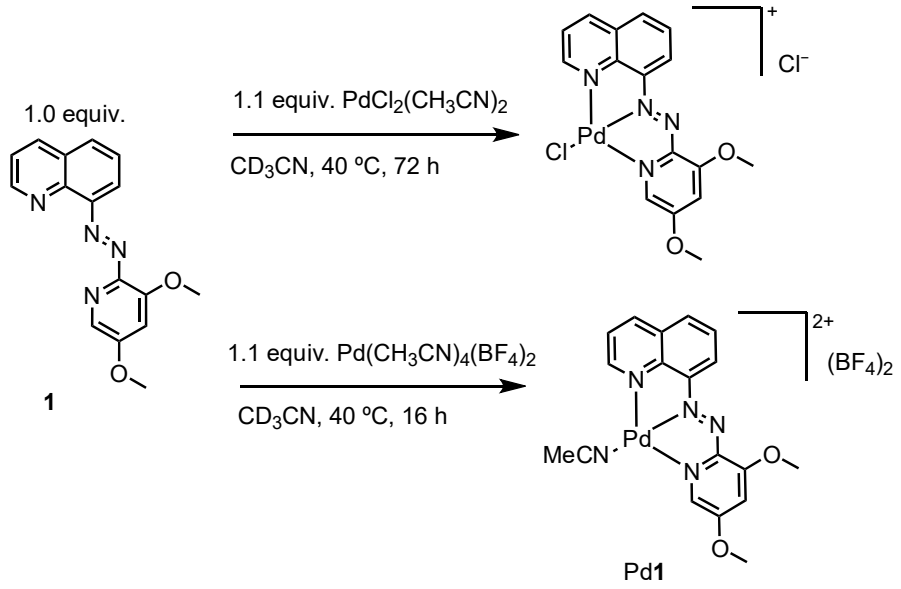

Scheme 26. Complex formation of ligand **1** with $PdCl_2(CH_3CN)_2$ and $Pd(CH_3CN)_4(BF_4)_2$ in acetonitrile.

The complex formation between ligand **1** and a Pd(II) salt was found to be highly dependent on the choice of counteranion (Scheme 26). When 1.0 equiv. of $PdCl_2(CH_3CN)_2$ was added to 1.0 equiv. of **1** in acetonitrile at 40 °C, an immediate colour change from light to dark red was observed. The immediate colour change is typically a strong indication of complex formation; however, the complex was only detectable by ESI^+ mass spectrometry. In the corresponding NMR spectrum, only signals corresponding to the deuterated solvent were observed, with no detectable signals of either free ligand **1** or the complex. This behaviour is likely due to the poor solubility of the chloride-containing complex in acetonitrile, limiting its detection by the less sensitive NMR technique.[155]

In contrast, when 1.0 equiv. of $Pd(CH_3CN)_4(BF_4)_2$ was used, the desired complex was readily characterised by NMR, ESI^+ mass spectrometry (Section 4.6.3, Figure 54), and UV-vis spectroscopy. These observations highlight the influence of the counteranion (Cl^- vs BF_4^-) on the stability and solubility of the Pd(II) complexes formed with ligand **1**. For this reason, all subsequent experiments were conducted using the metal salt $Pd(CH_3CN)_4(BF_4)_2$ and thus, references to Pd**1** in this chapter refer specifically to the complex formed with BF_4^- as the counteranion.

^1H NMR spectroscopy was used to compare free ligand **1** and its Pd**1** complex (Figure 13). In acetonitrile at 298 K, ligand **1** exists as a mixture of *E*- and *Z*-isomers in a ratio of 79:21, respectively. Strikingly, only a single ligand environment is observed in the spectrum of Pd**1**, consistent with exclusive coordination of the *E*-isomer to the metal centre. This indicates that metal complexation significantly shifts the isomeric equilibrium, favouring the *E*-isomer in solution. Furthermore, upon coordination to Pd(II), the ^1H NMR signals of ligand **1** shift predominantly downfield, consistent with deshielding upon metal binding. Only the quinoline proton adjacent to the coordinating nitrogen (H-a) shifts upfield, likely due to its spatial orientation relative to the aromatic system and metal centre, resulting in local shielding effects.

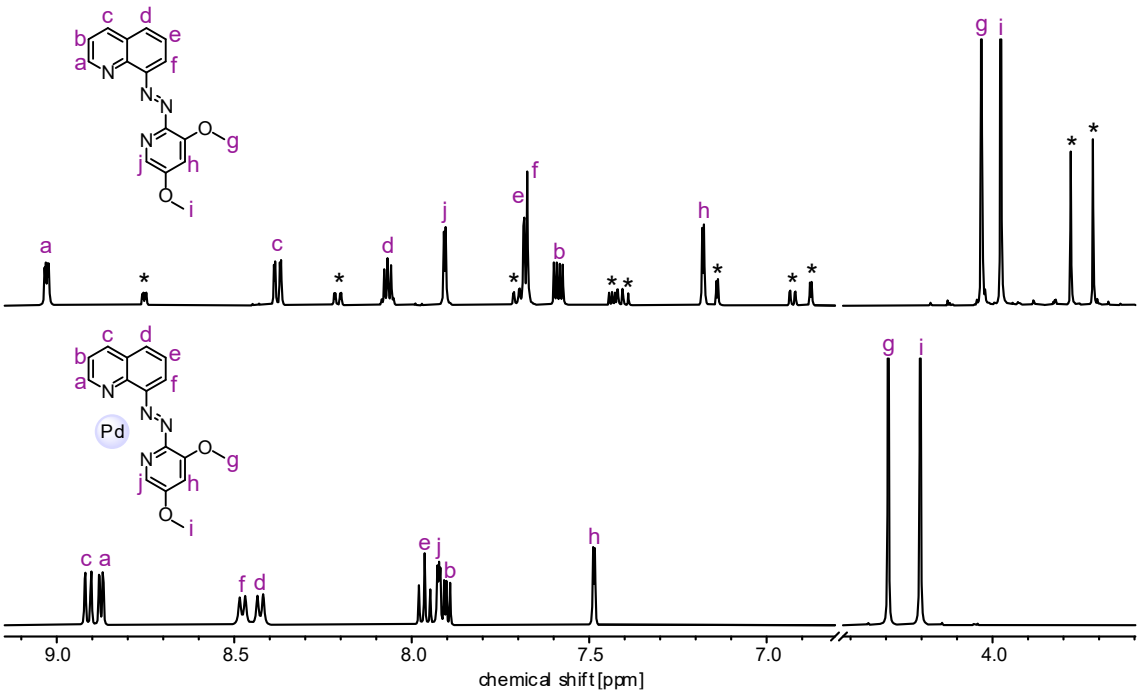

Figure 13. Stacked ^{1}H NMR spectra (500 MHz, CD_3CN, 298 K) of **1** (top) and Pd**1** (bottom). Signals marked with an asterisk correspond to *Z*-**1**.

Having established that Pd**1** exists exclusively in the *E*-configuration in solution, the key question is whether ligand **1** can undergo *E*→*Z* isomerisation while bound to Pd(II) (Scheme 27). This directly addresses one of the central aims of this chapter: to evaluate the extent to which metal coordination inhibits photoswitching, and to establish if such effects are linked to direct coordination to the azo core.

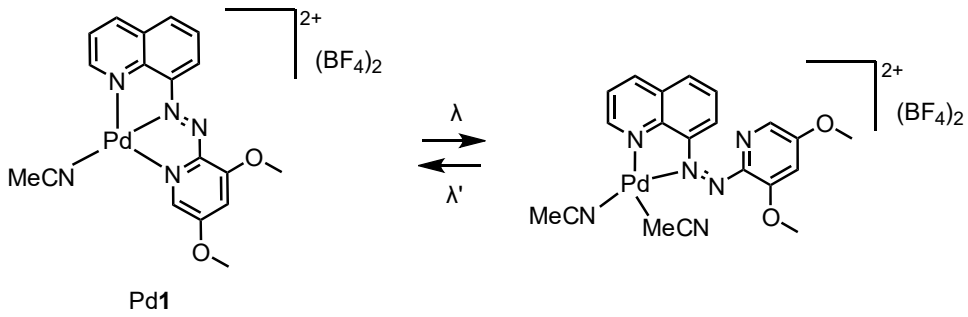

Scheme 27. Proposed reversible *E/Z* isomerisation of Pd**1** upon irradiation with UV light and visible light.

As only a single species was detected in the ^{1}H NMR spectrum of Pd**1**, *in-situ* UV-vis spectroscopy was employed to study its photoswitching behaviour, as it is more readily accessible for continuous irradiation studies. The UV-vis spectrum of Pd**1** in acetonitrile exhibited a red-shift in the absorption maximum compared to free ligand **1**; while *E*-**1**

displays a strong π→π* absorption band centred at 365 nm, Pd**1** showed this band shifted to 510 nm (Figure 14). Unlike free ligand **1**, Pd**1** exhibited no changes in its UV-vis spectrum upon irradiation with different wavelengths of light (Figure 14). Furthermore, repeated irradiation experiments were conducted at various temperatures (25-60 °C) to determine whether thermal energy could overcome the kinetic barriers to *E*/*Z* isomerisation imposed by coordination to Pd(II). However, no spectral changes were observed. This demonstrates that Pd**1** does not undergo detectable *E*/*Z* isomerisation under these conditions and that coordination to Pd(II) effectively suppresses photoswitching in solution. However, could the addition of a competitive ligand in solution enable photoswitching?

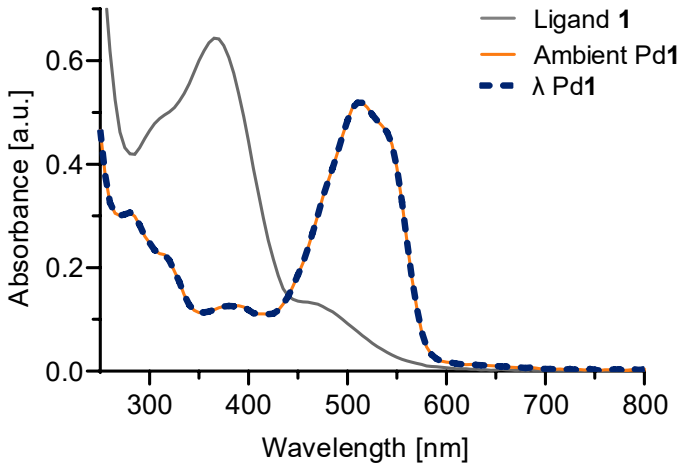

Figure 14. UV-vis spectra of ligand **1** (85 μM, CH_3CN, 25 °C) under ambient light and of Pd**1** in CH_3CN when exposed to different wavelengths of light (λ = 310, 325, 365, 390, 405, 430, 450, 500, 550, 590, 655 nm) at various temperatures (25 °C, 30 °C, 40 °C, 50 °C, 60 °C). No changes were observed for Pd**1** upon irradiation with UV and white light at various temperatures.

4.3 Photoswitching properties of Pd**1** in the presence of a competitive ligand

Coordination of **1** to Pd(II) inhibits the photoswitching of Pd**1** in solution, which motivated an investigation into whether competitive ligand binding could restore its light responsiveness. The underlying concept was that light-driven *E*→*Z* isomerisation of **1**, in combination with competition from an external ligand, would destabilise **1**'s tridentate binding mode and enforce bidentate coordination. This would create an open site on Pd(II) for substitution. Introducing a competitive ligand under irradiation was therefore

intended to both probe the stability of the Pd–ligand **1** coordination environment and test whether displacement of one coordination site could re-establish photoswitching of **1**.

Pyridine was selected as the competitive ligand due to its strong Pd(II)-N coordination affinity.[146] Under irradiation with light of a specific wavelength, pyridine binding was expected to displace one donor site of **1**, yielding a Pd**1**-pyridine complex in which **1** adopts its *Z*-configuration (Scheme 28). In this experiment, 2.0 equiv. of pyridine were added to a solution of Pd**1** (1.0 equiv.) and the resulting mixture, described as Pd**1**-pyridine, was immediately analysed by UV-vis spectroscopy to assess photoswitching.

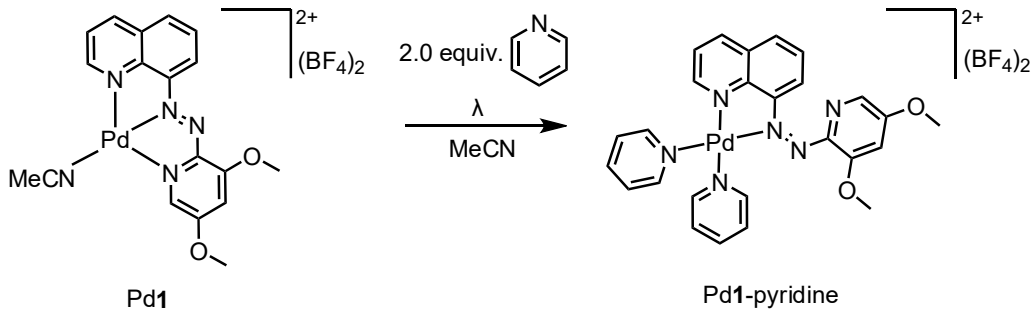

Pd**1** Pd**1**-pyridine

Scheme 28. Proposed formation of the pyridine adduct, labelled as Pd**1**-pyridine, upon addition of 2.0 equiv. of pyridine under irradiation with UV or white light in acetonitrile at various temperatures.

Irradiation of Pd**1**-pyridine at various wavelengths (310, 325, 365, 390, 405, 430, 450, 500, 550, 590, 655 nm) revealed minor spectral changes only upon exposure to 405 nm light for 5 min at 25 °C. Specifically, the major absorption peak at 500 nm decreased slightly, while a broader band around 600 nm increased, corresponding to the π-π* and n-π* transitions, respectively. Increasing the temperature enhanced these spectral changes, with higher temperatures resulting in greater absorbance differences. Measurements were carried out at 25, 35, 45, 55, and 65 °C, with irradiation at 405 nm light at 65 °C producing the greatest absorbance change of 0.2 a.u. (Figure 15).

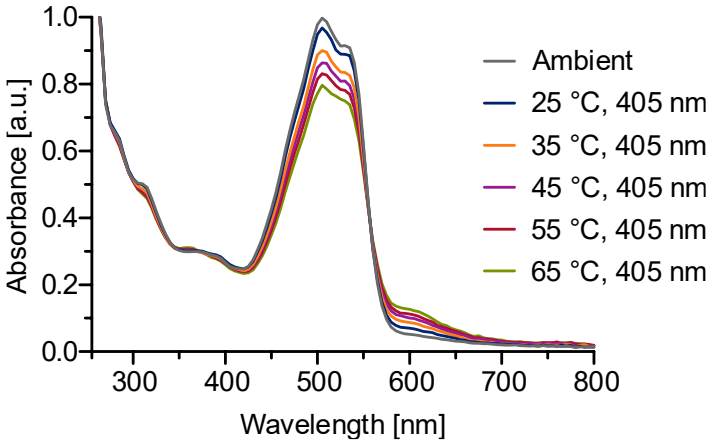

Figure 15. UV-vis spectra of the potential Pd**1**-pyridine complex in CH_3CN under 405 nm light irradiation at various temperatures (25 °C, 30 °C, 40 °C, 50 °C, 60 °C).

It should be noted that the observed spectral changes cannot be conclusively attributed to the formation of the described Pd**1**-pyridine complex (Scheme 28), as no follow-up characterisation by NMR or mass spectrometry was performed.

Attempts to reverse the changes observed in the UV-vis spectrum by irradiating the sample with white light were unsuccessful, as no spectral reversion was observed. These findings suggest that the process is irreversible to light, supporting the hypothesis of irreversible ligand displacement or structural modification.

To better understand the minimal spectral changes observed for Pd**1**-pyridine upon irradiation at different temperatures, it is important to consider the nature of the ligands involved. While pyridine is a monodentate ligand, ligand **1** coordinates in a tridentate manner, benefiting from the chelating effect which generally increases binding strength and complex stability.[156,157] This chelating effect is favoured both enthalpically and entropically, making the partial displacement of ligand **1** by pyridine to form a bidentate coordination mode unfavourable. In an attempt to overcome this limitation, the UV-vis photoswitching experiment was repeated with progressively increasing amounts of pyridine, up to 32 equiv., to evaluate whether higher pyridine concentrations could induce more significant changes in the UV-vis absorbance spectrum.

Increasing the equivalents of pyridine (x = 2, 4, 8, 16, 24, 32) failed to cause immediate changes in the UV-vis absorption spectra when irradiated with 405 nm light at 25 °C, indicating no rapid displacement or photoswitching under these conditions. Consequently, a more suitable competitive ligand was selected to repeat the experiment.

The bidentate ligand bipyridine was chosen for its stronger chelating effect compared to the monodentate pyridine ligand, making it a more competitive candidate for binding to the Pd(II) centre. Under irradiation with light of a specific wavelength, bipyridine binding was expected to displace one donor site of **1**, yielding a Pd**1**-bipyridine complex in which **1** adopts its *Z*-configuration (Scheme 29). In this experiment, 1.0 equiv. of bipyridine was added to a solution of Pd**1** (1.0 equiv.) and the resulting mixture, defined as Pd**1**-bipyridine, was analysed directly by UV-vis spectroscopy to assess photoswitching.

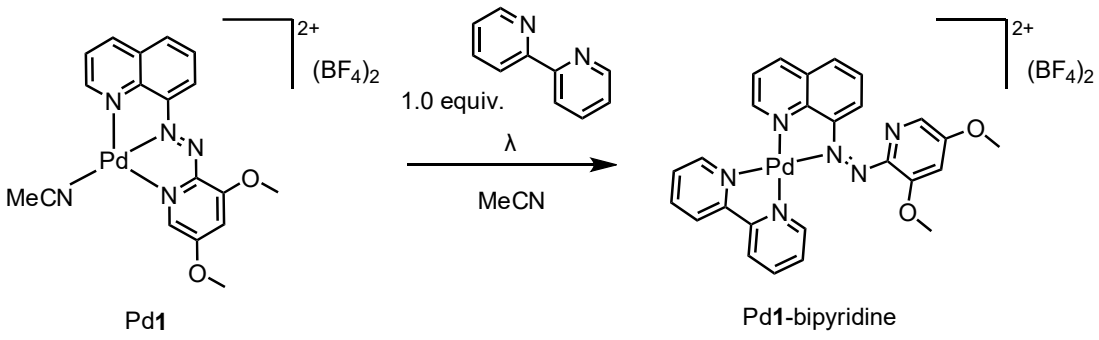

Scheme 29. Proposed formation of the bipyridine adduct, defined as Pd**1**-bipyridine, upon addition of 1.0 equiv. of bipyridine under irradiation in acetonitrile at 25 °C.

Irradiation with 405 nm light was again found to elicit the greatest change in absorbance amongst all wavelengths tested. Unlike in the experiments with Pd**1**-pyridine, changes in the UV-vis spectrum were still observed after 5 min of irradiation and thus, the sample was irradiated for 10 h to ensure sufficient exposure. This resulted in a significant change in UV-vis absorbance spectrum of Pd**1**-bipyridine, potentially indicating the breakage of the Pd-$N_{pyridine}$ bond (Figure 16). However, this cannot be confirmed solely through UV-vis spectroscopy, as supporting mass spectrometry and NMR data are lacking. Additionally, the stability of ligand **1** under prolonged 405 nm light irradiation remains unknown. Further experiments, including mass spectrometry and NMR analysis, are necessary before drawing definitive conclusions. Nonetheless, irradiating the sample with different wavelengths of light, in an attempt to reverse the spectral changes, produced no

observable changes to the UV-vis spectrum, indicating that the process was irreversible under the tested conditions.

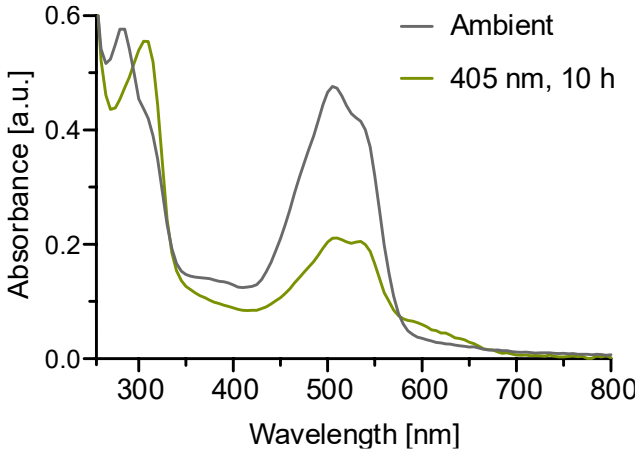

Figure 16. UV-vis spectra of the potential Pd**1**-bipyridine complex (CH_3CN, 25 °C) under 405 nm light irradiation for 10 h.

The inhibited photoswitching of Pd**1** may arise from coordination of the N=N azo moiety to the Pd centre, from the stabilising chelate effect of the tridentate ligand **1**, or from a combination of the two. To clarify the origin of this inertness, three new bidentate derivatives were designed and synthesised for further study.

4.4 Derivatives of **1**: synthesis, Pd complexes, and photoswitching studies

To clarify whether the lack of photoswitching in Pd**1** arises from coordination of the azo N=N group to the Pd(II) centre and/or from the strong chelating nature of **1**'s tridentate ligand framework, three new bidentate derivatives were designed (Figure 17). In these derivatives, the pyridine donor of **1** was replaced with a phenyl ring to eliminate the tridentate binding mode. Ligand **2** retains the same methoxy substitution pattern as **1**, two methoxy groups *ortho* and *para* on the phenyl ring, enabling direct comparison of the two scaffolds.

As discussed in Section 2.1.1, *ortho* substituents to the azo bond can sterically hinder back-rotation, thereby slowing down thermal relaxation.[59] Furthermore, tetra-*ortho*-substitution around the N=N unit in azobenzenes is known to distort the planarity of the

E-isomer, separating the n→π* absorption bands of the two isomers and improving photoswitchability in the visible region.[158] On this basis, ligands **3** and **4** introduce additional steric bulk by incorporating an extra methoxy group *ortho* to the N=N bond on the quinoline ring, intended to modulate the photoswitching behaviour. Both **3** and **4** also contain three methoxy groups on the phenyl ring, resulting in four substituents per ligand overall. However, in ligand **3**, three of these methoxy groups occupy *ortho* positions relative to the azo group, making it the most sterically hindered derivative. Whereas ligand **4** features *meta* and *para* substitution in the phenyl ring providing a slightly different steric and electronic environment to ligand **3**.

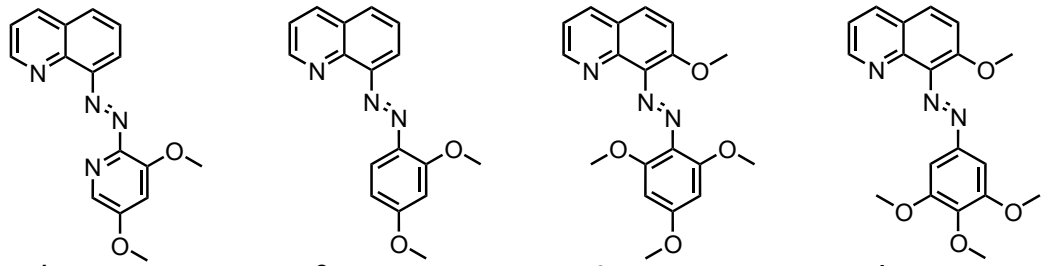

Figure 17. Structures of ligand **1** and its derivatives **2**-**4** prepared for comparative studies.

These structural variations were designed to probe both the coordination behaviour and photoswitching properties of the resulting Pd(II) complexes, as well as the substitution effect of the electron-donating OMe groups on the PSS and the thermal *Z*→*E* relaxation rates of the free ligands.

4.4.1 Studies of derivative **2**

Ligand **2** was synthesised following an azo coupling between quinolin-8-amine and resorcinol, proceeding through *in-situ* diazotisation, to give precursor $\mathbf{2^{OH}}$ (61% yield). Subsequent O,O-dimethylation of $\mathbf{2^{OH}}$ with dimethyl sulfate, via an S_N2 mechanism, produced ligand **2** (2% yield) (Scheme 30). The extremely low yield of **2** is attributed to purification challenges in separating singly and double methylated products. Despite numerous attempts using column chromatography and HPLC, minor impurities remain detectable in the aliphatic region of the ^{1}H NMR spectrum (Figure 21).

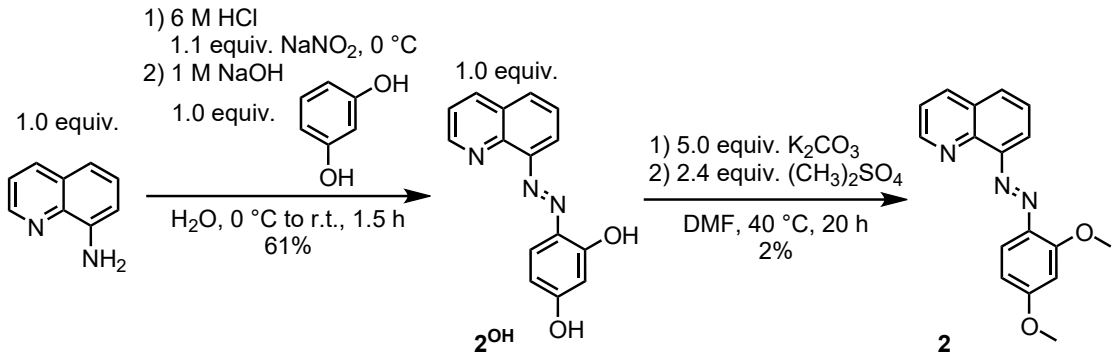

Scheme 30. Two step synthesis of ligand **2** via an azo coupling and subsequent methylation of **2^{OH}**.

The photoswitching behaviour of ligand **2**, summarised in Scheme 31, was investigated in acetonitrile at 25 °C by UV-vis and ^{1}H NMR spectroscopy. The optimal wavelength for *E*→*Z* isomerisation was identified as 405 nm via *in-situ* UV-vis measurements, as this produced the largest change in the absorbance spectrum (Figure 18). The UV-vis spectrum of the *E*-isomer (*E*-**2**) displayed a strong π→π* absorption band centred at 375 nm, which decreased upon exposure to 405 nm light, consistent with the conversion to its *Z*-isomer, *Z*-**2** (Figure 20a). Irradiation of *Z*-**2** with the available laboratory wavelengths did not restore the *E*-**2** absorbance to the value observed under ambient conditions prior to irradiation (Figure 18). Consequently, the thermal *Z*→*E* relaxation of **2** was next examined.

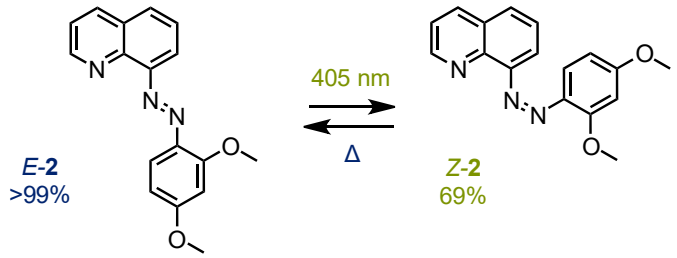

Scheme 31. *E*- and *Z*-isomer structures of ligand **2** upon irradiation with 405 nm light (*E*→*Z*, PSS 69% *Z*-**2**) and thermal relaxation (*Z*→*E*, >99% *E*-**2**).

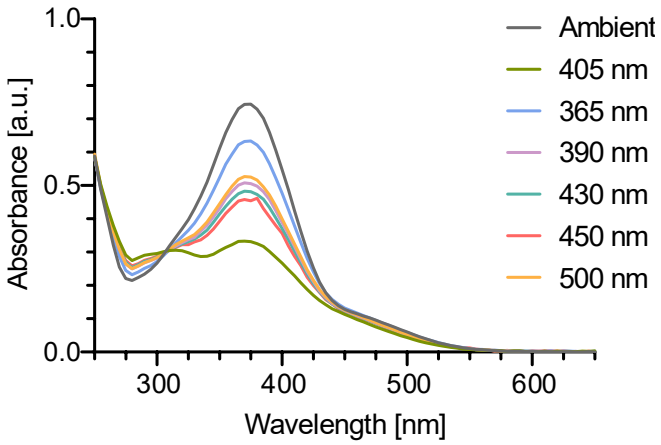

Figure 18. UV-vis spectra of ligand **2** (89 µM, CH_3CN, 25 °C) before and after irradiation with different wavelengths of light for 1 min each.

The thermal relaxation of *Z*-**2** in the dark at 25 °C was monitored using UV-vis spectroscopy (Figure 19), revealing a thermal half-life of 1.3 min for the *Z*→*E* isomerisation in acetonitrile. This is significantly faster than that of its parent ligand **1** ($\tau_{½}$ = 3.7 h). The short thermal lifetime of *Z*-**2** means that all controlled photoswitching experiments must be performed *in-situ*.

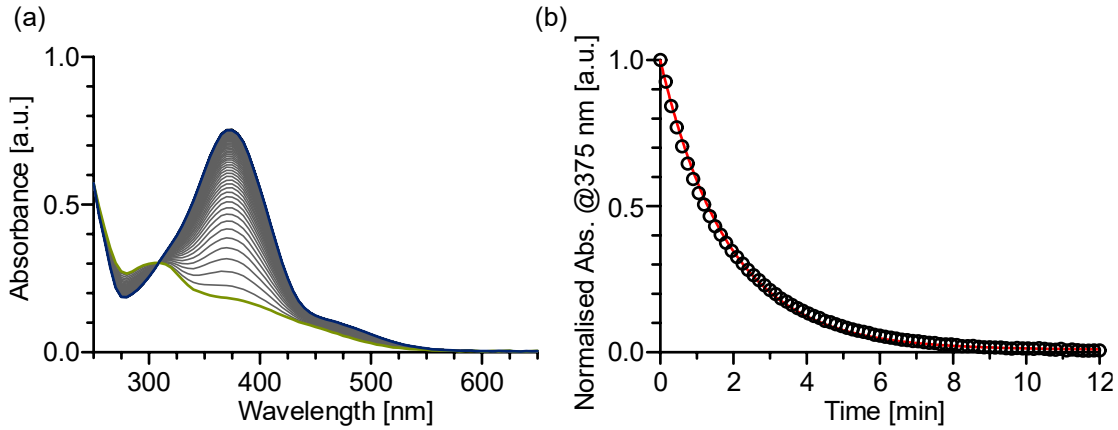

Figure 19. Thermal relaxation of ligand **2** (89 µM, CH_3CN, 25 °C). (a) UV-vis spectra of **1** measured every 9 s in the dark after irradiating with 405 nm light. (b) Change in absorption $(A_t - A_\infty) \cdot (A_0 - A_\infty)^{-1}$ plotted over time *t* following thermal relaxation of **1** to provide its half-life, $\tau_{½}$ = 1.3 min.

Investigated by *in-situ* UV-vis, the *E*→*Z* isomerisation with 405 nm light and the thermal *Z*→*E* relaxation were fully reversible over at least ten cycles, with no detectable photobleaching (Figure 20b).

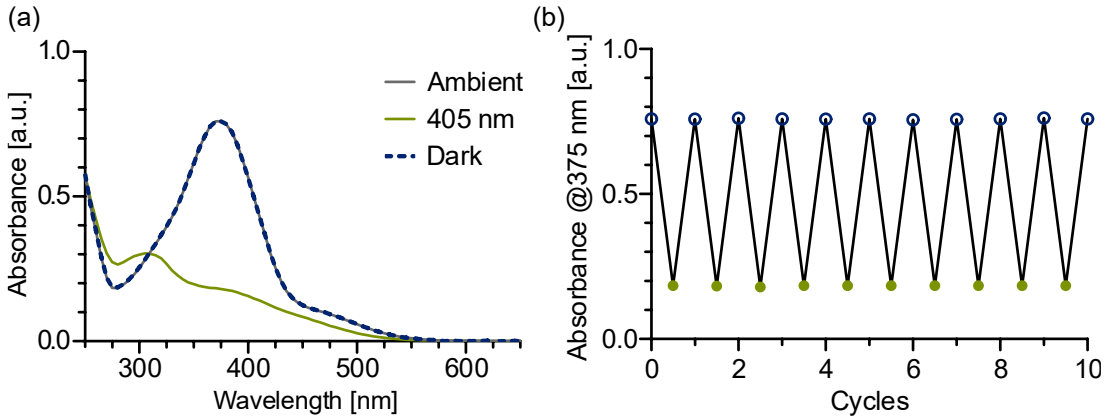

Figure 20. (a) UV-vis spectra of ligand **2** (89 μM, CH_3CN, 25 °C) under ambient light, after irradiation with 405 nm light for 1 min and after relaxing 5 min in the dark. (b) UV-vis switching reversibility experiment of **2** (89 μM, CH_3CN, 25 °C) showing absorbance at 375 nm after alternating light irradiation with 405 nm light (1 min) and relaxing in the dark (5 min).

Determined by *in-situ* ^{1}H NMR, upon irradiation with 405 nm light *E*-**2** was converted to *Z*-**2**, achieving a PSS comprising of 69% *Z*-**2** (Figure 21). Back-isomerisation of *Z*-**2** to *E*-**2** was accomplished by leaving the sample in the dark for 20 min, with >99% *E*-**2** (Figure 21).

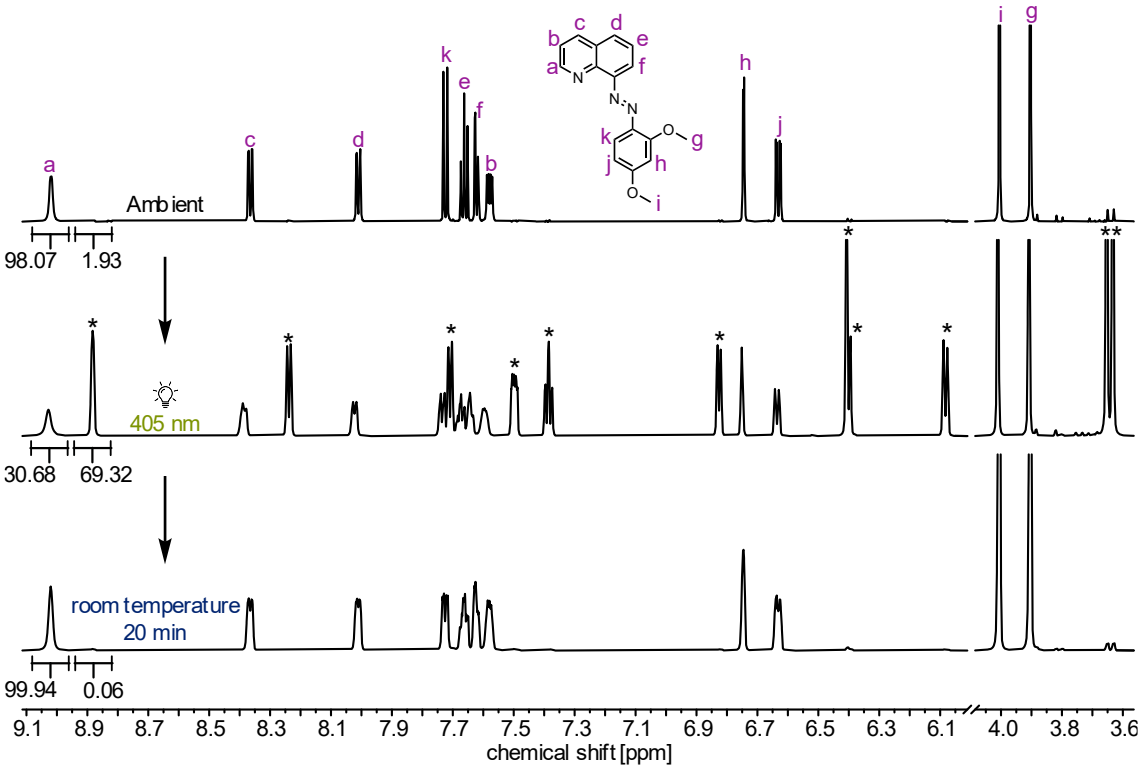

Figure 21. ^{1}H NMR spectra (500 MHz, CD_3CN, 298 K) of ligand **2** under ambient light, after irradiation with 405 nm light (5 min, PSS 69% *Z*-**2**), and after being in the dark (20 min, PSS 100% *E*-**2**). Signals marked with an asterisk correspond to *Z*-**2**.

Having established the photoswitching behaviour of ligand **2**, its coordination to Pd(II) was next investigated to assess the impact of metal complexation on isomerisation.

Unlike tridentate ligand **1**, which can only form a single ML_1 complex, bidentate ligand **2** allows for multiple coordination isomers. Even when reacted with Pd(II) in a 1:1 ligand-to-metal ratio, three complexes are possible: the monoligated Pd**2** complex, and the bis-ligated *cis*-Pd(**2**)$_2$ and *trans*-Pd(**2**)$_2$ isomers (Scheme 32).

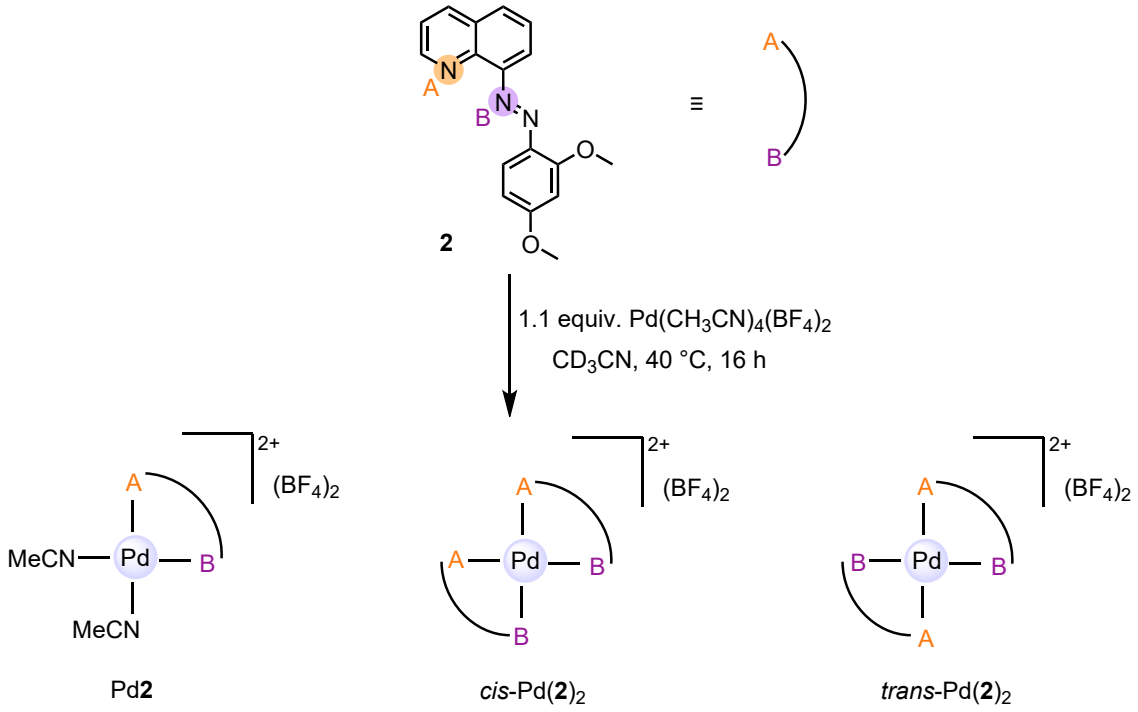

Scheme 32. A schematic representation of ligand **2** highlighting its two coordination sites: A = N-pyridine, and B = N-azo. Reaction of ligand **2** with $Pd(CH_3CN)_4(BF_4)_2$ under a 1:1 stoichiometry can theoretically yield three products: the monoligated Pd**2** complex and the bis-ligated *cis*-Pd(**2**)$_2$ and *trans*-Pd(**2**)$_2$ isomers.

Following the same synthetic procedure as for Pd**1**, equimolar amounts of **2** and $Pd(CH_3CN)_4(BF_4)_2$ were combined in CD_3CN at 40 °C (Scheme 32). Analysis by ESI^+ mass spectrometry revealed two peaks assignable to $[Pd + \mathbf{2} + CN]^+$ and $[Pd + \mathbf{2} - H + CH_3CN]^+$, with no evidence of any Pd(**2**)$_2$ species (Section 4.6.3, Figure 56). On this basis, the subsequent ^1H NMR analysis was interpreted under the working assumption that only monoligated Pd**2** species were present. Comparison of the ^1H NMR spectra of free ligand **2** (predominantly *E*-**2**, 98:22 *E:Z*) and its Pd(II) complex (Figure

22) showed that, upon coordination, two distinct ligand environments (x and y) appeared in a 35:65 ratio, with no detectable free ligand.

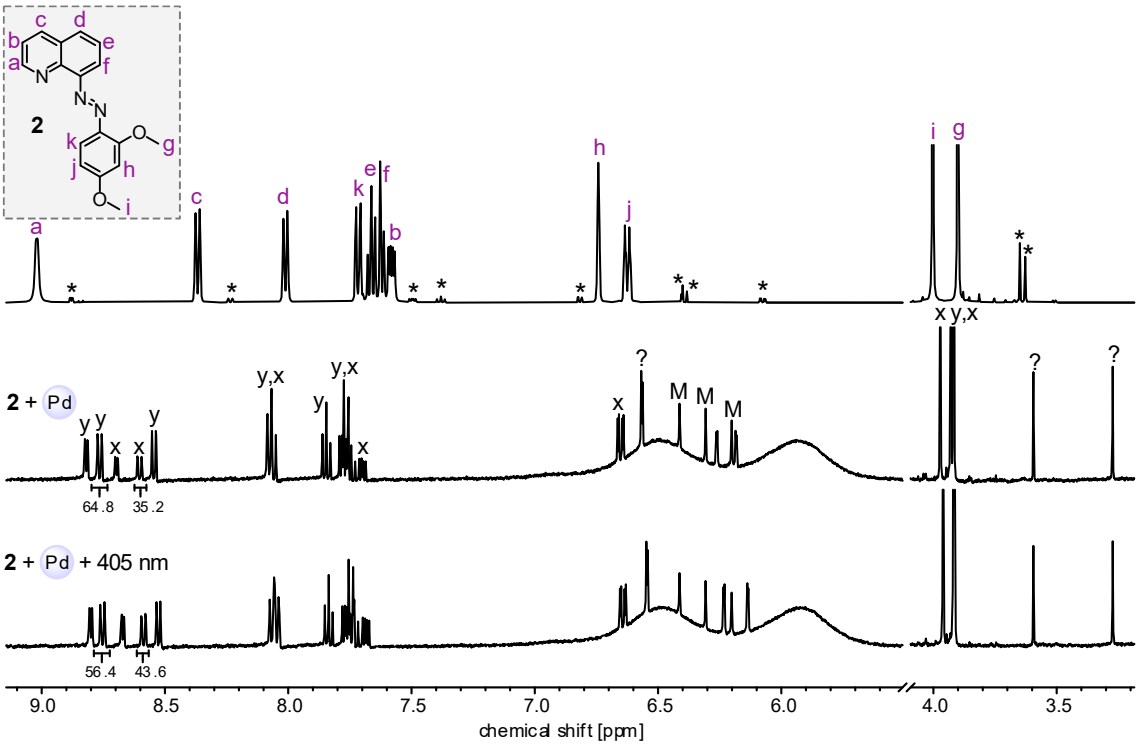

Figure 22. ^{1}H NMR spectra (500 MHz, CD_3CN, 298 K) of ligand **2** (top), its Pd(II) complex (middle), and the complex solution following 5 min irradiation with 405 nm light (bottom). Two distinct ligand environments in the complex are labelled as x and y; their assignment to specific isomers remains unresolved. Signals marked with an asterisk correspond to free ligand *Z*-**2**. Peaks marked with a question mark indicate unassigned resonances. Signals labelled M are tentatively attributed to decomposition products of MeCN.[159]

To investigate whether the two sets of signals (x and y) originated from different isomeric forms of a monoligated Pd**2** complex rather than from a Pd**2**: Pd(**2**)$_2$ mixture, the NMR sample of the Pd(II) complex was irradiated with 405 nm light for 5 min. This wavelength was chosen as it induces *E*→*Z* isomerisation in the free ligand form (Figure 21). Irradiation caused a slight change in the ratio of the two ligand environments (44:56, x:y), enriching environment x (Figure 22). These spectral changes suggest that the two environments are light-responsive and may correspond to different geometric isomers of Pd**2**. In azobenzene systems, π-π stacking anisotropy often causes the *Z*-isomer to resonate at slightly lower chemical shifts.[160,161] On this basis, environment x may correspond to *Z*-Pd**2**, as it resonates at a lower ppm value. However, a definitive

assignment would require further experiments, such as ROESY NMR, to identify key through-space correlations and proton interactions.

An important observation is that, while free ligand **2** is predominantly its *E*-isomer in solution (98:2, *E:Z*), the Pd(II) complex appears to have a much lower *E* content (either 35% or 65%, depending on the assignment). If these two environments indeed correspond to *E*-Pd**2** and *Z*-Pd**2**, this would suggest that Pd coordination does not prevent photoswitching, but rather reduces its efficiency. However, it should be emphasised that photoswitching of free ligand **2** was investigated via *in-situ* NMR due to its fast *Z*→*E* relaxation time; thus, larger changes in the x:y ratio might be observed if the irradiation experiment were to be repeated under *in-situ* conditions. These results are consistent with the hypothesis that the apparent inertness of Pd**1** stems from the rigid, tridentate chelation of ligand **1** rather than the Pd-azo interaction itself. However, further data would be needed to confirm this.

Although the ESI^+ data indicated only monoligated Pd**2** (Section 4.6.3, Figure 56), dilution of the MS sample could have favoured Pd**2** over Pd(**2**)$_2$. Thus, the presence of higher-order species cannot be completely excluded without targeted experiments. For example, a dilution series of the NMR sample would reveal whether the relative populations of x and y are concentration-dependant. Another experiment could involve preparing Pd(**2**)$_2$ at a 2:1 L:M ratio and comparing its ^{1}H NMR spectrum with that of the current sample to determine whether any of the observed environments correspond to an ML_2 species.

Having studied the photoswitching behaviour of free ligand **2**, with its coordination behaviour still only partially understood, attention next shifted to ligand **3**, which has an increased steric bulk. The main questions to be addressed were: (i) whether ligand **3** would also favour the ML_1 monoligated complex and (ii) if the coordinated form would retain photoresponsiveness.

4.4.2 Studies of derivative **3**

Ligand **3** was synthesised following an azo coupling between 2,4,6-trimethoxyaniline and quinolin-7-ol, proceeding through *in-situ* diazotisation, to give precursor $\mathbf{3^{OH}}$ (90% yield). Subsequent O-methylation of $\mathbf{3^{OH}}$ with methyl iodide, via an S_N2 mechanism, produced ligand **3** (10% yield) (Scheme 33).

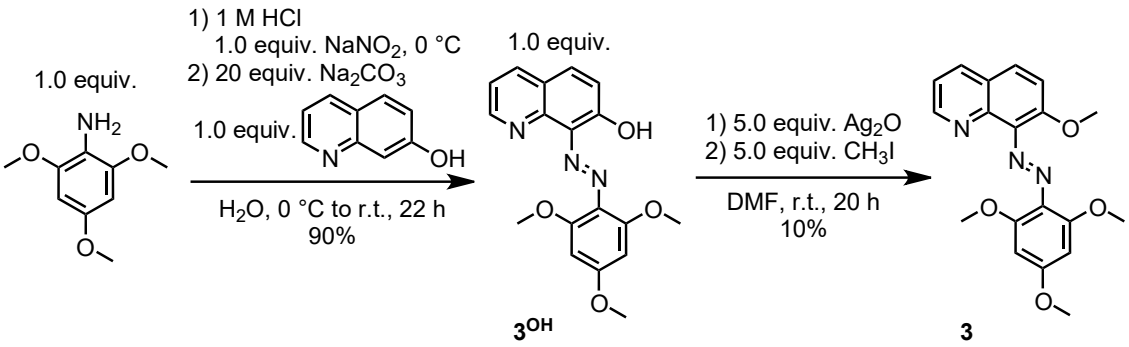

Scheme 33. Two step synthesis of ligand **3** via an azo coupling and subsequent methylation of $\mathbf{3^{OH}}$.

The photoswitching behaviour of ligand **3**, summarised in Scheme 34, was investigated in acetonitrile at 25 °C by UV-vis and ^{1}H NMR spectroscopy. The optimal wavelengths for bidirectional switching were identified as 550 nm (*E*→*Z*) and 405 nm (*Z*→*E*) via *in-situ* UV-vis measurements, as these produced the largest changes in the absorbance spectrum (Figure 23). The UV-vis spectrum of the *E*-isomer (*E*-**3**) displayed a strong π→π* absorption band centred at 320 nm (Figure 24a). Exposure to 550 nm light decreased the band intensity, consistent with conversion to its *Z*-isomer (*Z*-**3**) (Figure 24a). The switching process was fully reversible over at least ten irradiation cycles with no detectable photobleaching (Figure 24b), indicating good fatigue resistance.

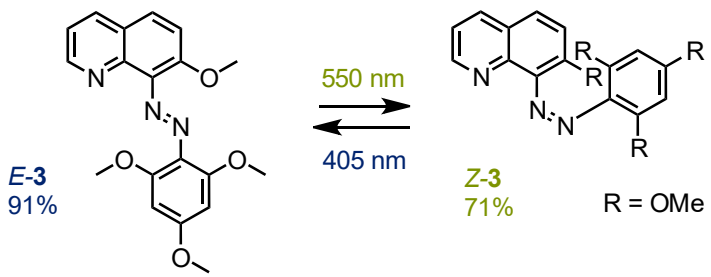

Scheme 34. *E*- and *Z*- isomer structures of ligand **3** upon irradiation with 550 nm light (*E*→*Z*, PSS 71% *Z*-**3**) and 405 nm light (*Z*→*E*, PSS 91% *E*-**3**).

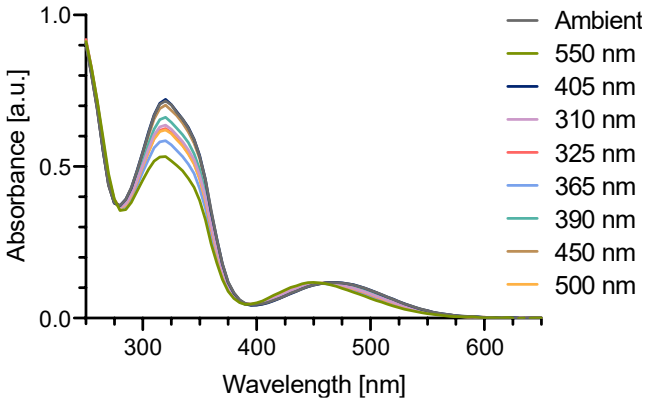

Figure 23. UV-vis spectra of ligand **3** (84 μM, CH_3CN, 25 °C) before and after irradiation with different wavelengths of light for 1 min each.

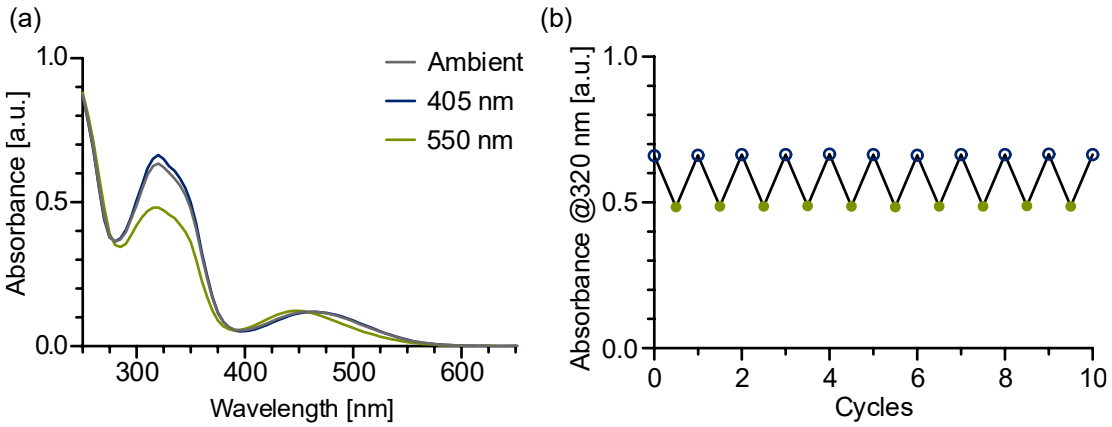

Figure 24. (a) UV-vis spectra of ligand **3** (84 μM, CH_3CN, 25 °C) under ambient light and after irradiation with 405 and 550 nm for 30 s and 3 min, respectively. (b) UV-vis switching reversibility experiment of **3** (84 μM, CH_3CN, 25 °C) showing absorbance at 320 nm after alternating light irradiation with 405 nm (30 s) and 550 nm (3 min), respectively. No apparent photodegradation was observed over 10 switching cycles.

Thermal relaxation of *Z*-**3** in the dark at 25 °C was monitored by UV-vis spectroscopy (Figure 25), revealing a thermal half-life of 29 min for the *Z*→*E* isomerisation in acetonitrile. This value falls between the thermal half-lives of *Z*-**1** and *Z*-**2** ($\tau_{½}$ = 3.7 h and 1.3 min, respectively). Although the thermal stability of *Z*-**3** is limited, it remains sufficient for subsequent NMR analysis within a few minutes after irradiation.

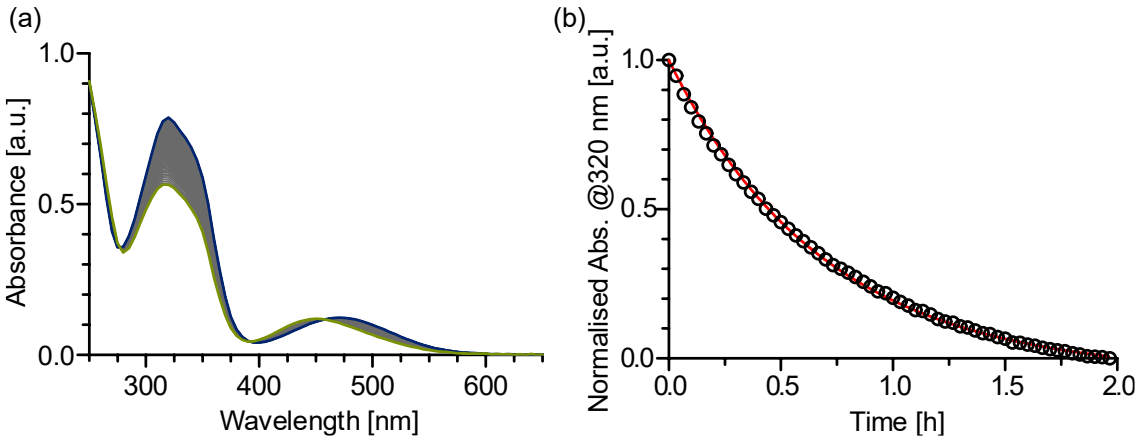

Figure 25. Thermal relaxation of ligand **3** (84 µM, CH_3CN, 25 °C). (a) UV-vis spectra of **3** measured every 1 min in the dark after irradiating with 550 nm light. (b) Change in absorption $(A_t - A_\infty) \cdot (A_0 - A_\infty)^{-1}$ plotted over time *t* following thermal relaxation of **3** to provide its half-life, $\tau_{½}$ = 29 min.

Determined by ^{1}H NMR, upon irradiation with 550 nm light *E*-**3** was converted to *Z*-**3**, achieving a PSS of 71% *Z*-**3** (Figure 26). Back-isomerisation of *Z*-**3** to *E*-**3** was accomplished by irradiation with 405 nm light, yielding a PSS of 91% *E*-**3** (Figure 26).

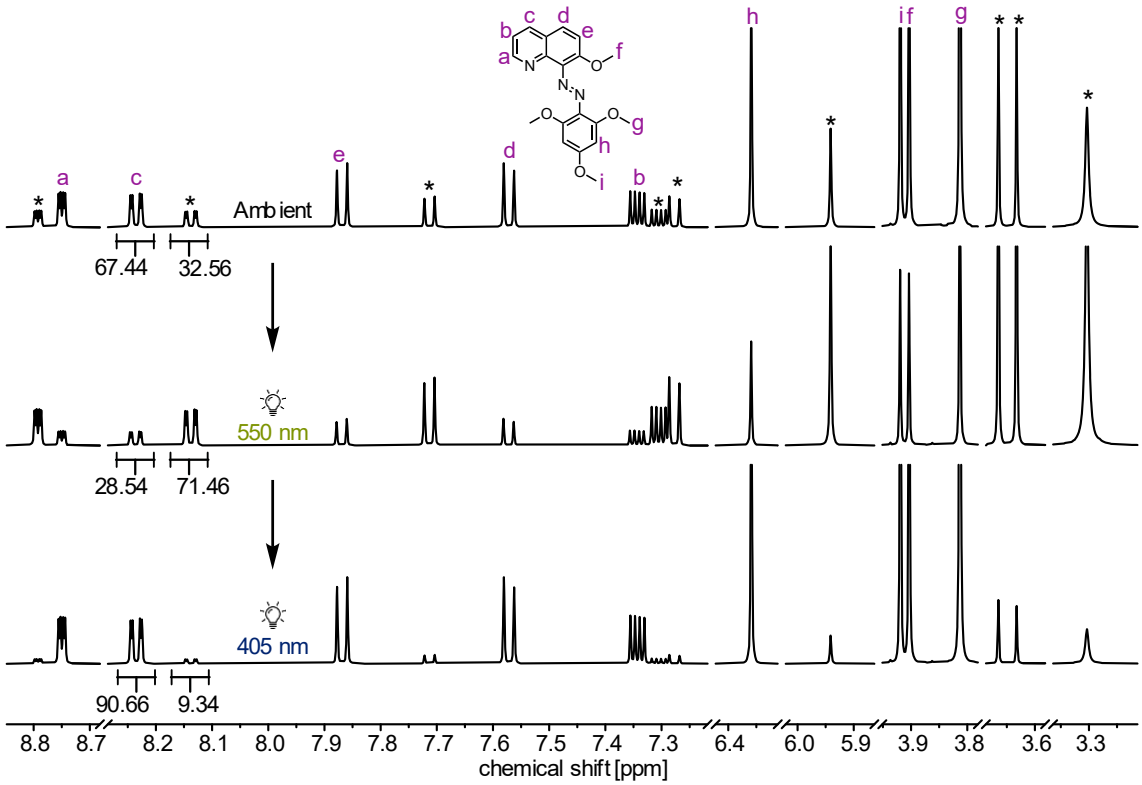

Figure 26. ^{1}H NMR spectra (500 MHz, CD_3CN, 298 K) of ligand **3** under ambient light, after irradiation with 550 nm light (10 min, PSS 71% *Z*-**3**), and after irradiation with 405 nm light (10 min, PSS 91% *E*-**3**). Signals marked with an asterisk correspond to *Z*-**3**.

Having established the photoswitching behaviour of ligand **3**, its coordination to Pd(II) was next investigated to determine how metal binding influences its switching properties. Specifically, whether ligand **3** behaves in a similar manner to the previously examined bidentate ligand **2**.

Tridentate ligand **1** can only form a single ML_1 complex, whereas the coordination mode of bidentate ligand **3** allows for multiple isomers. Even when reacted with Pd(II) in a 1:1 ligand-to-metal ratio, three complexes are possible: the monoligated Pd**3** complex, and the bis-ligated *cis*-Pd(**3**)$_2$ and *trans*-Pd(**3**)$_2$ isomers (Scheme 35).

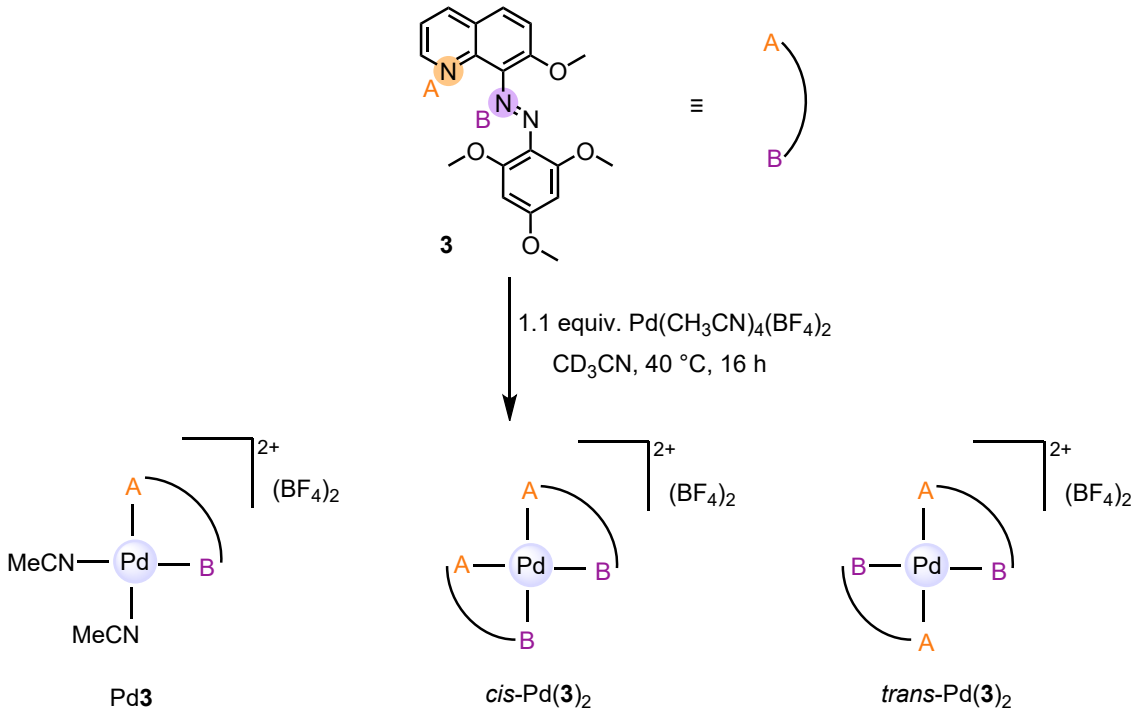

Scheme 35. A schematic representation of ligand **3** highlighting its two coordination sites: A = N-pyridine, and B = N-azo. Reaction of ligand **3** with $Pd(CH_3CN)_4(BF_4)_2$ under a 1:1 stoichiometry can theoretically yield three products: the monoligated Pd**3** complex and the bis-ligated *cis*-Pd(**3**)$_2$ and *trans*-Pd(**3**)$_2$ isomers.

Following the same synthetic procedure as for Pd**1**, equimolar amounts of ligand **3** and $Pd(CH_3CN)_4(BF_4)_2$ were combined in CD_3CN at 40 °C. ESI^+ mass spectrometry revealed three assignable peaks corresponding to $[Pd + \mathbf{3} + CN]^+$, $[Pd + (\mathbf{3})_2]^{2+}$, $[Pd + (\mathbf{3})_2 + BF_4]^+$ (Section 4.6.3, Figure 58). Notably, in contrast to the Pd(II) complex of bidentate ligand **2**, ligand **3** clearly formed a bis-ligated species detectable by mass spectrometry.

Comparison of the ^{1}H NMR spectra of free ligand **3** (*E:Z* = 67:33) and the solution after complexation with Pd(II) (Figure 27) showed complete consumption of free ligand and the appearance of two distinct ligand environments (x and y) in a 38:62 ratio. As mass spectrometry indicates the presence of both mono- and bis-ligated complexes (Section 4.6.3, Figure 58), the two distinct ligand environments observed in the ^{1}H NMR spectrum likely correspond to Pd**3** and Pd(**3**)$_2$. The bis-ligated complex displays only a single ligand environment, which is consistent with either a *trans* arrangement (C_2 symmetry) or a *cis* arrangement (inversion centre). However, the steric bulk introduced by the tetra-*ortho*-substitution strongly favours the *trans* configuration, as a *cis* arrangement would bring the OMe groups of each ligand into close proximity, resulting in unfavourable steric interactions. Although the formation of *trans*-Pd(**3**)$_2$ prevents a direct structural comparison with the parent complex Pd**1**, irradiation remains worthwhile to determine whether the coordinated ligand **3** can undergo photoisomerisation despite its altered coordination geometry.

Upon light irradiation of the Pd(II) complex mixture at 550 nm, a wavelength that efficiently induces *E*→*Z* isomerisation in free ligand **3** (Figure 26), no change was detected in the relative ratio of environments x and y (Figure 27). Moreover, no additional signals indicative of new species were observed (Figure 27).

Additional irradiation experiments with 365 nm and 405 nm light produced no observable changes in the ^{1}H NMR spectra (Figure 27), consistent with Pd(II) coordination suppressing photoswitching of **3**. The potential effect of other wavelengths could be examined in future *in-situ* ^{1}H NMR studies to account for rapid thermal relaxation of the Pd(II) complexes.

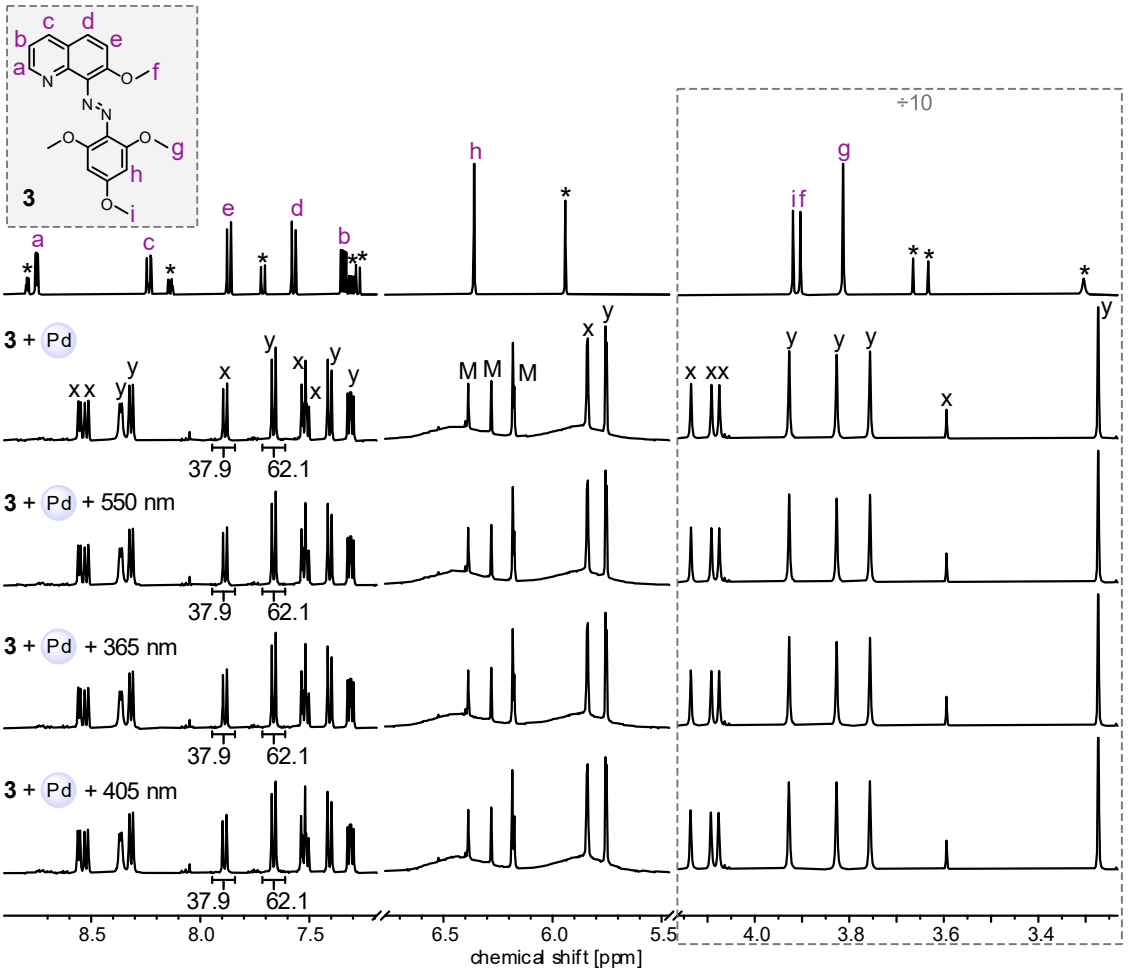

Figure 27. ^{1}H NMR spectra (500 MHz, CD_3CN, 298 K) of ligand **3**, its Pd(II) complex, and the complex solution following light irradiation with: 550 nm, 365 nm, and 405 nm (5 min each). Two distinct ligand environments in the complex are labelled as x and y; their assignment to specific complexes remains unresolved. Signals marked with an asterisk correspond to free ligand *Z*-**3**. Signals labelled M are tentatively attributed to decomposition products of MeCN.[159]

Although the precise assignment of ligand environments x and y to mono- versus bis-ligated complexes remains uncertain, the results suggest that Pd(II) coordination suppresses photoswitching of **3** under the conditions tested, as was also observed for tridentate ligand **1**. The greater steric bulk of ligand **3** compared to ligand **2** may further contribute to the loss of photoresponsiveness in its complexes.

Having established the behaviour of ligand **3**, attention then turned to ligand **4**, which is structurally related. The principal questions to address were whether ligand **4** would also form both ML_1 and bis-ligated species, and whether its coordinated forms would similarly exhibit complete suppression of photoresponsiveness upon light irradiation.

4.4.3 Studies of derivative **4**

Ligand **4** was synthesised following an azo coupling between 3,4,5-trimethoxyaniline and quinolin-7-ol, proceeding through *in-situ* diazotisation, to give precursor $\mathbf{4^{OH}}$ (55-95% yield). Subsequent O-methylation of $\mathbf{4^{OH}}$ with dimethyl sulfate, via an S_N2 mechanism, produced ligand **4** (15% yield) (Scheme 36).

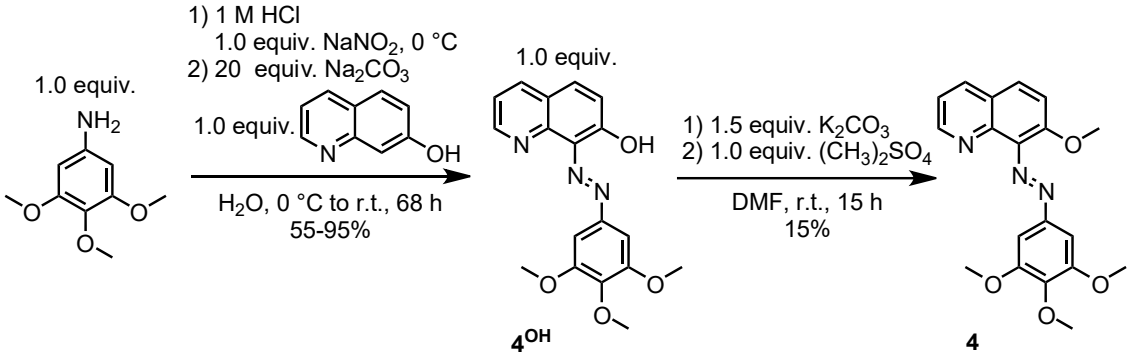

Scheme 36. Two step synthesis of ligand **4** via an azo coupling and subsequent methylation of $\mathbf{4^{OH}}$.

The photoswitching behaviour of ligand **4**, summarised in Scheme 37, was investigated in acetonitrile at 25 °C by UV-vis and ^{1}H NMR spectroscopy. The optimal wavelengths for bidirectional switching were identified as 365 nm (*E*→*Z*) and 405 nm (*Z*→*E*) via *in-situ* UV-vis measurements, as these produced the largest changes in the absorbance spectrum (Figure 28). The UV-vis spectrum of the *E*-isomer (*E*-**4**) displayed a strong π→π* absorption band centred at 335 nm (Figure 29a). Exposure to 405 nm light decreased the band intensity, consistent with conversion to its *Z*-isomer (*Z*-**4**) (Figure 29a). The switching process was fully reversible over at least ten irradiation cycles with no detectable photobleaching (Figure 29b), indicating good fatigue resistance.

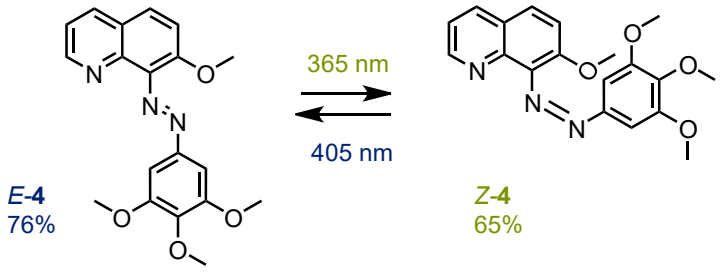

Scheme 37. *E*- and *Z*-isomer structures of ligand **4** upon irradiation with 365 nm light (*E*→*Z*, PSS 65% *Z*-**4**) and 405 nm light (*Z*→*E*, PSS 76% *E*-**4**).

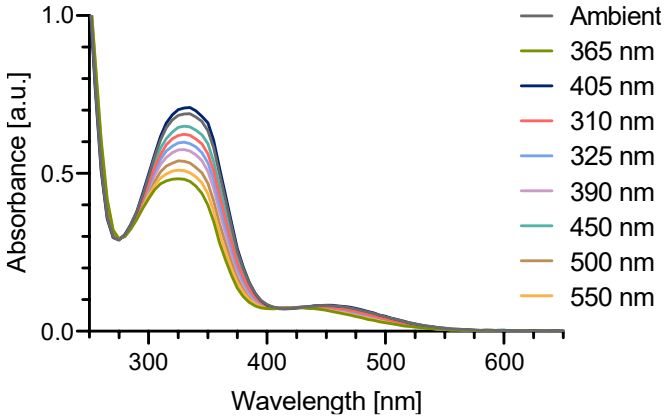

Figure 28. UV-vis spectra of ligand **4** (78 μM, CH_3CN, 25 °C) before and after irradiation with different wavelengths of light for 1 min each.

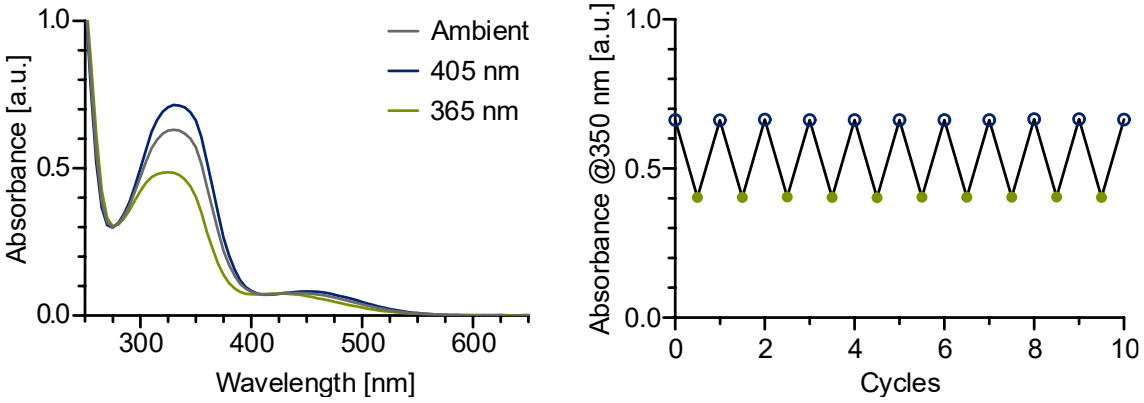

Figure 29. (a) UV-vis spectra of ligand **3** (78 μM, CH_3CN, 25 °C) under ambient light and after irradiation with 405 and 365 nm for 1 min, respectively. (b) UV-vis switching reversibility experiment of **4** (78 μM, CH_3CN, 25 °C) showing absorbance at 350 nm after alternating light irradiation with 405 nm (30 s) and 365 nm (30 s), respectively. No apparent photodegradation was observed over 10 switching cycles.

Thermal relaxation of *Z*-**4** in the dark at 25 °C was monitored by UV-vis spectroscopy (Figure 30), revealing a thermal half-life of 31 h for the *Z*→*E* isomerisation in acetonitrile. This value exceeds those measured for *Z*-**1**, *Z*-**2**, and *Z*-**3** ($\tau_{½}$ = 3.7 h, 1.3 min, and 29 min, respectively). The high thermal stability of *Z*-**4** readily permits controlled photoswitching experiments and ensures that the *Z*-isomer remains stable for subsequent NMR analysis without the need for *in-situ* irradiation.

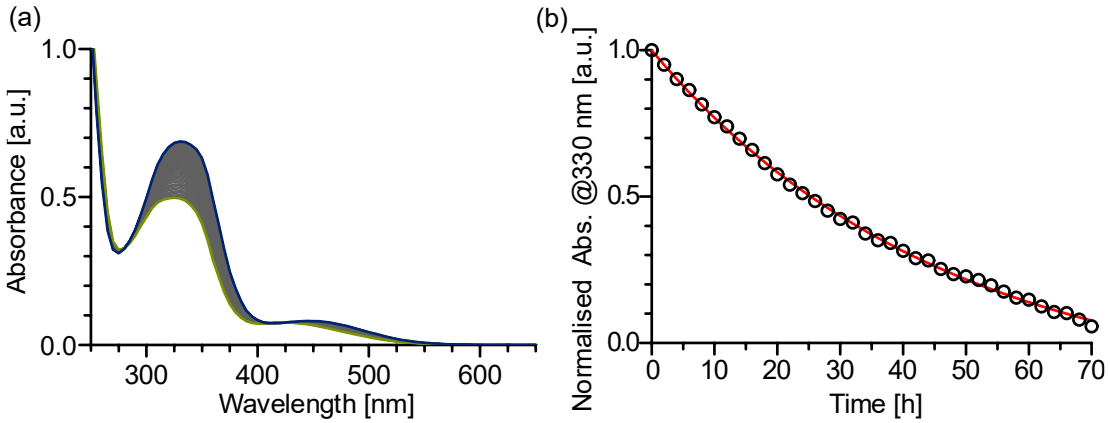

Figure 30. Thermal relaxation of ligand **4** (78 µM, CH_3CN, 25 °C). (a) UV-vis spectra of **4** measured every 1 h in the dark after irradiating with 365 nm light. (b) Change in absorption $(A_t - A_\infty) \cdot (A_0 - A_\infty)^{-1}$ plotted over time *t* following thermal relaxation of **4** to provide its half-life, $\tau_{½}$ = 31 h.

Determined by ^{1}H NMR, irradiation with 365 nm light converted *E*-**4** to *Z*-**4**, achieving a PSS of 65% *Z*-**4** (Figure 31). Back-isomerisation of *Z*-**4** to *E*-**4** was achieved by irradiating with 405 nm light, yielding a PSS of 76% *E*-**4** (Figure 31). Interestingly, in contrast to ligands **1**-**3**, the *Z*-isomer of **4** was present in slightly higher amounts than its *E*-isomer (47:53, *E:Z*). However, this does not necessarily indicate that *Z*-**4** is intrinsically more stable; the observed ratio is probably the result of partial photoisomerisation caused by exposure to ambient light during sample handling, since standard non-amberised NMR tubes were used.

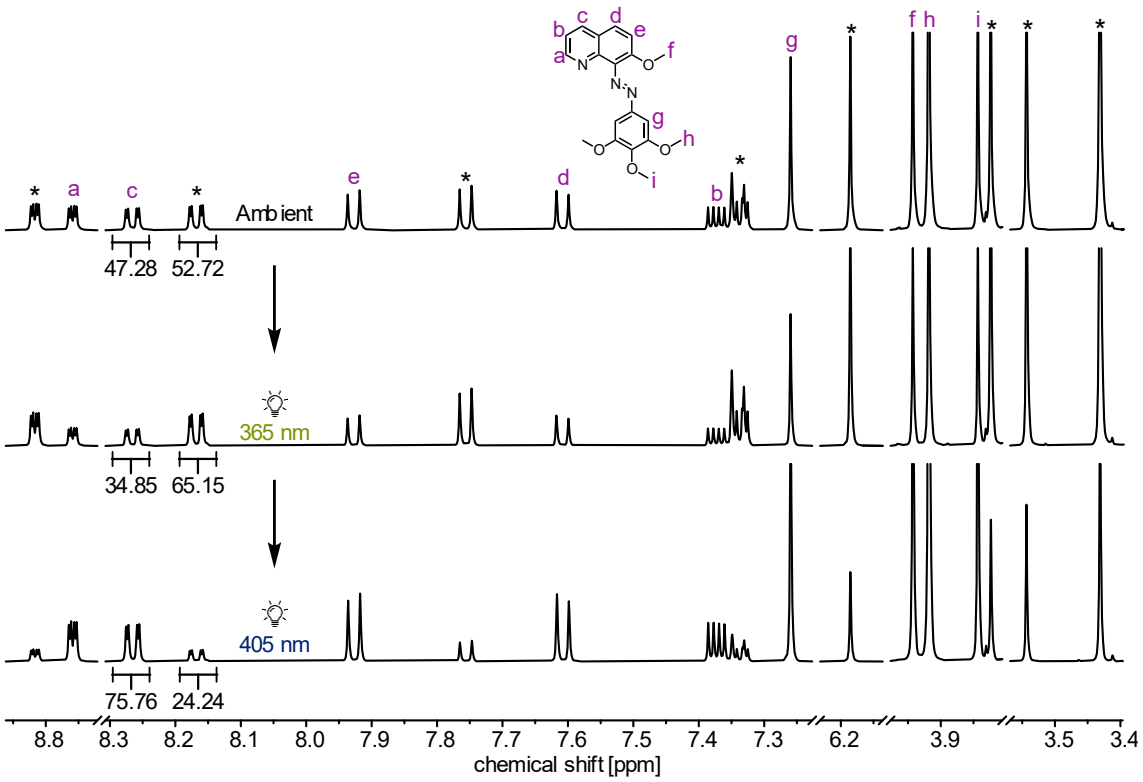

Figure 31. ^{1}H NMR spectra (500 MHz, CD_3CN, 298 K) of ligand **4** under ambient light, after irradiation with 365 nm light (10 min, PSS 65% *Z*-**4**), and after irradiation with 405 nm light (10 min, PSS 76% *E*-**4**). Signals marked with an asterisk correspond to *Z*-**4**.

Having established the photoswitching behaviour of ligand **4**, its coordination to Pd(II) was next examined to determine whether metal complexation affects its photoresponsive properties similarly to bidentate ligand **2** or ligand **3**.

Whereas tridentate ligand **1** forms only a single ML_1 complex, the bidentate nature of ligand **4** permits multiple isomeric assemblies. Even when reacted with Pd(II) in a 1:1 ligand-to-metal ratio, three complexes are possible: the monoligated Pd**4** complex, and the bis-ligated *cis*-Pd(**4**)$_2$ and *trans*-Pd(**4**)$_2$ isomers (Scheme 38).

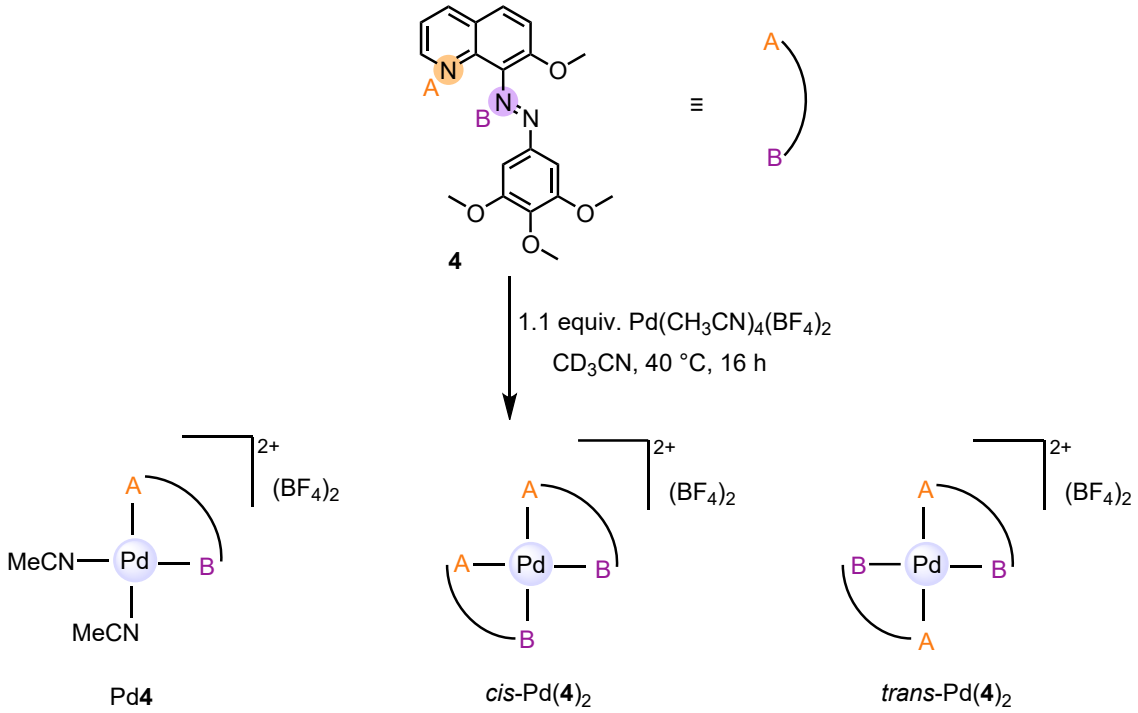

Scheme 38. A schematic representation of ligand **4** highlighting its two coordination sites: A = N-pyridine, and B = N-azo. Reaction of ligand **4** with $Pd(CH_3CN)_4(BF_4)_2$ under a 1:1 stoichiometry can theoretically yield three products: the monoligated Pd**4** complex and the bis-ligated *cis*-Pd(**4**)$_2$ and *trans*-Pd(**4**)$_2$ isomers.

Following the synthetic procedure established for Pd**1**, equimolar amounts of ligand **4** and $Pd(CH_3CN)_4(BF_4)_2$ were combined in CD_3CN and heated at 40 °C. ESI^+ mass spectrometry revealed four assignable peaks corresponding to $[Pd + \mathbf{4} - H]^+$, $[Pd + \mathbf{4} - H + CH_3CN]^+$, $[Pd + (\mathbf{4})_2]^{2+}$, and $[Pd + (\mathbf{4})_2 + BF_4]^+$ (Section 4.6.3, Figure 60). Notably, in contrast to the Pd(II) complex of bidentate ligand **2**, ligand **4** clearly formed a bis-ligated species detectable by mass spectrometry, reminiscent of the behaviour observed for ligand **3**.

Comparison of the ^1H NMR spectra of free ligand **4** ($E:Z = 47:53$) and the solution following Pd(II) (Figure 32) demonstrated complete consumption of free ligand **4** and the emergence of two distinct ligand environments (x and y) in a 45:55 ratio. Based on the mass spectrometry data showing both mono- and bis-ligated complexes (Section 4.6.3, Figure 60), one environment can be assigned to Pd**4** and the other to Pd(**4**)$_2$. The bis-ligated complex displays a single ligand environment, which could correspond to either a *trans* arrangement (C_2 symmetry) or a *cis* arrangement (inversion centre). However, the steric bulk introduced by the OMe groups favours the *trans* configuration, as a *cis*

arrangement would bring these substituents into close proximity, resulting in unfavourable steric interactions. Although the formation of *trans*-Pd(**4**)$_2$ prevents a direct structural comparison with Pd**1**, irradiation experiments can still assess whether ligand **4** retains its photoisomerisation capability when coordinated.

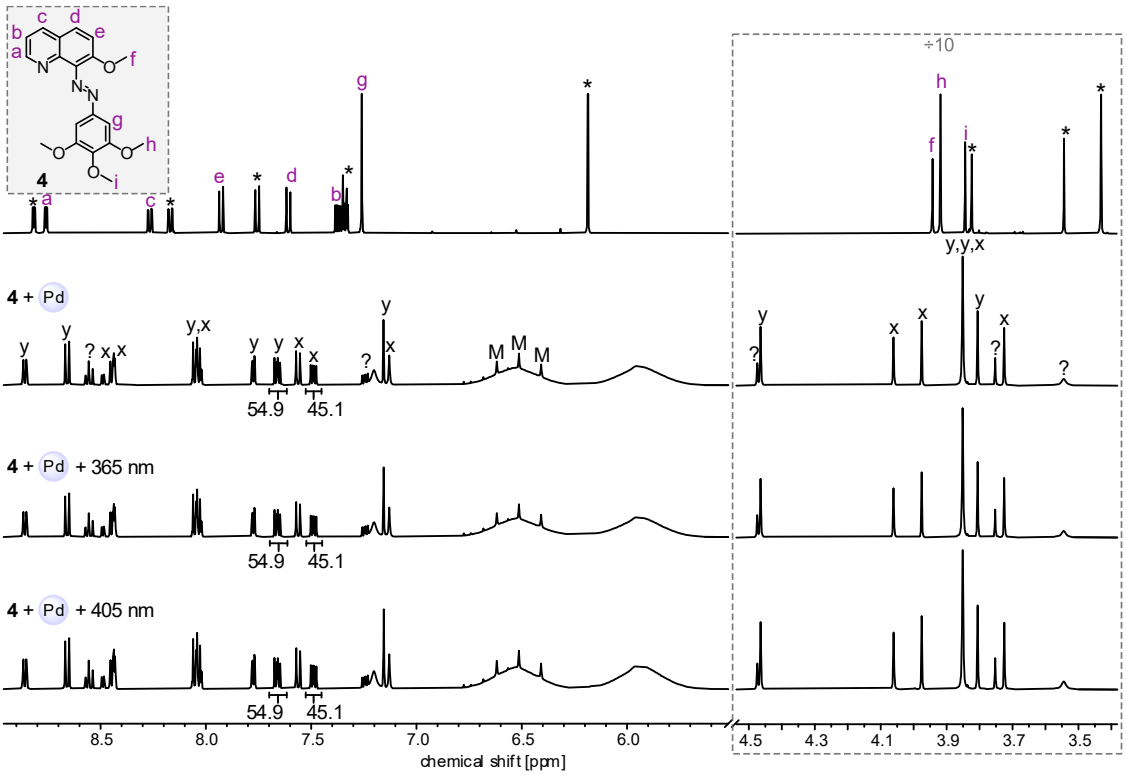

Figure 32. ^{1}H NMR spectra (500 MHz, CD_3CN, 298 K) of ligand **4**, its Pd(II) complex, and the complex solution following light irradiation with: 365 nm and 405 nm (5 min each). Two distinct ligand environments in the complex are labelled as x and y; their assignment to specific complexes remains unresolved. Signals marked with an asterisk correspond to free ligand *Z*-**4**. Peaks marked with a question mark indicate unassigned resonances. Signals labelled M are tentatively attributed to decomposition products of MeCN.[159]

Upon light irradiation of the Pd(II) complex mixture at 365 nm, a wavelength known to efficiently induce *E*→*Z* isomerisation in free ligand **4** (Figure 31), no changes were detected in the relative ratio of environments x and y, nor were any additional signals indicative of new species were observed (Figure 32).

Additional irradiation of the Pd(II) complexes with 405 nm light produced no observable changes in the ^{1}H NMR spectra (Figure 32), suggesting that photoswitching is suppressed upon coordination. Future *in-situ* ^{1}H NMR studies could: (i) establish whether other

wavelengths induce isomerisation, and (ii) exclude the possibility of rapid thermal relaxation of the Pd(II) complexes.

Although the precise assignment of ligand environments x and y to mono- versus bis-ligated complexes remains uncertain, the results suggest that Pd(II) coordination supressed photoswitching of **4** under the conditions tested, as was also observed for tridentate ligand **1** and bidentate ligand **3**.

4.5 Outlook and conclusion

This chapter examined the influence of metal coordination on the photoswitching properties of azobenzene-based ligands, using a tridentate quinoline–azo–pyridine scaffold (ligand **1**) and its bidentate derivatives (ligands **2**-**4**) as model systems. The free ligands exhibited distinct photophysical behaviours, summarised in Table 1. The *Z*-isomer PSS values where very similar across the series, differing by no more than 6% (65-71% *Z*-**L**). In contrast, the *E*-isomer PSS values showed greater variation: ligands **1**-**3** all exceeded 90% *E*-**L**, whereas ligand **4** was significantly lower at 76%. The most pronounced differences, however, were observed in the thermal half-lives (measured in acetonitrile at 25 °C), which spanned several orders of magnitude from 1.3 min to 31 h. Despite no clear trend being identified, these results underscore the importance of substitution pattern in tuning both switching efficiencies and *Z*-isomer stabilities.

Coordination to Pd(II) had a substantial effect on photoswitching. In the case of tridentate ligand **1**, complexation yielded a single, exclusively *E*-Pd**1** species that was inert to photoisomerisation across a wide range of wavelengths and temperatures. This complete suppression of photoswitching is likely a consequence of direct azo (N=N) coordination combined with the strong chelating effect of the tridentate ligand. Attempts to restore light-responsiveness through competitive ligand binding (pyridine or bipyridine) produced minor and irreversible spectral changes, with no conclusive evidence of *E*→*Z* isomerisation.

In contrast, bidentate ligand **2** formed Pd(II) complexes featuring two distinct ligand environments in solution. Preliminary ^{1}H NMR irradiation experiments suggest that some degree of isomerisation may occur, however, the precise assignment of these two ligand

environments remains unresolved and will require further structural (e.g., ROESY NMR) and photochemical analysis (*in-situ* UV-vis).

Ligands **3** and **4** formed mixtures of mono-ligated (ML_1) and bis-ligated (ML_2) complexes, complicating direct structural and photochemical comparison to parent model Pd**1**. Although the ^{1}H NMR assignment of the mono- and bis-ligated complexes remains uncertain, the key observation holds: Pd(II) coordination inhibits photoswitching of both **4** and **3**, as was also observed for tridentate ligand **1**. To enable cleaner comparisons in the future, *cis*-protected Pd(II) metal salts (e.g., cis-Pd(DPPP)$(CH_3CN)_2(BF_4)_2$) should be tested to ensure the exclusive formation of ML_1 species with ligands **2**-**4**.

Overall, these results show that Pd(II) coordination can either partially or completely inhibit the photoswitching of azobenzene derivatives, with the extent of suppression influenced by ligand denticity, donor arrangement, and substitution pattern. Across ligands **1**-**4**, the results indicated that direct N=N–metal coordination should be avoided if preserving the photoswitching capacity is essential. This principle forms the basis for larger light-responsive metal–ligand assemblies, which are explored in the subsequent chapters. In these assemblies, the deliberate avoidance of azo–metal binding enables the photoswitching behaviour to be preserved in more complex supramolecular systems.

Table 1. Summarised photoswitching properties of ligands **1**-**4** and their respective complexes in acetonitrile.

Ligand	PSS *E*-L (%)	PSS *Z*-L (%)	$\tau_{½}$ (298 K)	ML_1	ML_2	Complex switching
1	92[a]	67[b]	3.7 h	✓	n.d.	n.d.
2	>99	69[c]	1.3 min	✓	n.d.	✓
3	91[c]	71[d]	29 min	✓	✓	n.d.
4	76[c]	65[e]	31 h	✓	✓	n.d.

[a] 310 nm; [b] 390 nm; [c] 405 nm; [d] 550 nm; [e] 365 nm; n.d. = not detected by ^{1}H NMR and/or ESI^+.

4.6 Experimental

4.6.1 General information

Reagents and materials. Commercial solvents and reagents were purchased from abcr, Acros Organics, Alfa Aesar, BLD-Pharm, Merck, Sigma Aldrich, TCI, Thermo Fisher Scientific, and used as received unless otherwise stated.

Schlenk techniques. Reactions involving air-sensitive reagents were conducted under an argon atmosphere using standard Schlenk techniques. When moisture sensitivity was also a concern, all glassware was thoroughly heat-dried before use.

Column chromatography. Flash column chromatography was performed using a puriFlash 5.020 system (Interchim) equipped with PuriFlash 15 µm Si HP cartridges (Interchim).

NMR spectroscopy. NMR spectra were recorded on Bruker spectrometers operating at 400 MHz, 500 MHz, or 700 MHz (Avance I 400, Avance I 500, Avance III HD Prodigy 500, Avance III HD Ascend 700). Chemical shifts (δ, in ppm) are referenced to residual solvent peaks: CD_3CN (^1H: 1.94 ppm, ^{13}C: 1.32 ppm) or DMSO-d_6 (^1H: 2.50 ppm, ^{13}C: 39.52 ppm). Reported data include chemical shift, relative integral, multiplicity, coupling constants (in Hz), and assignment. Multiplicities are abbreviated as follows: s, singlet; d, doublet; t, triplet; m, multiplet. Spectra were processed (phase and baseline corrections, integration, peak assignment) using MestReNova 14.2.1 (Mestrelab) and TopSpin 4.1.3 (Bruker BioSpin), with all operations manually verified to ensure fidelity to the raw data.

Mass spectrometry. High resolution mass spectra were acquired on an Orbitrap XL instrument (Thermo Fischer Scientific) and analysed using XCalibur 4.2 software (Thermo Fischer Scientific).

UV-vis spectroscopy. UV-vis absorption spectra were measured on a Cary 60 spectrometer (Agilent) equipped with a flash lamp and temperature-controlled cuvette holder. Data analysis and visualisation were performed using Spectragryph (v1.2.16.1) and GraphPad Prism (v8.0.2).

Light sources. *In-situ* illumination during NMR and UV-vis measurements were conducted using Prizmatrix FC5-LED fibre collimated multichannel LED sources. Additional NMR illumination experiments with 365 nm and 405 nm light were performed using a custom-built portable light source incorporating commercial Nichia LED chips: NCSU275(T)-U365 (1.8 W) for 365 nm and NVSU233B(T)-U405 (1,4 W) for 405 nm.

Table 2. Light output of fibre coupled LEDs.

λ [nm]	**310**	**325**	**365**	**390**	**405**	**430**	**450**	**500**	**550**	**655**	**white**
Output power [mW] (1 m optical fibre)	1	8.6	170	220	260	160	440	165	165	140	74

4.6.2 Photoswitching studies

NMR LED irradiation. This method was previously described by our group.[74] The following description was added here for convenience: "Portable, in-house built light sources fitted with custom 3D-printed adapters were used to irradiate NMR samples. After the irradiation was completed, the samples were promptly subjected to measurement."

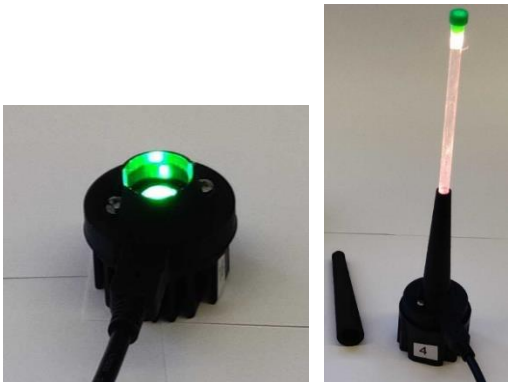

Figure 33. LED illumination setup with USB-powered homemade light sources using commercial LED chips with 3D-printed adaptors for 2 mL GC vials and 5 mm NMR tubes.[74] Reproduced from [74], © 2025 The Authors, published under CC BY 4.0 license. No changes were made.

***In-situ* NMR irradiation.** This method was adapted from literature[162,163] and previously described by our group.[164] The following description was added here for convenience: “An NMR sample tube was fitted with an insert tube made of quartz glass, and a quartz glass optical fibre was pushed down into the insert. The end of this fibre was non-terminated, and the exposed surface had been roughened to ensure even and omnidirectional illumination. This construction was lowered into the NMR device using an aluminium rod to avoid damage to the fibre. The other end of the optical fibre was connected to a fibre-collimated LED light source so the sample could be irradiated inside the spectrometer.”

Figure 34. NMR sample with quartz glass insert and optical fibre for *in-situ* illumination during NMR experiments.[164] Reproduced from [74], © 2025 The Authors, published under CC BY 4.0 license. No changes were made.

***In-situ* irradiation (UV-vis).** This method was previously described by our group.[74] The following description was added here for convenience: “Samples were irradiated perpendicularly to the measurement axis within the UV-vis spectrometer using optical fibres connected to an LED light source. To facilitate the irradiation of the cuvettes perpendicularly to the spectrometer's measurement axis, a hole matching the diameter of the quartz glass fibre was drilled at the centre of the Teflon stopper used to seal the UV-vis cuvettes. This configuration enabled the connection of an optical fibre to the cuvette, allowing the irradiation of the samples from above.”

Figure 35. UV-vis *in-situ* illumination setup showing fibre collimated LED-sources connected to the cuvette with open (left) and closed measurement chamber (right).[74] Reproduced from [74], © 2025 The Authors, published under CC BY 4.0 license. No changes were made.

Photostationary state determination. The PSS of each photoswitch was quantified by ^{1}H NMR spectroscopy. In line with literature guidelines,[73,165] the PSS was calculated for each compound by integrating two well-resolved, non-overlapping signals corresponding to the same proton and using their relative areas.

Thermal half-life determination. Thermal *Z*→*E* isomerisation kinetics were determined by UV-vis absorption spectroscopy. Samples of each ligand were first irradiated with an appropriate wavelength of light to generate a *Z* enriched PSS. The solutions were then kept in the dark at 25 °C while spectra were recorded at defined time. For each compound, the wavelength exhibiting the largest change in absorbance between the *E*- and *Z*-isomers was selected for analysis. The absorbance values at this wavelength were normalised to the initial spectrum and plotted against time (t). The resulting decay curves were fitted to a first-order exponential function (Equation **1**) to obtain the rate constant (k), from which the thermal half-life ($\tau_{½}$) was then calculated as $\tau_{½} = \ln(2)/k$.

$$A^{\text{normalised}} = \frac{A_t - A_\infty}{A_0 - A_\infty} = e^{-kt} \qquad \textbf{(1)}$$

4.6.3 Synthesis

(*E*)-2-(quinolin-8-yldiazenyl) pyridine-3,5-diol (**1^{OH}**)

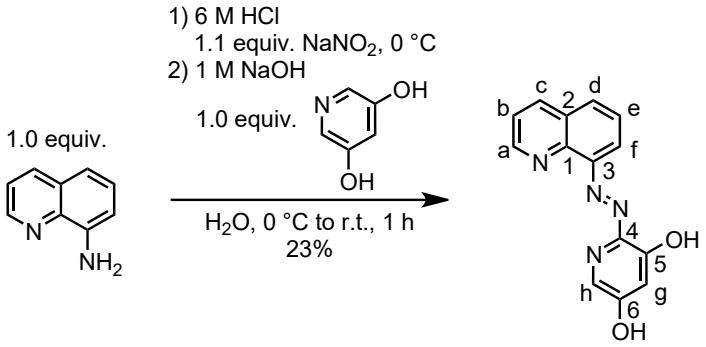

Quinolin-8-amine (100.6 mg, 693.6 µmol, 1.0 equiv.) was dissolved in HCl (6 M, 10 mL) and placed in an ice bath. Pyridine-3,5-diol (77.1 mg, 693.6 µmol, 1.0 equiv.) was dissolved in NaOH (1 M, 20 mL) and placed in an ice bath. $NaNO_2$ (52.6 mg, 763.0 µmol, 1.1 equiv.) was dissolved in 0 °C H_2O (5 mL) and added to the quinolin-8-amine solution. Subsequently, the quinoline solution was added dropwise to the pyridine-3,5-diol solution. A colour change from yellow to dark red was observed. After stirring for 1 h at room temperature, NaOH (1 M, 35 mL) was added until pH 5 was reached. Brown solid precipitated which was filtered through gravity filtration, washed with HCl (10^{-5} M, 100 mL) and left to dry in the filter for 48 h to yield the desired product as a dark brown solid (42.48 mg, 159.5 µmol, 23%).

$C_{14}H_{10}N_4O_2$ 266.26 g/mol

R_F value (CH_2Cl_2 / MeOH 95:5 (*v*/*v*)) = 0.26

^{1}H NMR (500 MHz, DMSO-d_6, 298 K) δ_H [ppm] = 6.54 (d, J = 2.6 Hz, 1H, H-g), 7.71 (dd, J = 8.3, 4.2 Hz, 1H, H-b), 7.78 (t, J = 7.9 Hz, 1H, H-e), 8.01 (d, J = 2.6 Hz, 1H, H-h), 8.06 (dd, J = 8.2, 1.3 Hz, 1H, H-d), 8.17 (dd, J = 7.7, 1.3 Hz, 1H, H-f), 8.51 (dd, J = 8.4, 1.7 Hz, 1H, H-c), 9.06 (dd, J = 4.2, 1.7 Hz, 1H, H-a).

^{13}C NMR (126 MHz, DMSO-d_6, 298 K) δ_C [ppm] = 110.2 (C-g), 114.3 (C-f), 123.1 (C-b), 127.6 (C-e), 129.1 (C-d), 137.0 (C-c), 137.5 (C-h), 139.9 (C-2), 140.9 (C-1), 141.2 (C-3), 142.7 (C-4), 150.8 (C-5), 151.5 (C-a), 159.6 (C-6).

HRMS (ESI$^+$): *m*/*z* (relative intensity) = 267.0873 (100%, [M+Na$^+$], calcd 267.0977).

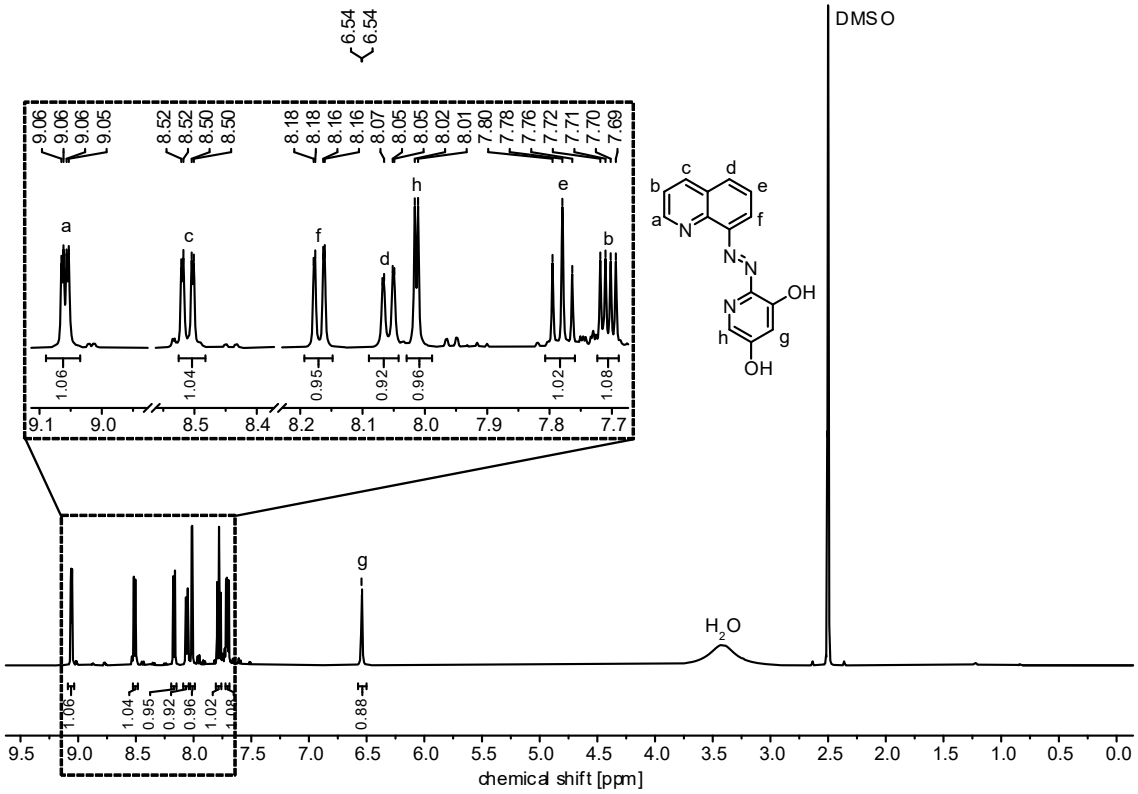

Figure 36. ^{1}H NMR spectrum (500 MHz, DMSO-*d*$_6$, 298 K) of **1**^{OH}.

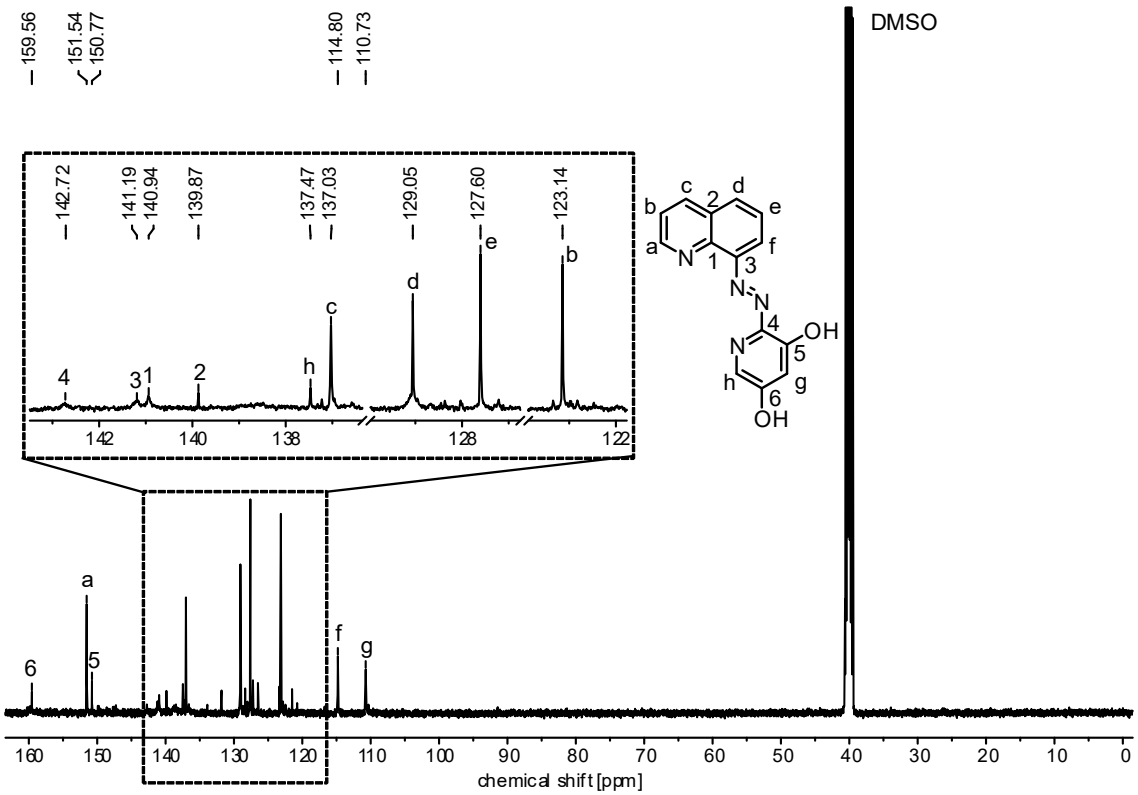

Figure 37. ^{13}C NMR spectrum (126 MHz, DMSO-*d*$_6$, 298 K) of **1**^{OH}.

(*E*)-8-((3,5-dimethoxypyridin-2-yl) diazenyl) quinoline (**1**)

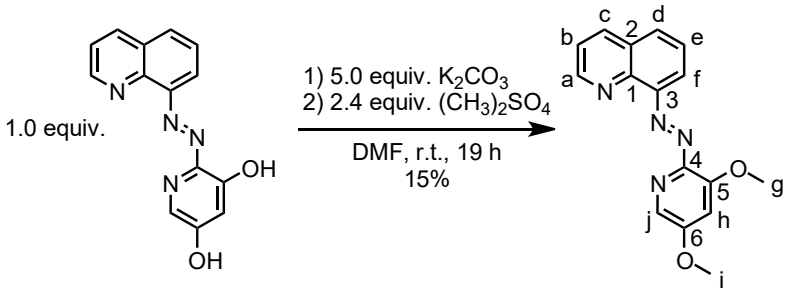

Under an argon atmosphere, $\mathbf{1^{OH}}$ (102.0 mg, 383.1 µmol, 1.0 equiv.) and dry K_2CO_3 (264.9 mg, 1.917 mmol, 5.0 equiv.) were dissolved in dry DMF (18 mL) and stirred for 15 min. Dimethyl sulfate (115.7 mg, 917.3 µmmol, 2.4 equiv.) was then added, and the mixture was stirred overnight (19 h) at ambient temperature. Then, H_2O (2 mL) was added, and the mixture was filtered through a celite plug using acetone (~20 mL). After the removal of acetone under reduced pressure, the remaining mixture was extracted with CH_2Cl_2 (3 x 15 mL), the combined organic layers were washed with brine (3 x 10 mL) and dried over Na_2SO_4. Residual solvents were removed under reduced pressure and the residue was subjected to column chromatography (DCM/*i*PrOH, 100/0 (*v/v*) to DCM/*i*PrOH, 0/100 (*v/v*)). (*E*)-8-((3,5-dimethoxypyridin-2-yl) diazenyl) quinoline **1** was isolated as a yellow-brown solid (16.91 mg, 57.46 µmol, 15%).

$C_{16}H_{14}N_4O_2$ 294.31 g/mol

R_F value (CH_2Cl_2 / *i*PrOH 95:5 (*v/v*)) = 0.22

^{1}H NMR (500 MHz, CD_3CN, 298 K) δ_H [ppm] = 3.98 (s, 3H, H-i), 4.03 (s, 3H, H-g), 7.18 (d, *J* = 2.5 Hz, 1H, H-h), 7.59 (dd, *J* = 8.3, 4.1 Hz, 1H, H-b), 7.67 (s, 1H, H-f), 7.68 (d, *J* = 2.9 Hz, 1H, H-e), 7.91 (d, *J* = 2.5 Hz, 1H, H-j), 8.07 (m, 1H, H-d), 8.38 (dd, *J* = 8.3, 1.7 Hz, 1H, H-c), 9.03 (dd, *J* = 4.2, 1.8 Hz, 1H, H-a).

^{13}C NMR (126 MHz, CD_3CN, 298 K) δ_C [ppm] = 57.2 (C-g), 57.2 (C-i), 107.4 (C-h), 116.5 (C-f), 123.1 (C-b), 127.6 (C-e), 128.7 (C-j), 130.2 (C-2), 131.8 (C-d), 137.2 (C-c), 145.3 (C-3), 147.4 (C-5), 151.5 (C-1), 152.1 (C-a), 155.7 (C-4), 160.4 (C-6).

HRMS (ESI^+): *m/z* (relative intensity) = 295.1185 (100%, [M+Na^+], calcd 295.1195).

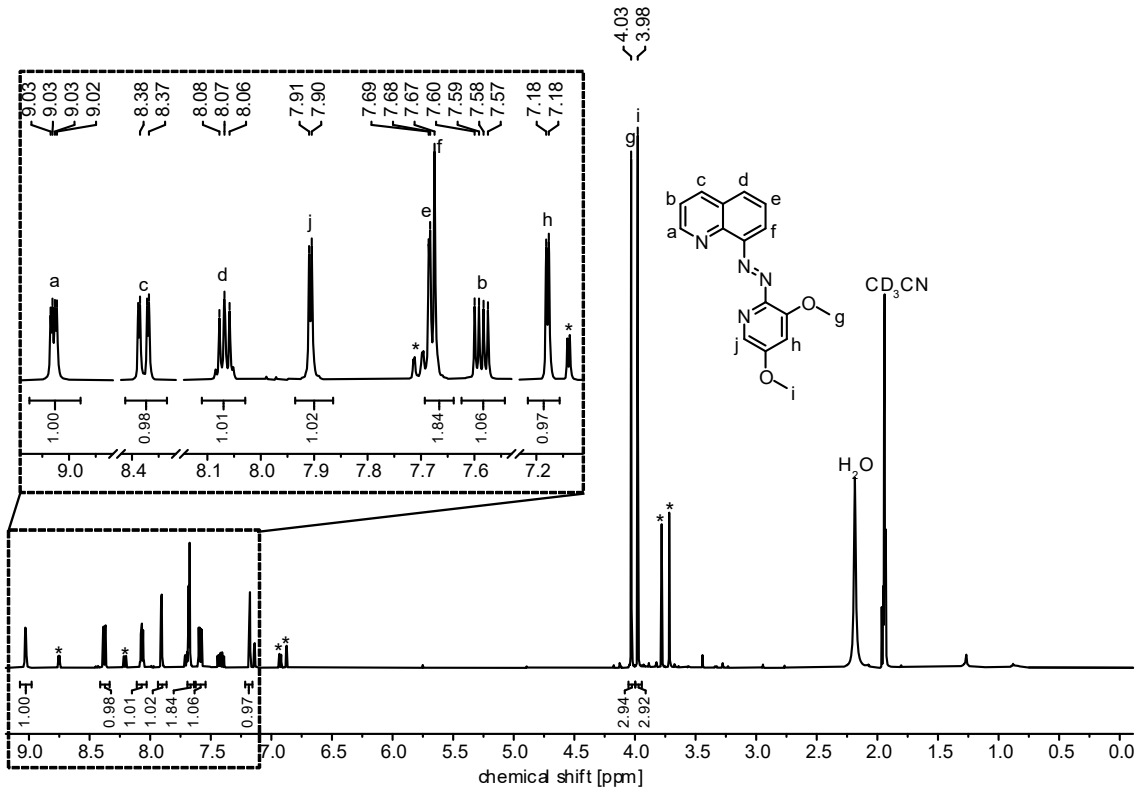

Figure 38. ^{1}H NMR spectrum (500 MHz, CD_3CN, 298 K) of **1**. Signals with an asterisk correspond to *Z*-**1**.

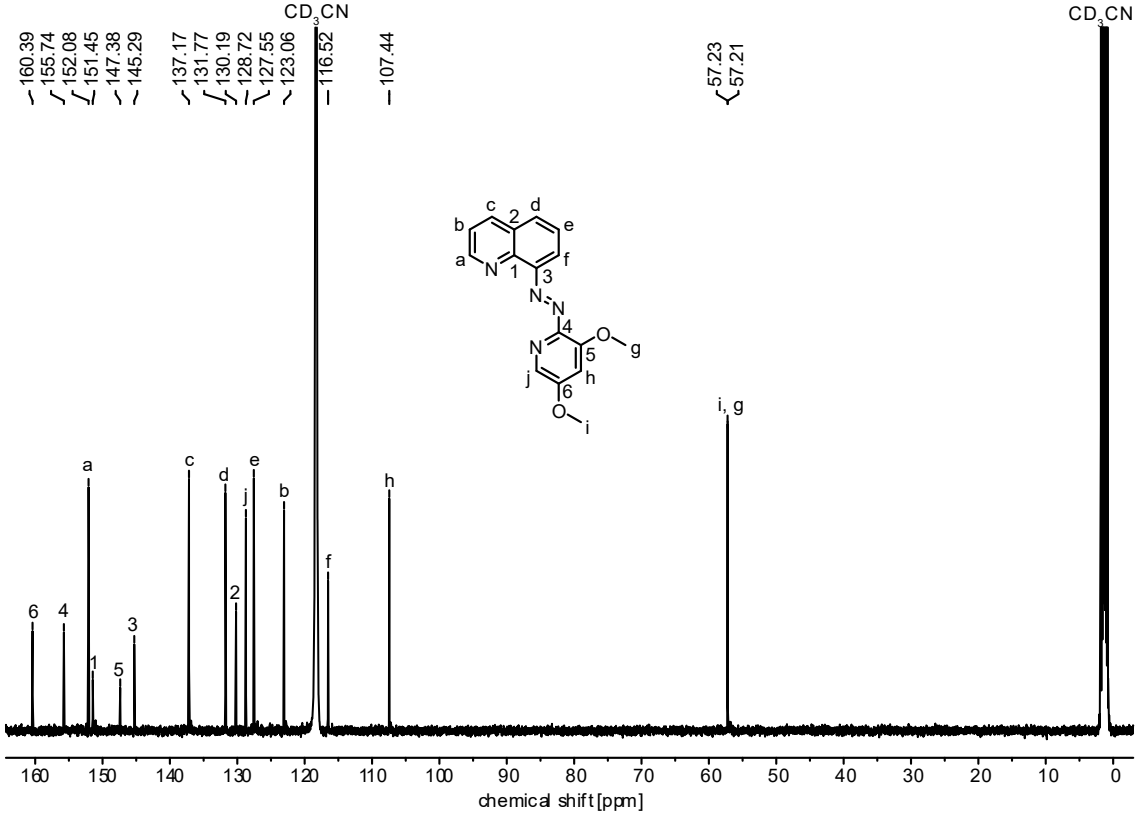

Figure 39. ^{13}C NMR spectrum (126 MHz, CD_3CN, 298 K) of **1**.

(*E*)-4-(quinolin-8-yldiazenyl) benzene-1,3-diol (**2^{OH}**)

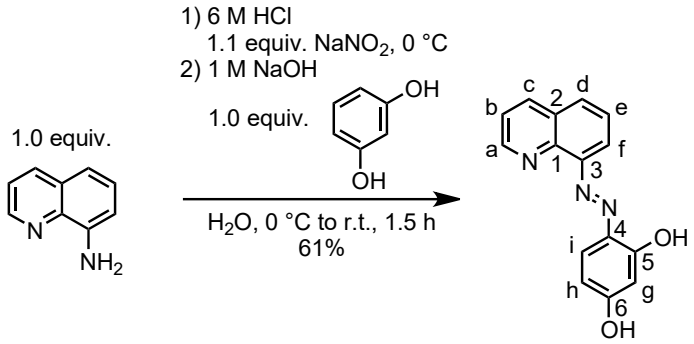

Quinolin-8-amine (100.5 mg, 693.6 µmol, 1.0 equiv.) was dissolved in HCl (6 M, 10 mL) and placed in an ice bath. Separately, resorcinol (77.9 mg, 693.6 µmol, 1.0 equiv.) was dissolved in NaOH (1 M, 20 mL) and placed in an ice bath. $NaNO_2$ (52.6 mg, 763.0 µmol, 1.1 equiv.) was dissolved in 0 °C water (5 mL) and added to the quinolin-8-amine solution. Subsequently, the quinoline solution was added dropwise to the resorcinol solution. A colour change from pale green to dark red was observed. After stirring for 1.5 h at ambient temperature, NaOH (1 M, 35 mL) was added until pH 5 was reached. Red solid precipitated which was filtered through gravity filtration, washed with HCl (10^{-5} M, 100 mL) and left to dry in the filter for 48 h to yield the desired product **2^{OH}** as a dark yellow-brown solid (112.2 mg, 423.1 µmol, 61%).

$C_{15}H_{11}N_3O_2$ 265.27 g/mol

R_F value (CH_2Cl_2 / MeOH 95:5 (*v/v*)) = 0.30

^{1}H NMR (500 MHz, DMSO-d_6, 298 K) δ_H [ppm] = 6.28 (ddt, J = 6.3, 4.2, 2.3 Hz, 1H, H-g), 6.53 (dd, J = 9.0, 2.5 Hz, 1H, H-h), 7.72 (s, 1H, H-i), 7.77 – 7.84 (m, 2H, H-b, H-d), 8.11 (d, J = 7.2 Hz, 1H, H-e), 8.23 (d, J = 8.5 Hz, 1H, H-c), 8.66 (s, 1H, H-f), 9.11 (d, J = 6.4 Hz, 1H, H-a).

^{13}C NMR (126 MHz, DMSO-d_6, 298 K) δ_C [ppm] = 103.6 (C-g), 111.6 (C-h), 115.1 (C-c), 122.6 (C-b), 127.1 (C-i), 127.5 (C-d), 128.6 (C-2), 128.8 (C-e), 133.9 (C-4), 138.4 (C-f), 139.6 (C-3), 141.9 (C-1), 150.1 (C-a), 163.8 (C-5), 165.2 (C-6).

HRMS (ESI$^+$): *m/z* (relative intensity) = 266.0924 (100%, [M+Na$^+$], calcd 266.0924).

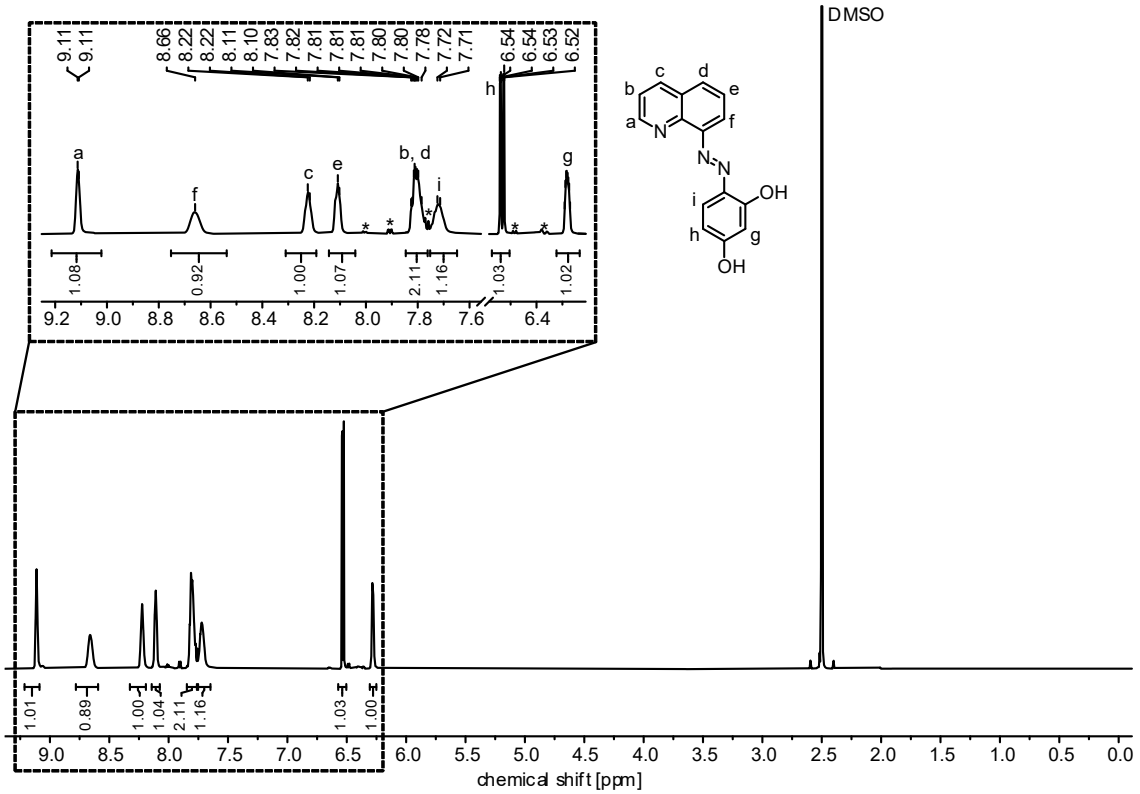

Figure 40. ^{1}H NMR spectrum (500 MHz, DMSO-d_6, 298 K) of **2^{OH}**. Signals with an asterisk correspond to *Z*-**2^{OH}**.

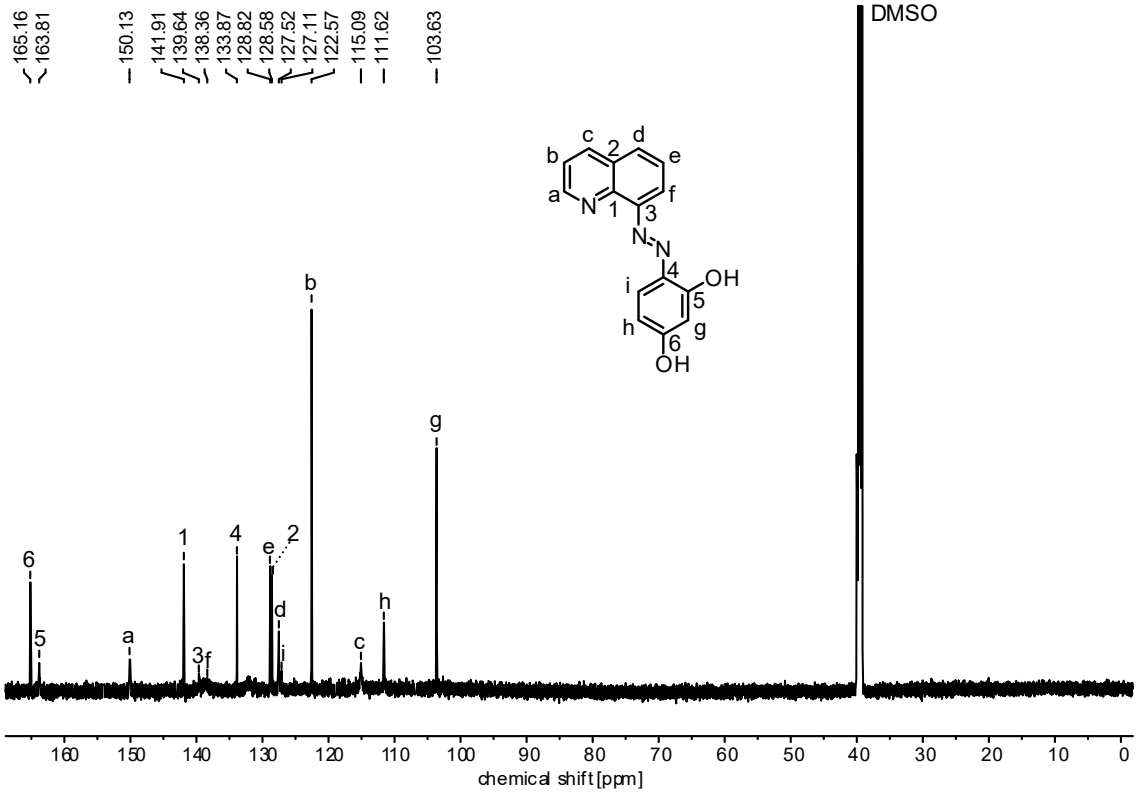

Figure 41. ^{13}C NMR spectrum (126 MHz, DMSO-d_6, 298 K) of **2^{OH}**.

(*E*)-8-((2,4-dimethoxyphenyl) diazenyl) quinoline (**2**)

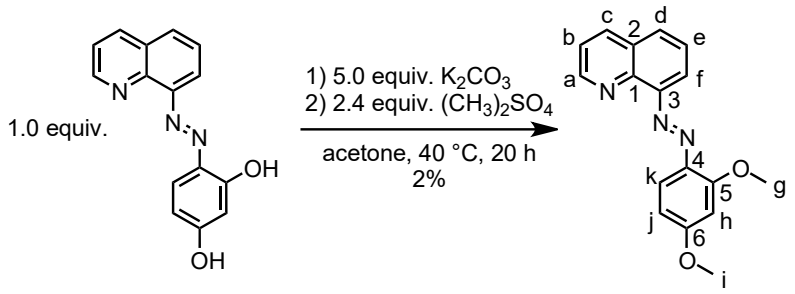

Under an argon atmosphere, $\mathbf{2^{OH}}$ (250.0 mg, 942.4 µmol, 1.0 equiv.) and dry K_2CO_3 (122.1 mg, 884.0 µmol, 1.5 equiv.) were dissolved in dry acetone (18 mL) and stirred for 15 min. Dimethyl sulfate (292.6 mg, 2.320 mmol, 2.5 equiv.) was added and the mixture was stirred overnight (20 h) at 40 °C. Then, H_2O (2 mL) was added, and the mixture was filtered through a celite plug using acetone. After the removal of acetone under reduced pressure, the remaining aqueous phase was extracted with EtOAc (3 x 15 mL), the combined organic layers were washed with brine (3 x 10 mL) and dried over Na_2SO_4. Residual solvents were removed under reduced pressure and the residue was subjected to column chromatography (CH_2Cl_2/*i*PrOH, 100/0 (*v/v*) to CH_2Cl_2/*i*PrOH, 90/10 (*v/v*)). Since purification was not achieved, the sample was further purified via high pressure liquid chromatography with an isocratic eluent mixture of CH_3CN and H_2O ((*v/v*), CH_3CN/H_2O, 45/55) over 30 min with a flow rate of 15 mL/min and a pressure of 152 bar. UV detection at 380 nm was used. (*E*)-8-((2,4-dimethoxyphenyl)-diazenyl) quinoline **2** was isolated as an orange solid (5.5 mg, 18.85 µmol, 2%).

$C_{17}H_{15}N_3O_2$ 293.33 g/mol

R_F value (cyclohexane / EtOAc 1:1 (*v/v*)) = 0.22

^{1}H NMR (500 MHz, CD_3CN, 298 K) δ_H [ppm] = 3.90 (s, 3H, H-g), 4.00 (s, 3H, H-i), 6.63 (dd, *J* = 8.9, 2.6 Hz, 1H, H-j), 6.74 (d, *J* = 2.5 Hz, 1H, H-h), 7.56 (dd, *J* = 8.3, 4.1 Hz, 1H, H-b), 7.61 (dd, *J* = 7.4, 1.6 Hz, 1H, H-f), 7.65 (t, *J* = 7.7 Hz, 1H, H-e), 7.72 (d, *J* = 9.0 Hz, 1H, H-k), 8.00 (dd, *J* = 7.9, 1.6 Hz, 1H, H-d), 8.34 (dd, *J* = 8.3, 1.8 Hz, 1H, H-c), 9.01 (dd, *J* = 4.1, 1.8 Hz, 1H, H-a).

^{13}C NMR (126 MHz, CD_3CN, 298 K) δ_C [ppm] = 56.6 (C-g), 57.0 (C-i), 100.1 (C-h), 107.2 (C-j), 116.9 (C-f), 119.1 (C-k), 122.9 (C-b), 127.6 (C-e), 130.1 (C-d), 130.8 (C-1), 137.1 (C-c), 138.5 (C-4), 145.0 (C-2), 151.2 (C-a), 151.8 (C-3), 160.3 (C-5), 165.3 (C-6).

HRMS (ESI^+): *m/z* (relative intensity) = 294.1235 (100%, $[M+H^+]$, calcd 294.1242).

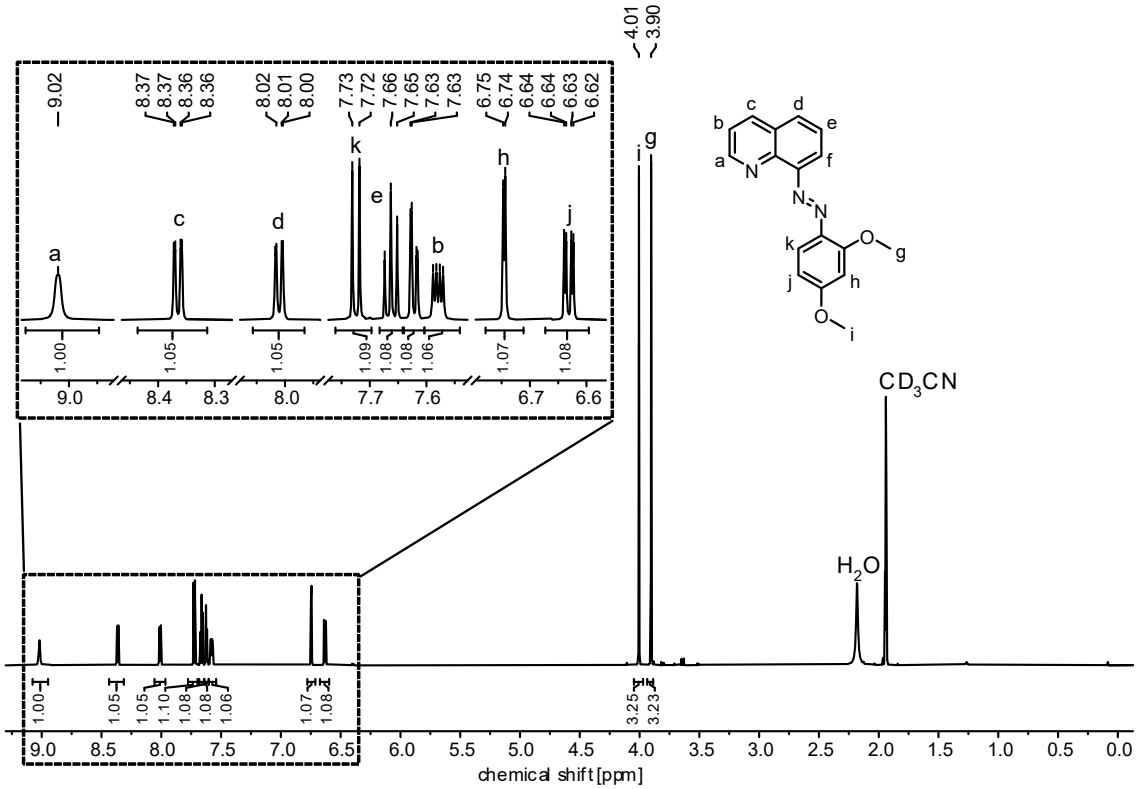

Figure 42. ^{1}H NMR spectrum (500 MHz, CD_3CN, 298 K) of **2**.

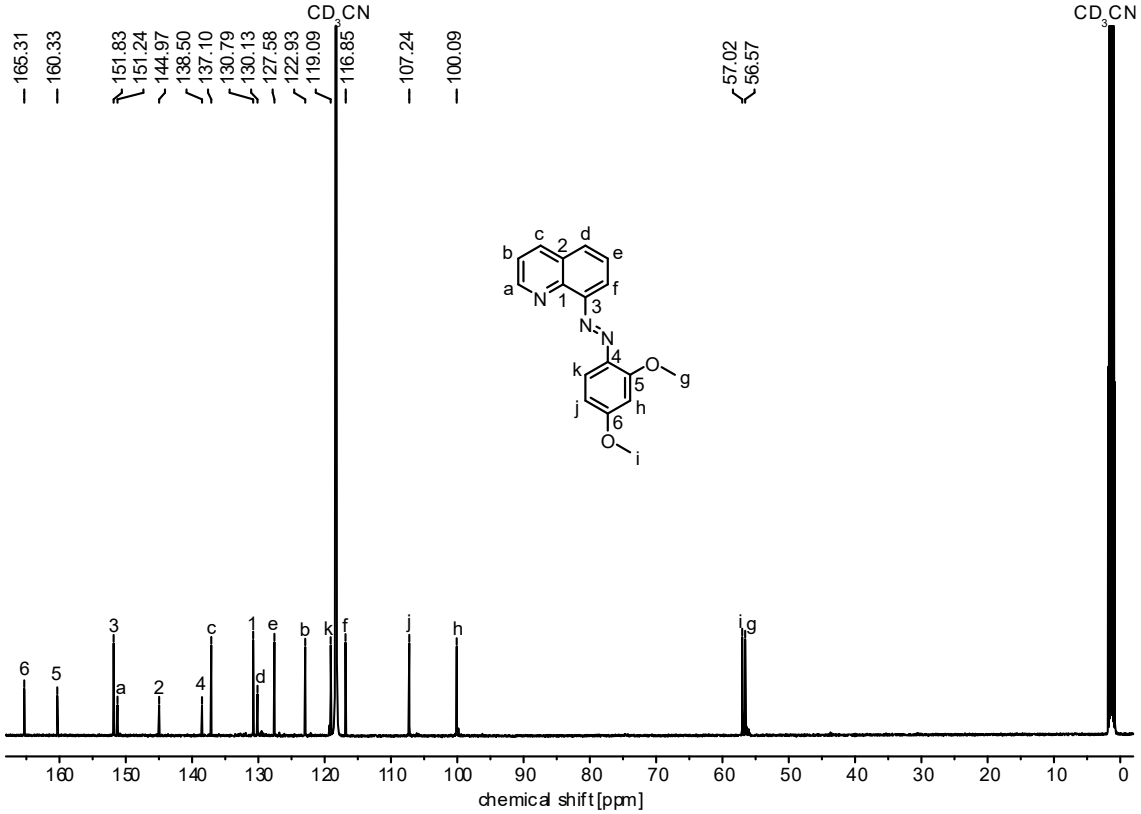

Figure 43. ^{13}C NMR spectrum (126 MHz, CD_3CN, 298 K) of **2**.

(*E*)-8-((2,4,6-trimethoxyphenyl) diazenyl) quinolin-7-ol (**3^{OH}**)

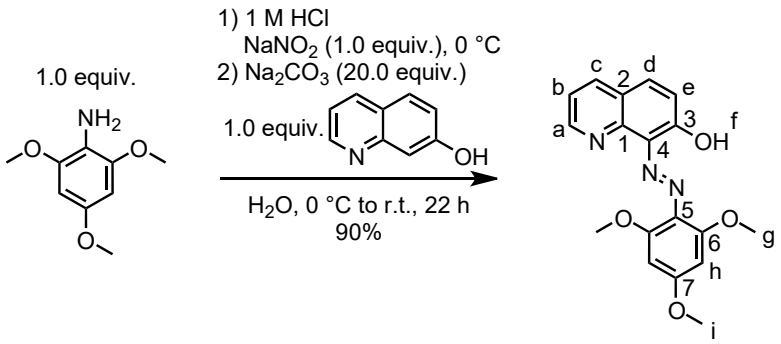

2,4,6-trimethoxyaniline (198.1 mg, 1.081 mmol, 1.0 equiv.) was dissolved in HCl (1 M, 5.5. mL) and was left cooling at 0 °C for 15 min. A solution of $NaNO_2$ in H_2O (1 mL) was added dropwise to the 2,4,6-trimethoxyaniline containing solution and was left stirring at 0 °C for 30 min. Meanwhile, Na_2CO_3 (2.309 g, 21.79 mmol, 20.0 equiv.) and 7-hydroxyquinoline (158.0 mg, 1.082 mmol, 1.0 equiv.) were dissolved in H_2O (12 mL) and left to stir at 0 °C. After 30 min, 2,4,6-trimethoxyaniline solution was added to the 7-hydroxyquinoline containing solution and an immediate colour change from yellow to red was observed. The solution was left stirring at ambient temperature for 22 h. To quench the reaction, HCl (6 M, 4 mL) was added to the reaction mixture until pH 7 was reached. The reaction mixture was extracted with CH_2Cl_2 (4 x 15 mL) and the organic layers were washed with brine (4 x 15 mL). The combined organic phases were dried over Na_2SO_4 and the residual solvent was removed under reduced pressure. The product **3^{OH}** was obtained as a red powder (332.5 mg, 972.6 µmol, 90%).

$C_{18}H_{17}N_3O_4$ 339.35 g/mol

R_F value (CH_2Cl_2 / MeOH 95:5 (*v/v*)) = 0.39

^{1}H NMR (500 MHz, DMSO-d_6, 298 K) δ_H [ppm] = 3.90 (s, 3H, H-i), 3.92 (s, 6H, H-g), 6.46 (s, 2H, H-h), 7.10 (d, J = 9.2 Hz, 1H, H-e), 7.42 (dd, J = 8.0, 4.3 Hz, 1H, H-b), 7.91 (d, J = 9.2 Hz, 1H, H-d), 8.21 (dd, J = 7.9, 1.8 Hz, 1H, H-c), 8.85 (dd, J = 3.8, 1.4 Hz, 1H, H-a), 16.41 (s, 1H, H-f).

^{13}C NMR (126 MHz, DMSO-d_6, 298 K) δ_C [ppm] = 55.6 (C-i), 56.6 (C-g), 92.3 (C-h), 119.0 (C-5), 119.7 (C-b), 122.1 (C-2), 123.6 (C-e), 130.8 (C-4), 135.0 (C-d), 135.9 (C-c), 146.9 (C-1), 150.5 (C-a), 154.7 (C-6), 161.7 (C-7), 163.4 (C-3).

HRMS (ESI^+): *m/z* (relative intensity) = 340.1288 (100%, [M+Na^+], calcd 340.1292).

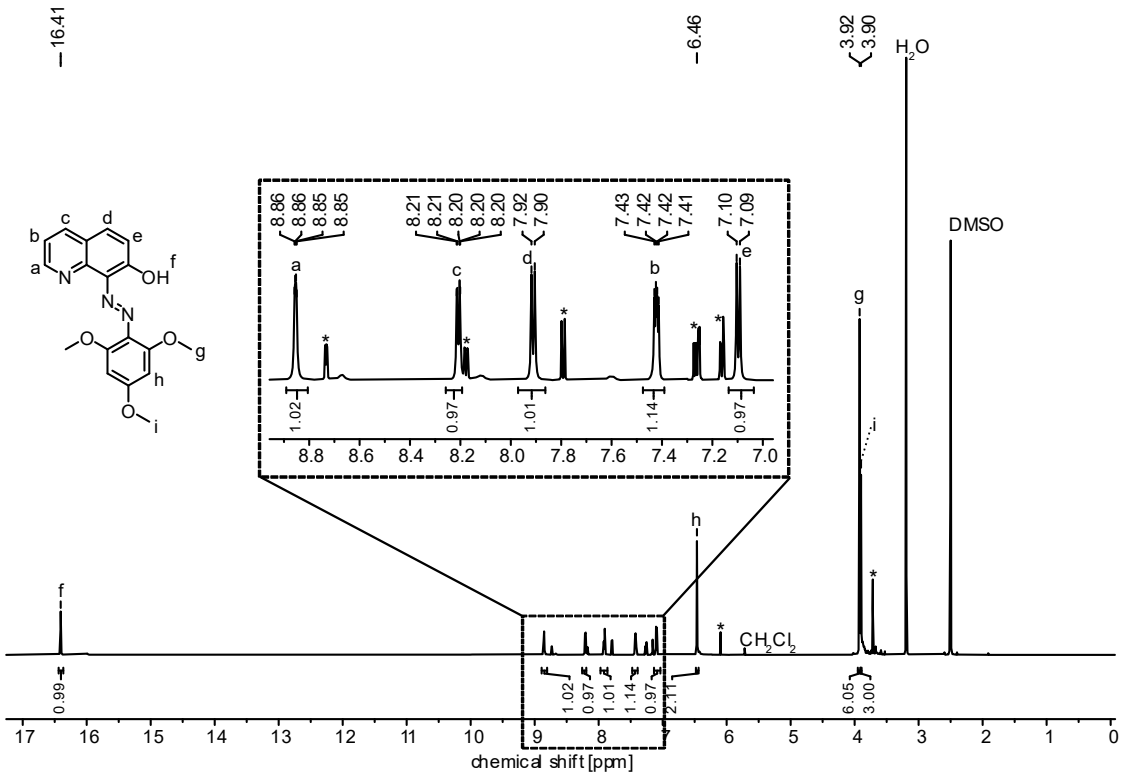

Figure 44. ^{1}H NMR spectrum (500 MHz, DMSO-d_6, 298 K) of **3^{OH}**. Signals with an asterisk correspond to *Z*-**3^{OH}**.

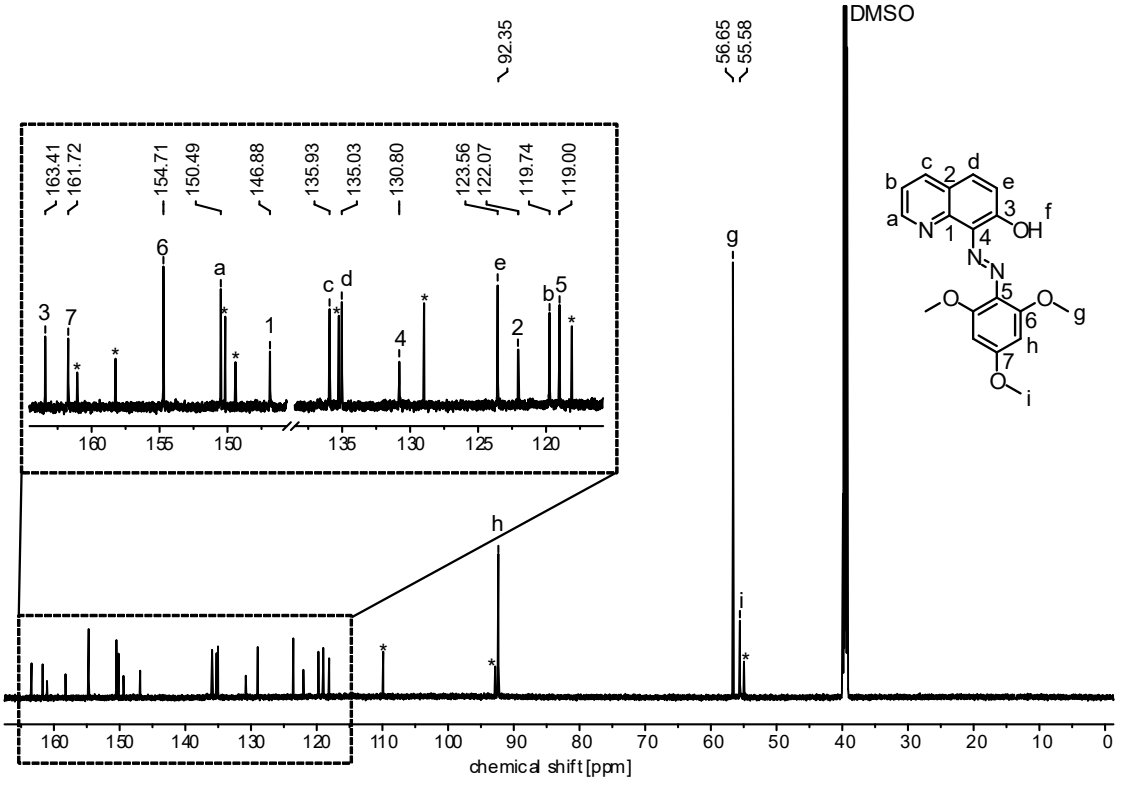

Figure 45. ^{13}C NMR spectrum (126 MHz, DMSO-d_6, 298 K) of **3^{OH}**. Signals with an asterisk correspond to *Z*-**3^{OH}**.

(*E*)-7-methoxy-8-((2,4,6-trimethoxyphenyl) diazenyl) quinoline (**3**)

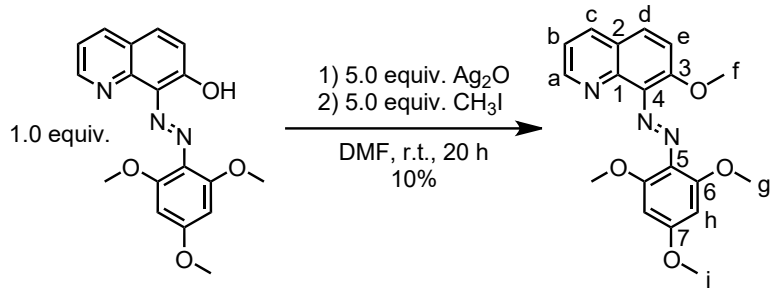

Under an argon atmosphere, **3^{OH}** (49.90 mg, 147.3 µmol, 1.0 equiv.) and Ag_2O (170.6 mg, 736.7 µmol, 5.0 equiv.) were dissolved in dry DMF (8 mL) and stirred for 10 min. Methyl iodide (104.6 mg, 736.7 µmol, 5.0 equiv.) was added and the mixture was stirred overnight (20 h) at 40 °C. The reaction mixture was filtered through a celite plug with acetone. After the removal of acetone and methyl iodide under reduced pressure, the residue was dissolved in H_2O (5 mL) and CH_2Cl_2 (15 mL). The aqueous phase was extracted with CH_2Cl_2 (3 x 15 mL), the combined organic layers were washed with brine (3 x 10 mL) and dried over Na_2SO_4. Residual solvents were removed under reduced pressure and the residue was subjected to column chromatography (silica gel, see Table 3 for solvent specifications). (*E*)-7-methoxy-8-((2,4,6-trimethoxyphenyl) diazenyl) quinoline **4** was isolated as a red-brown solid (5.210 mg, 14.37 µmol, 10%).

Table 3. Solvent mixtures used to purify **3** via flash column chromatography.

Column volume	Cyclohexane	CH_2Cl_2	EtOAc	*i*-PrOH
0	80	0	20	0
12	20	10	70	0
18	0	10	70	20
22	0	10	0	90

$C_{19}H_{19}N_3O_4$ 353.38 g/mol

R_F value (cyclohexane / EtOAc 1:1 (*v/v*)) = 0.28

^{1}H NMR (500 MHz, DMSO-d_6, 298 K) δ_H [ppm] = 3.77 (s, 6H, H-g), 3.88 (s, 3H, H-f), 3.89 (s, 3H, H-i), 6.39 (s, 2H, H-h), 7.39 (dd, J = 8.3, 4.1 Hz, 1H, H-b), 7.64 (d, J = 9.1 Hz, 1H, H-d), 7.94 (d, J = 9.1 Hz, 1H, H-e), 8.33 (dd, J = 8.3, 1.8 Hz, 1H, H-c), 8.75 (dd, J = 4.1, 1.8 Hz, 1H, H-a).

^{13}C NMR (126 MHz, DMSO-d_6, 298 K) δ_C [ppm] = 55.6 (C-i), 56.1 (C-g), 56.8 (C-f), 91.5 (C-h), 115.5 (C-d), 119.4 (C-b), 123.1 (C-2), 127.2 (C-e), 127.2 (C-5), 135.6 (C-c), 138.9 (C-4), 140.9 (C-1), 148.7 (C-3), 150.7 (C-a), 154.7 (C-6), 162.0 (C-7).

HRMS (ESI$^+$): *m*/*z* (relative intensity) = 354.1433 (80%, [M+H] $^+$, calcd 354.1448), 533.2031 (100%, $[M+C_9H_{10}NO_3]^+$, 533.2030).

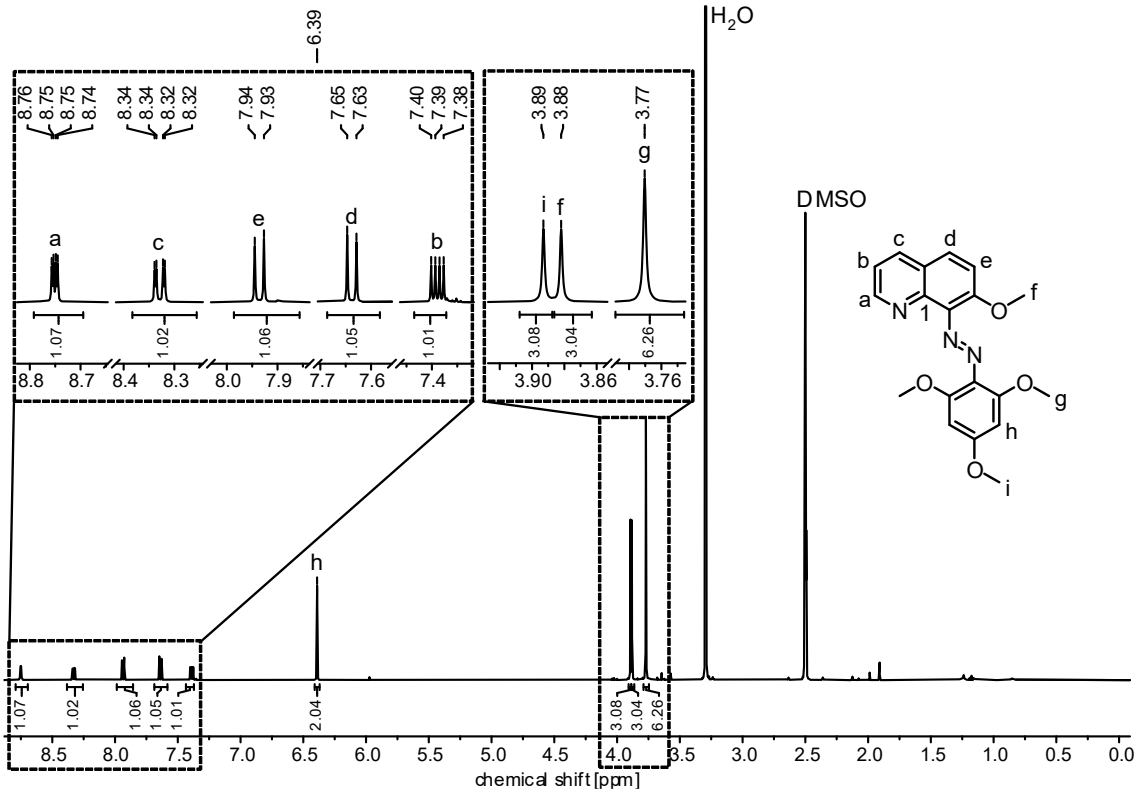

Figure 46. ^{1}H NMR spectrum (500 MHz, DMSO-d_6, 298 K) of **3**.

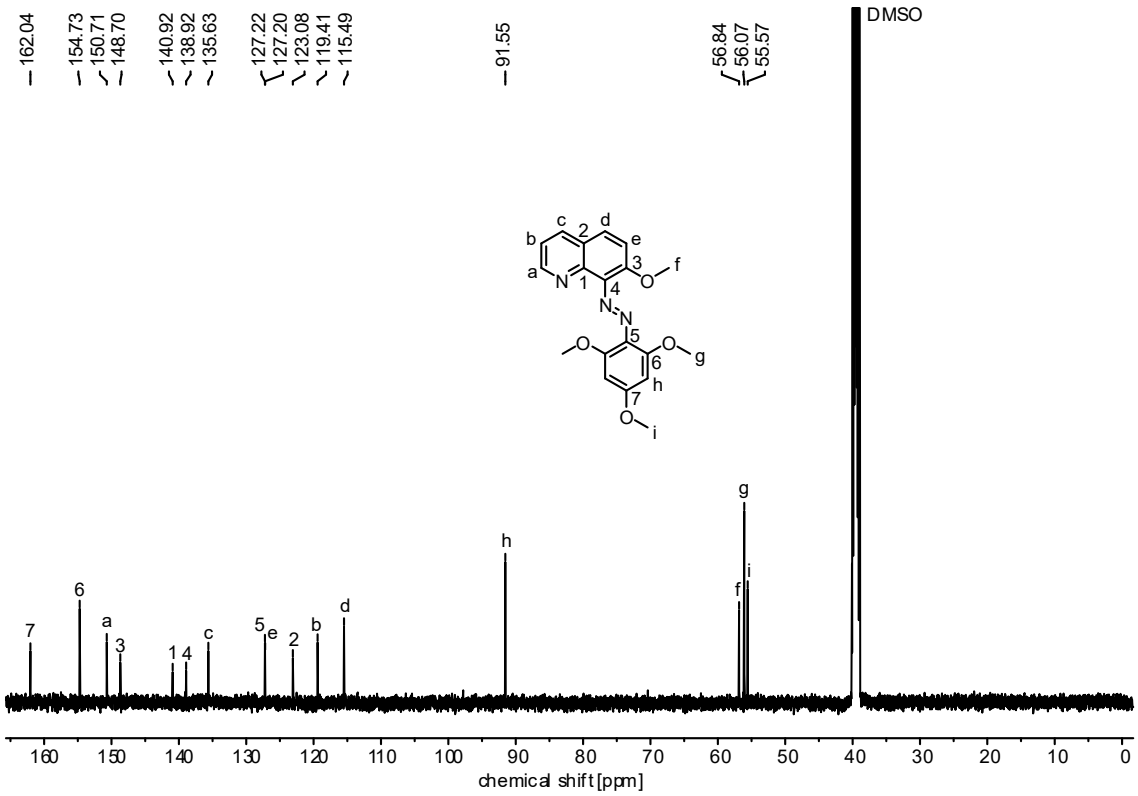

Figure 47. ^{13}C NMR spectrum (126 MHz, DMSO-d_6, 298 K) of **3**.

(*E*)-8-((3,4,5-trimethoxyphenyl) diazenyl) quinolin-7-ol (**4^{OH}**)

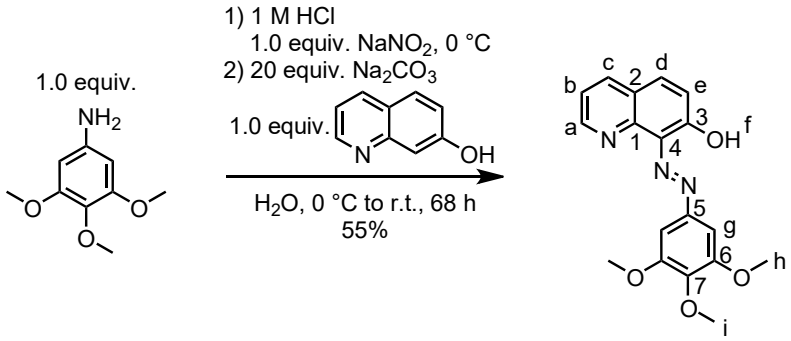

3,4,5-trimethoxyaniline (500 mg, 2.73 mmol, 1.0 equiv.) was dissolved in HCl (1 M, 14.8 mL) and was left cooling at 0 °C for 20 min. A solution of $NaNO_2$ (189.0 mg, 2.73 mmol, 1.0 equiv.) in H_2O (1 mL) was added dropwise to the 3,4,5-trimethoxyaniline solution and was left stirring at 0 °C for 30 minutes. Meanwhile, Na_2CO_3 (5.79 g, 54.58 mmol, 20.0 equiv.) and 7-hydroxyquinoline (396.2 mg, 2.73 mmol, 1.0 equiv.) were dissolved in H_2O (30 mL) and were left to stir at 0 °C. After 30 min, the 3,4,5-trimethoxyaniline solution was slowly added to the 7-hydroxyquinoline solution and a colour change from yellow to red was immediately observed. The solution was left stirring at ambient temperature for 29 h. To quench the reaction, HCl (6 M, 25 mL) was added to the reaction mixture and a red solid was formed at pH 7. The solid was washed with H_2O (40 mL). The aqueous phase was extracted with CH_2Cl_2 (4 x 20 mL) and brine (4 x 20 mL). The organic phase was dried over Na_2SO_4 and the residual solvent was removed under reduced pressure to yield the desired product **4^{OH}** as a dark red solid (509.4 mg, 1.50 mmol, 55%).

$C_{18}H_{17}N_3O_4$ 339.35 g/mol

R_F value (CH_2Cl_2 / MeOH 95:5 (*v*/*v*)) = 0.19

^{1}H NMR (500 MHz, DMSO-*d*$_6$, 298 K) δ_H [ppm] = 3.76 (s, 4H, H-i), 3.91 (s, 8H, H-h), 7.18 (d, *J* = 9.3 Hz, 1H, H-e), 7.33 (s, 2H, H-g), 7.50 (dd, *J* = 8.0, 4.5 Hz, 1H, H-b), 8.02 (d, *J* = 9.3 Hz, 1H, H-d), 8.28 (d, *J* = 7.9 Hz, 1H, H-c), 8.93 (s, 1H, H-a), 15.72 (m, 1H, H-f).

^{13}C NMR (126 MHz, DMSO-*d*$_6$, 298 K) δ_C [ppm] = 56.2 (C-h), 60.3 (C-i), 98.3 (C-g), 120.6 (C-b), 122.8 (C-1), 123.2 (C-e), 129.9 (C-4), 136.5 (C-d), 136.7 (C-c), 139.0 (C-7), 142.9 (C-5), 146.8 (C-2), 151.2 (C-a), 153.7 (C-6), 163.5 (C-3).

HRMS (ESI$^+$): *m*/*z* (relative intensity) = 340.1288 (100%, [M+H$^+$], calcd 340.1292).

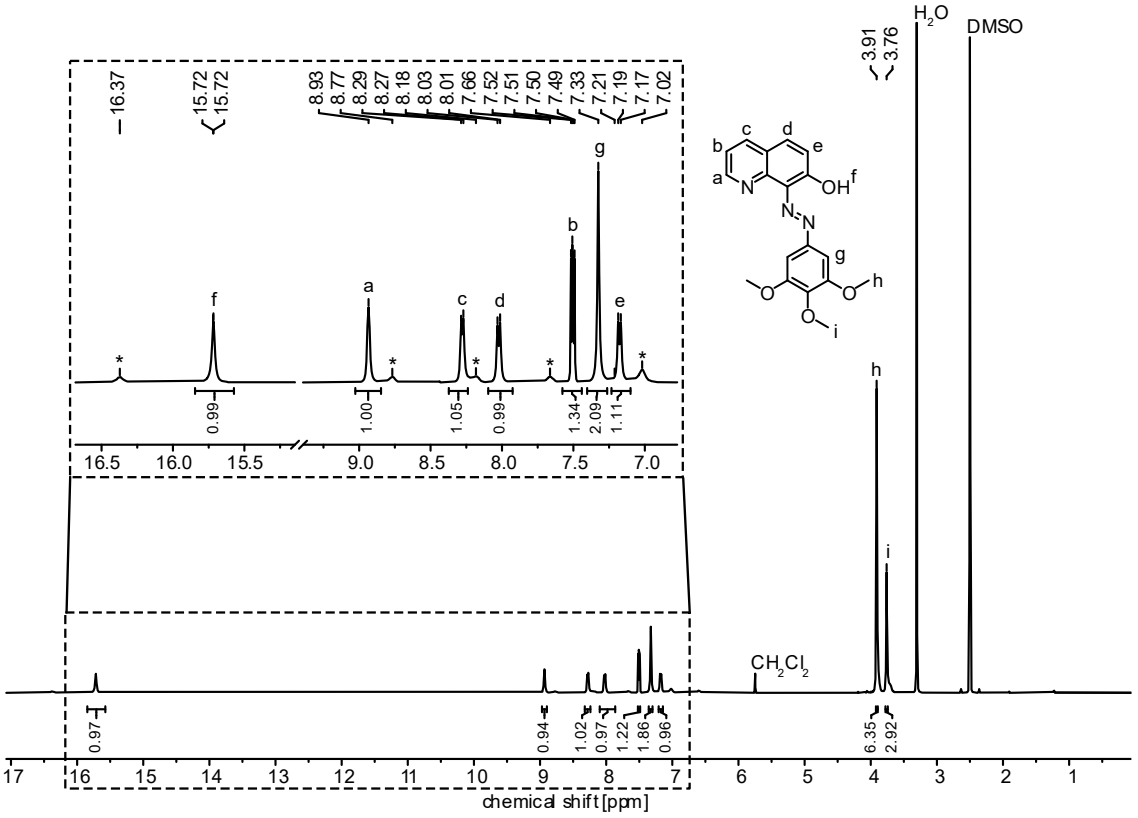

Figure 48. ^{1}H NMR spectrum (500 MHz, DMSO-d_6, 298 K) of **4^{OH}**. Signals with an asterisk correspond to *Z*-**4^{OH}**.

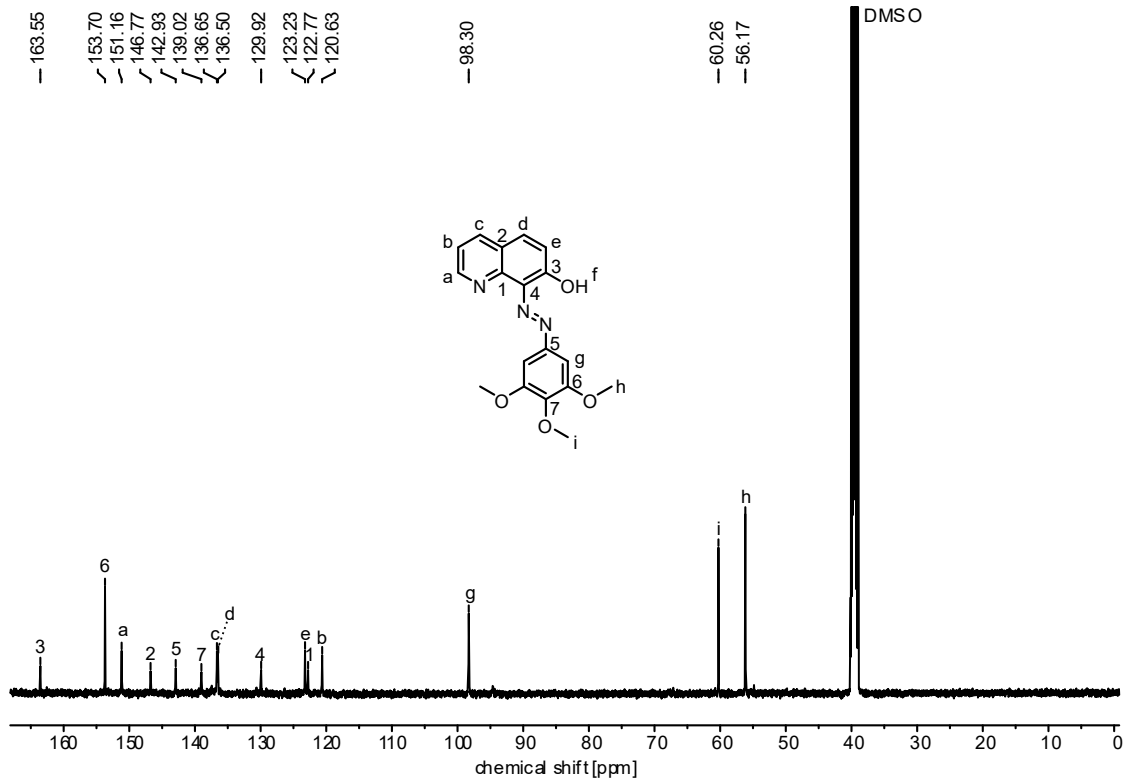

Figure 49. ^{13}C NMR spectrum (126 MHz, DMSO-d_6, 298 K) of **4^{OH}**.

(*E*)-7-methoxy-8-((3,4,5-trimethoxyphenyl) diazenyl) quinoline (**4**)

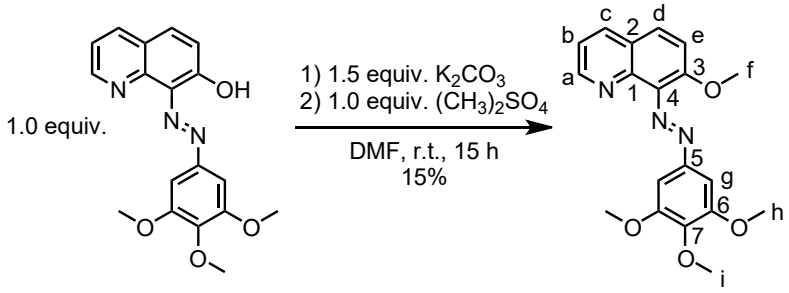

Under an argon atmosphere, $\mathbf{4^{OH}}$ (200 mg, 589.4 µmol, 1.0 equiv.) and dry K_2CO_3 (122 mg, 884.0 µmol, 1.5 equiv.) were dissolved in dry DMF (13 mL) and stirred for 15 min. Dimethyl sulfate (731.5 mg, 5.894 mmol, 10.0 equiv.) was added and the mixture was stirred overnight (15 h) at ambient temperature. H_2O (2 mL) was added and the reaction mixture was then extracted with EtOAc (3 x 15 mL), the combined organic layers were washed with brine (3 x 10 mL) and dried over Na_2SO_4. Residual solvents were removed under reduced pressure and the residue was subjected to column chromatography (silica gel, see Table 4 for solvent specifications). (*E*)-7-methoxy-8-((3,4,5-trimethoxyphenyl) diazenyl) quinoline **4** was isolated as a red solid (31.22 mg, 88.40 µmol, 15%).

Table 4. Solvent mixtures used to purify **4** via flash column chromatography.

Column volume	Cyclohexane	EtOAc	*i*-PrOH
0	40	60	0
5	25	75	0
8	0	80	20
10	0	50	50

$C_{19}H_{19}N_3O_4$ 353.38 g/mol

R_F value (Cyclohexane / EtOAc 8:2 (*v/v*)) = 0.45

^{1}H NMR† (700 MHz, CD_3CN, 298 K) δ_H [ppm] = 3.43 (s, 6H, H-h*), 3.55 (s, 3H, H-i*), 3.83 (s, 3H, H-f*), 3.85 (s, 3H, H-i), 3.92 (s, 6H, H-h), 3.94 (s, 3H, H-f), 6.19 (s, 2H, H-g*), 7.26 (s, 2H, H-g), 7.34 (dd, *J* = 8.6, 4.5 Hz, 1H, H-b*), 7.34 (d, *J* = 8.6, 1H, H-d*), 7.37 (dd, *J* = 8.3, 4.1 Hz, 1H, H-b), 7.61 (d, *J* = 9.1 Hz, 1H, H-d), 7.76 (d, *J* = 9.1 Hz, 1H, H-e*), 7.93 (d, *J* = 9.1 Hz, 1H, H-e), 8.17 (dd, *J* = 8.3, 1.8 Hz, 1H, H-c*), 8.26 (dd, *J* =

8.3, 1.8 Hz, 1H, H-c), 8.76 (dd, J = 4.1, 1.8 Hz, 1H, H-a), 8.82 (dd, J = 4.2, 1.7 Hz, 1H, H-a*).

^{13}C NMR† (126 MHz, CD_3CN, 298 K) δ_C [ppm] = 55.5 (C-h*), 55.9 (C-h), 56.0 (C-f*), 56.7 (C-f), 59.7 (C-i*), 60.1 (C-i), 96.1 (C-g*), 100.2 (C-g), 114.0 (C-d*), 115.2 (C-d), 119.7 (C-b), 119.7 (C-b*), 123.1 (C-2), 123.6 (C-2*), 127.5 (C-e*), 128.1 (C-e), 135.8 (C-6*), 135.9 (C-c), 135.9 (C-c*), 136.7 (C-5*), 138.4 (C-1), 138.4 (C-1*), 139.9 (C-4*), 141.1 (C-6), 141.5 (C-5), 145.1 (C-3*), 148.8 (C-4), 149.2 (C-3),151.4 (C-a), 151.4 (C-a*), 152.7 (C-7*), 153.8 (C-7).

HRMS (ESI^+): m/z (relative intensity) = 354.1449 (100%, [$M+H^+$], calcd 354.1448).

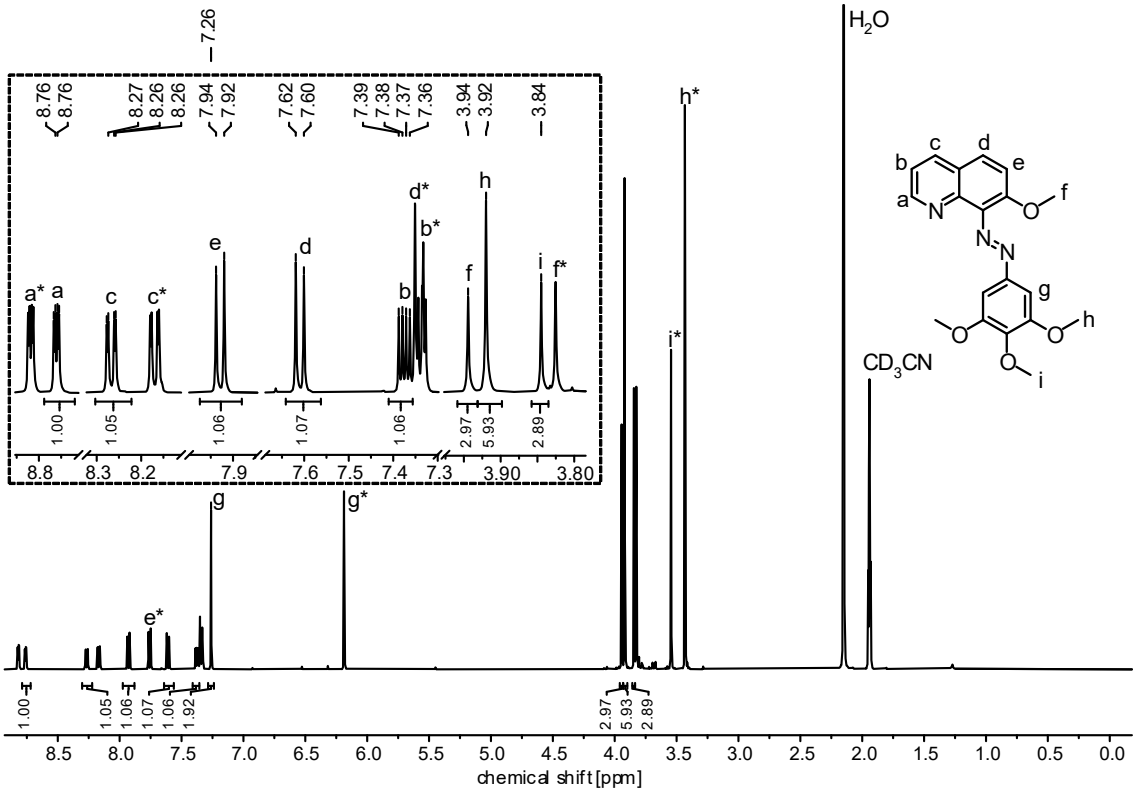

Figure 50. ^{1}H NMR spectrum (700 MHz, CD_3CN, 298 K) of **4**. Signals with an asterisk correspond to *Z*-**4**.

† Both *E*- and *Z*-isomers were assigned in the ^{1}H and ^{13}C NMR, the signals with an asterisk correspond to the *Z*-isomer of **4**.

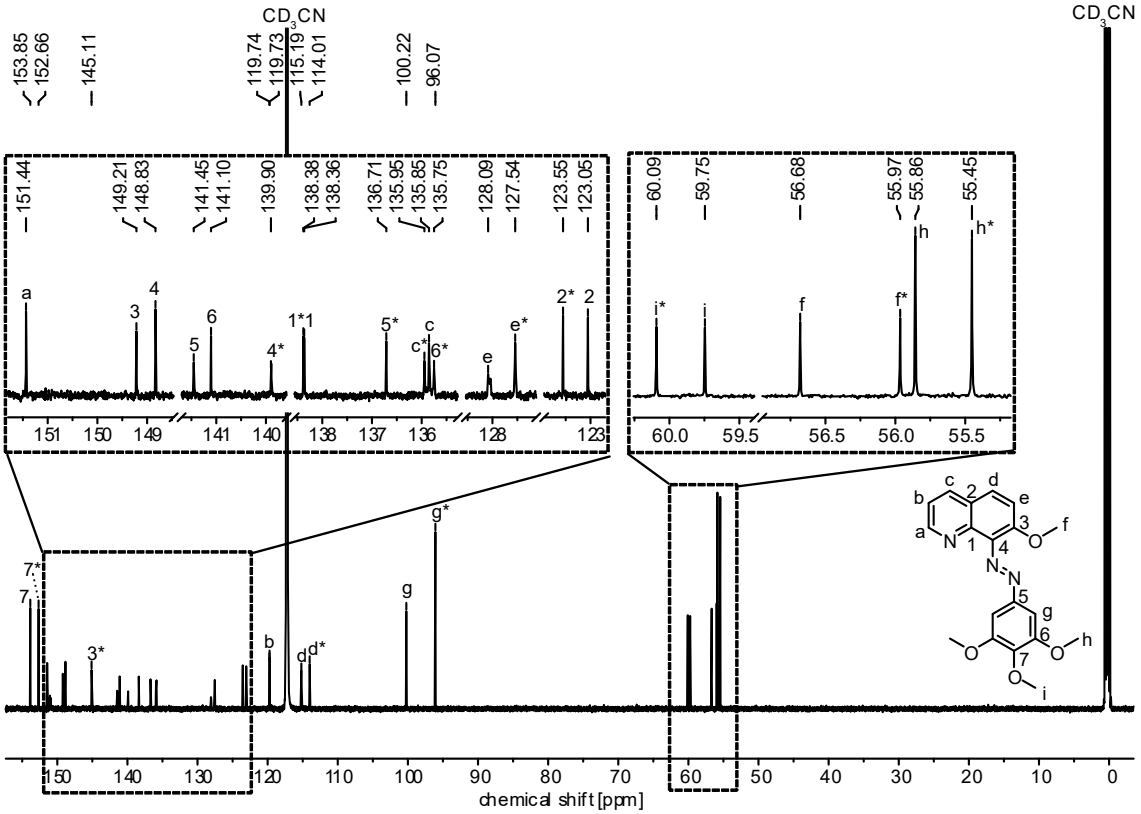

Figure 51. ^{13}C NMR spectrum (126 MHz, CD_3CN, 298 K) of **4**. Signals with an asterisk correspond to *Z*-**4**.

Complex Pd**1**

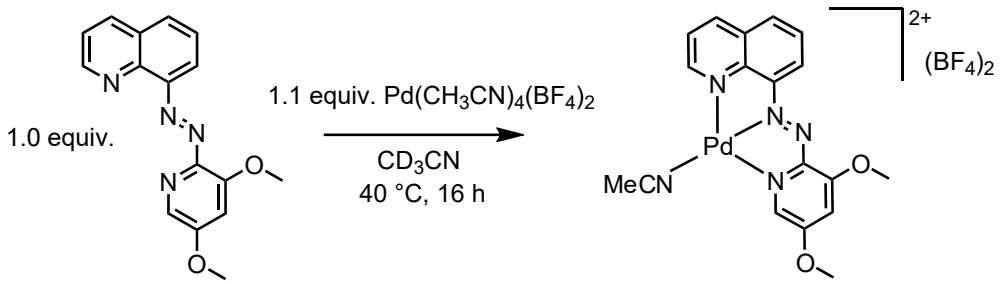

Ligand **1** (2.9 mg, 9.85 µmol, 1.0 equiv.) was dissolved in CD_3CN (0.6 mL), followed by the addition of $Pd(CH_3CN)_4(BF_4)_2$ (4.8 mg, 10.84 µmol, 1.1 equiv.). The resulting dark red solution was stirred at 40 °C for 16 h, after which it was allowed to cool to ambient temperature. The sample was then used for analysis without further purification.

$[Pd(C_{16}H_{14}N_4O_2)(CH_3CN)](BF_4)_2$ 615.05 g/mol

^{1}H NMR (500 MHz, CD_3CN, 298 K) δ_H [ppm] = 4.20 (s, 3H, H-i), 4.29 (s, 3H, H-g), 7.49 (d, J = 2.4 Hz, 1H, H-h), 7.91 (dd, J = 8.6, 5.4 Hz, 1H, H-b), 7.93 (d, J = 2.4 Hz, 1H, H-j), 7.96 (t, J = 8.0 Hz, 1H, H-e), 8.43 (d, J = 8.1 Hz, 1H, H-d), 8.48 (d, J = 7.9 Hz, 1H, H-f), 8.87 (dd, J = 5.2, 1.3 Hz, 1H, H-a), 8.91 (dd, J = 8.5, 1.3 Hz, 1H, H-c).

^{13}C NMR (126 MHz, CD_3CN, 298 K) δ_C [ppm] = 60.1 (C-i), 60.4 (C-g), 109.9 (C-h), 122.6 (C-f), 125.8 (C-b), 131.2 (C-e), 132.4 (C-3), 135.9 (C-d), 139.9 (C-j), 143.5 (C-c), 146.8 (C-1), 150.0 (C-2), 150.2 (C-4), 155.4 (C-a), 162.6 (C-5), 166.4 (C-6).

HRMS (ESI^+): m/z (relative intensity) = 426.0207 (70%, $[Pd + \mathbf{1} + CN]^+$, calcd 426.0182), 436.9842 (100%, $[Pd + \mathbf{1} + Cl]^+$, calcd 436.9832).

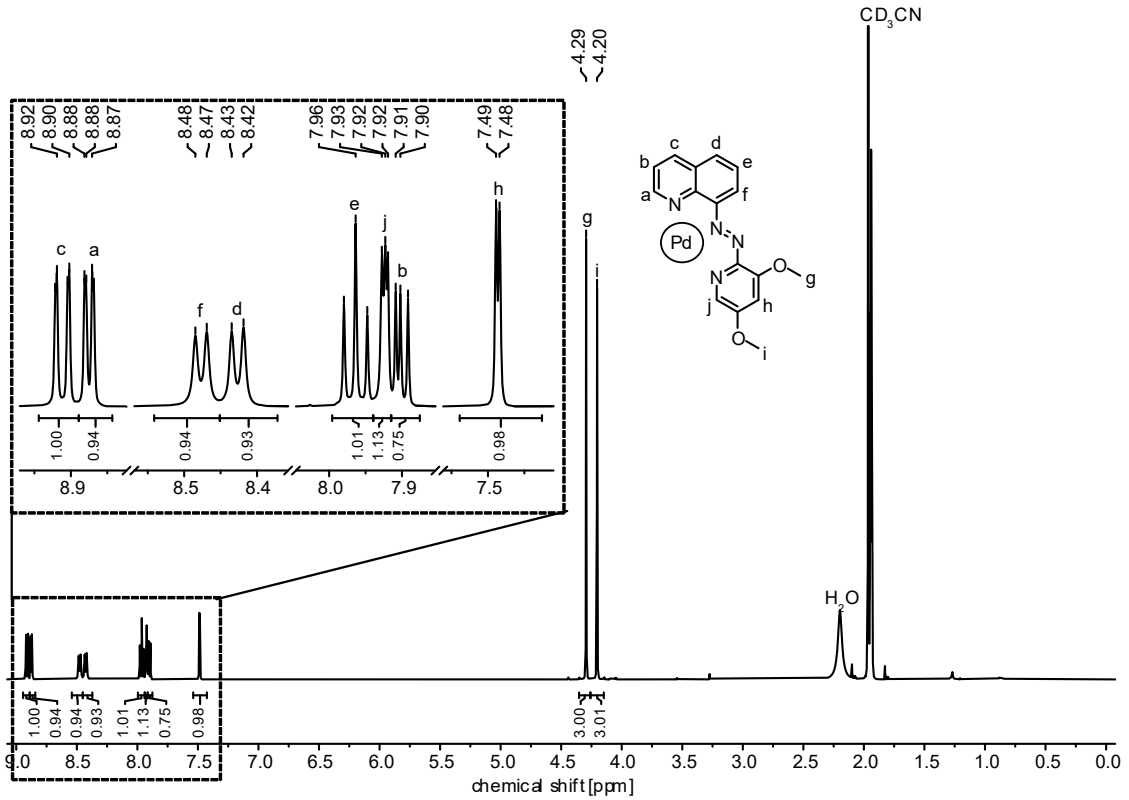

Figure 52. ^{1}H NMR spectrum (500 MHz, CD_3CN, 298 K) of Pd**1**.

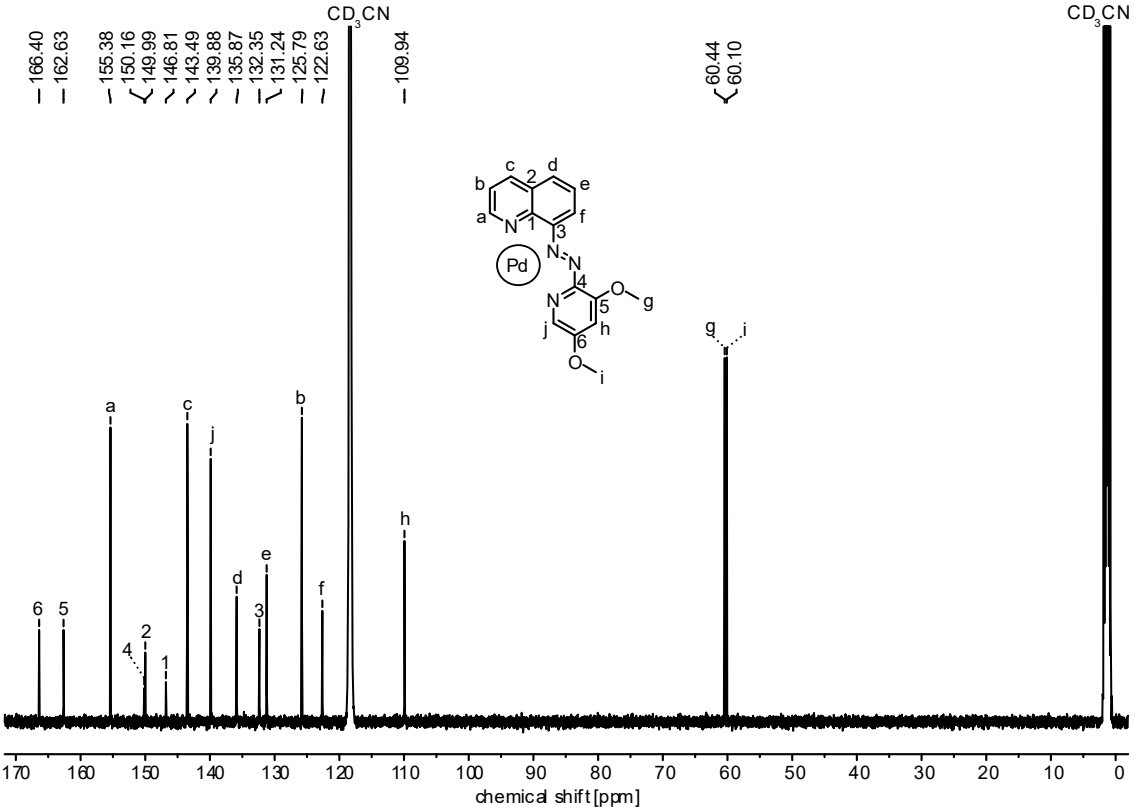

Figure 53. ^{13}C NMR spectrum (126 MHz, CD_3CN, 298 K) of Pd**1**.

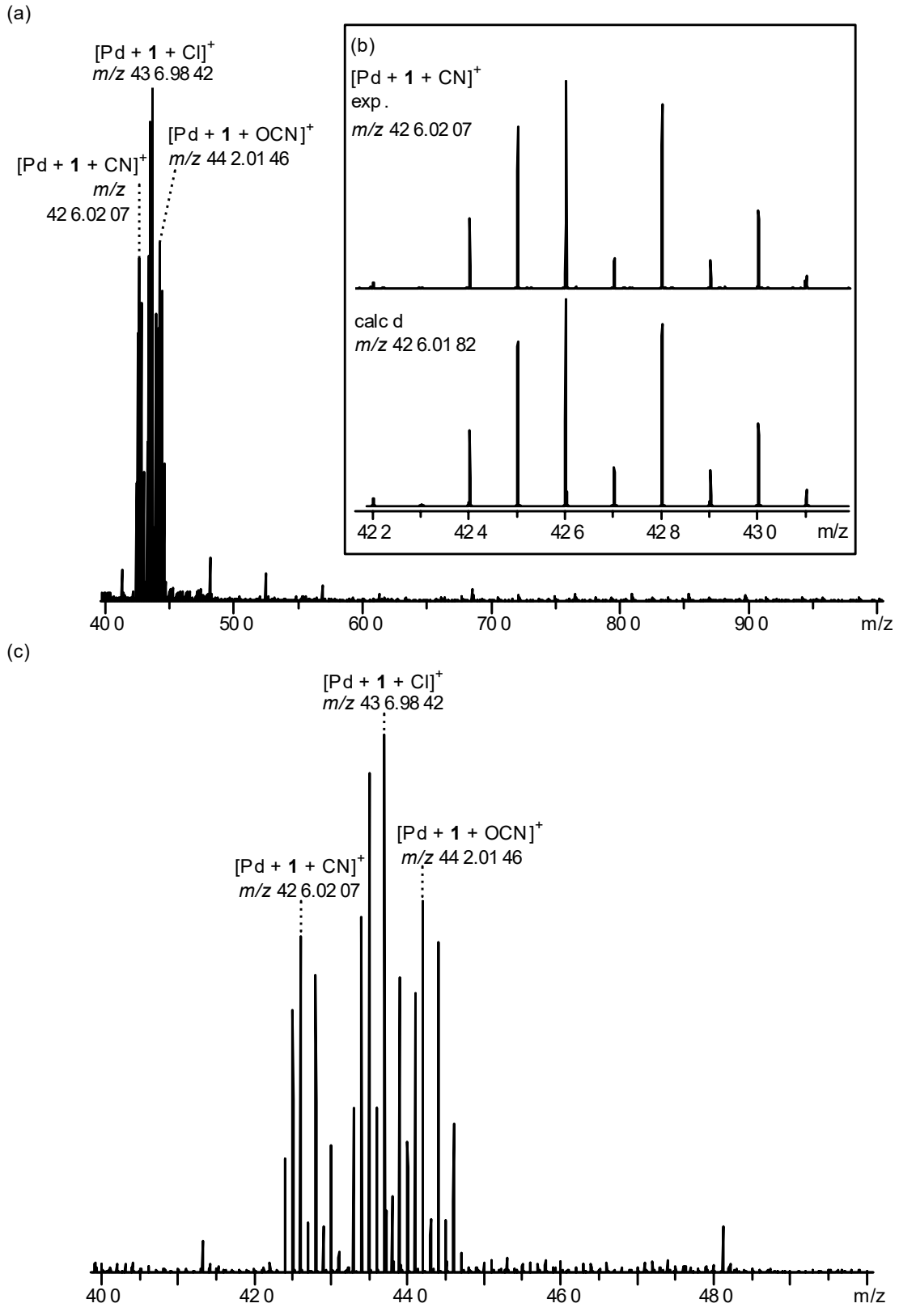

Figure 54. High-resolution ESI+ mass spectrum (CH_3CN) of (a) complex sample Pd**1**, (b) experimental and calculated isotope pattern of [Pd + **1** + CN]+, and (c) zoom-in of (a).

Complex Pd**2**

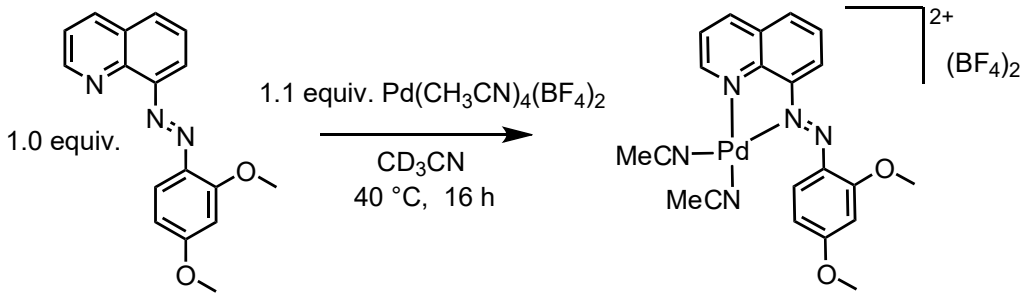

Ligand **2** (2.58 mg, 8.8 µmol, 1.0 equiv.) was dissolved in CD_3CN (0.6 mL) followed by the addition of $Pd(CH_3CN)_4(BF_4)_2$ (4.3 mg, 9.68 µmol, 1.1 equiv.). The resulting dark red solution was stirred at 40 °C for 16 h, after which it was allowed to cool to ambient temperature. The sample was then used for analysis without further purification. Note that no ^1H NMR assignments could be made and no signals were observed in the ^{13}C NMR due to low concentrations. See Section 4.4.1 for more information.

$[Pd(C_{17}H_{15}N_3O_2)(CH_3CN)_2](BF_4)_2$ 655.08 g/mol

HRMS (ESI^+): *m/z* (relative intensity) = 425.0225 (100%, [Pd + **2** + CN]$^+$, calcd 425.0230), 439.0375 (60%, [Pd + **2** – **H** + CH_3CN]$^+$, calcd 439.03808).

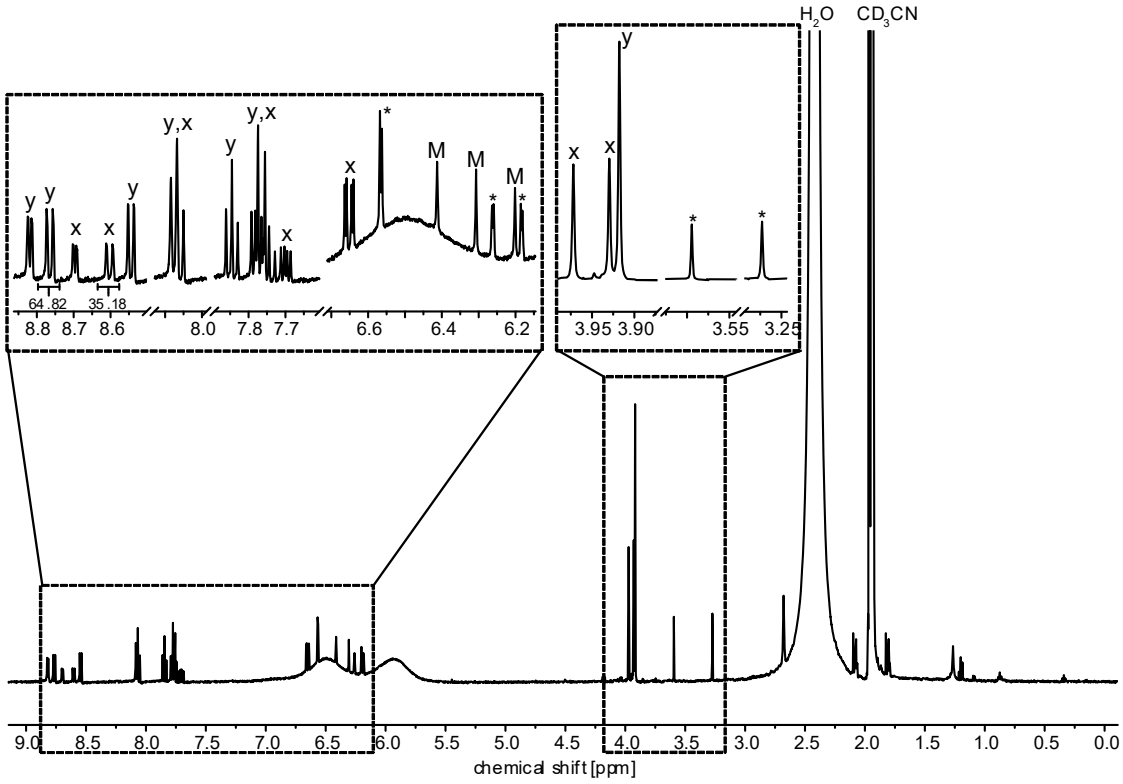

Figure 55. ^1H NMR spectrum (500 MHz, CD_3CN, 298 K) of Pd**2**. See Section 4.4.1 for signal interpretations.

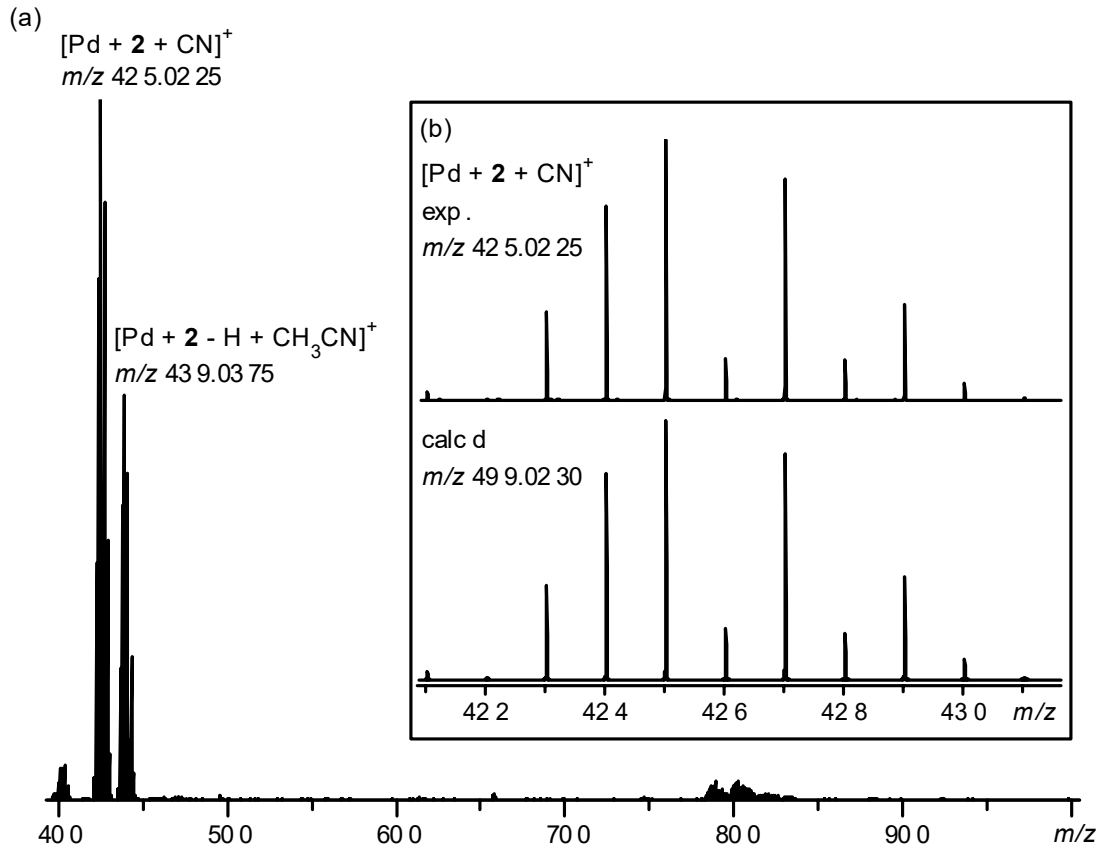

Figure 56. High-resolution ESI$^+$ mass spectrum (CH_3CN) of (a) complex sample Pd**2**, and (b) experimental and calculated isotope pattern of [Pd + **2** + CN]$^+$.

Complexes Pd**3** & Pd(**3**)$_2$

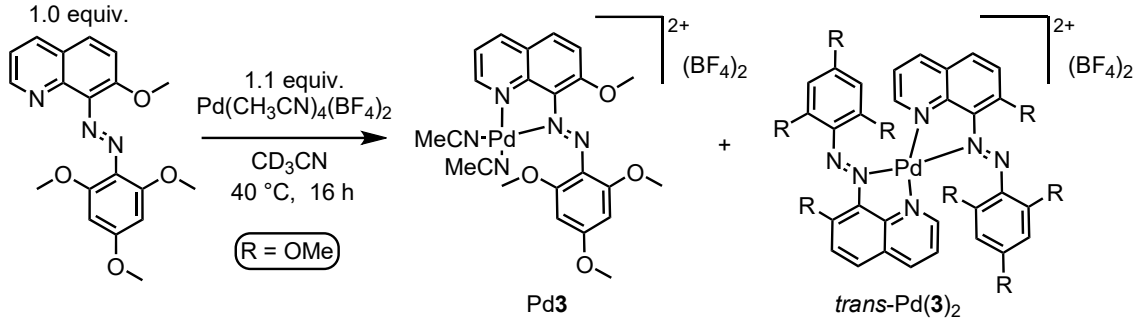

Ligand **3** (1.5 mg, 4.64 µmol, 1.0 equiv.) was dissolved in CD_3CN (0.6 mL) followed by the addition of $Pd(CH_3CN)_4(BF_4)_2$ (2.1 mg, 5.10 µmol, 1.1 equiv.). The resulting dark red solution was stirred at 40 °C for 16 h, after which it was allowed to cool to ambient temperature. The sample was then used for analysis without further purification. Note that no ^{1}H NMR assignments could be made and no signals were observed in the ^{13}C NMR due to low concentrations. See Section 4.4.2 for more information.

$[Pd(C_{19}H_{19}N_3O_4)(CH_3CN)_2](BF_4)_2$ 715.10 g/mol

$[Pd(C_{19}H_{19}N_3O_4)_2](BF_4)_2$ 986.18 g/mol

HRMS (ESI^+): *m/z* (relative intensity) = 406.0915 (65%, $[Pd + (\mathbf{3})_2]^{2+}$, calcd 406.0888), 485.0473 (100%, $[Pd + \mathbf{3} + CN]^+$, calcd 485.0442), 899.1869 (20%, $[Pd + (\mathbf{3})_2 + BF_4]^+$, calcd 899.1810).

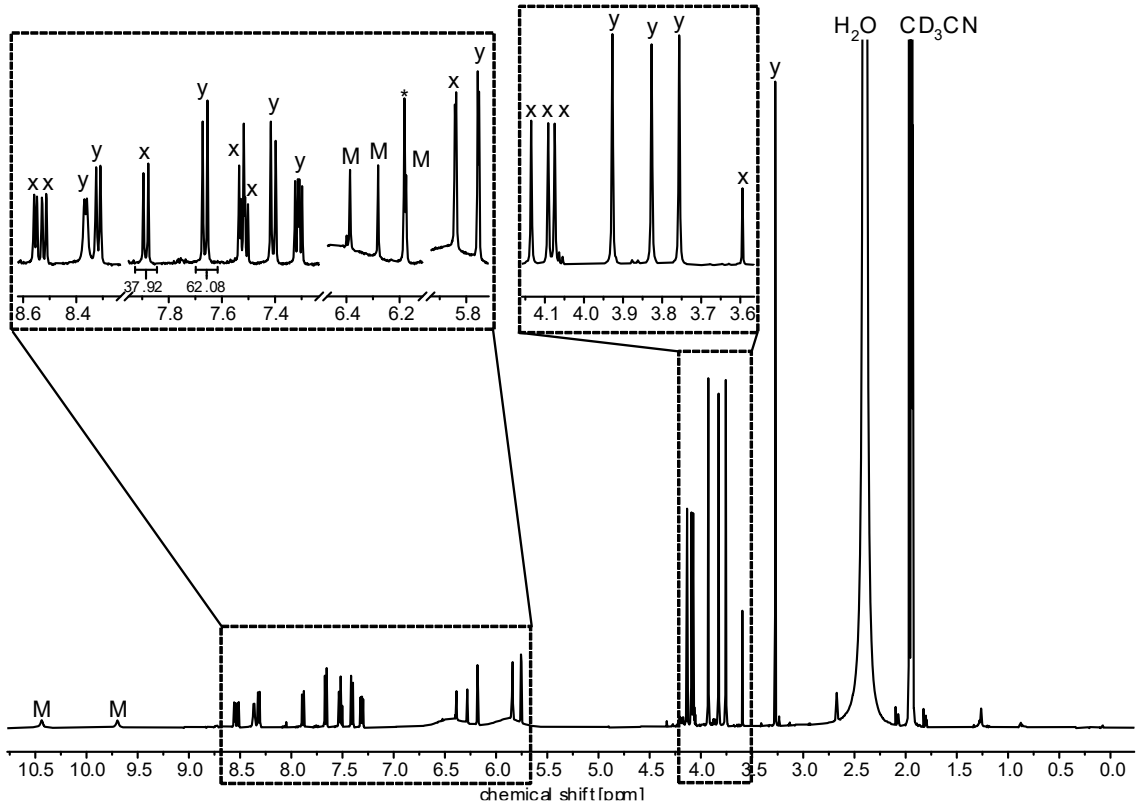

Figure 57. ^{1}H NMR spectrum (500 MHz, CD_3CN, 298 K) of Pd**3** and Pd(**3**)$_2$. See Section 4.4.2 for signal interpretations.

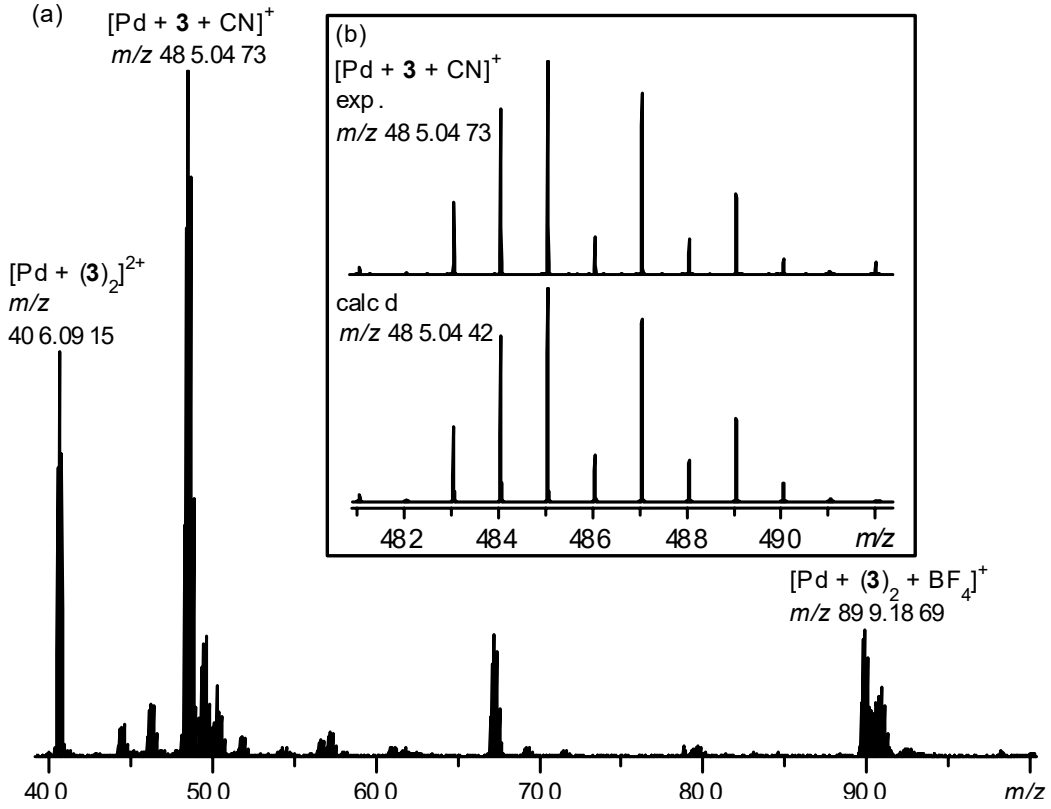

Figure 58. High-resolution ESI$^+$ mass spectrum (CH_3CN) of (a) complex sample Pd**3** and Pd(**3**)$_2$, and (b) experimental and calculated isotope pattern of [Pd + **3** + CN]$^+$.

Complexes Pd**4** & Pd(**4**)$_2$

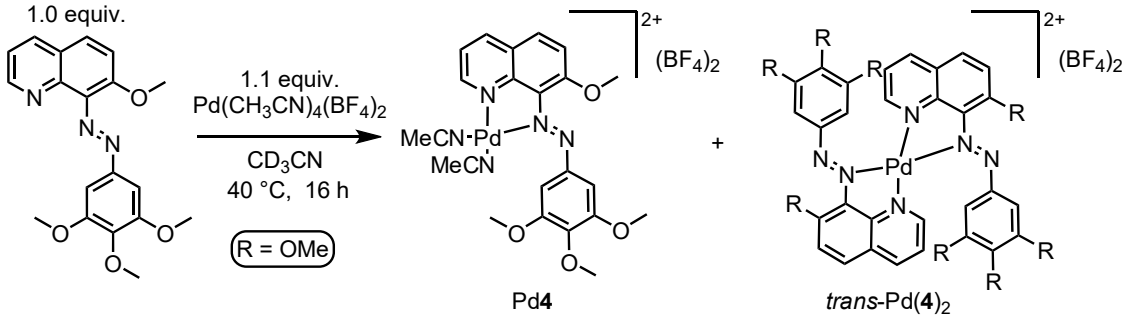

Ligand **4** (2.2 mg, 6.23 µmol, 1.0 equiv.) was dissolved in CD_3CN (0.6 mL) followed by the addition of $Pd(CH_3CN)_4(BF_4)_2$ (3.0 mg, 6.85 µmol, 1.1 equiv.). The resulting dark red solution was stirred at 40 °C for 16 h, after which it was allowed to cool to ambient temperature. The sample was then used for analysis without further purification. Note that no ^{1}H NMR assignments could be made and no signals were observed in the ^{13}C NMR due to low concentrations. See Section 4.4.3 for more information.

$[Pd(C_{19}H_{19}N_3O_4)(CH_3CN)_2](BF_4)_2$ 715.10 g/mol

$[Pd(C_{19}H_{19}N_3O_4)_2](BF_4)_2$ 986.18 g/mol

HRMS (ESI$^+$): *m/z* (relative intensity) = 406.0887 (80%, $[Pd + (\mathbf{4})_2]^{2+}$, calcd 406.0888), 459.0405 (5%, $[Pd + \mathbf{4}]^+$, calcd 459.0410), 499.0601 (100%, $[Pd + \mathbf{4} - \mathbf{H} + CH_3CN]^+$, calcd 499.0599), 899.1825 (45%, $[Pd + (\mathbf{4})_2 + BF_4]^+$, calcd 899.1810).

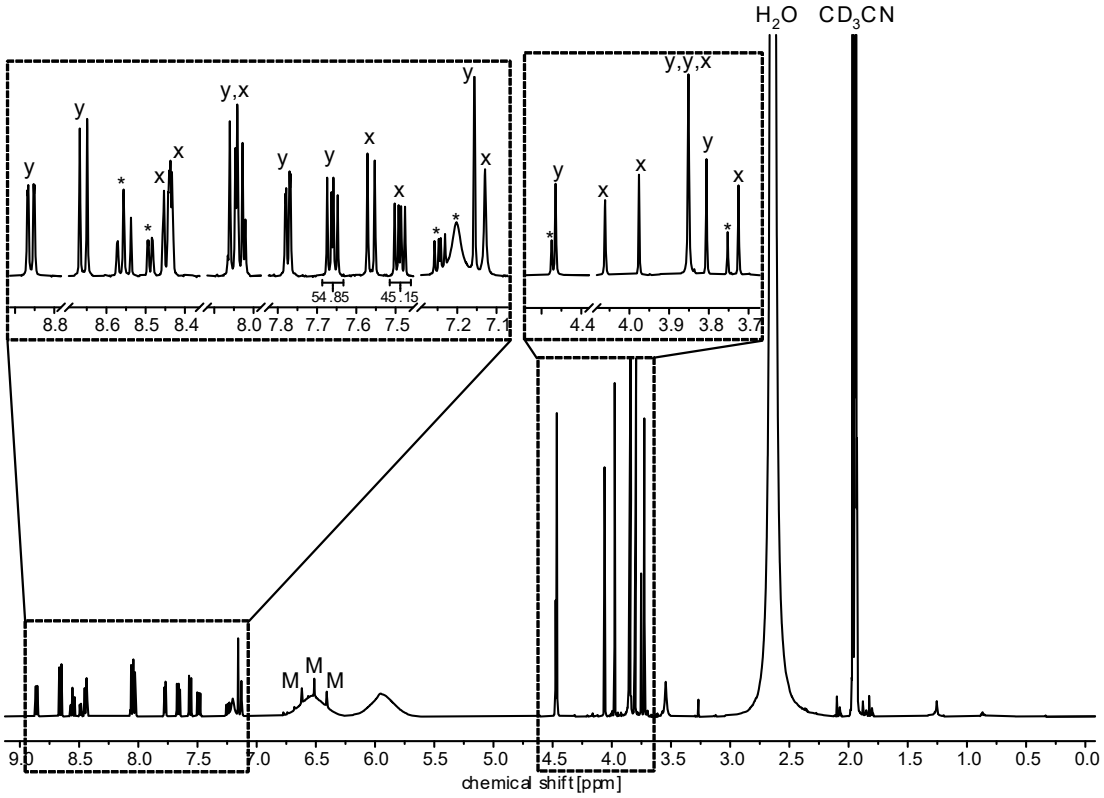

Figure 59. ^{1}H NMR spectrum (500 MHz, CD_3CN, 298 K) of Pd**4** and Pd(**4**)$_2$. See Section 4.4.3 for signal interpretations.

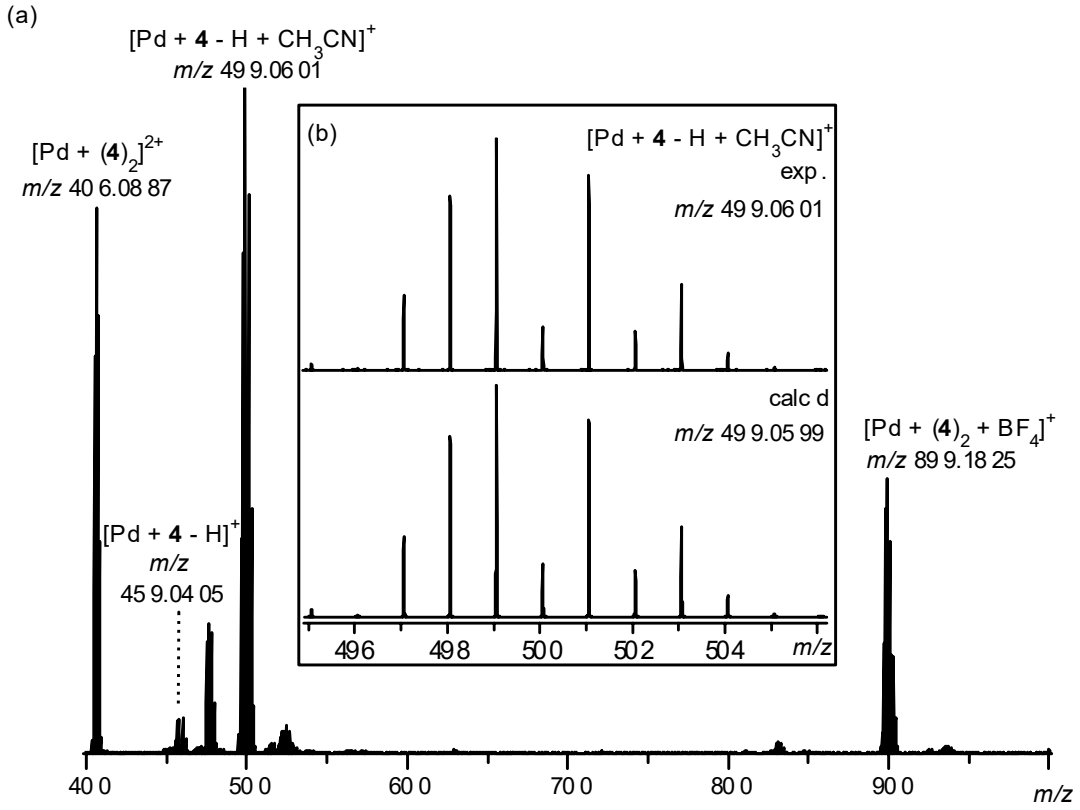

Figure 60. High-resolution ESI$^+$ mass spectrum (CH_3CN) of (a) complex sample Pd**4** and Pd(**4**)$_2$, and (b) experimental and calculated isotope pattern of [Pd + **4** – H + CH_3CN]$^+$.

5. Photoswitching of Co(II)-based coordination cages containing azobenzene backbones

Max B. Tipping, Lidón Pruñonosa Lara, Atena B. Solea, Larissa K.S. von Krbek, and Michael D. Ward

Chem. Sci., **2024**, 15, 8488-8499.
The article was submitted on 6 March 2024 and was first published in *Chemical Science* on 3 May 2024. An electronic version is available at DOI: 10.1039/D4SC01575D.

5.1 Project summary

Self-assembled metal-organic cages, as described in Section 2.4, represent a versatile class of supramolecular architectures capable of dynamic behaviour in response to external stimuli.[8] Amongst the possible stimuli employed, light is particularly advantageous for its ability to provide precise, reversible, and non-invasive control over structure and function.[13] Incorporating photoswitchable units, such as those introduced in Section 2.1, into cage-forming ligands is an attractive design strategy for making light-responsive assemblies, as it directly couples molecular photoisomerisation with supramolecular self-assembly.[12] The ability of these systems to undergo reversible changes in their structure and guest-binding properties has made them a focal point in the development of responsive supramolecular architectures.[14]

A central challenge in designing such systems is ensuring that photoisomerisation at the molecular-level reliably induces well-defined changes in the overall structure. As demonstrated by McConnell, Herges and co-workers (see Section 2.4), even subtle variations in ligand substitution patterns, e.g. *meta* versus *para* connectivity, can significantly influence coordination vectors and, consequently, the resulting architectures formed.[9] These effects are further amplified when combined with light-induced configurational changes, leading to systems with orthogonal assembly preferences that respond selectively to irradiation.

Azobenzene, a well-established molecular photoswitch introduced in Section 2.4.1, undergoes controllable and reversible *E/Z* isomerisation in response to light, resulting in distinct structural transformations.[15,40] Modifications to the azobenzene backbone allow the fine-tuning of electronic properties and coordination geometry through changes in ligand orientation and bite angles, making azobenzenes an ideal scaffold for investigating how photoinduced changes in ligand structure trigger supramolecular reorganisation.

Herein, we report how changes in coordination vectors arising from both photosiomerisation (*E*- versus *Z*-configuration) and ligand regioisomerism (*meta* versus *para* connectivity) impact the self-assembly of Co(II)-based cages.

In this project, photoswitchable azobenzene units were incorporated as spacers within ditopic bridging ligands to enable light-induced modulation of ligand geometry. Two regioisomeric ligands were synthesised, each bearing two pyrazolyl-pyridine coordination sites linked by an azobenzene backbone. In ligand **L*p***, the donor units are connected at the *para* position relative to the N=N azo bridge, whereas in ligand **L*m*** they are attached at the *meta* position (Scheme 39). As expected for azobenzenes, both ligands undergo reversible *E/Z* isomerisation: the thermodynamically stable *E*-isomer converts to the metastable *Z*-form upon irradiation with UV light (340 nm), and the reverse process occurs under blue light (450 nm) or via thermal relaxation. These two ligands therefore provided distinct coordination vectors, leading to structurally diverse, light-responsive assemblies.

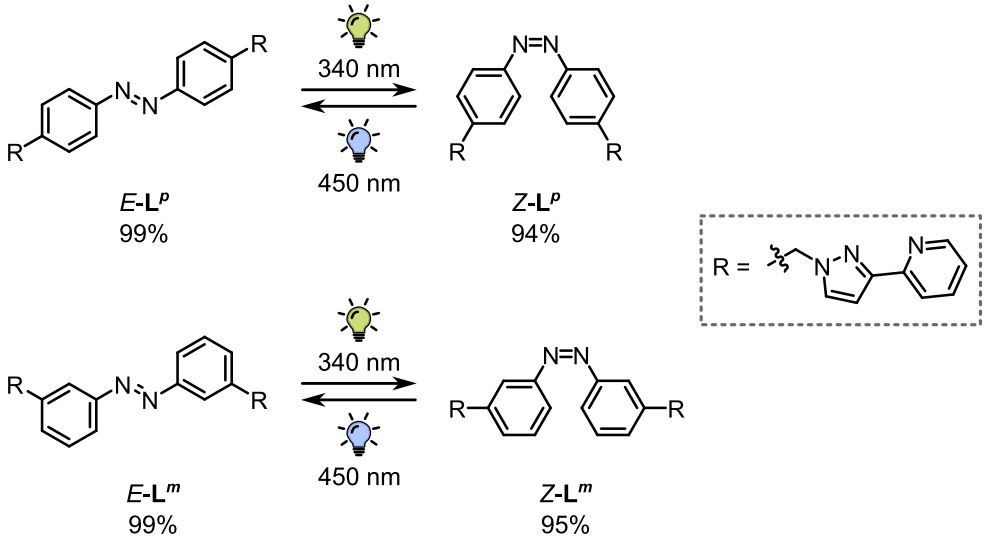

Scheme 39. Light-induced isomeric forms of ligands **L*p*** and **L*m*** with associated PSS compositions.

The self-assembly of $\mathbf{L}^{p}$ with Co(II) produced two distinct species, depending on the azobenzene configuration (Scheme 40). With *E*-$\mathbf{L}^{p}$, a dinuclear helicate of composition $Co_2(E\text{-}\mathbf{L}^{p})_3$ and D_3 symmetry was formed, consistent with linear coordination vectors favouring small, discrete architectures.[166] Irradiation with UV light (340 nm) induced *E*→*Z* isomerisation, which drove reorganisation into a larger C_3-symmetric $Co_4(Z\text{-}\mathbf{L}^{p})_6$ tetrahedral cage structure (Scheme 40). Reverse *Z*→*E* isomerisation converted the $Co_4(Z\text{-}\mathbf{L}^{p})_6$ structure back into the $Co_2(E\text{-}\mathbf{L}^{p})_3$ helicate, either under white light or thermally after five weeks. Photoisomerisation could be cycled over six times without any detectable photodegradation. Thus, establishing a fully reversibly, light-driven interconversion between two supramolecular assemblies of different nuclearity.

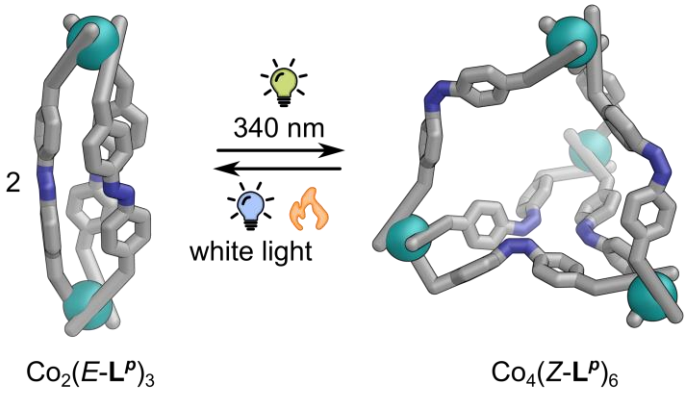

Scheme 40. MM2-optimised model of the dinuclear, triple-helicate $Co_2(E\text{-}\mathbf{L}^{p})_3$, and GFN-xTB generated structure of the photoisomerised tetrahedral cage $Co_4(Z\text{-}\mathbf{L}^{p})_6$. The pyrazolyl-pyridine coordination sites have been stylised to highlight the configurational change of azobenzene and to aid interpretation. Adapted from Tipping et al.[23]

On the other hand, $\mathbf{L}^{m}$ exhibited a more intricate assembly profile. Crystallographic analysis revealed that self-assembly with Co(II) formed a $Co_4(E\text{-}\mathbf{L}^{m})_6$ complex, in which two dinuclear double helicates are connected by two additional bridging ligands (Scheme 41). This architecture reflects the bent coordination vectors imposed by the *meta* connectivity. Studies of Co(II) assemblies with *Z*-$\mathbf{L}^{m}$ revealed greater complexity than those with *Z*-$\mathbf{L}^{p}$. When *Z*-$\mathbf{L}^{m}$ was first generated by photoirradiating the free ligand and then combined with Co(II), a species consistent with $Co_4(Z\text{-}\mathbf{L}^{m})_6$ was obtained (Scheme 41). In contrast, irradiating pre-assembled $Co_4(E\text{-}\mathbf{L}^{m})_6$ with UV light to induce *E*→*Z* isomerisation produced a more complex mixture of species, indicating that different isomeric cages coexist under these conditions. $Co_4(\mathbf{L}^{m})_6$ species can thus incorporate

either *E*- or *Z*- ligands, allowing a series of mixed-ligand $Co_4(Z\text{-}\mathbf{L}^m)_n(E\text{-}\mathbf{L}^m)_{6-n}$ complexes to exist without disrupting the overall stoichiometry. NMR titration experiments with defined mixtures of *E*-$\mathbf{L}^m$ and *Z*-$\mathbf{L}^m$ indicated that $Co_4(Z\text{-}\mathbf{L}^m)_2(E\text{-}\mathbf{L}^m)_4$ is a thermodynamically favoured assembly. Additionally, time-resolved *in-situ* NMR studies supported the formation of mixed assemblies with varying *E*:*Z* ratios. Importantly, these experiments revealed that in order to obtain $Co_4(Z\text{-}\mathbf{L}^m)_6$ as the major species, $\mathbf{L}^m$ must be switched to the *Z*-form prior to assembly. Thermal relaxation of $Co_4(Z\text{-}\mathbf{L}^m)_6$ occurred over ten months, much slower than for the analogous $Co_4(Z\text{-}\mathbf{L}^p)_6$ tetrahedral cage, and proceeded through $Co_4(Z\text{-}\mathbf{L}^m)_2(E\text{-}\mathbf{L}^m)_4$ as a long-lived intermediate.

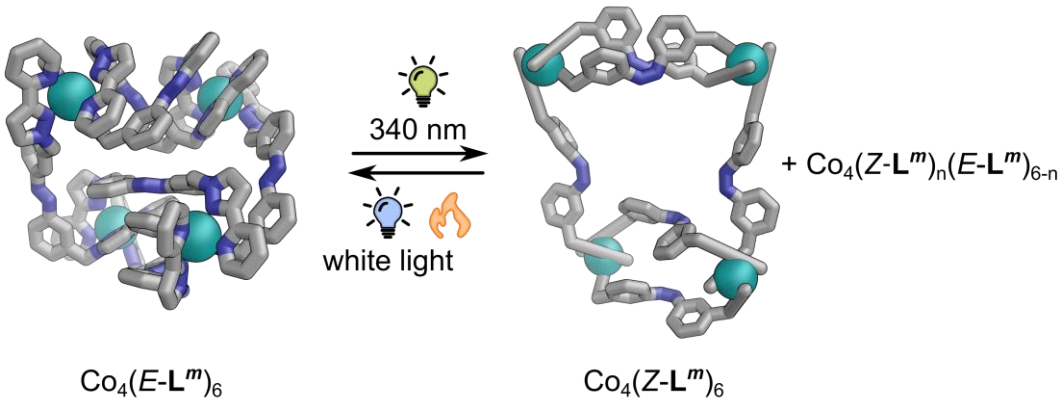

Scheme 41. Molecular structure of $Co_4(E\text{-}\mathbf{L}^m)_6$ from an X-ray crystal structure determination and a GFN-xTB generated structure of $Co_4(Z\text{-}\mathbf{L}^m)_6$ where the pyrazolyl-pyridine coordination sites have been stylised to aid interpretation. GFN-xTB generated structure of mixed-ligand $Co_4(Z\text{-}\mathbf{L}^m)_n(E\text{-}\mathbf{L}^m)_{6-n}$ complexes can be found in the Supporting Information (Figure S57). Adapted from Tipping et al.[23]

Together, these results exemplify how the self-assembly behaviour of metal-organic cages, in this case of Co(II), can be significantly influenced by both the substitution pattern and the photoisomeric state of the ligand. The *para*-substituted ligand ($\mathbf{L}^p$) enables reversible interconversion between assemblies of different nuclearity, while the *meta*-substituted ligand ($\mathbf{L}^m$) produces a family of $Co_4(\mathbf{L}^m)_6$ species in which assemblies containing either exclusively *E*- or *Z*-ligands, or mixtures of both, can be present depending on the irradiation pathway and assembly conditions. By incorporating azobenzene photoswitches into the ligand backbone, we achieved light-induced modulation of the ligand geometry, enabling reversible control over cage formation.

5.2 Author contributions

The general conception of the project was developed by Max B. Tipping and Michael D. Ward; the latter also supervised the research throughout. Max B. Tipping led the experimental work, which included the synthesis of both azobenzene-based ligands (**L**^{m} and **L**^{p}), the assembly of the Co(II)-based coordination cages, and their characterisation. He also conducted in-depth photoswitching studies and interpreted the photochemical behaviour and switching dynamics of the system, which formed the central focus of the investigation.

Lidón Pruñonosa Lara carried out *in-situ* ^{1}H NMR experiments, with data analysis and interpretation performed jointly with Max B. Tipping. Due to differences in LED equipment between institutions, she also conducted complementary photoswitching experiments using UV-vis spectroscopy to determine the optimal irradiation wavelengths. Additionally, she measured DOSY NMRs, including plotting the data and calculating diffusion coefficients. All molecular simulations to support structural analysis were carried out by Lidón Pruñonosa Lara, while Larissa K. S. von Krbek rendered the structural figures using PyMOL and supervised Lidón's work.

Atena B. Solea was responsible for the X-ray crystallographic measurements and structure refinement of all successfully crystallised ligand and cage assemblies.

The Supporting Information and manuscript were based on the doctoral thesis of Max B. Tipping. Michael D. Ward then prepared the manuscript and Supporting Information for journal submission, incorporating revisions and input from all the co-authors. All authors contributed to discussions throughout the project and provided feedback on the final manuscript.

The inclusion of this publication in the doctoral thesis has been approved by all of the co-authors.

6. White-light powered autonomous molecular ratchet drives Pd^{II} capsules out of equilibrium

Lidón Pruñonosa Lara, Benedikt Bädorf, Maximilian J. Notheis, Gregor Schnakenburg, Stefan Grimme, and Larissa K. S. von Krbek.

Preprint uploaded to ChemRxiv on 9 October 2025. Available at DOI: 10.26434/chemrxiv-2025-ck3gw.

6.1 Project summary

Metal-organic cages formed via coordination-driven self-assembly, as outlined in Section 2.4, offer a versatile platform for constructing dynamic supramolecular architectures.[111] These systems commonly operate under thermodynamic control, whereby the final structure corresponds to the global free-energy minimum under the given conditions.[24] Such equilibrium assemblies have enabled the development of well-defined cages with tailored guest-binding properties and have increasingly been recognised as dynamic molecular platforms capable of supporting mechanical motion.[120]

Nonetheless, as discussed in Section 2.5, operating supramolecular systems away from equilibrium allows access to structural outcomes that would otherwise be thermodynamically unfavourable.[130] Out-of-equilibrium assemblies require continuous energy input to maintain metastable states.[26] This energy can be supplied by external stimuli; light, in particular, offers high spatial and temporal precision, reversibility, and is non-invasive.[13] When coupled to reaction networks that selectively link energy-releasing and energy-consuming steps, light can bias molecular transformations and sustain non-equilibrium behaviour. This concept is formalised in the framework of molecular ratchets (see Section 2.6).[132] Molecular ratchets are reaction cycles that proceed preferentially in one direction, typically through energy gradients (energy ratchets) or kinetic asymmetry (information ratchets).[28] While molecular ratchets have been reported in diverse molecular systems, their integration into metallo-supramolecular cages, particularly for autonomous operation, remains rare.[29]

Photoswitchable ligands embedded within coordination assemblies (see Section 2.4) offer a powerful approach to modulating structure and behaviour using light. Herein, we report a light-powered molecular information ratchet embedded within a Pd(II)-based cage system.[140] This ratchet mechanism is enabled by a photoswitchable azobispyrazole-containing ligand (**1**), which undergoes reversible *E/Z* isomerisation with near-quantitative conversions and excellent fatigue resistance (Scheme 42). Upon irradiation with 365 nm light, ligand **1** achieves a PSS of 99% *Z*-**1** in CD_2Cl_2. Reverse *Z*→*E* isomerisation occurs either under 500 nm light (97% *E*-**1**) or via thermal relaxation, with a half-life of 10 h at 60 °C in DMF. Azobispyrazoles photoswitches (Section 2.1.2) have been scarcely explored in supramolecular systems and, to our knowledge, have not been previously incorporated into metal-organic cages.

The conformational flexibility of ligand **1**, arising from its pyrazole units, enables it to adopt distinct geometries depending on the orientation of the pyrazole rings. These rings can adopt either an *anti* or *syn* conformation, with protons H-a and H-b positioned either on opposite sides or on the same side of the azo bridge, respectively (Scheme 42). In its *E*-configuration, ligand **1** forms two discrete Pd(II) assemblies: a $Pd_3(E\text{-}\mathbf{1})_6$ double-walled triangle (*E*-**T**) and a $Pd_2(E\text{-}\mathbf{1})_4$ lantern (*E*-**L**), which coexist in a 78:22 equilibrium mixture (Scheme 42). In *E*-**T**, the ligands adopt an *anti*-conformation, giving a coordination vector angle of 60°, while in *E*-**L** they adopt a *syn*-conformation with an angle of 0°. These distinct bite angles thus enable structurally divergent assemblies to be formed from the same ligand.

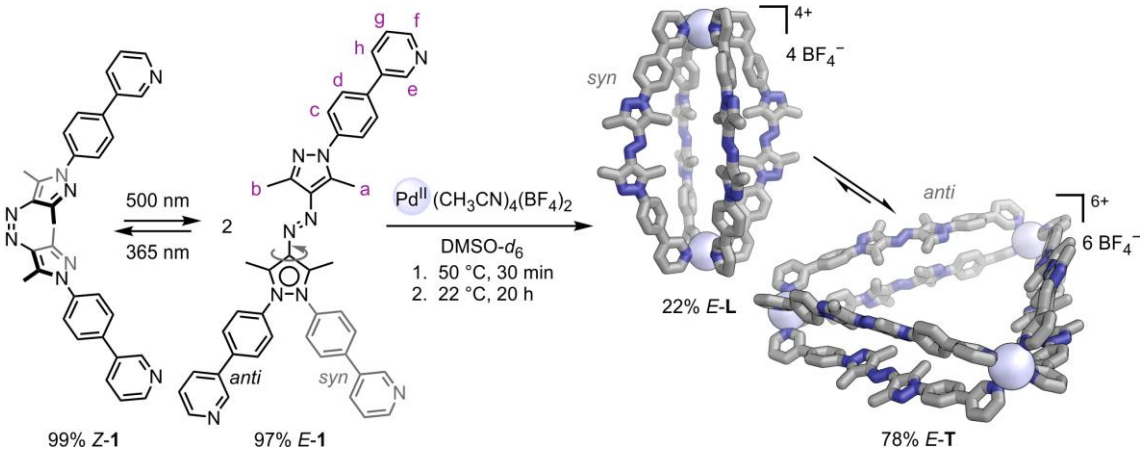

Scheme 42. Photoswitching of ligand **1** between its *E*- and *Z*-isomers. *E*-**1** adopts either a *syn* or *anti* conformation. Self-assembly of *E*-**1** with $Pd(CH_3CN)_4(BF_4)_2$ yields 78% triangle *E*-**T** (GFN2-xTB optimised structure) and 22% lantern *E*-**L** (X-ray structure). Reproduced from Pruñonosa Lara et al.[140]

Given the labile nature of the Pd(II)-pyridine bonds, *E*-**T** and *E*-**L** readily interconvert and coexist in a dynamic equilibrium. As expected for an equilibrium between a larger and a smaller species (see Section 2.3), diluting the complex mixture or increasing the temperature shifts the equilibrium towards the entropically favoured lantern *E*-**L**.

Upon UV light irradiation (365 nm), both *E*-**T** and *E*-**L** undergo complete *E*→*Z* isomerisation, resulting in a single Pd_2(*Z*-**1**)$_4$ lantern structure (*Z*-**L**) (Scheme 43). Minor signals in the ^{1}H NMR spectrum of *Z*-**L** are tentatively attributed to four additional diastereomers, arising from the chiral nature of *Z*-**1**. DFT calculations revealed only small energy differences between these diastereomers, supporting their coexistence in solution.

To gain insight into the thermal stability and relaxation pathway of *Z*-**L**, its time-dependent changes were monitored. *Z*-**L** exhibits high thermodynamic stability, with a thermal half-life of 21 min at 75 °C and a relaxation time of approximately one year at room temperature. During thermal relaxation, a series of intermediates were observed. Given the comparable solvodynamic diameters of *Z*-**L** and *E*-**L**, both lanterns appear sufficiently flexible to accommodate mixed *E/Z* ligand configurations. Accordingly, these intermediates were tentatively assumed to be *Z*,*Z*,*Z*,*E*-**L**, *cis*- and *trans*-*Z*,*Z*,*E*,*E*-**L**, and *Z*,*E*,*E*,*E*-**L** – consistent with the stepwise *E/Z* isomerisation of the four ligands. This assumption was supported by both experimental and computational data, the latter revealing a systematic increase in free energy with each successive *E*→*Z* conversion, consistent with the presence of mixed-ligand lantern intermediates.

Irradiating *Z*-**L** with visible light (500 nm) induces complete *Z*→*E* isomerisation. However, instead of regenerating the original 78:22 *E*-**T**/*E*-**L** mixture, only the lantern *E*-**L** is initially formed, bypassing the thermodynamically favoured *E*-**T** structure (Scheme 43). Nevertheless, the initial equilibrium mixture can be restored by leaving the sample to reach equilibrium at room temperature for at least 8 h. This light-induced switching and subsequent thermal equilibration can be repeated over multiple cycles without any detectable photodegradation.

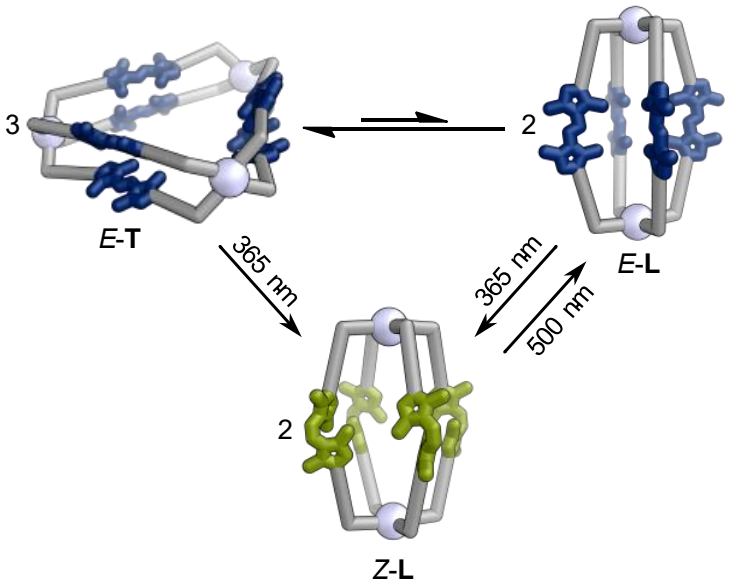

Scheme 43. Schematic representation of the molecular information ratchet. Irradiation of the *E*-**T**/*E*-**L** mixture with 365 nm light yields *Z*-**L** exclusively. Subsequent irradiation with 500 nm light reverts *Z*-**L** to *E*-**L**, which then equilibrates back to the original *E*-**T**/*E*-**L** ratio (78:22, respectively).

In-situ NMR studies confirmed that *E*-**T** and *E*-**L** convert to *Z*-**L** under 365 nm light irradiation, while *Z*-**L** exclusively reverts to *E*-**L** when exposed to 500 nm light. Kinetic modelling further supported these observations, revealing that the *Z*-**L**→*E*-**L** pathway is markedly favoured over the *Z*-**L**→*E*-**T** pathway, and that the original *E*-**T**/*E*-**L** mixture can only be regained through slow thermal equilibration. Together, these directional switching behaviours establish that the system operates as a molecular information ratchet, defined in Section 2.6.2. The kinetic asymmetry of the *Z*-**L**→*E*-**L** and *Z*-**L**→*E*-**T** back reactions result in the accumulation of the out-of-equilibrium *E*-**L** structure.

Remarkably, the molecular ratchet operates autonomously under white light or sunlight. This autonomy arises because both *E*- and *Z*-isomers absorb within the visible spectrum, ensuring that each state is repeatedly excited and interconverted, even under constant irradiation. As a result, the system continuously cycles through the ratcheting process and accumulates the out-of-equilibrium lantern *E*-**L**. Under steady-state irradiation, a 34:66 *E*-**T**/*E*-**L** ratio is reached after 5.5 h of white-light exposure, corresponding to a threefold enrichment of *E*-**L**. A similar enrichment (36:64 *E*-**T**/*E*-**L**) is obtained under sunlight, demonstrating that the system can temporarily convert light into stored chemical energy. This process is fully reversible; the original 78:22 (*E*-**T**:*E*-**L**) equilibrium mixture is restored when left in the dark at 22 °C.

Together, these results present a striking example of an autonomous, light-powered information ratchet integrated within a metallo-supramolecular cage. By embedding a photoswitchable ligand with conformational flexibility into a Pd(II) coordination framework, we demonstrate how kinetic asymmetry can be exploited to drive supramolecular assemblies away from equilibrium. The transient storage of chemical energy in a defined metastable structure opens up new possibilities for the developing functional, light-responsive supramolecular devices.

6.2 Author contributions

Lidón Pruñonosa Lara carried out all experimental work, including the synthesis of ligand **1** and its precursors, the preparation and characterisation of the Pd(II)-based coordination assemblies, and their detailed photoswitching studies. She also processed and interpreted the data, which formed the core of this investigation, prepared the majority of the Supporting Information, and wrote the first draft of the manuscript.

Larissa K. S. von Krbek supervised the project from start to finish, working closely with Lidón to develop the study's overall conception. Larissa K. S. von Krbek was instrumental in assembling the publication, making the manuscript figures, and shaping and refining the manuscript to its final polished form.

Benedikt Bädorf, under the supervision of Stefan Grimme, performed all quantum-chemical calculations to support the experimental structural analysis. Maximilian Notheis fitted the kinetic data and contributed significantly to the interpretation and discussion of the ratchet mechanism. Gregor Schnakenburg was responsible for the X-ray crystallographic measurements and structure refinements of all successfully crystallised ligands and coordination assemblies.

All authors contributed to discussions throughout the project and provided feedback on the final manuscript.

The inclusion of this publication in the doctoral thesis has been approved by all of the co-authors.

7. Conclusion

This thesis set out to explore how light can be used not only to control, but ultimately to drive, the behaviour of supramolecular assemblies. Specifically, it addressed three central questions: (i) How does metal coordination influence the photochemical properties of azobenzene ligands? (ii) How do variations in coordination vectors determine the geometry, responsiveness, and potential for concerted switching in photoswitchable metal-organic cages? and (iii) Can continuous light input drive a metallo-supramolecular system out of equilibrium, enabling autonomous, directional transformations via a molecular ratchet mechanism that converts light into stored chemical energy? Each project developed the work of the previous one, progressing from the photochemical behaviour of mononuclear complexes to the design of increasingly complex light-driven supramolecular assemblies.

The first project, investigated how metal coordination affects the intrinsic photoswitching behaviour of azobenzene derivatives in mononuclear complexes. It was found that coordination to Pd(II) substantially influences isomerisation behaviour, with direct N=N coordination leading to the partial or complete suppression of photoisomerisation depending on the ligand's denticity and donor arrangement. These findings established the design principle that preserving photoswitch function requires spatial separation between the azo unit and the metal-binding sites. This principle guided the design of the subsequent assemblies, ensuring that light responsiveness could be maintained in larger supramolecular architectures.

Building on these findings, the second project investigated how subtle differences in ligand connectivity and coordination vectors influence the geometry and photoresponsiveness of self-assembled metal-organic cages. Comparative studies of *para*- and *meta*-substituted azobenzene ligands revealed that small structural variations can have a significant impact on the nuclearity and the concertedness of photoinduced transformations in Co(II)-based cages. The *para*-substituted ligand enabled the reversible interconversion of well-defined assemblies of different nuclearity, whereas the *meta*-substituted ligand led to a family of $Co_4(\mathbf{L}^{m})_6$ species containing either *E*- or *Z*-ligands, or a mixture of both. These results demonstrate that even subtle geometric changes in

ligand structure and configuration can have a significant impact on the geometry and light responsiveness of the resulting cages.

The third project extended these principles into out-of-equilibrium systems, showing that a molecular ratchet mechanism can drive metallo-supramolecular assemblies away from equilibrium with continuous light input. Pd(II)-based assemblies incorporating azobispyrazole photoswitchable ligands were designed to undergo directional transformations between discrete cage structures under sustained irradiation. As both the *E* and *Z* states absorb visible light, the system remains responsive under continuous white light or sunlight exposure, autonomously cycling between structural forms and accumulating an out-of-equilibrium assembly. These findings demonstrate how kinetic asymmetry and continuous light input can be harnessed to achieve autonomous, light-driven operation and temporary chemical energy storage in supramolecular assemblies. This represents a significant step towards the development of functional systems capable of converting light energy into stored chemical energy.

Together, these three projects form a conceptual trajectory, progressing from an understanding of how metal coordination controls photoswitching to the translation of this knowledge into the design of responsive cages, and ultimately, the achievement of light-driven, out-of-equilibrium behaviour in a self-assembled molecular ratchet. Looking ahead, these findings open up new opportunities for developing light-responsive supramolecular systems capable of storing and using light energy. Future work could build on these concepts to create artificial molecular machines that are powered directly by sunlight, mimicking nature's strategies for light-driven energy storage and conversion.

8. References

[1] F. Huang, E. V. Anslyn, "Introduction: Supramolecular Chemistry" *Chem. Rev.* **2015**, *115*, 6999–7000.

[2] S. Talreja, S. Tiwari, "Supramolecular Chemistry: Unveiling the Fascinating World of Non-Covalent Interactions and Complex Assemblies" *J Pharm Pharmacol Res* **2023**, *7*, 133–139.

[3] L. E. Bickerton, T. G. Johnson, A. Kerckhoffs, M. J. Langton, "Supramolecular chemistry in lipid bilayer membranes" *Chem. Sci.* **2021**, *12*, 11252–11274.

[4] A. Barba-Bon, M. Nilam, A. Hennig, "Supramolecular Chemistry in the Biomembrane" *ChemBioChem* **2020**, *21*, 886–910.

[5] J.-M. Lehn, "Supramolecular chemistry: Where from? Where to?" *Chem. Soc. Rev.* **2017**, *46*, 2378–2379.

[6] S. Kubik, *Supramolecular Chemistry From Concepts to Applications*, De Gruyter, Berlin, Boston, **2024**.

[7] Prof. Dr. J. Lehn, *Supramolecular Chemistry: Concepts and Perspectives*, VCH, Weinheim, Germany, **1995**.

[8] T. R. Cook, P. J. Stang, "Recent Developments in the Preparation and Chemistry of Metallacycles and Metallacages via Coordination" *Chem. Rev.* **2015**, *115*, 7001–7045.

[9] D. Hugenbusch, M. Lehr, J. von Glasenapp, A. J. McConnell, R. Herges, "Light-Controlled Destruction and Assembly: Switching between Two Differently Composed Cage-Type Complexes" *Angew. Chem. Int. Ed.* **2023**, *62*, e202212571.

[10] W. Cullen, S. Turega, C. A. Hunter, M. D. Ward, "pH-dependent binding of guests in the cavity of a polyhedral coordination cage: reversible uptake and release of drug molecules" *Chem. Sci.* **2014**, *6*, 625–631.

[11] G. Szalóki, V. Croué, V. Carré, F. Aubriet, O. Alévêque, E. Levillain, M. Allain, J. Aragó, E. Ortí, S. Goeb, M. Sallé, "Controlling the Host–Guest Interaction Mode through a Redox Stimulus" *Angew. Chem. Int. Ed.* **2017**, *56*, 16272–16276.

[12] E. Benchimol, J. Tessarolo, G. H. Clever, "Photoswitchable coordination cages" *Nat. Chem.* **2024**, *16*, 13–21.

[13] D.-H. Qu, Q.-C. Wang, Q.-W. Zhang, X. Ma, H. Tian, "Photoresponsive Host–Guest Functional Systems" *Chem. Rev.* **2015**, *115*, 7543–7588.

[14] S. J. Wezenberg, "Light-switchable Metal-Organic Cages" *Chem. Lett.* **2020**, *49*, 609–615.

[15] J. Volarić, W. Szymanski, N. A. Simeth, B. L. Feringa, "Molecular photoswitches in aqueous environments" *Chem. Soc. Rev.* **2021**, *50*, 12377–12449.

[16] F. A. Jerca, V. V. Jerca, R. Hoogenboom, "Advances and opportunities in the exciting world of azobenzenes" *Nat. Rev. Chem.* **2022**, *6*, 51–69.

[17] Y. He, Z. Shangguan, Z. Zhang, M. Xie, C. Yu, T. Li, "Azobispyrazole Family as Photoswitches Combining (Near-) Quantitative Bidirectional Isomerization and Widely Tunable Thermal Half-Lives from Hours to Years**" *Angew. Chem. Int. Ed.* **2021**, *60*, 16539–16546.

[18] G. C. Thaggard, J. Haimerl, K. C. Park, J. Lim, R. A. Fischer, B. K. P. M. Kankanamalage, B. J. Yarbrough, G. R. Wilson, N. B. Shustova, "Metal–Photoswitch Friendship: From Photochromic Complexes to Functional Materials" *J. Am. Chem. Soc.* **2022**, *144*, 23249–23263.

[19] G. Morselli, C. Reber, O. S. Wenger, "Molecular Design Principles for Photoactive Transition Metal Complexes: A Guide for 'Photo-Motivated' Chemists" *J. Am. Chem. Soc.* **2025**, *147*, 11608–11624.

[20] D. Gupta, A. K. Gaur, H. Kumar, S. Singh, S. Venkataramani, "Light-Switchable Metal Complexes: Introducing Photoresponsive Behaviour Through Azoheteroarenes" *ChemPhotoChem* **2023**, *7*, DOI 10.1002/cptc.202300068.

[21] L. P. Wu, Y. Suenaga, T. Kuroda-Sowa, M. Maekawa, K. Furuichi, M. Munakata, "Syntheses, structures and properties of palladium (II) complexes with photochromic 4-methoxyazobenzene" *Inorg. Chim. Acta* **1996**, *248*, 147–152.

[22] S. Bhattacharyya, M. R. Black, B. S. Pilgrim, "Encapsulation of reactive species within metal–organic cages" *Chem. Sci.* **2025**, DOI 10.1039/d5sc02081f.

[23] M. B. Tipping, L. Pruñonosa Lara, A. B. Solea, L. K. S. von Krbek, M. D. Ward, "Photoswitching of Co(II)-based coordination cages containing azobenzene backbones" *Chem. Sci.* **2024**, *15*, 8488–8499.

[24] S. A. P. van Rossum, M. Tena-Solsona, J. H. van Esch, R. Eelkema, J. Boekhoven, "Dissipative out-of-equilibrium assembly of man-made supramolecular materials" *Chem. Soc. Rev.* **2017**, *46*, 5519–5535.

[25] G. Li, R. W. Lewis, R. Eelkema, "Out-of-Equilibrium Assembly Based on Host–Guest Interactions" *CCS Chem.* **2024**, *6*, 27–40.

[26] Q. Wang, Z. Qi, M. Chen, D. Qu, "Out-of-equilibrium supramolecular self-assembling systems driven by chemical fuel" *Aggregate* **2021**, *2*, DOI 10.1002/agt2.110.

[27] M. Kathan, S. Hecht, "Photoswitchable molecules as key ingredients to drive systems away from the global thermodynamic minimum" *Chem. Soc. Rev.* **2017**, *46*, 5536–5550.

[28] S. Borsley, D. A. Leigh, B. M. W. Roberts, “Molecular Ratchets and Kinetic Asymmetry: Giving Chemistry Direction” *Angew. Chem. Int. Ed.* **2024**, *63*, e202400495.

[29] M. J. Notheis, G. Schnakenburg, L. K. S. von Krbek, “Light-Driven Ratchet Mechanism Accelerates Regioselective Metal-Cation Exchange in a Heterobimetallic Helicate” *Angew. Chem. Int. Ed.* **2025**, e202508952.

[30] E. Benchimol, B.-N. T. Nguyen, T. K. Ronson, J. R. Nitschke, “Transformation networks of metal–organic cages controlled by chemical stimuli” *Chem. Soc. Rev.* **2022**, *51*, 5101–5135.

[31] S. J. Wezenberg, “Photoswitchable molecular tweezers: isomerization to control substrate binding, and what about vice versa ?” *Chem. Commun.* **2022**, *58*, 11045–11058.

[32] M. Russew, S. Hecht, “Photoswitches: From Molecules to Materials” *Adv. Mater.* **2010**, *22*, 3348–3360.

[33] A. Goulet-Hanssens, F. Eisenreich, S. Hecht, “Enlightening Materials with Photoswitches” *Adv. Mater.* **2020**, *32*, e1905966.

[34] C. Sun, C. Wang, R. Boulatov, “Applications of Photoswitches in the Storage of Solar Energy” *ChemPhotoChem* **2019**, *3*, 268–283.

[35] I. Tochitsky, M. A. Kienzler, E. Isacoff, R. H. Kramer, “Restoring Vision to the Blind with Chemical Photoswitches” *Chem. Rev.* **2018**, *118*, 10748–10773.

[36] D. Samanta, J. Gemen, Z. Chu, Y. Diskin-Posner, L. J. W. Shimon, R. Klajn, “Reversible photoswitching of encapsulated azobenzenes in water” *Proc. Natl. Acad. Sci.* **2018**, *115*, 9379–9384.

[37] J. Fitz, A. Mammana, “Spectroscopic study of the pH dependence of the optical properties of a water-soluble molecular photo-switch” *Spectrochim. Acta Part A: Mol. Biomol. Spectrosc.* **2020**, *227*, 117576.

[38] N. R. Krekiehn, M. Müller, U. Jung, S. Ulrich, R. Herges, O. M. Magnussen, “UV/Vis Spectroscopy Studies of the Photoisomerization Kinetics in Self-Assembled Azobenzene-Containing Adlayers” *Langmuir* **2015**, *31*, 8362–8370.

[39] Q. Thijssen, J. A. Carroll, F. Feist, A. Beil, H. Grützmacher, M. Wegener, S. V. Vlierberghe, C. Barner-Kowollik, “Beyond absorption maxima: the impact of wavelength-resolved photochemistry on materials science” *Mater. Horiz.* **2024**, *11*, 6184–6191.

[40] K. Kuntze, J. Isokuortti, J. J. van der Wal, T. Laaksonen, S. Crespi, N. A. Durandin, A. Priimagi, “Detour to success: photoswitching via indirect excitation” *Chem. Sci.* **2024**, *15*, 11684–11698.

[41] K. B. Jørgensen, “Photochemical Oxidative Cyclisation of Stilbenes and Stilbenoids—The Mallory-Reaction” *Molecules* **2010**, *15*, 4334–4358.

[42] H. Bouas-Laurent, H. Dürr, “Organic photochromism (IUPAC Technical Report)” *Pure Appl. Chem.* **2001**, *73*, 639–665.

[43] K. Nakatani, J. Piard, P. Yu, R. Métivier, “Photochromic Materials” **2018**, 1–45.

[44] E. Merino, M. Ribagorda, “Control over molecular motion using the cis–trans photoisomerization of the azo group” *Beilstein J. Org. Chem.* **2012**, *8*, 1071–1090.

[45] Ľ. Vetráková, V. Ladányi, J. A. Anshori, P. Dvořák, J. Wirz, D. Heger, “The absorption spectrum of cis -azobenzene” *Photochem. Photobiol. Sci.* **2017**, *16*, 1749–1756.

[46] A. A. Beharry, G. A. Woolley, “Azobenzene photoswitches for biomolecules” *Chem. Soc. Rev.* **2011**, *40*, 4422–4437.

[47] P. Bharmoria, S. Ghasemi, F. Edhborg, R. Losantos, Z. Wang, A. Mårtensson, M. Morikawa, N. Kimizuka, Ü. İşci, F. Dumoulin, B. Albinsson, K. Moth-Poulsen, “Far-red triplet sensitized Z -to- E photoswitching of azobenzene in bioplastics” *Chem. Sci.* **2022**, *13*, 11904–11911.

[48] A. H. Heindl, R. C. Wende, H. A. Wegner, “London dispersion as important factor for the stabilization of (Z)-azobenzenes in the presence of hydrogen bonding” *Beilstein J. Org. Chem.* **2018**, *14*, 1238–1243.

[49] X.-M. Liu, X.-Y. Jin, Z.-X. Zhang, J. Wang, F.-Q. Bai, “Theoretical study on the reaction mechanism of the thermal cis – trans isomerization of fluorine-substituted azobenzene derivatives” *RSC Adv.* **2018**, *8*, 11580–11588.

[50] A. Kerckhoffs, K. E. Christensen, M. J. Langton, “Fast relaxing red and near-IR switchable azobenzenes with chalcogen and halogen substituents: periodic trends, tuneable thermal half-lives and chalcogen bonding” *Chem. Sci.* **2022**, *13*, 11551–11559.

[51] A. L. Sanna, T. Pachova, A. Catellani, A. Calzolari, G. Sforazzini, “Meta-Substituted Asymmetric Azobenzenes: Insights into Structure–Property Relationship” *Molecules* **2024**, *29*, 1929.

[52] M. Quick, A. L. Dobryakov, M. Gerecke, C. Richter, F. Berndt, I. N. Ioffe, A. A. Granovsky, R. Mahrwald, N. P. Ernsting, S. A. Kovalenko, “Photoisomerization Dynamics and Pathways of trans- and cis-Azobenzene in Solution from Broadband Femtosecond Spectroscopies and Calculations” *J. Phys. Chem. B* **2014**, *118*, 8756–8771.

[53] H. M. D. Bandara, S. C. Burdette, “Photoisomerization in different classes of azobenzene” *Chem. Soc. Rev.* **2011**, *41*, 1809–1825.

[54] T. Cusati, G. Granucci, M. Persico, G. Spighi, “Oscillator strength and polarization of the forbidden n→π* band of trans-azobenzene: A computational study” *J. Chem. Phys.* **2008**, *128*, 194312.

[55] N. Eleya, S. Ghosh, E. Lork, A. Staubitz, "A new photo switchable azobenzene macrocycle without thermal relaxation at ambient temperature" *J. Mater. Chem. C* **2020**, *9*, 82–87.

[56] S. Crespi, N. A. Simeth, B. König, "Heteroaryl azo dyes as molecular photoswitches" *Nat. Rev. Chem.* **2019**, *3*, 133–146.

[57] F. A. Martins, R. V. Viesser, J. V. Schober, R. Herges, J. I. Wu, "Triplet Spin Delocalization and Temperature Dependence for Adiabatic and Non-Adiabatic Z–E Isomerization Pathways in Azoarenes" *J. Am. Chem. Soc.* **2025**, DOI 10.1021/jacs.5c09852.

[58] E. M. M. Tan, S. Amirjalayer, S. Smolarek, A. Vdovin, F. Zerbetto, W. J. Buma, "Fast photodynamics of azobenzene probed by scanning excited-state potential energy surfaces using slow spectroscopy" *Nat. Commun.* **2015**, *6*, 5860.

[59] F. Küllmer, L. Gregor, H.-D. Arndt, "Systematic modifications of substitution patterns for property tuning of photoswitchable asymmetric azobenzenes" *Org. Biomol. Chem.* **2022**, *20*, 4204–4214.

[60] D. Bléger, J. Schwarz, A. M. Brouwer, S. Hecht, "o-Fluoroazobenzenes as Readily Synthesized Photoswitches Offering Nearly Quantitative Two-Way Isomerization with Visible Light" *J. Am. Chem. Soc.* **2012**, *134*, 20597–20600.

[61] R. J. Mart, R. K. Allemann, "Azobenzene photocontrol of peptides and proteins" *Chem. Commun.* **2016**, *52*, 12262–12277.

[62] D. Cameron, S. Eisler, "Photoswitchable double bonds: Synthetic strategies for tunability and versatility" *J. Phys. Org. Chem.* **2018**, *31*, DOI 10.1002/poc.3858.

[63] M. Han, Y. Norikane, K. Onda, Y. Matsuzawa, M. Yoshida, M. Hara, "Light-driven modulation of fluorescence color from azobenzene derivatives containing electron-donating and electron-withdrawing groups" *N. J. Chem.* **2010**, *34*, 2892–2896.

[64] J. García-Amorós, D. Velasco, "Recent advances towards azobenzene-based light-driven real-time information-transmitting materials" *Beilstein J. Org. Chem.* **2012**, *8*, 1003–1017.

[65] S. Samanta, A. A. Beharry, O. Sadovski, T. M. McCormick, A. Babalhavaeji, V. Tropepe, G. A. Woolley, "Photoswitching Azo Compounds in Vivo with Red Light" *J. Am. Chem. Soc.* **2013**, *135*, 9777–9784.

[66] S. Millan, B. Gil-Hernández, E. Hastürk, A. Schmitz, C. Janiak, "A 2D Zinc Coordination Polymer Built from the Mono-deprotonated 4,4′-Azobis(3,5-dimethyl-1H-pyrazole) Ligand" *Z. für Anorg. Allg. Chem.* **2018**, *644*, 1311–1316.

[67] S. Millan, J. Nasir, B. Gil-Hernández, T.-O. Knedel, B. Moll, I. Boldog, O. Weingart, J. S. auf der Günne, C. Janiak, "Solid-State Landscape of 4,4′-Azobis(3,5-dimethyl-1H-pyrazole) with the Isolation of Conformer-Dependent Polymorphs" *Cryst. Growth Des.* **2020**, *20*, 2721–2733.

[68] C. E. Weston, R. D. Richardson, M. J. Fuchter, "Photoswitchable basicity through the use of azoheteroarenes" *Chem. Commun.* **2016**, *52*, 4521–4524.

[69] A. Gonzalez, M. Odaybat, M. Le, J. L. Greenfield, A. J. P. White, X. Li, M. J. Fuchter, G. G. D. Han, "Photocontrolled Energy Storage in Azobispyrazoles with Exceptionally Large Light Penetration Depths" *J. Am. Chem. Soc.* **2022**, *144*, 19430–19436.

[70] P. Lentes, P. Frühwirt, H. Freißmuth, W. Moormann, F. Kruse, G. Gescheidt, R. Herges, "Photoswitching of Diazocines in Aqueous Media" *J. Org. Chem.* **2021**, *86*, 4355–4360.

[71] S. Li, N. Eleya, A. Staubitz, "Cross-Coupling Strategy for the Synthesis of Diazocines" *Org. Lett.* **2020**, *22*, 1624–1627.

[72] J. Isokuortti, T. Griebenow, J.-S. von Glasenapp, T. Raeker, M. A. Filatov, T. Laaksonen, R. Herges, N. A. Durandin, "Triplet sensitization enables bidirectional isomerization of diazocine with 130 nm redshift in excitation wavelengths" *Chem. Sci.* **2023**, *14*, 9161–9166.

[73] M. S. Maier, K. Hüll, M. Reynders, B. S. Matsuura, P. Leippe, T. Ko, L. Schäffer, D. Trauner, "Oxidative Approach Enables Efficient Access to Cyclic Azobenzenes" *J. Am. Chem. Soc.* **2019**, *141*, 17295–17304.

[74] M. J. Notheis, V. Sahiti, V. Prangenberg, J. S. Kruse, L. K. S. von Krbek, "2,8-Dihalogenated Diazocines: Versatile Reactants for Functionalized Photoswitches" *Synlett* **2025**, *36*, 1569–1573.

[75] R. Siewertsen, H. Neumann, B. Buchheim-Stehn, R. Herges, C. Näther, F. Renth, F. Temps, "Highly Efficient Reversible Z−E Photoisomerization of a Bridged Azobenzene with Visible Light through Resolved S1(nπ*) Absorption Bands" *J. Am. Chem. Soc.* **2009**, *131*, 15594–15595.

[76] A. Mukherjee, M. D. Seyfried, B. J. Ravoo, "Azoheteroarene and Diazocine Molecular Photoswitches: Self-Assembly, Responsive Materials and Photopharmacology" *Angew. Chem. Int. Ed.* **2023**, *62*, e202304437.

[77] E. Salazar, S. Reinink, S. Faraji, "Providing theoretical insight into the role of symmetry in the photoisomerization mechanism of a non-symmetric dithienylethene photoswitch" *Phys. Chem. Chem. Phys.* **2022**, *24*, 11592–11602.

[78] H. Xi, Z. Zhang, W. Zhang, M. Li, C. Lian, Q. Luo, H. Tian, W.-H. Zhu, "All-Visible-Light-Activated Dithienylethenes Induced by Intramolecular Proton Transfer" *J. Am. Chem. Soc.* **2019**, *141*, 18467–18474.

[79] H. Lu, H. Ye, M. Zhang, Z. Liu, H. Zou, L. You, "Photoswitchable dynamic conjugate addition-elimination reactions as a tool for light-mediated click and clip chemistry" *Nat. Commun.* **2023**, *14*, 4015.

[80] D. Wilson, N. R. Branda, “Turning ‘On’ and ‘Off’ a Pyridoxal 5′-Phosphate Mimic Using Light” *Angew. Chem. Int. Ed.* **2012**, *51*, 5431–5434.

[81] D. Majee, S. Presolski, “Dithienylethene-Based Photoswitchable Catalysts: State of the Art and Future Perspectives” *ACS Catal.* **2021**, *11*, 2244–2252.

[82] S. Qiu, A. T. Frawley, K. G. Leslie, H. L. Anderson, “How do donor and acceptor substituents change the photophysical and photochemical behavior of dithienylethenes? The search for a water-soluble visible-light photoswitch” *Chem. Sci.* **2023**, *14*, 9123–9135.

[83] I. Hamdi, G. Buntinx, A. Perrier, O. Devos, N. Jaïdane, S. Delbaere, A. K. Tiwari, J. Dubois, M. Takeshita, Y. Wada, S. Aloïse, “New insights into the photoswitching mechanisms of normal dithienylethenes” *Phys. Chem. Chem. Phys.* **2016**, *18*, 28091–28100.

[84] M. Irie, “Diarylethenes for Memories and Switches” *Chem. Rev.* **2000**, *100*, 1685–1716.

[85] Z. Li, J. Song, Q. Wang, Y. Qi, X. Gao, Y. Feng, H. Zhang, Y.-J. Chen, H. Guo, X.-G. Yang, J. Yin, “Near-infrared light-activated switchable antibacterial agent based on dithienylethene photoswitch” *Chin. Chem. Lett.* **2025**, 111139.

[86] J. Yu, M. Luo, Z. Lv, S. Huang, H.-H. Hsu, C.-C. Kuo, S.-T. Han, Y. Zhou, “Recent advances in optical and optoelectronic data storage based on luminescent nanomaterials” *Nanoscale* **2020**, *12*, 23391–23423.

[87] D. Dai, Y. Zhang, S. Yang, W. Kong, J. Yang, J. Zhang, “Recent Advances in Functional Materials for Optical Data Storage” *Molecules* **2024**, *29*, 254.

[88] W. A. Wani, A. H. Malik, A. Hussain, M. F. Alajmi, S. Shreaz, I. Kostova, “Recent advances in metal complexes for the photodynamic therapy of cancer” *N. J. Chem.* **2025**, *49*, 13244–13268.

[89] H. Shi, R. C. Marchi, P. J. Sadler, “Advances in the Design of Photoactivatable Metallodrugs: Excited State Metallomics” *Angew. Chem. Int. Ed.* **2025**, *64*, e202423335.

[90] S. Petrovskii, A. Senchukova, V. Sizov, A. Paderina, M. Luginin, E. Abramova, E. Grachova, “Efficient photoswitchable organometallic complexes with azobenzene and stilbene units: the case of Au(i)” *Mol. Syst. Des. Eng.* **2022**, *7*, 1249–1262.

[91] V. W.-W. Yam, A. K.-W. Chan, E. Y.-H. Hong, “Charge-transfer processes in metal complexes enable luminescence and memory functions” *Nat. Rev. Chem.* **2020**, *4*, 528–541.

[92] C.-C. Ko, V. W.-W. Yam, “Transition metal complexes with photochromic ligands—photosensitization and photoswitchable properties” *J. Mater. Chem.* **2009**, *20*, 2063–2070.

[93] J. Long, D. Kumar, C. Deo, P. Retailleau, G. V. Dubacheva, G. Royal, J. Xie, N. Bogliotti, "Photo-/Electroinduced Irreversible Isomerization of 2,2'-Azobispyridine Ligands in Arene Ruthenium(II) Complexes" *Chem. A Eur. J.* **2021**, *27*, 9563–9570.

[94] J. Long, P. Retailleau, J. Xie, N. Bogliotti, "Steric Bulk-Dependent Photoresponse of Sulfonamide Azobenzene Ligand in Arene Ruthenium(II) Complexes" *Helvetica Chim. Acta* **2024**, *107*, DOI 10.1002/hlca.202300190.

[95] M. Han, T. Hirade, M. Hara, "A reversibly photoswitchable mononuclear palladium(ii) complex with ortho -diethylated azobenzene ligands" *N. J. Chem.* **2010**, *34*, 2887–2891.

[96] J. L. Atwood, G. W. Gokel, L. Barbour, Eds. , *Comprehensive Supramolecular Chemistry II*, Elsevier, Amsterdam, **2017**.

[97] Á. M. Pendás, J. Contreras-García, "Topological Approaches to the Chemical Bond" *Theor. Chem. Comput. Model.* **2023**, 175–218.

[98] B. Zhang, H. Lee, J. J. Holstein, G. H. Clever, "Shape-Complementary Multicomponent Assembly of Low-Symmetry Co(III)Salphen-Based Coordination Cages" *Angew. Chem. Int. Ed.* **2024**, *63*, e202404682.

[99] C. Piguet, "Enthalpy–entropy correlations as chemical guides to unravel self-assembly processes" *Dalton Trans.* **2011**, *40*, 8059–8071.

[100] A. E. MARTELL, *Chelating Agents and Metal Chelates*, American Chemical Society, **1967**.

[101] M. D. Ward, C. A. Hunter, N. H. Williams, "Coordination Cages Based on Bis(pyrazolylpyridine) Ligands: Structures, Dynamic Behavior, Guest Binding, and Catalysis" *Acc. Chem. Res.* **2018**, *51*, 2073–2082.

[102] D. A. P. III, E. O. Bobylev, S. Mathew, J. N. H. Reek, "Entropy directs the self-assembly of supramolecular palladium coordination macrocycles and cages" *Chem. Sci.* **2022**, *13*, 10141–10148.

[103] B. Widom, P. Bhimalapuram, K. Koga, "The hydrophobic effect" *Phys. Chem. Chem. Phys.* **2003**, *5*, 3085–3093.

[104] J. H. Jordan, B. C. Gibb, "Molecular containers assembled through the hydrophobic effect" *Chem. Soc. Rev.* **2014**, *44*, 547–585.

[105] Y. Liu, L. Wang, L. Zhao, Y. Zhang, Z.-T. Li, F. Huang, "Multiple hydrogen bonding driven supramolecular architectures and their biomedical applications" *Chem. Soc. Rev.* **2024**, *53*, 1592–1623.

[106] X. Zhang, X. Dai, L. Gao, D. Xu, H. Wan, Y. Wang, L.-T. Yan, "The entropy-controlled strategy in self-assembling systems" *Chem. Soc. Rev.* **2023**, *52*, 6806–6837.

[107] W. Cullen, C. A. Hunter, M. D. Ward, “An Interconverting Family of Coordination Cages and a meso-Helicate; Effects of Temperature, Concentration, and Solvent on the Product Distribution of a Self-Assembly Process” *Inorg. Chem.* **2015**, *54*, 2626–2637.

[108] J. Martí-Rujas, “Mechanical interlocking of metal organic cages” *Commun. Chem.* **2025**, *8*, 92.

[109] A. Stephenson, S. P. Argent, T. Riis-Johannessen, I. S. Tidmarsh, M. D. Ward, “Structures and Dynamic Behavior of Large Polyhedral Coordination Cages: An Unusual Cage-to-Cage Interconversion” *J. Am. Chem. Soc.* **2011**, *133*, 858–870.

[110] F. A. Cotton, C. A. Murillo, R. Yu, “Dynamic equilibrium between cyclic oligomers. Thermodynamic and structural characterization of a square and a triangle” *Dalton Trans.* **2006**, *0*, 3900–3905.

[111] L. Chen, Q. Chen, M. Wu, F. Jiang, M. Hong, “Controllable Coordination-Driven Self-Assembly: From Discrete Metallocages to Infinite Cage-Based Frameworks” *Acc. Chem. Res.* **2015**, *48*, 201–210.

[112] S. Hiraoka, “Self-Assembly Processes of Pd(II)- and Pt(II)-Linked Discrete Self-Assemblies Revealed by QASAP” *Isr. J. Chem.* **2019**, *59*, 151–165.

[113] B. H. Northrop, Y.-R. Zheng, K.-W. Chi, P. J. Stang, “Self-Organization in Coordination-Driven Self-Assembly” *Acc. Chem. Res.* **2009**, *42*, 1554–1563.

[114] F. Ibukuro, T. Kusukawa, M. Fujita, “A Thermally Switchable Molecular Lock. Guest-Templated Synthesis of a Kinetically Stable Nanosized Cage” *J. Am. Chem. Soc.* **1998**, *120*, 8561–8562.

[115] I. A. Riddell, Y. R. Hristova, J. K. Clegg, C. S. Wood, B. Breiner, J. R. Nitschke, “Five Discrete Multinuclear Metal-Organic Assemblies from One Ligand: Deciphering the Effects of Different Templates” *J. Am. Chem. Soc.* **2013**, *135*, 2723–2733.

[116] M. D. Ward, “Polynuclear coordination cages” *Chem. Commun.* **2009**, *0*, 4487–4499.

[117] S. Tashiro, Y. Yamada, L. A. Kringe, Y. Okajima, M. Shionoya, “Intricate Low-Symmetry Ag6 L 4 Capsules Formed by Anion-Templated Self-Assembly of the Stereoisomers of an Unsymmetric Ligand” *J. Am. Chem. Soc.* **2024**, *146*, 34501–34509.

[118] R. J. Severinsen, G. J. Rowlands, P. G. Plieger, “Coordination cages in catalysis” *J. Incl. Phenom. Macrocycl. Chem.* **2020**, *96*, 29–42.

[119] Z. Ashbridge, J. N. H. Reek, “The multifaceted roles of MnL2n cages in catalysis” *Nat. Synth.* **2024**, *3*, 1197–1207.

[120] L. K. Moree, L. A. V. Faulkner, J. D. Crowley, “Heterometallic cages: synthesis and applications” *Chem. Soc. Rev.* **2023**, *53*, 25–46.

[121] N. Judge, L. Wang, Y. Y. L. Ho, Y. Wang, "Molecular Engineering of Metal-Organic Cycles/Cages for Drug Delivery" *Macromol. Res.* **2018**, *26*, 1074–1084.

[122] A. Ghosh, J. Pruchyathamkorn, C. F. Espinosa, J. R. Nitschke, "Light-Driven Purification of Progesterone from Steroid Mixtures Using a Photoresponsive Metal–Organic Capsule" *J. Am. Chem. Soc.* **2024**, *146*, 2568–2573.

[123] X. Sun, K. Wu, P. C. P. Teeuwen, P. Pracht, D. J. Wales, J. R. Nitschke, "Proton-driven lithium separation using alkali-templated coordination cages" *Chem* **2025**, 102556.

[124] Y. Yang, Y. Du, A. W. Heard, J. R. Nitschke, "Allosteric regulation in metal–organic cages" *Nat. Synth.* **2025**, *4*, 537–551.

[125] E.-S. M. El-Sayed, D. Yuan, "Metal-Organic Cages (MOCs): From Discrete to Cage-based Extended Architectures" *Chem. Lett.* **2019**, *49*, 28–53.

[126] M. Han, R. Michel, B. He, Y. Chen, D. Stalke, M. John, G. H. Clever, "Light-Triggered Guest Uptake and Release by a Photochromic Coordination Cage" *Angew. Chem. Int. Ed.* **2013**, *52*, 1319–1323.

[127] R. G. DiNardi, A. O. Douglas, R. Tian, J. R. Price, M. Tajik, W. A. Donald, J. E. Beves, "Visible-Light-Responsive Self-Assembled Complexes: Improved Photoswitching Properties by Metal Ion Coordination**" *Angew. Chem. Int. Ed.* **2022**, *61*, e202205701.

[128] H. Lee, J. Tessarolo, D. Langbehn, A. Baksi, R. Herges, G. H. Clever, "Light-Powered Dissipative Assembly of Diazocine Coordination Cages" *J. Am. Chem. Soc.* **2022**, *144*, 3099–3105.

[129] M. F. Hagan, G. M. Grason, "Equilibrium mechanisms of self-limiting assembly" *Rev. Mod. Phys.* **2021**, *93*, 025008.

[130] R. D. Astumian, "Kinetic Asymmetry and Directionality of Nonequilibrium Molecular Systems" *Angew. Chem.* **2024**, *136*, DOI 10.1002/ange.202306569.

[131] C. Pezzato, C. Cheng, J. F. Stoddart, R. D. Astumian, "Mastering the non-equilibrium assembly and operation of molecular machines" *Chem. Soc. Rev.* **2017**, *46*, 5491–5507.

[132] T. Sangchai, S. A. Shehimy, E. Penocchio, G. Ragazzon, "Artificial Molecular Ratchets: Tools Enabling Endergonic Processes" *Angew. Chem. Int. Ed.* **2023**, *62*, e202309501.

[133] E. Olivieri, J. M. Gallagher, A. Betts, T. W. Mrad, D. A. Leigh, "Endergonic synthesis driven by chemical fuelling" *Nat. Synth.* **2024**, *3*, 707–714.

[134] S. Borsley, J. M. Gallagher, D. A. Leigh, B. M. W. Roberts, "Ratcheting synthesis" *Nat. Rev. Chem.* **2024**, *8*, 8–29.

[135] D. Thomas, D. J. Tetlow, Y. Ren, S. Kassem, U. Karaca, D. A. Leigh, "Pumping between phases with a pulsed-fuel molecular ratchet" *Nat. Nanotechnol.* **2022**, *17*, 701–707.

[136] M. Baroncini, S. Silvi, A. Credi, "Photo- and Redox-Driven Artificial Molecular Motors" *Chem. Rev.* **2020**, *120*, 200–268.

[137] M. Ovalle, M. Kathan, R. Toyoda, C. N. Stindt, S. Crespi, B. L. Feringa, "Light-Fueled Transformations of a Dynamic Cage-Based Molecular System" *Angew. Chem. Int. Ed.* **2023**, *62*, e202214495.

[138] V. Serreli, C.-F. Lee, E. R. Kay, D. A. Leigh, "A molecular information ratchet" *Nature* **2007**, *445*, 523–527.

[139] N. Tamaoki, M. Wada, "Dynamic Control of Racemization Rate through E − Z Photoisomerization of Azobenzene and Subsequent Partial Photoresolution under Circular Polarized Light" *J. Am. Chem. Soc.* **2006**, *128*, 6284–6285.

[140] L. Pruñonosa Lara, B. Bädorf, M. J. Notheis, G. Schnakenburg, S. Grimme, L. K. S. von Krbek, "White-light powered autonomous molecular ratchet drives PdII capsules out of equilibrium" *ChemRxiv (Preprint)* **2025**, DOI 10.26434/chemrxiv-2025-ck3gw.

[141] J. E. M. Lewis, E. L. Gavey, S. A. Cameron, J. D. Crowley, "Stimuli-responsive Pd 2 L 4 metallosupramolecular cages: towards targeted cisplatin drug delivery" *Chem. Sci.* **2011**, *3*, 778–784.

[142] O. R. Panisello, J. Jover, C. Puigjaner, M. Ferrer, M. Martínez, "No Switching Cooperativity between Coordinated Azo Ligands on Complexes Having {MII(phosphane-κ2 P)}2+ (M = Pd, Pt) Scaffolds" *Inorg. Chem.* **2024**, *63*, 16251–16263.

[143] G. Markiewicz, A. Walczak, F. Perlitius, M. Piasecka, J. M. Harrowfield, A. R. Stefankiewicz, "Photoswitchable transition metal complexes with azobenzene-functionalized imine-based ligands: structural and kinetic analysis" *Dalton Trans.* **2018**, *47*, 14254–14262.

[144] J. Long, L. Rocard, E. V. Elslande, P. Retailleau, J. Xie, N. Bogliotti, "Light-Promoted Basic Nitrogen Unmasking in Arene Ruthenium Complexes Derived from Z-Configured 2,2′-Azobispyridine" *Chem. A Eur. J.* **2023**, *29*, e202301301.

[145] P. Cecot, A. Walczak, G. Markiewicz, A. R. Stefankiewicz, "Gating the photoactivity of azobenzene-type ligands trapped within a dynamic system of an M 4 L 6 tetrahedral cage, an M 2 L 2 metallocycle and mononuclear ML n complexes" *Inorg. Chem. Front.* **2021**, *8*, 5195–5200.

[146] G. Kurpik, A. Walczak, M. Gołdyn, J. Harrowfield, A. R. Stefankiewicz, "Pd(II) Complexes with Pyridine Ligands: Substituent Effects on the NMR Data, Crystal Structures, and Catalytic Activity" *Inorg. Chem.* **2022**, *61*, 14019–14029.

[147] M. R. J. Elsegood, M. B. Smith, S. H. Dale, “Two square-planar palladium(II) complexes with P,O-bidentate hybrid ligands” *Acta Crystallogr. Sect. C: Cryst. Struct. Commun.* **2007**, *63*, m7–m9.

[148] K. M. Dyumaev, L. D. Smirnov, “The Structure and Reactivity of 3-Hydroxypyridine Derivatives in Electrophilic Substitution” *Russ. Chem. Rev.* **1975**, *44*, 823–832.

[149] E. F. V. Scriven, “Comprehensive Heterocyclic Chemistry” *Part 2A: Six-membered Rings One Nitrogen At.* **1984**, 165–314.

[150] A. Müller-Deku, O. Thorn-Seshold, “Exhaustive Catalytic ortho-Alkoxylation of Azobenzenes: Flexible Access to Functionally Diverse Yellow-Light-Responsive Photoswitches” *J. Org. Chem.* **2022**, *87*, 16526–16531.

[151] H. M. D. Bandara, T. R. Friss, M. M. Enriquez, W. Isley, C. Incarvito, H. A. Frank, J. Gascon, S. C. Burdette, “Proof for the Concerted Inversion Mechanism in the trans→cis Isomerization of Azobenzene Using Hydrogen Bonding To Induce Isomer Locking” *J. Org. Chem.* **2010**, *75*, 4817–4827.

[152] K. Ichimura, “Isosbestic Points Do Not Always Work as the Measure to Determine the Oneness of a Reaction as Exemplified by the Photoisomerization of Azobenzene Tethered to Polymer Chains” *Chem. Lett.* **2018**, *47*, 1247–1250.

[153] M. Dong, A. Babalhavaeji, S. Samanta, A. A. Beharry, G. A. Woolley, “Red-Shifting Azobenzene Photoswitches for in Vivo Use” *Acc. Chem. Res.* **2015**, *48*, 2662–2670.

[154] C. L. Forber, E. C. Kelusky, N. J. Bunce, M. C. Zerner, “Electronic spectra of cis- and trans-azobenzenes: consequences of ortho substitution” *J. Am. Chem. Soc.* **1985**, *107*, 5884–5890.

[155] R. M. Gathungu, R. Kautz, B. S. Kristal, S. S. Bird, P. Vouros, “The integration of LC-MS and NMR for the analysis of low molecular weight trace analytes in complex matrices” *Mass Spectrom. Rev.* **2020**, *39*, 35–54.

[156] J. J. R. F. da Silva, “The chelate effect redefined” *J. Chem. Educ.* **1983**, *60*, 390.

[157] A. E. Martell, R. D. Hancock, R. J. Motekaitis, “Factors affecting stabilities of chelate, macrocyclic and macrobicyclic complexes in solution” *Coord. Chem. Rev.* **1994**, *133*, 39–65.

[158] J. Volarić, J. Buter, A. M. Schulte, K.-O. van den Berg, E. Santamaría-Aranda, W. Szymanski, B. L. Feringa, “Design and Synthesis of Visible-Light-Responsive Azobenzene Building Blocks for Chemical Biology” *J. Org. Chem.* **2022**, *87*, 14319–14333.

[159] A. Lifshitz, C. Tamburu, “Thermal decomposition of acetonitrile. Kinetic modeling” *Int. J. Chem. Kinet.* **1998**, *30*, 341–347.

[160] K. F. Sheberstov, H.-M. Vieth, H. Zimmermann, K. L. Ivanov, A. S. Kiryutin, A. V. Yurkovskaya, “cis Versus trans-Azobenzene: Precise Determination of NMR Parameters and Analysis of Long-Lived States of 15N Spin Pairs” *Appl. Magn. Reson.* **2018**, *49*, 293–307.

[161] N. H. Martin, N. W. Allen, K. D. Moore, L. Vo, “A proton NMR shielding model for the face of a benzene ring” *J. Mol. Struct.: THEOCHEM* **1998**, *454*, 161–166.

[162] C. Feldmeier, H. Bartling, E. Riedle, R. M. Gschwind, “LED based NMR illumination device for mechanistic studies on photochemical reactions – Versatile and simple, yet surprisingly powerful” *J. Magn. Reson.* **2013**, *232*, 39–44.

[163] Y. Ji, D. A. DiRocco, J. Kind, C. M. Thiele, R. M. Gschwind, M. Reibarkh, “LED-Illuminated NMR Spectroscopy: A Practical Tool for Mechanistic Studies of Photochemical Reactions” *ChemPhotoChem* **2019**, *3*, 984–992.

[164] R. Falkenburg, M. J. Notheis, G. Schnakenburg, L. K. S. von Krbek, “Twelve-membered ring photoswitches with excellent Z → E conversion under ambient light” *Org. Biomol. Chem.* **2023**, *21*, 4993–4998.

[165] S. Ghosh, C. Eschen, N. Eleya, A. Staubitz, “Synthesis of a Series of 12-Membered Azobenzene Macrocycles and Tuning of the Half-Life of the Thermal Z–E Isomerization” *J. Org. Chem.* **2023**, *88*, 3372–3377.

[166] A. P. Paneerselvam, S. S. Mishra, D. K. Chand, “Linear and circular helicates: A brief review” *J. Chem. Sci.* **2018**, *130*, 96.

9. Appendix

This appendix contains all the publications relevant to the doctoral thesis: a peer-reviewed article and a preprint deposited in a recognised repository. They are presented in the order in which they appear in the thesis and are reproduced in full, without modification, including all supporting information. In accordance with the University of Bonn's doctoral regulations, each publication is accompanied by a summary and a detailed description of the contributions of all authors within the main body of the thesis. All co-authors have approved the inclusion of their respective publications and the accompanying text. Bibliographic details and copyright information are provided for each publication.

9.1 Photoswitching of Co(II)-based coordination cages containing azobenzene backbones

Max B. Tipping, Lidón Pruñonosa Lara, Atena B. Solea, Larissa K.S. von Krbek, and Michael D. Ward

Chem. Sci., **2024**, 15, 8488-8499.

The article was submitted on 6 March 2024 and was first published in *Chemical Science* on 3 May 2024. An electronic version is available at DOI: 10.1039/D4SC01575D.

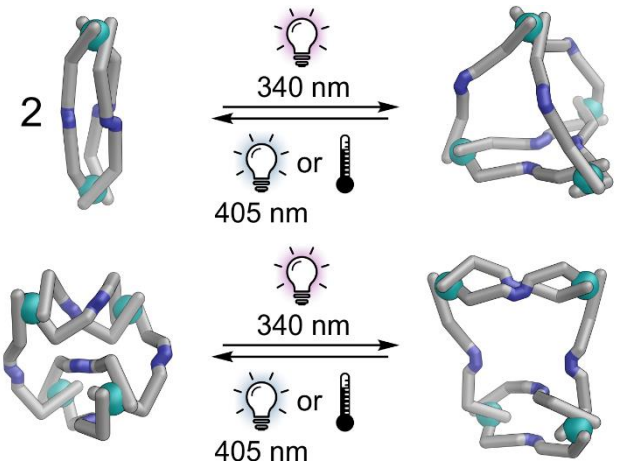

Figure A1. Graphical abstract. Reprinted with permission from Tipping et al.[23] Reproduced under the terms of the Creative Commons Attribution 3.0 Unported Licence. © 2024 The Royal Society of Chemistry.

Chemical Science

ROYAL SOCIETY OF CHEMISTRY

EDGE ARTICLE

View Article Online
View Journal | View Issue

Cite this: *Chem. Sci.*, 2024, **15**, 8488

All publication charges for this article have been paid for by the Royal Society of Chemistry

Photoswitching of Co(II)-based coordination cages containing azobenzene backbones†

Max B. Tipping, [a] Lidón Pruñonosa Lara, [b] Atena B. Solea, [a] Larissa K. S. von Krbek *[b] and Michael D. Ward *[a]

Inclusion of photoswitchable azobenzene units as spacers into ditopic bridging ligands L^m and L^p, containing two chelating pyrazolyl-pyridine termini, allows formation of metal complex assemblies with Co(II) that undergo a range of light-induced structural transformations. One notable result is the light-induced conversion of a $Co_2(L^p)_3$ dinuclear triple helicate (based on the *E* ligand isomer) to a C_3-symmetric $Co_4(L^p)_6$ assembly, assumed to be an edge-bridged tetrahedral cage, based on the *Z* ligand isomer. Another is the preparation of a series of $Co_4(L^m)_6$ complexes, of which $Co_4(E\text{-}L^m)_6$ was crystallographically characterised and consists of a pair of $Co_2(L^m)_2$ double helicates connected by an additional two bridging ligands which span the pair of helicate units, giving a cyclic Co_4 array in which one and then two bridging ligands alternate around the periphery. A set of $Co_4(L^m)_6$ complexes could be prepared containing different ratios of *Z* : *E* ligand isomers (0 : 6, 2 : 4, 4 : 2 and 6 : 0) of which $Co_4(Z\text{-}L^m)_2(E\text{-}L^m)_4$ was particularly stable and dominated the speciation behaviour, either during light-induced switching of the ligand geometry in pre-formed complexes, or when ligand isomers were combined in different proportions during the preparation. These examples of (i) interconversion between Co_2L_3 (helicate) and (ii) Co_4L_6 (cage) assemblies with L^p, and the interconversion between a series of Co_4L_6 assemblies $Co_4(Z\text{-}L^m)_n(E\text{-}L^m)_{6-n}$ with L^m, constitute significant advances in the field of photoswitchable supramolecular assemblies.

Received 6th March 2024
Accepted 2nd May 2024

DOI: 10.1039/d4sc01575d

rsc.li/chemical-science

Introduction

The ability of hollow metal–ligand coordination cages to accommodate small-molecule guests inside their central cavity[1] can be made more valuable and widely applicable if the host–guest interactions can be controllably modulated, allowing for switchable guest uptake/release in response an external stimulus. These external stimuli may be chemical,[2] electrochemical,[3] or photochemical:[4] light, in particular, is perceived as an excellent method for *in situ* manipulation of guest binding because of the precise tunability of wavelength and intensity, inherent cleanliness, and extreme ease of physical delivery.[5]

Many small molecules can undergo reversible structural changes when exposed to light, with one wavelength triggering a rearrangement and another wavelength triggering the reverse reaction – an obviously appealing way to modulate the structures of metal/ligand assemblies and hence control guest binding. These may include bond breaking and bond forming reactions that result in a significant chemical change in the unit concerned as shown by the photochromic dithienyl-ethene units from Irie and co-workers,[6] which undergo reversible 6π-electron cyclisation/cyclo-reversion reactions (ring-closing and ring-opening) under light illumination at different wavelengths: this has been exploited by Clever and co-workers to make a Pd_2L_4 cage with 'open' and 'closed' forms which display different guest binding properties.[7]

Another popular photo-switching modality is provided by the *E*/*Z* isomerisation of stilbenes and azo-benzenes which can be exploited to allow control of the conformations of ligands where those units are incorporated into the backbone.[5b] The first light-modulated coordination cage, based on azobenzene photo-switching units, was a $Pd_{12}L_{24}$ cage from Fujita's group: azo-benzene units were bound to the concave side of each ligand (*i.e.* were inwardly-directed into the cavity) to form a 24-fold, endohedrally-functionalised 'nanosphere'.[8] This enabled the *in situ* manipulation of the hydrophobic interior surface of the cavity under light irradiation, causing the switchable uptake of the guest 1-pyrenecarboxaldehyde. Wu and co-workers prepared an azobenzene-containing ligand with anion-binding bis-urea end groups which, when combined with phosphate, formed

[a]*Department of Chemistry, University of Warwick, Coventry CV4 7AL, UK. E-mail: M.D.Ward@warwick.ac.uk*

[b]*Kekulé-Institut für Organische Chemie und Biochemie, Rheinische Friedrich-Wilhelms-Universität Bonn, Gerhard-Domagk-Str. 1, 53121 Bonn, Germany. E-mail: larissa.vonkrbek@uni-bonn.de*

† Electronic supplementary information (ESI) available: Detailed experimental and characterisation data including NMR and mass spectra; X-ray crystallographic information; additional details of computational structure simulations. CCDC 2301496 and 2301498. For ESI and crystallographic data in CIF or other electronic format see DOI: https://doi.org/10.1039/d4sc01575d

an A_4L_6 tetrahedron; irradiation with 380 nm light transformed the *E*-ligand tetrahedron into a A_2L_3 *Z*-ligand helicate, with concomitant release of a cavity-bound guest; this example was not reversibly photoswitchable however due to conformational restrictions associated with the rigid supramolecular structures.[9] Beves and co-workers produced the first example of a visible-light responsive azobenzene-containing cage – a $[Pd_2L_4]^{4+}$ lantern-shaped cage based on square-planar Pd(II) ions which, when exposed to red light, isomerised to 2 equivalents of a PdL_2 mononuclear complex. While the process was reversible with violet light, the photoisomerization yield and stability of the *Z*-ligand isomer were shown to improve with metal coordination.[10] McConnell's and Herges's groups embedded the azobenzene photochromic unit into a cyclic diazocine unit, in which steric strain ensures that the *Z*-azo group is more stable; conformational changes induced by photoswitching of this diazocine ring enabled self-sorting of a mixture of regioisomers *via* formation and destruction of M_2L_3 helicates in the presence of Co(II) ions.[11]

In this paper, we report how incorporation of the well-known azobenzene photochromic unit into our bis(pyrazolyl-pyridine) ligand system[12] can be used as a basis to control the course of the self-assembly with metal ions. We have reported numerous examples of coordination cage complexes with ligands from this family,[12] including some in which dynamic equilibria between cages of different nuclearity can be identified in solution.[13] Here, the inclusion of the photochromic unit provides an additional light-based method to control the course of the self-assembly and allows, unusually, (i) switching between different complex forms such as dinuclear helicates and tetrahedral cages; and (ii) switching between isomeric forms of assemblies with the same composition.

Results and discussion

Synthesis, characterisation and photoswitching behaviour of ligands

The ligands used are shown in Scheme 1. The bridging ligand $\mathbf{L^p}$ was reported several years ago and used to prepare an Ag(I) metallamacrocycle: no photoswitching investigations were performed at that time.[14] For this work we have also studied the isomeric ligand $\mathbf{L^m}$, which was prepared using the same general method as used for $\mathbf{L^p}$. Specifically, bromination of the methyl groups of 3,3′-dimethyl-azobenzene with *N*-bromo-succinimide in acetonitrile afforded 3,3′-bis(bromomethyl)-azobenzene in 70% isolated yield: reaction of this with two equivalents of 3-(2-pyridyl)pyrazole, under basic conditions to deprotonate the pyrazole NH group and in the presence of tetrabutylammonium iodide as a catalyst, afforded $\mathbf{L^m}$ in 75% isolated yield.

Crystals of $\mathbf{L^m}$ were grown by diffusion of hexane vapour into a solution of the compound in ethyl acetate: the X-ray crystal structure is in Fig. 1 and shows the expected approximately transoid coplanar conformation of the pyrazolyl-pyridine as well as the *E* configuration of the N=N bond (length 1.234 Å). Extensive π–π interactions are apparent between centrosymmetric molecules of $\mathbf{L^m}$ in the stacked arrays.

Following synthesis of the two ligands, it was important to confirm that they showed photo-switching behaviour. The UV/Vis spectra of both of the ligands in acetonitrile exhibited absorption bands at *ca.* 320 nm, corresponding to a π–π* transition, with the low-energy tail of the absorbance extending out to *ca.* 370 nm (Fig. 2a). Irradiation of 10 μM samples at 340 or 365 nm resulted in an immediate loss in intensity of the π–π* transition for the *E* isomer of each ligand, and an increased intensity for the weaker symmetry-allowed n–π* transition of the *Z* isomer of each ligand, at *ca.* 430 nm. Both azobenzene ligands had reached photostationary states (PSS) following 30 minutes of irradiation. The process could be mostly reversed by irradiation with white light, with a small difference in absorbance between the white-light-induced PSS and the thermally relaxed samples. In addition, the light-induced switching could

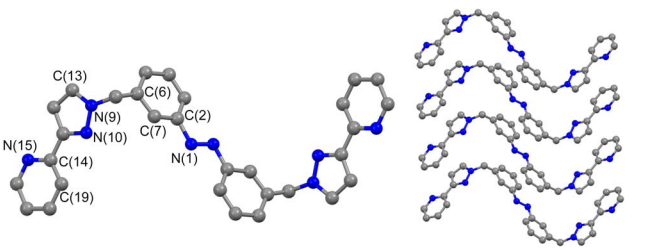

Fig. 1 Molecular structure of $\mathbf{L^m}$ from crystallographic data, including the atomic labelling scheme and the packing arrangement.

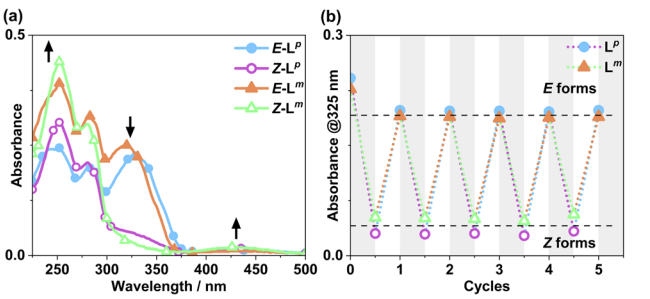

Fig. 2 (a) Absorption spectra of 10 μM solutions of $\mathbf{L^m}$ and $\mathbf{L^p}$ in MeCN, pre (*E* form) and post (*Z* form) irradiation with 340 nm light. Arrows indicate changes in absorbance maxima. (b) Switching reversibility experiment monitoring absorbance of each ligand (10 μM) at 325 nm, after alternating irradiation with 340 nm and white light.

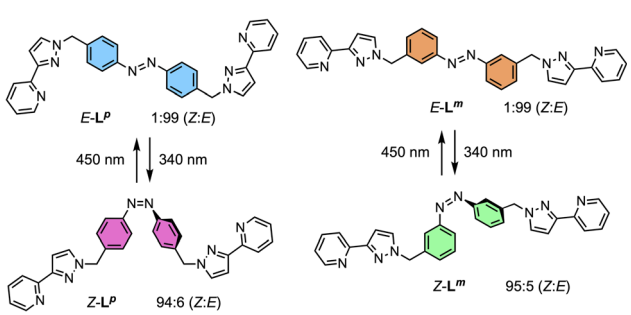

Scheme 1 Ligands used in this paper and their isomeric forms.

be repeated for several cycles with no appreciable photobleaching (Fig. 2b).

NMR spectroscopy was used to quantify the PSSs of both ligands, using the integration ratios of the methylene protons which are well-separated from other signals (Fig. 3). Prior to irradiation of the sample, a solution of $\mathbf{L^P}$ in acetonitrile contained a mixture of 1% *Z* and 99% *E* isomers (note, all ratios will be presented as *Z* : *E*, with individual values to the nearest 1%). Following irradiation at 340 nm overnight, the sample composition was 94 : 6 *Z* : *E* (Fig. 3b). Similarly, an initial solution of $\mathbf{L^m}$ in acetonitrile containing a 1 : 99 *Z* : *E* isomeric mixture prior to irradiation switched to 95 : 5 *Z* : *E* post-irradiation (Fig. 3a).

Following determination of PSSs, photoconversion was studied using NMR spectroscopy during *in situ* illumination experiments whereby a quartz optical fibre was inserted into a sample tube such that the solution could be irradiated inside the spectrometer.[15] Spectra were recorded every 17 seconds during both the forward and backward reactions. Due to the limited availability of LEDs it was not possible to irradiate the samples with 340 nm light during the NMR experiments, however 365 nm and 325 nm sources were available, of which the 365 nm source gave more photoswitching of $\mathbf{L^P}$ whereas the 325 nm source gave more photoswitching of $\mathbf{L^m}$: both ligands converted back from *Z* to *E* forms under 450 nm irradiation. Advantageously, the 325 and 365 nm LEDs are also much more powerful – 170 and 13 mW respectively – than the 1.7 mW 340 nm LED.

Fig. 4 shows the resulting changes in isomeric composition of each ligand with time under irradiation as measured during the *in situ* NMR experiments. After approximately 5 minutes of irradiation with 365 nm light, isomerisation of $\mathbf{L^P}$ showed no further changes, with a PSS_{365nm} ratio of 79 : 21 *Z* : *E* being obtained under these conditions. Subsequent exposure to 450 nm light caused a fast return to the original composition, with 20 minutes of additional irradiation causing no further changes. The much shorter timescale for the reverse reaction is likely due to the higher power of the 450 nm LED (440 mW, compared to 170 mW for the 365 nm LED) and not necessarily to any differences in isomerisation mechanisms.[16] In a similar way a solution of $\mathbf{L^m}$, after approximately 20 minutes of irradiation

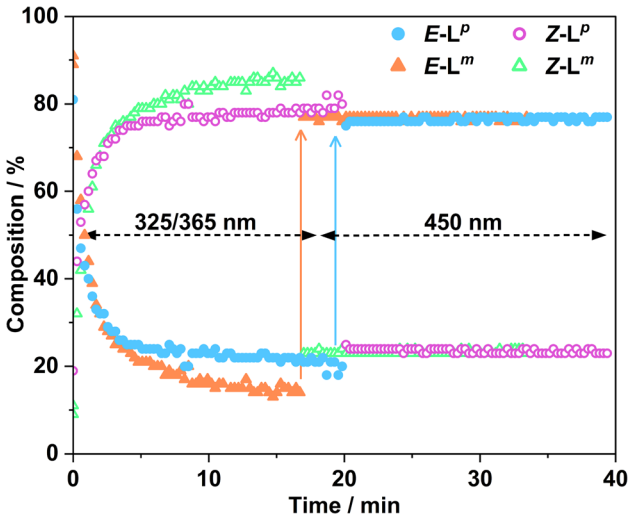

Fig. 4 Changes in composition of *Z*/*E* mixtures of L^P (blue and pink for *E* and *Z* isomers, respectively) and L^m (orange and green for *E* and *Z* isomers, respectively) measured by *in situ* illumination ^{1}H NMR (700 MHz, CD_3CN, 298 K). A sample of *E*-L^m (2.0 mM) was irradiated with 325 nm light for *ca.* 17 minutes to induce the *E* to *Z* isomerisation; followed by illumination with 450 nm light for *ca.* 17 minutes, to switch the ligands back to the *E* configuration. A sample of *E*-L^P (2.0 mM) was irradiated with 365 nm light for *ca.* 20 minutes, with subsequent irradiation with 450 nm light for *ca.* 20 minutes. In both cases the slow change to the *Z* isomer during the first 17–20 minutes with the UV irradiation, and then the very fast change back to the *E* isomer following visible light irradiation, are clear.

with 325 nm light, achieved a PSS_{325nm} ratio of 85 : 15 *Z* : *E* isomers under the same conditions. Again, the reverse reaction with 450 nm light was fast with all changes complete after 17 seconds.

This sample did not return completely to its original state however, instead consisting of a PSS_{450nm} ratio of 22 : 78 *Z* : *E*, so for $\mathbf{L^m}$ the photo-isomerisation is not fully reversible under 450 nm light irradiation (Fig. 4).

Usefully, azobenzenes may also undergo specifically the *Z* to *E* isomerisation by thermal relaxation. To test this, solutions of $\mathbf{L^m}$ and $\mathbf{L^P}$ in acetonitrile were first irradiated until PSSs were

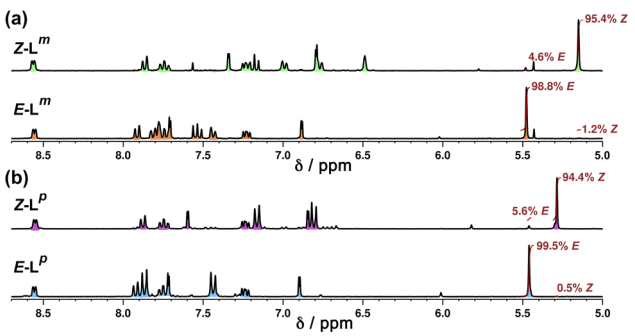

Fig. 3 Stacked ^{1}H NMR spectra (300 MHz, MeCN-d_3, 10 μM, 298 K) of (a) L^m and (b) L^P showing changes between *E* forms (bottom) and predominantly *Z* forms (top), following photoirradiation at 340 nm, which generates a *Z* : *E* mixtures of 95 : 5 (L^m) and 94 : 6 (L^P).

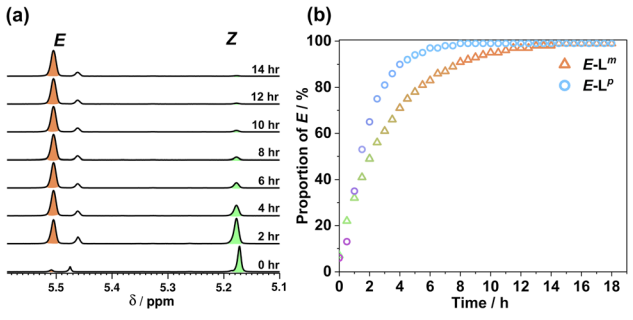

Fig. 5 (a) ^{1}H NMR spectra (400 MHz, CD_3CN, 338 K) indicating the change in the methylene proton signals of (predominantly) *Z*-L^m peaks following heating at 65 °C in CD_3CN to effect thermal relaxation back to *E*-L^m; (b) proportion of *E*-L^m and *E*-L^P with time during this heating process.

reached, producing a 93 : 7 and 94 : 6 Z : E ratio, respectively. Fig. 5 shows how the composition of isomers in solution varies after heating this sample to 65 °C for 18 hours. Both ligands showed complete conversion back to the E form with a thermal half-life $\tau_{1/2}$ of 2.36 h for $\mathbf{L^m}$ and 1.38 h for $\mathbf{L^p}$, demonstrating an alternative thermal method for isomerisation of the Z form back to the E form.

Metal complexes with $\mathbf{L^p}$: synthesis and characterisation

Reaction of $\mathbf{L^p}$ (1.5 equivalents) with 1 equivalent of an appropriate metal salt [$Co(BF_4)_2$ or $Zn(BF_4)_2$] at 60 °C overnight in MeOH afforded a precipitate which was washed with methanol, CH_2Cl_2 and diethyl ether to remove any unreacted metal salts and ligand. The 1.5 : 1 ligand : metal ratio reflects the generally six-coordinate preference of the metal ion and the bis-bidentate nature of the ligands, and this ligand : metal ratio routinely appears in this family of complexes based on bis(pyrazolylpyridine) ligands.[12]

We denote the Co(II) complex that was prepared with the (predominantly) E form of ligand as $E\cdot\mathbf{Co}\cdot\mathbf{L^p}$. The high-resolution electrospray ionisation (ESI) mass spectrum showed a sequence of signals corresponding to the species $[Co_2(\mathbf{L^p})_3(BF_4)_n]^{(4-n)+}$ (n = 0, 1, 2) suggesting that the complex formed is $[Co_2(\mathbf{L^p})_3](BF_4)_4$ with three bridging ligands spanning two Co(II) centres to give a triple-stranded structure which could be either a helicate or a mesocate.[17] The ^{1}H NMR spectrum, characteristically dispersed over a range of nearly 200 ppm due to the paramagnetism of high-spin Co(II), clearly contains major and minor signals (Fig. 6): but the number of signals associated with the major component is consistent with one half of one ligand environment being unique, *i.e.* all three ligands are the same and have twofold symmetry, which (in conjunction with the ESI-MS data) is consistent with a dinuclear triple helicate structure for $E\cdot\mathbf{Co}\cdot\mathbf{L^p}$.

As no *X*-ray quality crystals could be obtained for $E\cdot\mathbf{Co}\cdot\mathbf{L^m}$, a minimum-energy structure was calculated using an MM2 force-field (Fig. 7). The two metal centres possess *fac* tris-chelate coordination geometries and the three ligands adopt continuous spiral conformations, characteristic of helicates. The resulting D_3 symmetry is consistent with the ^{1}H NMR spectrum of the major solution species (Fig. 6) with one half of a ligand environment being unique.

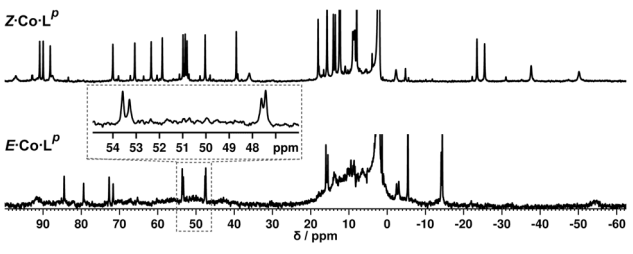

Fig. 6 (Top) ^{1}H NMR spectrum (300 MHz, CD_3CN, 298 K) of $Z\cdot\mathbf{Co}\cdot\mathbf{L^p}$, prepared by irradiation at 340 nm of a solution of $E\cdot\mathbf{Co}\cdot\mathbf{L^p}$. (Bottom) ^{1}H NMR spectrum (300 MHz, CD_3CN, 298 K) of $E\cdot\mathbf{Co}\cdot\mathbf{L^p}$. An expansion of the 47–54 ppm region makes clear the presence of two closely-spaced signals: this is also apparent in the signal at −14 ppm.

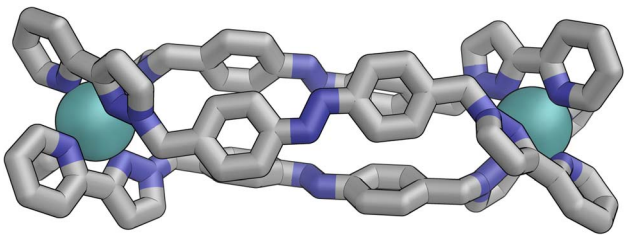

Fig. 7 MM2-optimised model of $E\cdot\mathbf{Co}\cdot\mathbf{L^p}$ showing a dinuclear, triple-helicate with D_3 symmetry.

Close examination of the ^{1}H NMR spectrum reveals that some of the signals are split into two closely-spaced components of comparable intensity (particularly the signals at *ca.* −14, 48 and 53 ppm, see inset in lower part of Fig. 6 showing expansions of the latter two), which could indicate the presence of slightly different environments associated with a guest (such as a counter-anion) binding to the helicate, possibly in the central cavity,[18] such that there are separate signals for 'free' and 'guest-bound' helicate. Indirect evidence for this suggestion comes from preparing the analogous Zn(II) complex $E\cdot\mathbf{Zn}\cdot\mathbf{L^p}$ which has the composition (from high-resolution ESI-MS) $[Zn_2(\mathbf{L^p})_3](BF_4)_4$ and is likely to be isostructural to the Co(II) analogue. The ^{19}F NMR spectrum of $E\cdot\mathbf{Zn}\cdot\mathbf{L^p}$ (Fig. 8) showed that the signals associated with the fluoroborate anions (separate ^{19}F signals for the ^{10}B and ^{11}B isotopomers are clearly visible) are split into two closely-spaced components, consistent with the anions being in two different environments: such splitting is not present in the ^{19}F NMR spectrum of $Zn(BF_4)_2$ (Fig. 8).‡ The two component spectrum suggests that BF_4^- anions from $E\cdot\mathbf{Zn}\cdot\mathbf{L^p}$ are found free in solution or are associated with the $[Zn_2(\mathbf{L^p})_3]^{4+}$ core, with any free/bound anion

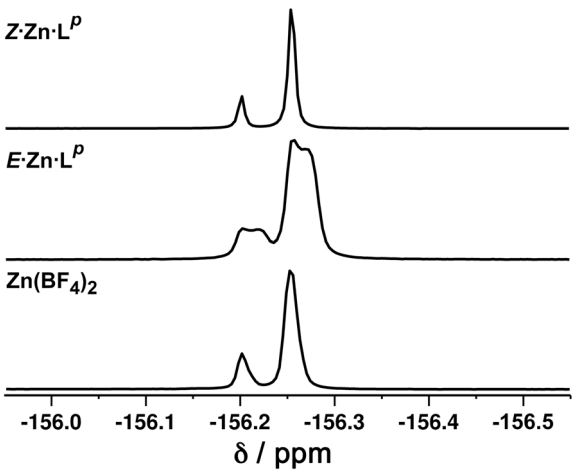

Fig. 8 ^{19}F NMR spectra (400 MHz, CD_3CN, 298 K) of (bottom) $Zn(BF_4)_2$ showing the presence of only one anion environment (the two separate signals arise from the ^{10}B and ^{11}B isotopomers which give slightly different chemical shifts for attached ^{19}F atoms); (middle) $E\cdot\mathbf{Zn}\cdot\mathbf{L^p}$ showing by the extra splitting the presence of two BF_4^- anion environments in the complex; and (top) $Z\cdot\mathbf{Zn}\cdot\mathbf{L^p}$ showing the presence of only one anion environment.

exchange being slow on the NMR timescale. We were unable to obtain X-ray quality crystals of these complexes but the NMR evidence for anion interaction with the complex cation is clear, though the close overlap of the ^{19}F signals precludes accurate integration. Association of anions to the surface of cages formed using ligands of this family has been firmly established crystallographically and also underpins the solution catalytic activity of this family of cages.[12,19] A possible (calculated) structure for $E\cdot\mathbf{Co}\cdot\mathbf{L^P}$ containing one fluoroborate anion inside the triple helicate is in ESI, Fig. S51.†

Metal complexes with $\mathbf{L^P}$: photoswitching

Irradiation of a CD_3CN solution of $E\cdot\mathbf{Co}\cdot\mathbf{L^P}$ with 340 nm light results in the major component of the ^{1}H NMR spectrum becoming significantly more complex, with >30 new ^{1}H signals (the major component of the spectrum) appearing, indicating formation of a new species with lower internal symmetry (Fig. 6, top). Significantly, the sharp signals associated with $E\cdot\mathbf{Co}\cdot\mathbf{L^P}$ are now completely absent. On the basis that irradiation at this wavelength converts the E form of $\mathbf{L^P}$ to the Z form, we denote this new species $Z\cdot\mathbf{Co}\cdot\mathbf{L^P}$. The high-resolution ESI-MS of this solution revealed a new series of signals corresponding to the species $[Co_4(\mathbf{L^P})_6(BF_4)_n]^{(8-n)+}$ (n = 2, 3, 4, 5), suggesting that an M_4L_6 tetrahedral cage had formed. The number of new ^{1}H NMR signals is consistent with the presence of two different ligand environments, each with no internal symmetry: even if we cannot observe all 48 expected signals (because some are overlapping, or paramagnetically highly broadened, or obscured by residual solvent/water signals in the 0–10 ppm region) the number is clearly larger than the 24 signals that would arise from a structure associated with one independent, non-symmetrical ligand environment. This, together with the ESI-MS data, implies formation of an M_4L_6 cage that has C_3 symmetry because one vertex is different from the other three (which are equivalent) such that there is an $M^AM_3^B$ arrangement of metal types. This can arise when one metal centre has a *fac* tris-chelate coordination geometry and the other three have *mer* tris chelate coordination geometries, as we have reported;[20] or it can arise when one metal centre has Λ chirality and the other three have Δ (or *vice versa*).[21] We note in the NMR spectrum (Fig. 6, top) the presence of a set of much weaker signals, associated with a minor component. As the ES mass spectrum of $Z\cdot\mathbf{Co}\cdot\mathbf{L^P}$ indicates the formulation $Co_4(\mathbf{L^P})_6(BF_4)_8$ with no evidence for other cage sizes, a plausible explanation for the minor peaks is formation of an alternate cage isomer (T and S_4 isomers for tetrahedral cages are also possible).[21]

Fig. 9 shows the GFN-xTB optimised geometry[22] of a C_3 symmetric M_4L_6 tetrahedral cage, $Z\cdot\mathbf{Co}\cdot\mathbf{L^m}$, with one *fac* and three *mer* vertices. The resulting structure possesses, as required by the ^{1}H NMR spectrum, two distinct ligand environments (with one ligand spanning *fac* and *mer* tris-chelate metal vertices; and the other spanning two *mer* vertices but with no internal symmetry due to the chirality of the cage), which follows a previously-observed structure in this cage family.[20] Such C_3-symmetric M_4L_6 tetrahedra are less common than T-symmetric M_4L_6 tetrahedra in which all four metal centres are identical and are usually *fac* tris-chelates.

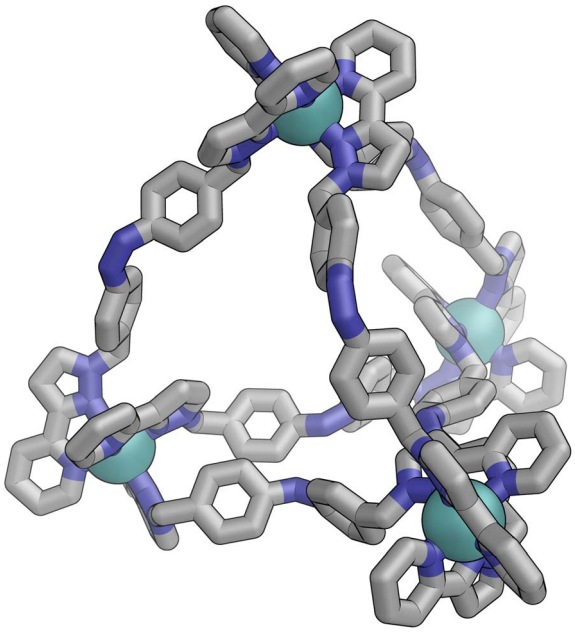

Fig. 9 GFN-xTB generated structure of the C_3 symmetric M_4L_6 tetrahedral cage $Z\cdot\mathbf{Co}\cdot\mathbf{L^P}$. The structure contains two distinct ligand environments, with one ligand environment spanning *fac* (top metal ion in Figure) and *mer* (other three metal ions at base of Figure) metal vertices, and the other spanning two *mer* vertices but with no internal symmetry due to the cage chirality.

We note that there is no splitting of signals indicative of slow-exchange guest binding in the ^{1}H NMR spectrum of $Z\cdot\mathbf{Co}\cdot\mathbf{L^P}$, or in the ^{19}F NMR spectrum of the Zn analogue ($Z\cdot\mathbf{Zn}\cdot\mathbf{L^P}$) (Fig. 8). This could be due to fluoroborate anions binding to the more accessible cavity of the tetrahedron in fast exchange on the NMR timescale,[20] or no binding occurring at all due to restructuring of the assembly from helicate to tetrahedron triggering guest release.

The photo-conversion of $E\cdot\mathbf{Co}\cdot\mathbf{L^P}$ to $Z\cdot\mathbf{Co}\cdot\mathbf{L^P}$ (Co_2L_3 form to Co_4L_6 form) proceeded to completion within the detection

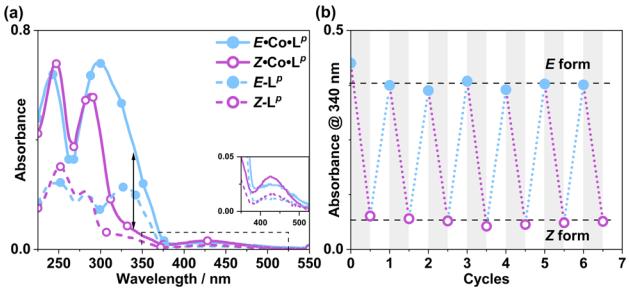

Fig. 10 (a) UV/Vis spectra of $E\cdot\mathbf{Co}\cdot\mathbf{L^P}$ and $Z\cdot\mathbf{Co}\cdot\mathbf{L^P}$ (MeCN, 13 μg ml^{-1}), as well as E-$\mathbf{L^P}$ and Z-$\mathbf{L^P}$ (MeCN, 10 μM). (b) Switching stability experiment monitoring the absorbance at 340 nm [black arrow in part (a)] of a 13 μg ml^{-1} sample after alternating irradiation with 340 nm for 30 minutes and then white light for 30 minutes, to switch between $E\cdot\mathbf{Co}\cdot\mathbf{L^P}$ and $Z\cdot\mathbf{Co}\cdot\mathbf{L^P}$ complexes.

limits of NMR spectroscopy, with complete loss of $E{\cdot}\mathbf{Co}{\cdot}\mathbf{L^P}$. This photoswitching is more effective (in terms of completeness) than was observed for free $\mathbf{L^P}$ in acetonitrile (Fig. 10), which may be ascribed to the greater separation between the π–π* and n–π* bands in the absorption spectrum (13 μg ml^{-1} $\mathbf{Co}{\cdot}\mathbf{L^P}$ and 10 μM $\mathbf{L^P}$)(Fig. 10a) and also, possibly, to a greater steric barrier to relaxation when the ligand is incorporated into a cage structure compared to being free. Similarly, the reverse photoswitching of $Z{\cdot}\mathbf{Co}{\cdot}\mathbf{L^P}$ back to $E{\cdot}\mathbf{Co}{\cdot}\mathbf{L^P}$ (Co_4L_6 form back to Co_2L_3 form) went to completion on irradiation with white light, indicating complete chemically reversible photoswitching between Co_2L_3 (likely a triple helicate) and Co_4L_6 (likely a C_3-symmetric tetrahedral cage) species.

In situ NMR measurements during illumination were used to probe the kinetics of this metal complex photoswitching, again using a quartz optical fibre inserted into the sample in the NMR cavity (Fig. 11 and S48/49†).[15] ^{1}H NMR spectra were recorded every 40 seconds for 20 minutes under irradiation with 365 nm and subsequently 405 nm light. Given the high dispersion of NMR signals arising from the paramagnetism of high-spin Co(II), a relatively narrow NMR spectral width (50–75 ppm) containing two (for $E{\cdot}\mathbf{Co}{\cdot}\mathbf{L^P}$) or three (for $Z{\cdot}\mathbf{Co}{\cdot}\mathbf{L^P}$) characteristic signals was used to provide good resolution of the signals in those selected windows. To help compensate for any uncertainty in integration of the broad signals associated with paramagnetism, integrals were recorded for all of the signals associated with each compound in the relevant window, and then averaged, with the resulting average being used to determine the ratio of isomers in solution.

Prior to irradiation, the sample of $\mathbf{Co}{\cdot}\mathbf{L^P}$ used was prepared using the as-isolated ligand $\mathbf{L^P}$ (3 : 97, $Z:E$), *i.e.* predominantly the M_2L_3 complex containing the E form of the ligand, *i.e.* $E{\cdot}\mathbf{Co}{\cdot}\mathbf{L^P}$. Following approximately 5 minutes of irradiation a PSS was reached comprising 90 : 10 $Z:E$ $\mathbf{Co}{\cdot}\mathbf{L^P}$ (Fig. 11). Subsequent exposure to 405 nm light showed complete reversion to the original mixture after 3 minutes. Moreover, UV/Vis spectroscopy could also be used to show cycling between the two species (Fig. 10): the spectrum of $E{\cdot}\mathbf{Co}{\cdot}\mathbf{L^P}$ showed a small blue shift of the ligand's π–π* transition following coordination to Co(II), from 327 nm to 305 nm, which ensured a better separation from the n–π* transition for $Z{\cdot}\mathbf{Co}{\cdot}\mathbf{L^P}$ than is possible for the free ligands. Light-induced switching between the M_2L_3 complex $E{\cdot}\mathbf{Co}{\cdot}\mathbf{L^P}$ (presumed triple helicate) and the M_4L_6 complex $Z{\cdot}\mathbf{Co}{\cdot}\mathbf{L^P}$ (presumed C_3-symmetric cage isomer) could be repeated for many cycles with no appreciable photobleaching (Fig. 10b).

Finally, we note that $Z{\cdot}\mathbf{Co}{\cdot}\mathbf{L^P}$ showed good thermal stability, taking approximately 5 weeks to return to $E{\cdot}\mathbf{Co}{\cdot}\mathbf{L^P}$ in solution at ambient temperature (Fig. 12): the high kinetic inertness of coordination cages compared to mononuclear species, even when based on individually labile metal complex vertices, is well known.[13,23] We also note that thermal relaxation is expected to be slower than light-induced isomerisations which are – effectively – performed under forcing non-equilibrium conditions.[24]

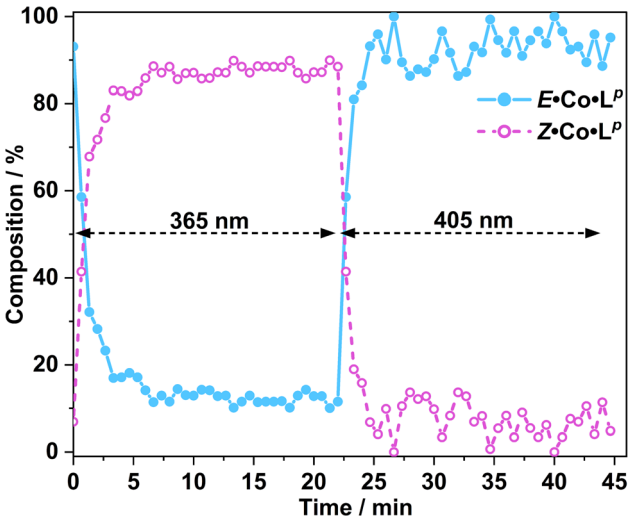

Fig. 11 Photoswitching of a solution of $E{\cdot}\mathbf{Co}{\cdot}\mathbf{L^P}$ to $Z{\cdot}\mathbf{Co}{\cdot}\mathbf{L^P}$ and back, using 365 nm and then 405 nm irradiation respectively, monitored by *in situ* ^{1}H NMR spectroscopy (700 MHz, CD_3CN, 298 K); see main text. The light blue trace shows the initial solution containing 3 : 97 $Z:E$ complexes converting over several minutes to a PSS containing *ca.* 90 : 10 $Z:E$ forms under UV irradiation, followed by rapid conversion back to the starting composition under 405 nm light excitation.

Metal complexes with $\mathbf{L^m}$: synthesis and characterisation

These complexes were prepared in exactly the same way as the complexes of $\mathbf{L^P}$, by reaction of 1.5 equivalents of $\mathbf{L^m}$ (in the as-isolated 3 : 97 $Z:E$ form) with one equivalent of $Co(BF_4)_2$ or $Zn(BF_4)_2$ in methanol overnight. After evaporation of solvent to give a solid product, any unreacted ligand and metal salt were removed with ethyl acetate and diethyl ether washes. High-resolution ESI-MS of the Co(II) product, which we denote $E{\cdot}\mathbf{Co}{\cdot}\mathbf{L^m}$, showed a sequence of signals for the species $[Co_4(\mathbf{L^m})_6(BF_4)_n]^{(8-n)+}$ (n = 2, 3, 4, 5), suggesting that an M_4L_6 complex (possibly, but not necessarily, a tetrahedral cage) had formed. The mass spectra however also showed signals corresponding to $[Co_2(\mathbf{L^m})_3(BF_4)_n]^{(4-n)+}$ (n = 1, 2, 3, 4): and whilst some of these will have the same m/z values as signals from $[Co_4(\mathbf{L^m})_6(BF_4)_n]^{(8-n)+}$ and hence overlap (see ESI†), the different

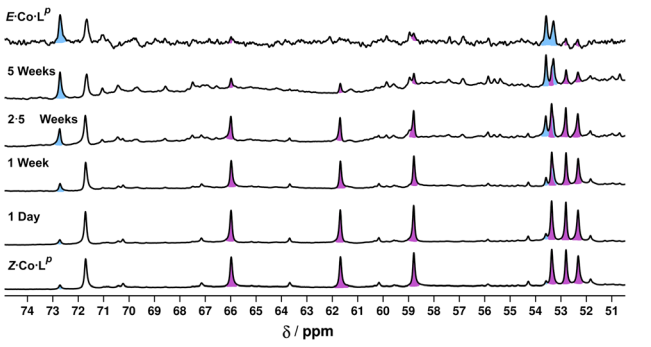

Fig. 12 Series of ^{1}H NMR spectra (400 MHz, CD_3CN, RT) showing the slow thermal conversion of $Z{\cdot}\mathbf{Co}{\cdot}\mathbf{L^P}$ (bottom spectrum) back to $E{\cdot}\mathbf{Co}{\cdot}\mathbf{L^P}$ (top spectrum) over 5 weeks. The top and bottom spectra match those in Fig. 6.

isotopic spacings make the presence of $[Co_2(\mathbf{L^m})_3(BF_4)_n]^{(4-n)+}$ in the sample quite clear, though whether this is a separate species or just a fragment induced by ESI conditions is not known. The high-resolution ESI-MS of $E{\cdot}\mathbf{Zn}{\cdot}\mathbf{L^m}$ showed a signal corresponding to $[Zn_4(\mathbf{L^m})_6(BF_4)_5]^{3+}$.

Slow cooling of a solution of $E{\cdot}\mathbf{Co}{\cdot}\mathbf{L^m}$ in methanol afforded X-ray quality crystals; the molecular structure of the complex is shown in Fig. 13. The M_4L_6 composition as shown by ESI-MS is confirmed. The structure is not that of a conventional edge-bridged tetrahedral cage, but consists of a pair of (crystallographically inequivalent) M_2L_2 double helicate units which are connected at each end by an additional bridging ligand spanning the two helicate units. The connectivity is therefore that of a closed (non-planar) M_4 cycle with alternately 1 and then 2 bridging ligands spanning successive edges – a structural type that has been reported before.[25] The ligands are coloured as three pairs in Fig. 13 for clarity, with one M_2L_2 unit having ligands coloured green, the other having ligands coloured orange, and the cross-piece ligands connecting the helicates coloured grey. Note that the same colouring does not imply crystallographic equivalence as the complex molecule has no internal crystallographic symmetry, with an entire molecule in the asymmetric unit. All metal centres have a *mer* tris-chelate coordination geometry and all have the same optical configuration (Δ in the figure shown, with the enantiomeric assembly also present in the other half of the $P\bar{1}$ unit cell).

The flexibility of the ligands associated with the $-CH_2-$ spacer units, as well as rotation of the aromatic rings about the Ph–N bonds, provide substantial conformational freedom. The two ligands coloured green in Fig. 13 have a conformation in which the internal twofold symmetry of each ligand is lost, *i.e.* the 'head' and 'tail' ends are different, but the head-to-tail disposition of the pair of similar (but not crystallographically equivalent) ligands provides approximate local C_2 symmetry for this helical unit (Fig. 14).

In contrast the pair of orange-coloured ligands in the other M_2L_2 helicate have a conformation in which both retain (non-crystallographic) internal C_2 symmetry and are also very similar to one another, giving this fragment local D_2 symmetry (Fig. 15), though this is removed by one face of that helicate being closer to the other M_2L_2 unit, pointing 'into' the centre of the complex, than the other which lies on the exterior surface. In both M_2L_2 helicate units we can see inter-ligand π-stacking with phenyl rings of one ligand stacked with electron-deficient, coordinated, pyrazolyl-pyridine units from other ligands. The grey-coloured ligands connecting the two helicate fragments have no internal symmetry. The Zn(II) analogue $E{\cdot}\mathbf{Zn}{\cdot}\mathbf{L^m}$ was also crystallographically characterised and is isostructural, but provided significantly poorer quality data: accordingly it is not included here but we just note that it is isostructural/isomorphous to $E{\cdot}\mathbf{Co}{\cdot}\mathbf{L^m}$.

In solution, allowing for adoption of formally higher symmetry due to relaxation from what is observed in the crystal structure, the cation of $E{\cdot}\mathbf{Co}{\cdot}\mathbf{L^m}$ could display twofold

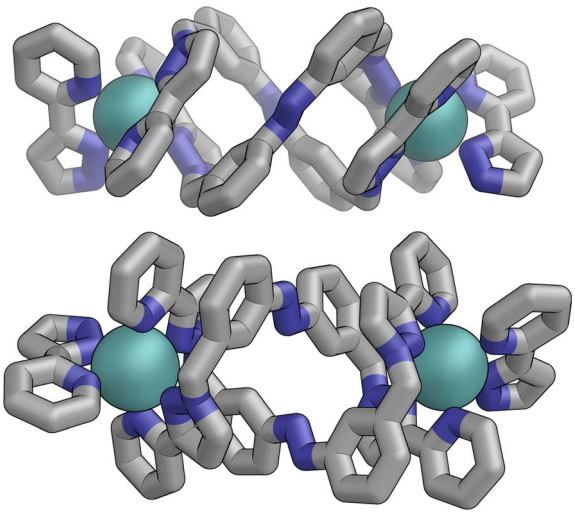

Fig. 14 Structure of the M_2L_2 double-helicate unit coloured green in Fig. 13, with approximate (non-crystallographic) C_2 internal symmetry in which the two ligands are essentially identical but conformational details two ends of each ligand are different (*i.e.* both adopt the same 'head to tail' arrangement within the M_2L_2 unit).

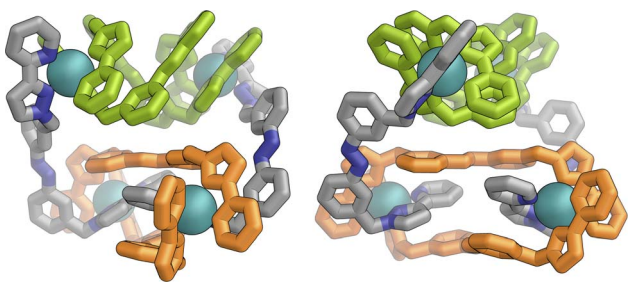

Fig. 13 Two views of the molecular structure of the M_4L_6 complex cation of $E{\cdot}\mathbf{Co}{\cdot}\mathbf{L^m}$ from an X-ray crystal structure determination, with different types of ligand environment highlighted in green or orange (within the two M_2L_2 helicate units), or grey (cross-linking the two helicate units).

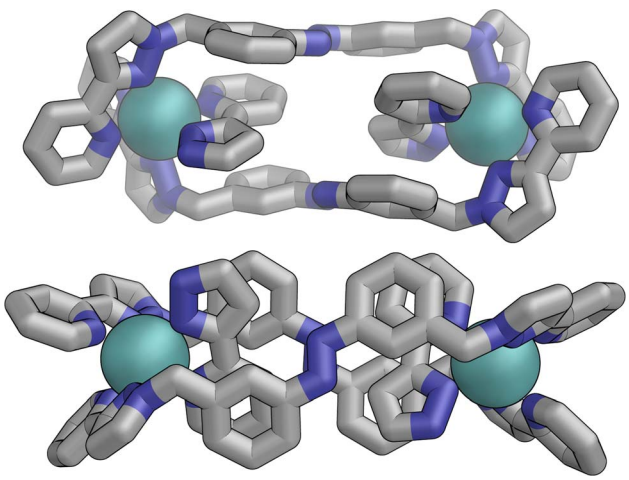

Fig. 15 Structure of the M_2L_2 double-helicate unit coloured orange in Fig. 14, with each ligand having approximate (non-crystallographic) C_2 internal symmetry with each end the same: the two ligands are essentially identical, giving local D_2 symmetry for the M_2L_2 unit.

symmetry, with a single C_2 axis bisecting the two helicates: this would lead to three independent ligand environments – the orange, green and grey ligand types shown in Fig. 14 – and, in principle, 72 different ^{1}H NMR signals. The observed ^{1}H NMR spectrum (from redissolved crystals) reveals a complicated mixture of signals of different intensities that is not susceptible to simple analysis (Fig. 16a): there are clearly major and minor components present whose relative intensities were concentration dependent, with the weaker signals becoming relatively more intense compared to the stronger signals at higher concentrations, possibly indicating aggregation into a larger structure. This is consistent with what would be expected for a combination of M_2L_3 and M_4L_6 (and perhaps other) species in solution, *cf.* the ESI mass spectrum which revealed the presence of both M_2L_3 and M_4L_6 species, and it is to be expected on the basis of the Le Chatelier principle that the larger assembly dominates at the high local concentrations when crystal nucleation occurs. We have seen concentration-dependence in the speciation behaviour of other metal/ligand assemblies from this general family of ligands,[13] and we note that McConnell and Herges,[26] and Clever,[27] have similarly observed complex mixtures of species forming in solution using bridging ligands incorporating diazocene units into the spacers.

Metal complexes with L^m: preparation and identification of mixed-ligand-isomer complexes

Following photo-irradiation of E·**Co**·$\mathbf{L^m}$ with 340 nm light to induce E to Z isomerisation of the ligands, ESI-MS showed that signals corresponding to an M_4L_6 complex stoichiometry were retained in Z·**Co**·$\mathbf{L^m}$; this photochemical switching is discussed in more detail in the next section. In the absence of crystallographic data, the geometry of Z·**Co**·$\mathbf{L^m}$ was optimised using GFN-xTB assuming a similar M_4 cyclic structure as for E·**Co**·$\mathbf{L^m}$ with (i) all metal centres possessing a *mer* tris-chelate coordination geometry and (ii) having same optical configuration as one another (Δ, Fig. 17).

The structure adopts a similar conformation to E·**Co**·$\mathbf{L^m}$, displaying two inequivalent M_2L_2 helical units, connected at each end by two additional bridging ligands. This generated structure of an isolated molecule of Z·**Co**·$\mathbf{L^m}$ is less compact than the molecular structure observed in crystals of E·**Co**·$\mathbf{L^m}$, which we attribute to the greater solid-state constraints associated with crystal packing. In this calculated structure of Z·**Co**·$\mathbf{L^m}$, inter-ligand π-stacking was observed between relatively electron-rich phenyl rings of one ligand and coordinated pyrazolyl-pyridine units from other ligands which are relatively electron-deficient due to their coordination to +2 ions. In contrast to E·**Co**·$\mathbf{L^m}$, both helical units in the calculated structure of Z·**Co**·$\mathbf{L^m}$ displayed local C_2 symmetry, which is removed by the orientation of the two helical units with respect to each other. This calculated M_4 cyclic structure therefore possesses no symmetry elements, which would lead to 6 independent ligand environments displaying 144 different ^{1}H-NMR signals in solution.

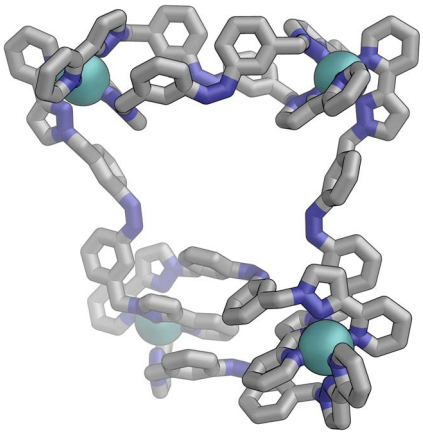

Fig. 17 GFN-xTB generated structure of the M_4L_6 complex cation of Z·**Co**·L^m comprising two M_2L_2 helicate units joined by two cross-linking ligands, with no internal symmetry.

Samples of Z·**Co**·$\mathbf{L^m}$ could be prepared by two procedures: (i) reaction of $Co(BF_4)_2$ (7.0 mM) with a sample of Z-$\mathbf{L^m}$ (10.5 mM) in acetonitrile; or (ii) irradiation of pre-formed E·**Co**·$\mathbf{L^m}$ in acetonitrile with 340 nm light. Comparison of the observed ^{1}H NMR spectra of the two samples (Fig. 16b and c, respectively) show that they are generally similar but contain major and minor components, whose relative intensities were dependent on the method by which the samples were prepared. The latter method [direct reaction of Co(II) with photo-generated Z-$\mathbf{L^m}$, Fig. 16b] afforded a ^{1}H NMR spectrum with a major component of >100 signals, consistent with the optimised structure generated by GFN-xTB (Fig. 17). In contrast, irradiation of E·**Co**·$\mathbf{L^m}$ in acetonitrile with 340 nm generated a more complex NMR spectrum containing additional minor signals (compare the features labelled * between Fig. 16b and c), implying formation of a less clean mixture of multiple species by photoswitching of pre-assembled E·**Co**·$\mathbf{L^m}$.

If cyclic M_4L_6 species can form with the ligands in either E (crystal structure, Fig. 13) or Z (calculated structure, Fig. 17) geometries, this implies that other intermediate M_4L_6 structures might exist containing different proportions of Z- and E-$\mathbf{L^m}$ ligands, *viz.* a series of $M_4(E\text{-}\mathbf{L^m})_n(Z\text{-}\mathbf{L^m})_{6-n}$ species which can

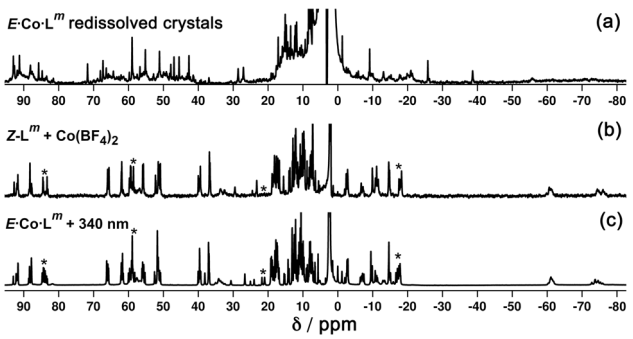

Fig. 16 ^{1}H NMR spectra (300 MHz, CD_3CN, 298 K) of (a) redissolved crystals of E·**Co**·L^m; (b) Z·**Co**·L^m prepared by combination of Z-L^m with $Co(BF_4)_2$; and (c) Z·**Co**·L^m prepared by irradiation of a sample of E·**Co**·L^m at 340 nm. Comparison of signals labelled * between parts (b) and (c) show additional complexity in the spectrum of the sample generated by photoswitching.

tolerate *Z*/*E* configurational changes to individual ligands without disrupting the overall complex formulation, and that is the focus of this section.

We investigated this possibility by combining $Co(BF_4)_2$ with mixtures of *Z* and *E* forms of $\mathbf{L^m}$ in different proportions. Due to the low solubility of free $\mathbf{L^m}$ in acetonitrile, 15% (*v*/*v*) chloroform was added to aid dissolution. Two titrations were performed, whereby the free ligand *Z*-$\mathbf{L^m}$ was gradually added to the complex mixture *E*·**Co**·$\mathbf{L^m}$, and *vice versa*, with free *E*-$\mathbf{L^m}$ being added to the complex *Z*·**Co**·$\mathbf{L^m}$ [prepared by addition of $Co(BF_4)_2$ (4 mM) to *Z*-$\mathbf{L^m}$ (6 mM)]. The first titration, therefore, had the starting composition $Co(BF_4)_2$ (4 mM) and *E*-$\mathbf{L^m}$ (6 mM), to which was added aliquots of *Z*-$\mathbf{L^m}$ (0 → 6 mM): the second titration, conversely, started with a mixture of $Co(BF_4)_2$ (4 mM) and *Z*-$\mathbf{L^m}$ (6 mM), to which was added aliquots of *E*-$\mathbf{L^m}$ (0 → 6 mM). This meant that by the end of each titration it would be possible for the solution to select whichever combination of ligand isomers gave the most stable cage if one particular cage was significantly favoured, or a mixture of species otherwise. Any ligand not needed for the minimum-energy complex assembly would be free in solution. Performing this titration in both directions but to the same compositional end point (4 Co^{2+} ions: 6 *Z*-$\mathbf{L^m}$: 6 *E*-$\mathbf{L^m}$) avoids any issues with one of the species being particularly kinetically inert and thereby giving a misleading impression of thermodynamic stability.

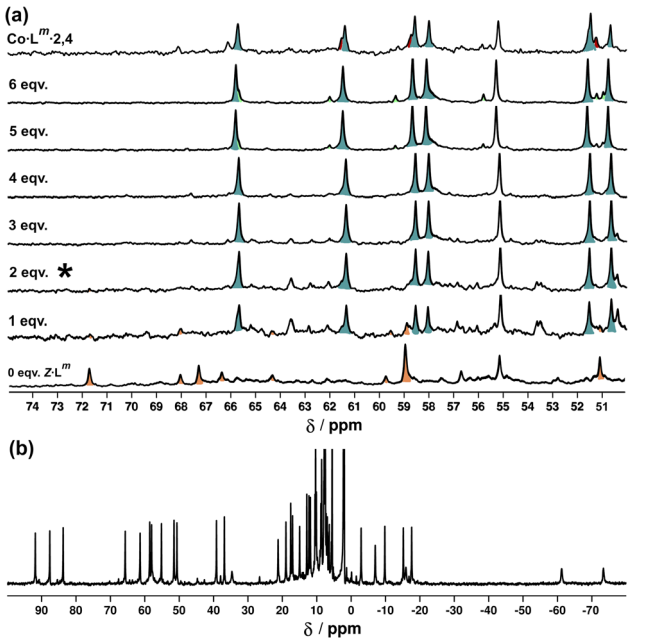

Fig. 18 (a) ^{1}H NMR spectra [300 MHz, MeCN-d_3/$CDCl_3$ (85 : 15 *v*/*v*), 298 K] recorded during addition of 0–6 equivalents (from bottom up) of *Z*-$\mathbf{L^m}$ to a solution of *E*·**Co**·$\mathbf{L^m}$. The spectrum labelled * (after addition of two equivalents of *Z*-$\mathbf{L^m}$) signals the point at which **Co**·$\mathbf{L^m}$·**2,4** is the dominant species present with little change thereafter. (b) ^{1}H-NMR spectrum (300 MHz, MeCN-d_3/$CDCl_3$ (85 : 15 *v*/*v*), 298 K) of **Co**·$\mathbf{L^m}$·**2,4** prepared separately in the same solvent mixture – compare the 50–70 ppm region with the spectrum labelled * in Fig. 18a.

Fig. 18a shows the sequence of ^{1}H NMR spectra measured during stepwise addition of portions of *Z*-$\mathbf{L^m}$ (1 mM) to *E*·**Co**·$\mathbf{L^m}$ in 85 : 15 (*v*/*v*) $CD_3CN/CDCl_3$. Addition of 1 equivalent of *Z*-$\mathbf{L^m}$ immediately resulted in appearance of a clear set of signals for a new complex: these new signals grew in intensity as the amount of *Z*-$\mathbf{L^m}$ increased to two equivalents (spectrum labelled * in Fig. 18a) with little change thereafter, and this species remains as the only metal complex structure following the addition of further equivalents of *Z*-$\mathbf{L^m}$ up to 6 mM. The pronounced appearance of this species after addition of two equivalents of *Z*-$\mathbf{L^m}$, and its retention thereafter, implies the formation of a complex with a 2 : 4 *Z* : *E* ligand ratio – which we denote **Co**·$\mathbf{L^m}$·**2,4**, with the numerals indicating the numbers of *Z* and *E* ligands respectively. **Co**·$\mathbf{L^m}$·**2,4** therefore appears to be a particularly thermodynamically favoured mixed-ligand product. It could be prepared directly using the appropriate mixture of ligand isomers and $Co(BF_4)_2$ in the required proportions. The relatively simple and clean spectrum for **Co**·$\mathbf{L^m}$·**2,4** suggests a single species, with ≈40 signals clearly resolved (Fig. 18b), consistent with the presence of two independent ligand environments having no internal symmetry which would give 48 distinct signals if all signals were clearly resolved with no overlap.

A similar result was obtained from the second titration in the opposite direction: on addition of portions of *E*-$\mathbf{L^m}$ to the complex *Z*·**Co**·$\mathbf{L^m}$, signals for **Co**·$\mathbf{L^m}$·**2,4** dominated the spectra over a wide range of compositions (see ESI†). From this we can conclude that **Co**·$\mathbf{L^m}$·**2,4**, with the composition M_4(*Z*-$\mathbf{L^m}$)$_2$(*E*-$\mathbf{L^m}$)$_4$, is the most stable of the ligand–isomer complex possibilities and we assume that it has the same cyclic structure as that observed for the crystal structure of *E*·**Co**·$\mathbf{L^m}$ but with two of the six ligands adopting the *Z* geometry: possibly the two 'crosslinking' ligands, as isomerisation of these would not disrupt the dinuclear helicate subunits.

Metal complexes with $\mathbf{L^m}$: photoswitching

UV/Vis spectroscopy (Fig. 19) was used to demonstrate repeated cycling between complexes containing *E*·**Co**·$\mathbf{L^m}$ (M_4L_6 complex possibly also containing other species such as M_2L_3 as part of a concentration-dependent equilibrium, see above) and the

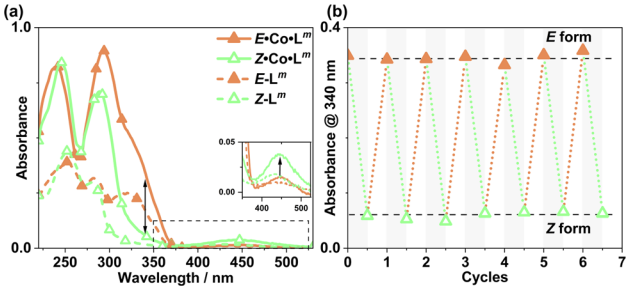

Fig. 19 (a) UV/Vis spectra of *Z*·**Co**·$\mathbf{L^m}$ and *E*·**Co**·$\mathbf{L^m}$ in MeCN (20 μg ml^{-1}), as well as *E*-$\mathbf{L^p}$ and *Z*-$\mathbf{L^p}$ (MeCN, 10 μM). (b) Switching stability experiment monitoring the absorbance of **Co**·$\mathbf{L^m}$ (20 μg ml^{-1}) species at 340 nm, after alternating irradiation with 340 nm for 30 minutes and white light for 30 minutes.

photoswitched Z·**Co**·$\mathbf{L^m}$ species whose mass spectrum indicates an M_4L_6 complex. As the UV/Vis spectra of the two forms have good separation of key absorption features, selective irradiation can be applied, and light-induced switching could be repeated over multiple cycles (Fig. 19b) with no appreciable photobleaching. We emphasise that this is not complete switching of the 'molecule A converts to molecule B' type, but switching of the composition of two metal complex ensembles in which the ligands are E to start with, but have the Z structure after photo-switching. The UV/Vis spectra (**Co**·$\mathbf{L^m}$, 20 μg ml^{-1}; and $\mathbf{L^m}$, 10 μM in acetonitrile) clearly confirm basically complete disappearance of the lower-energy absorption shoulder associated with the E form of $\mathbf{L^m}$ (Fig. 19a) following irradiation at 340 nm. Indeed, the similarity to the UV/Vis spectra associated with the E/Z switching of free $\mathbf{L^m}$ is striking (Fig. 2a), implying that the PSS under the forcing conditions of UV irradiation can be considered as approximately all-Z·**Co**·$\mathbf{L^m}$. After irradiation of the PSS with white light, the system completely reverted to the E·**Co**·$\mathbf{L^m}$ mixture of species, and the process could be repeated reversibly over several switching cycles.

We also used *in situ* illumination during NMR measurements to study the photo-induced interconversions between the set of complexes based on different ligand isomers, starting from E·**Co**·$\mathbf{L^m}$. Spectra were recorded every 40 seconds for 20 minutes under 325 nm irradiation for the E to Z switching, and then with 405 nm irradiation to reverse the ligand isomerisation (Fig. 20). As in the earlier photoswitching experiments, a narrow NMR spectral window (50–75 ppm) was selected in order to maximise the frequency resolution of the signals in this region and facilitate analysis.

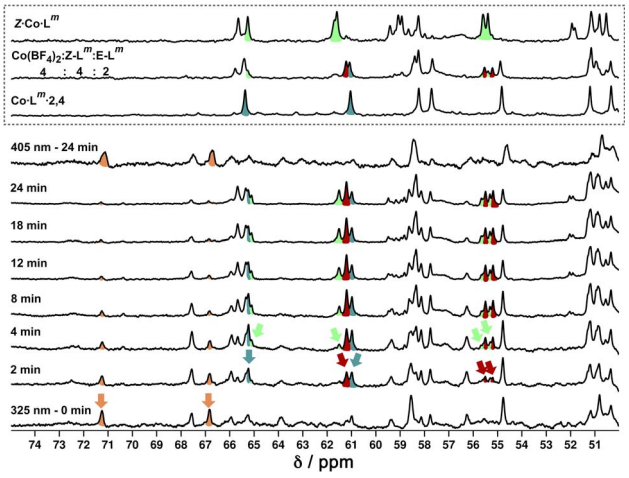

Fig. 20 ^{1}H NMR (700 MHz, CD_3CN, 298 K) spectral changes during illumination of E·**Co**·$\mathbf{L^m}$ (orange) with 325 nm light for 24 minutes, with subsequent illumination with 405 nm light for 24 minutes. Characteristic spectra of Z·**Co**·$\mathbf{L^m}$ (green) and **Co**·$\mathbf{L^m}$·**2,4** (teal blue) prepared by combination of stoichiometric quantities of Z and E-$\mathbf{L^m}$ with $Co(BF_4)_2$, are shown for comparison. A third spectrum prepared by combination of Z-$\mathbf{L^m}$, E-$\mathbf{L^m}$ and $Co(BF_4)_2$ in a 4 : 2 : 4 ratio shows the presence of a fourth species (red) amongst signals associated with Z·**Co**·$\mathbf{L^m}$ and **Co**·$\mathbf{L^m}$·**2,4**. For discussion of signals labelled with coloured arrows, see main text.

Overlap of some ^{1}H NMR signals due to the similarities between NMR spectra of isomeric structures made determination of integrals unreliable even after attempts at deconvolution, and also made evolution of spectra during the photoswitching difficult to follow with precision. However, it was still possible to see some diagnostic changes in the NMR spectra with time under irradiation. Starting with a solution of E·**Co**·$\mathbf{L^m}$, which has a messy spectrum as mentioned earlier, irradiation at 325 nm results in disappearance of some of the starting signals (denoted with orange arrows in Fig. 20, at around 67 and 71 ppm) over a period of ≈10 minutes. In parallel with this, new signals appeared at different rates. Signals labelled with a red arrow were not present in the starting spectrum of E·**Co**·$\mathbf{L^m}$ but appeared quickly during the irradiation, plateauing in intensity on a similar timescale to disappearance of E·**Co**·$\mathbf{L^m}$. The signals indicated with a teal blue arrow, in contrast, appeared to grow and then reduce in intensity, being most intense at around the 4–6 minutes mark before shrinking; and finally signals indicated with a green arrow were slowest to appear but then persisted.

This behaviour is consistent with photoswitched species containing different amounts of Z-$\mathbf{L^m}$ appearing in sequence, with the first such complex likely being **Co**·$\mathbf{L^m}$·**2,4** – which is the complex that appears first and then disappears (teal blue signals) as it is further converted to species containing a higher proportion of Z-$\mathbf{L^m}$. Red signals seem to match numerous peaks visible in spectra containing a $Z:E$ ligand ratio of 4 : 2. Literature precedents shows a tendency for cyclic bis-azobenzenes to favour *EE* and *ZZ* states, leading us tentatively to suggest concerted switching of pairs of azo-units *i.e.* two M_2L_2 units and the pair of cross-piece ligands connecting these helicates,[24,28] as suggested earlier. Given the obvious complexity/high overlap between signals in these evolving spectra of mixtures we cannot assign confidently the nature of the new photoswitched species beyond that: we just note that (i) E to Z photoswitching occurs of ligands within the complexes, without changing the overall M_4L_6 stoichiometry; and (ii) the appearance and then disappearance of signals associated with **Co**·$\mathbf{L^m}$·**2,4** is apparent as the complex population shifts towards species containing a higher proportion of the Z isomer under the forcing conditions (prolonged UV irradiation). After 25 minutes, a PSS was reached with no further significant changes in the ^{1}H NMR spectra. Like the spectrum obtained following 340 nm irradiation, incomplete switching to Z·**Co**·$\mathbf{L^m}$ was observed, showing that in order to form Z·**Co**·$\mathbf{L^m}$ as the major species, $\mathbf{L^m}$ must be switched to the Z form by photoirradiation prior to assembly. As with the UV/Vis experiments, after 2 minutes of irradiation at 405 nm, the system completely reverted to the E·**Co**·$\mathbf{L^m}$ mixture of species.

Finally, we note (again) that thermal relaxation, after photoswitching, is slow. A solution subjected to photoswitching using 340 nm irradiation, as described above, had partially reverted after 2.5 weeks at ambient temperature with complete loss of the photoswitched species Z·**Co**·$\mathbf{L^m}$. After this time ^{1}H NMR signals associated with the particularly stable species **Co**·$\mathbf{L^m}$·**2,4** were present: but even after 5 weeks there was no E·**Co**·$\mathbf{L^m}$, with the presence of stable intermediate species such

as **Co·L^m·2,4** hindering relaxation. After 10 months the complex had completely reverted to *E*·**Co·L^m**.

Conclusions

The bis-bidentate bridging ligands **L^p** and **L^m** contain two chelating pyrazolyl-pyridine coordination sites separated by photochromic azobenzene units based on *para* or *meta* substitution patterns, respectively. The light-induced $E \rightarrow Z$ conversion (under UV excitation) and subsequent reversion (under visible excitation) was clearly established by *in situ* NMR spectroscopic measurements which established compositions of the PSS as 94 : 6 *Z* : *E* and 95 : 5 *Z* : *E* for **L^p** and **L^m** respectively in MeCN.

The photochromic properties of the ligands could be exploited to effect photoswitching between different complex structures. The Co(II) complex with *E*-**L^p** (denoted *E*·**Co·L^p**) has NMR and MS data consistent with the dominant structure being a symmetric Co_2L_3 helicate with all three ligands equivalent and each ligand having twofold symmetry. Photoswitching (complete within detection limits of NMR spectroscopy) to *Z*·**Co·L^p** shows appearance by MS of a new M_4L_6 species whose more complex NMR spectrum is consistent with two independent ligand environments, characteristic of a C_3-symmetric isomer of an M_4L_6 tetrahedral cage. The interconversion is fully reversible, and whilst we were unable to obtain X-ray quality crystals of these species, the combination of NMR and MS data points to fully reversible photo-switching between a Co_2L_3 helicate and a Co_4L_6 cage.

The Co(II) complex with *E*-**L^m** (denoted *E*·**Co·L^m**) has an ill-defined NMR spectrum indicative of a mixture of species, but it contains at least Co_2L_3 and Co_4L_6 species by ESI MS. It crystallises as a Co_4L_6 complex which is a pair of Co_2L_2 dinuclear double helicates crosslinked by two additional bridging ligands, such that the cyclic array of four Co(II) ions has alternately one or two bridging ligands along each edge. NMR titrations, to examine the dominant speciation that occurred when Co(II) ions could select from different proportions of *Z*-**L^m** and *E*-**L^m** in solution, indicated that the most stable assembly of composition $M_4(Z\text{-L})_n(E\text{-L})_{6-n}$ has $n = 2$ (two *Z* ligands and four *E* ligands, denoted **Co·L^m·2,4**), which persisted over a wide range of ligand isomer compositions. Photoswitching showed, by UV/Vis spectroscopy, conversion of the ligands to the *Z* form to give the species *Z*·**Co·L^m** amongst other *Z*-**L^m** complex species, which – by ESI MS – retain M_4L_6 compositions; *in situ* NMR experiments to monitor the photoswitching could not be fully interpreted but did show the appearance and then disappearance of a photoswitched initial product which is likely to be **Co·L^m·2,4** *en route* to eventual formation of *Z*·**Co·L^m**. Thermal relaxation of *Z*·**Co·L^m** was slow, with **Co·L^m·2,4** being the dominant species after several weeks: complete reversion to *E*·**Co·L^m** was complete by 10 months.

Overall the pair of ligands **L^p** and **L^m** both display photoswitching behaviour which translates into major structural changes in their metal complex assemblies, with unusual examples of (i) interconversion between Co_2L_3 (helicate) and Co_4L_6 (cage) assemblies with **L^p**; and interconversion between a series of Co_4L_6 assemblies $Co_4(Z\text{-L}^m)_n(E\text{-L}^m)_{6-n}$ with **L^m**.

Experimental

All experimental information (synthesis, characterisation data, X-ray crystallography, photoswitching instrumentation and methodologies, calculations of model structures and software used) are in the ESI.†

Data availability

The datasets supporting this article have been uploaded as part of the ESI.†

Author contributions

M. B. T.: synthesis, characterisation and UV/Vis based photoswitching studies. L. P. L.: NMR-based photoswitching studies and calculations of molecular models. A. B. S.: X-ray crystallography. L. K. S. v. K and M. D. W.: project conception and supervision.

Conflicts of interest

There are no conflicts to declare.

Acknowledgements

We thank the University of Warwick for a PhD studentship to M. B. T.; the Swiss National Science Foundation for an Early Postdoc Mobility fellowship (project P2FRP2/199583) to A. B. S.; and the Leverhulme Trust for a research project grant (RPG 2022–232). L. K. S. v. K. thanks the Fonds der Chemischen Industrie (FCI, Liebig Fellowship) and the German Research Foundation (DFG; Emmy Noether Programme, 446317932).

Notes and references

‡ We used the Zn(II) complex for this experiment because paramagnetic broadening in the Co(II) complex meant that the closely-spaced signals for the two forms of the complex (with free or bound anion) could not be resolved.

1 (*a*) T. R. Cook and P. J. Stang, *Chem. Rev.*, 2015, **115**, 7001; (*b*) M. M. J. Smulders, I. A. Riddell, C. Browne and J. R. Nitschke, *Chem. Soc. Rev.*, 2013, **42**, 1728; (*c*) D. Zhang, T. K. Ronson and J. R. Nitschke, *Acc. Chem. Res.*, 2018, **51**, 2423; (*d*) H. Vardhan, M. Yusubov and F. Verpoort, *Coord. Chem. Rev.*, 2016, **306**, 171; (*e*) E. G. Percástegui, T. K. Ronson and J. R. Nitschke, *Chem. Rev.*, 2020, **120**, 13480; (*f*) F. J. Rizzuto, L. K. S. von Krbek and J. R. Nitschke, *Nat. Rev. Chem*, 2019, **3**, 204; (*g*) T. K. Ronson, W. Meng and J. R. Nitschke, *J. Am. Chem. Soc.*, 2017, **139**, 9698; (*h*) C. G. P. Taylor, S. P. Argent, M. D. Ludden, J. R. Piper, C. Mozaceanu, S. A. Barnett and M. D. Ward, *Chem.–Eur. J.*, 2020, **26**, 3054; (*i*) W. Cullen, S. Turega, C. A. Hunter and M. D. Ward, *Chem. Sci.*, 2015, **6**, 2790.

2 W. Cullen, S. Turega, C. A. Hunter and M. D. Ward, *Chem. Sci.*, 2015, **6**, 625–631.
3 G. Szalóki, V. Croué, V. Carré, F. Aubriet, O. Alévêque, E. Levillain, M. Allain, J. Aragó, E. Ortí, S. Goeb and M. Sallé, *Angew. Chem., Int. Ed.*, 2017, **56**, 16272–16276.
4 (*a*) S. J. Wezenberg, *Chem. Lett.*, 2020, **49**, 609; (*b*) E. Benchimol, J. Tessarolo and G. H. Clever, *Nat. Chem.*, 2024, **16**, 13.
5 (*a*) D.-H. Qu, Q.-C. Wang, Q.-W. Zhang, X. Ma and H. Tian, *Chem. Rev.*, 2015, **115**, 7543–7588; (*b*) S. J. Wezenberg, *Chem. Commun.*, 2022, **58**, 11045; (*c*) A. Ghosh, L. Slappendel, B.-N. T. Nguyen, L. K. S. von Krbek, T. K. Ronson, A. M. Castilla and J. R. Nitschke, *J. Am. Chem. Soc.*, 2023, **145**, 3828.
6 (*a*) K. Matsuda and M. Irie, *J. Photochem. Photobiol., C*, 2004, **5**, 169; (*b*) M. Irie, *Chem. Rev.*, 2000, **100**, 1685; (*c*) M. Irie, T. Fukaminato and S. Kobatake, *Chem. Rev.*, 2014, **114**, 12174.
7 (*a*) R.-J. Li, J. Tessarolo, H. Lee and G. H. Clever, *J. Am. Chem. Soc.*, 2021, **143**, 3865; (*b*) R.-J. Li, J. J. Holstein, W. G. Hiller, J. Andréasson and G. H. Clever, *J. Am. Chem. Soc.*, 2019, **141**, 2097; (*c*) S. Juber, S. Wingbermühle, P. Nuernberger, G. H. Clever and L. V. Schäfer, *Phys. Chem. Chem. Phys.*, 2021, **23**, 7321; (*d*) R.-J. Li, M. Han, J. Tessarolo, J. J. Holstein, J. Lübben, B. Dittrich, C. Volkmann, M. Finze, C. Jenne and G. H. Clever, *ChemPhotoChem*, 2019, **3**, 378; (*e*) M. Han, R. Michel, B. He, Y. S. Chen, D. Stalke, M. John and G. H. Clever, *Angew. Chem., Int. Ed.*, 2013, **52**, 1319.
8 T. Murase, S. Sato and M. Fujita, *Angew. Chem., Int. Ed.*, 2007, **46**, 5133.
9 Y. Wang, B. Li, J. Zhu, W. Zhang, B. Zheng, W. Zhao, J. Tang, X.-J. Yang and B. Wu, *Angew. Chem., Int. Ed.*, 2022, **61**, e202201789.
10 R. G. DiNardi, A. O. Douglas, R. Tian, J. R. Price, M. Tajik, W. A. Donald and J. E. Beves, *Angew. Chem., Int. Ed.*, 2022, **61**, e202205701.
11 (*a*) H. Lee, J. Tessarolo, D. Langbehn, A. Baksi, R. Herges and G. H. Clever, *J. Am. Chem. Soc.*, 2022, **144**, 3099; (*b*) D. Hugenbusch, M. Lehr, J.-S. von Glasenapp, A. J. McConnell and R. Herges, *Angew. Chem., Int. Ed.*, 2023, **62**, e202212571.
12 M. D. Ward, C. A. Hunter and N. H. Williams, *Acc. Chem. Res.*, 2018, **51**, 2073.
13 (*a*) A. Stephenson, S. P. Argent, T. Riis-Johannessen, I. S. Tidmarsh and M. D. Ward, *J. Am. Chem. Soc.*, 2011, **133**, 858; (*b*) W. Cullen, C. A. Hunter and M. D. Ward, *Inorg. Chem.*, 2015, **54**, 2626.
14 A. Stephenson and M. D. Ward, *RSC Adv.*, 2012, **2**, 10844.
15 (*a*) R. Falkenburg, M. J. Notheis, G. Schnakenburg and L. K. S. von Krbek, *Org. Biomol. Chem.*, 2023, **21**, 4993; (*b*) Y. Ji, D. A. DiRocco, J. Kind, C. M. Thiele, R. M. Gschwind and M. Reibarkh, *ChemPhotoChem*, 2019, **3**, 984.
16 W. Moormann, T. Tellkamp, E. Stadler, F. Röhricht, C. Näther, R. Puttreddy, K. Rissanen, G. Gescheidt and R. Herges, *Angew. Chem., Int. Ed.*, 2020, **59**, 15081.
17 (*a*) Z. Zhang and D. Dolphin, *Chem. Commun.*, 2009, 6931; (*b*) J. Xu, T. N. Parac and K. N. Raymond, *Angew. Chem., Int. Ed. Engl.*, 1999, **38**, 2878; (*c*) F. Cui, S. Li, C. Jia, J. S. Mathieson, L. Cronin, X.-J. Yang and B. Wu, *Inorg. Chem.*, 2012, **51**, 179; (*d*) M. Albrecht, *Chem.–Eur. J.*, 2000, **6**, 3485.
18 (*a*) M. Albrecht, *Top. Curr. Chem.*, 2004, **248**, 105; (*b*) M. Albrecht, O. Blau and R. Fröhlich, *Proc. Natl. Acad. Sci. U. S. A.*, 2002, **99**, 4867; (*c*) L. A. Barrios, R. Diego, M. Darawsheh, J. I. Martínez, O. Roubeau and G. Aromí, *Chem. Commun.*, 2022, **58**, 5375; (*d*) S. Goetz and P. E. Kruger, *Dalton Trans.*, 2006, 1277; (*e*) C. J. Massena, N. B. Wageling, D. A. Decato, E. M. Rodriguez, A. M. Rose and O. B. Berryman, *Angew. Chem., Int. Ed. Engl.*, 2016, **55**, 12398; (*f*) M. Albrecht, O. Blau and J. Zauner, *Eur. J. Org Chem.*, 1999, 3165; (*g*) D. Van Craen, M. G. Kalarikkal and J. J. Holstein, *J. Am. Chem. Soc.*, 2022, **144**, 18135.
19 (*a*) W. Cullen, M. C. Misuraca, C. A. Hunter, N. H. Wiilliams and M. D. Ward, *Nat. Chem.*, 2016, **8**, 231; (*b*) M. D. Ludden, C. G. P. Taylor, M. B. Tipping, J. S. Train, N. H. Williams, J. C. Dorratt, K. L. Tuck and M. D. Ward, *Chem. Sci.*, 2021, **12**, 14781; (*c*) M. D. Ludden, C. G. P. Taylor and M. D. Ward, *Chem. Sci.*, 2021, **12**, 12640; (*d*) M. D. Ludden and M. D. Ward, *Dalton Trans.*, 2021, **50**, 2782; (*e*) X. Zhang, B. Suditapong and M. D. Ward, *Inorg. Chem. Front.*, 2023, **10**, 1270.
20 (*a*) R. L. Paul, S. P. Argent, J. C. Jeffery, L. P. Harding, J. M. Lynam and M. D. Ward, *Dalton Trans.*, 2004, 3453; (*b*) B. R. Hall, L. E. Manck, I. S. Tidmarsh, A. Stephenson, B. F. Taylor, E. J. Blaikie, D. A. Vander Griend and M. D. Ward, *Dalton Trans.*, 2011, **40**, 12132.
21 (*a*) W. Meng, J. K. Clegg, J. D. Thoburn and J. R. Nitschke, *J. Am. Chem. Soc.*, 2011, **133**, 13652; (*b*) T. Beissel, R. E. Powers, T. N. Parac and K. N. Raymond, *J. Am. Chem. Soc.*, 1999, **121**, 4200.
22 S. Grimme, C. Bannwarth and P. Shushkov, *J. Chem. Theory Comput.*, 2017, **13**, 1989.
23 (*a*) M. D. Ward, *Chem. Commun.*, 2009, 4487; (*b*) A. J. Terpin, M. Ziegler, D. W. Johnson and K. N. Raymond, *Angew. Chem., Int. Ed.*, 2001, **40**, 157; (*c*) S. Sato, Y. Ishido and M. Fujita, *J. Am. Chem. Soc.*, 2009, **131**, 6064; (*d*) S. P. Argent, F. C. Jackson, H. M. Chan, S. Meyrick, C. G. P. Taylor, T. K. Ronson, J. P. Rourke and M. D. Ward, *Chem. Sci.*, 2020, **11**, 10167.
24 M. Müri, K. C. Schuermann, L. De Cola and M. Mayor, *Eur. J. Org Chem.*, 2009, 2562.
25 A. Stephenson and M. D. Ward, *Dalton Trans.*, 2011, **40**, 10360.
26 D. Hugenbusch, M. Lehr, J.-S. von Glasenapp, A. J. McConnell and R. Herges, *Angew. Chem., Int. Ed.*, 2023, **62**, e202212571.
27 H. Lee, J. Tessarolo, D. Langbehn, A. Baksi, R. Herges and G. H. Clever, *J. Am. Chem. Soc.*, 2022, **144**, 3099.
28 (*a*) Y. Norikane and N. Tamaoki, *Org. Lett.*, 2004, **6**, 2595; (*b*) A. H. Heindl, L. Schweighauser, C. Logemann and H. A. Wegner, *Synthesis*, 2017, **49**, 2632.

Supporting Information For: Photoswitching of Co(II)-based coordination cages containing azobenzene backbones

Max B. Tipping,[a] Lidón Pruñonosa Lara,[b] Atena B. Solea,[a] Larissa K. S. von Krbek*[b] and Michael D. Ward*[a]

a Department of Chemistry, University of Warwick, Coventry CV4 7AL, UK

b Kekulé-Institut für Organische Chemie und Biochemie, Rheinische Friedrich-Wilhelms-Universität Bonn, Gerhard-Domagk-Str. 1, 53121 Bonn, Germany

Corresponding Authors Email: m.d.ward@warwick.ac.uk, larissa.vonkrbek@uni-bonn.de

Contents

Materials

Starting materials were purchased from the following commercial sources: Fluorochem, Sigma-Aldrich, Fisher Scientific and Alfa Aesar and used as supplied. The following materials were prepared using literature procedures: 3,3'-bis(bromomethyl)-azobenzene and 4,4'-bis(bromomethyl)-azobenzene;[1] 3-(2-pyridyl)-1H-pyrazole;[2] **L^P**.[3]

Methods

NMR Spectroscopy - ^{1}H NMR and ^{13}C{^{1}H} NMR spectra were recorded at 300, 400, 500 or 700 MHz (^{1}H) and 125 MHz (^{13}C) respectively on Bruker Avance (300 MHz), Bruker Avance III HD (400 MHz), Bruker Avance III HD (500 MHz), Bruke Avance I (500 MHz) or Bruker Avance III HD Ascend (700 MHz) spectrometers. ^{19}F{^{1}H} NMR were also recorded on a Bruker Avance III HD (400 MHz). All NMR spectra were measured at 25°C in the indicated deuterated solvents unless stated otherwise. Proton and carbon chemical shifts (δ) are reported in ppm and coupling constants (*J*) are reported in Hertz (Hz). The resonance multiplicity in the ^{1}H NMR spectra are described as "s" (singlet), "d" (doublet), "t" (triplet), "q" (quartet), ''dd'' (doublet of doublets), ''ddd'' (doublet of doublet of doublets) and "m" (multiplet) and broad resonances are indicated by "br". 2D homonuclear correlation ^{1}H-^{1}H COSY and 2D heteronuclear correlation ^{1}H-^{13}C HETCOR experiments (HSQC, HMBC) were used to confirm NMR peak assignments.

Mass Spectrometry - Low resolution ESI mass spectrometry was performed using an Agilent 6130B ESI-MS; high resolution ESI mass spectra were acquired on a Bruker Compact ESI-Q-TOF.

UV/Vis Spectroscopy - recorded on an Implen C40 Nanophotometer and/or a Clariostar Plus (BMG Labtech) plate reader.

IR Spectroscopy - recorded on a Bruker Alpha FTIR Spectrometer.

Light Sources - Illumination experiments were carried out using Prizmatrix fiber collimated LEDs and a Thorlabs single colour UV LED (340 nm light source).

Table S1. Light output of LEDs used.

λ / nm	**310**	**325**	**340***	**365**	**390**	**405**	**450**	**500**	**550**
Output power (1 m optical fiber) / mW	1	8.6	1.7	170	220	260	440	165	230

* 340 nm is not a fibre collimated LED and, hence, output power is given directly at the light source.

340 nm LEDs (only) were unavailable for *in situ* illumination NMR experiments, but were used for endpoint experiments and synthesis.

Preparations

***L**^{m}:* Aqueous KOH (5.5 M, 51 cm^3, 280.5 mmol) was added to a stirred solution of 3-(2-pyridyl)-1H-pyrazole (4.20 g, 28.9 mmol) in THF (250 cm^3). Once effervescence had ceased, 3,3'-bis(bromomethyl)-azobenzene (5.00 g, 13.7 mmol) was added along with a catalytic quantity of tetrabutylammonium iodide and the solution heated to 74 °C for 20 h. Once cooled to RT, the crude mixture was diluted with H_2O and then reduced in volume by 50% under reduced pressure. The crude product was extracted using DCM (3 x 50 cm^3), dried over $MgSO_4$, filtered and solvent removed by rotary evaporation. Column chromatography on silica (THF/$CHCl_3$, 1:9 v/v) yielded **L**^{m} as an orange powder (4.1 g, 61%). High-resolution ESI-MS: m/z 497.2192; calcd. for $C_{30}H_{25}N_8^+$ $(M + H)^+$, 497.2197. IR: ν_{max}/cm^{-1} 3121w, 3048w, 2918m, 2850w, 1743w, 1707w, 1591m, 1564m, 1491m, 1459m, 1226m, 1143m, 1048m, 993m, 755s, 695s, 634m, 621m, 539m. ^{1}H-NMR (500 MHz, $CDCl_3$, RT): δ 8.69 (2H, d, J 4.3 Hz, pyridyl H^6); 7.96 (2H, d, J 7.9 Hz, pyridyl H^3); 7.84 (2H, d, J 8.0 Hz, phenyl H^6), 7.81 (2H, s, phenyl H^2), 7.71 (2H, td, J 7.9, 1.8 Hz, pyridyl H^4), 7.49-7.47 (4H, m, pyrazole H^5 and phenyl H^5), 7.35 (2H, d, J 7.9 Hz, phenyl H^4), 7.19 (2H, dd, J 6.9, 5.4 Hz, pyridyl H^5), 6.96 (2H, d, J 2.1 Hz, pyrazole H^4), 5.48 (4H, s, CH_2). ^{13}C-NMR (125 MHz, $CDCl_3$, RT): δ152.7 (Phenyl C^1), 152.0 Pyridyl C^2), 151.7 Pyrazole C^3), 149.2 (Pyridyl C^6), 137.6 (Phenyl C_3), 136.7 (Pyridyl C^4), 131.0 (Pyrazole C^5), 130.2 (Phenyl C^4), 129.6 (Phenyl C^5), 122.7 (Phenyl C^6), 122.4 (Pyridyl C^5), 122.0 (Phenyl C^2), 120.2 (Pyridyl C^3), 105.1 (Pyrazole C^4), 55.9 (CH_2).

E•***Co•L**^{p}*: **L**^{p} (50 mg, 101 μmol) and $Co(BF_4)_2.6H_2O$ (23 mg, 68 μmol) were combined in methanol (10 cm^3) and heated to 60 °C overnight. The suspension was centrifuged and the solid washed with methanol, CH_2Cl_2, and diethyl ether. The resulting compound was dried in air. Yield: 60 mg (91%). High-resolution ESI-MS: m/z 890.2472 (calcd. for $\{Co_2(\mathbf{L}^p)_3(BF_4)_2\}^{2+}$, 890.2554); 564.4983 (calcd. for $\{Co_2(\mathbf{L}^p)_3(BF_4)\}^{3+}$, 564.5021); 401.8743 (calcd. for $\{Co_2(\mathbf{L}^p)_3\}^{4+}$, 401.8761). ^{1}H NMR spectra shown in **Figure 6**.

E•***Zn•L**^{p}* was prepared in the same way as *E*•**Co•L**^{p}, but using $Zn(BF_4)_2.xH_2O$ (21 mg, 68 μmol, assumed to be the hexahydrate) in place of $Co(BF_4)_2.6H_2O$. Yield: 58 mg (88%). High-resolution ESI-MS: m/z 897.2521 (calcd. for $\{Zn_2(\mathbf{L}^p)_3(BF_4)_2\}^{2+}$, 897.2501); 569.1662 (calcd. for $\{Zn_2(\mathbf{L}^p)_3(BF_4)\}^{3+}$, 569.1653); 405.1236 (calcd. for $\{Zn_2(\mathbf{L}^p)_3\}^{4+}$, 405.1229). ^{1}H NMR spectra shown in **Figure S4**.

Z•***Co•L**^{p}*: A sample of *E*•**Co•L**^{p} (10 mg) was dissolved in MeCN-d_3 (1 cm^3), transferred to a quartz cuvette and irradiated with a 1.7 mW 340 nm LED overnight. High-resolution ESI-MS: m/z 1216.3280 (calcd. for $\{Co_4(\mathbf{L}^p)_6(BF_4)_5\}^{3+}$, 1216.3428); 890.4975 (calcd. for $\{Co_4(\mathbf{L}^p)_6(BF_4)_4\}^{4+}$, 890.5060); 694.9983 (calcd. for $\{Co_4(\mathbf{L}^p)_6(BF_4)_3\}^{5+}$, 695.0039); 564.6636 (calcd. for $\{Co_4(\mathbf{L}^p)_6(BF_4)_2\}^{6+}$, 564.6692). ^{1}H NMR spectrum shown in Figure 6 and spectra recorded during the interconversion are shown in **Figure S45**.

Z•***Zn•L**^{p}:* A sample of *E*•**Zn•L**^{p} (10 mg) was dissolved in MeCN-d_3 (1 cm^3), transferred to a quartz cuvette and irradiated with a 1.7 mW 340 nm LED overnight. High-resolution ESI-

MS: m/z 1224.6689 (calcd. for $\{Zn_4(\mathbf{L}^{p})_6(BF_4)_5\}^{3+}$, 1224.6692). For ^{1}H NMR spectrum, see **Figure S6**.

***E*•Co•L^m:** **L^m** (50 mg, 101 μmol) and $Co(BF_4)_2.6H_2O$ (23 mg, 68 μmol) were combined in methanol and stirred at 60 °C overnight. After cooling to room temperature, the solvent was removed via rotary evaporation. The resulting solid was washed with ethyl acetate and diethyl ether. Yield: 60 mg, (91%). For ^{1}H NMR spectrum, see main text. High-resolution ESI-MS: m/z 1216.2931 (calcd. for $\{Co_4(\mathbf{L}^{m})_6(BF_4)_5\}^{3+}$, 1216.3428); 890.4694 (calcd. for $\{Co_4(\mathbf{L}^{m})_6(BF_4)_4\}^{4+}$, 890.5060); 694.9746 (calcd. for $\{Co_4(\mathbf{L}^{p})_6(BF_4)_3\}^{5+}$, 695.0039). For ^{1}H NMR spectrum, see **Figure 16**.

***E*•Zn•L^m:** this was prepared exactly as for ***E*•Co•L^m** but using $Zn(BF_4)_2$ (21 mg, 68 μmol, assumed to be the hexahydrate) in place of $Co(BF_4)_2.6H_2O$. Yield: 59 mg, (89%). High-resolution ESI-MS: *m/z* 1225.0099 (calcd. for $\{Zn_4(\mathbf{L}^{m})_6(BF_4)_5\}^{3+}$, 1225.0020). For ^{1}H NMR spectrum, see **Figure S10**.

***Z*•Co•L^m:** **L^m** (6.0 mg, 12 μmol) was dissolved in MeCN (1 cm^3) and irradiated with 340 nm overnight, to produce ***Z*-L^m.** $Co(BF_4)_2.6H_2O$ (19.2 mg, 56 μmol) was dissolved in acetonitrile (1 cm^3). ***Z*-L^m** solution (0.7 cm^3) and $Co(BF_4)_2$ solution (0.1 cm^3) were combined and vortexed. High resolution ESI-MS: m/z 1867.9415 (calcd. for $\{Co_4(\mathbf{L}^{m})_6(BF_4)_6\}^{2+}$, 1868.0164); 1216.2930 (calcd. for $\{Co_4(\mathbf{L}^{m})_6(BF_4)_5\}^{3+}$, 1216.3428); 890.4697 (calcd. for $\{Co_4(\mathbf{L}^{m})_6(BF_4)_4\}^{4+}$, 890.5060); 694.9747 (calcd. for $\{Co_4(\mathbf{L}^{p})_6(BF_4)_3\}^{5+}$, 695.0039). ^{1}H NMR spectrum shown in Figure 16 and spectra recorded during the interconversion are shown in **Figure 16** and **Figure S48**.

Selected NMR Spectra

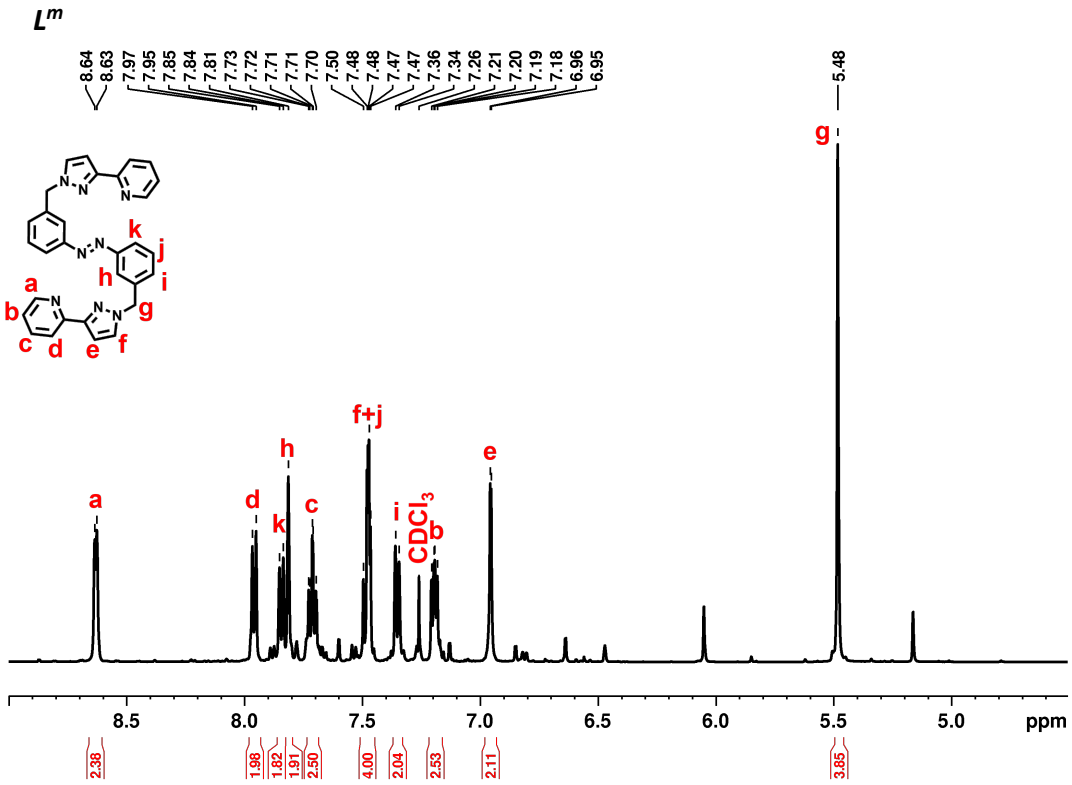

Figure S1. ^{1}H NMR spectrum (500 MHz, $CDCl_3$, 298 K) of *E*-**L**^{m}.

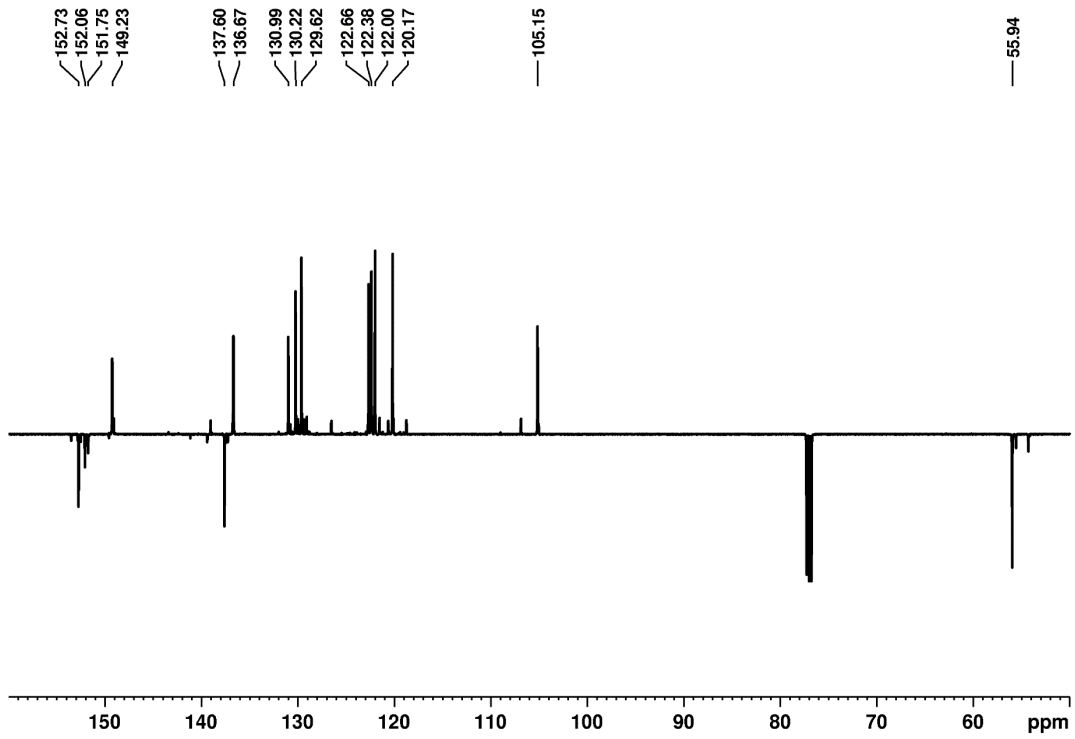

Figure S2. $^{13}C\{^{1}H\}$ APT NMR spectrum (125 MHz, $CDCl_3$, 298 K) of *E*-**L**^{m}.

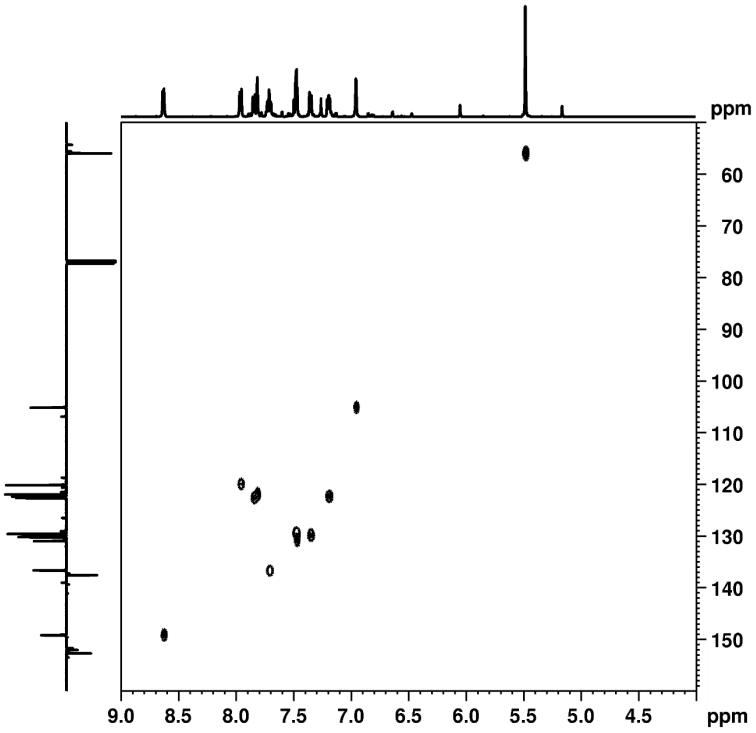

Figure S3. 2D ^{1}H-^{13}C HSQC NMR spectrum ($CDCl_3$, 298 K) of *E*-**L**^{m}

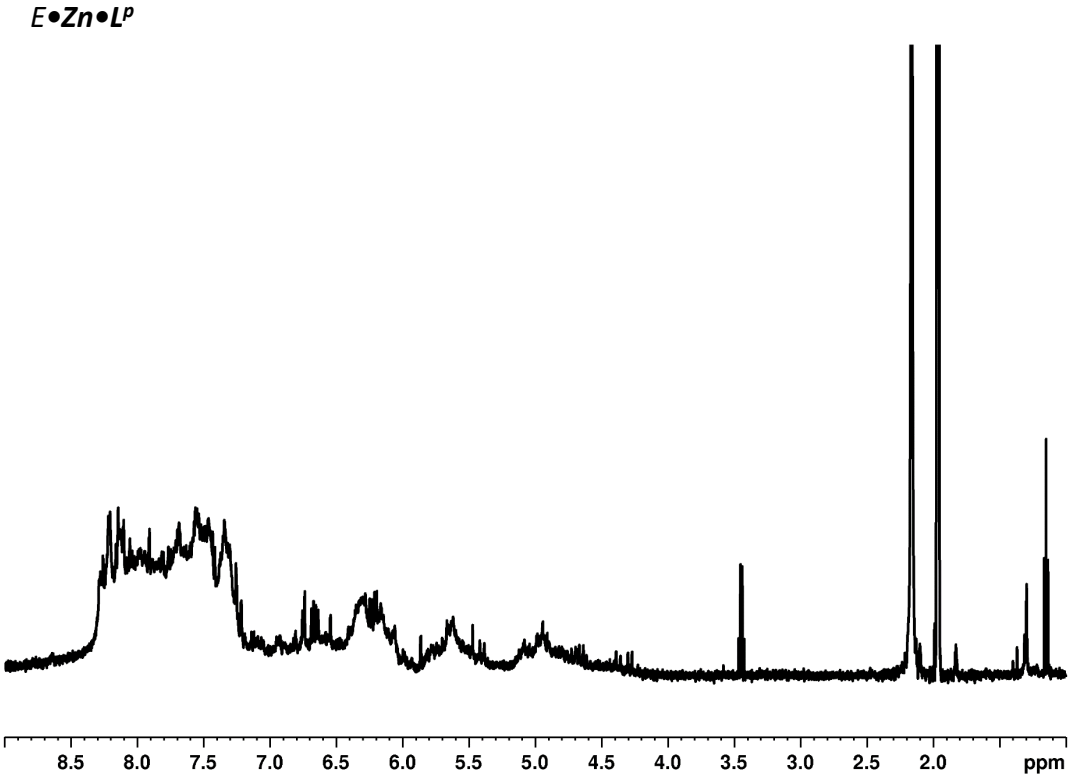

Figure S4. ^{1}H NMR spectrum (500 MHz, MeCN-d_3, 298 K) of *E*•**Zn**•**L**^{p}

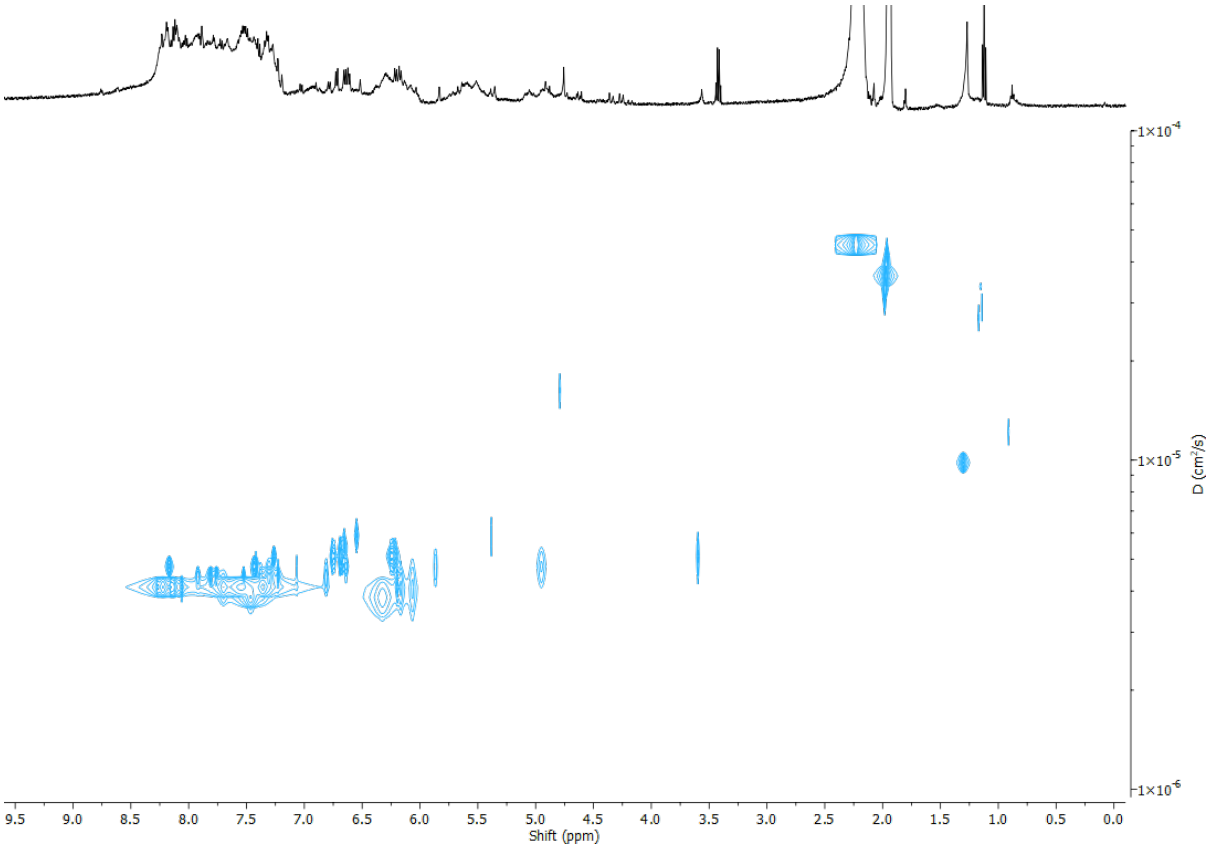

Figure S5. 2D-DOSY NMR spectrum (500 MHz, MeCN-d_3, 298 K) of *E*•**Zn**•**L**^{p}

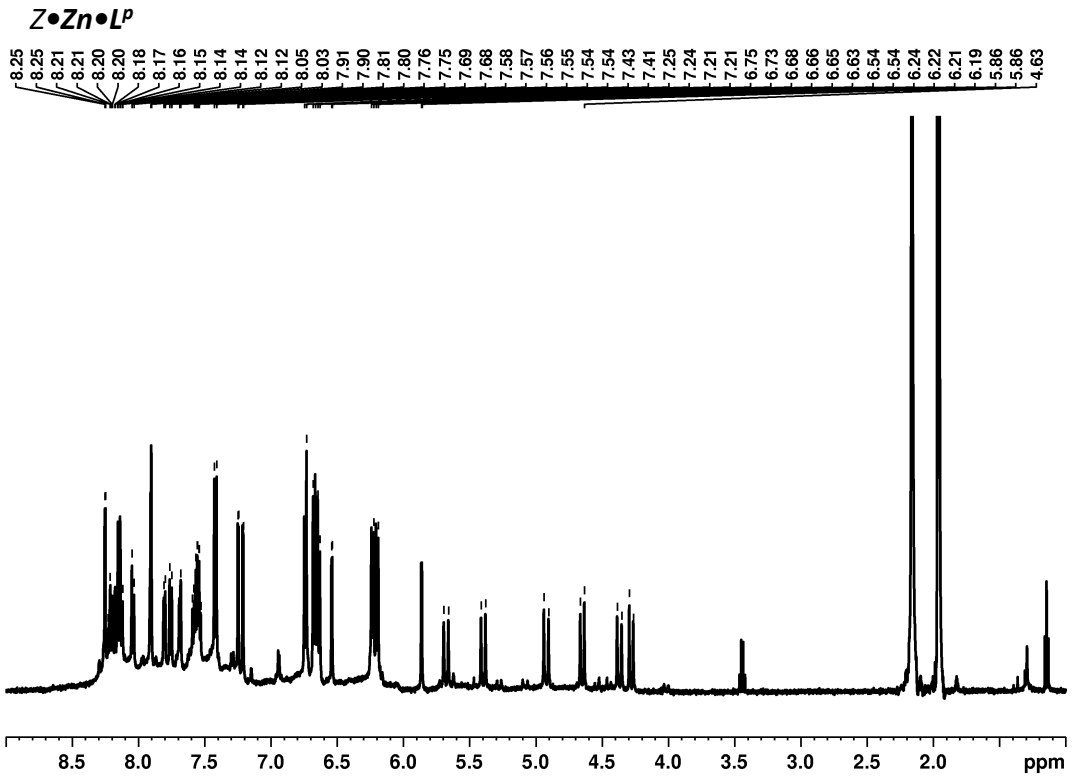

Figure S6. ^{1}H NMR spectrum (500 MHz, MeCN-d_3, 298 K) of *Z*•**Zn**•**L**^{p}

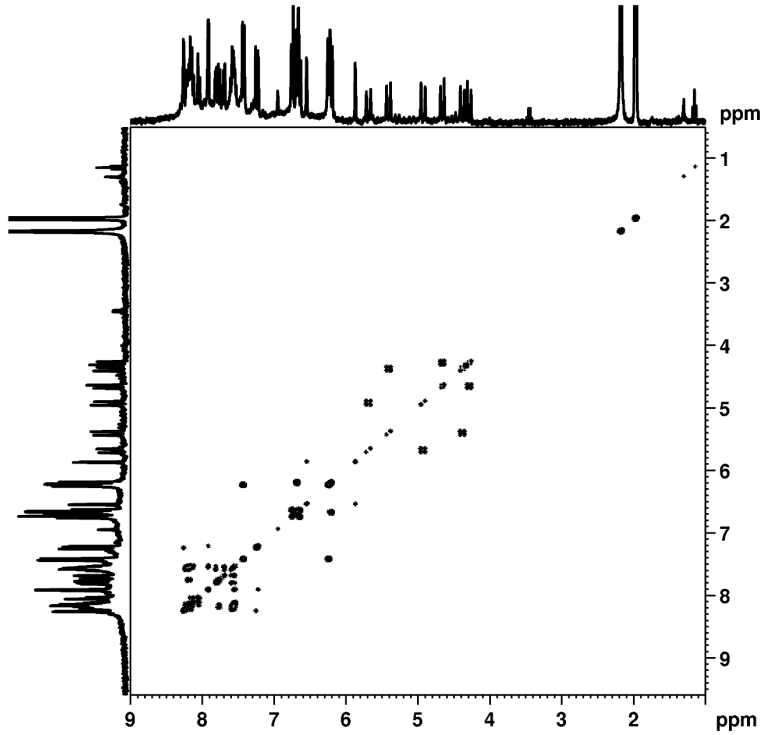

Figure S7. 1H-1H COSY spectrum (300 MHz, MeCN-d_3, 298 K) of *Z*•**Zn**•**L***P*.

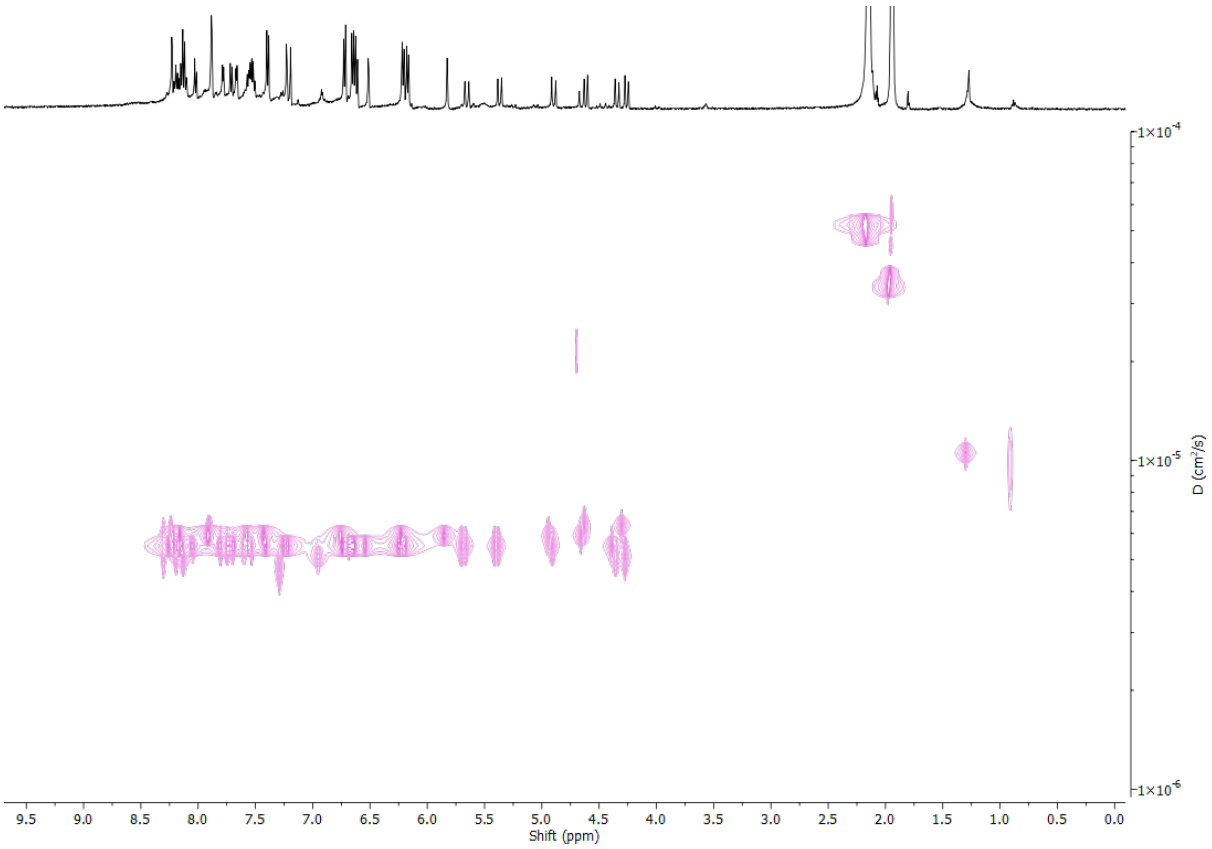

Figure S8. 2D-DOSY NMR spectrum (500 MHz, MeCN-d_3, 298 K) of *Z*•**Zn**•**L***P*

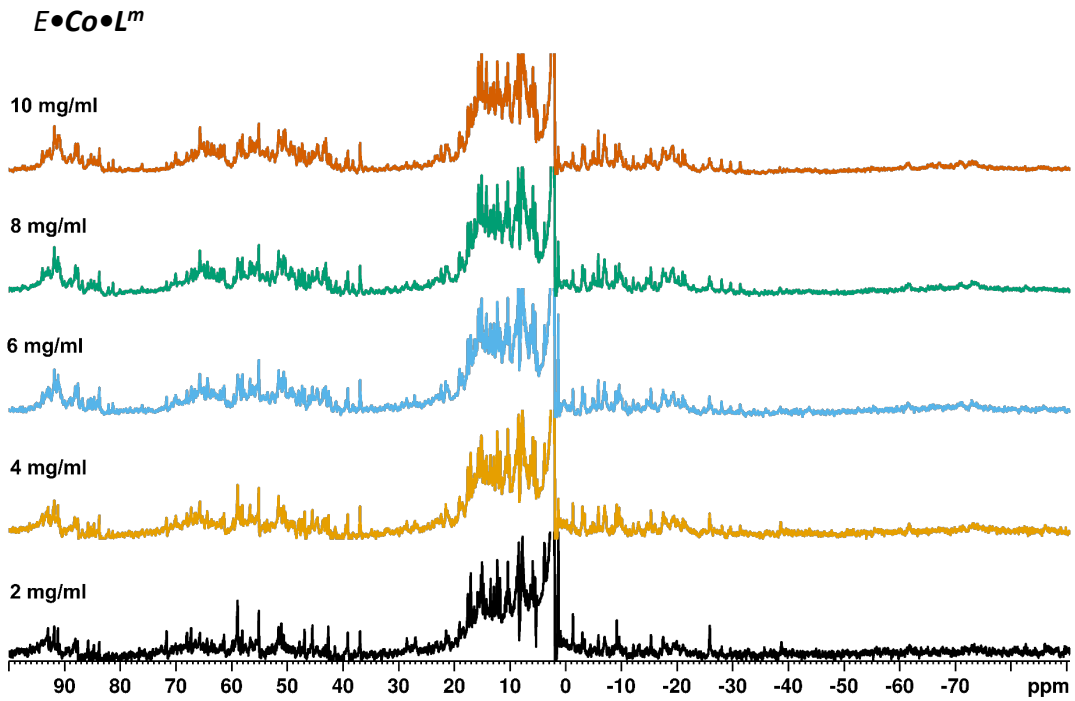

Figure S9. ^{1}H NMR spectrum (300 MHz, CD_3CN-d_3, 298 K) of *E*•**Co**•**L**^{m} at various concentrations.

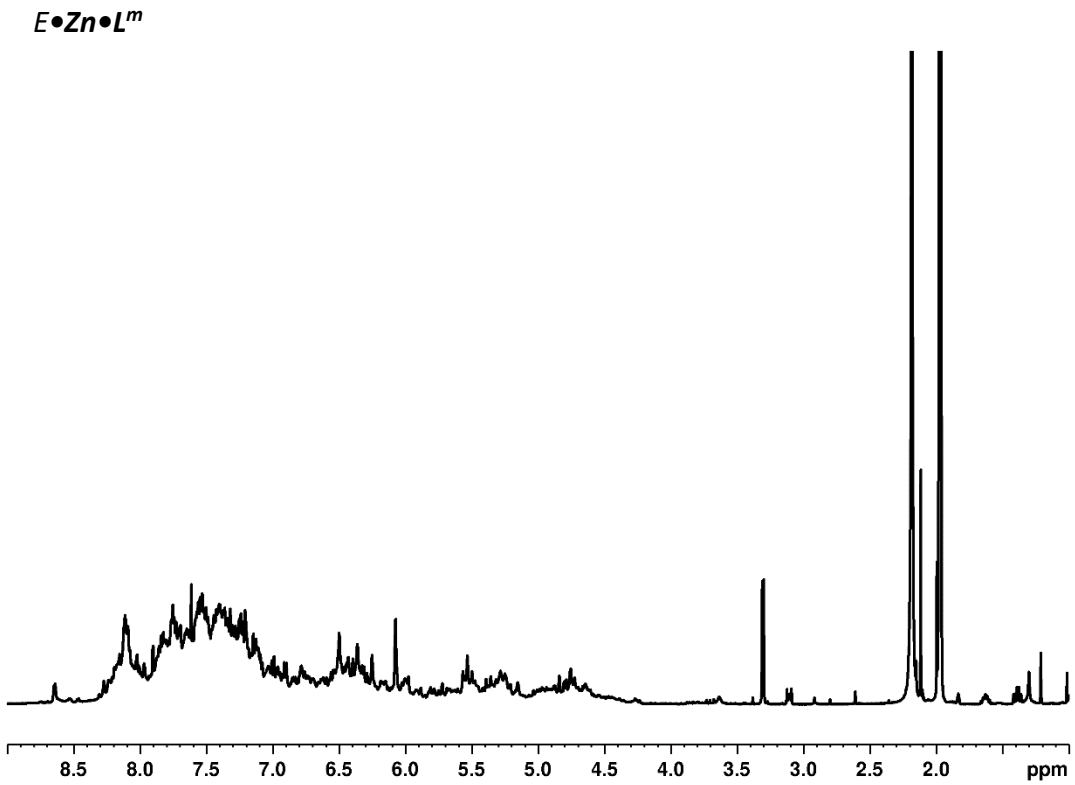

Figure S10. ^{1}H NMR spectrum (500 MHz, MeCN-d_3, 298 K) of *E*•**Zn**•**L**^{m}

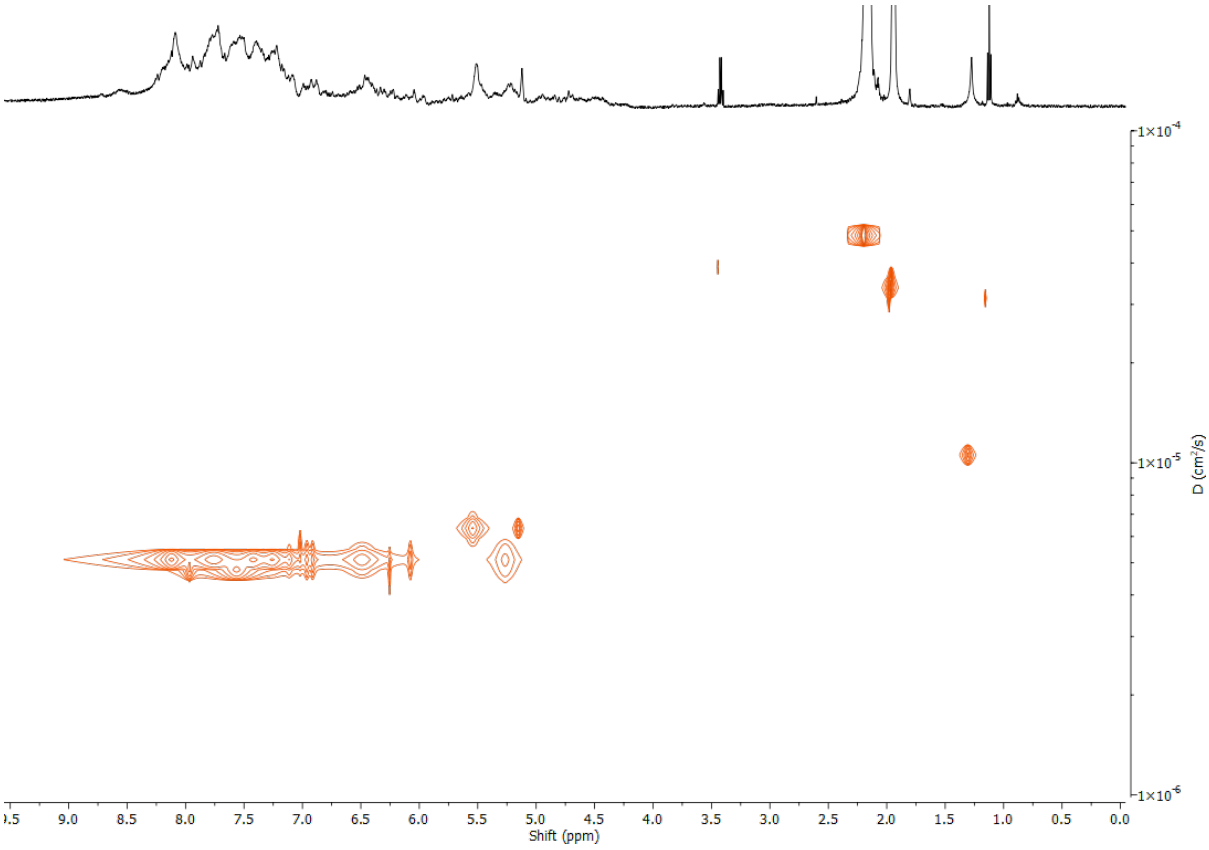

Figure S11. 2D-DOSY NMR spectrum (500 MHz, MeCN-d_3, 298 K) of ***E*•Zn•L^m**

***Z*•Zn•L^m**

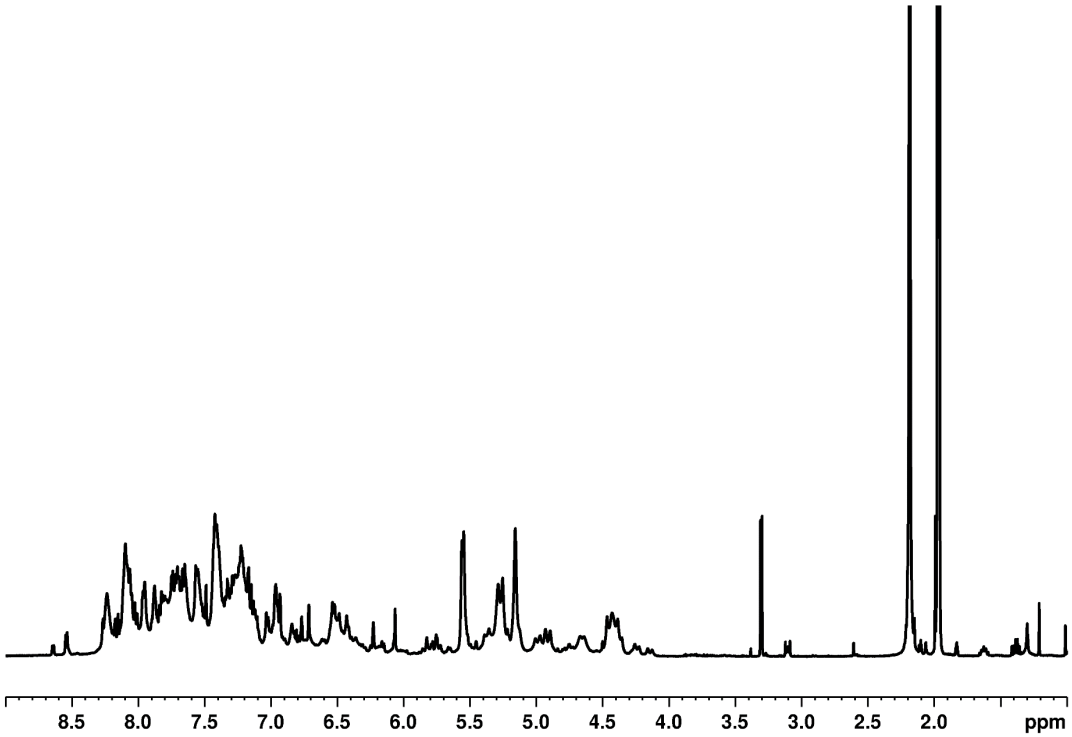

Figure S12. ^{1}H NMR spectrum (500 MHz, MeCN-d_3, 298 K) of ***Z*•Zn•L^m**

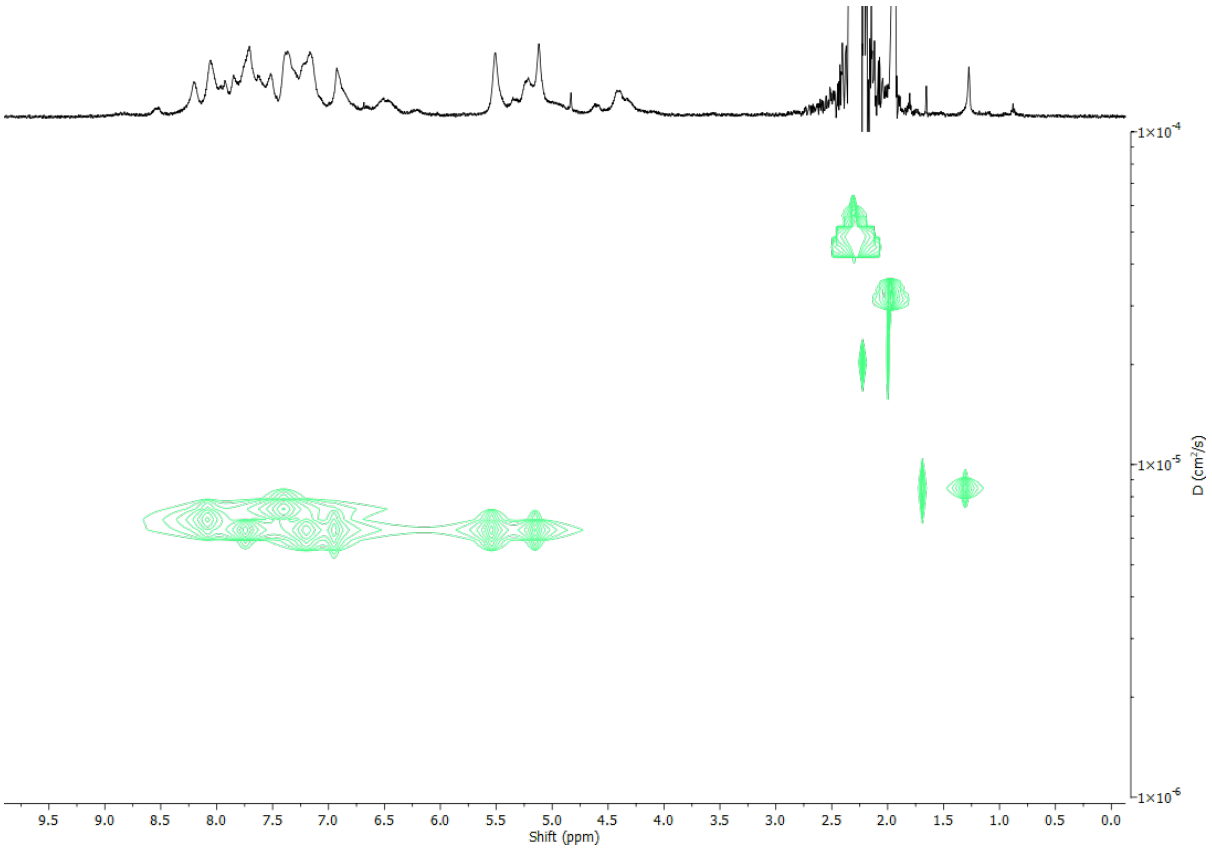

Figure S13. 2D-DOSY NMR spectrum (500 MHz, MeCN-d_3, 298 K) of ***Z*•Zn•L^m**

Mass Spectra

***E*•Co•L^p**

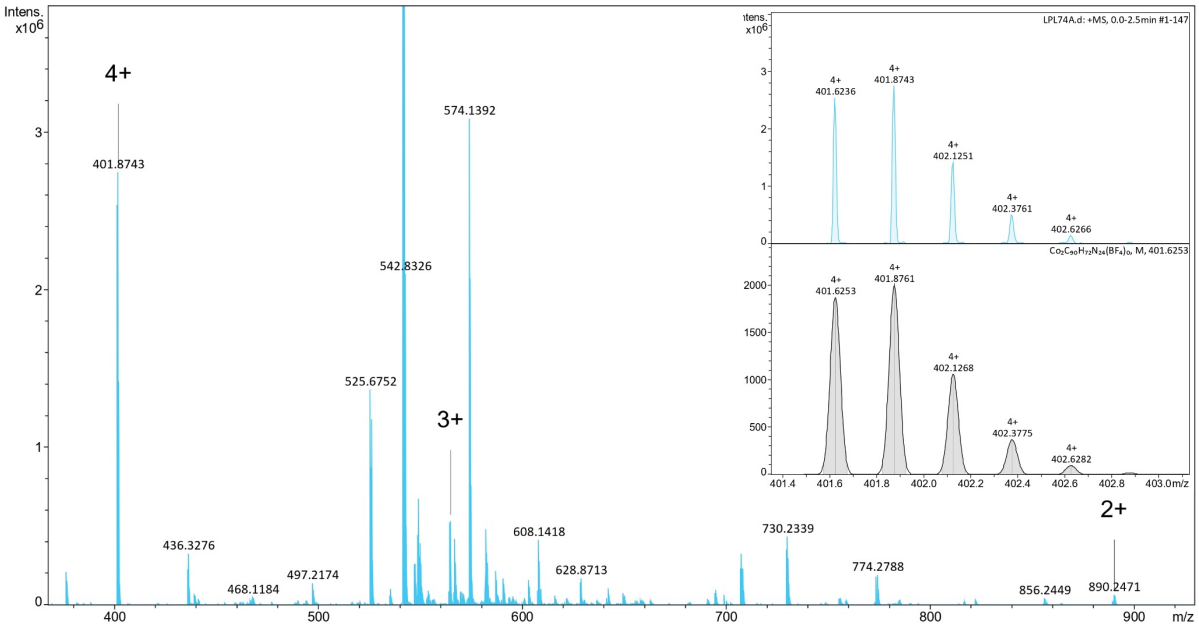

Figure S14. HR-ESI-MS of $[Co_2(E\text{-}\mathbf{L}^p)_3(BF_4)_4]$ [*E*•**Co**•**L**^{p}] in CH_3CN with signals corresponding to $[Co_2(E\text{-}\mathbf{L}^p)_3(BF_4)_n]^{(4-n)+}$ (n = 0, 1, 2). Expansion of $[Co_2(E\text{-}\mathbf{L}^p)_3]^{4+}$ is inset.

***E*•Zn•L^p**

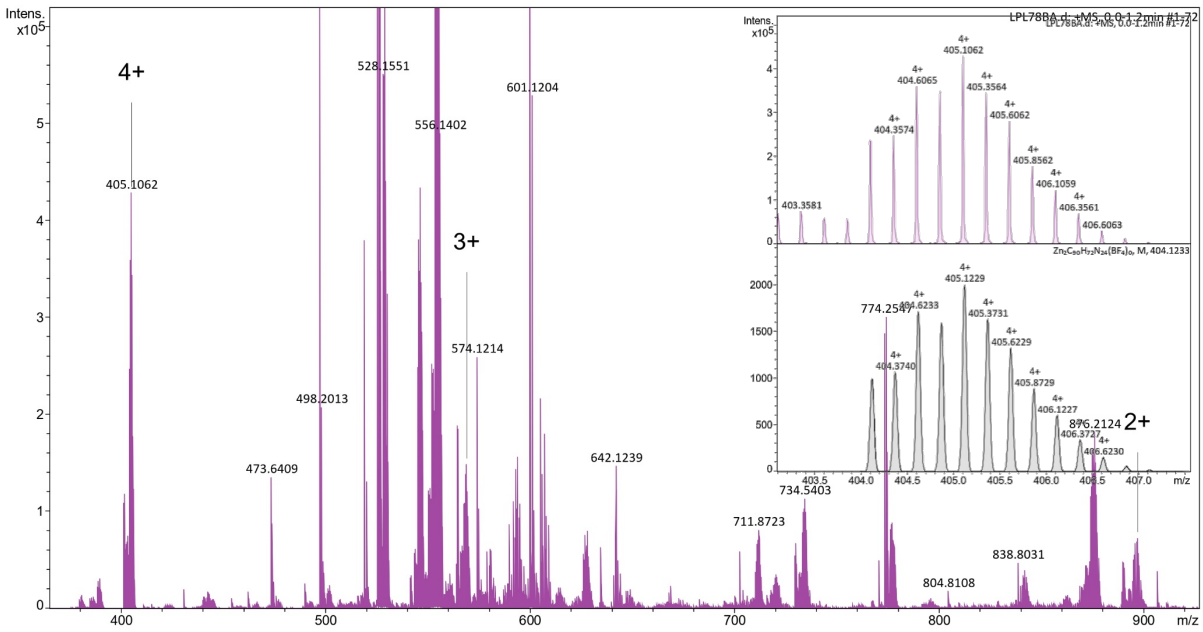

Figure S15. HR-ESI-MS of $[Zn_2(E\text{-}\mathbf{L}^p)_3(BF_4)_4]$ [*E*•**Zn**•**L**^{p}] in CH_3CN with signals corresponding to $[Zn_2(E\text{-}\mathbf{L}^p)_3(BF_4)_n]^{(4-n)+}$ (n = 0, 1, 2). Expansion of $[Zn_2(E\text{-}\mathbf{L}^p)_3]^{4+}$ is inset.

***Z*•Co•L^p**

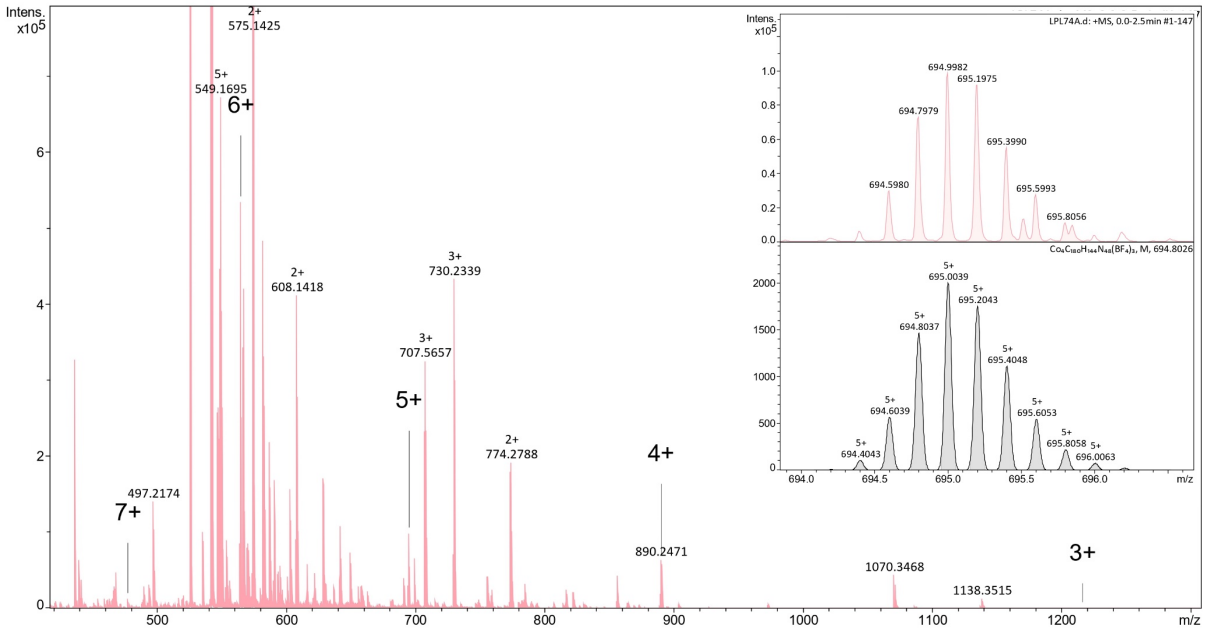

Figure S16. HR-ESI-MS of $[Co_4(Z\text{-}\mathbf{L}^p)_6(BF_4)_8]$ [*Z*•**Co**•**L**^{p}] in CH_3CN with signals corresponding to $[Co_4(Z\text{-}\mathbf{L}^p)_6(BF_4)_n]^{(8-n)+}$ (n = 1, 2, 3, 4, 5). Expansion of $[Co_4(Z\text{-}\mathbf{L}^p)_6(BF_4)_3]^{5+}$ is inset.

***Z*•Zn•L^p**

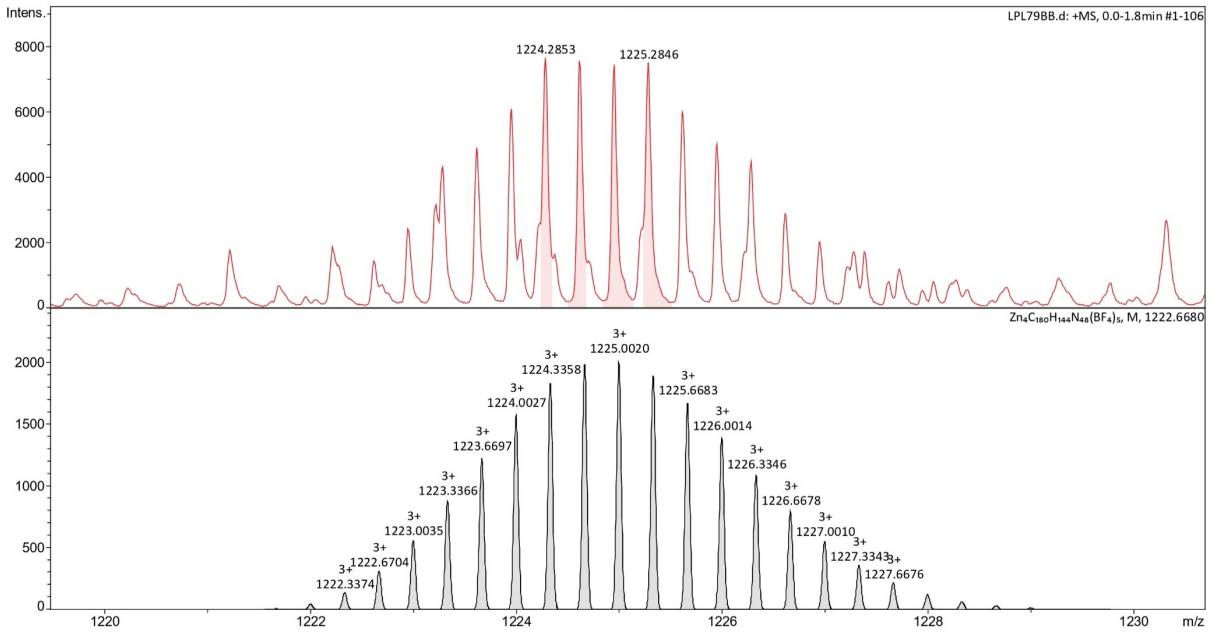

Figure S17. HR-ESI-MS of $[Zn_4(Z\text{-}\mathbf{L}^p)_6(BF_4)_8]$ [*Z*•**Zn**•**L**^{p}] showing expansion of $[Zn_4(Z\text{-}\mathbf{L}^p)_6(BF_4)_5]^{3+}$.

***E*•Co•L^m**

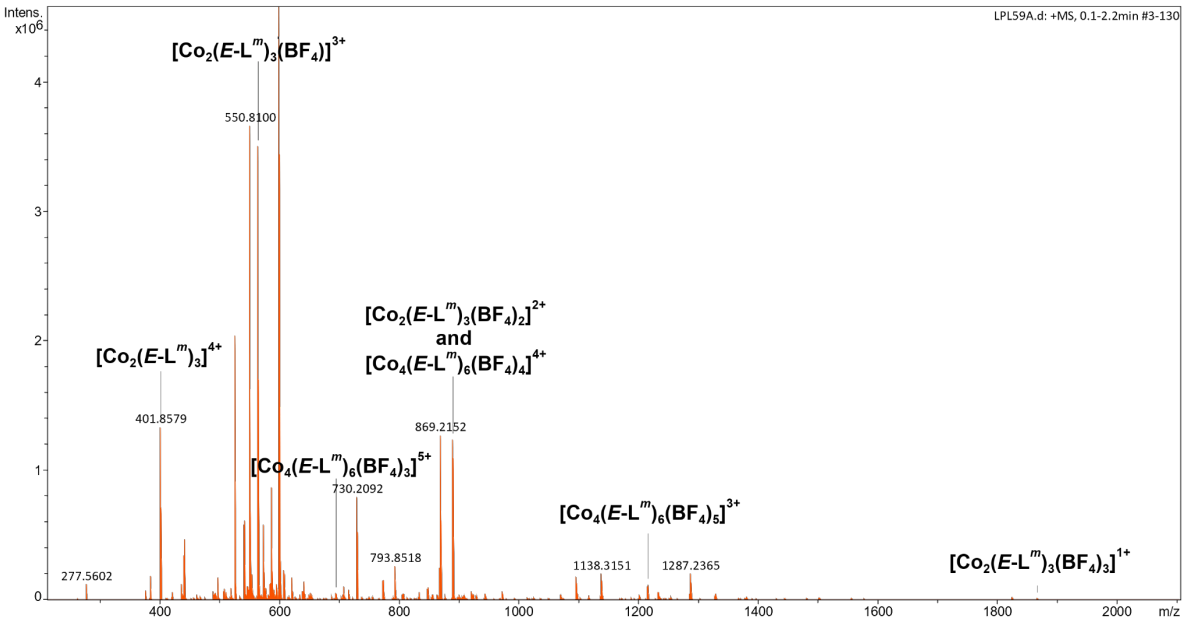

Figure S18. HR-ESI-MS of ***E*•Co•L^m** in CH_3CN with peaks labelled for the M_4 cyclic species $[Co_4(E\text{-}\mathbf{L^m})_6(BF_4)_{(n)}]^{(8-n)+}$ (n = 3, 4, 5) and the dinuclear triple helicate $[Co_2(E\text{-}\mathbf{L^m})_3(BF_4)_n]^{(4-n)+}$ (n = 0, 1, 2, 3).

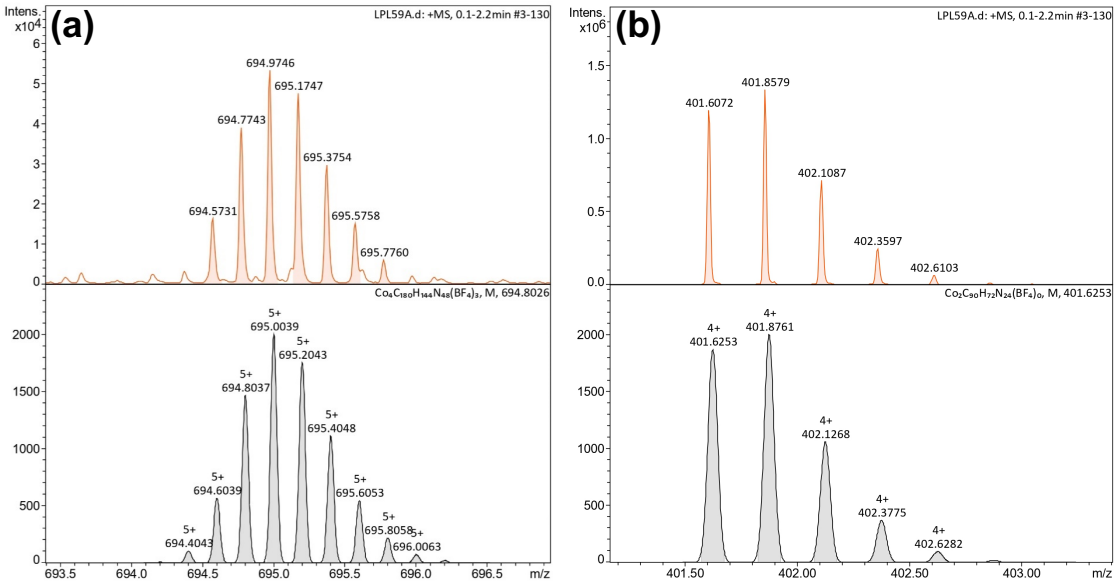

Figure S19. (a) Expansion of $[Co_4(E\text{-}\mathbf{L^m})_6(BF_4)_3]^{5+}$ with simulated isotope distribution shown below for comparison. (b) Expansion of $[Co_2(E\text{-}\mathbf{L^m})_3]^{4+}$ with simulated isotope distribution shown below for comparison.

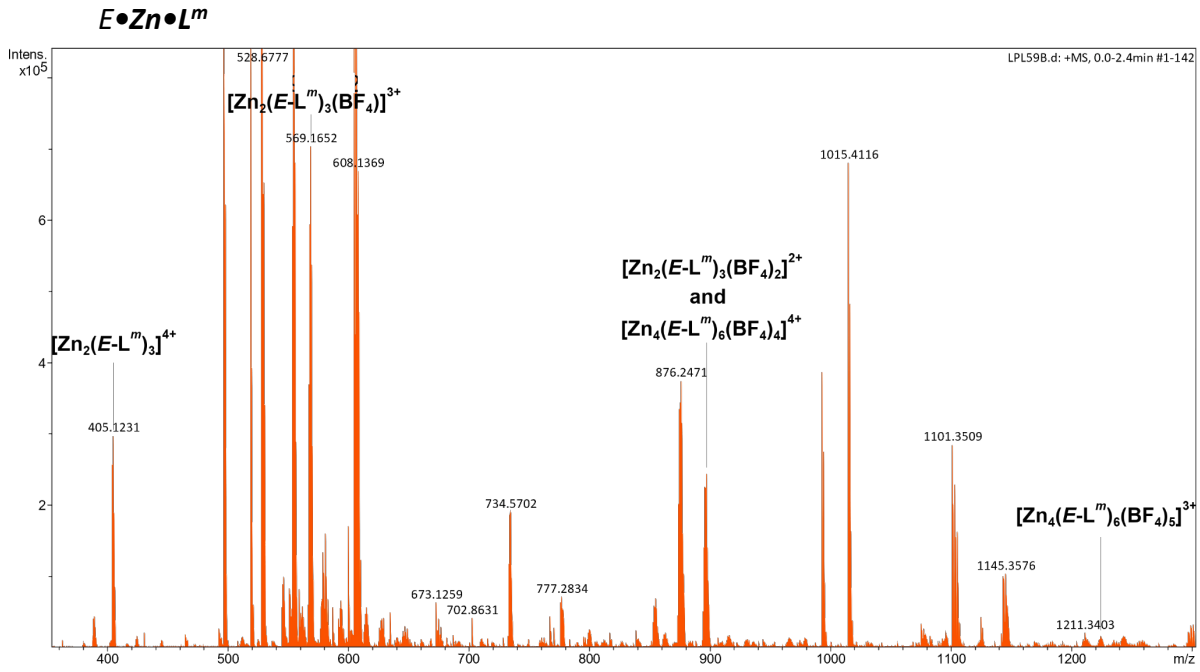

Figure S20. HR-ESI-MS of *E*•**Zn**•**L*m*** in CH_3CN with peaks labelled for the M_4 cyclic species $[Zn_4(E\text{-}\mathbf{L}^{m})_6(BF_4)_n]^{(8-n)+}$ (n = 4, 5) and the dinuclear triple helicate $[Zn_2(E\text{-}\mathbf{L}^{m})_3(BF_4)_n]^{(4-n)+}$ (n = 0, 1, 2).

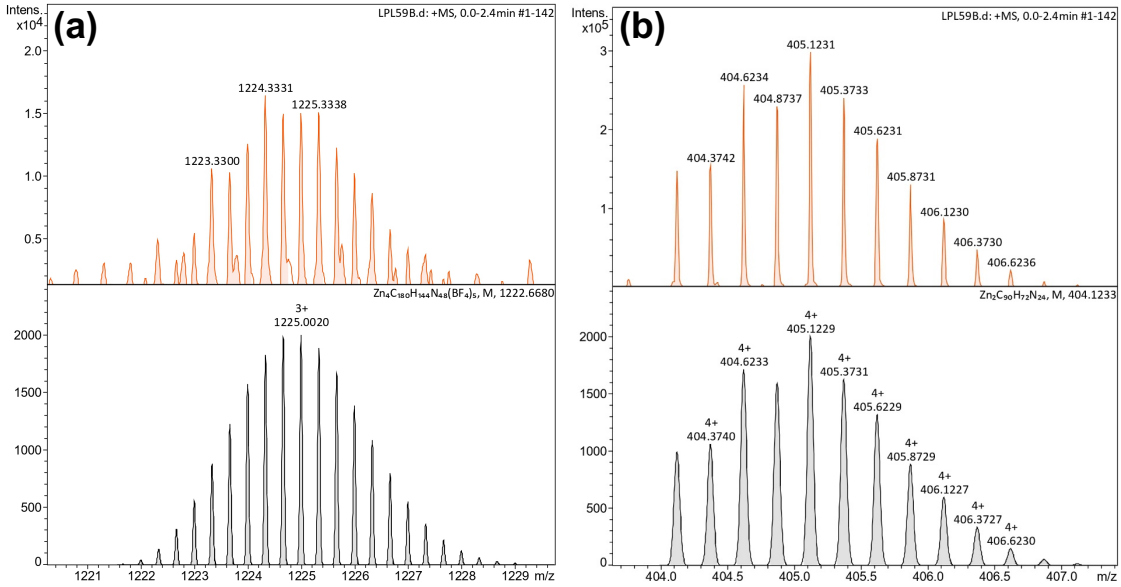

Figure S21. (a) Expansion of $[Zn_4(E\text{-}\mathbf{L}^{m})_6(BF_4)_5]^{3+}$ with simulated isotope distribution shown below for comparison. (b) Expansion of $[Zn_2(E\text{-}\mathbf{L}^{m})_3]^{4+}$ with simulated isotope distribution shown below for comparison.

***Z*•Co•L^m**

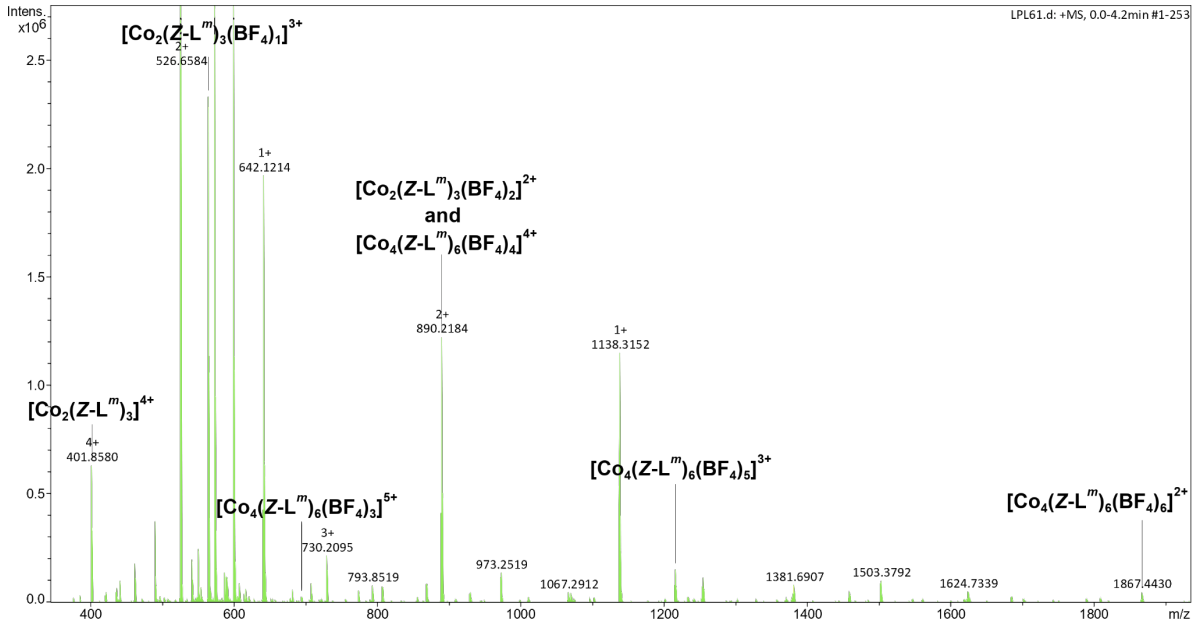

Figure S22. HR-ESI-MS of *Z*•**Co•L^m** in CH_3CN with peaks labelled for the M4 cyclic species $[Co_4(Z\text{-}\mathbf{L}^m)_6(BF_4)_n]^{(8-n)+}$ (n = 3, 4, 5, 6) and the dinuclear triple helicate $[Co_2(Z\text{-}\mathbf{L}^m)_3(BF_4)_n]^{(4-n)+}$ (n = 0, 1, 2).

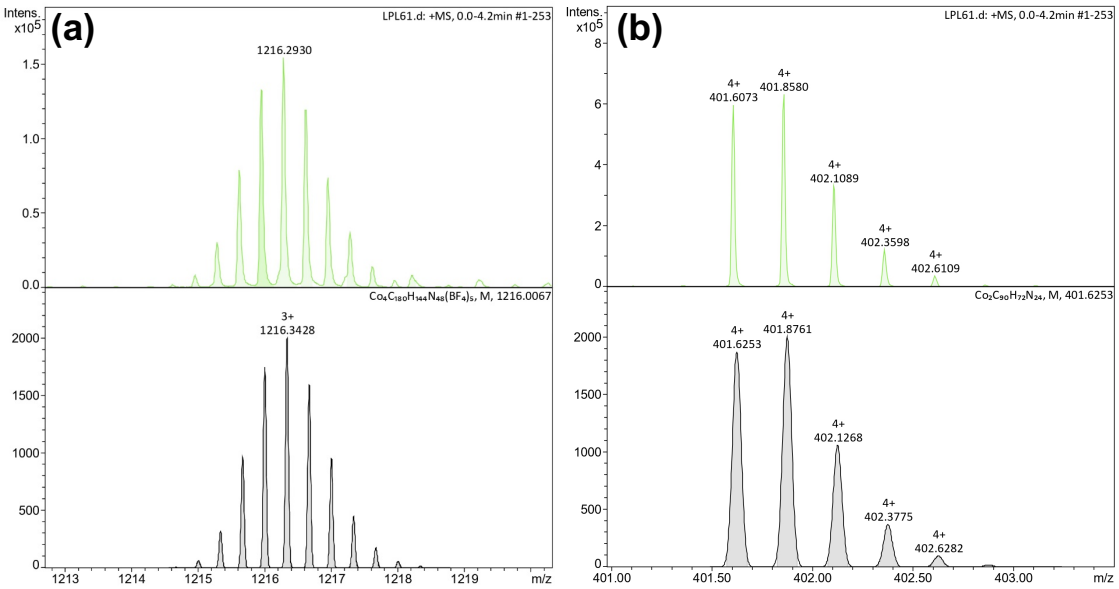

Figure S23. (a) Expansion of $[Co_4(Z\text{-}\mathbf{L}^m)_6(BF_4)_5]^{3+}$ with simulated isotope distribution shown below for comparison. (b) Expansion of $[Co_2(Z\text{-}\mathbf{L}^m)_3]^{4+}$ with simulated isotope distribution shown below for comparison.

Co•L^m•2,4

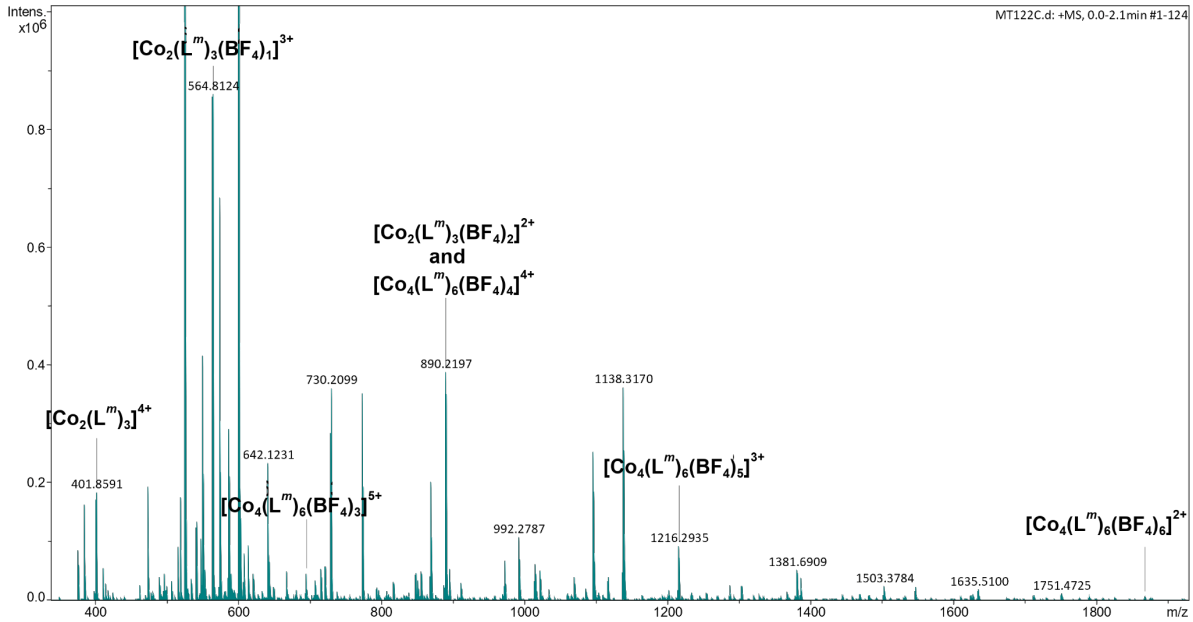

Figure S24. HR-ESI-MS of **Co•L^m•2,4** in CH_3CN with peaks labelled for the M_4 cyclic species $[Co_4(\mathbf{L^m})_6(BF_4)_n]^{(8-n)+}$ (n = 3, 4, 5, 6) and the dinuclear triple helicate $[Co_2(\mathbf{L^m})_3(BF_4)_n]^{(4-n)+}$ (n = 0, 1, 2).

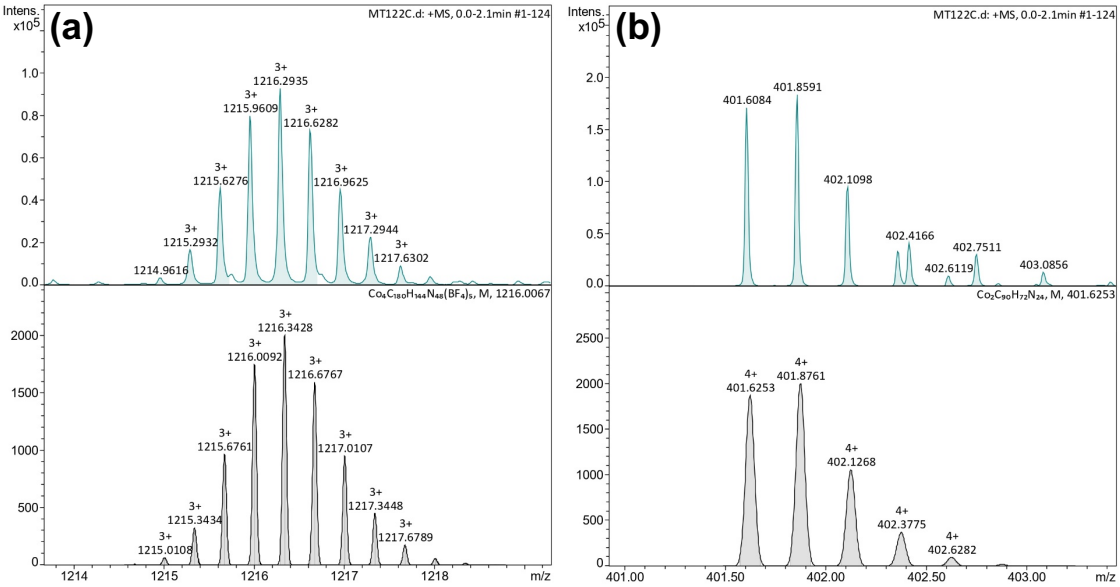

Figure S25. (a) Expansion of $[Co_4(\mathbf{L^m})_6(BF_4)_5]^{3+}$ with simulated isotope distribution shown below for comparison. (b) Expansion of $[Co_2(\mathbf{L^m})_3]^{4+}$ with simulated isotope distribution shown below for comparison.

UV/Vis Spectroscopy

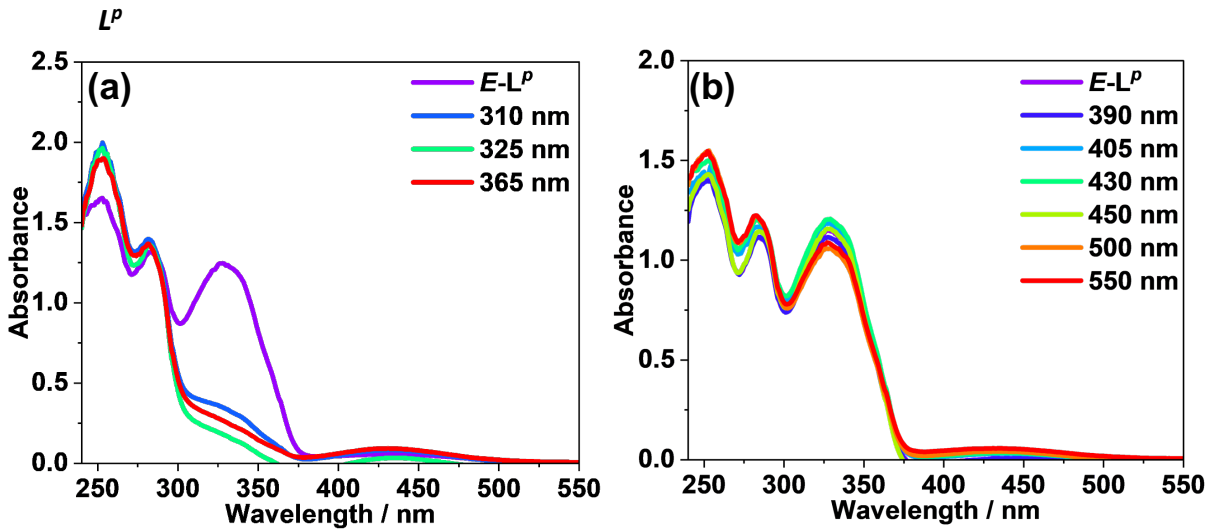

Figure S26. UV-vis spectra of **L^p** (MeCN, 55.9 µM) at ambient temperature, after irradiation with different wavelengths (310, 325, 365, 390, 405, 430, 450, 500 and 550 nm, respectively) to determine the optimum wavelengths for photoswitching.

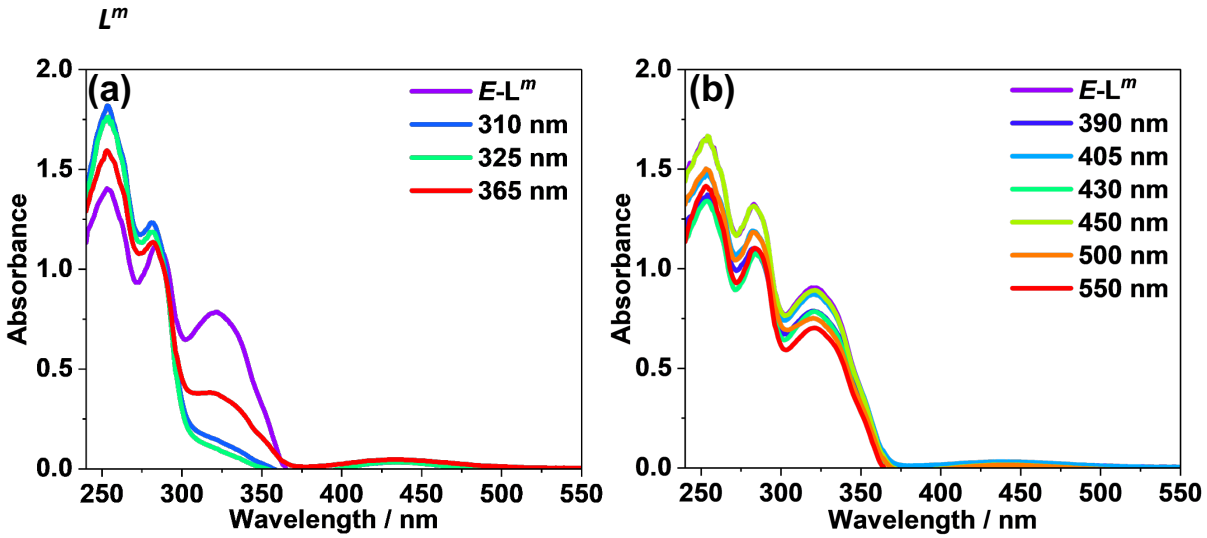

Figure S27. UV-vis spectra of **L^m** (MeCN, 56.0 µM) after irradiation with different wavelengths (310, 325, 365, 390, 405, 430, 450, 500 and 550 nm, respectively) to determine the optimum wavelengths for photoswitching.

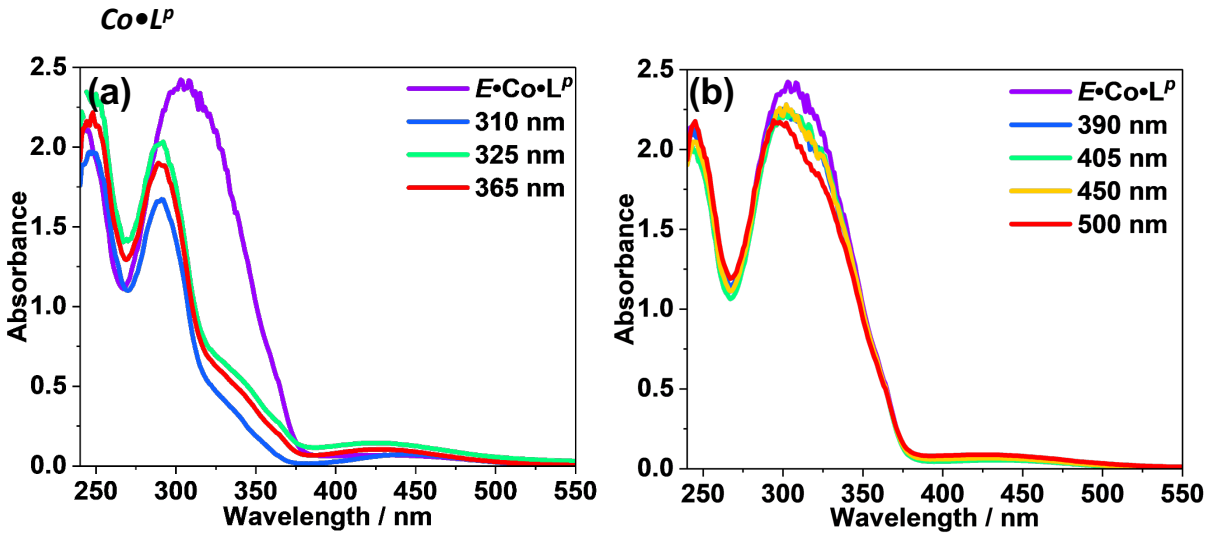

Figure S28. UV-vis spectra of **Co•L^p** (MeCN, 28.4 µM) after irradiation with different wavelengths (310, 325, 365, 390, 405, 450, and 500 nm, respectively) to determine the optimum wavelengths for photoswitching.

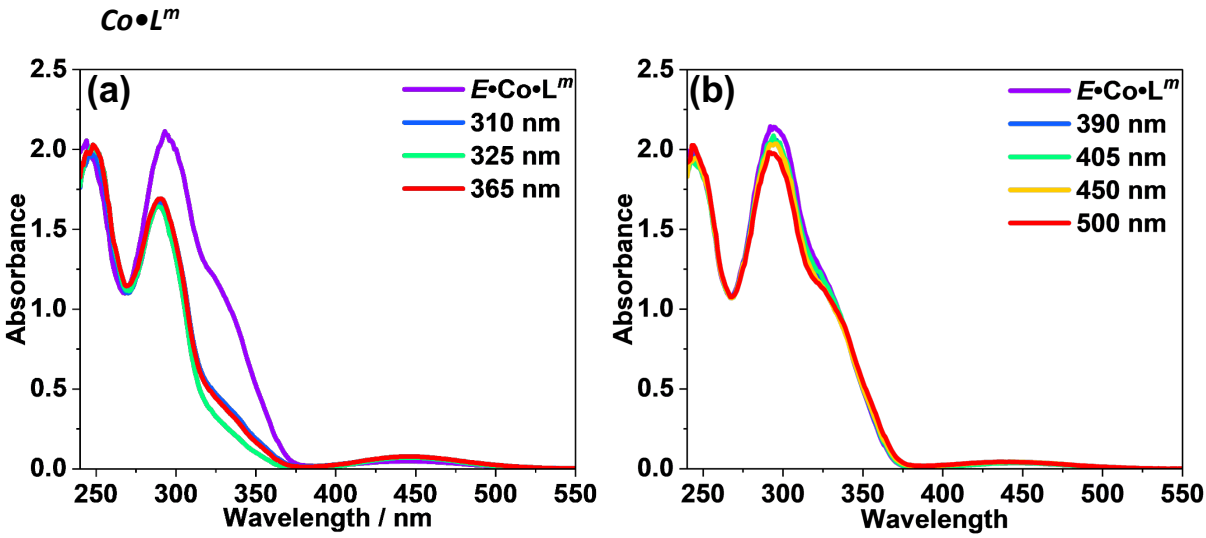

Figure S29. UV-vis spectra of **Co•L^m** (MeCN, 14.2 µM) after irradiation with different wavelengths (310, 325, 365, 390, 405, 450, and 500 nm, respectively) to determine the optimum wavelengths for photoswitching.

Variable Temperature NMR

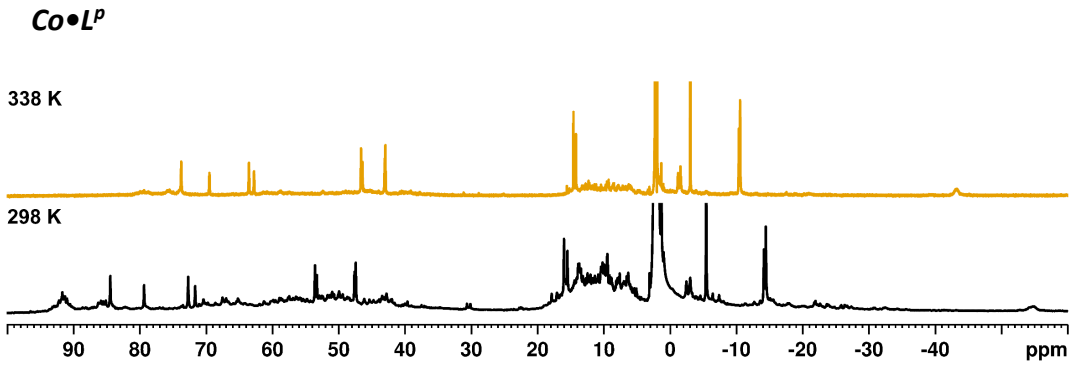

Figure S30. Variable Temperature ^{1}H-NMR spectra (400 MHz, MeCN-d_3, 298, 338 K) of ***E*•Co•Lᵖ.**

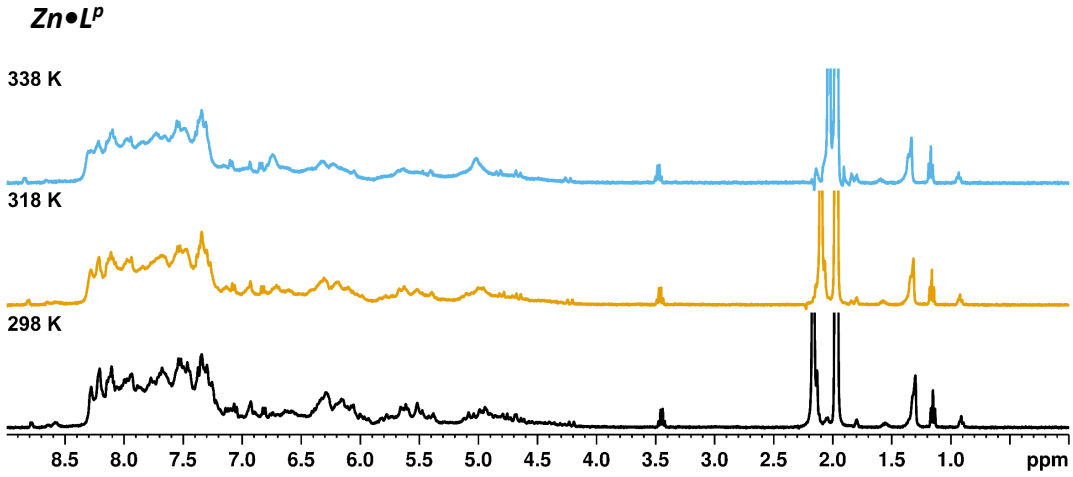

Figure S31. Variable Temperature ^{1}H-NMR spectra (400 MHz, MeCN-d_3, 298, 318, 338 K) of ***E*•Zn•Lᵖ.**

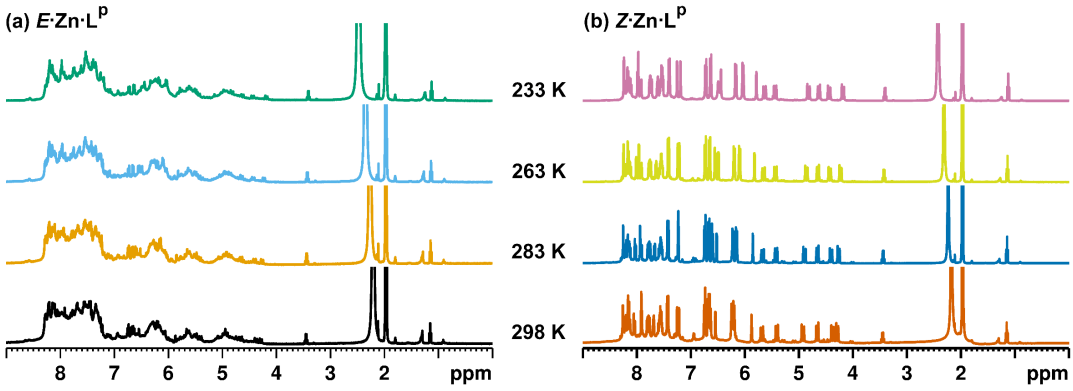

Figure S32. Variable temperature ^{1}H-NMR spectra (400 MHz, MeCN-d_3, 298, 283, 263, 233 K) with a sodium triflate (2 mM) internal standard of (a) ***E*•Zn•Lᵖ** and (b) ***Z*•Zn•Lᵖ**.

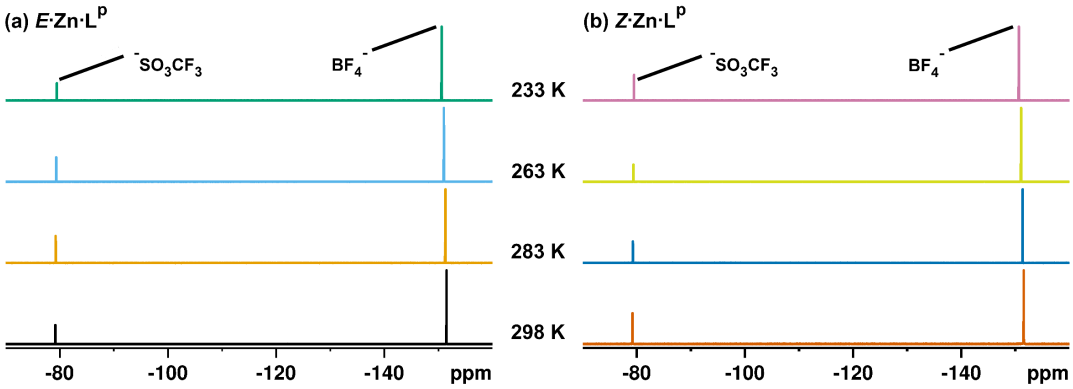

Figure S33. Variable temperature ^{19}F-NMR spectra (400 MHz, MeCN-d_3, 298, 283, 263, 233 K) with a sodium triflate (2 mM) internal standard of (a) ***E*•Zn•L^p** and (b) ***Z*•Zn•L^p**.

Thermal Relaxation NMR Experiments

Ligands

Ligands (5 mg, 10 µmol) were dissolved in MeCN-d_3 (1 cm^3) and irradiated with 340 nm light until a photostationary state was reached. Spectra were recorded every 30 minutes for 18 hours at 65 °C and every 30 minutes for 60 hours at 25 °C.

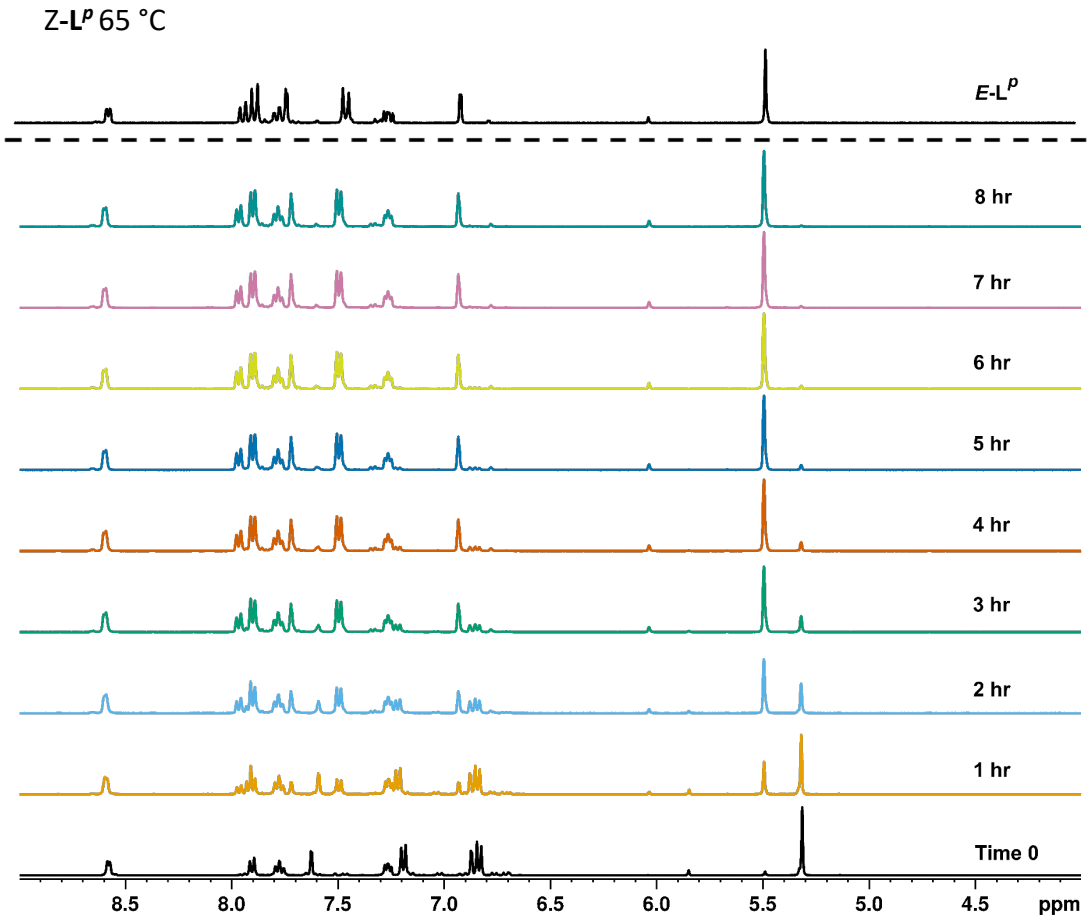

Figure S34. ^{1}H-NMR spectra (400 MHz, MeCN-d_3, 338 K) of *Z*-**L**^{p} over 8 hours.

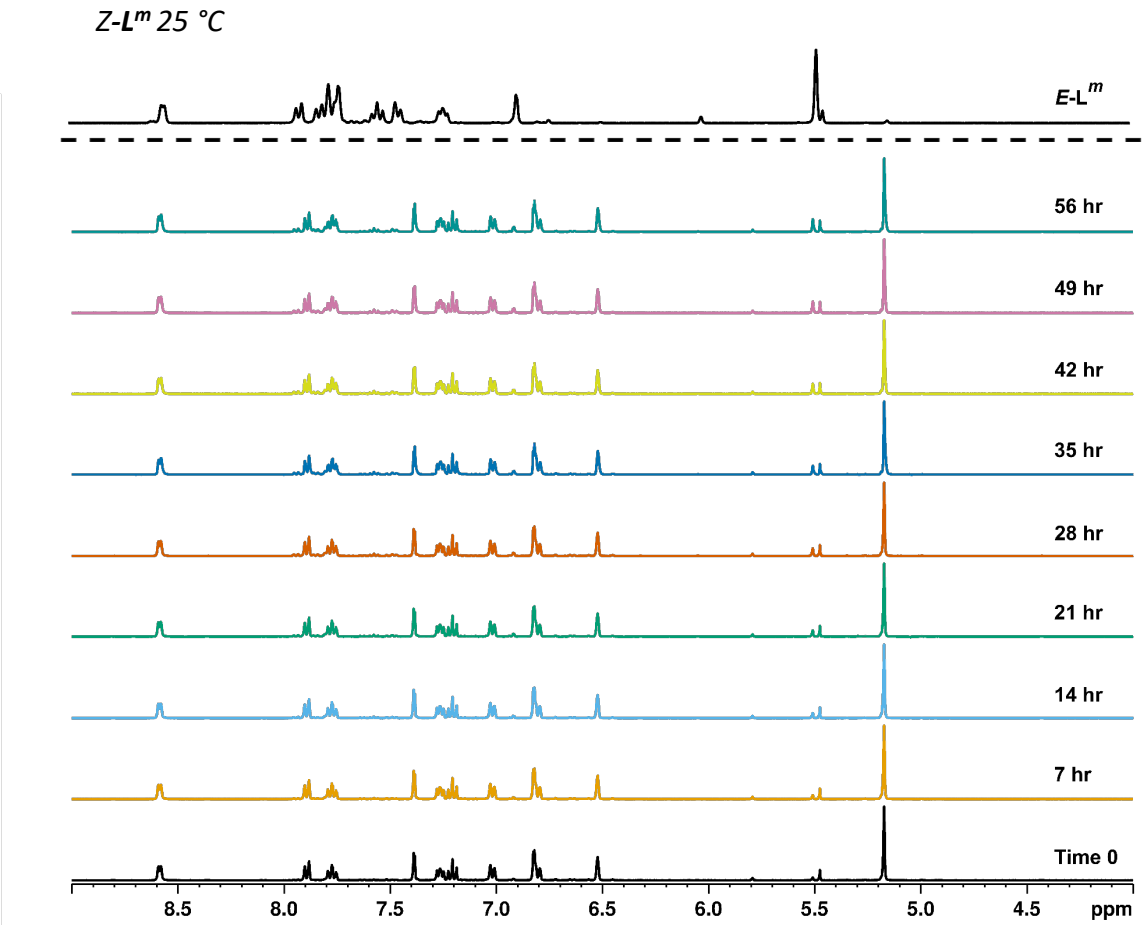

Figure S35. ^{1}H-NMR spectra (400 MHz, MeCN-d_3, 298 K) of *Z*-**L*m*** over 56 hours.

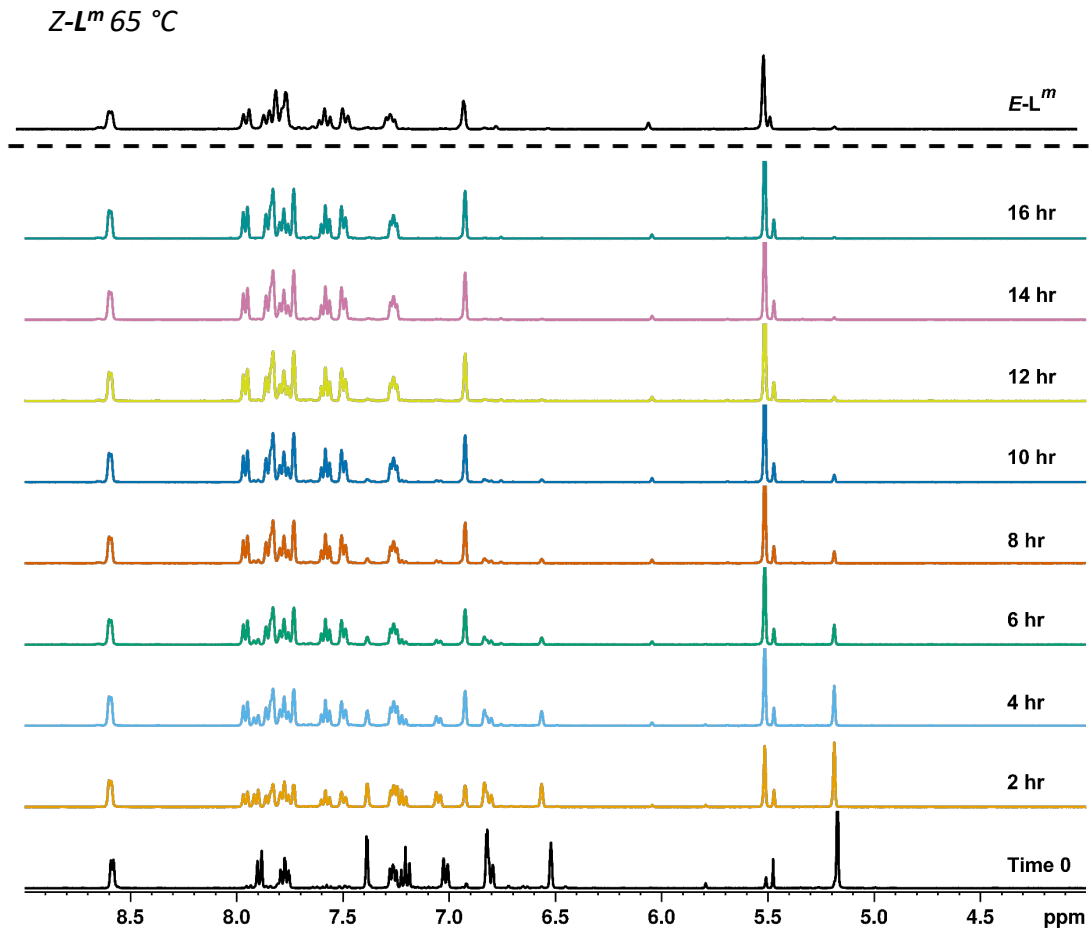

Figure S36. ^{1}H-NMR spectra (400 MHz, MeCN-d_3, 338 K) of *Z*-**L**^{m} over 16 hours.

Ligand Half-Life

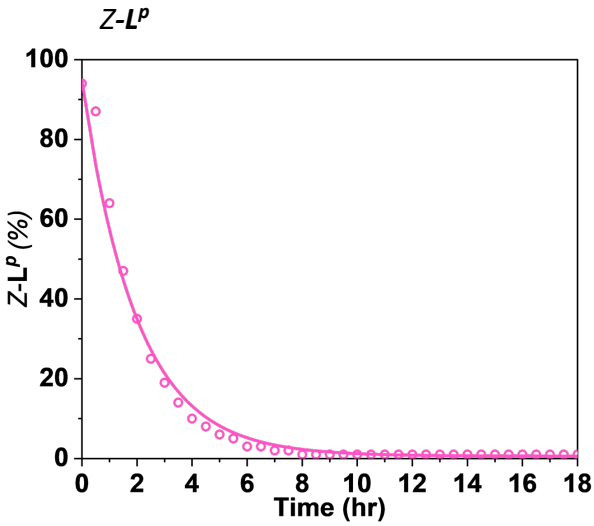

Figure S37. Thermal relaxation of L^p in acetonitrile (2 mM, ^{1}H NMR) at 65 °C after irradiation at 340 nm overnight.

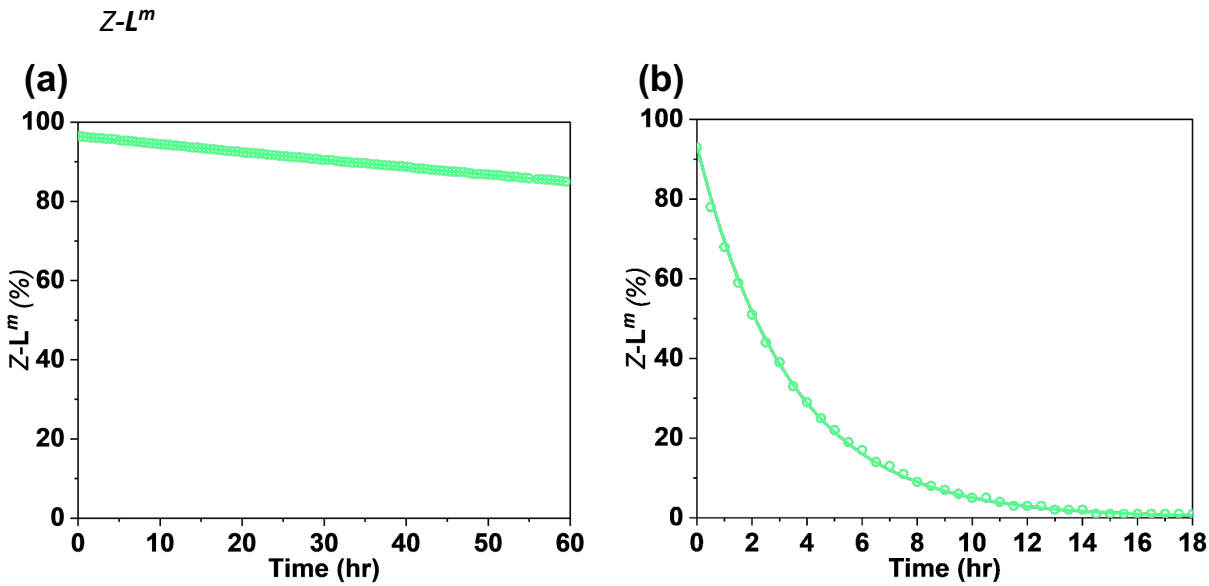

Figure S38. (a) Thermal relaxation of L^m in acetonitrile (2 mM, ^{1}H NMR) at 25 °C after irradiation at 340 nm overnight. (b) Thermal relaxation of L^m in acetonitrile (2 mM, ^{1}H NMR) at 65 °C after irradiation at 340 nm overnight.

Table S2. Rate constants (k), mean lifetimes (τ = k −1), and half-lives ($\tau_{½}$) obtained by thermal relaxation experiments of L^m and L^p (65 °C, MeCN-d_3, 2 mM) using NMR. Relaxation of L^m was also investigated at 25 °C (MeCN-d_3, 2 mM).

	L^p (65 °C)	L^m (25 °C)	L^m (65 °C)
$\tau_{½}$ (hr)	1.38	326.36	2.36
τ (hr)	1.99	470.84	3.40
k (hr^{-1})	0.504	0.002	0.294

Cages

Cages – ***E*•Co•L^p** (2 mg, 1 mM) and ***E*•Co•L^m** (2 mg, 0.5 mM) – were dissolved in MeCN-d_3 (1 cm^3) and irradiated with 340 nm light until a photostationary state was reached. Spectra were recorded at a series of time points of 5 weeks, with the samples stored in darkness at ambient temperature between time points.

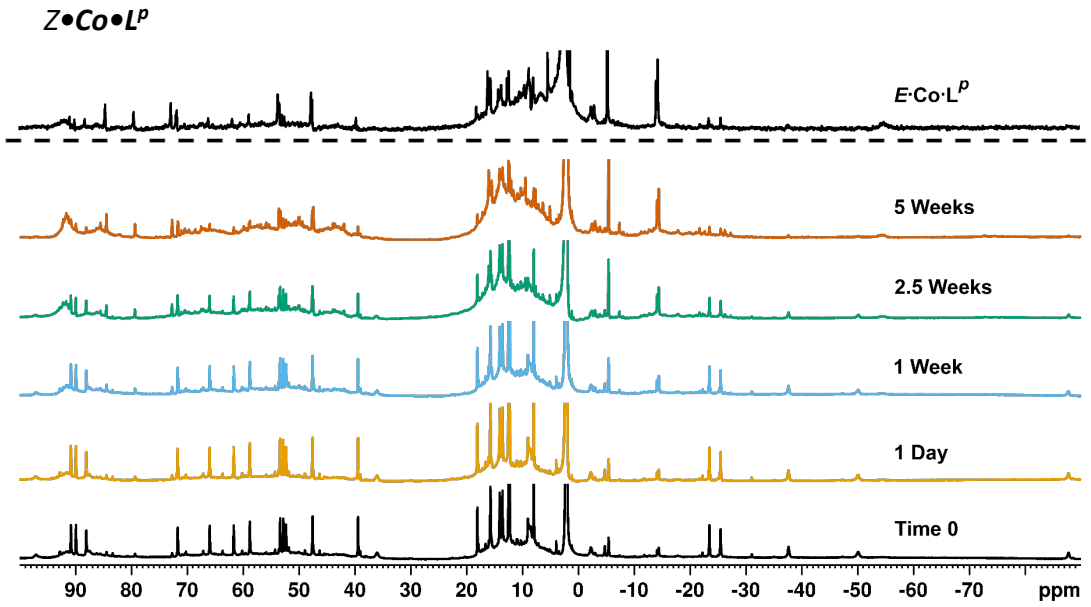

Figure S39. Series of ^{1}H NMR spectra (400 MHz, CD_3CN, MeCN-d_3, RT) showing the slow thermal conversion of ***Z*•Co•L^p** (bottom spectrum) back to ***E*•Co•L^p** (top spectrum) over 5 weeks.

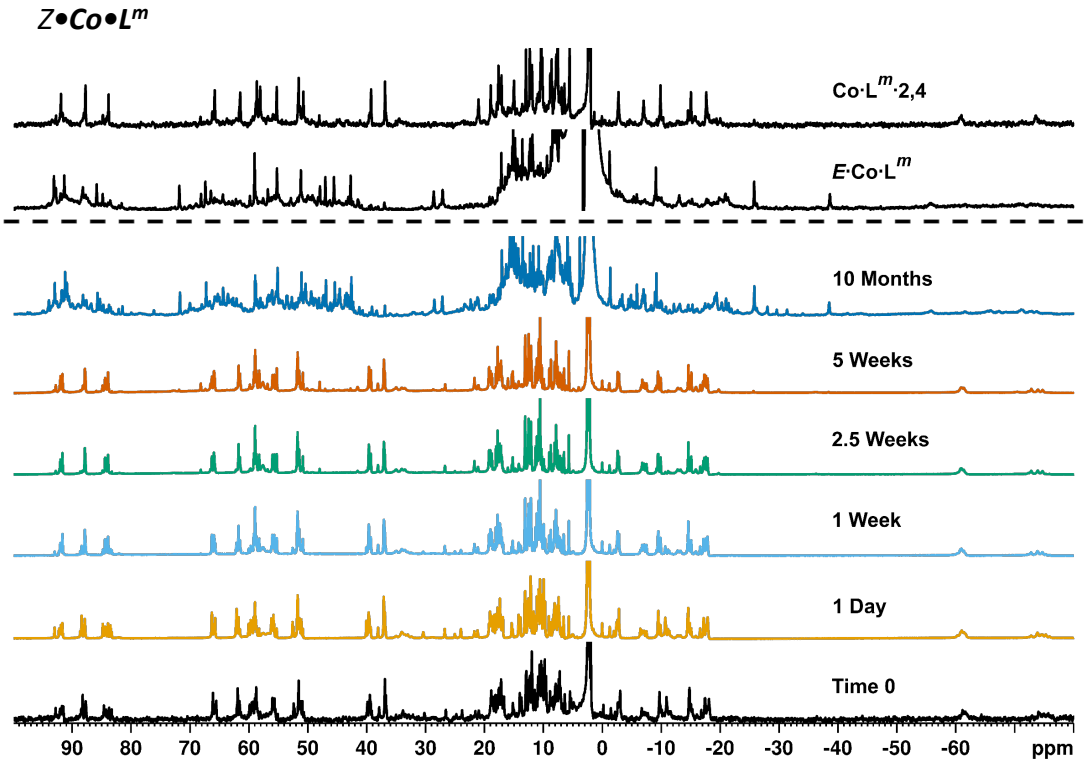

Figure S40. Series of ^{1}H NMR spectra (400 MHz, CD_3CN, MeCN-d_3, RT) showing the slow thermal conversion of *Z*•**Co**•**L**^{m} (bottom spectrum) back to *E*•**Co**•**L**^{m} (top spectrum) over 5 weeks.

Titrations

Mixed Ligand Cage Formation

E-**L**^{m} (30 mg, 60 µmol) was dissolved in a $CDCl_3$:MeCN-d_3 (85:15 *v/v*, 6 cm^3) mixture. 3 cm^3 of the ligand solution was irradiated with 340 nm light until a photostationary state was reached. A series of NMR tubes were prepared, containing 0.7 cm^3 of solution by combining the two samples in various ratios and NMR spectra recorded. $Co(BF_4)_2{\cdot}6H_2O$ (16 mg, 47 µmol) was dissolved in $CDCl_3$:MeCN-d_3 (85:15 *v/v*, 1 cm^3). 0.1 cm^3 of metal salt solution was added to each tube and spectra recorded.

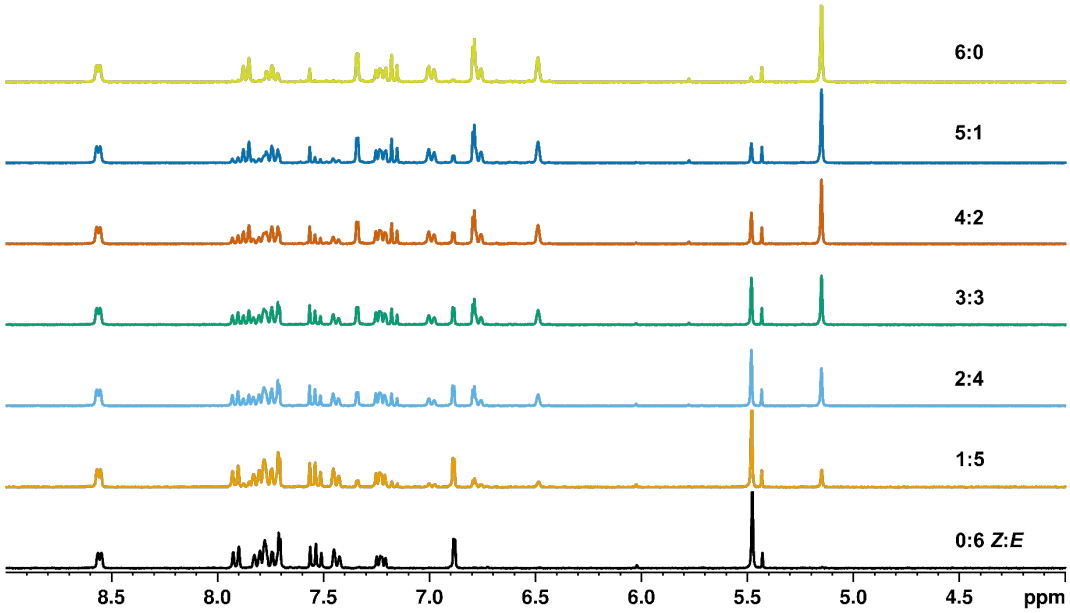

Figure S41. A series of ^{1}H-NMR spectra (300 MHz, MeCN-d_3/$CDCl_3$ (85:15 *v/v*), 298 K) recorded during the combination of *E*-**L**^{m} (10 mM) and *Z*-**L**^{m} (10 mM) in the specified ratios.

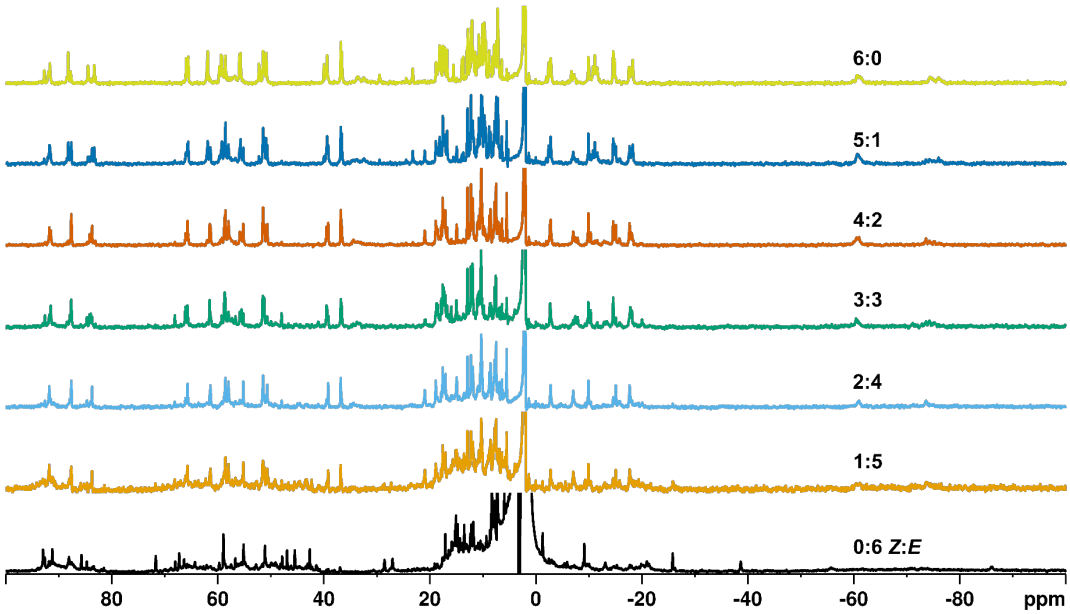

Figure S42. A series of ^{1}H-NMR spectra (300 MHz, MeCN-d_3/$CDCl_3$ (85:15 *v/v*), 298 K) recorded during the combination of a series of mixtures, containing *E*-**L**^{m} and *Z*-**L**^{m} in the specified ratios, with $Co(BF_4)_2$.

*Addition of Z-**L**^{m} to E•**Co**•**L**^{m}*

E-**L**^{m} (15 mg, 30 µmol) was dissolved in $CDCl_3$:MeCN-d_3 (85:15 *v/v*, 3 cm^3) and irradiated with 340 nm light. *E*•**Co**•**L**^{m} (62.5 mg, 16 µmol) was dissolved in $CDCl_3$:MeCN-d_3 (85:15 *v/v*, 2 cm^3). 0.1 cm^3 of cage solution was added to a series of NMR tubes. *Z*-**L**^{m} solution and $CDCl_3$:MeCN-d_3 (85:15 *v/v*) were added to each tube in various ratios to form 0.7 cm^3 samples containing excess ligand and NMR spectra recorded.

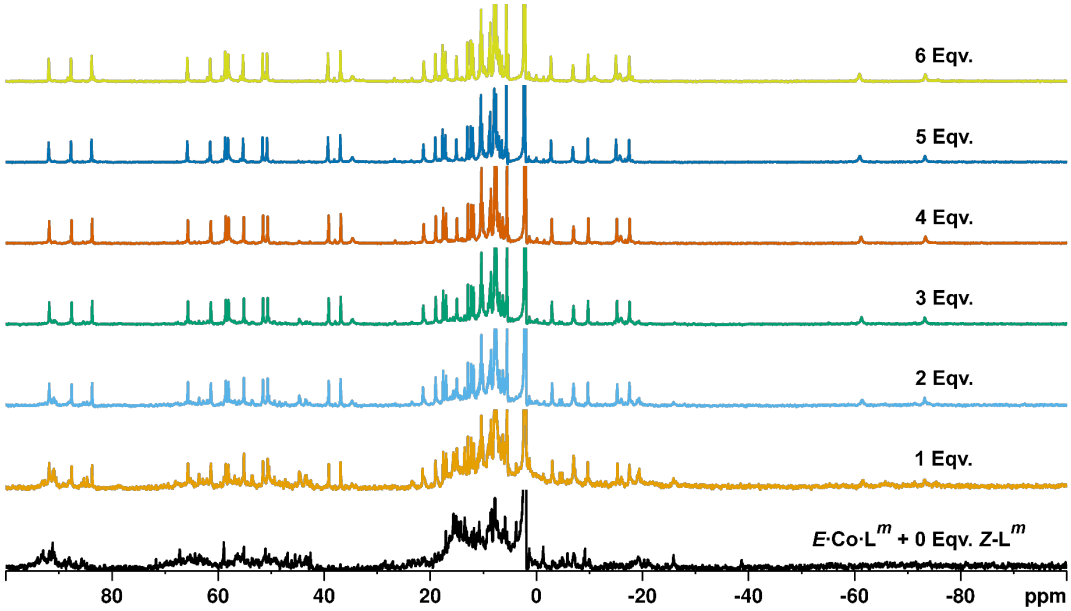

Figure S43. ^{1}H NMR spectra (300 MHz, MeCN-d_3/$CDCl_3$ (85:15 v/v), 298 K) recorded during addition of 0 – 6 equivalents (from bottom up) of *Z*-**L**^{m} to a solution of *E*•**Co**•**L**^{m}.

*Addition of E-**L**^{m} to Z•**Co**•**L**^{m}*

E-**L**^{m} (16 mg, 32 µmol) was dissolved in $CDCl_3$:MeCN-d_3 (85:15 *v/v*, 3.2 cm^3) and irradiated with 340 nm light overnight. $Co(BF_4)_2 \cdot 6H_2O$ (7.3 mg, 21 µmol) was added to form *Z*•**Co**•**L**^{m}. 0.43 mL of *Z*•**Co**•**L**^{m} solution was added to a series of NMR tubes. *E*-**L**^{m} (18 mg, 36 µmol) was dissolved in $CDCl_3$:MeCN-d_3 (85:15 *v/v*, 3 cm^3). *E*-**L**^{m} solution and $CDCl_3$:MeCN-d_3 (85:15 *v/v*) were added to the NMR tubes in various ratios to form 0.7 cm^3 samples such that *E*-**L**^{m} was in excess and NMR spectra recorded.

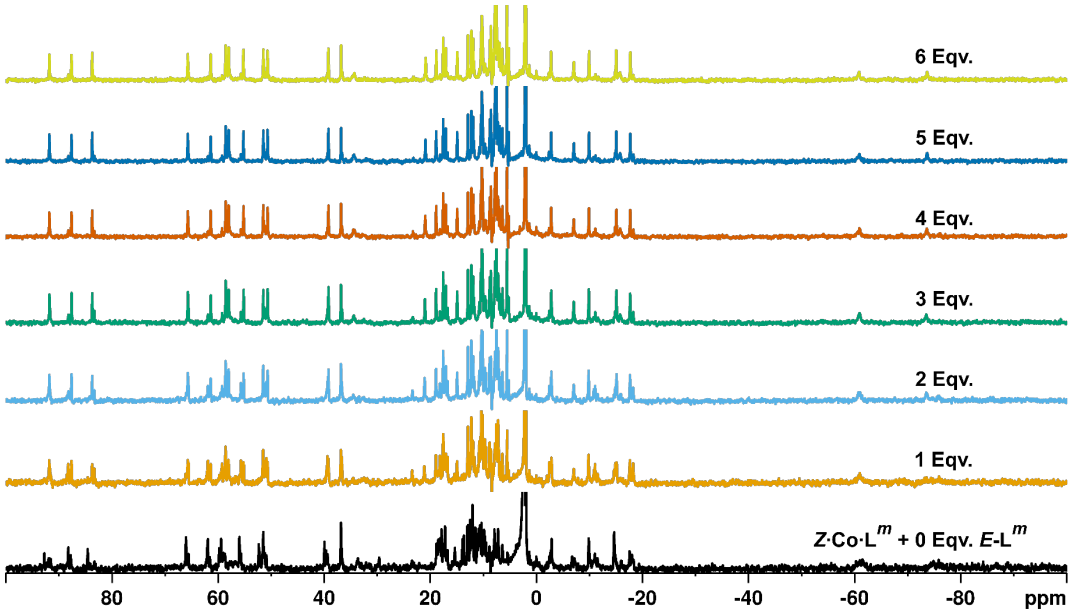

Figure S44. ^{1}H NMR spectra (300 MHz, MeCN-d_3/$CDCl_3$ (85:15 v/v), 298 K) recorded during addition of 0 – 6 equivalents (from bottom up) of *Z*-**L**^{m} to a solution of *E*•**Co**•**L**^{m}.

In situ NMR Spectra

We have adapted this method from literature[4] and described it previously.[5] We add this description here for convenience:

The NMR sample used for the *in-situ* illumination experiments was fitted with an insert tube made from quartz glass. A quartz glass optical fibre with a non-terminated end and its exposed surface and the exposed surface roughened to ensure even and omnidirectional illumination was subsequently inserted into the insert. In order to avoid damaging the fibre, an aluminium rod was used to lower this construction into the NMR spectrometer. The opposite end of the optical fibre was connected to the light source to allow for the irradiation of the sample inside the spectrometer.[4]

Figure S45. Visual presentation of the in-situ NMR irradiation set up: An NMR sample with a quartz-glass insert and an optical fibre.[5]

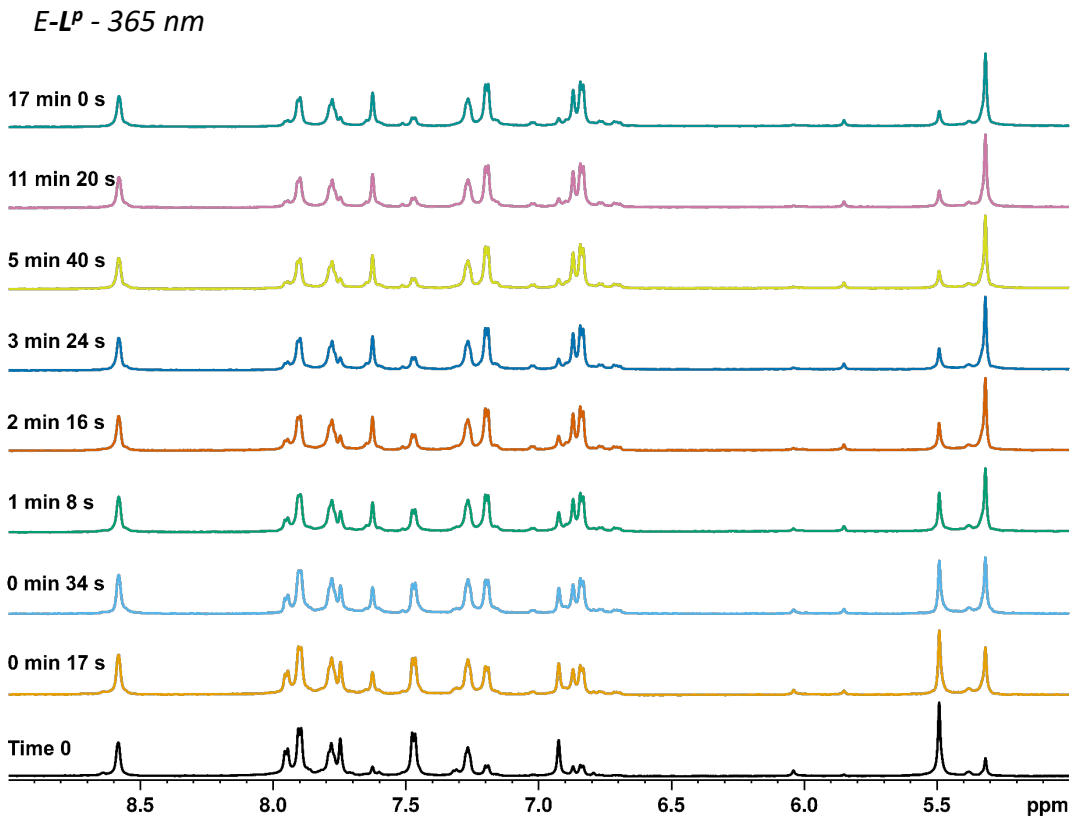

Figure S46. Series of ^{1}H-NMR (700 MHz, CD_3CN, 298 K) spectra during illumination of *E*-**L**^{p} with 365 nm light for 17 minutes.

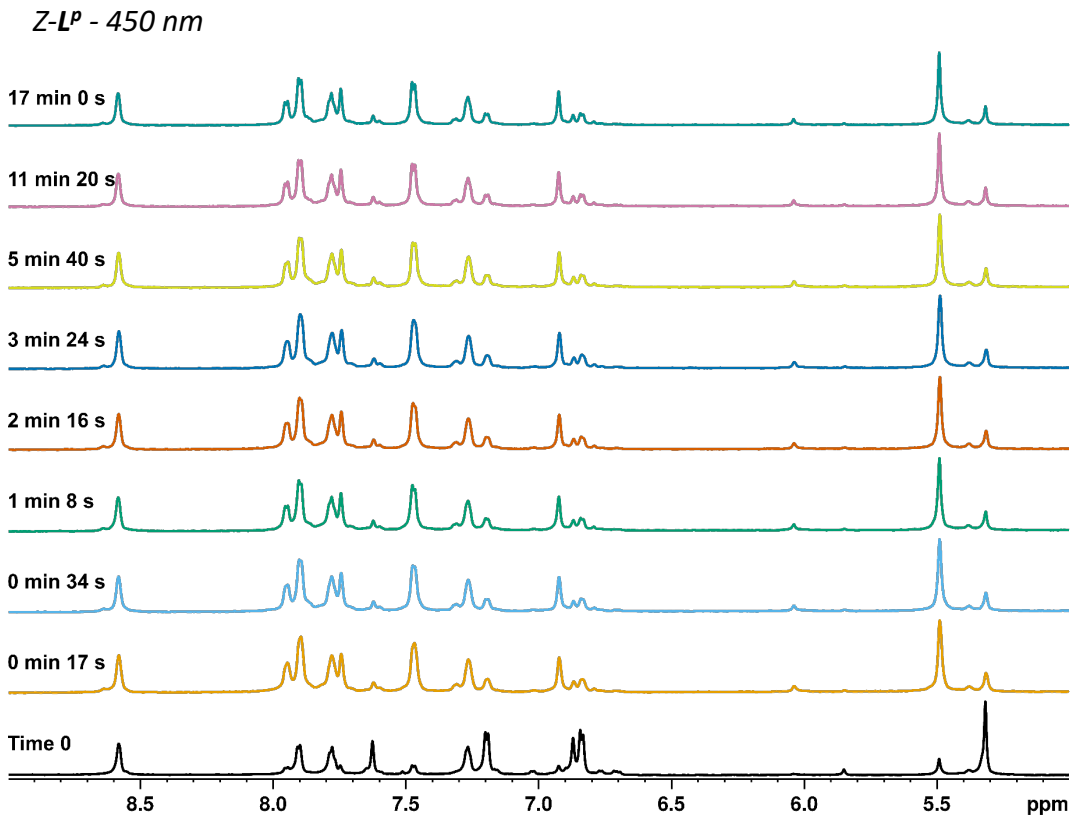

Figure S47. Series of ^{1}H-NMR (700 MHz, CD_3CN, 298 K) spectra during illumination of *Z*-**L**^{p} with 450 nm light for 17 minutes.

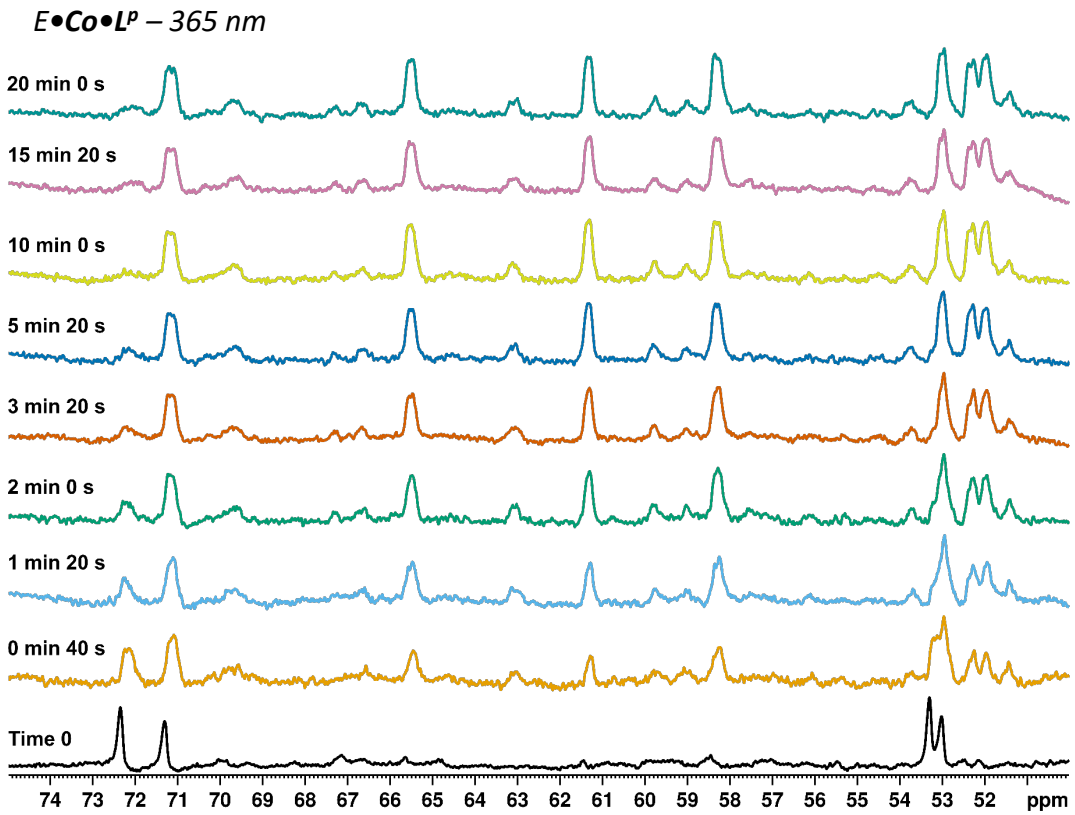

Figure S48. Series of ^{1}H-NMR (700 MHz, CD_3CN, 298 K) spectra during illumination of *E*•**Co**•**L**^{p} with 365 nm light for 20 minutes.

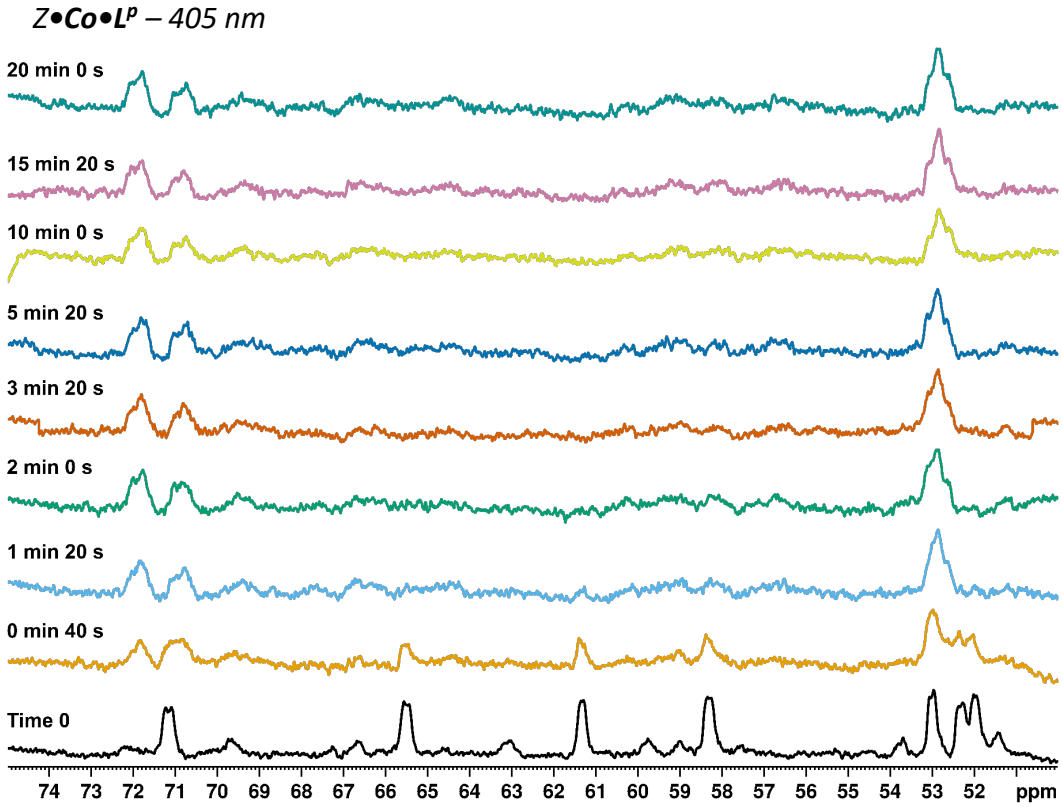

Figure S49. Series of ^{1}H-NMR (700 MHz, CD_3CN, 298 K) spectra during illumination of *Z*•**Co**•**L**^{p} with 405 nm light for 20 minutes.

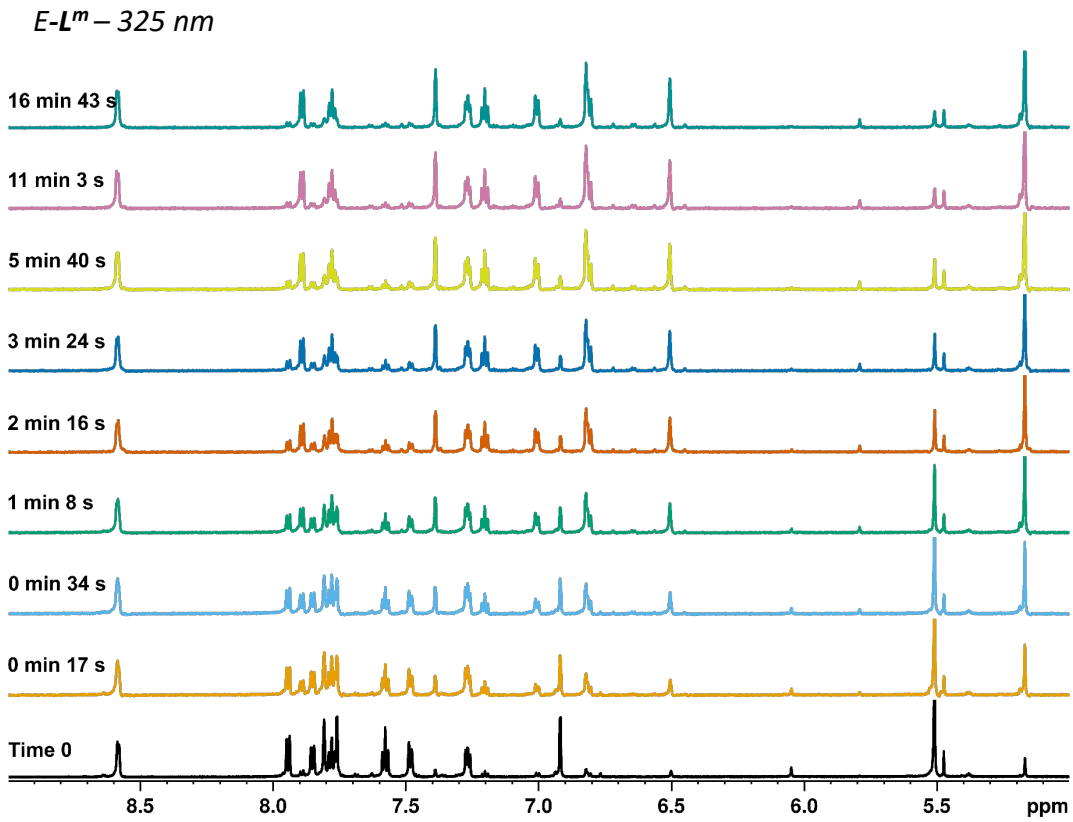

Figure S50. Series of ^{1}H-NMR (700 MHz, CD_3CN, 298 K) spectra during illumination of *E*-**L^{m}** with 325 nm light for 17 minutes.

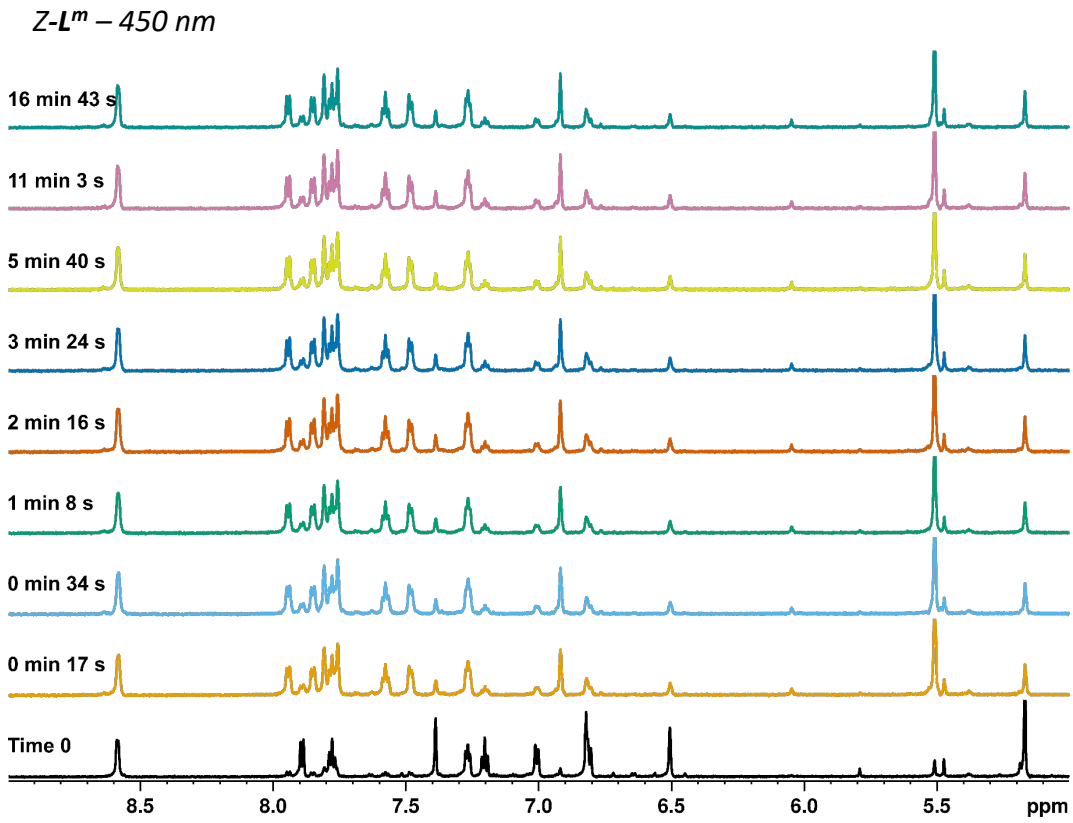

Figure S51. Series of ^{1}H-NMR (700 MHz, CD_3CN, 298 K) spectra during illumination of *Z*-**L^{m}** with 450 nm light for 17 minutes.

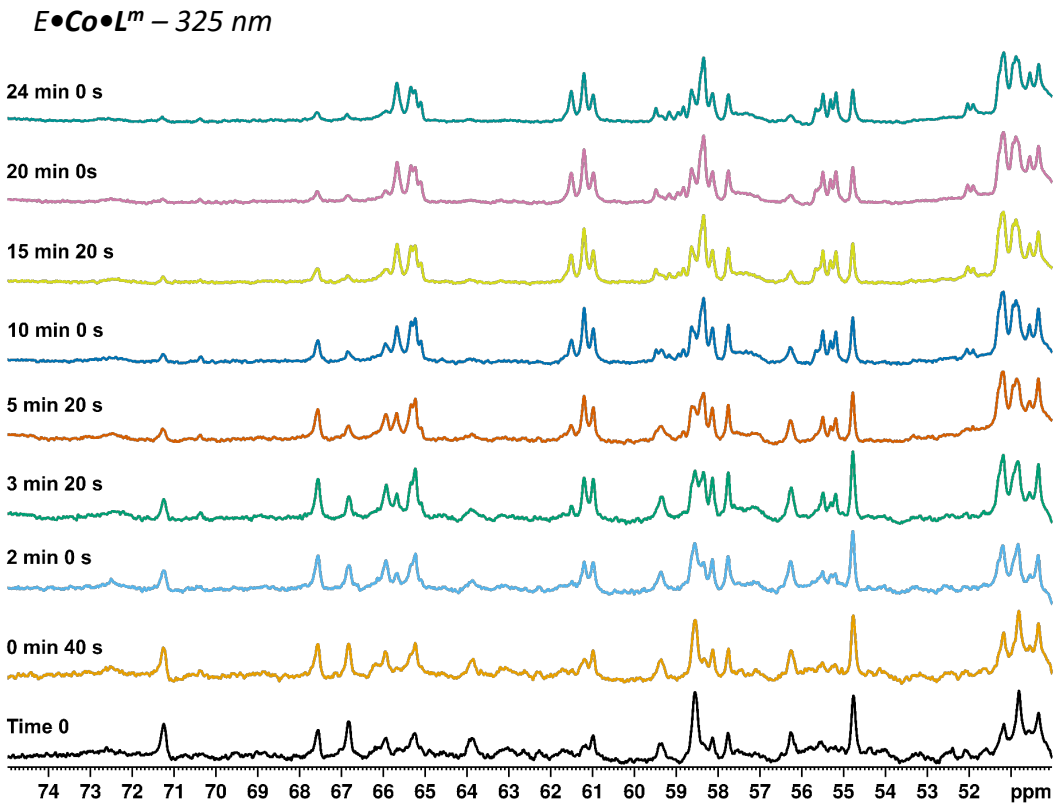

Figure S52. Series of ^{1}H-NMR (700 MHz, CD_3CN, 298 K) spectra during illumination of *E*•**Co**•**L**^{m} with 325 nm light for 24 minutes.

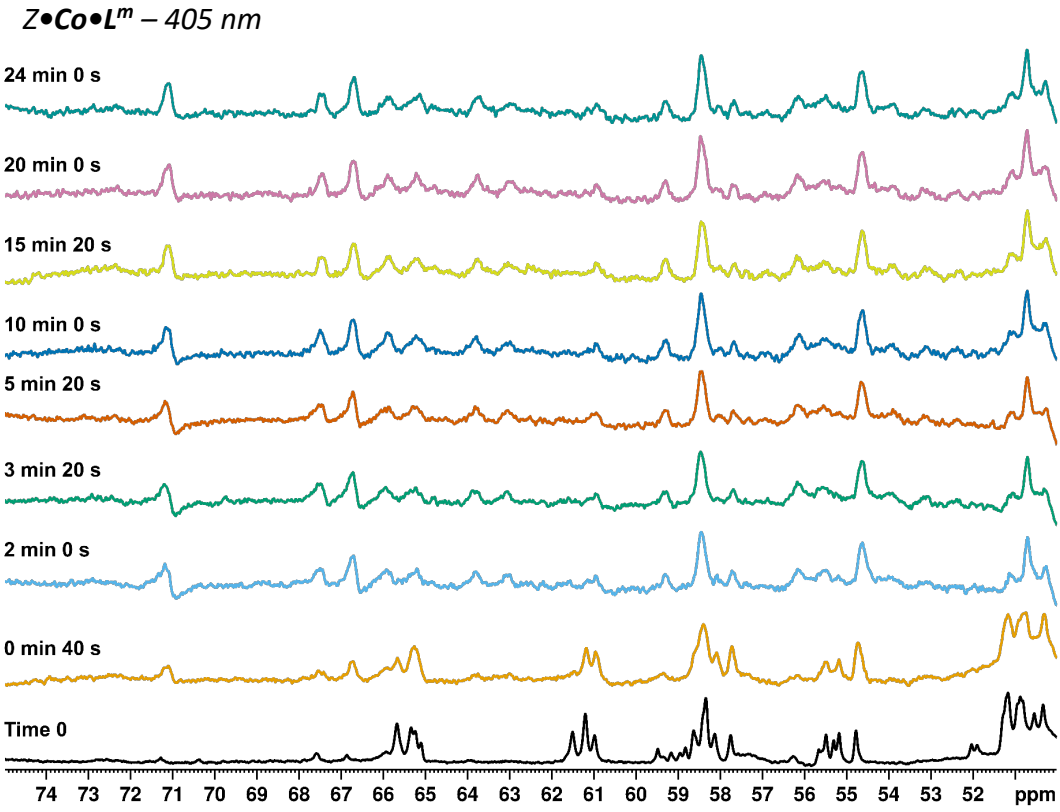

Figure S53. Series of ^{1}H-NMR (700 MHz, CD_3CN, 298 K) spectra during illumination of *Z*•**Co**•**L**^{m} with 405 nm light for 24 minutes.

X-ray crystallography

Details of the crystals used, data collection and refinements are given in Table 1. The structural determination of ligand **L*m*** was performed on a Rigaku Supernova diffractometer. The data was integrated and absorption corrections were applied using a Gaussian numerical method using the CrysAlisPro software.[6]

The data collection for *E*•**Co•L*m*** was performed in Experiment Hutch 1 of beamline I-19 at the UK Diamond Light Source synchrotron facility,[7] using methodology, data processing and software described previously.[1h] The structures were solved with Olex2,[8] using dual space iterative methods (SHELXT)[9] and refined by a full-matrix least-squares algorithm (SHELXL).[9]

As is usual with crystallographic structure determinations of this kind of elaborate supramolecular assemblies, for *E*•**Co•L*m*** scattering is weak and refinement problems are significant due to substantial disorder, principally of anions and solvent molecules, although the Co_4L_6 cage superstructure itself showed disorder of some ligand fragments over two closely-spaced positions. These problems required (i) extensive use of restraints to ensure geometrically reasonable structures (in particular: the geometries of pyrazole and pyridine rings were fixed with AFIX commands due to high disorder, and rigid bond (RIGU) and similarity (SIMU) restraints were applied to the anisotropic displacement parameters of all atoms in the structure; and (ii) elimination of regions of diffuse electron density using the solvent mask feature in OLEX leaving apparent voids in the lattices equating to 513 electrons *per* complex molecule. Details pertaining to each structure are included in the individual CIFs. Discussion of the structure of *E*•**Co•L*m*** in the main text is accordingly at the level of demonstrating the gross geometry of the complex with detailed discussion of structural minutiae kept to a minimum.

Structure name	**L*m***	*E*•**Co•L*m***
CCDC number	2301496	2301498
Empirical formula	$C_{30}H_{24}N_8$	$B_{7.94}C_{191.88}Co_4F_{32.28}H_{203.94}N_{48.11}O_{17.88}$
Formula weight	496.57	4405.01
T / K	100	100
Radiation	Cu Kα (λ = 1.54184)	Synchrotron (λ = 0.6889 Å)
Crystal system	monoclinic	triclinic
Space group	$P2_1/n$	*P*–1
a/Å	12.4889(8)	20.35937(13)
b/Å	4.8850(3)	21.05549(13)
c/Å	20.2570(12)	23.94804(13)
α/°	90	93.3668(5)
β/°	92.563(6)	93.7613(5)
γ/°	90	94.7042(6)
Volume/Å^3	1234.61(13)	10188.21(8)

Z	2	2
ρ_{calc} / g cm^3	1.336	1.436
μ/mm^{-1}	0.664	0.393
Crystal size/mm^3	0.17 × 0.05 × 0.03	0.10 x 0.08 x 0.07
2Θ range for data collection/°	8.158 – 154.29	1.88 – 45.00
Reflections collected	10836	203895
Independent reflections /R_{int}	2364 / 0.1565	29237 / 0.0390
Data/restraints/ parameters	2364 / 252 / 225	29237 / 6264 / 2943
Goodness-of-fit on F^2	1.092	1.073
Final R_1 / wR_2 [a]	0.0736 / 0.1982	0.0638 / 0.1986
Largest diff. peak/hole / e Å^{-3}	0.31/-0.35	0.90 / -0.57

[a] The value of *R*1 is based on 'observed' data with $I > 2\sigma(I)$; the value of w*R*2 is based on all data.

Simulations

The geometries of the cages *Z*•**Co•L^{p}**, *E*•**Co•L^{m}** *Z*•**Co•L^{m}** , and (BF_4^-)@*E*•**Co•L^{p}** (Figures 10 and 18, main text, S50, S51d, and S52) as well as potential structures for **Co•L^{m}•2,4** and **Co•L^{m}•4,2** (Figure S53) were optimised with a semi-empirical tight-binding quantum chemical method denoted as GFN-xTB.[10] For these geometry optimisations the stand-alone program xtb was used.[11] The molecular mechanics simulations (MM2 force field) of *E*•**Co•L^{p}** (Figure 7, main text, and S51a) and (BF_4^-)@*E*•**Co•L^{p}** (Figure S51b) were performed using SCiGRESS (version FQ 3.4.5, Build 1669.13197, Serial No. 1620809473902 (copyright 2008-2024, Fujitsu Limited)).

Co•L^{p}

For *Z*•**Co•L^{p}** (Figures 9 and S50) two potential structures exist with C_3 symmetry, arising from one metal centre with an opposing Δ/Λ (*Z*•**Co•L^{p}**•Δ/Λ) or *fac/mer* (*Z*•**Co•L^{p}**•*fm*) tris-chelate coordination geometry to the other three tris-chelate coordination geometries. The vertices and geometries of *Z*•**Co•L^{p}**•*fm* were based on a previously published X-ray crystal structure of a C_3 symmetric tetrahedron with the same metal-ligand coordination motif.[12] The one *fac* and three *mer* vertices were connected by six *Z*-*p*-azobenzenes using Avogadro[13] (an open-source molecular builder and visualisation tool, Version 1.2.0, http://avogadro.cc/) and the complete supramolecular structure subjected to modelling in xtb.

The all *fac* M_4L_6 tetrahedral isomer, *Z*•**Co•L^{p}**•Δ/Λ (Figure S50b), was based on the same previously published X-ray crystal structure.[12] The Δ *fac* vertex was copied four times and one of them mirrored using SCiGRESS (version FQ 3.4.5, Build 1669.13197, Serial No. 1620809473902 (copyright 2008-2024, Fujitsu Limited)). The one Λ and three Δ vertices were connected by six *Z*-*p*-azobenzenes using Avogadro and the complete supramolecular structure subsequently subjected to modelling in xtb.

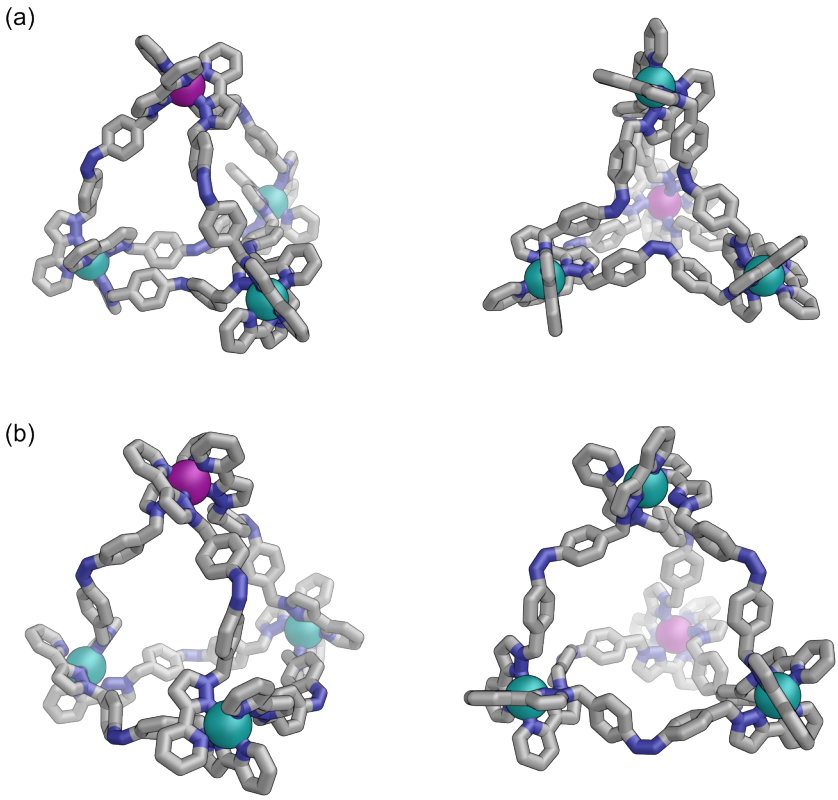

Figure S54. (a) GFN-xTB structures of two potential C_3 symmetric isomers of M_4L_6 structure *Z*•**Co**•**L**^{p}: (a) an M_4L_6 tetrahedron with one *fac* (purple) and three *mer* vertices (teal) (*Z*•**Co**•**L**^{p}•*fm*) and (b) an M_4L_6 tetrahedron with all *fac* vertices of different chiralities, one Λ (purple) and three Δ (teal) (*Z*•**Co**•**L**^{p}•Δ/Λ).

For *E*•**Co**•**L**^{p} (Figure 7, main text, and S51a), an MM2 force field was needed, because dispersion interactions in GFN-xTB caused the helicate structure to collapse in order to allow for π-stacking between two of the ligands. Since ^{1}H NMR suggests approximate D_3 symmetry of the *E*•**Co**•**L**^{p} helicate in solution, we reverted to a model which does not take dispersion interactions into account as strongly as GFN-xTB. The models of the vertices were based on the *fac* vertex obtained from a previously published X-ray crystal structure.[12] The cobalt(II) ions were set to octahedral geometry with sp^3d^2 hybridization to maintain Co–N bond angles. (BF_4^-)@*E*•**Co**•**L**^{p} was simulated with a MM2 model for comparison (Figure S51b), showing that the flexibility of the ligands allows them to bend to accommodate the BF_4^- guest thereby reducing the Co—Co distance (Figure S51c). The MM2 coordinates for (BF_4^-)@*E*•**Co**•**L**^{p} were also subjected to GFN-xTB which resulted in a similar geometry (Figure S51d).

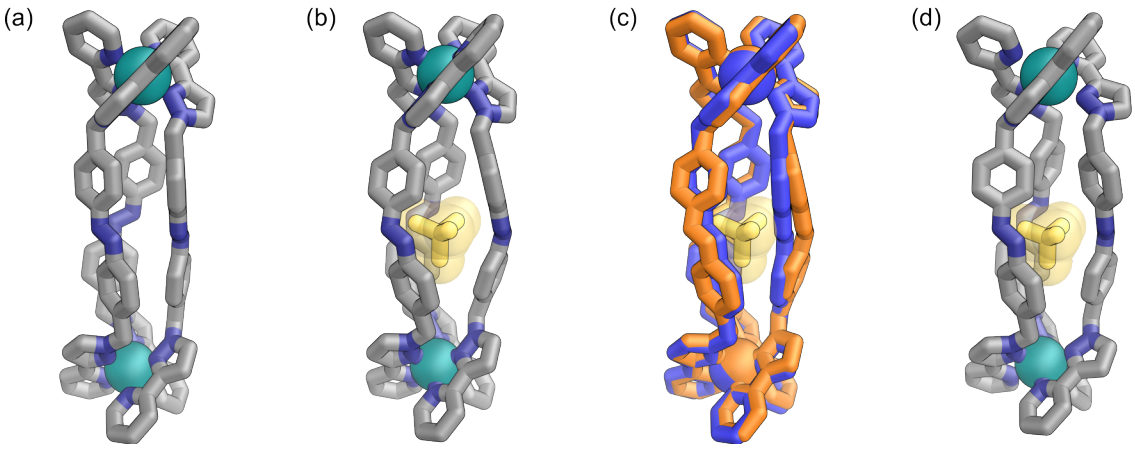

Figure S55. MM2 structures of (a) *E*•**Co•L^p**, (b) (BF_4^-)@*E*•**Co•L^p**, and (c) the comparison of *E*•**Co•L^p** (blue) and (BF_4^-)@*E*•**Co•L^p** (orange, with BF_4^- in yellow) showing the flexible ligands to bend slightly to accommodate the BF_4^- guest thereby reducing the Co—Co distance. (d) GFN-xTB structure of (BF_4^-)@*E*•**Co•L^p**.

Co•L^m

The models of the vertices for E•Co•Lm and Z•Co•Lm were based on the vertices obtained from the X-ray crystal structure of *E*•**Co•L^m**, which were connected by the respective ligand structures using Avogadro and the complete supramolecular structures subsequently subjected to modelling in xtb. The modelled structure of *Z*•**Co•L^m** is significantly expanded in comparison with the X-ray crystal structure of *E*•**Co•L^m**. To demonstrate that this is due to the lack of crystal packing forces in the molecular model, we subjected the coordinates of *E*•**Co•L^m** obtained from its X-ray crystal structure to the same modelling method (GFN-xTB; Figure S52). Comparing the GFN-xTB structure of *E*•**Co•L^m** to the X-ray crystal structure (Figure S52b) shows that subjection of the crystal structure coordinates to the GFN-xTB method causes the structure to unwind significantly, presumably due to the lack of crystal packing constraints. The structure of *E*•**Co•L^m** seems to exhibit considerable flexibility, so that changing the ligand configuration from *E* to Z does not cause significant changes in the Co_4 framework (Figure S52c).

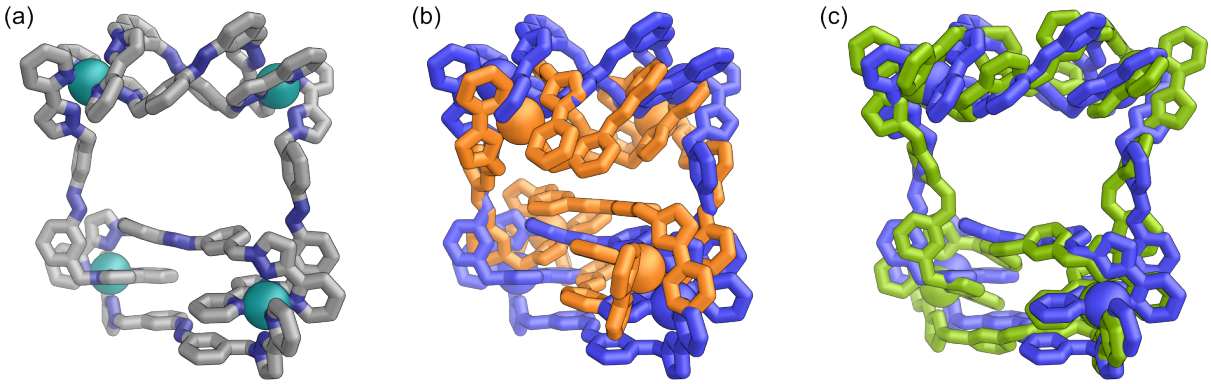

Figure S56. (a) GFN-xTB structure of *E*•**Co•L^m**. Comparison of GFN-xTB structure of *E*•**Co•L^m** (blue) to (b) X-ray crystal structure of *E*•**Co•L^m** (orange), that subjection of the crystal structure coordinates to the GFN-xTB method causes the structure to unwind significantly, and (c) GFN-xTB structure of *Z*•**Co•L^m** (green), showing that the size of the Co_4 metallacycle barely changes upon *E*→*Z* isomerisation.

In cyclic bis-azobenzenes, virtually concerted switching of both azobenzenes can be observed,[14,15] with the *EZ* state being considerably less stable than the *EE* and *ZZ* states, respectively, leading to a short lifetime of the *EZ* state and a long thermal half-life of the *ZZ* state.[15] If the flexibility of the bis-azobenzene macrocycle is not sufficient, switching of the azo-units can be prevented entirely.[16] This literature precedence and the fact that we only seem to observe discrete structures with *Z*/*E* ratios of 0:6, 2:4, and 6:0, with an apparent fourth species likely possessing a 4:2 ratio, lead us to the assumption that the azo-units of **Co•L^m** would switch in pairs, i.e. the two helicate subunits and the two parallel connecting ligands, reducing the number of possible isomers for the structures with *Z*/*E* ligand mixtures, **Co•L^m•2,4** and **Co•L^m•4,2**, to three, respectively (Figure S53). We optimized the geometries of those possible isomers with GFN-xTB. Structures highlighted in yellow seem more likely to form.

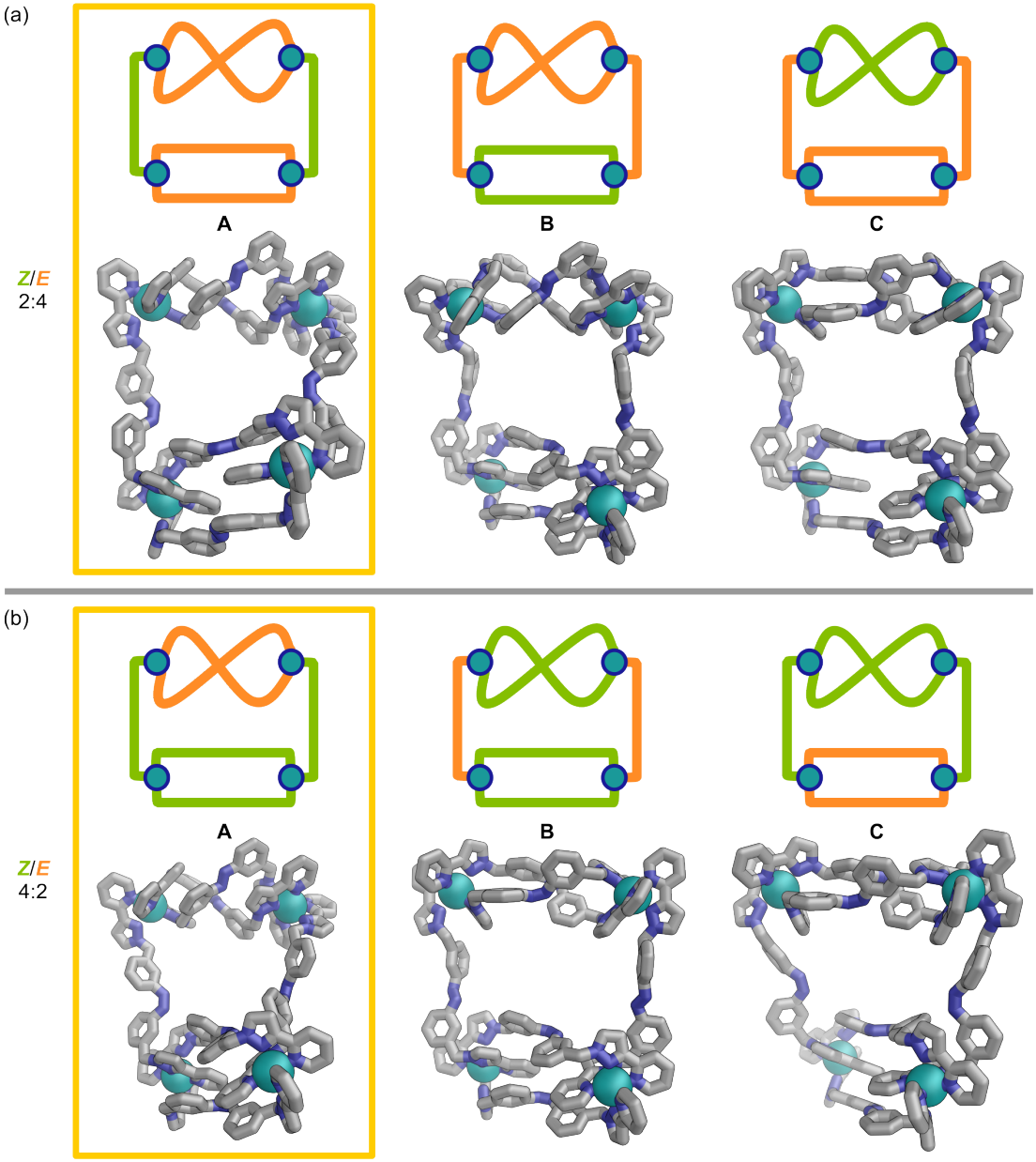

Figure S57. Possible structures (GFN-xTB) of **Co•L^m•2,4** and **Co•L^m•4,2**. Structures highlighted in yellow, seem more likely.

References

1. B. Jousselme, P. Blanchard, N. Gallego-Planas, E. Levillain, J. Delaunay, M. Allain, P. Richomme and J. Roncali, *Chem. Eur. J.,* 2003, **9**, 5297.
2. (a) A. J. Amoroso, A. M. W. Cargill Thompson, J. C. Jeffery, P. L. Jones, J. A. McCleverty and M. D. Ward, *J. Chem. Soc., Chem. Commun.,* 1994, 2751; (b) H. Brunner and T. Scheck, *Chem. Ber.,* 1992, **125**, 701; (c) Y. Lin and S. A. Lang, *J. Heterocycl. Chem.,* 1977, **14**, 345.
3. A. Stephenson and M. D. Ward, *RSC Adv.,* 2012, **2**, 10844.
4. C. Feldmeier, H. Bartling, E. Riedle and R. M. Gschwind, *J. Magn. Reson.*, 2013, **232**, 39.
5. R. Falkenburg, M. J. Notheis, G. Schnakenburg, L. K. S. von Krbek, *Org. Biomol. Chem.* 2023, **21**, 4993.
6. CrysAlisPro Software system (version 1.171.40.45a), Rigaku Oxford Diffraction, UK (2018).
7. D. R. Allan, H. Nowell, S. A. Barnett, M. R. Warren, A. Wilcox, J. Christensen, L. K. Saunders, A. Peach, M. T. Hooper, L. Zaja, S. Patel, L. Cahill, R. Marshall, S. Trimnell, A. J. Foster, T. Bates, S. Lay, M. A. Williams, P. V. Hathaway, G. Winter, M. Gerstel, R. W. Wooley, *Crystals,* 2017, **7**, 336.
8. O. V. Dolomanov, L. J. Bourhis, R. J. Gildea, J. A. K. Howard and H. Puschmann, *J. Appl. Cryst.,* 2009, **42**, 339.
9. G. M. Sheldrick, *Acta Cryst. A,* 2015, **71**, 3.
10. S. Grimme, C. Bannwarth, P. Sushkov, *J. Chem. Theory Comput.*, 2017, **13**, 1989-2009.
11. Please contact xtb@thch.uni–bonn.de to obtain the programme.
12. R. L. Paul, S. P. Argent, J. C. Jeffery, L. P. Harding, J. M. Lynam and M. D. Ward, *Dalton Trans.,* 2004, 3453.
13. M. D. Hanwell, D. E. Curtis, D. C. Lonie, T. Vandermeersch, E. Zurek, G. R. Hutchison *J. Cheminf.*, 2012, **4**.
14. M. Müri, K. C. Schuermann, L. De Cola, M. Mayor, *Eur. J. Org. Chem.*, 2009, 2562.
15. Y. Norikane, N. Tamaoki, *Org. Lett.*, 2004, **6**, 15, 2595–2598.
16. A. H. Heindl, L. Schweighauser, C. Logemann, H. A. Wegner, *Synthesis*, 2017, **49**, 2632.

9.2 White-light powered autonomous molecular ratchet drives Pd^{II} capsules out of equilibrium

Lidón Pruñonosa Lara, Benedikt Bädorf, Maximilian J. Notheis, Gregor Schnakenburg, Stefan Grimme, and Larissa K. S. von Krbek.

Preprint uploaded to ChemRxiv on 9 October 2025. Available at DOI: 10.26434/chemrxiv-2025-ck3gw.

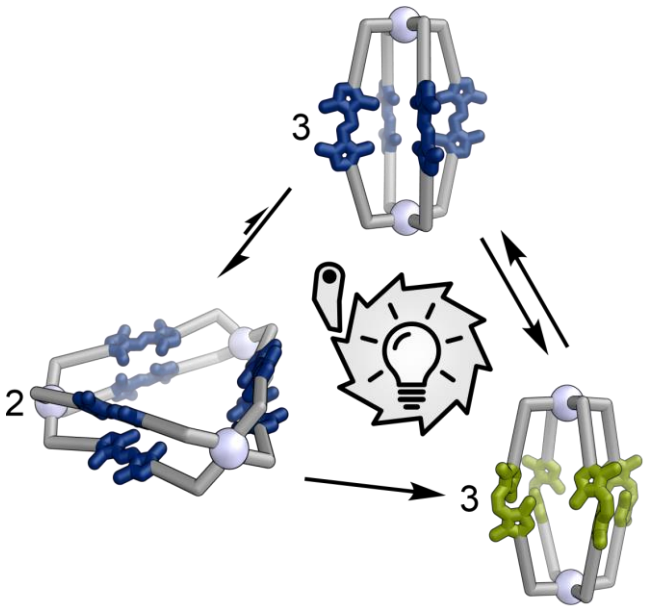

Figure A2. Graphical abstract. Reproduced from Pruñonosa Lara et al. under the terms of the Creative Commons Attribution-NonCommercial-NoDerivatives 4.0 International Licence (CC BY-NC-ND-4.0). © 2025 The Authors.[140]

White-light powered autonomous molecular ratchet drives Pd^{II} capsules out of equilibrium

Lidón Pruñonosa Lara,[a] Benedikt Bädorf,[b] Maximilian J. Notheis,[a] Gregor Schnakenburg,[c] Stefan Grimme,[b] and Larissa K. S. von Krbek*[a]

a. Kekulé-Institut für Organische Chemie and Biochemie, Rheinische Friedrich-Wilhelms-Universität Bonn, Gerhard-Domagk-Str. 1, 53121 Bonn, Germany. E-mail: larissa.vonkrbek@uni-bonn.de.
b. Mulliken Center for Theoretical Chemistry, University of Bonn, Beringstr. 4, 53115 Bonn, Germany.
c. Institut für Anorganische Chemie, Rheinische Friedrich-Wilhelms-Universität Bonn, Gerhard-Domagk-Str. 1, 53121 Bonn, Germany.

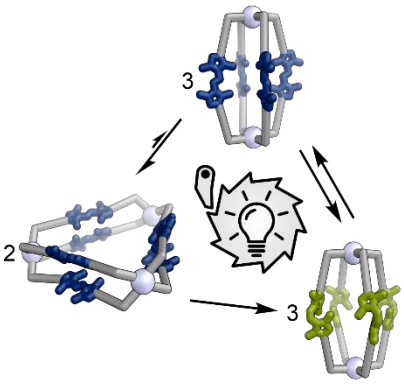

Keywords: self-assembly, photoswitches, metallo-supramolecular capsules, molecular ratchet, kinetic asymmetry, out of equilibrium

Abstract

Using an energy source to drive chemical reactions away from equilibrium is essential for life and remains a significant challenge in designing artificial out-of-equilibrium nanosystems and molecular machines. Achieving autonomous operation of such systems, as observed in nature, presents an even greater difficulty.

Here, we report Pd^{II}-mediated coordination capsules based on ligand **1** embedding an azobispyrazole photoswitch. The more thermodynamically stable *E*-photoisomer forms an equilibrium mixture of a Pd^{II}_3(*E*-**1**)$_6$ double-walled triangle and a Pd^{II}_2(*E*-**1**)$_4$ lantern in a 78:22 ratio. UV-light irradiation transforms both structures into a Pd^{II}_2(*Z*-**1**)$_4$ lantern, which then reverts solely to the out-of-equilibrium Pd^{II}_2(*E*-**1**)$_4$ lantern when exposed to visible light. The complete photoisomerisation proceeds through an information ratchet mechanism that can operate autonomously under continuous white light or sunlight exposure, selectively accumulating the out-of-equilibrium Pd^{II}_2(*E*-**1**)$_4$ structure.

This work demonstrates how autonomous, light-driven processes can be harnessed to direct non-equilibrium behaviour in complex coordination assemblies.

Introduction

Driving chemical systems away from equilibrium and harnessing endergonic reactions are essential for powering molecular machinery and developing adaptive materials.[1–4] One method to accomplish this is through molecular ratchets.[1,3–8] Just as a mechanical ratchet allows movement in only one direction, a molecular ratchet is a chemical reaction cycle, in which the components react exclusively in a single direction.[1,2,9] If this unidirectionality results from kinetic asymmetry,[10,11] where one intermediate along the reaction pathway reacts more quickly than another, the ratchet is known as an information ratchet.[1–4,12–16] In contrast, an energy ratchet[17–19] relies on the energy differences between intermediates in the reaction cycle to determine its directionality.[1–4] Operating molecular ratchets autonomously, like most natural processes, still presents a significant challenge.[1,20,21] When operating molecular ratchets, light acts as an advantageous stimulus for *in-situ* control, allowing precise spatial and temporal regulation without producing unwanted side products.[22,23] Additionally, it can be tuned to a specific wavelength, which activates both forward and reverse reactions, potentially enabling autonomous operation of information and energy ratchets alike.[1]

Harnessing light in molecular ratchets requires integrating photoswitches, such as azobenzenes,[24–29] diazocines,[30–32] crowded alkenes,[33,34] imines[35,36] or dithienylethanes (DTE)[37–40] into the system components. Aligning multiple switches inside a self-assembled supramolecular organic or metal-organic capsule can amplify the switching effect. Despite this advantage, examples of molecular ratchets and out-of-equilibrium structures in supramolecular capsules are still scarce.[1,26,30–32,41] Feringa, Kathan, and colleagues[26] described a supramolecular organic capsule that acts as a molecular ratchet, leveraging photoisomerisation and imine exchange to create an out-of-equilibrium open capsule. In previous work,[32] we demonstrated how a diazocine-containing, triple-stranded bimetallic helicate can autonomously operate as a molecular energy ratchet, furthermore using this mechanism to accelerate regioselective metal cation exchange within the structure.

Here, we describe the formation of metallo-supramolecular capsules from a bispyridine ligand **1** with an azo-bispyrazole[42–46] backbone (Scheme 1). Azo-bispyrazoles are photoswitches derived from azobenzene and arylazopyrazole, which have been scarcely explored in supramolecular systems. The ligand exhibits outstanding photophysical properties, with near-quantitative $E \rightarrow Z$ and $Z \rightarrow E$

conversions and no appreciable photobleaching. Moreover, the pyrazole units offer conformational flexibility, enabling the *E*-configuration of the ligand to self-assemble both into a Pd^{II}_3(*E*-**1**)$_6$ double-walled triangle and a Pd^{II}_2(*E*-**1**)$_4$ lantern structure in the presence of Pd^{II} ions. Photoswitching and subsequent capsule rearrangement occur via a molecular information ratchet that drives the system away from thermodynamic equilibrium. We elucidated the complex ratchet mechanism experimentally and through quantum chemistry-based calculations, regarding its thermodynamics and kinetics. Crucially, continuous white light or sunlight irradiation operates the molecular ratchet autonomously, enriching the mixture with the out-of-equilibrium Pd^{II}_2(*E*-**1**)$_4$ lantern. Our system exemplifies a rare autonomous, light-powered molecular ratchet within a supramolecular structure: it exhibits directional behaviour under constant illumination, continuously pushing the system out of equilibrium without requiring alternating stimuli. This system could advance the development of autonomous molecular ratchets, serving as an initial step toward harnessing out-of-equilibrium systems for light-driven reaction cascades or molecular machines.

Results and discussion

Synthesis and photoswitching of ligand **1**

Photoswitchable azobispyrazole-containing ligand **1** was synthesised by Chan-Lam coupling between (4-(pyridin-3-yl)phenyl)boronic acid and azobispyrazole photoswitch (*E*)-1,2-bis(3,5-dimethyl-1H-pyrazol-4-yl)diazene (**S4**; SI Figure S1 and Section S2.5)

At ambient conditions, ligand **1** predominantly exists in its thermodynamically more stable *E*-configuration (85% *E*-**1**). This is supported by the DFT-computed free energy difference‡ between *E*-**1** and *Z*-**1** of ΔG = +47.4 kJ mol^{-1} in favour of *E*-**1** (SI, Section S8.2). Single crystals of ligand *E*-**1** were grown by slow evaporation of solvent from a CD_2Cl_2 solution of **1**. The X-ray crystal structure shows the expected *E*-configuration of the N=N double bond (SI, Section S7).

Irradiation of **1** with 365 nm light causes *E*→*Z* isomerisation, reaching a photostationary state (PSS) of 99% *Z*-**1** (CD_2Cl_2, Scheme 1, left; SI, Section S4.2). This process can be reversed either by exposing *Z*-**1** to 500 nm light (97% *E*-**1**) or through thermal relaxation, which has a half-life of $\tau_{½}$ = 10 h at 60 °C in DMF (SI, Figure S59). The photoswitching of ligand **1** is rapid and fully reversible, usually requiring less

than 1 minute of irradiation in either direction (24 μM in DMF, 0.2 mW light power), with no appreciable photobleaching over ten switching cycles (SI, Figure S57, right). Notably, the photostationary states of ligand **1** were quite similar to those of the parent photoswitch **S4**. However, ligand **1** exhibited a significant increase in thermal half-life. This suggests that the 4-(pyridin-3-yl)phenyl substitution did not hinder photoswitching. The substitution of other azo-based photoswitches is known to impede photoswitching.[47]

Synthesis of Pd^{II} capsules

Mixing ligand **1** with $Pd(CH_3CN)_4(BF_4)_2$ in a 2:1 stoichiometric ratio in deuterated dimethyl sulfoxide (DMSO-d_6) at 50 °C yielded two Pd^{II} complexes after 30 minutes: a Pd^{II}_3(*E*-**1**)$_6$ double-walled triangle *E*-**T** and a Pd^{II}_2(*E*-**1**)$_4$ lantern *E*-**L** (Scheme 1). Triangle *E*-**T** and lantern *E*-**L** equilibrated to a 78:22 ratio at 22 °C over 20 hours (SI, Figure S43), and the mixture was characterised using single-crystal X-ray diffraction, mass spectrometry, ^{1}H NMR, and UV-vis spectroscopy (Figure 1; SI, Sections S2.6 and S7).

The pyrazole groups in ligand **1** can adopt either an *anti* or *syn* orientation, with protons H-a and H-b positioned on opposite sides of the azo bridge or on the same side. This conformational shift from *anti* to *syn* results in a change in the angle between the pyridine nitrogens' coordination vectors: 60° for *anti* and 0° for *syn*. This

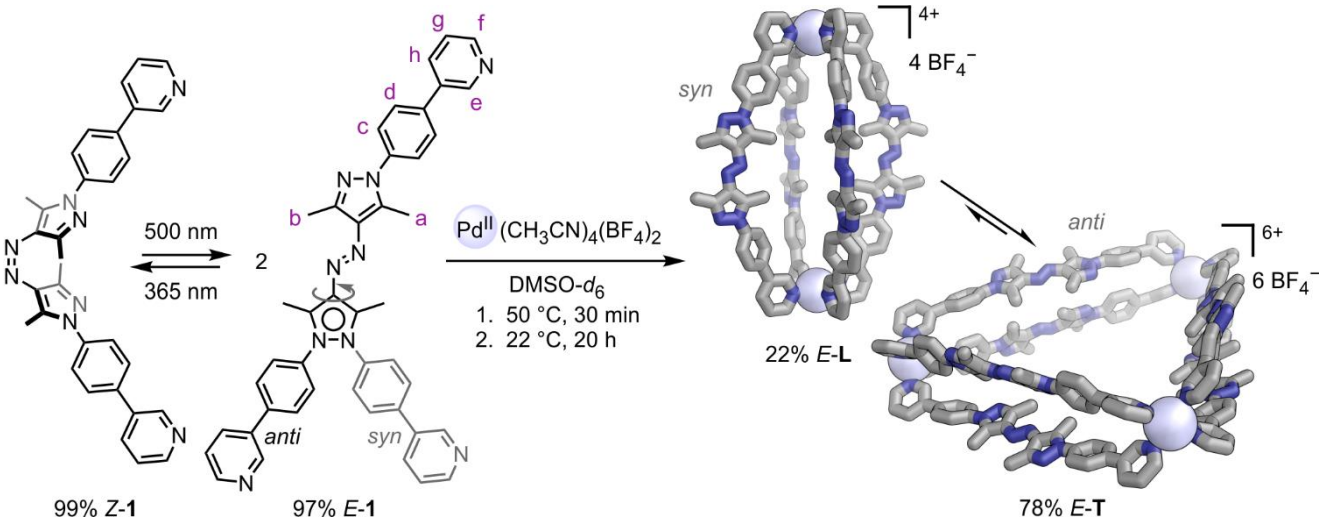

Scheme 1. *Left*: Photoswitching between the two isomers of **1**. Ligand *E*-**1** exhibits two distinct conformations: *syn* and *anti*. *Right*: Self-assembly of ligand *E*-**1** and $Pd(CH_3CN)_4(BF_4)_2$ yielding 22% lantern *E*-**L** (containing *syn*-*E*-**1**; single crystal X-ray structure shown) and 78% triangle *E*-**T** (containing *anti*-*E*-**1**; GFN2-xTB [ALPB: DMSO][48,49],‡ structure shown). Hydrogens and counterions omitted for clarity; C: grey, N: blue, Pd^{II}: blue white.

notable conformational flexibility in ligand **1** enables the formation of both triangle *E*-**T** and lantern *E*-**L** from the same ligand, despite the vastly different angles required[50–53] between the pyridine nitrogens' coordination vectors. We could confirm the *anti*-conformation of the ligands in triangle *E*-**T** using one-dimensional ^{1}H ROESY NMR, based on contacts between protons H-a and H-b, which are absent in lantern *E*-**L**, in line with the expected *syn*-conformation of the ligands in *E*-**L** (SI, Section S2.6).

Lantern *E*-**L** crystallised in the triclinic space group $P\bar{1}$ (Scheme 1; SI, Section S7). Four ligands **1** connect two Pd^{II} centres, with the crystallographic inversion centre located in the centre of the capsule. The pyrazole groups in ligand **1** display the expected *syn*-orientation, with protons H-a and H-b on opposite sides of the azo bridge, enabling the pyridine units to have a 0° angle between their coordination vectors, which is essential for lantern formation (SI, Section S2.6). This *syn*-ligand conformation is not C_2 symmetric; therefore, the ligands can be oriented either pointing "up" or "down" within the lantern structure (SI, Figure S13). The X-ray crystal structure shows two ligands pointing upwards and two pointing downwards in a *cis*-arrangement of the two ligand orientations. In theory, three additional and downwards, three ligands pointing up and one pointing down, or all ligands pointing in the same direction (SI, Figure S13). A large number of possible isomers were computationally modelled, revealing only low relative energy differences of 6.3 kJ mol^{-1} or less between these isomers (SI, Section S8.4), which suggests that lantern *E*-**L** might exist in different isomers in solution. Our computationally predicted structure, with the ligands arranged in a *cis*-configuration, shows excellent agreement with the X-ray crystal structure, validating the computational approach‡ (Figure 2; SI, Section S8.5).

The high-resolution electrospray ionisation (ESI) mass spectrum of the 78:22 triangle *E*-**T** / lantern *E*-**L** mixture under light exclusion displayed two series of signals corresponding to the species $[\mathbf{T}-n(BF_4)]^{n+}$ (n = 3, 4, 5, 6) and $[\mathbf{L}-n(BF_4)]^{n+}$ (n = 2, 3, 4; Figure 1c, top, SI, Figure S24), respectively. The ^{1}H NMR spectrum exhibited two sets of ligand signals in a 78:22 ratio (Figure 1d, top). The number of signals related to the major and minor components is consistent with one-half of one ligand environment being unique, meaning all ligands are identical and have twofold symmetry. This fits well with a triangle and a lantern structure coexisting in solution. Note that some very minor species were also observed, which we tentatively assign to other possible isomers of lantern *E*-**L** (see above and SI Section S8.4), while we

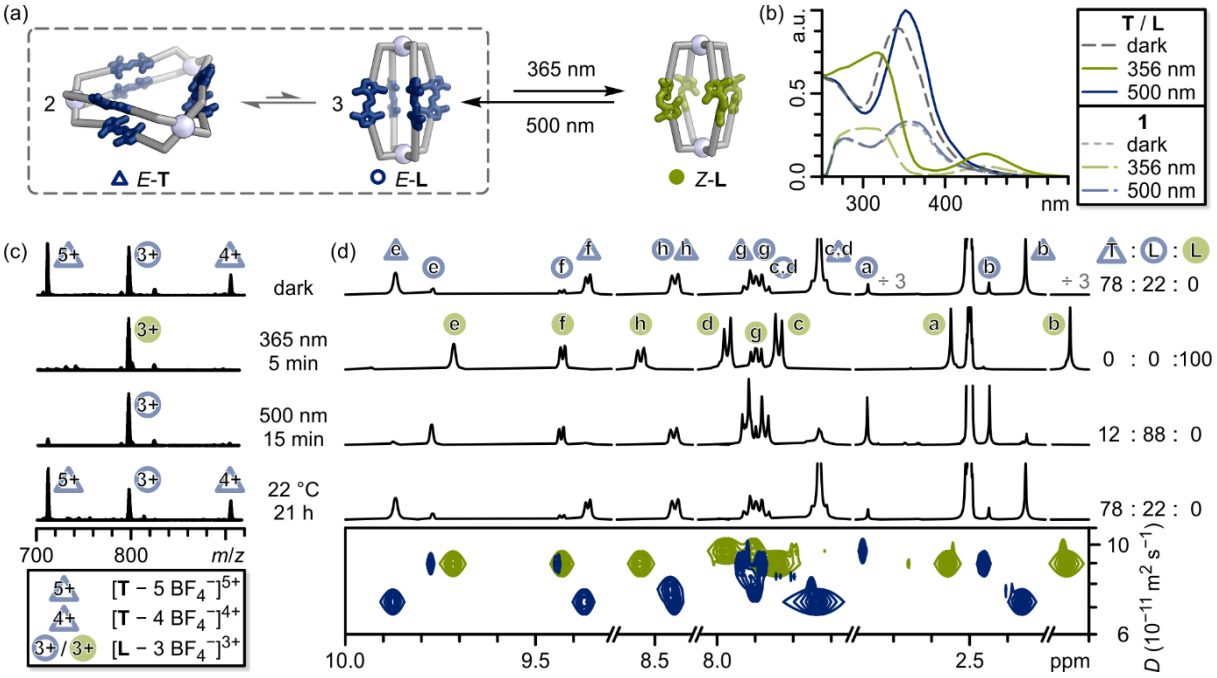

Figure 1. (a) The triangle *E*-**T** / lantern *E*-**L** mixture converts to lantern *Z*-**L** upon irradiation with 365 nm light. Irradiation of lantern *Z*-**L** with 500 nm light reverts it to *E*-**L**, exclusively, which then equilibrates back to the original triangle *E*-**T** / lantern *E*-**L** ratio over time. (b) Normalised UV-vis spectra of the triangle *E*-**T** / lantern *E*-**L** mixture and ligand **1** (DMSO) before and after irradiation with 365 nm and 500 nm light for 1 min, respectively. Spectra of *E*-**T** / *E*-**L** and **1** are normalised to 1.0 and 0.375, respectively, for clarity. (c,d) Triangle *E*-**T** / lantern *E*-**L** mixture before and after irradiation with 365 nm and 500 nm light for 1 min, respectively, as well as after equilibration under light exclusion at 22 °C for at least 21 h (top to bottom) monitored by (c) ESI mass spectrometry (DMSO/CH_3CN) and (d) ^{1}H NMR spectroscopy (700 MHz, DMSO-d_6, 298 K), including ^{1}H DOSY NMR of the triangle *E*-**T** / lantern *E*-**L** mixture before and after irradiation with 365 nm light (blue and green, respectively). Note that proton H-a of triangle *E*-**T** is below the DMSO solvent signal, but can be observed by VT NMR (SI, Figure S46).

assume the major isomer to be the *cis*-isomer observed in the X-ray crystal structure. UV-vis revealed a strong π→π* absorption band at $\lambda_{\pi\rightarrow\pi^*}$ = 335 nm, reminiscent of the π→π* absorption band in free ligand *E*-**1** ($\lambda_{\pi\rightarrow\pi^*}$ = 350 nm), indicating that all ligands are in their *E*-configurations in both metallo-supramolecular structures (Figure 1b). ^{1}H DOSY NMR revealed, that the two species have clearly distinguishable diffusion coefficients ($D_{E\text{-}\mathbf{T}}$ = 7.3 × 10^{-11} and $D_{E\text{-}\mathbf{L}}$ = 9.1 × 10^{-11} m^2 s^{-1}) corresponding to the major and minor species in ^{1}H NMR, respectively. This allowed us to identify the major species as triangle *E*-**T** and the minor species as lantern *E*-**L**. The solvodynamic diameters of $d_{E\text{-}\mathbf{T}}$ = 27.8 Å and $d_{E\text{-}\mathbf{L}}$ = 22.4 Å align well with the dimensions of the computational structure of triangle *E*-**T** and the X-ray crystal structure of lantern *E*-**L** ($d_{E\text{-}\mathbf{T}}$ = 25.2 Å and $d_{E\text{-}\mathbf{L}}$ = 19.8 Å, respectively; SI, Figures S23). UV-vis, NMR, and ESI MS data are consistent with the coexistence of a double-walled triangle *E*-**T** and a lantern *E*-**L**.

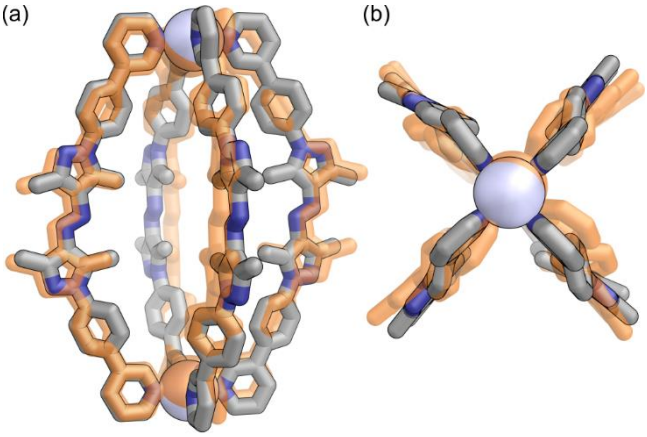

Figure 2. Overlay of the experimental structure of lantern *E*-**L** (orange) with the computationally obtained structure‡ (C: grey, N: blue, Pd^{II}: blue white) from a CREST[54] conformational search, reoptimized at the ωB97X-3c [CPCM: DMSO] level of theory.[55] The structures have a permutation-invariant root-mean-square deviation (iRMSD)[56] of 1.1 Å.

Due to the lability of the Pd^{II}–pyridine bonds, triangle *E*-**T** and lantern *E*-**L** exist in a dynamic equilibrium. As expected for an equilibrium between a larger and a smaller species, entropically favoured lantern *E*-**L** could be enriched in the mixture by diluting the complex mixture solution (SI, Section S3.3). At ligand concentrations below 7.0 mM, signals of free ligand *E*-**1** began to appear, which is why all studies on the triangle *E*-**T** / lantern *E*-**L** mixture were conducted at a ligand concentration between 7.5–8.5 mM. Similarly, increasing the temperature of the triangle *E*-**T** / lantern *E*-**L** mixture shifted the equilibrium towards the entropically favoured lantern *E*-**L** (SI, Section S3.4). Van't Hoff analysis showed that the enthalpic and entropic contributions of the 3 *E*-**L** ⇌ 2 *E*-**T** equilibrium are $\Delta H = -50.6 \pm 7.7$ kJ mol^{-1} and $\Delta S = -76.3 \pm 29.9$ J K^{-1} mol^{-1}, respectively. These values correspond to a Gibbs free energy difference of $\Delta G = -27.8 \pm 13.0$ kJ mol^{-1}, consistent with a higher thermodynamic stability of triangle *E*-**T**, and an equilibrium constant of $K = 76{,}000 \pm 36{,}000$ M^{-1} at 298 K.

Photoswitching of Pd^{II} capsules

Irradiation of the 78:22 triangle *E*-**T** / lantern *E*-**L** mixture in DMSO-d_6 with 365 nm light produced a single component: a lantern with all ligands in their *Z*-configurations, namely *Z*-**L**, which was characterised by mass spectrometry, NMR, and UV-vis spectroscopy (Figure 1; SI Section S2.7). In ^{1}H NMR, the proton signals of triangle *E*-**T** and lantern *E*-**L** completely disappeared after irradiation with 365 nm light, and a new set of signals appeared, consistent with one half of one ligand environment being unique (Figure 1d, second from top). This suggests all ligands are

identical and possess twofold symmetry, which would align with a lantern-shaped structure. Protons H-a and H-b were high-field shifted by 0.22 and 1.09 ppm, respectively, when comparing lanterns *E*-**L** and *Z*-**L**, indicating H-b to feel the anisotropy of the neighbouring pyrazole ring, which would be expected, if the ligands were in their *Z*-configurations (compare SI, Figures S51 and S55). Additionally, ROESY contacts between protons H-a and H-b align with the *Z*-configurations of ligands in *Z*-**L** (SI, Figure S30). UV-vis spectra after 365 nm irradiation showed a less intense and blue-shifted π→π* absorption band ($\lambda_{\pi\rightarrow\pi^*}$ = 310 nm), along with a new n→π* absorption band ($\lambda_{n\rightarrow\pi^*}$ = 435 nm), which resembles the UV-vis spectrum of ligand **1** in its *Z*-configuration (Figure 1b). This further supports that the ligands in lantern *Z*-**L** are all in their *Z*-states. High-resolution ESI mass spectrometry revealed a series of signals corresponding to the species $[\mathbf{L}-n(BF_4)]^{n+}$ (n = 2, 3, 4), indicating the presence of a lantern-shaped capsule (Figure 1c, second from top). ^{1}H DOSY NMR revealed a diffusion coefficient similar to that of lantern *E*-**L**, indicating a comparable solvodynamic diameter of $d_{Z\text{-}\mathbf{L}}$ = 21.8 Å, suggesting the presence of a lantern-shaped capsule in solution as well. Hence, we conclude that 365 nm light irradiation of the triangle *E*-**T** / lantern *E*-**L** mixture converts the structures to lantern *Z*-**L**.

Besides the main species observed in the ^{1}H NMR spectrum of *Z*-**L**, several sets of minor signals could be observed (SI, Figure S27), which are significantly more pronounced than in lantern *E*-**L** (compare SI, Figure S15). Since the ESI mass spectrum of lantern *Z*-**L** indicates clean formation of lantern *Z*-**L** and ligand **1** is chiral in its *Z*-configuration, we tentatively assume these minor signals are caused by the four additional possible diastereomers of lantern *Z*-**L**.§ We calculated‡ all possible diastereomers and obtained only minor differences in their free energies (approx. 5.0 kJ mol^{-1} or less), which supports our hypothesis (SI, Section S8.3).

Lantern *Z*-**L** demonstrates good thermodynamic stability with a thermal half-life of $\tau_{½}$ = 21 min at 75 °C in DMSO, as determined by ^{1}H NMR spectroscopy. At room temperature, thermal relaxation takes approximately one year to complete (SI, Figure S73). Over that period, several distinguishable intermediates were observed. We tentatively assume these to be the four possible intermediates: *Z,Z,Z,E*-**L**, *cis*- and *trans*-*Z,Z,E,E*-**L**, and *Z,E,E,E*-**L**. These intermediates might occur during the stepwise thermal relaxation of the four ligands from *Z,Z,Z,Z*-**L** to *E,E,E,E*-**L** (i.e. *Z*-**L** → *E*-**L**). Since lanterns *Z*-**L** and *E*-**L** are similar in size, both lanterns are presumably flexible enough to accommodate both *E*- and *Z*-ligands within the same capsule structure, as has been observed for other capsules containing photoswitchable ligands.[38,39,57] By mixing lanterns *E*-**L** and *Z*-**L** in various ratios, we could generate lanterns with mixed

ligand configurations (SI, Section S2.8), although not selectively, resulting in mixtures of species. Nevertheless, these lantern mixtures exhibited comparable ^{1}H NMR signals to those observed during thermal relaxation (SI, Figure S74), supporting our assumption that the intermediates observed during thermal relaxation could be *Z*,*Z*,*Z*,*E*-**L**, *cis*- and *trans*-*Z*,*Z*,*E*,*E*-**L**, and *Z*,*E*,*E*,*E*-**L**. The computed free energy differences[‡] among the five states — *Z*,*Z*,*Z*,*Z*-**L** (*Z*-**L**), *Z*,*Z*,*Z*,*E*-**L**, *Z*,*Z*,*E*,*E*-**L**, *Z*,*E*,*E*,*E*-**L**, and *E*,*E*,*E*,*E*-**L** (*E*-**L**) — further solidify this conclusion. These energy differences show a systematic trend, in which each successive ligand change from *E*- to *Z*-configuration increases the relative energy of the given lantern on average by ΔG = +48 kJ mol^{-1}, closely matching the computed *E*→*Z* isomerisation of a free ligand in solution (+47.4 kJ mol^{-1}).

Irradiating lantern *Z*-**L** with 500 nm light causes all ligands to switch back to their respective *E*-configurations, resulting not in the reformation of the 78:22 triangle *E*-**T** / lantern *E*-**L** mixture, but in the exclusive formation of lantern *E*-**L** as demonstrated by mass spectrometry, ^{1}H NMR, and DOSY NMR spectroscopy (Figure 1; SI Section S4.3). The initial 78:22 triangle *E*-**T** / lantern *E*-**L** mixture could be regained by equilibrating the sample at 22 °C for at least 8 hours, usually overnight. Furthermore, the light-induced switching and subsequent thermal equilibration could be repeated for five cycles with no appreciable photobleaching (Figure 3a; SI, Figure S68).

Since 78:22 *E*-**T** / *E*-**L** → *Z*-**L** switching under 365 nm light and *Z*-**L** → *E*-**L** switching under 500 nm light are not entirely reversible, resulting in the accumulation of the out-of-equilibrium structure lantern *E*-**L**, we propose, that the switching operates via a molecular ratchet mechanism.

An information ratchet

To verify the operation of a molecular ratchet mechanism in the *E*-**T** / *E*-**L** → *Z*-**L** and *Z*-**L** → *E*-**L** switching cycle, we investigated both processes via *in-situ* illumination ^{1}H NMR spectroscopy (Figure 3b; SI, Section S4.3).

During 365 nm light irradiation (LED power reduced to 10%), both triangle *E*-**T** and lantern *E*-**L** are converted to lantern *Z*-**L**. After approximately 15 min, the transformation was complete with a PSS of 100% *Z*-**L** and no further changes were observed. Subsequent irradiation with 500 nm light (LED power reduced to 2%)

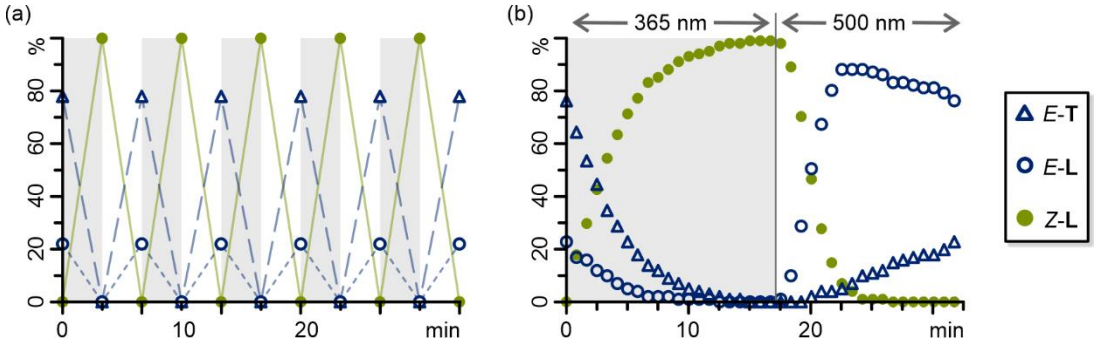

Figure 3. (a) Investigation of switching reversibility by ^{1}H NMR (500 MHz, DMSO-d_6, 298 K) of triangle *E*-**T**, lantern *E*-**L**, and lantern *Z*-**L**. A 78:22 triangle *E*-**T** / lantern *E*-**L** mixture was subjected to alternating light irradiation with 365 nm (5 min) and 500 nm (5 min), respectively. After irradiation with 500 nm light, the sample was left equilibrating for 22 h in an amberised NMR tube wrapped in aluminium foil in an air-conditioned room (22 °C) to allow for equilibration to the 78:22 triangle *E*-**T** / lantern *E*-**L** ratio. No apparent photodegradation was observed after five switching cycles. (b) Changes in composition between triangle *E*-**T**, lantern *E*-**L**, and lantern *Z*-**L** measured by *in-situ* illumination ^{1}H NMR (700 MHz, DMSO-d_6, 298 K). A sample of 78:22 triangle *E*-**T** / lantern *E*-**L** was irradiated with 365 nm light (LED power reduced to 10%) for approx. 17 min to induce *E*→*Z* isomerisation, followed by illumination with 500 nm light (LED power reduced to 2%) for approx. 16 min.

caused the amount of lantern *Z*-**L** to decrease in favour of lantern *E*-**L** rapidly. Lantern *E*-**L**, in turn, instantly begins equilibrating to triangle *E*-**T**, resulting in a maximum population of 11:89 triangle *E*-**T** / lantern *E*-**L** after 3 min of 500 nm light irradiation. Lantern *Z*-**L** is entirely consumed after about 10 min of 500 nm light irradiation, after which the gradual equilibration of lantern *E*-**L** to triangle *E*-**T** can be observed. A maximum population of 2:98 triangle *E*-**T** / lantern *E*-**L** could be reached upon 500 nm light irradiation by increasing the LED power from 10% to 100% (SI, Figure S65). In both processes, no half-assembled structures were observed within the detection limits of NMR spectroscopy (SI, Figures S63 and S64). However, some intermediates could be detected, which we tentatively assign to be the partly switched lantern structures already observed in the thermal relaxation of lantern *Z*-**L**, i.e. *Z*,*Z*,*Z*,*E*-**L**, *Z*,*Z*,*E*,*E*-**L**, and *Z*,*E*,*E*,*E*-**L** (see above and SI, Figure S74). Since these intermediates were minor and could not be clearly identified, we excluded them from the kinetic investigation of the switching cycle.

To further strengthen our hypothesis, that a molecular ratchet mechanism operates within the switching cycle of *E*-**L** + *E*-**T** → *Z*-**L** → *E*-**L** ⇌ *E*-**T**, we tentatively modelled the kinetics of this intricate process to compare the orders of magnitude of the rate-limiting steps using two independent kinetic models (Scheme 2; SI, Section S5.2).

The kinetic constants of the rate-determining steps of the switching cycle obtained by both models support our previous qualitative observations, demonstrating the molecular information ratchet mechanism at work (Scheme 2, values of Model II provided; SI, Section S5.2):

(i) Under 365 nm light irradiation, both triangle *E*-**T** and lantern *E*-**L** switch to lantern *Z*-**L** with comparable rate constants ($k_{E\text{-}\mathbf{T}\rightarrow Z\text{-}\mathbf{L}} = 4 \cdot 10^{-3}$ s^{-1}; $k_{E\text{-}\mathbf{L}\rightarrow Z\text{-}\mathbf{L}} = 10^{-4}$ s^{-1}).

(ii) When irradiating lantern *Z*-**L** with 500 nm light, the slowest step is the *Z*→*E* switching, which is, by definition, the same for both pathways ($k_{Z\text{-}\mathbf{L}} \approx k_{Z\text{-}\mathbf{L}} = 8 \cdot 10^{-3}$ s^{-1}; SI, Figure S75). The switched state then rapidly rearranges to lantern *E*-**L** with a rate constant of $k_{Z\text{-}\mathbf{L}\rightarrow E\text{-}\mathbf{L}} = 10^{3}$ M^{-1}s^{-1}, while the pathway from lantern *Z*-**L** to triangle *E*-**T** is negligible ($k_{Z\text{-}\mathbf{L}\rightarrow E\text{-}\mathbf{T}} = 5 \cdot 10^{-5}$ M^{-1}s^{-1}).

(iii) Reformation of triangle *E*-**T** predominantly occurs via the equilibrium between triangle *E*-**T** and lantern *E*-**L**, which is slow at room temperature.

Hence, this molecular information ratchet exploits the kinetic asymmetry in both the thermal and photochemical *Z*-**L**→*E*-**L** and *Z*-**L**→*E*-**T** isomerisations (and subsequent rearrangement) and can therefore be used to accumulate the out-of-equilibrium structure *E*-**L**.

To fully elucidate the thermodynamics of the molecular ratchet, we calculated[‡] the energy difference between lantern *Z*-**L** and lantern *E*-**L** using a model system derived from the crystal structure of lantern *E*-**L**. This model system features the respective lantern with its cavity occupied by four DMSO solvent molecules. Additionally, two BF_4^- anions coordinate to the Pd^{II} cations' octahedral positions outside the lanterns

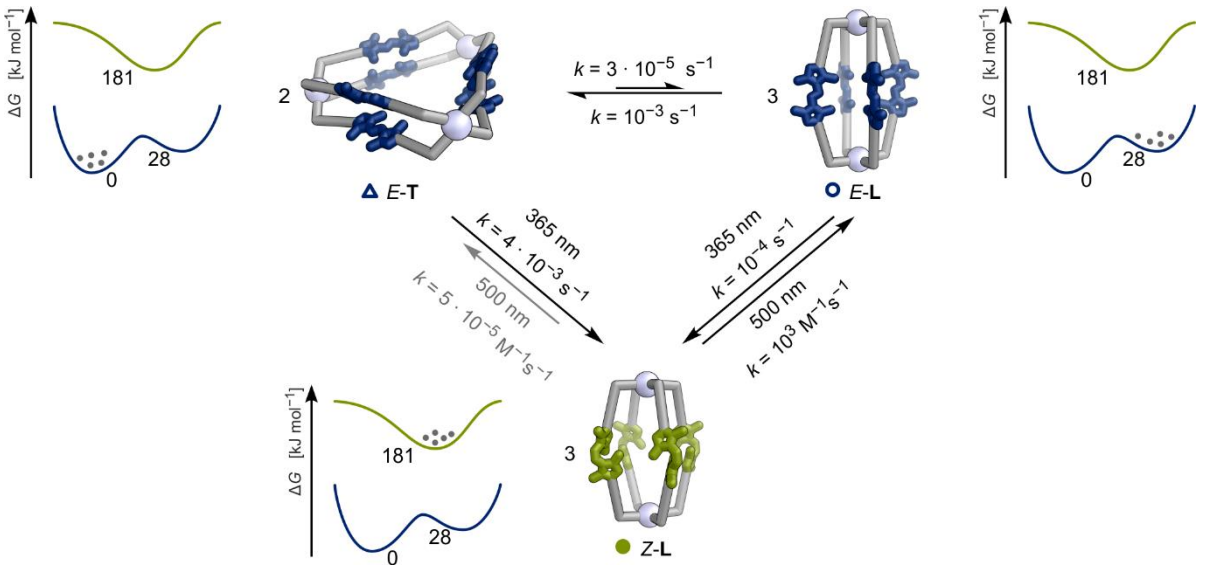

Scheme 2. Schematic representation of the molecular information ratchet governing the triangle *E*-**T** / lantern *E*-**L** → lantern *Z*-**L** switching cycle, with the rate constants of the respective rate-determining steps obtained from one of the kinetic models indicated alongside the reaction arrows. Next to each state, a schematic diagram of the potential energy surface and its population is illustrated along with the respective energies — both experimental and computed — of the three states (*Z*-states: blue; *E*-states: green).

(SI, Section S8.6). From this model system, a free energy difference of ΔG = −181.2 kJ mol^{-1} was obtained. Along with the energy difference between triangle *E*-**T** and lantern *E*-**L** of ΔG = −27.8 ± 13 kJ mol^{-1} determined via Van't Hoff analysis, this completes the thermodynamic picture of the ratchet.

Crucially, the molecular ratchet operates autonomously under continuous white light irradiation, as minor proportions of both the *E*- and *Z*-states are constantly excited by the white light spectrum (SI, Figure S93). The nature of the molecular ratchet then causes the accumulation of the thermodynamically less stable lantern *E*-**L** (Figure 4; SI, Section S6). White-light irradiation of the 78:22 triangle *E*-**T** / lantern *E*-**L** mixture *in situ* in the ^{1}H NMR spectrometer for 5.5 h results in a triangle *E*-**T** / lantern *E*-**L** ratio of 34:66, indicating a threefold increase in lantern *E*-**L** population. After leaving the sample at 22 °C in the dark for at least 8 hours, the initial 78:22 triangle *E*-**T** / lantern *E*-**L** mixture is restored. The same threefold increase in lantern *E*-**L** population can be reached by exposing the sample to sunlight for 7 hours, effectively converting sunlight into chemical energy.

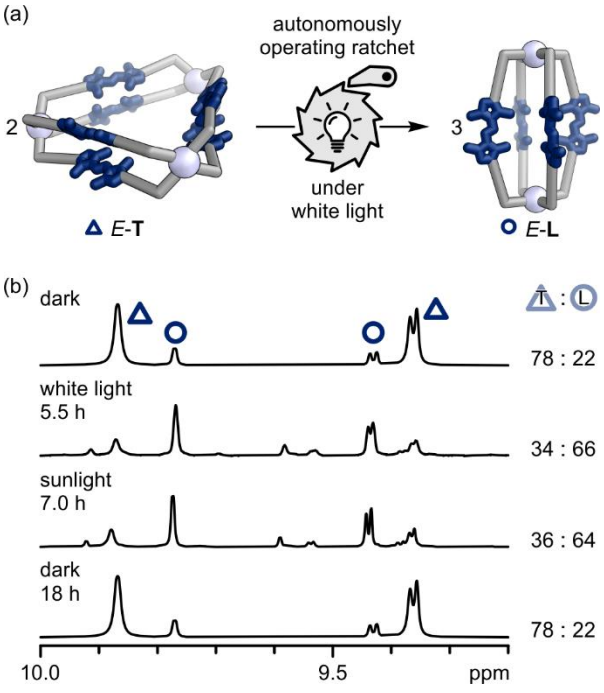

Figure 4. (a) Continuous exposure to white light powers the ratchet autonomously, leading to the formation of lantern *E*-**L**. (b) ^{1}H NMR spectra (700 MHz, DMSO-d_6, 298 K) of the 78:22 triangle *E*-**T** / lantern *E*-**L** mixture under light exclusion, after *in-situ* illumination with white light for 5.5 h (*E*-**T** / *E*-**L** 34:66), after exposing the sample to sunlight on a sunny spring day for 7 h (*E*-**T** / *E*-**L** 36:64), and after equilibrating the sample under light exclusion at 22 °C for 22 h (*E*-**T** / *E*-**L** 78:22; top to bottom).

Conclusion

In summary, azobispyrazol-based ligand **1** is an excellent photoswitch, exhibiting near-quantitative *E*→*Z* and *Z*→*E* conversions. Due to the conformational flexibility provided by the five-membered pyrazole rings, the ligand can adopt two conformations with coordination-vector bite angles of 0° and 60°, respectively, which both lead to metallo-supramolecular architectures: a double-walled triangle *E*-**T** and a lantern *E*-**L**. Since these structures require different ligand coordination vector bite angles (60° and 0°, respectively), they are usually not accessible from the same ligand structure.

Photoswitching of the equilibrated 78:22 triangle *E*-**T** / lantern *E*-**L** mixture occurs via a molecular ratchet mechanism, which we have elucidated in terms of both kinetics and thermodynamics, with the aid of quantum chemistry-based calculations: irradiation with 365 nm light affords lantern *Z*-**L** exclusively, which then switches back to lantern *E*-**L** exclusively. Triangle *E*-**T** subsequently forms from lantern *E*-**L** through thermodynamic equilibration. Crucially, the molecular ratchet operates autonomously under white light, effectively converting sunlight into an out-of-equilibrium structure, i.e. chemical energy, and temporarily storing it.

After developing molecular ratchet mechanisms, the next step will be to couple their energy-releasing step to molecular machines, thereby harnessing the stored energy rather than releasing it as heat.

Methods

Further details regarding the methods can be found in the supplemental information. The authors have cited additional references within the supplemental information.[32,46,48,49,54–56,58–82]

Resource availability

Lead contact

Requests for further information and resources should be directed to the lead contact, Larissa K. S. von Krbek (larissa.vonkrbek@uni-bonn.de).

Data and code availability

The accession numbers for the crystal structures reported in this paper are: CCDC-2488074 (*E*-**1**) and CCDC-2488075 (*E*-**L**). These data can be obtained free of charge from the CCDC at http://www.ccdc.cam.ac.uk/data_request/cif.

Acknowledgements

This work is supported by the Fonds der Chemischen Industrie (FCI, Liebig Fellowship) and the German Research Foundation (DFG; Emmy Noether Programme, 446317932). L. P. L. thanks U. Weynand and Dr. S. Nozinovic for support with NMR measurements. M. J. N. and L. K. S. v. K. thank Dr B. M. W. Roberts and Dr. R. J. Mayer for the helpful discussions regarding the fitting of kinetic data. B. B. and S. G. gratefully acknowledge the access to the Marvin cluster of the University of Bonn. G. S. thanks Prof. Dr. A. C. Filippou for providing X-ray infrastructure.

Author contributions

L. P. L.: synthesis, characterisation, photoswitching studies. B. B.: computational studies. M. J. N.: fitting of kinetic data. G. S.: X-ray crystallography. S. G.: supervision. L. K. S. v. K.: project conception and supervision.

Declaration of interests

The authors declare no conflicts of interest.

References

‡ All computed lantern structures were conformationally sampled using the CREST[54] program at the GFN2-xTB [ALPB: DMSO][48,49] level of theory. Using the ORCA software package,[78] the lowest conformers were optimised at the ωB97X-3c [CPCM: DMSO][55,64] level of theory, while the SMD[82] model was used for the final single-point calculations. Thermal corrections were computed at the GFN2-xTB [ALPB: DMSO] level of theory employing the mRRHO approximation,[77] using the xtb software package.[66,77,83]

§ Although *Z*-**1** is chiral and *Z*-**L** exists as a mixture of diastereomers, only minor shifts and no signal splitting were observed upon addition of the chiral shifting reagent Δ-TRISPHAT (SI, Figure S27). This suggests that the diastereomers are likely

the two *meso* forms or that their interaction with Δ-TRISPHAT occurs on fast exchange on the NMR timescale.

[1] T. Sangchai, S. A. Shehimy, E. Penocchio, G. Ragazzon, 'Artificial Molecular Ratchets: Tools Enabling Endergonic Processes' *Angew. Chem. Int. Ed.* **2023**, *62*, e202309501.

[2] S. Borsley, D. A. Leigh, B. M. W. Roberts, 'Molecular Ratchets and Kinetic Asymmetry: Giving Chemistry Direction' *Angew. Chem. Int. Ed.* **2024**, *63*, e202400495.

[3] R. D. Astumian, 'Trajectory and Cycle-Based Thermodynamics and Kinetics of Molecular Machines: The Importance of Microscopic Reversibility' *Acc. Chem. Res.* **2018**, *51*, 2653–2661.

[4] A. W. Heard, S. M. Goldup, 'Simplicity in the Design, Operation, and Applications of Mechanically Interlocked Molecular Machines' *ACS Cent. Sci.* **2020**, *6*, 117–128.

[5] E. R. Kay, D. A. Leigh, F. Zerbetto, 'Synthetic Molecular Motors and Mechanical Machines' *Angew. Chem. Int. Ed.* **2006**, *46*, 72–191.

[6] M. Kathan, S. Crespi, N. O. Thiel, D. L. Stares, D. Morsa, J. de Boer, G. Pacella, T. van den Enk, P. Kobauri, G. Portale, C. A. Schalley, B. L. Feringa, 'A light-fuelled nanoratchet shifts a coupled chemical equilibrium' *Nat. Nanotechnol.* **2022**, *17*, 159–165.

[7] R. D. Astumian, I. Derényi, 'Fluctuation driven transport and models of molecular motors and pumps' *Eur. Biophys. J.* **1998**, *27*, 474–489.

[8] M. Kathan, F. Eisenreich, C. Jurissek, A. Dallmann, J. Gurke, S. Hecht, 'Light-driven molecular trap enables bidirectional manipulation of dynamic covalent systems' *Nat. Chem.* **2018**, *10*, 1031–1036.

[9] K. Das, L. Gabrielli, L. J. Prins, 'Chemically Fueled Self-Assembly in Biology and Chemistry' *Angew. Chem. Int. Ed.* **2021**, *60*, 20120–20143.

[10] I. Aprahamian, S. M. Goldup, 'Non-equilibrium Steady States in Catalysis, Molecular Motors, and Supramolecular Materials: Why Networks and Language Matter' *J. Am. Chem. Soc.* **2023**, *145*, 14169–14183.

[11] R. D. Astumian, 'Microscopic reversibility as the organizing principle of molecular machines' *Nat. Nanotechnol.* **2012**, *7*, 684–688.

[12] M. Alvarez-Pérez, S. M. Goldup, D. A. Leigh, A. M. Z. Slawin, 'A Chemically-Driven Molecular Information Ratchet' *J. Am. Chem. Soc.* **2008**, *130*, 1836–1838.

[13] V. Serreli, C.-F. Lee, E. R. Kay, D. A. Leigh, 'A molecular information ratchet' *Nature* **2007**, *445*, 523–527.

[14] R. E. Spinney, M. Prokopenko, D. Chu, 'Information ratchets exploiting spatially structured information reservoirs' *Phys. Rev. E* **2018**, *98*, 022124.

[15] E. Liu, S. Cherraben, L. Boulo, C. Troufflard, B. Hasenknopf, G. Vives, M. Sollogoub, 'A molecular information ratchet using a cone-shaped macrocycle' *Chem* **2023**, *9*, 1147–1163.

[16] E. Liu, D. Daou, B. Hasenknopf, G. Vives, M. Sollogoub, 'Not going back: Unidirectional movement by intramolecular one-way ratcheting of functionalized cyclodextrin' *Chem* **2025**, 102623.

[17] J. A. Berrocal, C. Biagini, L. Mandolini, S. D. Stefano, 'Coupling of the Decarboxylation of 2-Cyano-2-phenylpropanoic Acid to Large-Amplitude Motions: A Convenient Fuel for an Acid–Base-Operated Molecular Switch' *Angew. Chem. Int. Ed.* **2016**, *55*, 6997–7001.

[18] S. Erbas-Cakmak, S. D. P. Fielden, U. Karaca, D. A. Leigh, C. T. McTernan, D. J. Tetlow, M. R. Wilson, 'Rotary and linear molecular motors driven by pulses of a chemical fuel' *Science* **2017**, *358*, 340–343.

[19] S. Erbas-Cakmak, D. A. Leigh, C. T. McTernan, A. L. Nussbaumer, 'Artificial Molecular Machines' *Chem. Rev.* **2015**, *115*, 10081–10206.

[20] M. A. Watson, S. L. Cockroft, 'Man-made molecular machines: membrane bound' *Chem. Soc. Rev.* **2016**, *45*, 6118–6129.

[21] G. Ragazzon, M. Malferrari, A. Arduini, A. Secchi, S. Rapino, S. Silvi, A. Credi, 'Autonomous Non-Equilibrium Self-Assembly and Molecular Movements Powered by Electrical Energy**' *Angew. Chem. Int. Ed.* **2023**, *62*, e202214265.

[22] S. J. Wezenberg, 'Photoswitchable molecular tweezers: isomerization to control substrate binding, and what about vice versa ?' *Chem. Commun.* **2022**, *58*, 11045–11058.

[23] D.-H. Qu, Q.-C. Wang, Q.-W. Zhang, X. Ma, H. Tian, 'Photoresponsive Host–Guest Functional Systems' *Chem. Rev.* **2015**, *115*, 7543–7588.

[24] R. G. DiNardi, A. O. Douglas, R. Tian, J. R. Price, M. Tajik, W. A. Donald, J. E. Beves, 'Visible-Light-Responsive Self-Assembled Complexes: Improved Photoswitching Properties by Metal Ion Coordination**' *Angew. Chem. Int. Ed.* **2022**, *61*, e202205701.

[25] R. G. DiNardi, S. Rasheed, S. S. Capomolla, M. H. Chak, I. A. Middleton, L. K. Macreadie, J. P. Violi, W. A. Donald, P. J. Lusby, J. E. Beves, 'Photoswitchable Catalysis by a Self-Assembled Molecular Cage' *J. Am. Chem. Soc.* **2024**, *146*, 21196–21202.

[26] M. Ovalle, M. Kathan, R. Toyoda, C. N. Stindt, S. Crespi, B. L. Feringa, 'Light-Fueled Transformations of a Dynamic Cage-Based Molecular System' *Angew. Chem. Int. Ed.* **2023**, *62*, e202214495.

[27] R. I. Petrikat, J. Hornbogen, M. J. P. Schmitt, E. Resmann, C. Wiedemann, N. I. Dilmen, H. Schneider, A. M. Pick, C. Riehn, R. Diller, S. Becker, 'A Photoswitchable Metallocycle Based on Azobenzene: Synthesis, Characterization, and Ultrafast Dynamics' *Chem. A Eur. J.* **2024**, *30*, e202400205.

[28] J. Gemen, J. R. Church, T.-P. Ruoko, N. Durandin, M. J. Białek, M. Weißenfels, M. Feller, M. Kazes, M. Odaybat, V. A. Borin, R. Kalepu, Y. Diskin-Posner, D. Oron, M. J. Fuchter, A. Priimagi, I. Schapiro, R. Klajn, 'Disequilibrating azobenzenes by visible-light sensitization under confinement' *Science* **2023**, *381*, 1357–1363.

[29] I. Neira, C. Taticchi, F. Nicoli, M. Curcio, M. D. Garcia, C. Peinador, S. Silvi, M. Baroncini, A. Credi, 'Light-driven ratcheted formation of diastereomeric host-guest systems' *Chem* **2025**, *11*, 102375.

[30] D. Hugenbusch, M. Lehr, J. von Glasenapp, A. J. McConnell, R. Herges, 'Light-Controlled Destruction and Assembly: Switching between Two Differently Composed Cage-Type Complexes' *Angew. Chem. Int. Ed.* **2023**, *62*, e202212571.

[31] H. Lee, J. Tessarolo, D. Langbehn, A. Baksi, R. Herges, G. H. Clever, 'Light-Powered Dissipative Assembly of Diazocine Coordination Cages' *J. Am. Chem. Soc.* **2022**, *144*, 3099–3105.

[32] M. J. Notheis, G. Schnakenburg, L. K. S. von Krbek, 'Light-Driven Ratchet Mechanism Accelerates Regioselective Metal-Cation Exchange in a Heterobimetallic Helicate' *Angew. Chem. Int. Ed.* **2025**, e202508952.

[33] C. Stuckhardt, D. Roke, W. Danowski, E. Otten, S. J. Wezenberg, B. L. Feringa, 'A chiral self-sorting photoresponsive coordination cage based on overcrowded alkenes' *Beilstein J. Org. Chem.* **2019**, *15*, 2767–2773.

[34] D. Villarón, S. J. Wezenberg, 'Stiff-Stilbene Photoswitches: From Fundamental Studies to Emergent Applications' *Angew. Chem. Int. Ed.* **2020**, *59*, 13192–13202.

[35] J. Wu, J. L. Greenfield, 'Harnessing light to drive a non-photoresponsive reaction out of equilibrium' *Chem* **2025**, 102579.

[36] J. Wu, L. Kreimendahl, J. L. Greenfield, 'Switching Sides: Regiochemistry and Functionalization Dictate the Photoswitching Properties of Imines' *Angewandte Chemie International Edition* **2025**, *64*, e202415464.

[37] M. Han, R. Michel, B. He, Y. Chen, D. Stalke, M. John, G. H. Clever, 'Light-Triggered Guest Uptake and Release by a Photochromic Coordination Cage' *Angew. Chem. Int. Ed.* **2013**, *52*, 1319–1323.

[38] R. Li, M. Han, J. Tessarolo, J. J. Holstein, J. Lübben, B. Dittrich, C. Volkmann, M. Finze, C. Jenne, G. H. Clever, 'Successive Photoswitching and Derivatization Effects in Photochromic Dithienylethene-Based Coordination Cages' *ChemPhotoChem* **2019**, *3*, 378–383.

[39] R.-J. Li, Julian. J. Holstein, W. G. Hiller, J. Andréasson, G. H. Clever, 'Mechanistic Interplay between Light Switching and Guest Binding in Photochromic [Pd2Dithienylethene4] Coordination Cages' *J. Am. Chem. Soc.* **2019**, *141*, 2097–2103.

[40] A. Carbonell, I. Izquierdo, D. B. G. Ríos, G. Norjmaa, G. Ujaque, A. J. Martínez-Martínez, U. Pischel, 'Synthesis, Characterization, and Photochemistry of a Ga2L3 Coordination Cage with Dithienylethene-Catecholate Ligands' *Inorg. Chem.* **2024**, *63*, 19872–19884.

[41] E. Benchimol, J. Tessarolo, G. H. Clever, 'Photoswitchable coordination cages' *Nat. Chem.* **2024**, *16*, 13–21.

[42] S. Millan, J. Nasir, B. Gil-Hernández, T.-O. Knedel, B. Moll, I. Boldog, O. Weingart, J. S. auf der Günne, C. Janiak, 'Solid-State Landscape of 4,4′-Azobis(3,5-dimethyl-1H-pyrazole) with the Isolation of Conformer-Dependent Polymorphs' *Cryst. Growth Des.* **2020**, *20*, 2721–2733.

[43] A. Gonzalez, M. Odaybat, M. Le, J. L. Greenfield, A. J. P. White, X. Li, M. J. Fuchter, G. G. D. Han, 'Photocontrolled Energy Storage in Azobispyrazoles with Exceptionally Large Light Penetration Depths' *J. Am. Chem. Soc.* **2022**, *144*, 19430–19436.

[44] Y. He, Z. Shangguan, Z. Zhang, M. Xie, C. Yu, T. Li, 'Azobispyrazole Family as Photoswitches Combining (Near-) Quantitative Bidirectional Isomerization and Widely Tunable Thermal Half-Lives from Hours to Years**' *Angew. Chem. Int. Ed.* **2021**, *60*, 16539–16546.

[45] Y. He, T. Dang, A. G. Leach, Z.-Y. Zhang, T. Li, 'Photoswitchable Azobispyrazole Crystals Achieving Near-Quantitative Crystalline-State Bidirectional E ⇆ Z Conversions' *J. Am. Chem. Soc.* **2024**, *146*, 29237–29244.

[46] S. Millan, B. Gil-Hernández, E. Hastürk, A. Schmitz, C. Janiak, 'A 2D Zinc Coordination Polymer Built from the Mono-deprotonated 4,4′-Azobis(3,5-dimethyl-1H-pyrazole) Ligand' *Z. für Anorg. Allg. Chem.* **2018**, *644*, 1311–1316.

[47] D. Pirone, N. A. G. Bandeira, B. Tylkowski, E. Boswell, R. Labeque, R. G. Valls, M. Giamberini, 'Contrasting Photo-Switching Rates in Azobenzene Derivatives: How the Nature of the Substituent Plays a Role' *Polymers* **2020**, *12*, 1019.

[48] S. Ehlert, M. Stahn, S. Spicher, S. Grimme, 'Robust and Efficient Implicit Solvation Model for Fast Semiempirical Methods' *J. Chem. Theory Comput.* **2021**, *17*, 4250–4261.

[49] C. Bannwarth, S. Ehlert, S. Grimme, 'GFN2-xTB—An Accurate and Broadly Parametrized Self-Consistent Tight-Binding Quantum Chemical Method with Multipole Electrostatics and Density-Dependent Dispersion Contributions' *J. Chem. Theory Comput.* **2019**, *15*, 1652–1671.

[50] S. S. Mishra, S. Krishnaswamy, D. K. Chand, 'Neighboring Cage Participation for Assisted Construction of Self-Assembled Multicavity Conjoined Cages and Augmented Guest Binding' *Journal of the American Chemical Society* **2024**, *146*, 4473–4488.

[51] S. M. Jansze, K. Severin, 'Palladium-Based Metal–Ligand Assemblies: The Contrasting Behavior upon Addition of Pyridine or Acid' *J. Am. Chem. Soc.* **2019**, *141*, 815–819.

[52] G. H. Clever, P. Punt, 'Cation–Anion Arrangement Patterns in Self-Assembled Pd2L4 and Pd4L8 Coordination Cages' *Acc. Chem. Res.* **2017**, *50*, 2233–2243.

[53] M. R. Black, S. Bhattacharyya, S. P. Argent, B. S. Pilgrim, 'Structural Transformations of Metal–Organic Cages through Tetrazine-Alkene Reactivity' *J. Am. Chem. Soc.* **2024**, *146*, 28233–28241.

[54] P. Pracht, S. Grimme, C. Bannwarth, F. Bohle, S. Ehlert, G. Feldmann, J. Gorges, M. Müller, T. Neudecker, C. Plett, S. Spicher, P. Steinbach, P. A. Wesołowski, F. Zeller, 'CREST—A program for the exploration of low-energy molecular chemical space' *J. Chem. Phys.* **2024**, *160*, 114110.

[55] M. Müller, A. Hansen, S. Grimme, 'ωB97X-3c: A composite range-separated hybrid DFT method with a molecule-optimized polarized valence double-ζ basis set' *J. Chem. Phys.* **2023**, *158*, 014103.

[56] P. Pracht, 'Conformational Pruning via the Permutation Invariant Root-Mean-Square Deviation of Atomic Positions' *J. Chem. Inf. Model.* **2025**, *65*, 4501–4511.

[57] M. B. Tipping, L. Pruñonosa Lara, A. B. Solea, L. K. S. von Krbek, M. D. Ward, 'Photoswitching of Co(II)-based coordination cages containing azobenzene backbones' *Chem. Sci.* **2024**, *15*, 8488–8499.

[58] M. J. Notheis, V. Sahiti, V. Prangenberg, J. S. Kruse, L. K. S. von Krbek, '2,8-Dihalogenated Diazocines: Versatile Reactants for Functionalized Photoswitches' *Synlett* **2025**, *36*, 1569–1573.

[59] S. Takahashi, Y. Sasaki, S. Hiraoka, H. Sato, 'A stochastic model study on the self-assembly process of a Pd 2 L 4 cage consisting of rigid ditopic ligands' *Phys. Chem. Chem. Phys.* **2018**, *21*, 6341–6347.

[60] M. D. Hanwell, D. E. Curtis, D. C. Lonie, T. Vandermeersch, E. Zurek, G. R. Hutchison, 'Avogadro: an advanced semantic chemical editor, visualization, and analysis platform' *J. Cheminformatics* **2012**, *4*, 17.

[61] P. V. D. Sluis, A. L. Spek, 'BYPASS: an effective method for the refinement of crystal structures containing disordered solvent regions' *Acta Crystallogr. Sect. A* **1990**, *46*, 194–201.

[62] S. Hoops, S. Sahle, R. Gauges, C. Lee, J. Pahle, N. Simus, M. Singhal, L. Xu, P. Mendes, U. Kummer, 'COPASI—a COmplex PAthway SImulator' *Bioinformatics* **2006**, *22*, 3067–3074.

[63] G. M. Sheldrick, 'Crystal structure refinement with SHELXL' *Acta Crystallogr. Sect. C: Struct. Chem.* **2015**, *71*, 3–8.

[64] M. Cossi, N. Rega, G. Scalmani, V. Barone, 'Energies, structures, and electronic properties of molecules in solution with the C-PCM solvation model' *J. Comput. Chem.* **2003**, *24*, 669–681.

[65] S. Grimme, 'Exploration of Chemical Compound, Conformer, and Reaction Space with Meta-Dynamics Simulations Based on Tight-Binding Quantum Chemical Calculations' *J. Chem. Theory Comput.* **2019**, *15*, 2847–2862.

[66] C. Bannwarth, E. Caldeweyher, S. Ehlert, A. Hansen, P. Pracht, J. Seibert, S. Spicher, S. Grimme, 'Extended tight-binding quantum chemistry methods' *Wiley Interdiscip. Rev.: Comput. Mol. Sci.* **2021**, *11*, DOI 10.1002/wcms.1493.

[67] C. Feldmeier, H. Bartling, E. Riedle, R. M. Gschwind, 'LED based NMR illumination device for mechanistic studies on photochemical reactions – Versatile and simple, yet surprisingly powerful' *J. Magn. Reson.* **2013**, *232*, 39–44.

[68] Y. Ji, D. A. DiRocco, J. Kind, C. M. Thiele, R. M. Gschwind, M. Reibarkh, 'LED-Illuminated NMR Spectroscopy: A Practical Tool for Mechanistic Studies of Photochemical Reactions' *ChemPhotoChem* **2019**, *3*, 984–992.

[69] T. Tateishi, T. Kojima, S. Hiraoka, 'Multiple Pathways in the Self-Assembly Process of a Pd4L8 Coordination Tetrahedron' *Inorg. Chem.* **2018**, *57*, 2686–2694.

[70] T. Tateishi, S. Takahashi, A. Okazawa, V. Martí-Centelles, J. Wang, T. Kojima, P. J. Lusby, H. Sato, S. Hiraoka, 'Navigated Self-Assembly of a Pd2L4 Cage by Modulation of an Energy Landscape under Kinetic Control' *J. Am. Chem. Soc.* **2019**, *141*, 19669–19676.

[71] O. V. Dolomanov, L. J. Bourhis, R. J. Gildea, J. A. K. Howard, H. Puschmann, 'OLEX2: a complete structure solution, refinement and analysis program' *J. Appl. Crystallogr.* **2009**, *42*, 339–341.

[72] M. S. Maier, K. Hüll, M. Reynders, B. S. Matsuura, P. Leippe, T. Ko, L. Schäffer, D. Trauner, 'Oxidative Approach Enables Efficient Access to Cyclic Azobenzenes' *J. Am. Chem. Soc.* **2019**, *141*, 17295–17304.

[73] S. Grimme, A. Hansen, S. Ehlert, J.-M. Mewes, 'r2SCAN-3c: A "Swiss army knife" composite electronic-structure method' *J. Chem. Phys.* **2021**, *154*, 064103.

[74] B. A. Inc., *SADABS-2016/2*, Madison, Wisconsin, USA, **2016**.

[75] S. Kai, T. Tateishi, T. Kojima, S. Takahashi, S. Hiraoka, 'Self-Assembly of a Pd4L8 Double-Walled Square Takes Place through Two Kinds of Metastable Species' *Inorg. Chem.* **2018**, *57*, 13083–13086.

[76] G. M. Sheldrick, 'SHELXT– Integrated space-group and crystal-structure determination' *Acta Crystallogr. Sect. A* **2015**, *71*, 3–8.

[77] S. Spicher, S. Grimme, 'Single-Point Hessian Calculations for Improved Vibrational Frequencies and Rigid-Rotor-Harmonic-Oscillator Thermodynamics' *J. Chem. Theory Comput.* **2021**, *17*, 1701–1714.

[78] F. Neese, 'Software update: The ORCA program system—Version 5.0' *Wiley Interdiscip. Rev.: Comput. Mol. Sci.* **2022**, *12*, DOI 10.1002/wcms.1606.

[79] S. Ghosh, C. Eschen, N. Eleya, A. Staubitz, 'Synthesis of a Series of 12-Membered Azobenzene Macrocycles and Tuning of the Half-Life of the Thermal Z–E Isomerization' *J. Org. Chem.* **2023**, *88*, 3372–3377.

[80] T. Tateishi, S. Kai, Y. Sasaki, T. Kojima, S. Takahashi, S. Hiraoka, 'Two dominant self-assembly pathways to a Pd 3 L 6 double-walled triangle' *Chem. Commun.* **2018**, *54*, 7758–7761.

[81] E. F. Pettersen, T. D. Goddard, C. C. Huang, E. C. Meng, G. S. Couch, T. I. Croll, J. H. Morris, T. E. Ferrin, 'UCSF ChimeraX: Structure visualization for researchers, educators, and developers' *Protein Sci.* **2021**, *30*, 70–82.

[82] A. V. Marenich, C. J. Cramer, D. G. Truhlar, 'Universal Solvation Model Based on Solute Electron Density and on a Continuum Model of the Solvent Defined by the Bulk Dielectric Constant and Atomic Surface Tensions' *J. Phys. Chem. B* **2009**, *113*, 6378–6396.

[83], 'GitHub - grimme-lab/xtb: Semiempirical Extended Tight-Binding Program Package', can be found under https://github.com/grimme-lab/xtb(accessed 12 August 2025), **n.d.**

Supporting information

for

White-light powered autonomous molecular ratchet drives Pd^{II} capsules out of equilibrium

Lidón Pruñonosa Lara,[a] Benedikt Bädorf,[b] Maximilian J. Notheis,[a] Gregor Schnakenburg,[c] Stefan Grimme,[b] and Larissa K. S. von Krbek*[a]

a. Kekulé-Institut für Organische Chemie und Biochemie, Rheinische Friedrich-WilhelmsUniversität Bonn, Gerhard-Domagk-Str. 1, 53121 Bonn, Germany.
E-mail: larissa.vonkrbek@uni-bonn.de

b. Mulliken Center for Theoretical Chemistry, Rheinische Friedrich-Wilhelms-Universität Bonn, Beringstr. 4, 53115 Bonn, Germany

c. Institut für Anorganische Chemie, Rheinische Friedrich-Wilhelms-Universität Bonn, Gerhard-Domagk-Str. 1, 53121 Bonn

Table of Contents

S1 General information

Reagents and materials. Commercial solvents and reagents were obtained from the following suppliers and used without further purification unless specified otherwise: abcr, Acros Organics, Alfa Aesar, BLD-Pharm, Merck, Sigma Aldrich, TCI, Thermo Fisher Scientific.

Column chromatography. Column chromatography was carried out using a puriFlash 5.020 (Interchim) flash chromatography machine with PuriFlash 15 µm Si HP (Interchim) flash cartridges.

NMR spectroscopy. All NMR spectroscopic measurements were carried out using 400 MHz, 500 MHz or 700 MHz spectrometers (Bruker Avance I 400, Bruker Avance I 500, Bruker Avance III HD Prodigy 500, Bruker Avance III HD Ascend 700). ^{1}H and ^{13}C NMR spectra are referenced to the residual solvent peak for CD_3CN (^{1}H: 1.94 ppm, ^{13}C: 1.32 ppm), CD_2Cl_2 (^{1}H: 5.32 ppm, ^{13}C: 53.5 ppm), DMSO-d_6 (^{1}H: 2.50 ppm, ^{13}C: 39.52 ppm) or DMF-d_7 (^{1}H: 8.03 ppm, ^{13}C: 163.15 ppm). NMR signals are reported in terms of chemical shift (δ) in ppm, relative integral, multiplicity, coupling constants (in Hz), and assignment, in that order. The following abbreviations for multiplicity are used: s, singlet; d, doublet. Spectra were processed (phase and baseline corrections, integration, peak analysis), evaluated, and plotted using MestReNova 14.2.1 (Mestrelab) and TopSpin 4.1.3 (BrukerBioSpin). All processing operations were manually checked to ensure that the processed spectra accurately represented the raw data.

Mass spectrometry. Mass spectra were acquired using an Orbitrap XL (Thermo Fischer Scientific) and evaluated and plotted using XCalibur 4.2 (Thermo Fischer Scientific).

UV-vis spectroscopy. All UV-vis spectroscopy measurements were carried out using a Cary 60 (Agilent) utilising a flash lamp style spectrometer with a temperature-controlled sample holder.

Elemental analysis. Elemental analysis was carried out using a Vario Micro Cube (Elementar). Approximately 2 mg of the compound were used, and all measurements were carried out in triplicate.

Light sources. All illumination experiments with 500 nm and *in-situ* illumination experiments (NMR and UV-vis) and were carried out using Prizmatrix fibre collimated LEDs (Table S1, for further details see Section S4). Illumination experiments (NMR

and MS) with 365 nm were carried out using a portable, self-built light source incorporating a commercial 365 nm LED chip (Nichia, NCSU275(T)-U365, 1.8 W).

Table S1. Light output of fibre collimated LEDs.

λ [nm]	**310**	**325**	**365**	**390**	**405**	**430**	**450**	**500**	**white**
Output power [mW] (1 m optical fibre)	1	8.6	170	220	260	160	440	165	74

S2 Synthesis

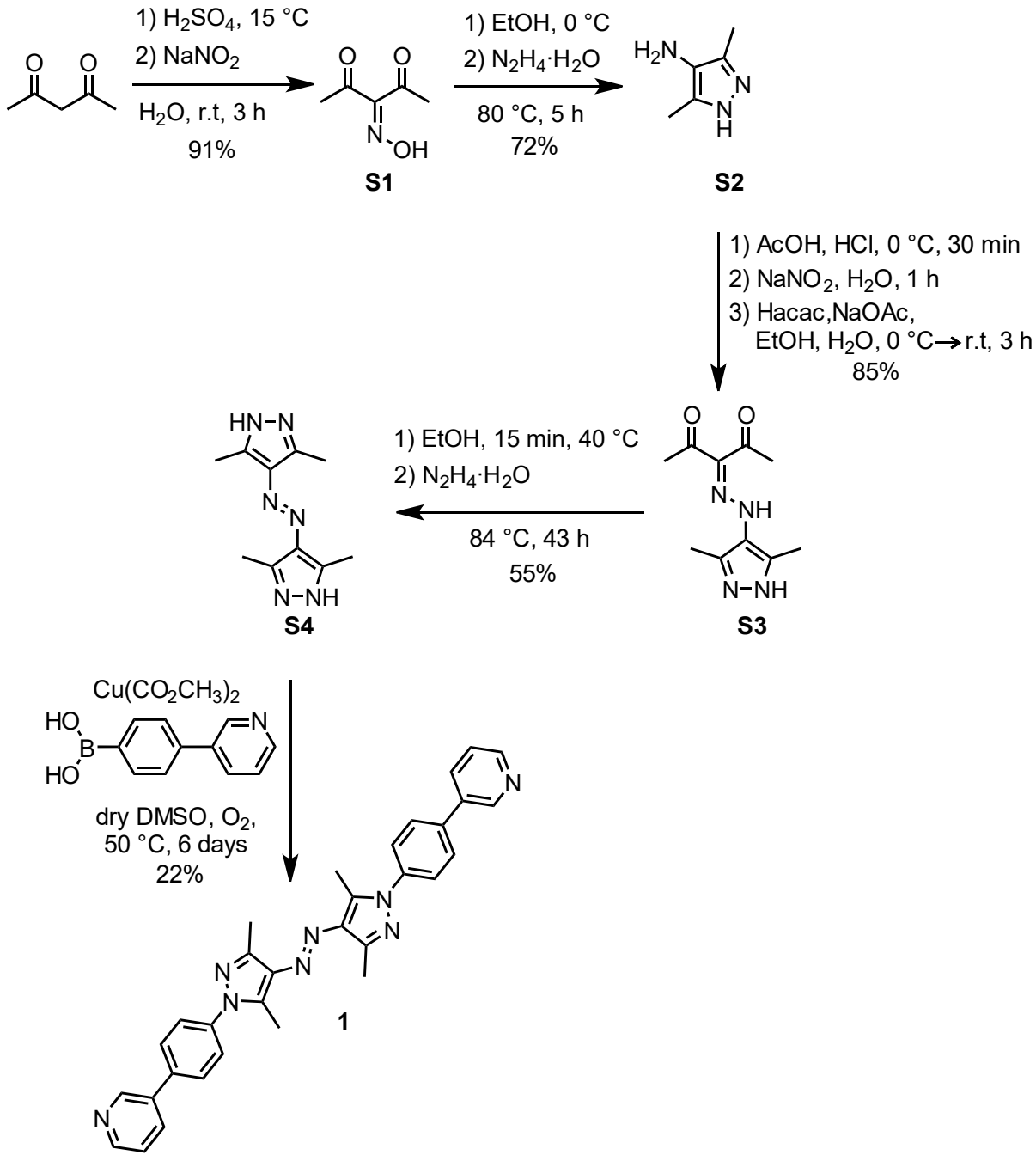

Scheme S1. Synthetic route to azobispyrazole-containing ligand **1**.

S2.1 3-(Hydroxyimino)pentane-2,4-dione (**S1**)

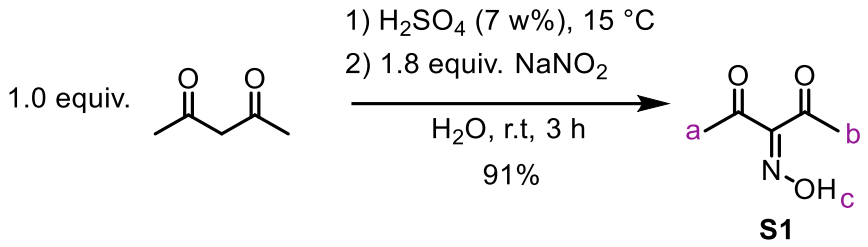

3-(Hydroxyimino)pentane-2,4-dione (**S1**) was synthesised after a modified literature procedure.[1]

Pentane-2,4-dione (5.0 g, 49.94 mmol, 1.0 equiv.) was dissolved in sulfuric acid (7%, 50 mL) at 15 °C. Subsequently, a solution of $NaNO_2$ (6.20 g, 89.89 mmol, 1.8 equiv.) in water (30 mL) was added dropwise at 15 °C. After the slightly yellow reaction solution was stirred at room temperature for 3 h, the product was extracted with ethyl acetate (4 × 15 mL) and the combined organic layers dried over anhydrous Na_2SO_4. The solvent was removed under reduced pressure on a rotary evaporator and the orange (slushy) solid was washed with cold toluene and later dissolved in methanol. After removing residual solvents under reduced pressure, 3-(hydroxyimino)pentane-2,4-dione (**S1**) was isolated as white crystals with a 91% yield (5.85 g, 45.31 mmol).

$C_5H_7NO_3$ 129.12 g/mol

R_F value (CH_2Cl_2 / CH_3OH 95:5 (v/v)) = 0.67

^{1}H NMR (400 MHz, CD_3CN, 293 K) δ_H [ppm] = 2.26 (s, 3H, H-a/b), 2.32 (s, 3H, H-a/b), 10.15 (s, 1H, H-c).

The obtained spectrum matches the literature data.[1]

HRMS (ESI^+): *m/z* (relative intensity) = 152.0320 (100%, [M+Na^+], calcd 152.0318).

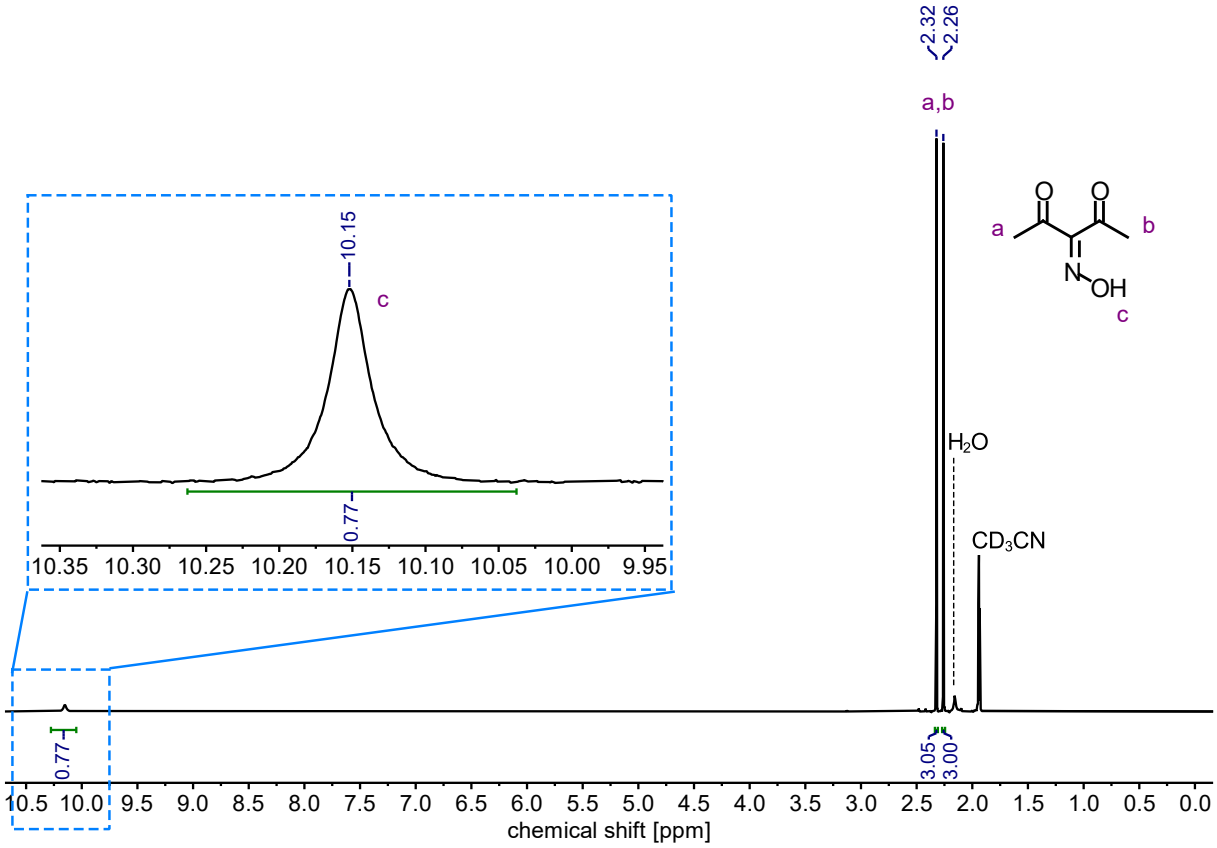

Figure S1. ^{1}H NMR spectrum (400 MHz, CD_3CN, 298 K) of dione **S1**.

S2.2 3,5-Dimethyl-1*H*-pyrazol-4-amine (**S2**)

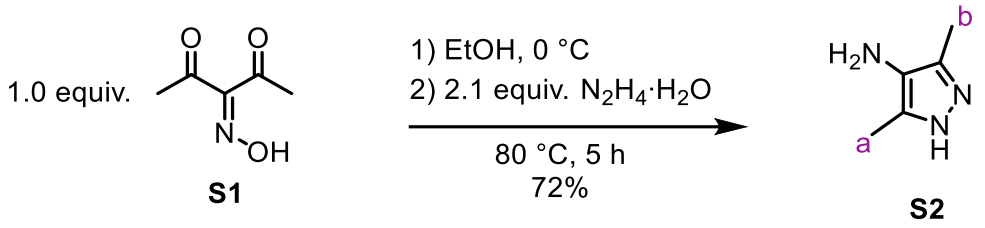

3,5-Dimethyl-1*H*-pyrazol-4-amine (**S2**) was synthesised after a modified literature procedure.[1]

Hydrazine monohydrate (0.8 mL, 19.52 mmol, 2.10 equiv.) was added dropwise to a solution of dione **S1** (1.0 g, 9.29 mmol, 1.0 equiv.) in ethanol (12 mL) at 0 °C. The resulting turquoise solution was stirred at 80 °C. After 90 min, additional hydrazine monohydrate (0.3 mL, 7.44 mmol, 0.8 equiv.) was added and the turquoise solution was stirred for a further 3.5 h at 80 °C. After allowing the reaction to cool to room temperature, water (20 mL) was added and the aqueous phase was extracted with ethyl acetate (4 × 10 mL). The combined organic layers were washed with water (1 × 10 mL) and dried over Na_2SO_4. The residual solvent was removed under reduced pressure on a rotary evaporator. 3,5-Dimethyl-1H-pyrazol-4-amine (**S2**) was obtained as an off-white powder with a yield of 72% (618 mg, 5.56 mmol).

$C_5H_9N_3$ 111.15 g/mol

R_F value (CH_2Cl_2 / CH_3OH 98:2 (v/v)) = 0.22

^{1}H NMR (400 MHz, DMSO-d_6, 293 K) δ_H [ppm] = 1.99 (s, 6H, H-a/b), 11.37 (s, 1H, NH).

The obtained spectrum matches the literature data.[1]

HRMS (ESI^+): m/z (relative intensity) = 112.0870 (100%, [$M+H^+$], calcd 112.0869).

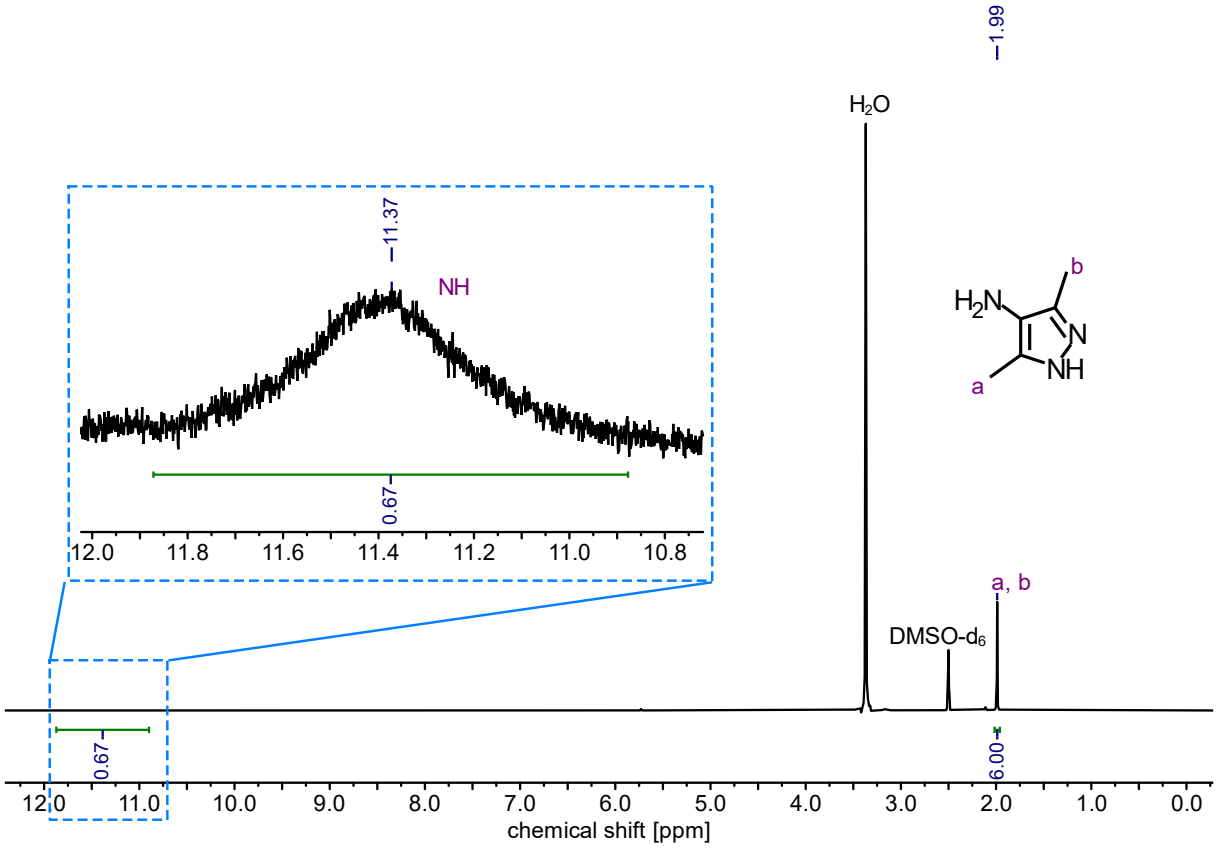

Figure S2. ^{1}H NMR spectrum (400 MHz, DMSO-d_6, 298 K) of pyrazole **S2**.

S2.3 3-(2-(3,5-Dimethyl-1*H*-pyrazol-4-yl)hydrazineylidene)pentane-2,4-dione (**S3**)

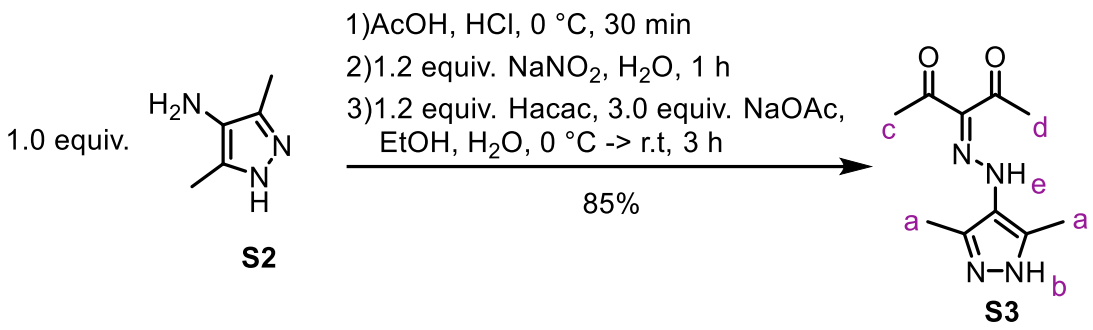

3-(2-(3,5-Dimethyl-1*H*-pyrazol-4-yl)hydrazineylidene)pentane-2,4-dione (**S3**) was synthesised after a modified literature procedure.[1]

A suspension of pyrazol amine **S2** (100 mg, 899.70 µmol, 1.0 equiv.) in glacial acetic acid (1.3 mL) and conc. HCl (0.3 mL) was stirred at 4 °C for 30 min. Subsequently, a solution of $NaNO_2$ (74.5 mg, 1.08 mmol, 1.2 equiv.) in water (1.0 mL) was added dropwise and the resulting clear yellow solution stirred at 4 °C for 1 h. This cold solution of the diazonium salt was added dropwise to a solution of acetylacetone (0.1 mL, 1.0 mmol, 1.2 equiv.) and NaOAc (0.22 g, 2.70 mmol, 3.0 equiv.) in ethanol (2.0 mL) and water (1.0 mL) at 4 °C. The resulting solution was warmed to room temperature and stirred for an additional 3 h. The aqueous phase was then extracted with ethyl acetate (4 × 20 mL). The combined organic layers were washed with water (1 × 15 mL) and dried over Na_2SO_4. The residual solvent was removed under reduced pressure on a rotary evaporator and the residue was subjected to column chromatography (silica gel, CH_2Cl_2/EtOAc 100:0→75:25 (v/v) over 15 column volumes). Dione **S3** was obtained as a yellow powder with an overall yield of 85% (170 mg, 764.91 µmol).

$C_{10}H_{14}N_4O_2$ 222.25 g/mol

R_F value (CH_2Cl_2 / CH_3OH, 95:5 (v/v)) = 0.55

^{1}H NMR (400 MHz, CD_3CN, 293 K) δ_H [ppm] = 2.32 (s, 9H, H-a, H-b, and H-d/e), 2.49 (s, 3H, H-d/e), 10.6 (s, 1H, H-c), 15.07 (s, 1H, H-f).

The obtained spectrum matches the literature data.[1]

HRMS (ESI^+): *m/z* (relative intensity) = 223.1191 (100%, [M+H^+], calcd 223.1190).

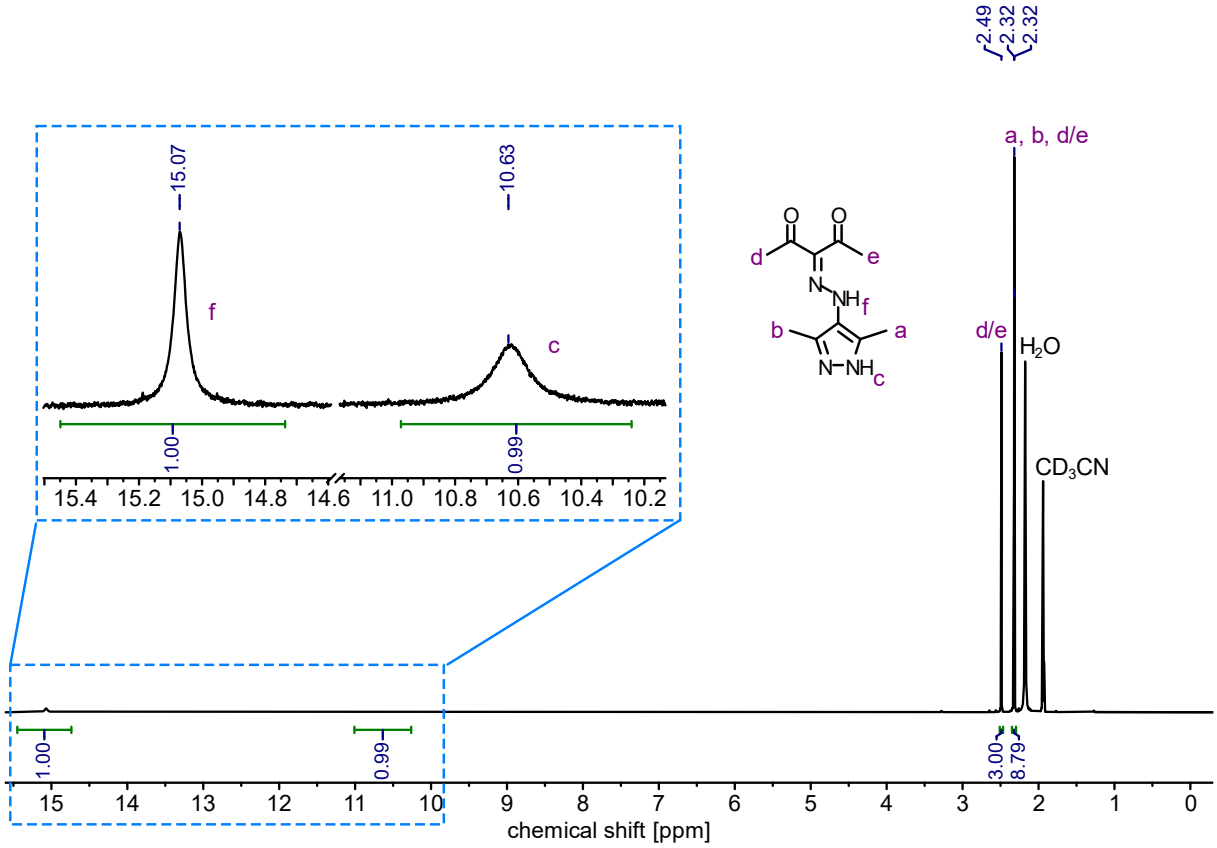

Figure S3. ^{1}H NMR spectrum (400 MHz, CD_3CN, 298 K) of **S3**.

S2.4 (*E*)-1,2-Bis(3,5-dimethyl-1*H*-pyrazol-4-yl)diazene (**S4**)

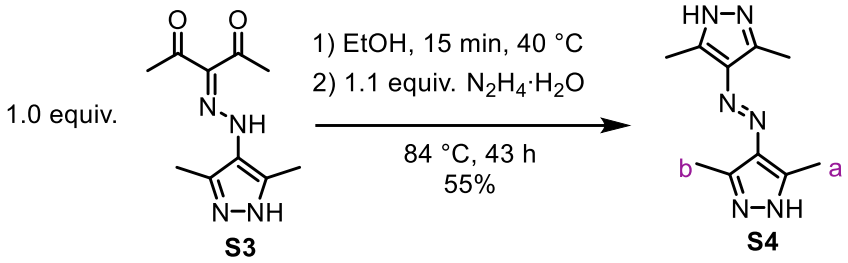

(*E*)-1,2-Bis(3,5-dimethyl-1*H*-pyrazol-4-yl)diazene (**S4**) was synthesised after a modified literature procedure.[1]

Dione **S3** (3.7 g, 16.6 mmol, 1.0 equiv.) was dissolved in ethanol (150 mL) by stirring the mixture for 15 min at 40 °C. Hydrazine monohydrate (890 µL, 18.3 mmol, 1.1 equiv.) was added and the solution was stirred under reflux (84 °C) for 43 h, during which a colour change from yellow to orange was observed and a yellow precipitate formed. After allowing the reaction mixture to cool down to room temperature, water (150 mL) was added upon which more precipitate formed. The formed precipitate was filtered via gravity filtration and washed with water (20 mL). After allowing the solid to air dry for 5 d, (*E*)-1,2-bis(3,5-dimethyl-1H-pyrazol-4-yl)diazene (**S4**) was obtained as a yellow solid in 55% yield (2.0 g, 9.16 mmol).

$C_{10}H_{14}N_6$ 218.26 g/mol

R_F value (CH_2Cl_2 / *i*-PrOH 9:1 (v/v)) = 0.63

^{1}H NMR (400 MHz, DMSO-d_6, 298 K) δ_H [ppm] = 2.34 (s, 3H, H-a/b), 2.40 (s, 3H, H-a/b), 12.53 (s, 1H, NH).

The obtained spectrum matches the literature data.[1]

HRMS (ESI^+): *m*/*z* (relative intensity) = 219.1349 (100%, $[M+H^+]$, calcd 219.1353).

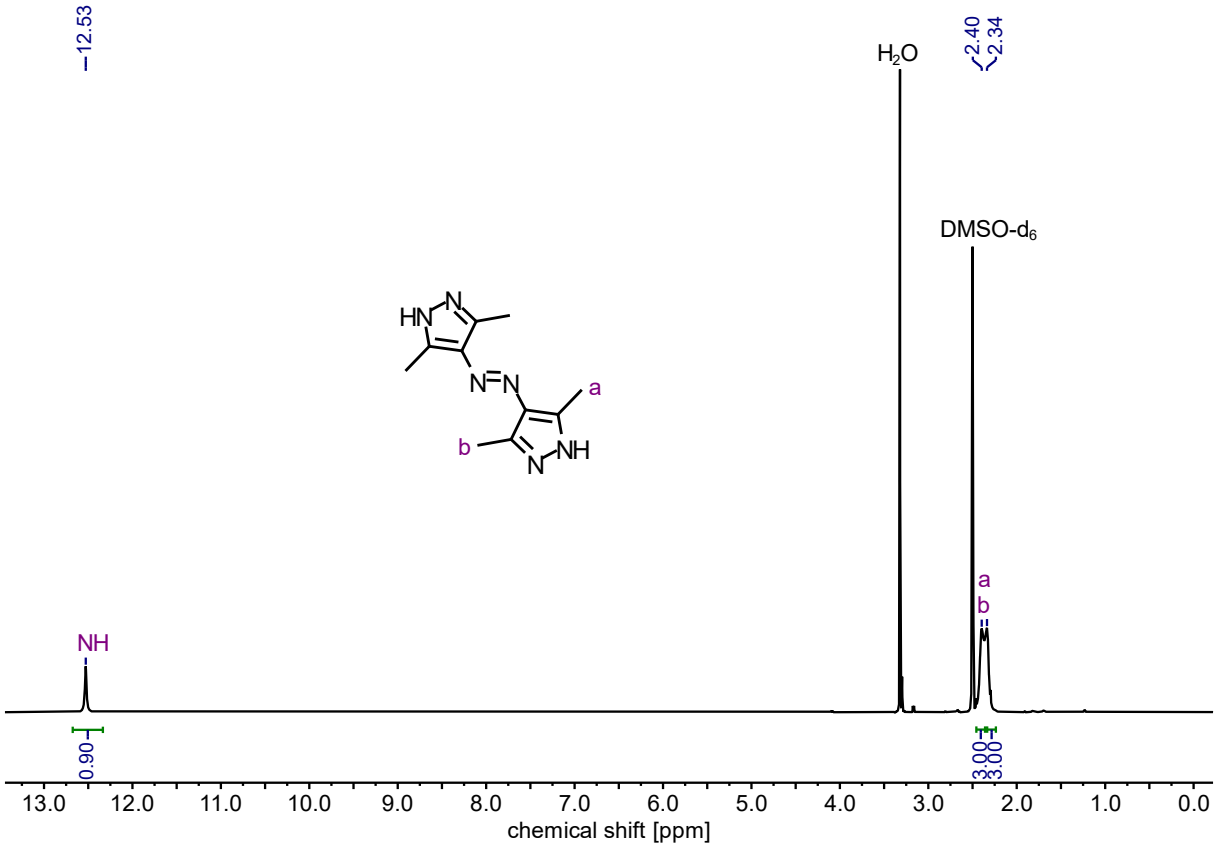

Figure S4. ^{1}H NMR spectrum (400 MHz, DMSO-d_6, 298 K) of azobispyrazole photoswitch **S4**.

S2.5 (*E*)-1,2-Bis(3,5-dimethyl-1-(4-(pyridin-3-yl)phenyl)-1*H*-pyrazol-4-yl)diazene (**1**)

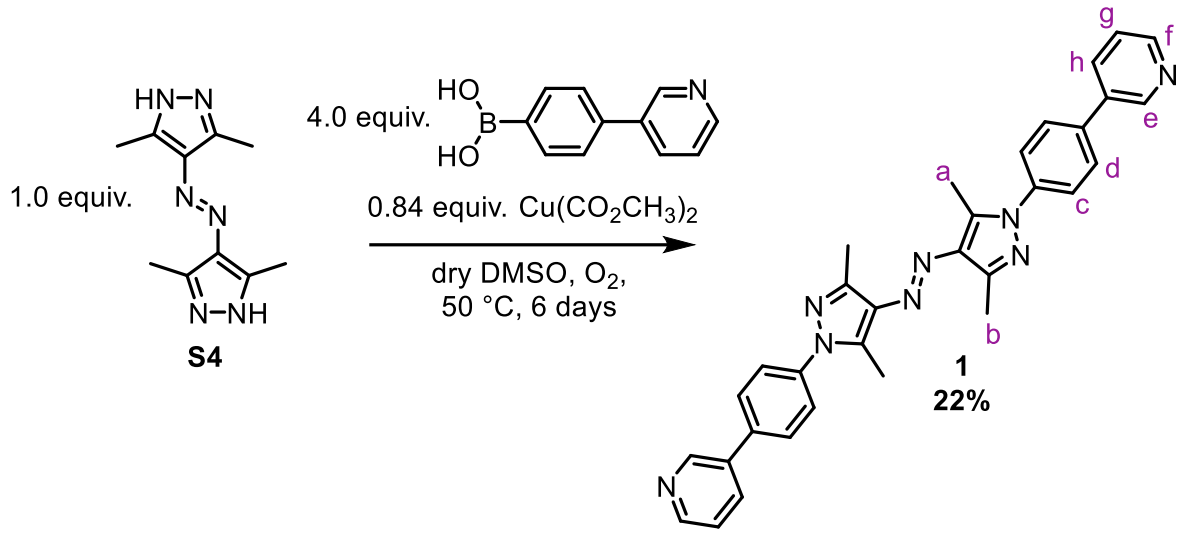

$Cu(CO_2CH_3)_2$ (160 mg, 885 µmol, 0.84 equiv.) was added to a solution of azobispyrazole photoswitch **S4** (230 mg, 1.05 mmol, 1.0 equiv.) and (4-(pyridin-3-yl)phenyl)boronic acid (839 mg, 4.22 mmol, 4.0 equiv.) in dry dimethyl sulfoxide (25 mL). The reaction mixture was equipped with an oxygen balloon and was stirred at 50 °C for 6 d, upon which a green solid precipitated. After allowing the reaction to cool down to ambient temperature, the green solid was filtered via gravity filtration and washed with water. After air drying the solid for 24 h, the green solid was collected and the residue was subjected to column chromatography (silica gel, see Table S2 for solvent specifications). The solid obtained after column chromatography was further purified by liquid-liquid (dichloromethane/ethyl acetate) diffusion-assisted crystallisation: The solid was dissolved in a minimum amount of dichloromethane (1 mL) and the solution carefully layered with ethyl acetate (2 mL) upon which yellow crystals formed. The mixture was cooled to 4 °C overnight or longer to afford ligand **1** as a yellow crystalline solid in 22% yield (125 mg, 238 µmol).

Table S2. Solvent gradient used to purify ligand **1** via flash column chromatography.

Column volume	**EtOAc / NEt_3** (97:3)	**CH_2Cl_2**	***i*-PrOH**
0	0	100	0
10	50	50	0
14	100	0	0
16	100	0	0
18	80	0	20

$C_{32}H_{28}N_8$ 524.63 g/mol

R_F value (EtOAc / NEt_3, 97:3 (v/v)) = 0.27

Elemental Analysis ($C_{32}H_{28}N_8$):

Calcd (%)	C: 73.26	H: 5.38	N: 21.36
Found (%)	C: 73.43	H: 5.39	N: 21.25

^{1}H NMR* (400 MHz, CD_2Cl_2, 298 K) δ_H [ppm] = 1.89 (s, 3H, H-b^Z), 2.25 (s, 3H, H-a^Z), 2.56 (s, 3H, H-b), 2.69 (s, 3H, H-a), 7.41 (ddd, *J* = 7.8, 4.8, 0.9, 1H, H-g), 7.52 – 7.59 (m, 2H, H-c^Z), 7.63 – 7.69 (m, 2H, H-c), 7.73 – 7.78 (m, 2H, H-d), 7.92 (dd, *J* = 2.4, 1.6, 1H, H-h^Z), 7.96 (ddd, *J* = 7.9, 2.4, 1.7, 1H, H-h), 8.61 (dd, *J* = 4.8, 1.6, 1H, H-f), 8.88 (d, *J* = 1.6, 1H, H-e^Z), 8.90 (dd, *J* = 2.4, 0.9, 1H, H-e).

^{13}C NMR (176 MHz, CD_2Cl_2, 298 K) δ_C [ppm] = 11.7 (C-a), 14.6 (C-b), 124.0 (C-g), 125.3 (C-c), 128.2 (C-d), 134.6 (C-h), 135.9 (C-6), 137.4 (C-1), 137.5 (C-5), 138.1 (C-2), 139.8 (C-4), 143.3 (C-3), 148.6 (C-e), 149.3 (C-f).

HRMS (ESI^+): *m/z* (relative intensity) = 525.2509 (100%, [$M+H^+$], calcd 525.2510).

* Signals with a ^{Z} represent *Z*-**1**. Not all signals of *Z*-**1** are visible due to peak overlap with *E*-**1** (Figure S55). One dimensional ^{1}H-ROESY spectra enabled the assignment of H-a, H-b, H-a^Z, and H-b^Z.

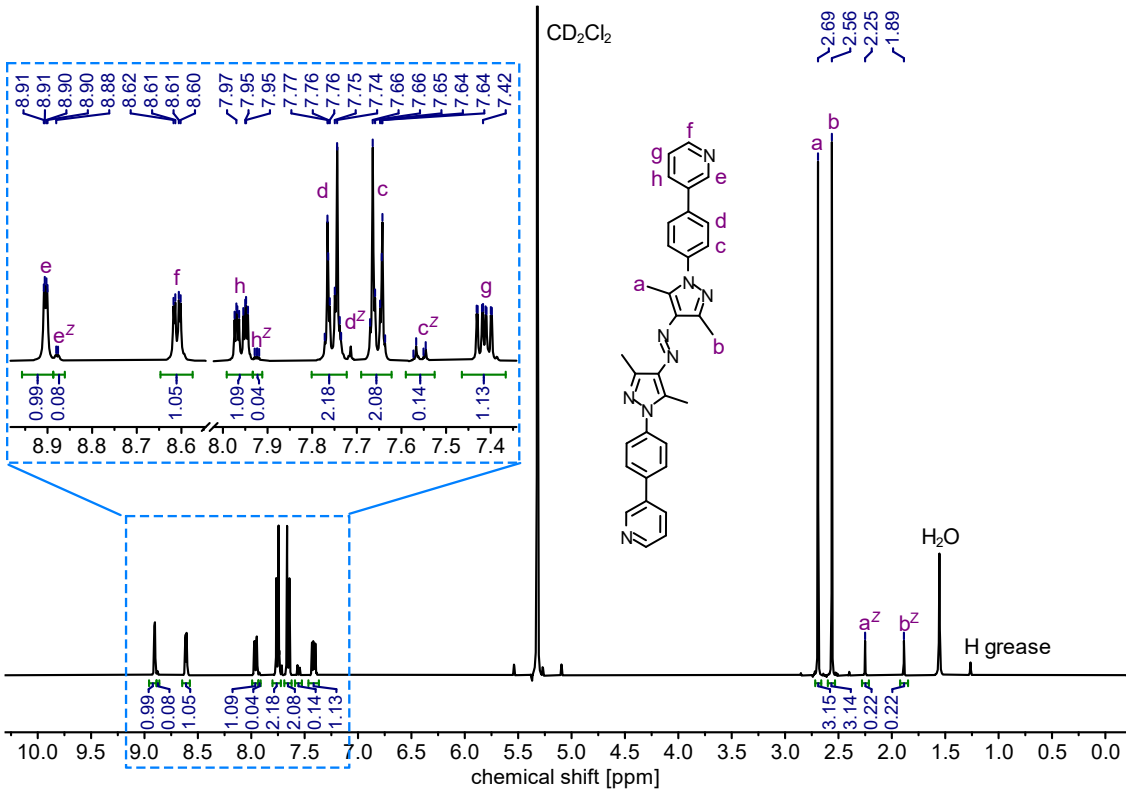

Figure S5. ^{1}H NMR spectrum (400 MHz, CD_2Cl_2, 298 K) of ligand **1**. Signals with a ^{Z} represent *Z*-**1** (92:8, *E*:*Z*).

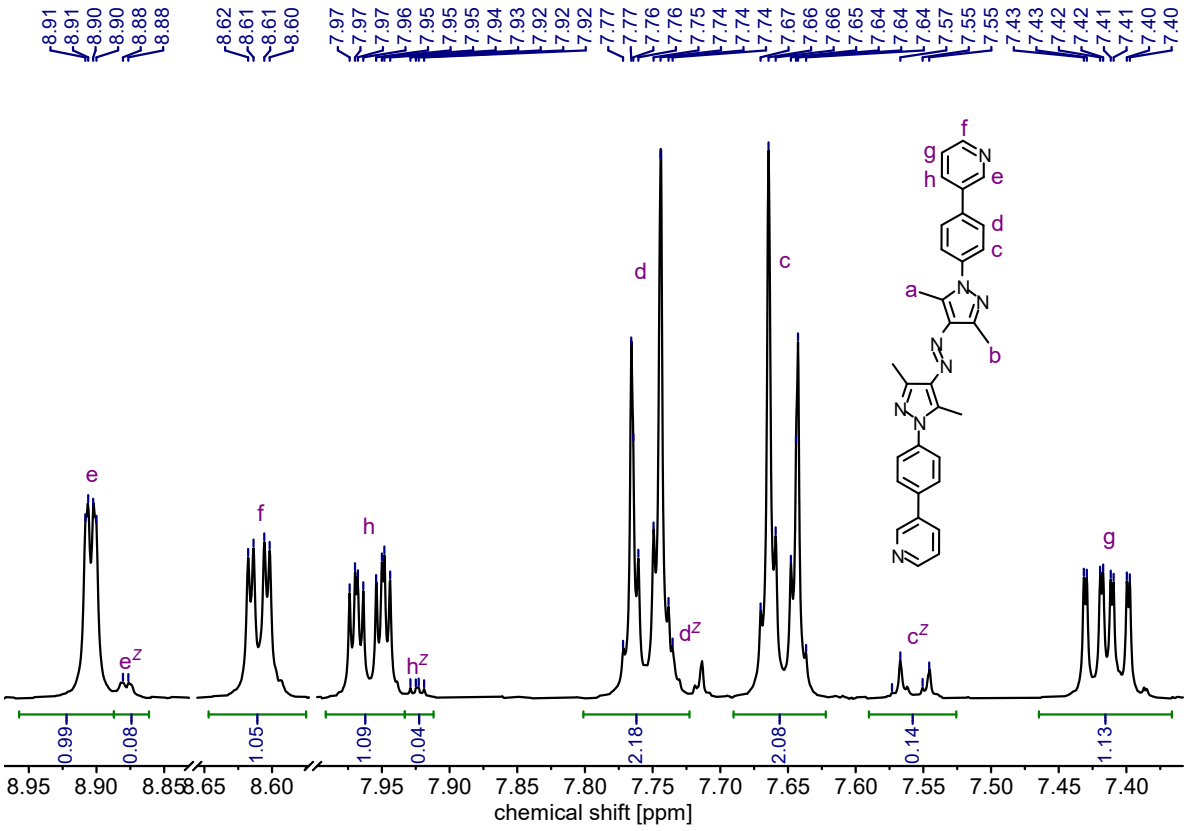

Figure S6. Partial ^{1}H NMR spectrum (400 MHz, CD_2Cl_2, 298 K) of ligand **1**. Signals with a ^{Z} represent *Z*-**1** (92:8, *E*:*Z*).

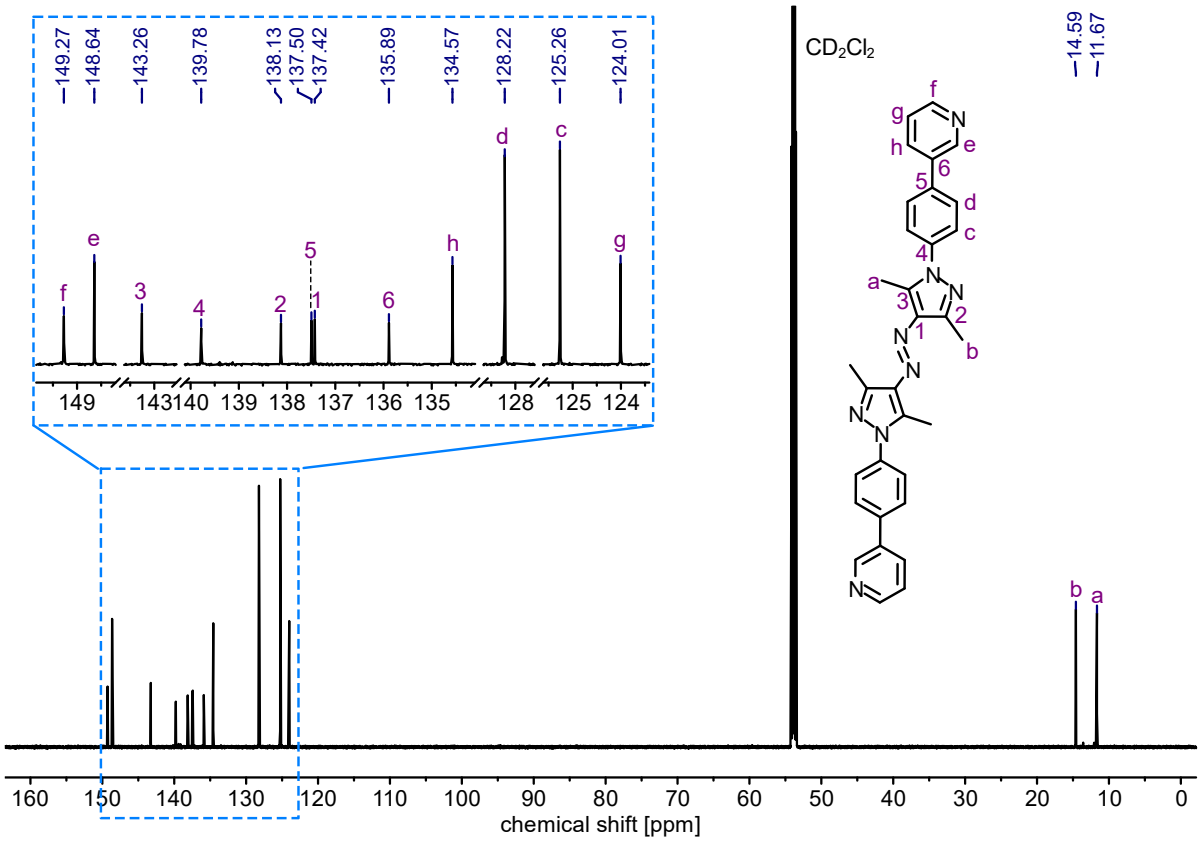

Figure S7. ^{13}C NMR spectrum (176 MHz, CD_2Cl_2, 298 K) of ligand **1**.

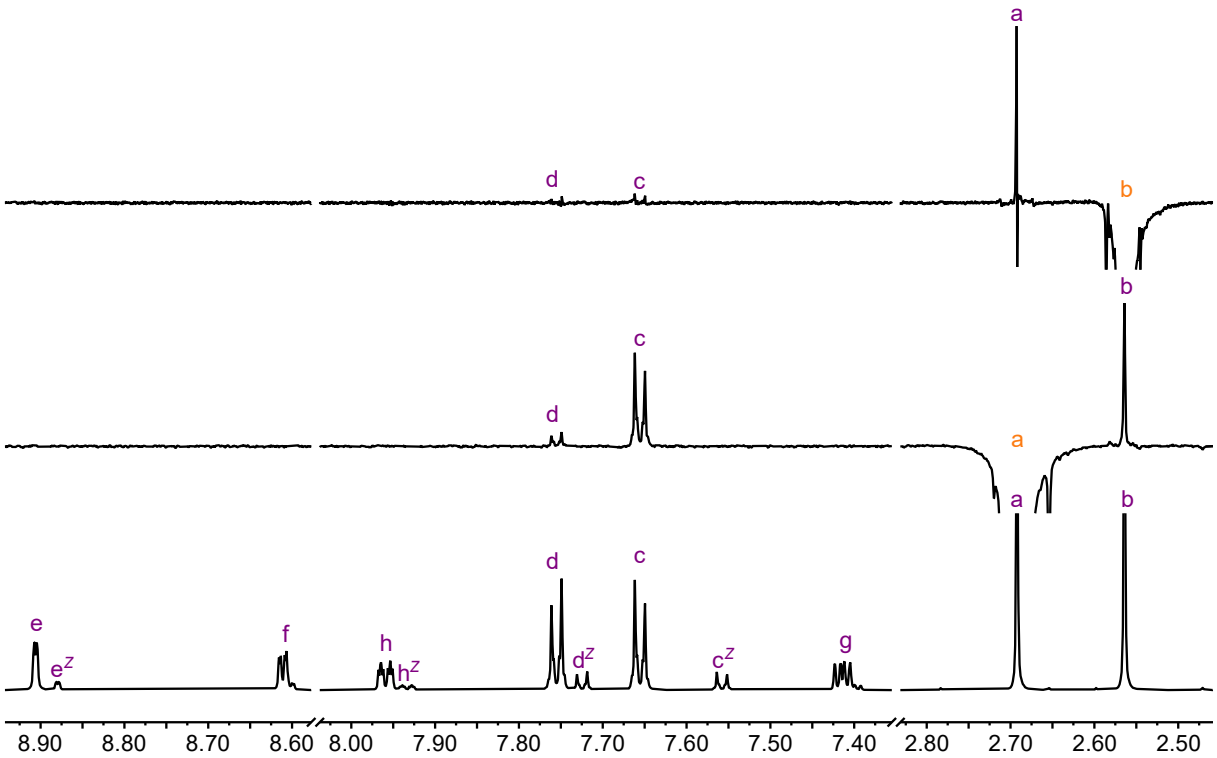

Figure S8. One-dimensional ^{1}H-ROESY NMR spectra (700 MHz, CD_2Cl_2, 298 K) of *E*-**1** for signals H-a, and H-b. Signals with a ^{Z} represent *Z*-**1** (85:15, *E*:*Z*).

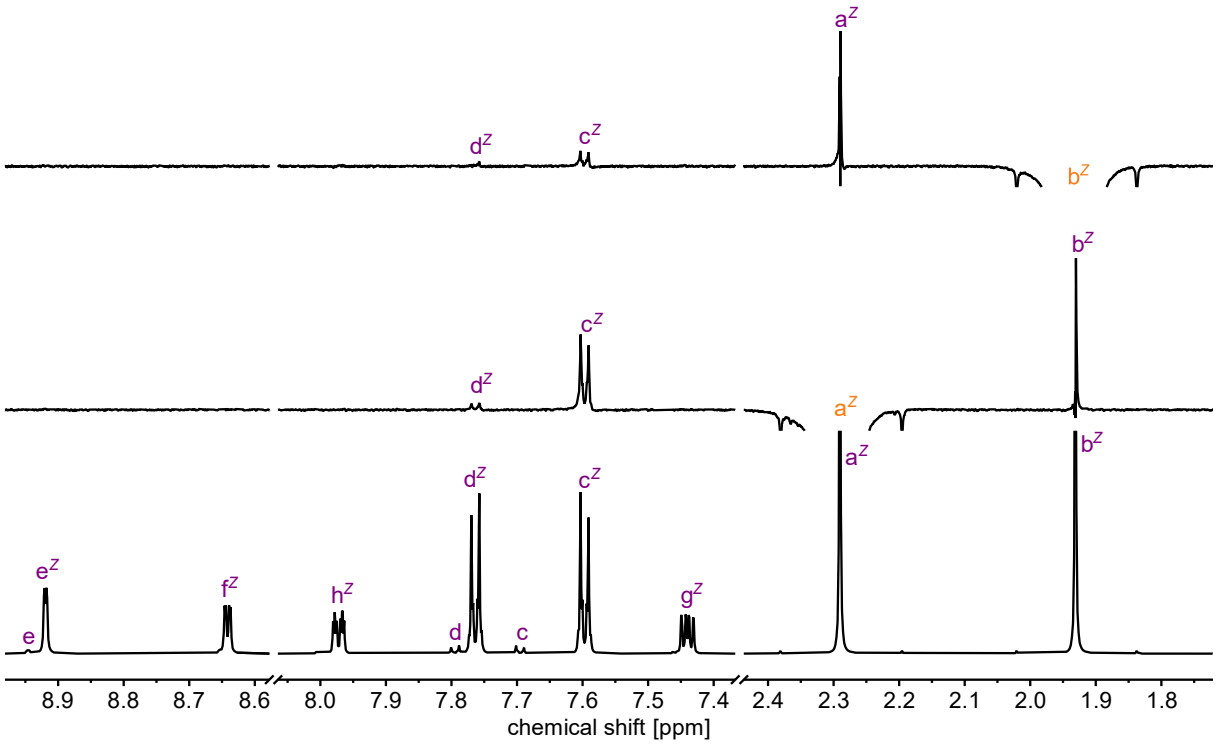

Figure S9. One-dimensional ^{1}H-ROESY NMR spectra (700 MHz, CD_2Cl_2, 298 K) of *Z*-**1** for signals H-a^{Z}, and H-b^{Z}. Signals with a ^{Z} represent *Z*-**1** (5:95, *E*:*Z*).

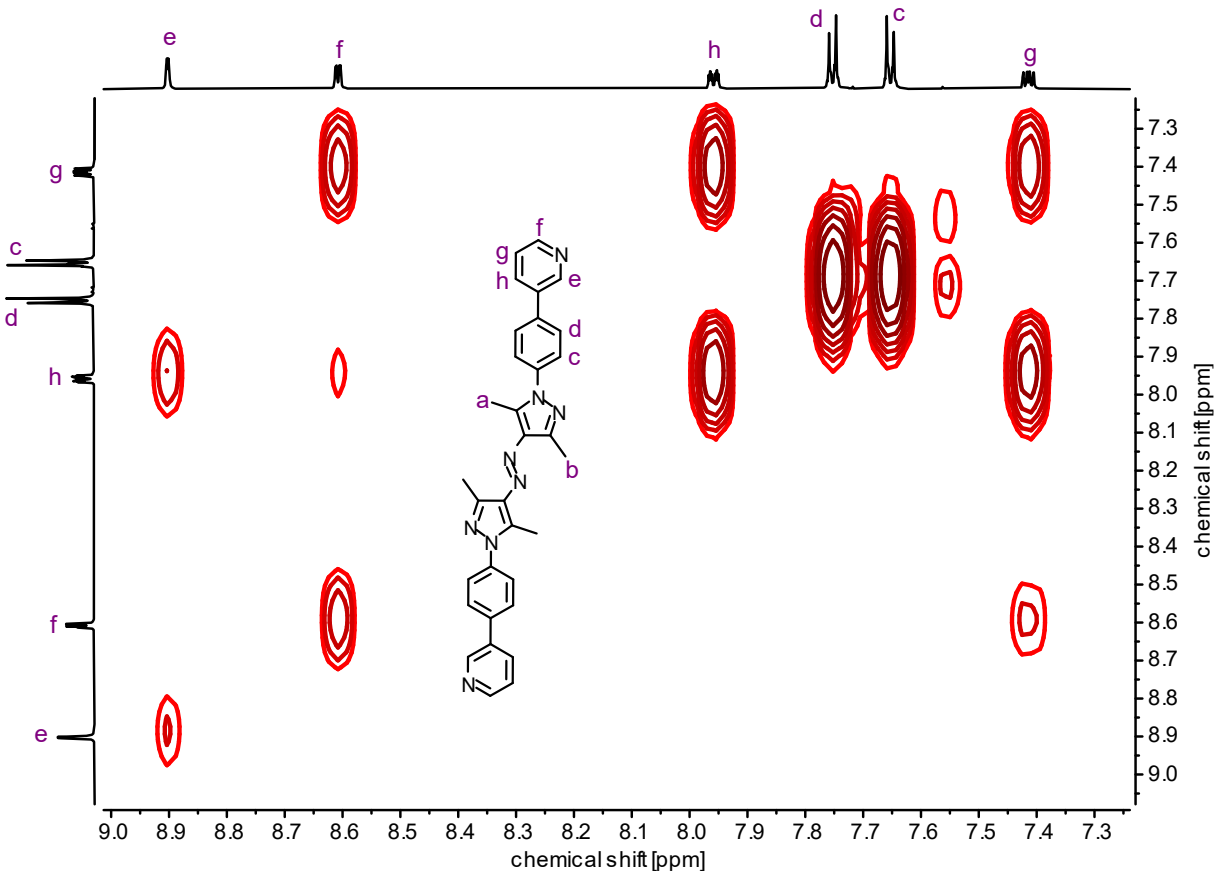

Figure S10. ^{1}H,^{1}H COSY NMR spectrum (700 MHz, CD_2Cl_2, 298 K) of ligand **1**.

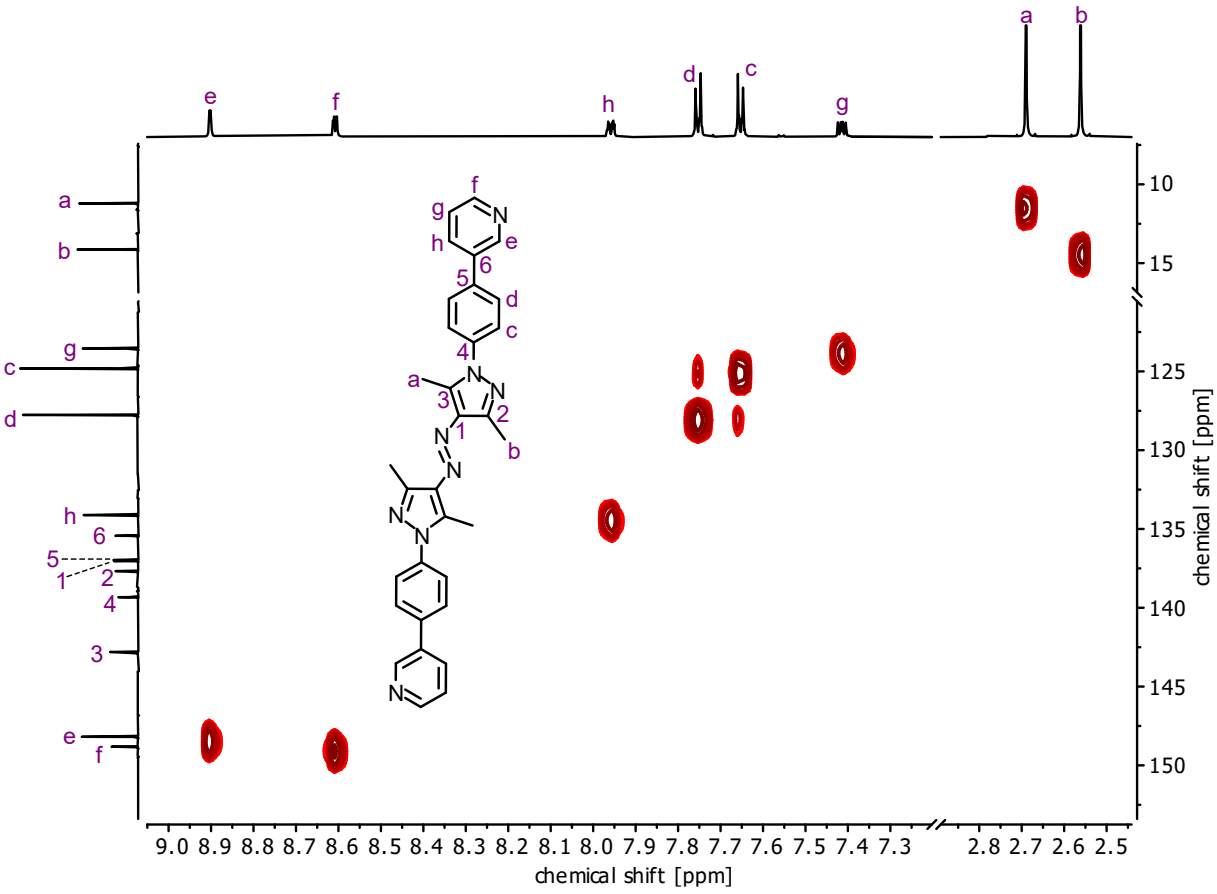

Figure S11. $^{1}H,^{13}C$ HSQC NMR spectrum (700/176 MHz, CD_2Cl_2, 298 K) of ligand **1**.

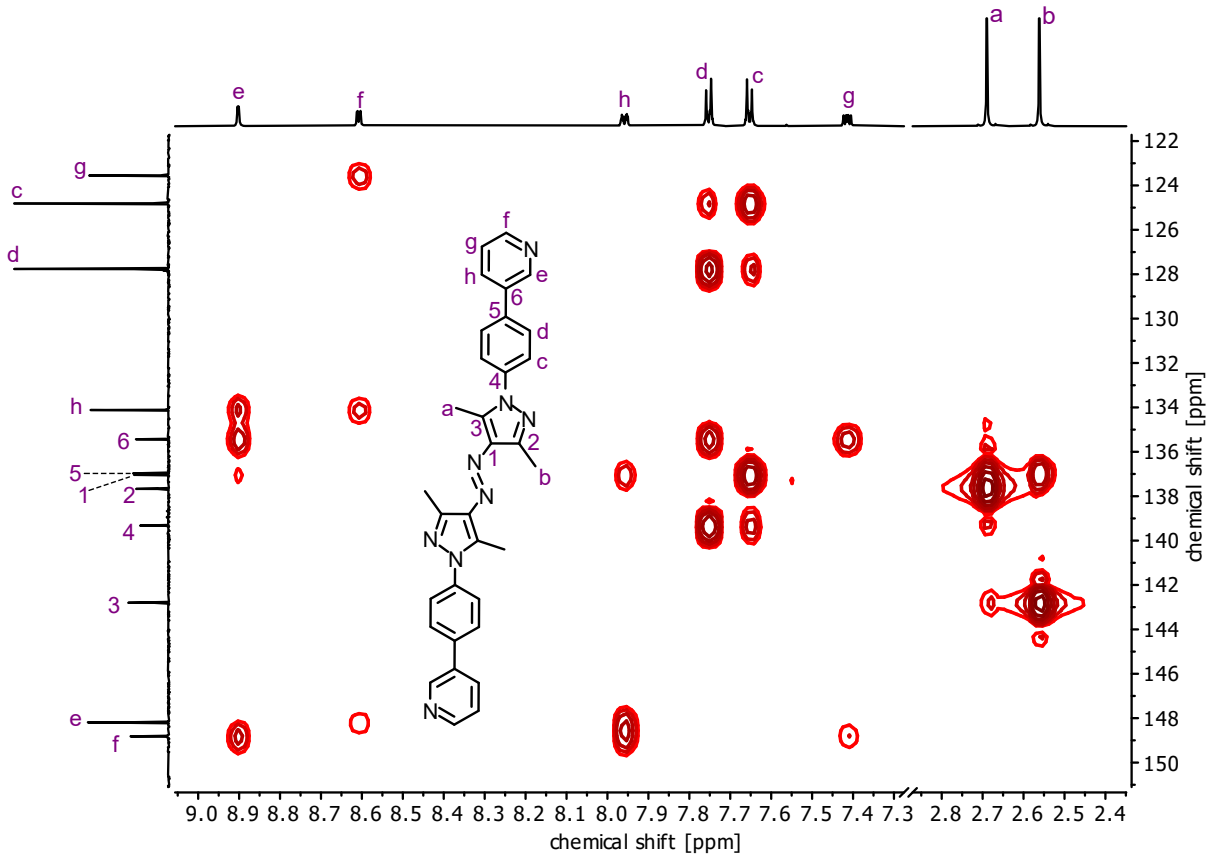

Figure S12. $^{1}H,^{13}C$ HMBC NMR spectrum (700/176 MHz, CD_2Cl_2, 298 K) of ligand **1**.

S2.6 Self-assembly of the triangle *E*-**T** / lantern *E*-**L** mixture

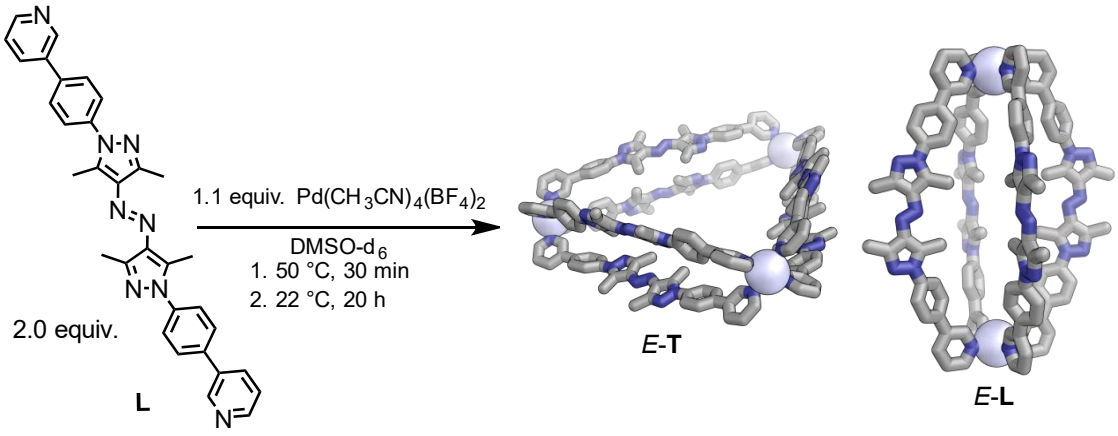

Ligand **1** (2.53 mg, 4.82 µmol, 2.0 equiv.) was suspended in DMSO-d_6 (522 µL) and sonicated for 2 min. A solution of $Pd(CH_3CN)_4(BF_4)_2$ (77 µL, [**1**] = 8.0 mM, 1.18 mg, 2.65 µmol, 1.1 equiv.) in DMSO-d_6 was added and the mixture was stirred at 50 °C for 30 min. The reaction mixture, initially observed as a turbid suspension, became a clear yellow solution after 5 min at 50 °C. The resulting complex solution was then left to equilibrate at 22 °C for a minimum of 6 h (usually overnight, approx. 20 h), resulting in a 78:22 *E*-**T** / *E*-**L** mixture.

In some instances, additional minor signals were observed in ^{1}H NMR (Figure S15). However, no other Pd species (e.g., Pd_4L_8) nor partially self-assembled structures (e.g., Pd_2L_5) were found in the ESI mass spectrum, which led us to tentatively assume that these minor signals correspond to different lantern *E*-**L** isomers (Figure S24 and Section S8.4). It was possible to reproducibly reduce the signals of these lantern *E*-**L** isomers by irradiating the sample with 365 nm light for 10 min (forming *Z*-**L**) and immediately heat it to 85 °C for 6 h. After allowing the mixture to cool to room temperature and equilibrate overnight (approx. 20 h), ^{1}H NMR revealed a clean 78:22 *E*-**T** / *E*-**L** mixture.

For more details on the equilibrium between *E*-**T** and *E*-**L**, see Section S3.

$[Pd_3(C_{32}H_{28}N_8)_6](BF_4)_6$	3987.82 g/mol
$[Pd_2(C_{32}H_{28}N_8)_4](BF_4)_4$	2658.54 g/mol

^{1}H NMR[†,‡] (500 MHz, DMSO-d_6, 298 K) δ_H [ppm] = 2.35 (s, 3H, H-b^T), 2.45 (s, 3H, H-b^L), 2.77 (s, 3H, H-a^L)[‡], 7.67z – 7.79 (m, 4H, H-c^T, d^T), 7.82 – 7.98 (m, 6H, H-g^T, g^L, c^L, d^L), 8.44 (s,1H, H-h^T), 8.46 (s,1H, H-h^L), 9.36 (d, J = 6.6 Hz, 1H, H-f^T), 9.43 (d, J = 7.2 Hz, 1H, H-f^L), 9.77 (d, J = 2.4 Hz, 1H, H-e^L), 9.87 (s, 1H, H-e^T).

^{13}C NMR[§] (176 MHz, DMSO-d_6, 298 K) δ_C [ppm] = 10.3 (C-a^T), 11.8 (C-a^L), 13.2 (C-b^L), 15.1 (C-b^T), 118.1, 124.6 (C-c^T/d^T), 125.1 (C-g^T/g^L/c^L/d^L), 128.1 (C-g^T/g^L/c^L/d^L), 128.3 (C-c^T/d^T), 136.5, 139.8, 140.3, 140.5, 148.3 (C-e^T), 144.8, 149.2 (C-e^L), 149.7 (C-f^L), 149.9 (C-f^T).

^{19}F NMR (470 MHz, DMSO-d_6, 298 K) δ_F [ppm] = −148.24, −148.18.

HRMS (ESI$^+$, DMSO-d_6/CH_3CN, 298 K): m/z (relative intensity) = 542.2474 (15%, [**1**]$^{\bullet+}$, calcd 542.2431), 577.7012 (100%, [**T** – 6 BF_4]$^{6+}$ and [**L** – 4 BF_4]$^{4+}$, calcd 577.6962), 710.6426 (20%, [**T** – 5 BF_4]$^{5+}$, calcd 710.6363), 799.2692 (22%, [**L** – 3 BF_4]$^{3+}$, calcd 799.2630), 909.8038 (10%, [**T** – 4 BF_4]$^{4+}$, calcd 910.0465), 1242.4077 (8%, [**T** – 3 BF_4]$^{3+}$ and [**L** – 2 BF_4]$^{2+}$, calcd 1242.3966).

[†] The ^{1}H and ^{13}C signals corresponding to *E*-**T** and *E*-**T** are depicted with a T and an L, respectively. One dimensional ^{1}H-ROESY spectra enabled the assignment of H-a^T, H-b^T, H-a^L, and H-b^L (Figure S19).

[‡] The H-a^T singlet is underneath the DMSO-d_6 signal and can only be observed at higher temperatures, see Section S3.4.

[§] Not all ^{13}C signals could be assigned unambiguously. C-H couplings for C-e^T, C-e^L, C-f^L, and C-f^T could be observed in the HSQC (Figure S22). However, individual signals could not be observed in the ^{13}C NMR (Figure S16).

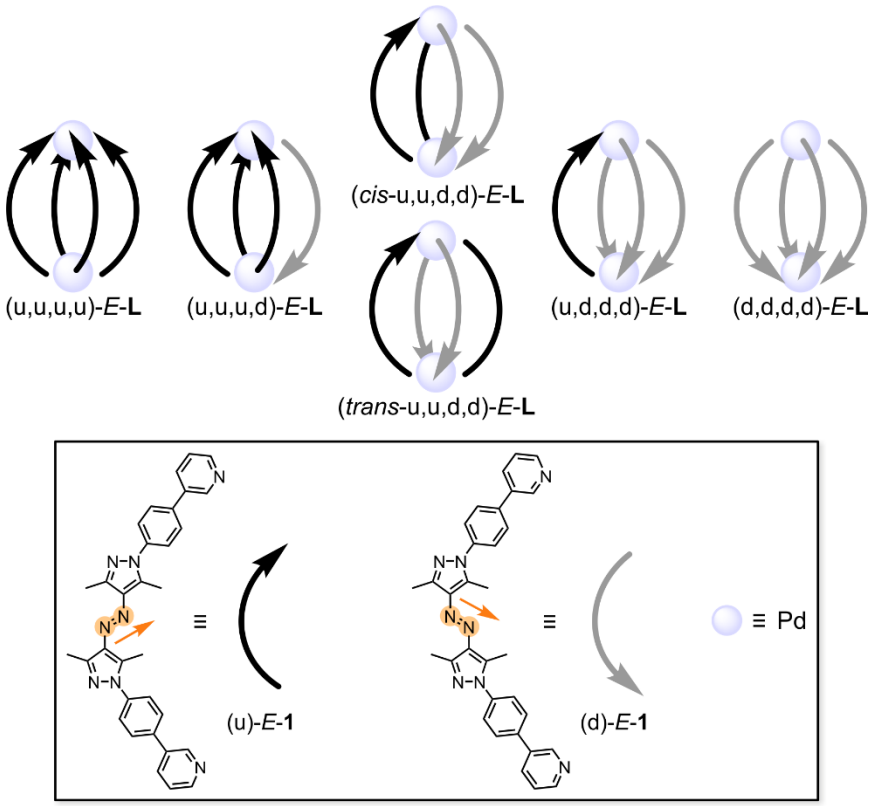

Figure S13. Cartoon representations of the six different possible isomers of *E*-**L**: (u,u,u,u)-*E*-**L** and its enantiomer (d,d,d,d)-*E*-**L**, (u,u,u,d)-*E*-**L** and its enantiomer (u,d,d,d)-*E*-**L**, (*cis*-u,u,d,d)-*E*-**L**, and (*trans*-u,u,d,d)-*E*-**L**. Ligand orientations are labelled “up” (u) and “down” (d), respectively, with respect to the orientations of the azo groups: If the N=N double bond of the azo bridge tilts slightly upward and points into the concave side of the ligand (orange arrow), a ligand is assigned the “up” (u) orientation (black curved arrow); if it tilts slightly downward and points into the concave side of the ligand (orange arrow), it is assigned the “down” (d) orientation (grey curved arrow). Computations of these isomers are detailed in Section S8.4. Note that the X-ray crystal structure showed the (*cis*-u,u,d,d)-*E*-**L** isomer (Section S7).

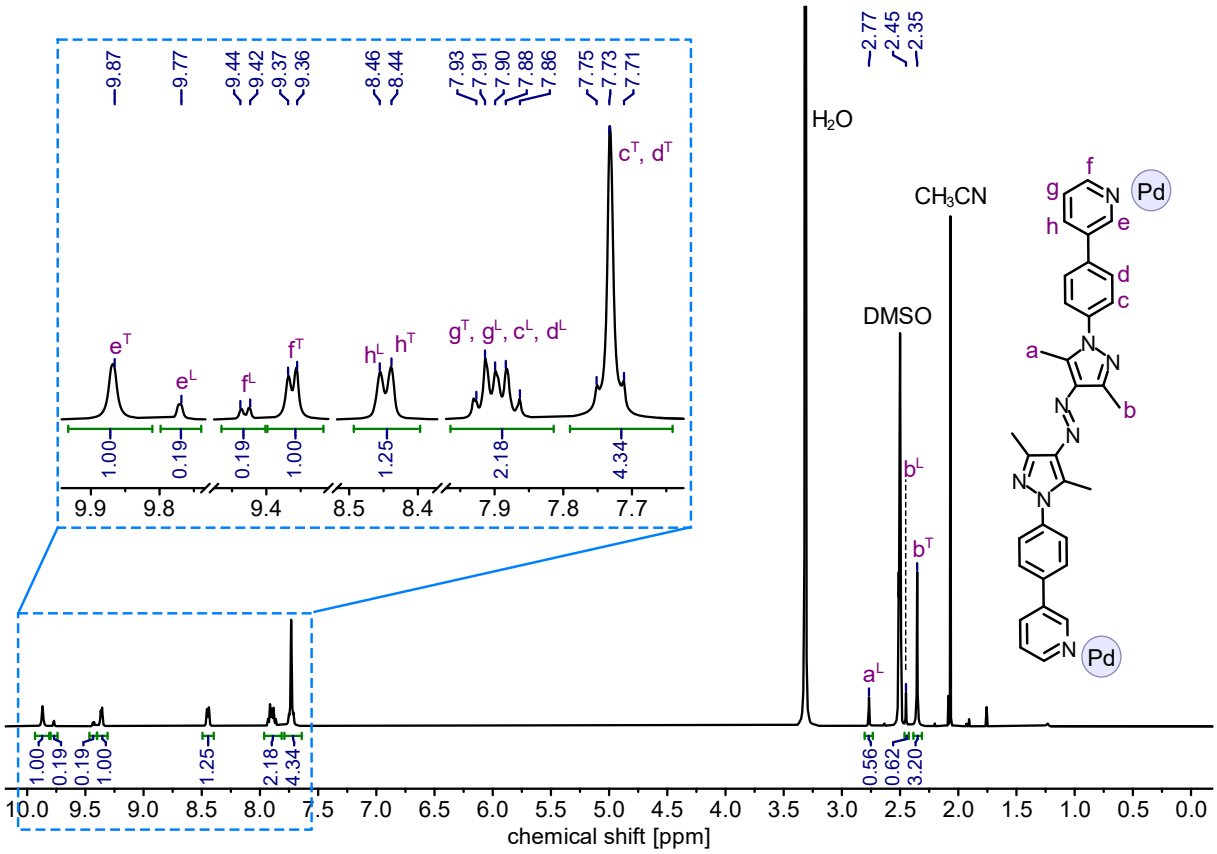

Figure S14. ^{1}H NMR spectrum (500 MHz, DMSO-d_6, 298 K) of 78% *E*-**T** (denoted as T) and 22% *E*-**L** (denoted as L).

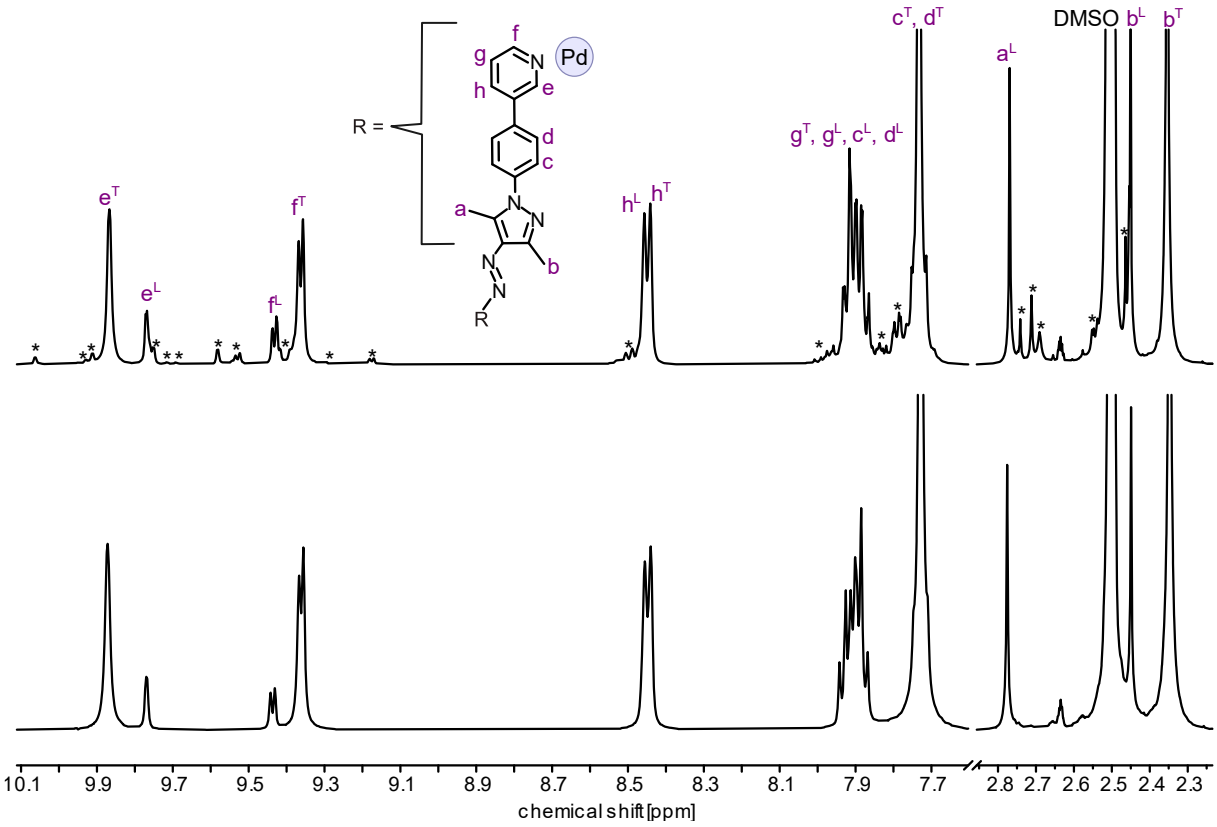

Figure S15. ^{1}H NMR spectrum (500 MHz, DMSO-d_6, 298 K) of 78% *E*-**T** (denoted as T) and 22% *E*-**L** (denoted as L) before (top) and after (bottom) “clean up”. Minor species highlighted with an asterisk.

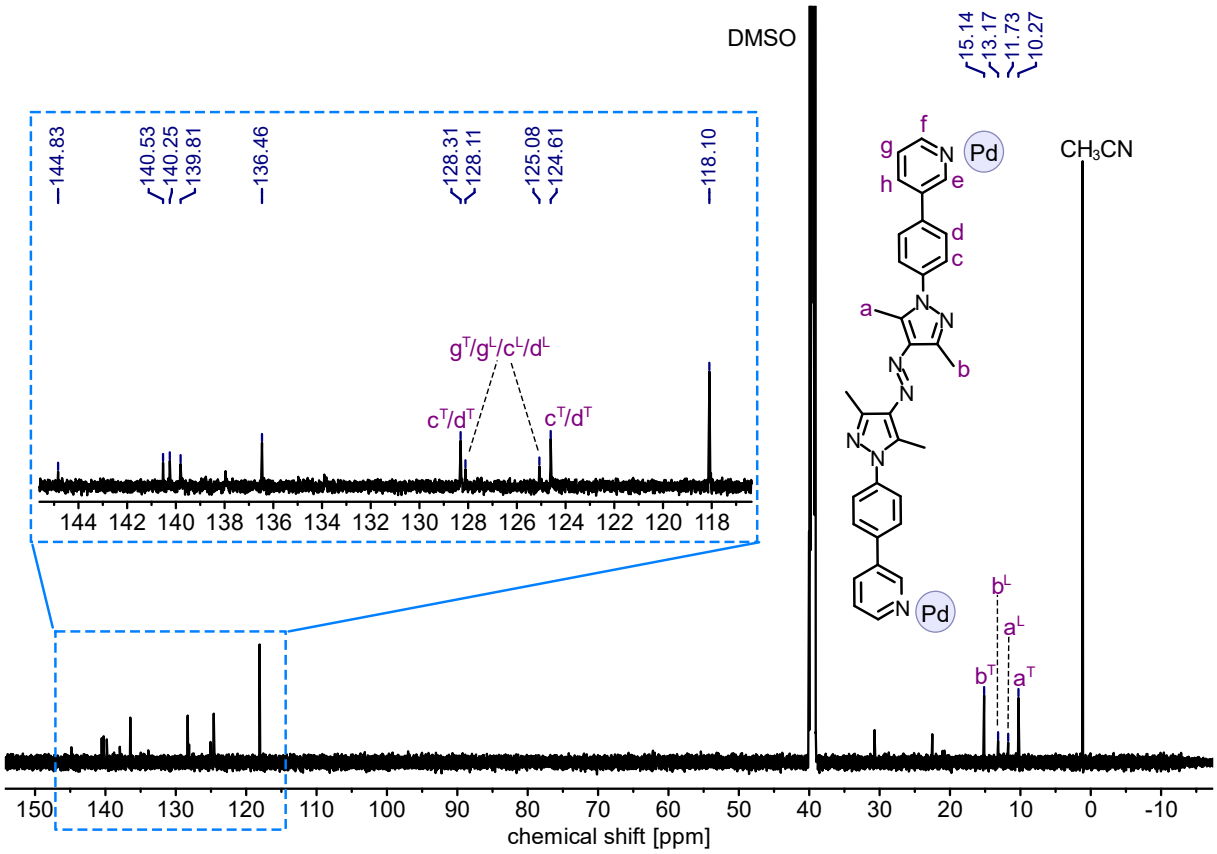

Figure S16. ^{13}C NMR spectrum (176 MHz, DMSO-d_6, 298 K) of 78% *E*-**T** (denoted as T) and 22% *E*-**L** (denoted as L).

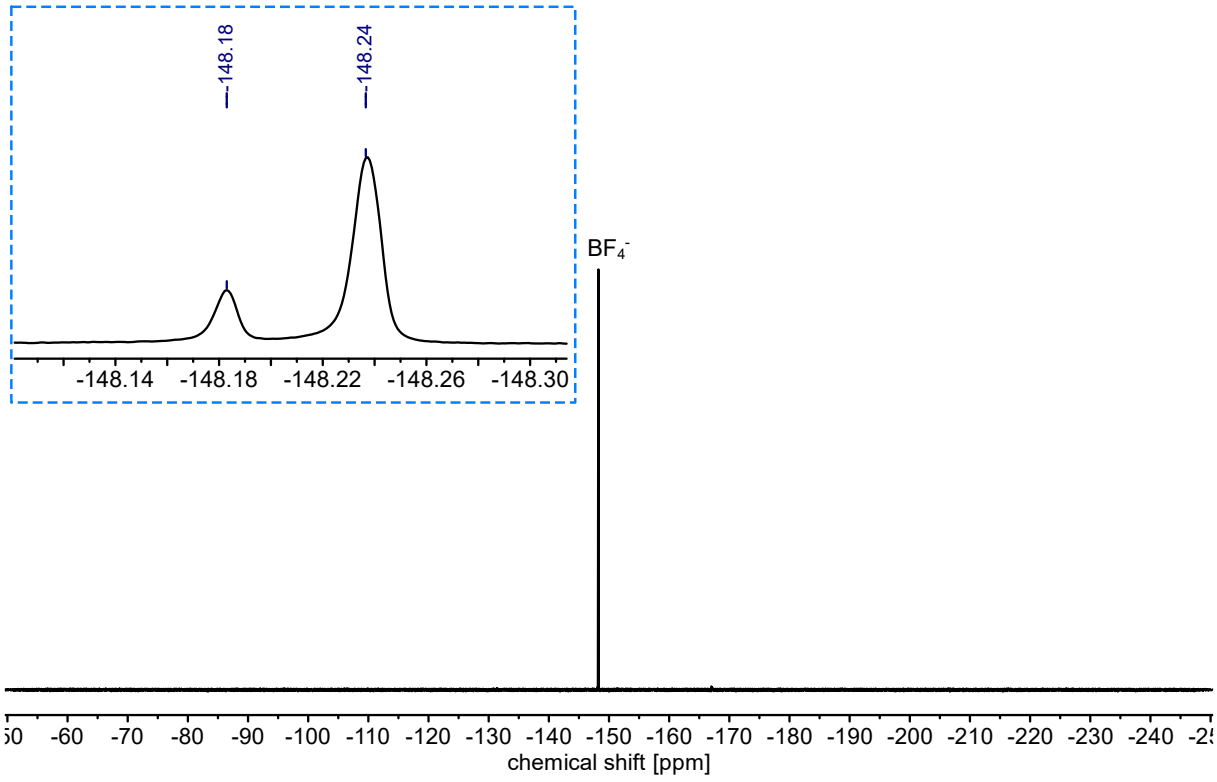

Figure S17. ^{19}F NMR spectrum (470 MHz, DMSO-d_6, 298 K) of 78% *E*-**T** and 22% *E*-**L** showing the presence of only one anion environment (the two separate signals arise from the ^{10}B and ^{11}B isotopomers).

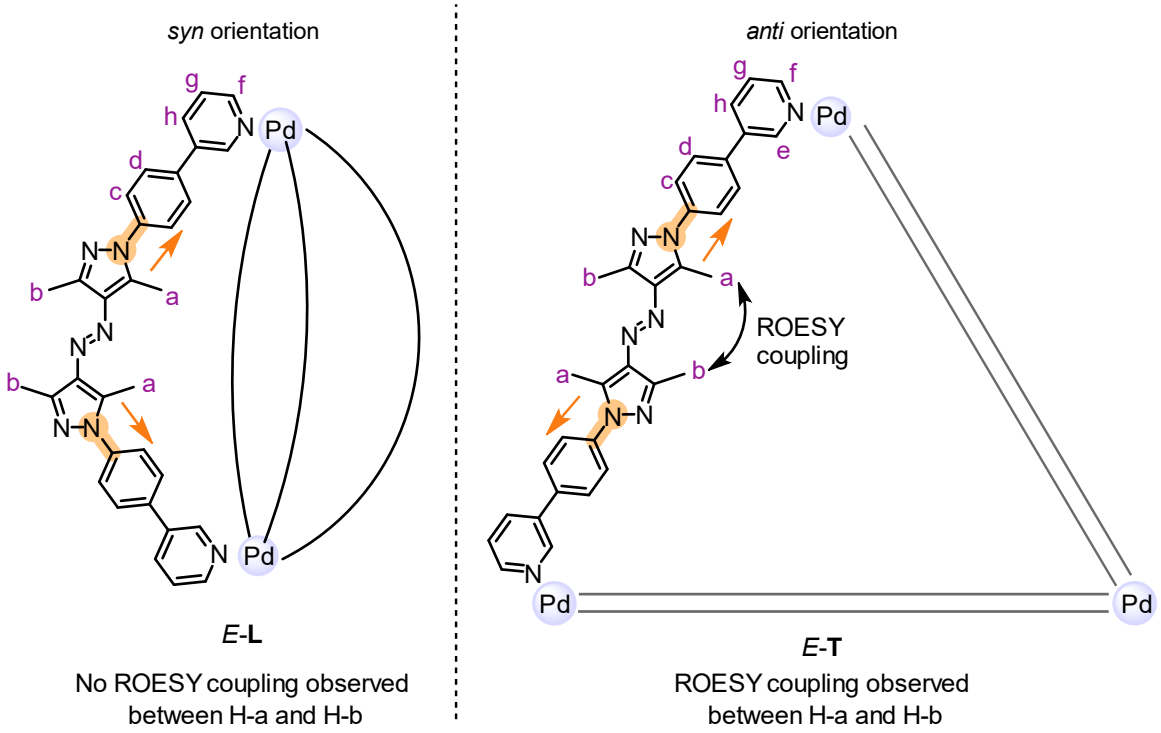

Figure S18. Graphical representation of the *syn* and *anti*-conformers of ligand **1** conformers within *E*-**L** and *E*-**T**, respectively. H-a and H-b only show ROESY contacts in the *anti*-conformation present in *E*-**T**.

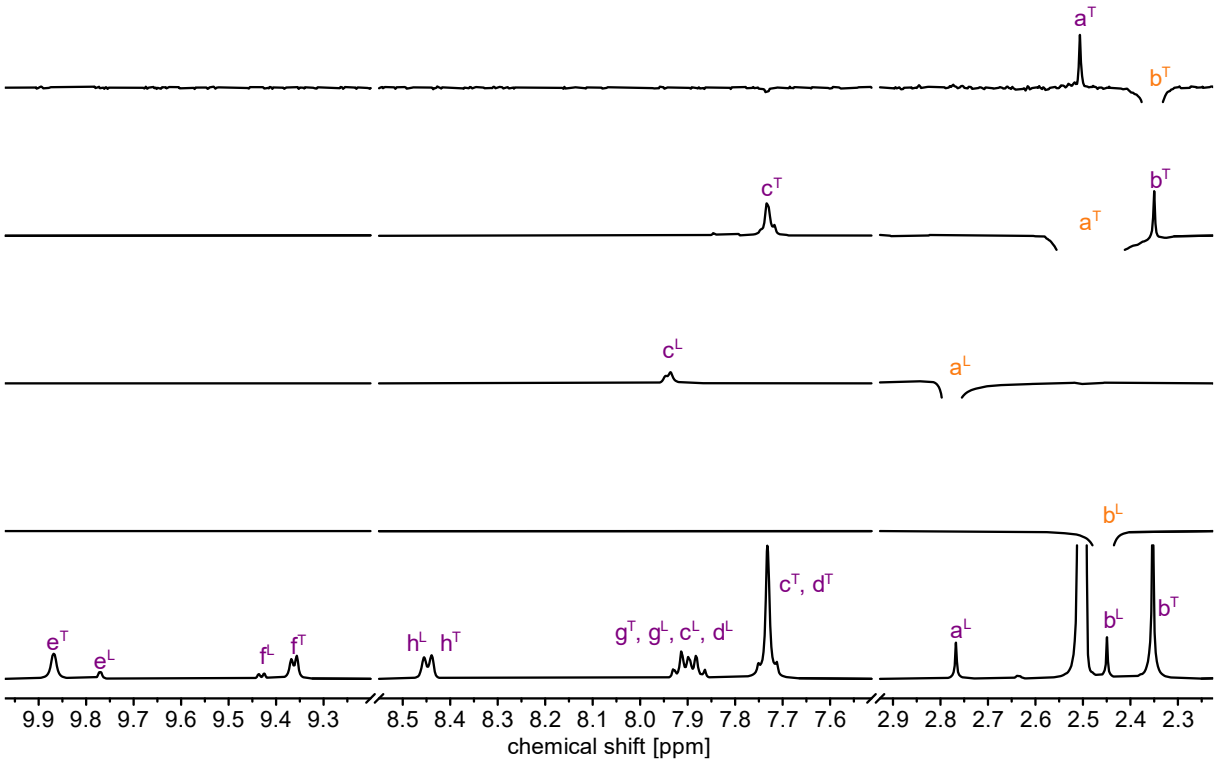

Figure S19. One-dimensional ^{1}H ROESY NMR spectra (700 MHz, DMSO-d_6, 298 K) of 78% *E*-**T** (denoted with T) and 22% *E*-**L** (denoted with L) for signals H-a^{L}, H-b^{L}, H-a^{T}, and H-b^{T}. Clear couplings between H-a^{T} and H-b^{T} confirm ligand **1**'s *anti*-conformation within *E*-**T**. As expected for the *syn*-conformation of ligand **1** in *E*-**L**, no cross peaks were observed for H-a^{L} and H-b^{L}.

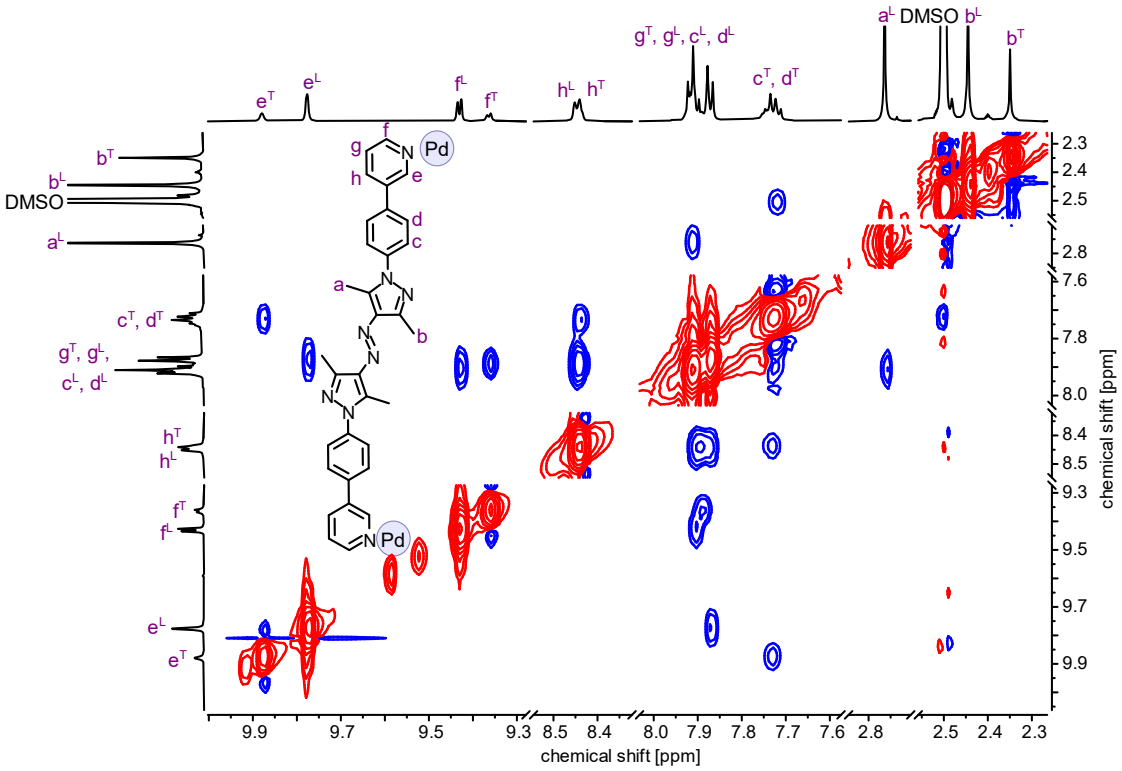

Figure S20. ^{1}H,^{1}H ROESY NMR spectrum (700 MHz, DMSO-d_6, 298 K) of 24% *E*-**T** (denoted as T) and 76% *E*-**L** (denoted as L). This mixture enriched with *E*-**L** was obtained by irradiating *Z*-**L** with 500 nm light and measuring the resulting spectrum immediately afterwards. This was necessary to obtain sufficiently intense signals of *E*-**L**, which helped with the proton assignment of *E*-**T** and *E*-**L**. As expected for the *syn*-conformation of ligand **1** in *E*-**L**, no cross peaks were observed for H-a^L and H-b^L.

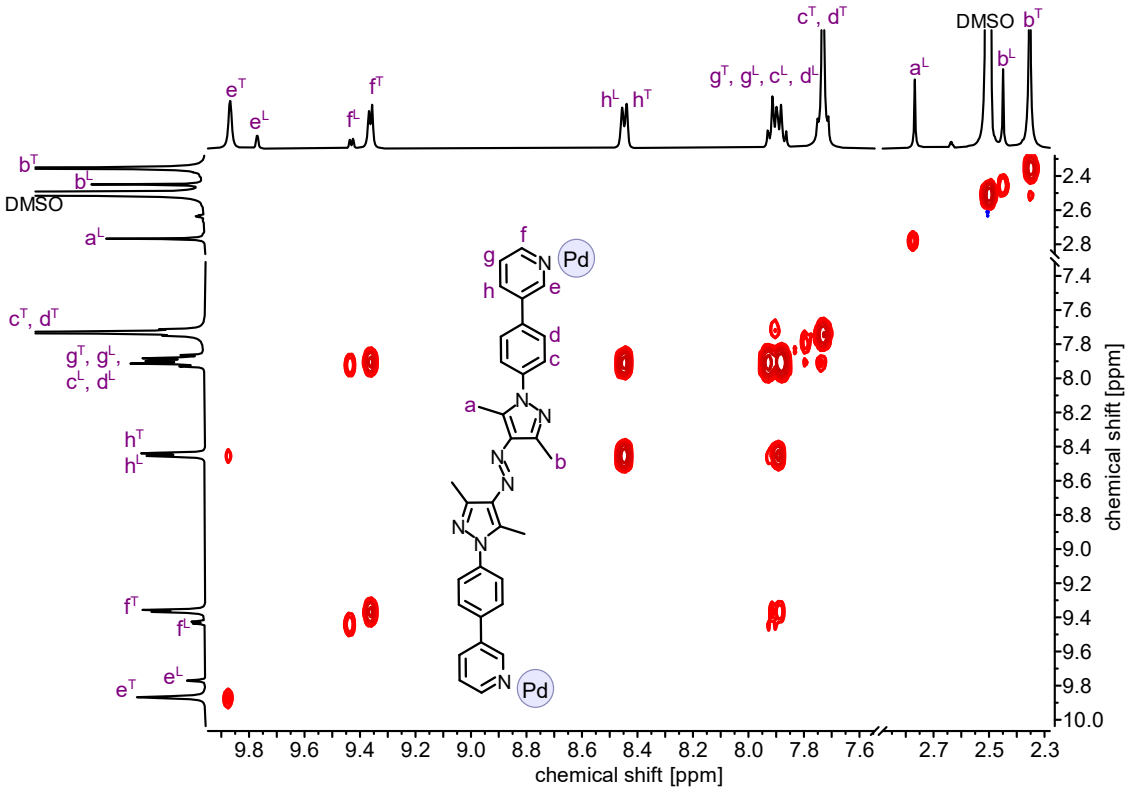

Figure S21. ^{1}H,^{1}H COSY NMR spectrum (700 MHz, DMSO-d_6, 298 K) of 78% *E*-**T** (denoted with T) and 22% *E*-**L** (denoted with L).

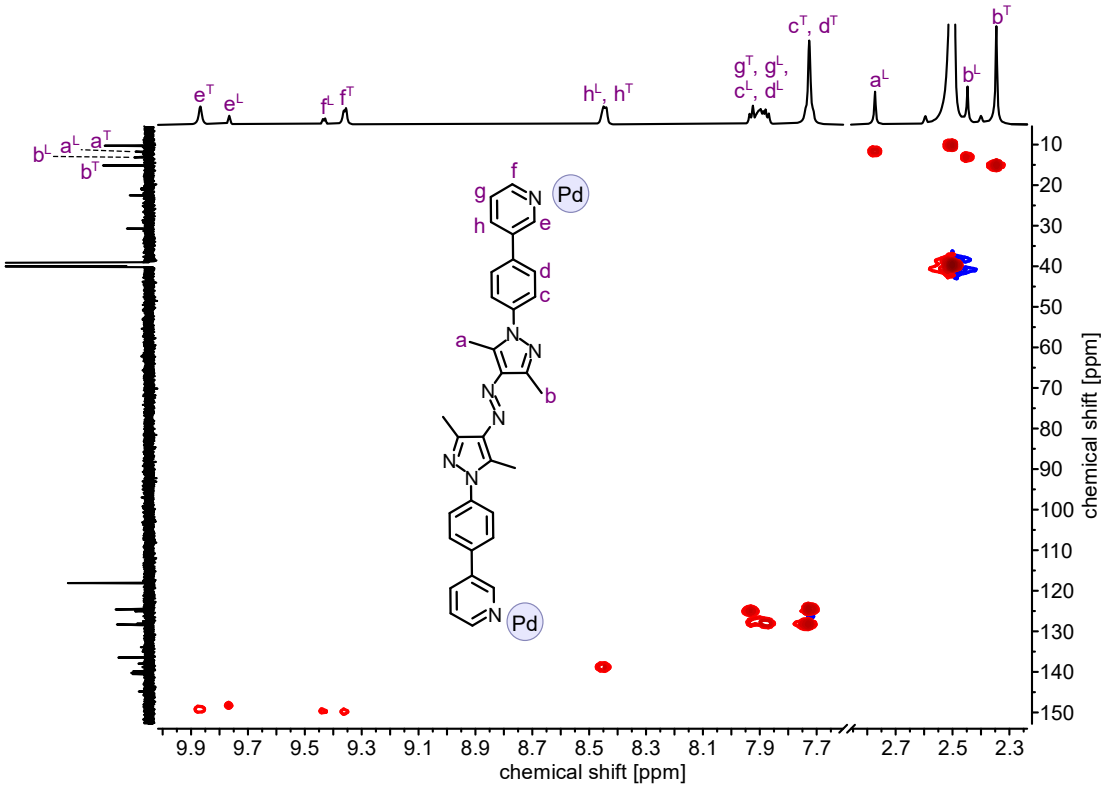

Figure S22. ^{1}H,^{13}C HSQC NMR spectrum (700/176 MHz, DMSO-d_6, 298 K) of 78% *E*-**T** (denoted with T) and 22% *E*-**L** (denoted with L).

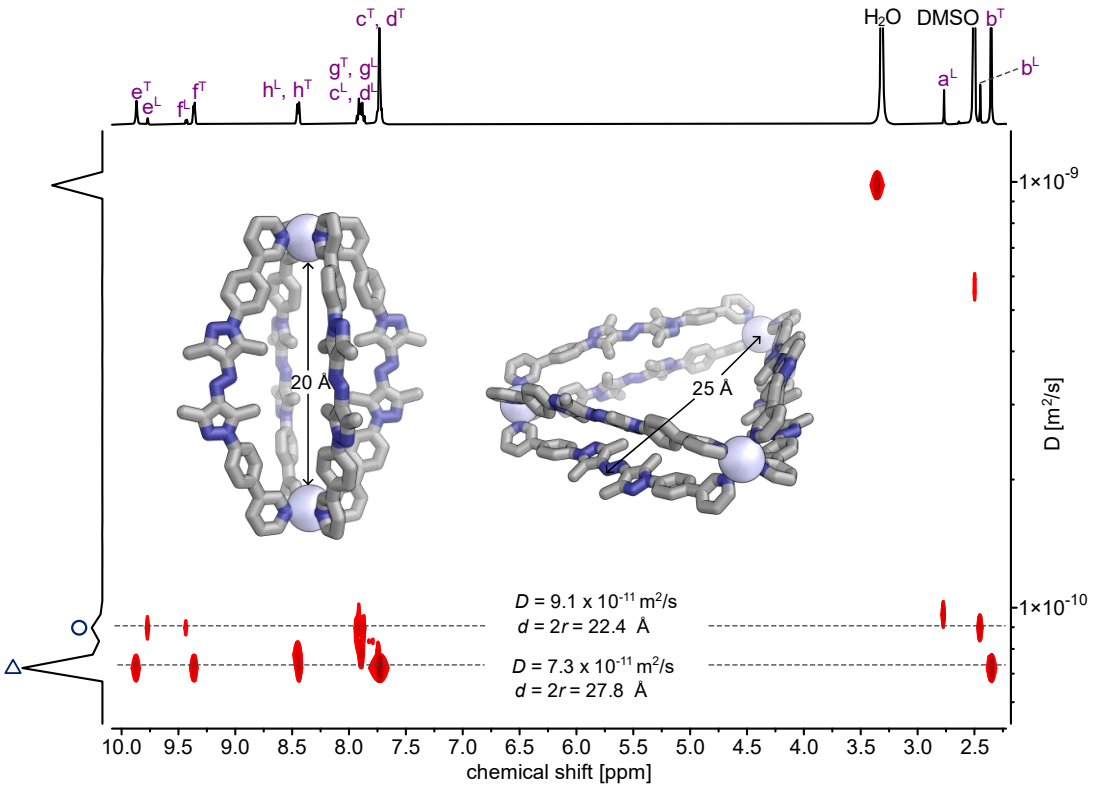

Figure S23. 2D-DOSY NMR spectrum (700 MHz, DMSO-d_6, 298 K, D20 = 0.35 s) of 78% *E*-**T** (denoted with T) and 22% *E*-**L** (denoted with L). Calculated diffusion constants (*D*) and solvodynamic diameters (*d* = 2*r*) for each complex are depicted in the spectrum. The crystal structure of *E*-**L** and the GFN2-xTB structure of *E*-**T** are shown with their respective distances (Pd – Pd and Pd – N_{azo}) as calculated by Avogadro (Version 1.2.0).[2]

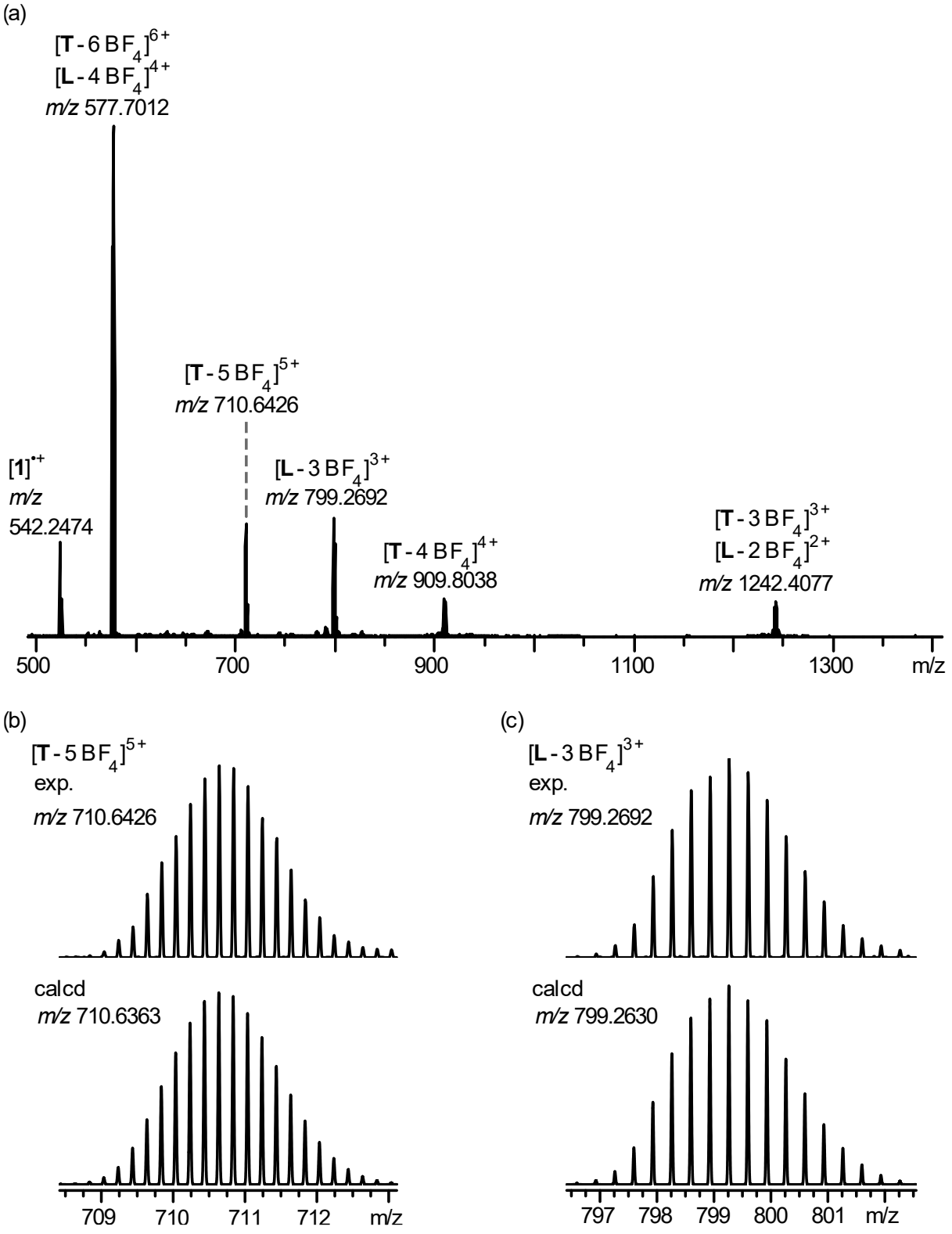

Figure S24. (a) High-resolution ESI$^+$ mass spectrum (DMSO/CH_3CN) of *E*-**T** and *E*-**L**. Experimental and calculated isotope patterns of (b) [**T** − 5 BF_4]$^{5+}$ and (c) [**L** − 3 BF_4]$^{3+}$.

S2.7 Formation of *Z*-**L**

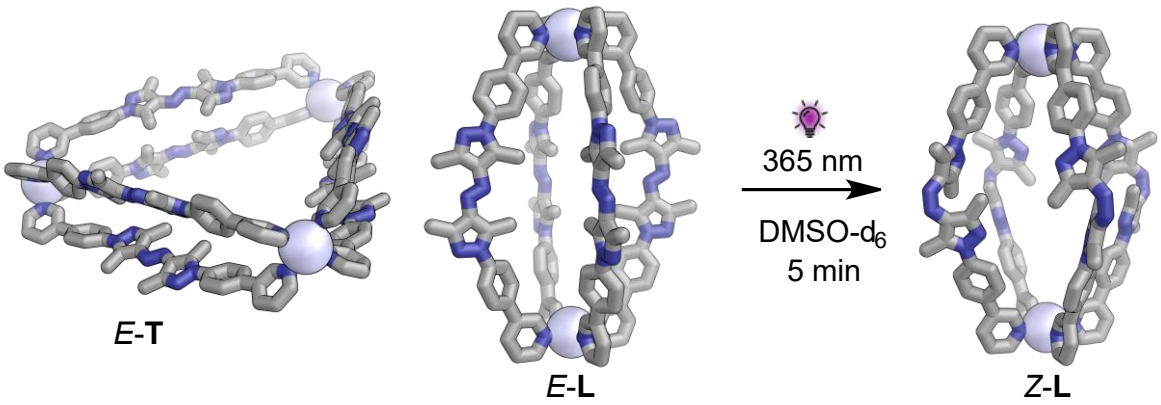

The previously prepared 78:22 triangle *E*-**T** / lantern *E*-**L** mixture (8.0 mM, 0.6 mL) was irradiated with 365 nm light for 5 min, and complete conversion to *Z*-**L** was achieved. A slight colour change from yellow to dark yellow/orange was observed upon irradiation. The sample was then kept in an amberised NMR tube wrapped in aluminium foil to avoid any *Z*→*E* isomerisation under ambient light.

Additional minor signals were observed in ^{1}H NMR (Figure S27a). However, no other Pd species (e.g., Pd_4L_8) nor partially self-assembled structures (e.g., Pd_2L_5) were found in the ESI mass spectrum, which led us to tentatively assume that these minor signals correspond to the five other lantern *Z*-**L** diastereomers, due to *Z*-**1** being chiral (Figure S36 and Section S8.3).

$[Pd_2(C_{32}H_{28}N_8)_4](BF_4)_4$ 2658.54 g/mol

^{1}H NMR[**] (500 MHz, DMSO-d_6, 298 K) δ_H [ppm] = 1.36 (s, 3H, H-b), 2.55 (s, 3H, H-a), 7.81 – 7.86 (m, 2H, H-c), 7.87 – 7.93 (m, 1H, H-g), 7.94 – 7.98 (m, 2H, H-d), 8.54 (d, J = 8.1, 1H, H-h), 9.43 (d, J = 7.2, 1H, H-f), 9.71 (d, J = 1.7, 1H, H-e).

^{13}C NMR (176 MHz, DMSO-d_6, 298 K) δ_C [ppm] = 10.7 (C-a), 13.7 (C-b), 124.6 (C-c), 127.6 (C-g), 127.9 (C-d), 133.2 (C-5), 135.3 (C-3), 137.6 (C-6), 138.3 (C-1/2), 138.6 (C-h), 139.8 (C-4), 148.4 (C-e), 149.9 (C-f).

^{19}F NMR (470 MHz, DMSO-d_6, 298 K) δ_F [ppm] = −148.24, −148.18

HRMS (ESI$^+$, DMSO-d_6/CH_3CN, 298 K): m/z (relative intensity) = 542.2485 (55%, [**1**]$^{\bullet+}$, calcd 542.2431), 577.7024 (100%, [**L** – 4 BF_4]$^{4+}$, calcd 577.6962), 799.2709 (20%, [**L** – 3 BF_4]$^{3+}$, calcd 799.2630), 1242.4095 (5%, [**L** – 2 BF_4]$^{2+}$, calcd 1242.3966).

[**] One dimensional ^{1}H-ROESY spectra enabled the assignment of H-a and H-b (Figure S30).

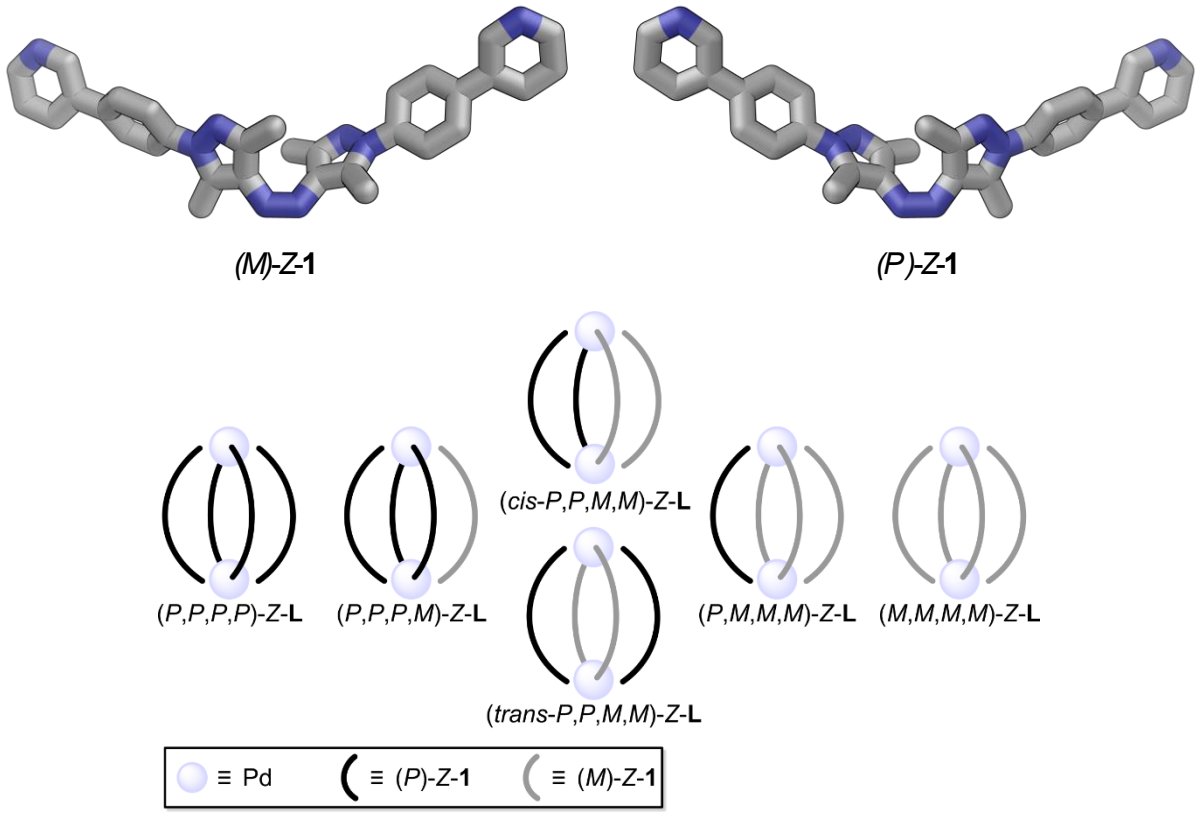

Figure S25. *Top*: Enantiomers of *Z*-**1**. *Bottom*: Cartoon representations of the six diastereomers of *Z*-**L**: *M*,*M*,*M*,*M*)-*Z*-**L** and its enantiomer (*P*,*P*,*P*,*P*)-*Z*-**L**, (*P*,*M*,*M*,*M*)-*Z*-**L** and its enantiomer (*P*,*P*,*P*,*M*)-*Z*-**L**, (*cis*-*P*,*P*,*M*,*M*)-*Z*-**L**, and (*trans*-*P*,*P*,*M*,*M*)-*Z*-**L**. Computations of these isomers are detailed in Section S8.3.

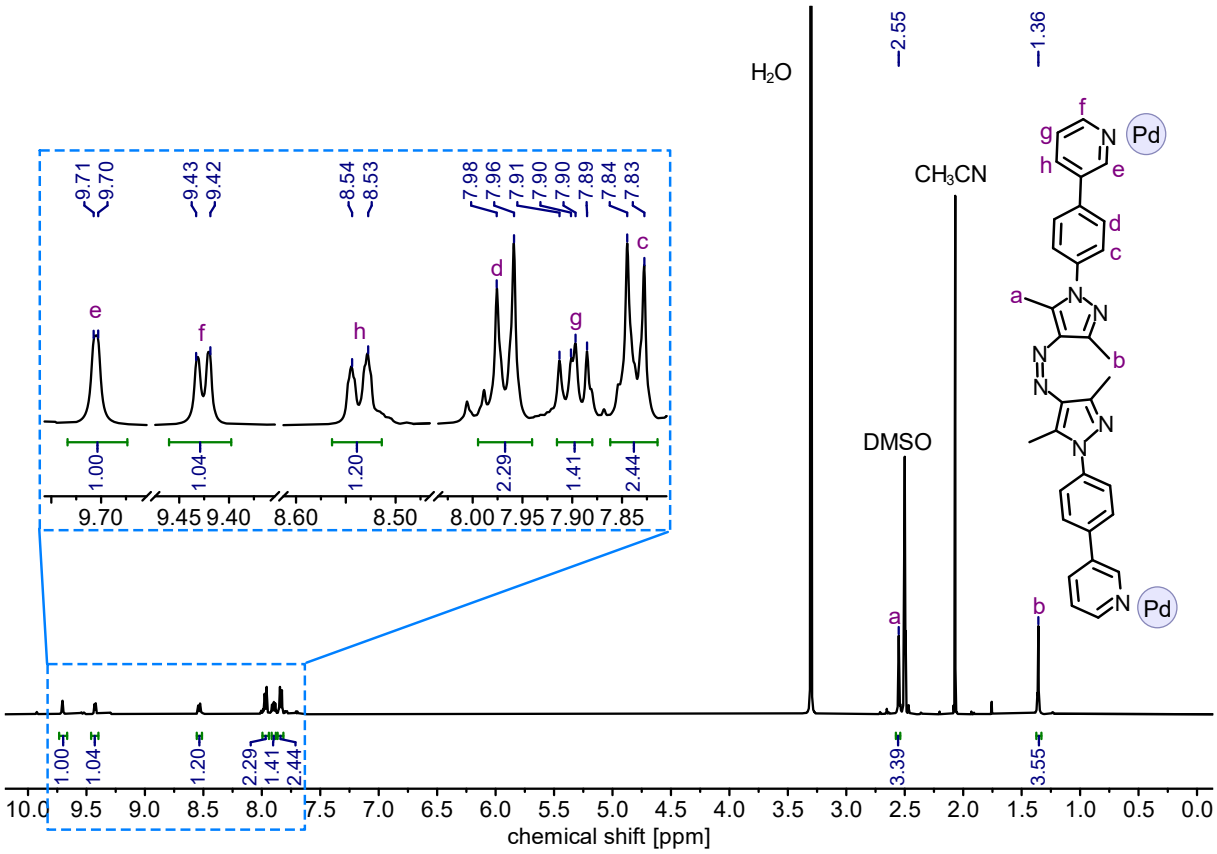

Figure S26. ^{1}H NMR spectrum (500 MHz, DMSO-d_6, 298 K) of *Z*-**L**.

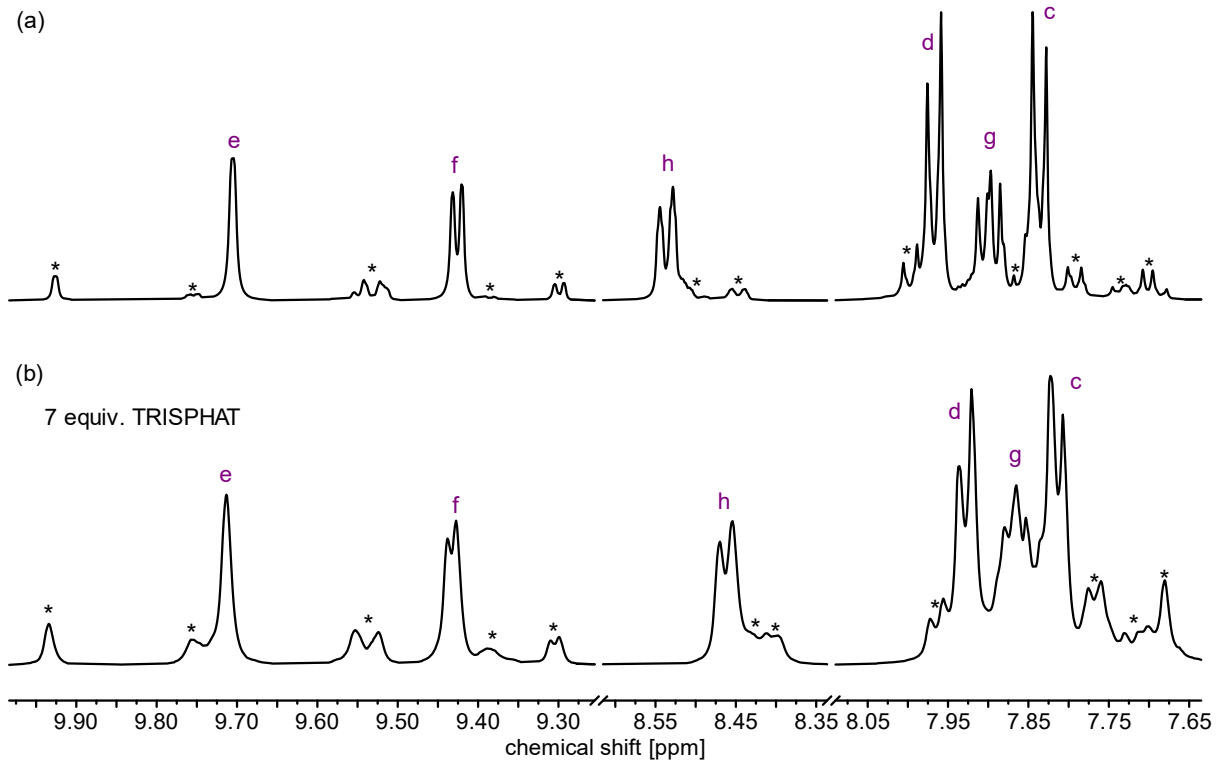

Figure S27. Stacked ^{1}H NMR spectra (500 MHz, DMSO-d_6, 298 K) of (a) *Z*-**L** and (b) *Z*-**L** + 7.0 equiv. tetra-*N*-butylammonium Δ-TRISPHAT. Minor species highlighted with an asterisk.

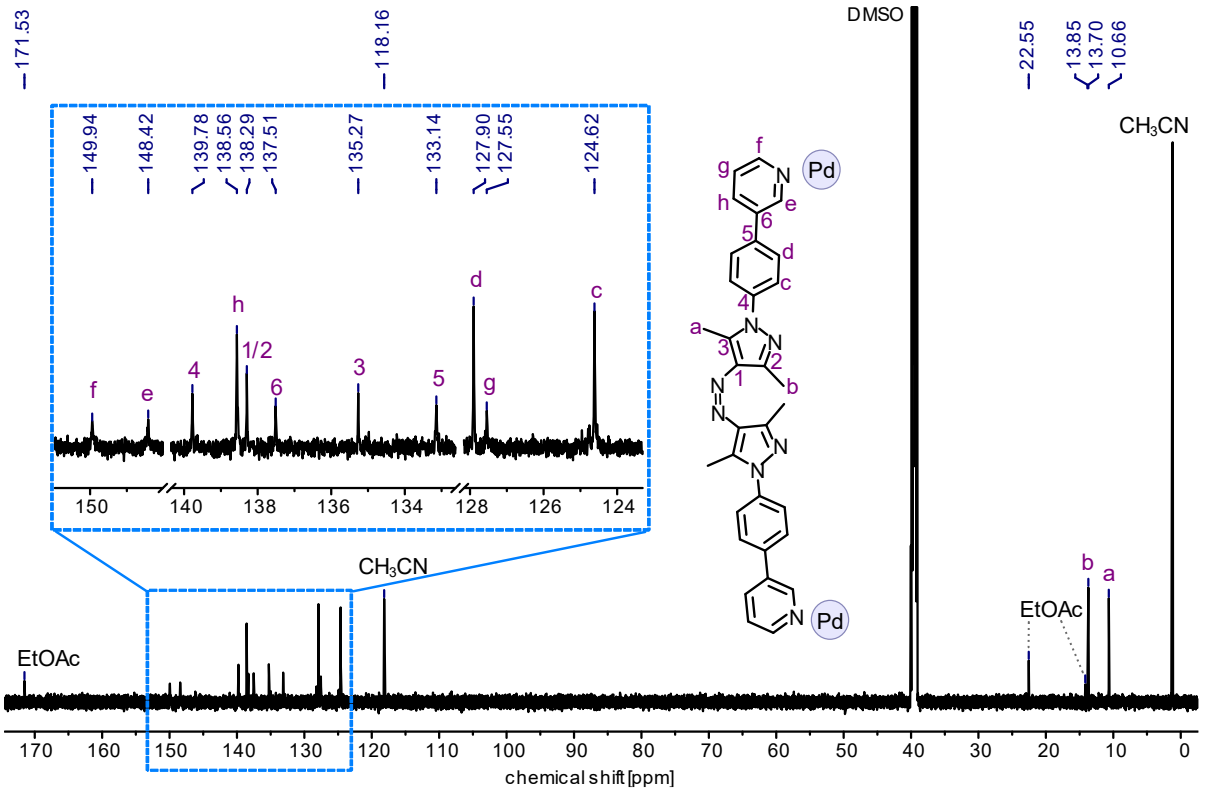

Figure S28. ^{13}C NMR spectrum (176 MHz, DMSO-d_6, 298 K) of *Z*-**L**.

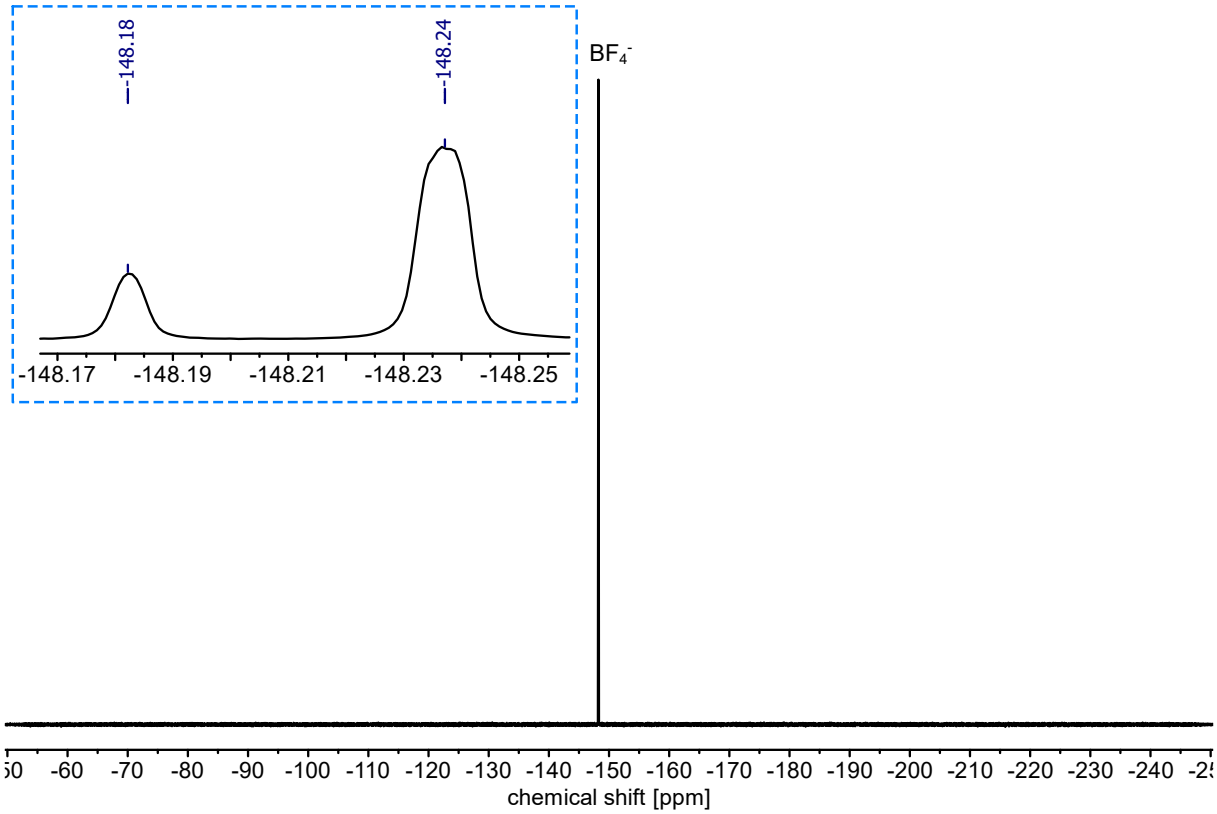

Figure S29. ^{19}F NMR spectrum (470 MHz, DMSO-d_6, 298 K) of *Z*-**L** showing the presence of only one anion environment (the two separate signals arise from the ^{10}B and ^{11}B isotopomers).

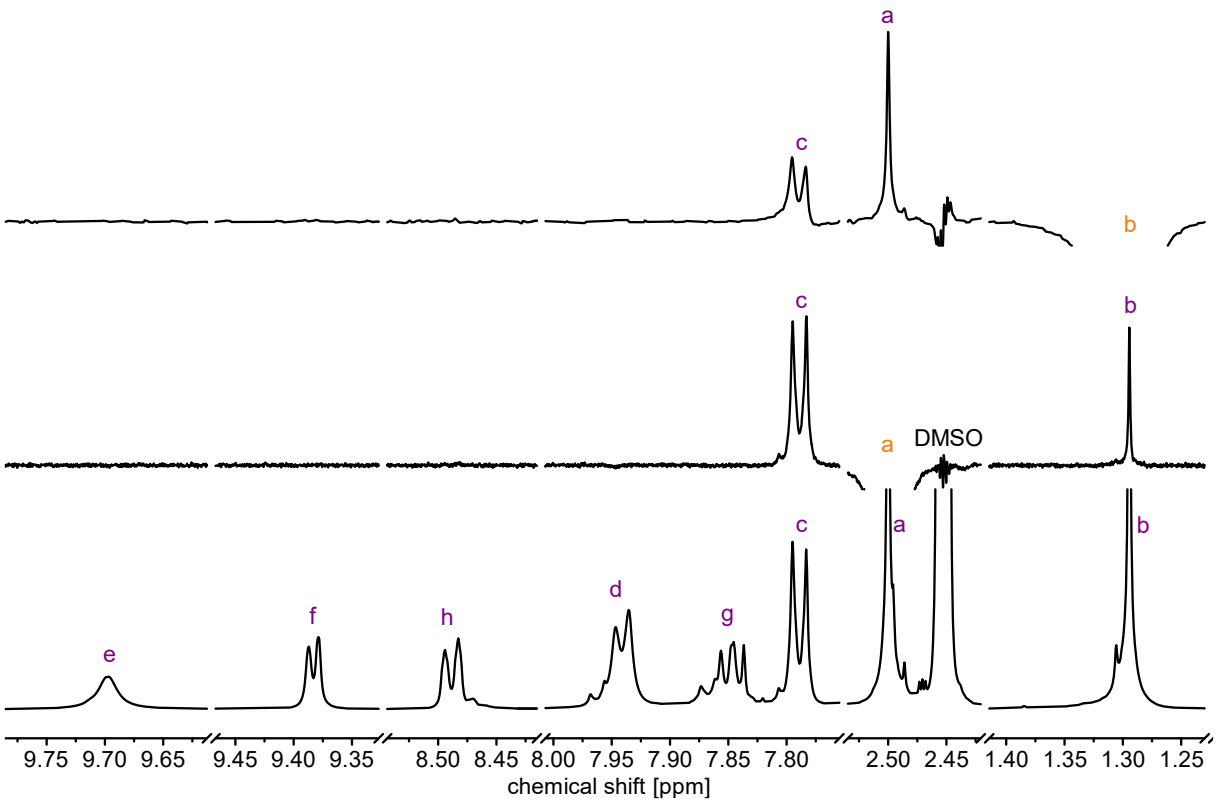

Figure S30. One-dimensional ^{1}H ROESY NMR spectra (700 MHz, DMSO-d_6, 298 K) of *Z*-**L** for signals H-a and H-b showing clear couplings between H-a and H-b, confirming ligand **1**'s *Z*-configuration within *Z*-**T**.

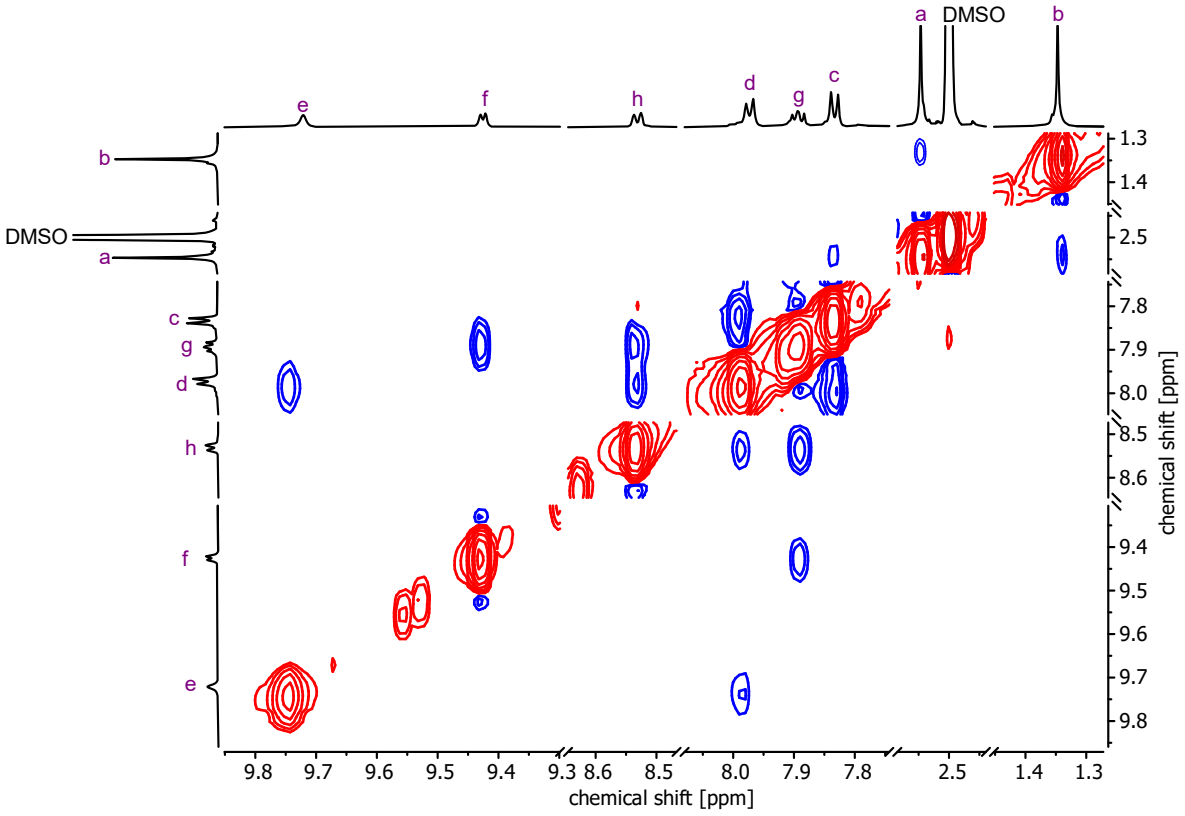

Figure S31. ^{1}H,^{1}H ROESY NMR spectrum (700 MHz, DMSO-d_6, 298 K) of *Z*-**L** showing clear coupling between H-a and H-b, confirming ligand **1**'s *Z*-configuration within *Z*-**T**.

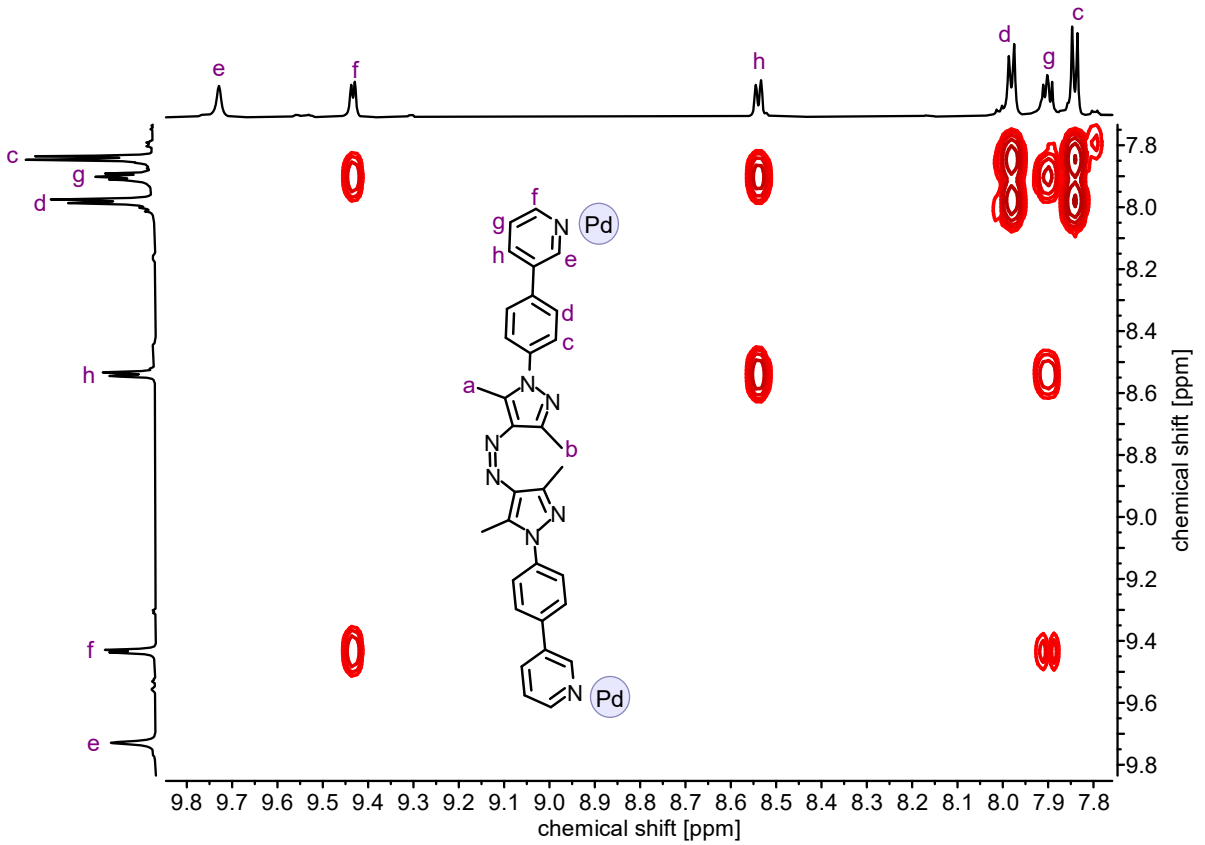

Figure S32. ^{1}H,^{1}H COSY NMR spectrum (700 MHz, DMSO-d_6, 298 K) of *Z*-**L**.

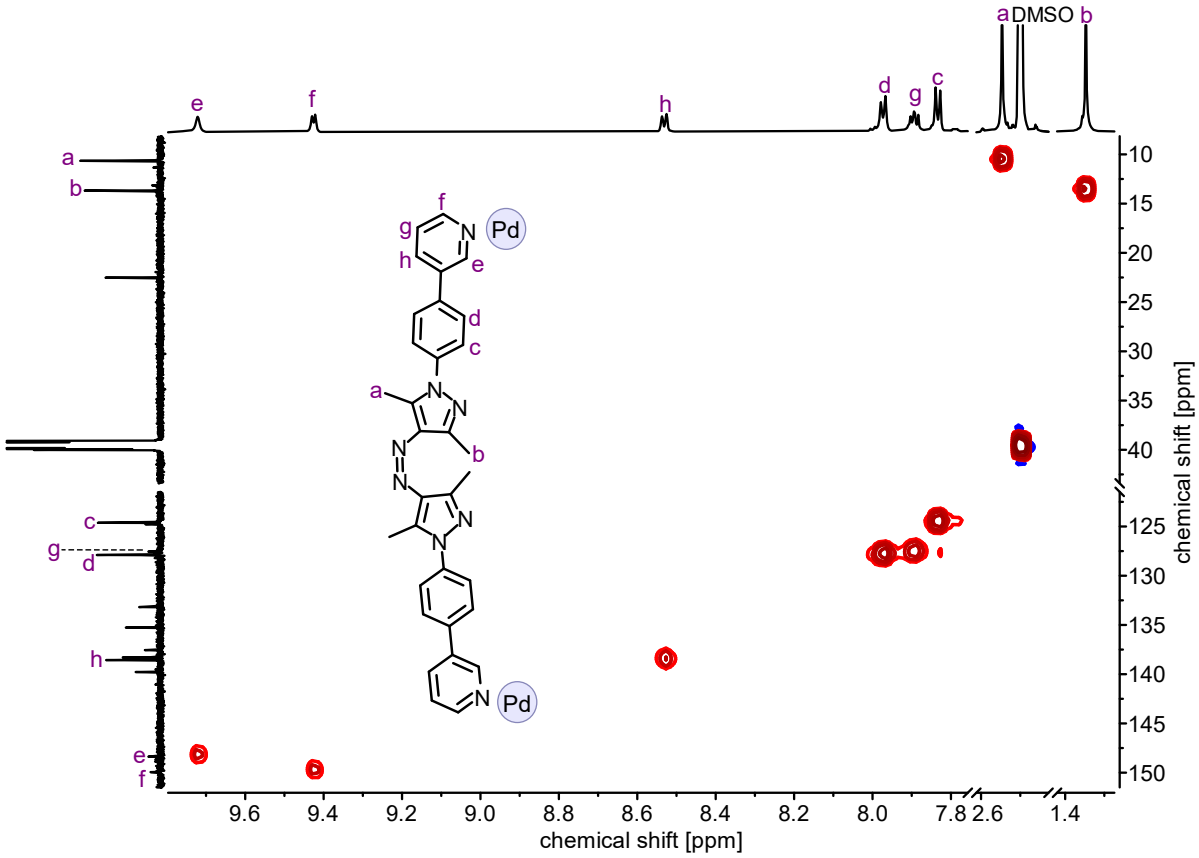

Figure S33. ^{1}H,^{13}C HSQC NMR spectrum (700/176 MHz, DMSO-d_6, 298 K) of *Z*-**L**.

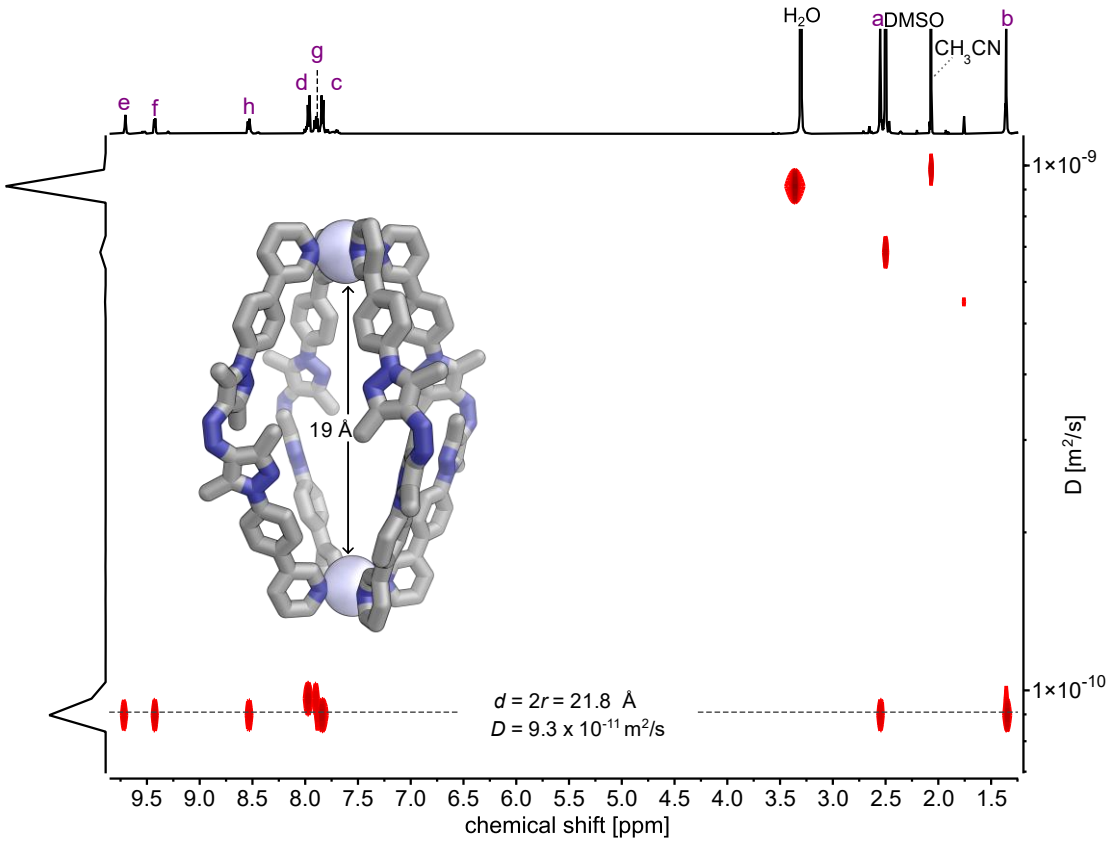

Figure S34. 2D-DOSY NMR spectrum (700 MHz, DMSO-d_6, 298 K, D20 = 0.35 s) of *Z*-**L**. Calculated diffusion constant (*D*) and solvodynamic diameter (*d* = 2*r*) are depicted in the spectrum. The GFN2-xTB structure of *Z*-**L** is shown with its Pd − Pd distance, calculated using Avogadro (Version 1.2.0).[2]

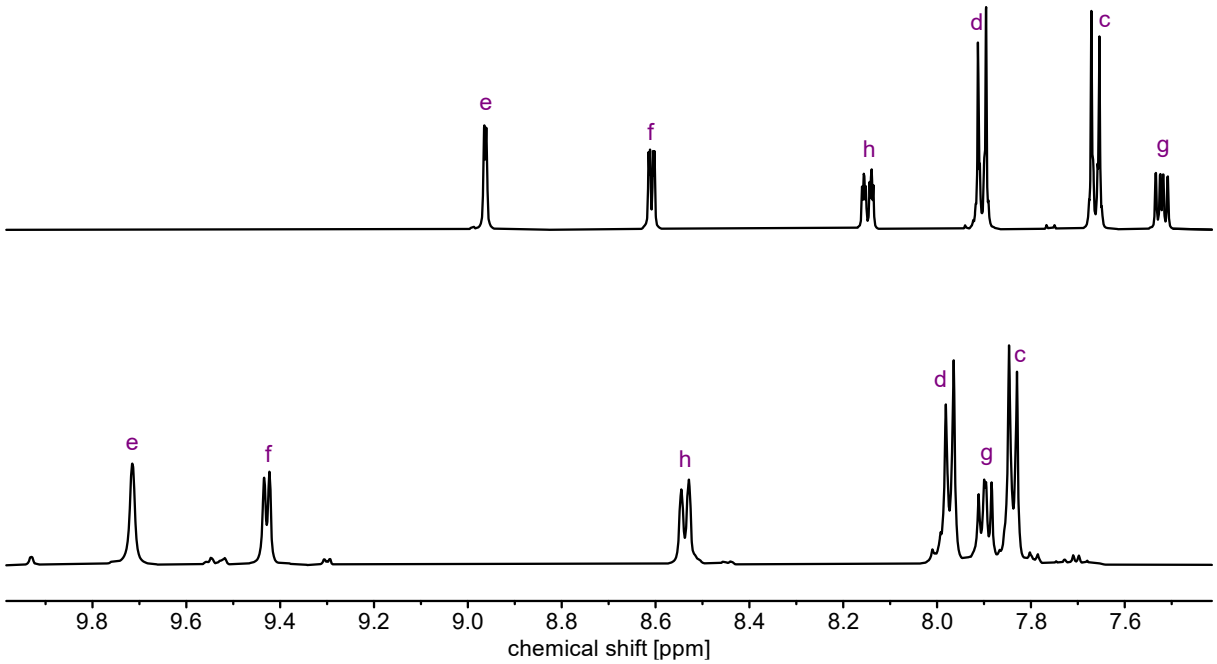

Figure S35. Stacked ^{1}H NMR spectra (500 MHz, DMSO-d_6, 298 K) of *Z*-**1** (top) and *Z*-**L** (bottom).

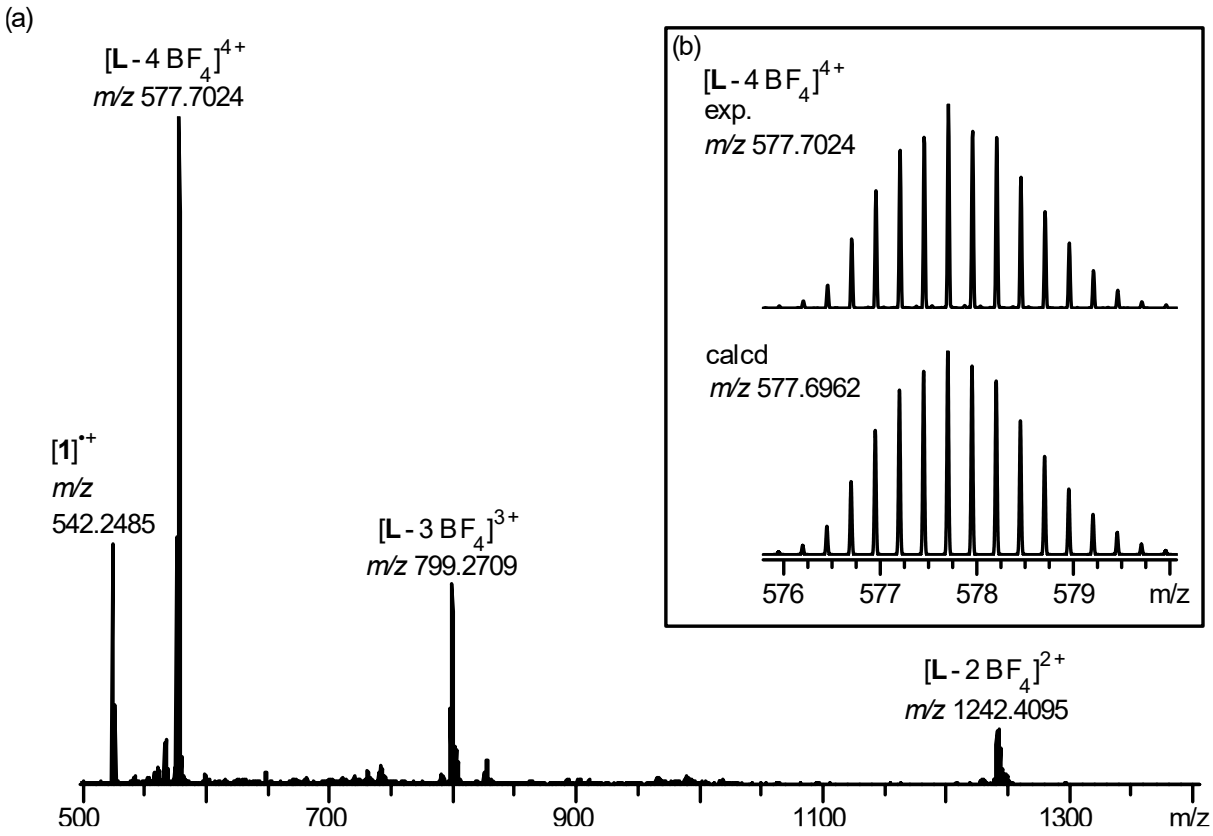

Figure S36. (a) High-resolution ESI$^+$ mass spectrum (DMSO/CH_3CN) of *Z*-**L**. (b) Experimental and calculated isotope patterns of [**L** − 4 BF_4]$^{4+}$.

S2.8 Lantern scrambling between *E*-**L** and *Z*-**L**

To investigate whether assemblies with both ligand *E*-**1** and *Z*-**1** within the same lantern structure, namely *Z,E,E,E*-**L**, *cis*-*Z,Z,E,E*-**L**, *trans*-*Z,Z,E,E*-**L**, *Z,Z,Z,E*-**L**, are able to form, as indicated by our computational studies (Section S8.2), lantern scrambling experiments were performed by combining pre-assembled lanterns *E*-**L** and *Z*-**L** in ratios of 1:3, 1:1, and 3:1 (*E*-**L** / *Z*-**L**). Direct mixing of isomeric ligands was not feasible, because of free ligand **1**'s low solubility in DMSO (the solvent used for cage formation).

Z-**L** was obtained by irradiating a sample of *E*-**T** / *E*-**L** at 365 nm to induce *E*→*Z* isomerisation. As complete thermal relaxation of *Z*-**L** requires approximately one year (Figure S73), no significant relaxation was expected during the course of the experiment. *E*-**L** was generated by irradiating a sample of *Z*-**L** at 500 nm. Due to the equilibration between *E*-**T** and *E*-**L** (see Section S3), small amounts of *E*-**T** were always present in the samples and increased within the course of the experiment.

Each sample was prepared using a freshly irradiated *E*-**L** solution and mixing it with the *Z*-**L** solution in 1:3, 1:1, and 3:1 (*E*-**L** / *Z*-**L**) ratios. The samples were investigated by ^{1}H NMR spectroscopy immediately after mixing (2 min / 5 min), and the mixtures were monitored over time (17 min / 20 min, 13 h, 7 d; Figure S37−S39). In all cases, the lantern mixtures gave rise to new sets of signals (highlighted in yellow, orange, and red, respectively, depending on whether they were predominantly found in the 1:3, 1:1 or 3:1 *E*-**L** / *Z*-**L** mixtures), which reached their maximum intensity after 13 h. While it was not possible to definitely assign the newly emerged signals to specific lantern structures, namely *Z,E,E,E*-**L**, *cis*-*Z,Z,E,E*-**L**, *trans*-*Z,Z,E,E*-**L**, *Z,Z,Z,E*-**L**, we tentatively assume these signals to arise from the lanterns with mixed ligand configurations, supporting our computational results that formation of such structures should be possible (Section S8.2). After 7 d all mixtures had formed significant amounts of triangle *E*-**T**, indicating its thermodynamic stability.

Some of the identified signals of lanterns with mixed ligand configurations can also be observed during the thermal relaxation of *Z*-**L** (Figure S74), further supporting our hypothesis regarding the identity of these signals.

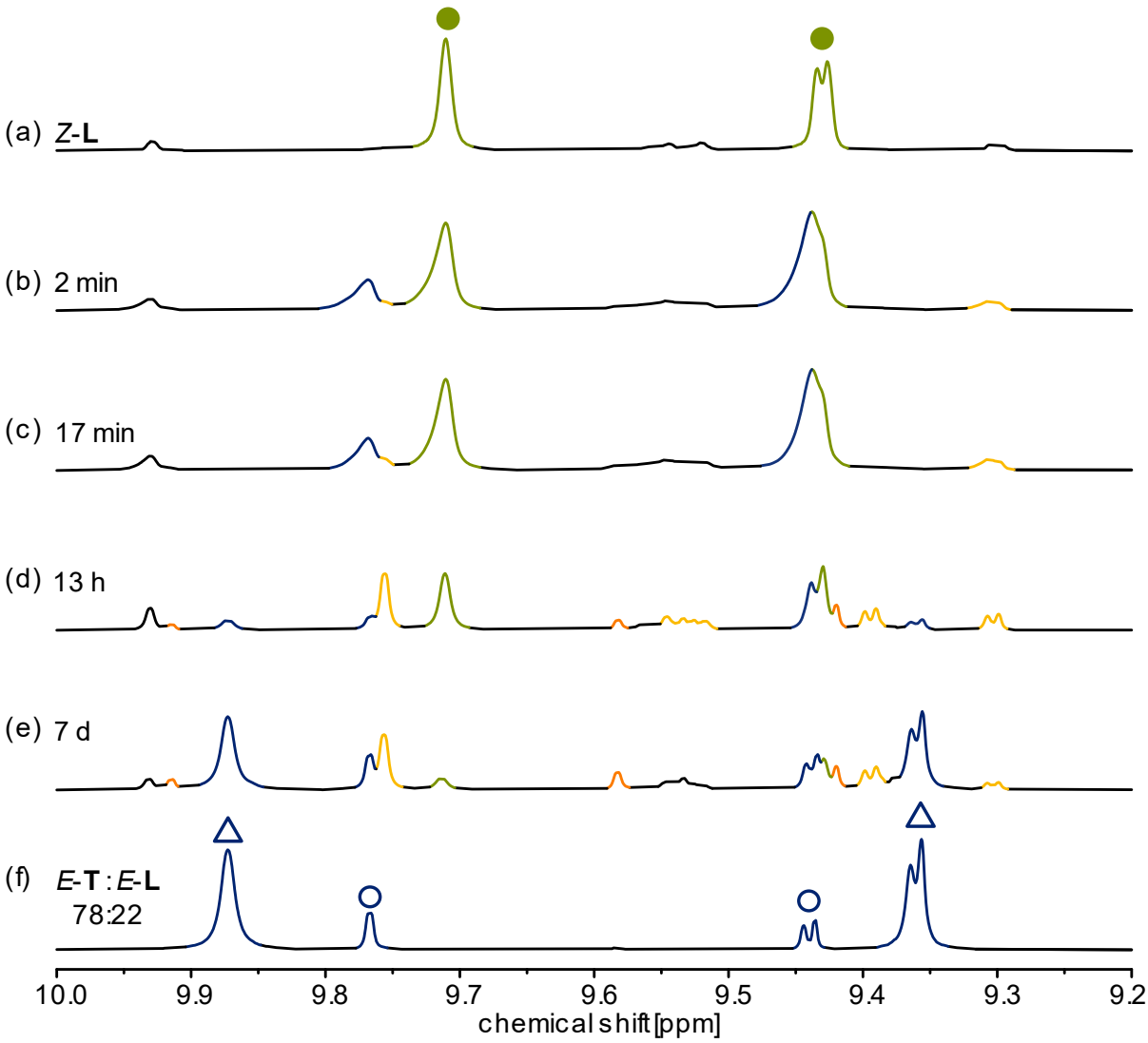

Figure S37. ^{1}H NMR (700 MHz, DMSO-d_6, 298 K) spectra of the lantern-scrambling experiment with *E*-**L** / *Z*-**L** (1:3) after (b) 2 min, (c) 17 min, (d) 13 h, and (e) 7 d. For reference: (a) *Z*-**L** and (f) *E*-**T** / *E*-**L** mixture under light exclusion (*E*-**T** / *E*-**L**, 78:22). *E*-**T** is denoted with **Δ**, *E*-**L** is denoted with **O**, and *Z*-**L** is denoted with ●. Newly emerged signals are tentatively highlighted in yellow, orange, and red, respectively, depending on whether they were predominantly found in the 1:3, 1:1 or 3:1 *E*-**L** / *Z*-**L** mixtures.

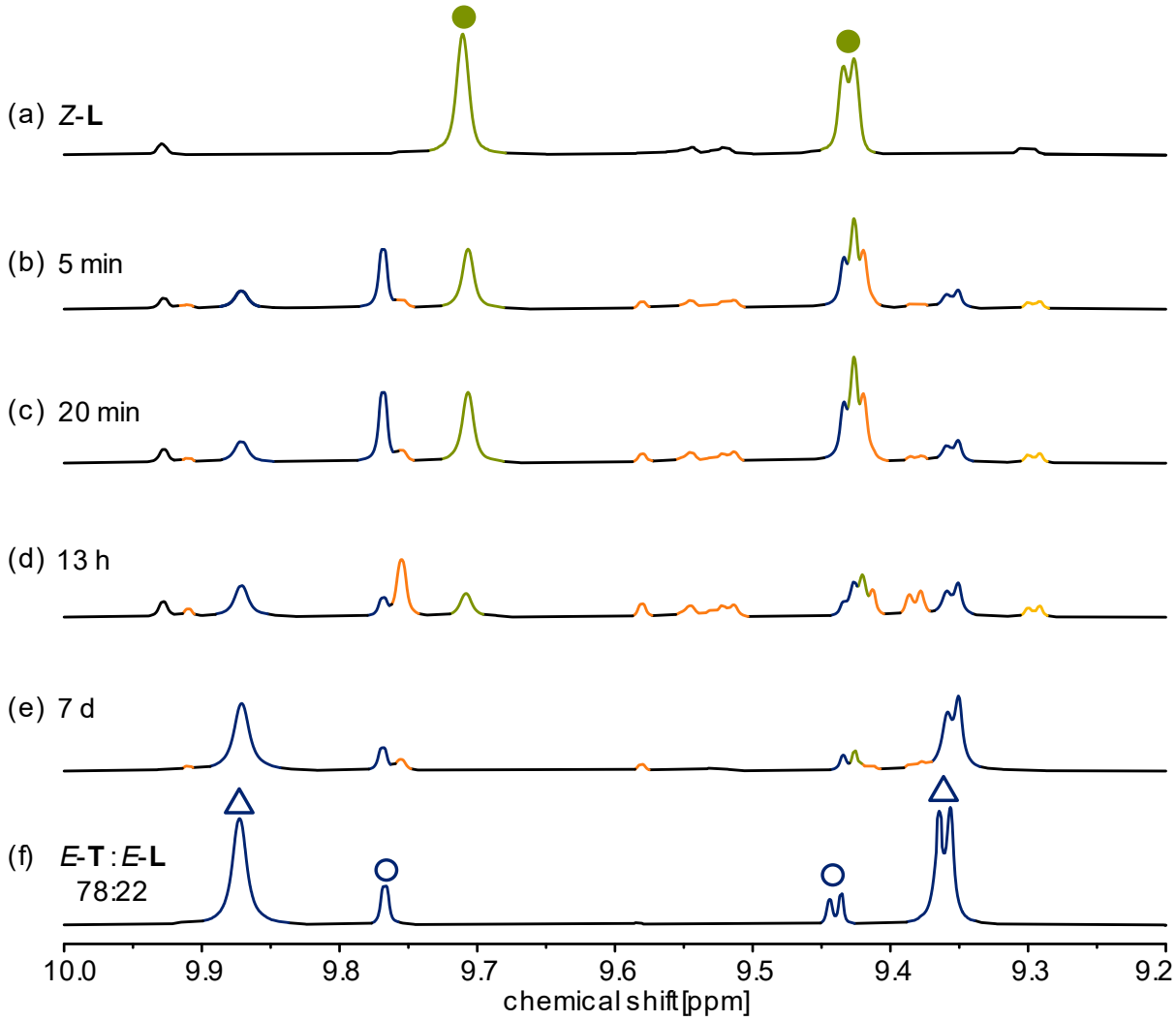

Figure S38. ^{1}H NMR (700 MHz, DMSO-d_6, 298 K) spectra of the lantern-scrambling experiment with *E*-**L** / *Z*-**L** (1:1) after (b) 5 min, (c) 20 min, (d) 13 h, and (e) 7 d. For reference: (a) *Z*-**L** and (f) *E*-**T** / *E*-**L** mixture under light exclusion (*E*-**T** / *E*-**L**, 78:22). *E*-**T** is denoted with **Δ**, *E*-**L** is denoted with **O**, and *Z*-**L** is denoted with ●. Newly emerged signals are tentatively highlighted in yellow, orange, and red, respectively, depending on whether they were predominantly found in the 1:3, 1:1 or 3:1 *E*-**L** / *Z*-**L** mixtures.

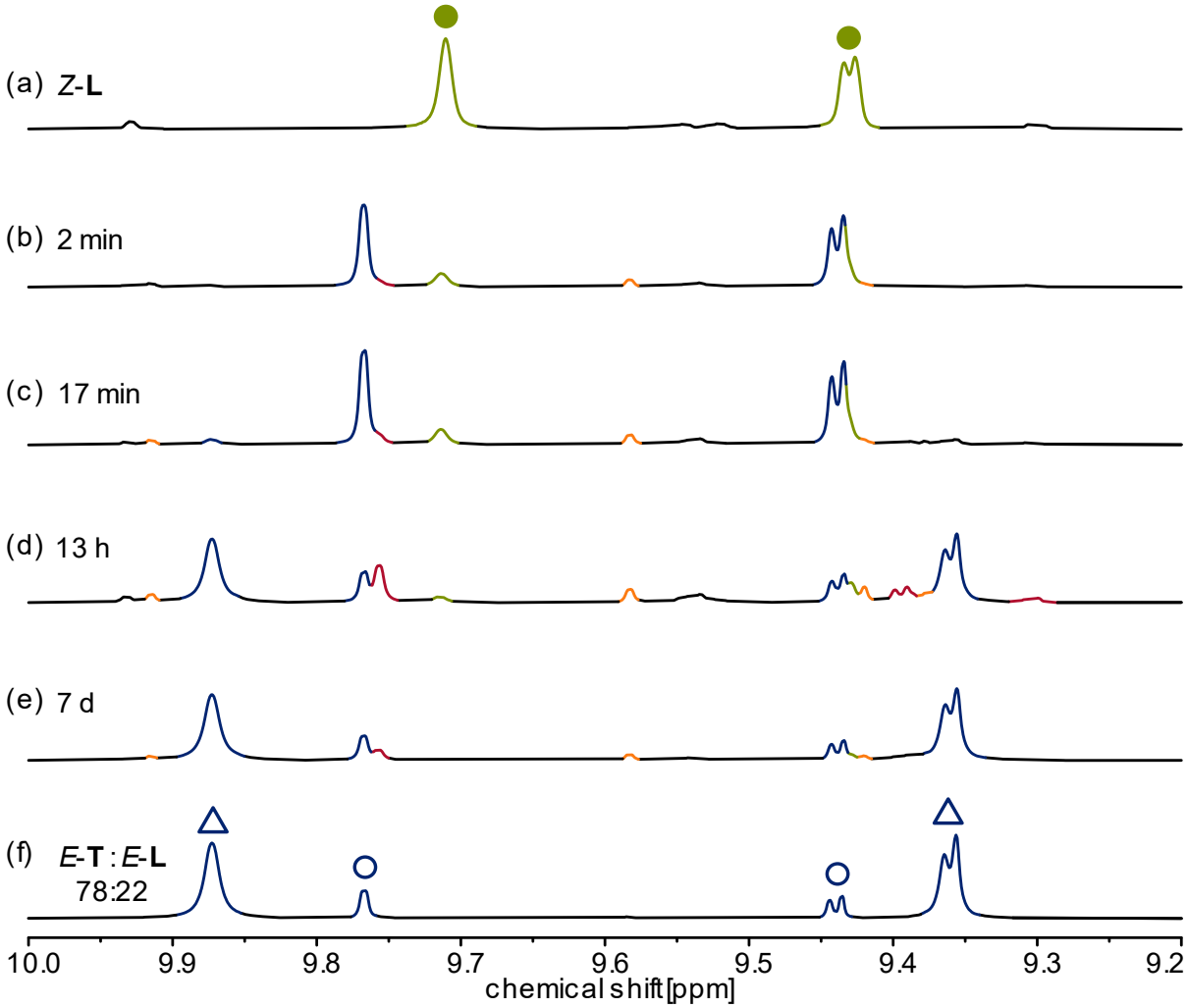

Figure S39. ^{1}H NMR (700 MHz, DMSO-d_6, 298 K) spectra of the lantern-scrambling experiment with *E*-**L** / *Z*-**L** (1:3) after: (b) 2 min, (c) 17 min, (d) 13 h, and (e) 7 d. For reference: (a) *Z*-**L** and (f) *E*-**T** / *E*-**L** mixture under light exclusion (*E*-**T** / *E*-**L**, 78:22). *E*-**T** is denoted with **Δ**, *E*-**L** is denoted with **O**, and *Z*-**L** is denoted with ●. Newly emerged signals are tentatively highlighted in yellow, orange, and red, respectively, depending on whether they were predominantly found in the 1:3, 1:1 or 3:1 *E*-**L** / *Z*-**L** mixtures.

S3 Investigation of the triangle *E*-**T** / lantern *E*-**L** equilibrium

All samples were prepared according to the experimental procedure outlined in Section S2.6 and were stored in amberised NMR tubes wrapped in aluminium foil in an air-conditioned room at 22 °C to prevent any disruption of the equilibrium caused by either temperature or ambient light.

S3.1 Triangle *E*-**T** / lantern *E*-**L** equilibrium

The thermal interconversion between triangle *E*-**T** and lantern *E*-**L** was investigated at 298 K and 348 K. For this, an NMR sample containing 78:22 triangle *E*-**T** / lantern *E*-**L** mixture was irradiated with 365 nm light for 5 min to obtain *Z*-**L**. The sample was then immediately irradiated with 500 nm light to obtain a sample that contains almost exclusively *E*-**L** lantern (Figure S61). The equilibration between triangle *E*-**T** and lantern *E*-**L** was followed over time by ^{1}H NMR spectroscopy (500 MHz, DMSO-d_6, 298 K or 348 K, Figure S41 and Figure **S42**) and the triangle *E*-**T** / lantern *E*-**L** composition plotted over time (Figure S40).

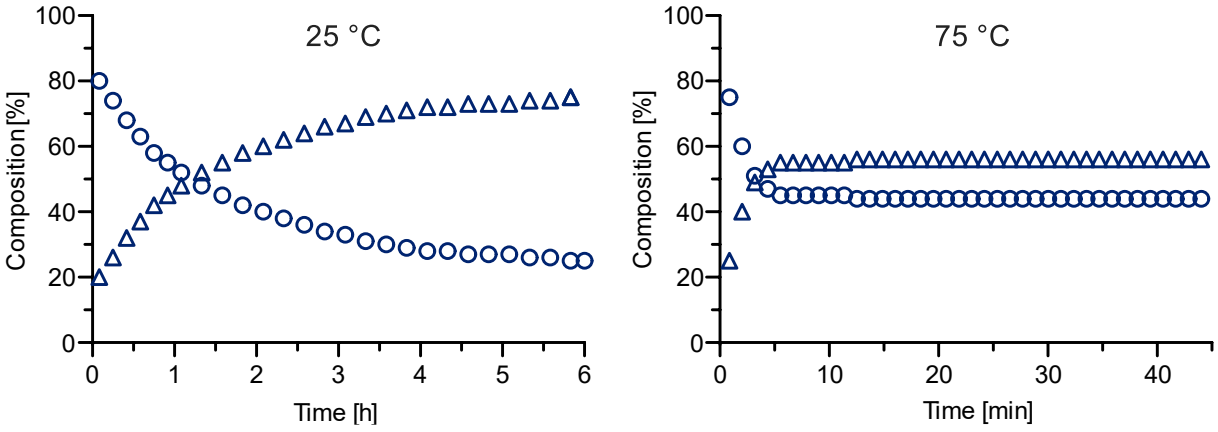

Figure S40. At room temperature, *Z*-**L** was irradiated with 500 nm for approx. 5 min to induce *Z*→*E* isomerisation. *Left*: A ^{1}H NMR (500 MHz, DMSO-d_6, 298 K) spectrum was measured every 5 min for 6 h to monitor the equilibrium between *E*-**T** triangle and *E*-**L** at 298 K. Between 0 h and 1 h, every second data point was removed for clarity; between 1 h and 6 h, only every third data point was plotted. *Right*: A ^{1}H NMR (500 MHz, DMSO-d_6, 348 K) spectrum was measured every 70 s for 45 min to monitor the equilibrium between *E*-**T** and *E*-**L** at 348 K. *E*-**T** is denoted with **Δ**, *E*-**L** is denoted with **O**.

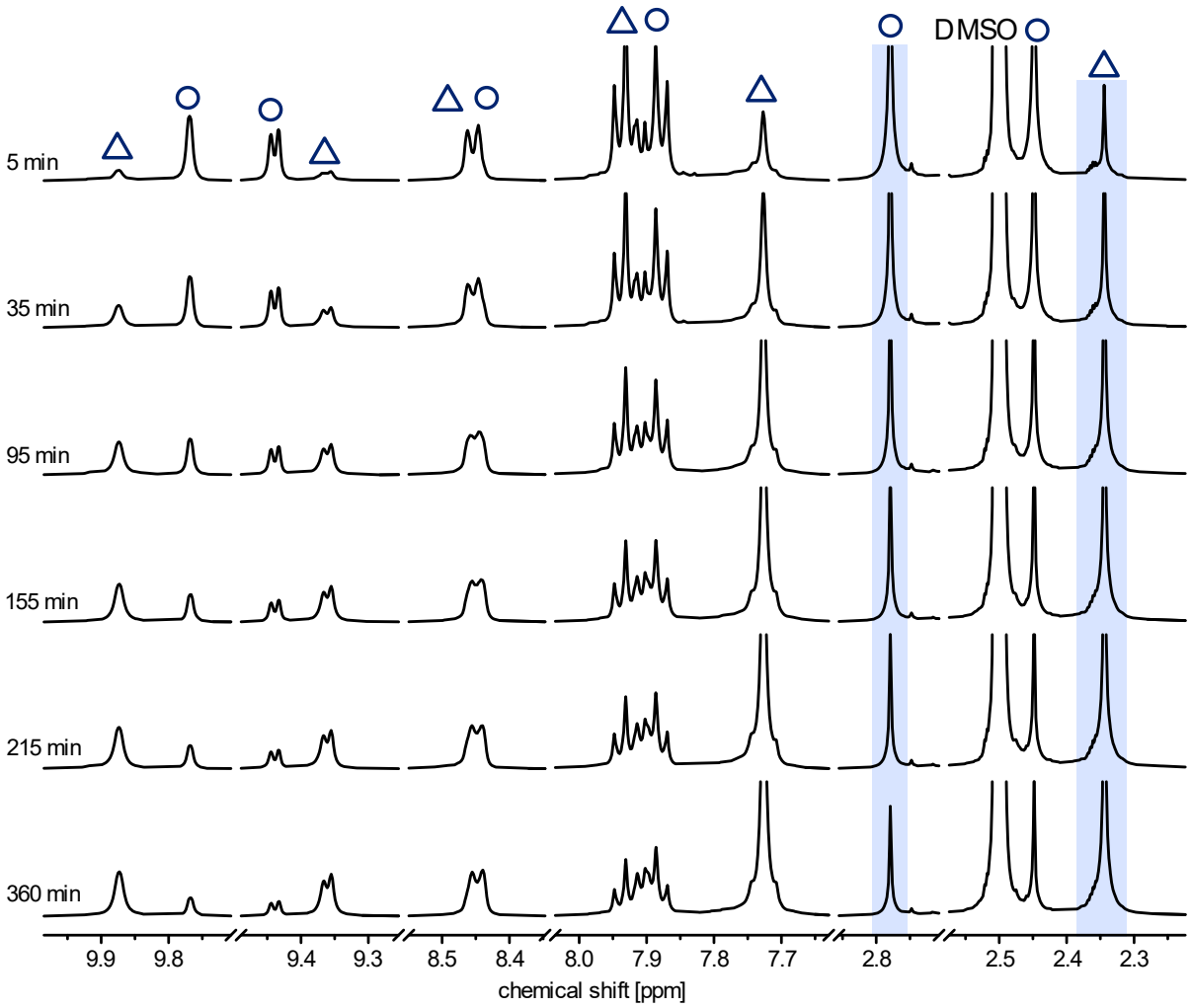

Figure S41. ^{1}H NMR (500 MHz, DMSO-d_6, 298 K) spectra of the equilibration between *E*-**T** triangle and *E*-**L** at 298 K. A ^{1}H NMR spectrum was measured every 5 min for 6 h. The signals highlighted in blue were chosen to be line-fitted and plotted to display changes in composition between *E*-**T** and *E*-**L** (Figure S40). *E*-**T** is denoted with **Δ**, *E*-**L** is denoted with **O**.

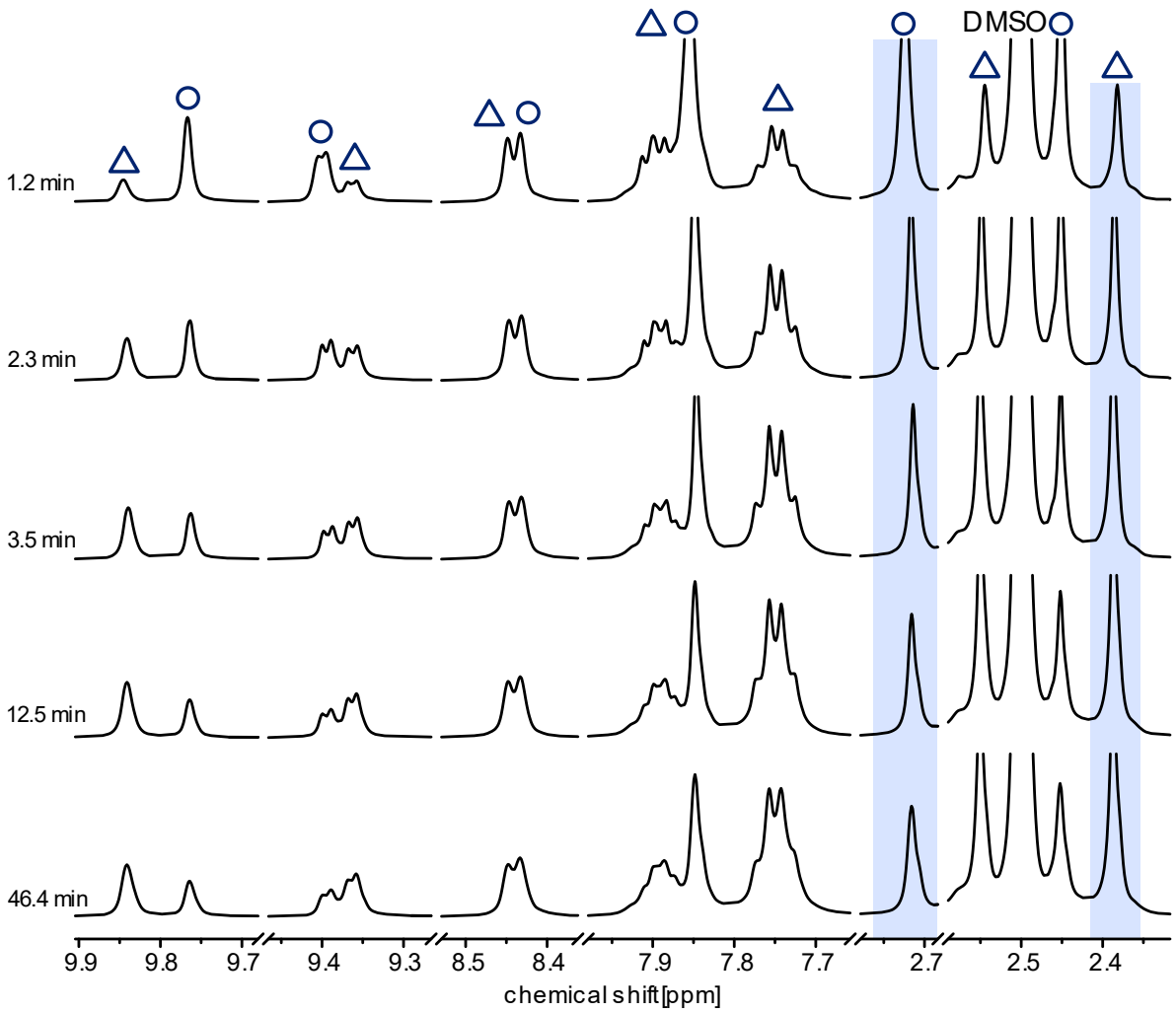

Figure S42. ^{1}H NMR (500 MHz, DMSO-d_6, 348 K) spectra of the equilibration between *E*-**T** triangle and *E*-**L** at 348 K. A ^{1}H NMR spectrum was measured every 70 s for 45 min. The signals highlighted in blue were chosen to be line-fitted and plotted to display changes in composition between *E*-**T** and *E*-**L** (Figure S40). *E*-**T** is denoted with **Δ**, *E*-**L** is denoted with **O**.

S3.2 Long-term stability of the triangle *E*-**T** / lantern *E*-**L** ratio

To test whether the triangle *E*-**T** / lantern *E*-**L** ratio of 78:22 indeed represented the thermodynamic equilibrium of the mixture, ^{1}H NMR spectra were measured for one month (Figure S43). The spectra show that the ratio of 78:22 between *E*-**T** and *E*-**L** is achieved after allowing the complex mixture to equilibrate for a minimum of 6 h (usually overnight) and remains unchanged thereafter.

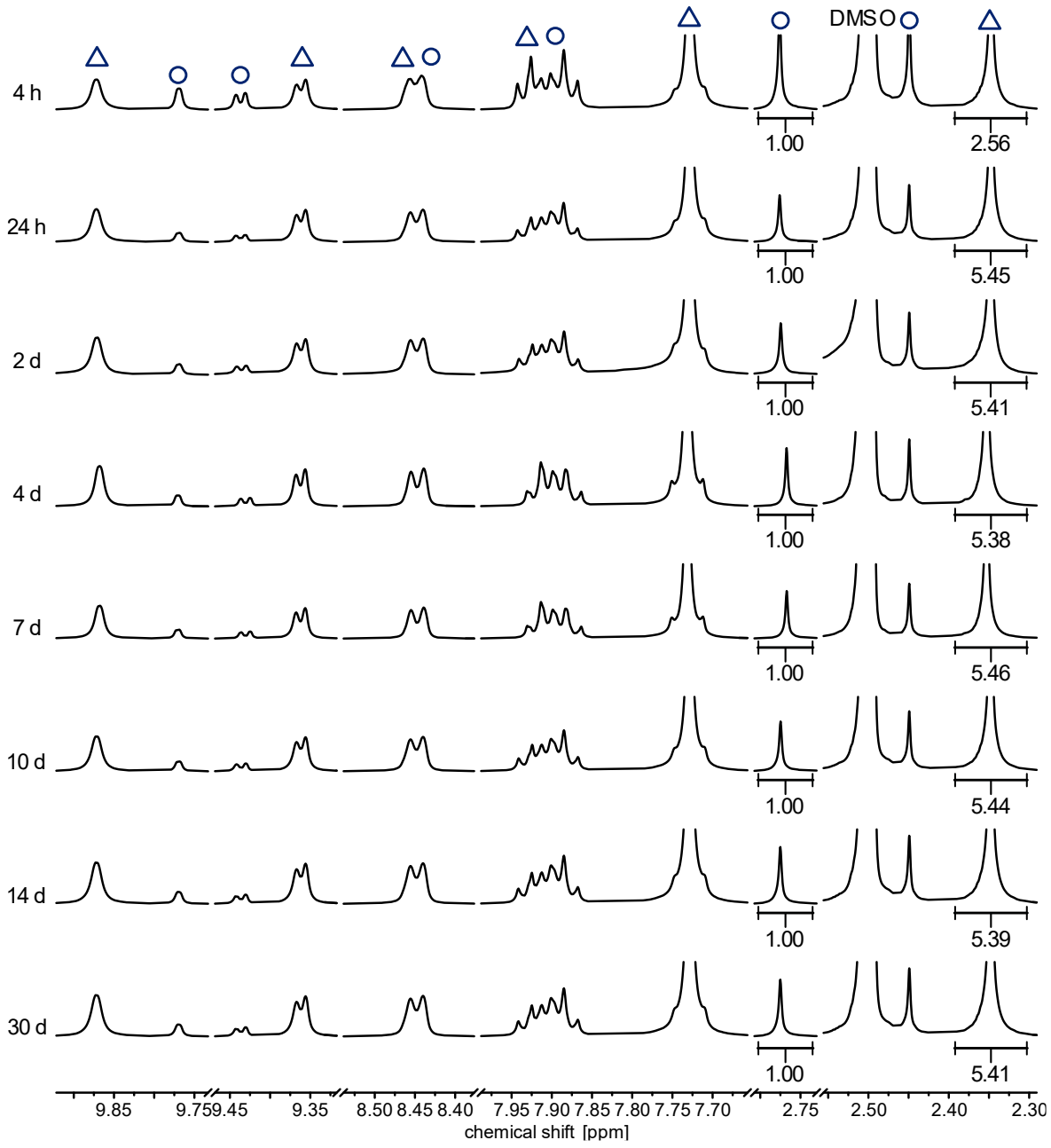

Figure S43. Stacked ^{1}H NMR (500 MHz, DMSO-d_6, 298 K) spectra of *E*-**T** (denoted with **Δ**) and *E*-**L** (denoted with **O**) over 30 d. Four hours after the reaction turned from turbid to a clear yellow, indicating complex formation, the ratio between *E*-**T** and *E*-**L** was 63:37. From day 1 onwards, the ratio between *E*-**T** and *E*-**L** remained at 78:22.

S3.3 Concentration dependence

To assess the concentration dependence of the triangle *E*-**T** / lantern *E*-**L** equilibrium, a total of 17 samples were prepared with concentrations ranging from 0.2 to 8 mM and a ^{1}H NMR spectrum was measured from each of them (Figure S44). The signals highlighted in orange were chosen to be line-fitted and plotted against the concentration to illustrate the concentration dependence of the *E*-**T** / *E*-**L** equilibrium (Figure S45). This dilution series demonstrated that the complex sample of *E*-**T** and *E*-**L** (78:22, respectively) has a critical self-assembly concentration of *csac*(**1**) ≈ 1.75 mM. Additionally, the ligand concentration should be at least 7 mM to prevent the presence of free ligand in solution and maintain the 78:22 *E*-**T** / *E*-**L** ratio.

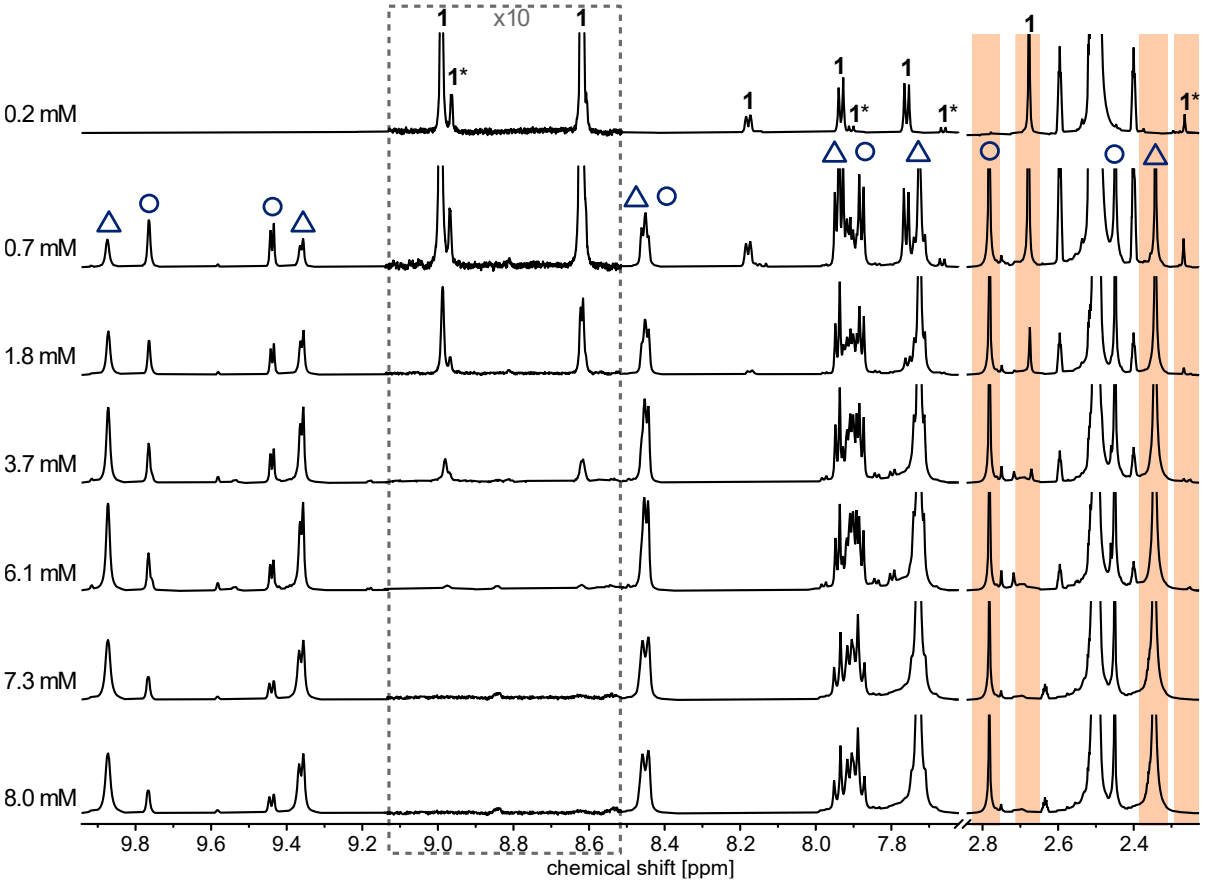

Figure S44. Stacked ^{1}H NMR (700 MHz, DMSO-d_6, 298 K) spectra of complexation mixtures at different concentrations. *E*-**T** is denoted with **Δ**, *E*-**L** is denoted with **O**, *E*-**1** is denoted with **1**, and *Z*-**1** is denoted with **1***. The signals highlighted in orange were chosen to be line-fitted and plotted to display the concentration dependence of *E*-**T** / *E*-**L** equilibrium (Figure S45).

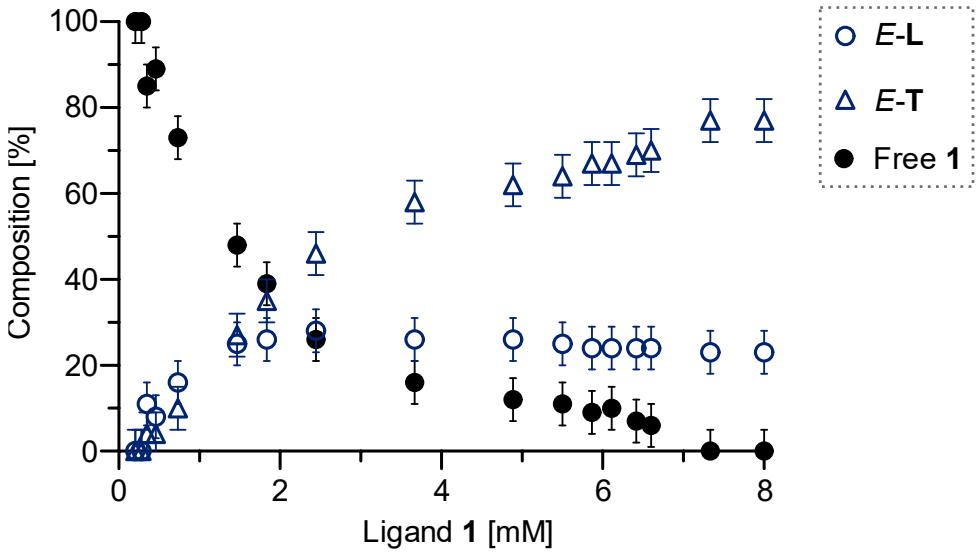

Figure S45. Plot of the percentage of triangle *E*-**T**, lantern *E*-**L**, and free ligand **1** as determined by ^{1}H NMR integration (Figure S44) against the concentration of **1**, showing the concentration dependence of the equilibrium between *E*-**T** and *E*-**L**.

S3.4 Temperature dependence

The temperature dependence of the triangle *E*-**T** / lantern *E*-**L** equilibrium was investigated using variable temperature ^{1}H NMR (303 K, 313 K, 323 K, 333 K, 343 K; Figure S46). By integrating the NMR signals corresponding to *E*-**T** and *E*-**L**, the equilibrated concentrations for each assembly were calculated based on the initial ligand concentration. Following Eq. 1, ln K_{eq} was calculated for all temperatures and plotted against T^{-1} (Figure S47). Fitting the data through linear regression and applying the Van't Hoff equation (Eq. 4) allowed for the determination of the thermodynamic parameters ΔH, ΔS, and ΔG (Table S3).

$$K_{eq} = \frac{[E\text{-}\mathbf{T}]^2}{[E\text{-}\mathbf{L}]^3} \quad (1)$$

$$\Delta G = \Delta H - T\,\Delta S \quad (2)$$

$$\Delta G = -R\,T \cdot \ln K_{eq} \quad (3)$$

$$\ln K_{eq} = -\frac{\Delta G_{eq}}{R\,T} = -\frac{\Delta H_{eq}}{R\,T} + \frac{\Delta S_{eq}}{R} \quad (4)$$

Table S3. Thermodynamic data as obtained from Van't Hoff analysis (Figure S46 and Figure **S47**). *K*, Δ*G* and *T* Δ*S* are given for *T* = 298 K.

K [M^{-1}]	**Δ*G*** [kJ mol^{-1}]	**Δ*H*** [kJ mol^{-1}]	**Δ*S*** [J K^{-1} mol^{-1}]	***T* Δ*S*** [kJ mol^{-1}]
76080 ± 36,000	−27.8 ± 13.0	−50.6 ± 7.7	−76.3 ± 23.9	−22.7 ± 7.1

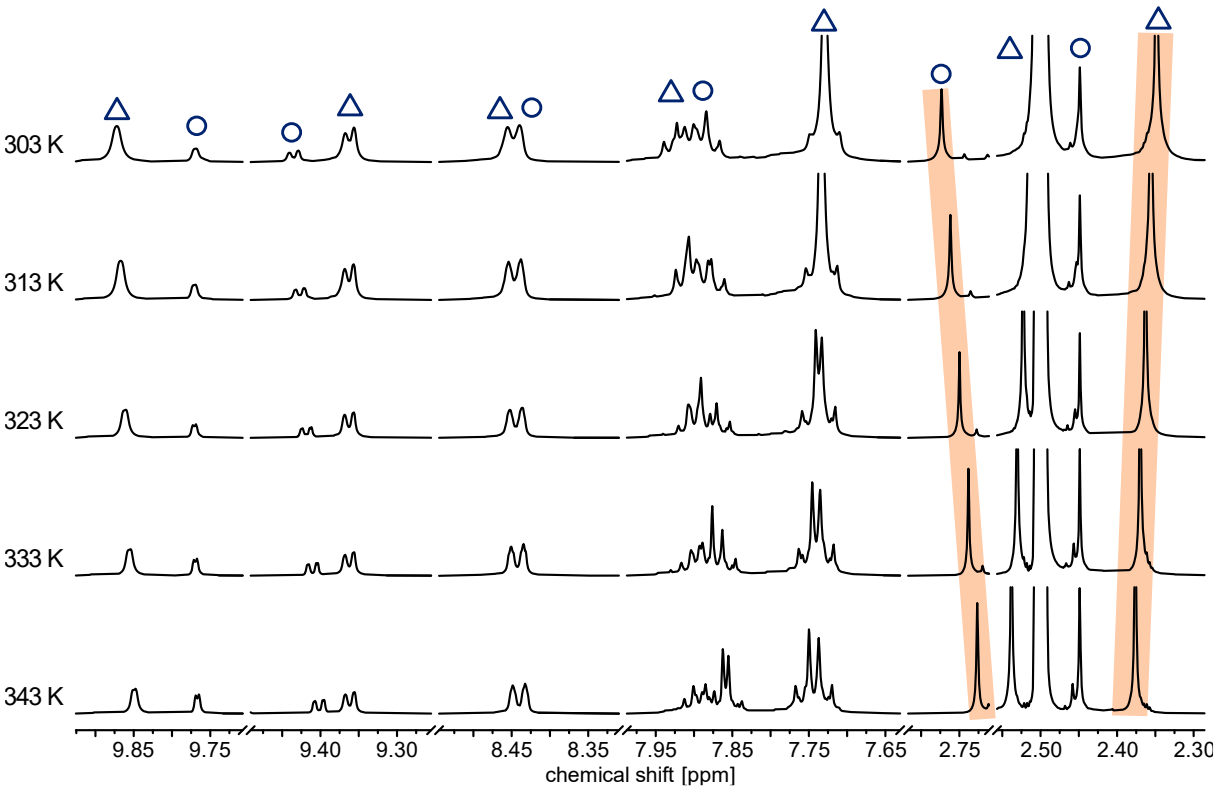

Figure S46. ^{1}H NMR spectra (500 MHz, DMSO-d_6) of the equilibrium between *E*-**T** (denoted with **Δ**) and *E*-**L** (denoted with **O**) at different temperatures (303 K, 313 K, 323 K, 333 K, 343 K). The signals highlighted in orange were integrated to determine the respective concentrations at each temperature for Van't Hoff analysis (Figure S47).

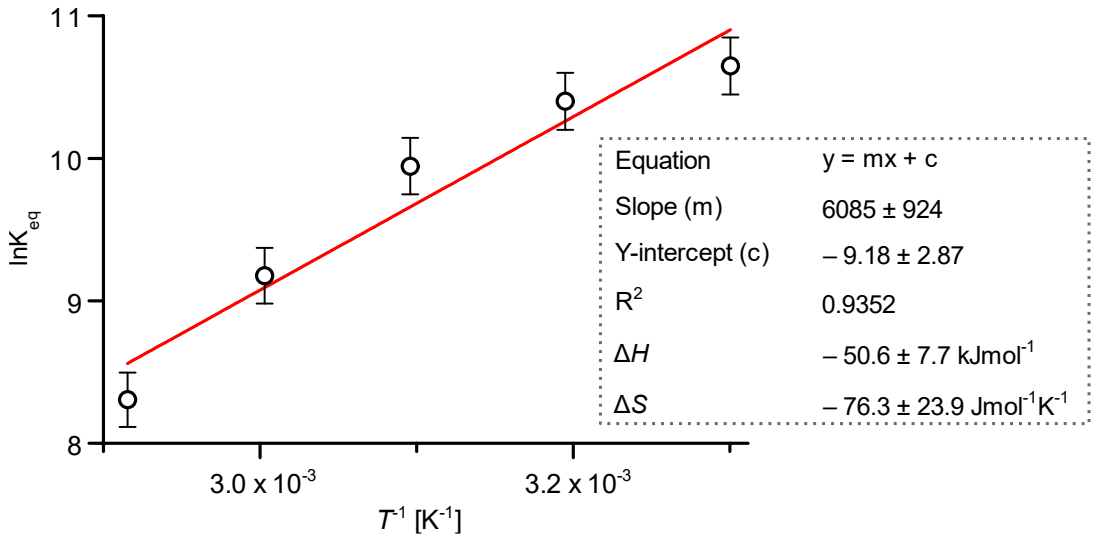

Figure S47. Van't Hoff plot of the equilibrium between *E*-**T** and *E*-**L** at different temperatures.

S4 Photoswitching studies

LED irradiation (NMR and MS). This method was previously described by our group.[3,4] The following description was added here for convenience:

A portable, built-in-house 365 nm LED light source using a commercial LED chip and 3D-printed adapters was employed to irradiate NMR and MS samples. For 500 nm light irradiation, a fibre collimated LED light source was used. Following irradiation, the samples were promptly subjected to measurement to reduce thermal relaxation to a minimum.

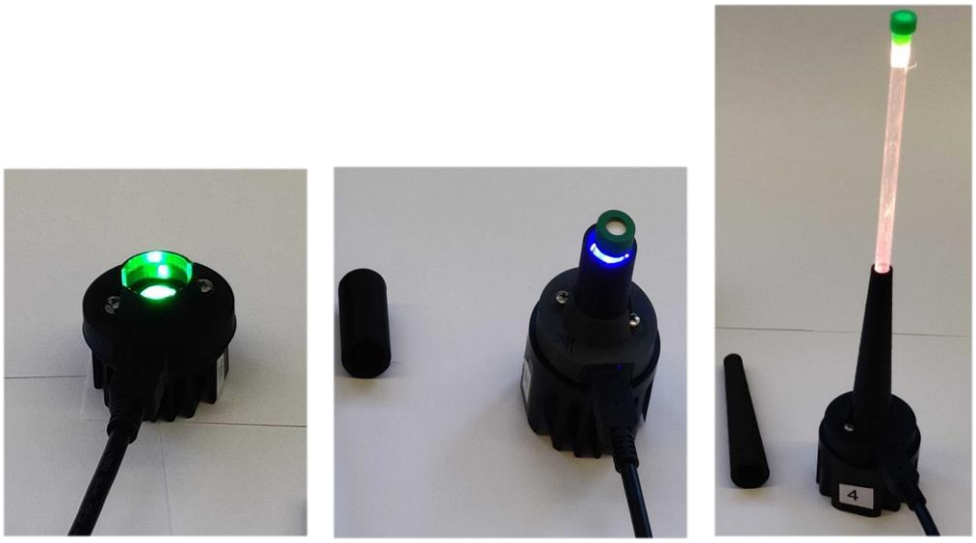

Figure S48. LED illumination setup with USB-powered homemade light sources using commercial LED chips with 3D-printed adaptors for 2 mL GC vials and 5 mm NMR tubes.

***In-situ* irradiation (NMR).** This method was adapted from literature[5,6] and previously described by our group.[3,4] The following description was added here for convenience:

An NMR sample tube was fitted with an insert tube made of quartz glass, and a quartz glass optical fibre was pushed down into the insert. The end of this fibre was non-terminated, and the exposed surface had been roughened to ensure even and omnidirectional illumination (Figure S49). This construction was lowered into the NMR device using an aluminium rod to avoid damage to the fibre. The other end of the optical fibre was connected to a fibre-collimated LED light source (see Section S1) so the sample could be irradiated inside the spectrometer.

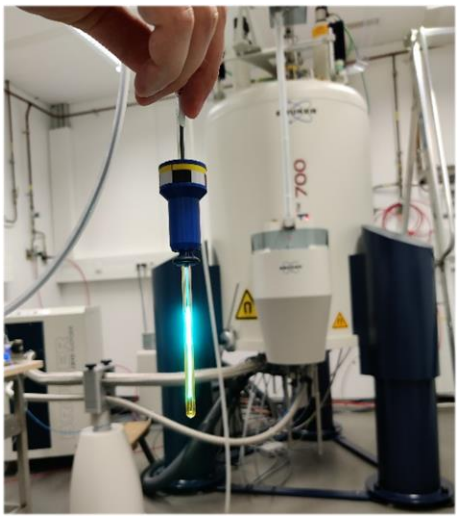

Figure S49. NMR sample with quartz glass insert and optical fibre for *in-situ* illumination during NMR experiments.

***In-situ* irradiation (UV-vis).** This method was previously described by our group.[3,4] The following description was added here for convenience:

Samples were irradiated perpendicularly to the measurement axis within the UV-vis spectrometer using optical fibres connected to an LED light source (see Section S1). To facilitate the irradiation of the cuvettes perpendicularly to the spectrometer's measurement axis, a hole matching the diameter of the quartz glass fibre was drilled at the centre of the Teflon stopper used to seal the UV-vis cuvettes. This configuration enabled the connection of an optical fibre to the cuvette, allowing the irradiation of the samples from above (Figure S50).

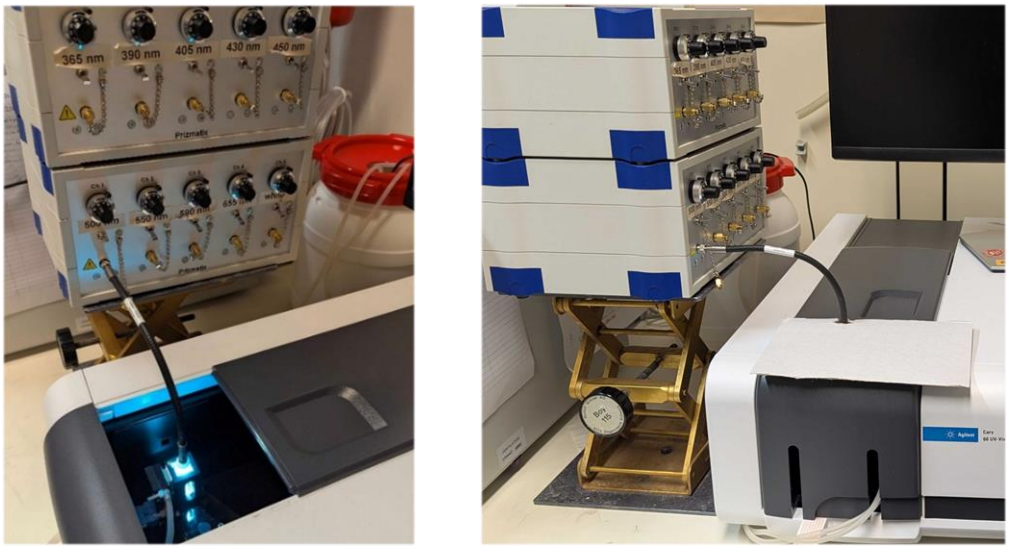

Figure S50. UV-vis *in-situ* illumination setup showing fibre collimated LED-sources connected to the cuvette with open (left) and closed measurement chamber (right).

Determination of the photostationary state (PSS). Photostationary states of the photoswitches were determined using ^{1}H NMR spectroscopy. For this purpose, two signals corresponding to the same proton were integrated, and the PSS was calculated based on the resulting integral ratios.[4] To ensure the highest accuracy, well-separated and clearly resolved signals were selected for the analysis, as recommended in the literature.[7,8]

S4.1 Azobispyrazole photoswitch (**S4**)

To the best of our knowledge, the photoswitching properties of **S4** have not been previously investigated; therefore, we have included their investigation here for convenience.

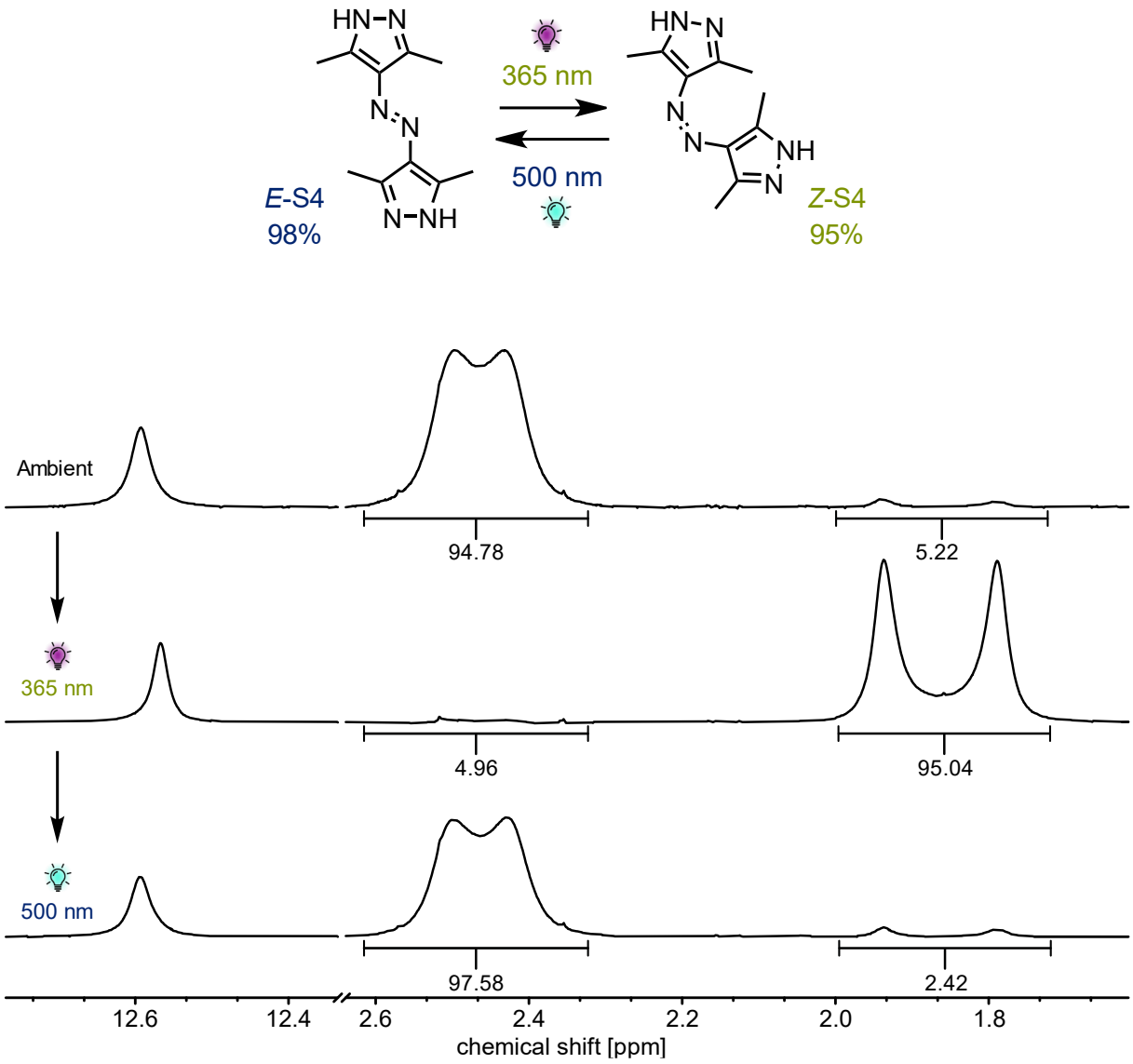

Figure S51. *In-situ* ^{1}H NMR (700 MHz, DMF-d_7, 298 K) of azobispyrazole photoswitch **S4** under ambient light, after irradiation with 365 nm light (1 min, PSS 95% *Z*-**S4**), and after irradiation with 500 nm light (3 min, PSS 98% *E*-**S4**).

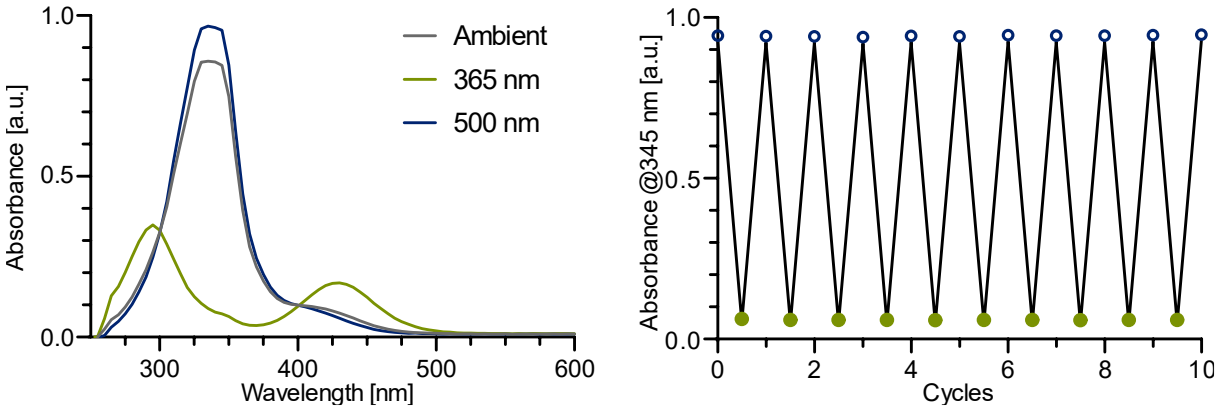

Figure S52. *Left*: UV-vis spectra of azobispyrazole photoswitch **S4** (69 µM, DMSO, 25 °C) under ambient light and after irradiation with 365 and 500 nm for 1 min, respectively. *Right*: UV-vis switching reversibility experiment of azobispyrazole photoswitch **S4** (69 µM, DMSO, 25 °C) showing the absorbance at 345 nm after alternating irradiation with 365 nm (1 min) and 500 nm light (1 min), respectively. No apparent photodegradation was observed over 10 switching cycles.

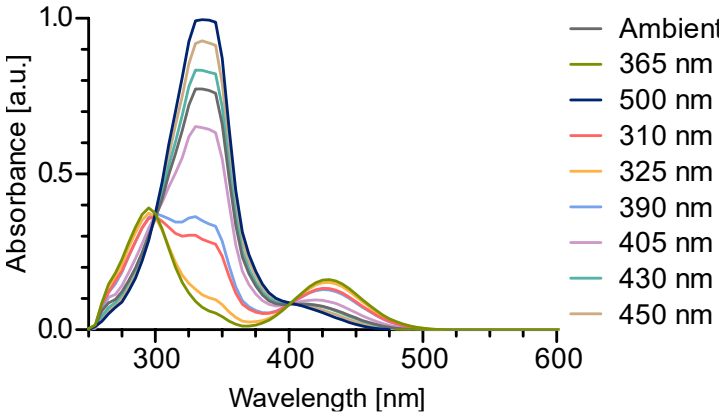

Figure S53. UV-vis spectra of azobispyrazole photoswitch **S4** (69 µM, DMSO, 25 °C) before and after irradiation with different wavelengths of light for 1 min each.

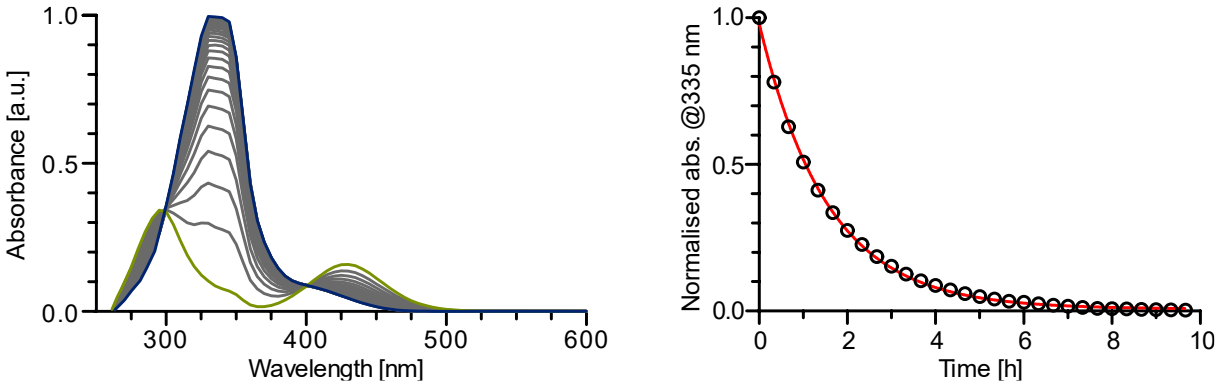

Figure S54. Thermal relaxation of azobispyrazole photoswitch **S4** (69 µM, DMSO, 25 °C). *Left*: UV-vis spectra of azobispyrazole photoswitch **S4** measured every 20 min in the dark after irradiating with 365 nm light. *Right*: Change in absorption $(A_t - A_\infty) \cdot (A_0 - A_\infty)^{-1}$ plotted over time t following thermal relaxation of azobispyrazole photoswitch **S4** to provide its half-life, $\tau_{½}$ = 69 min.

S4.2 Ligand (**1**)

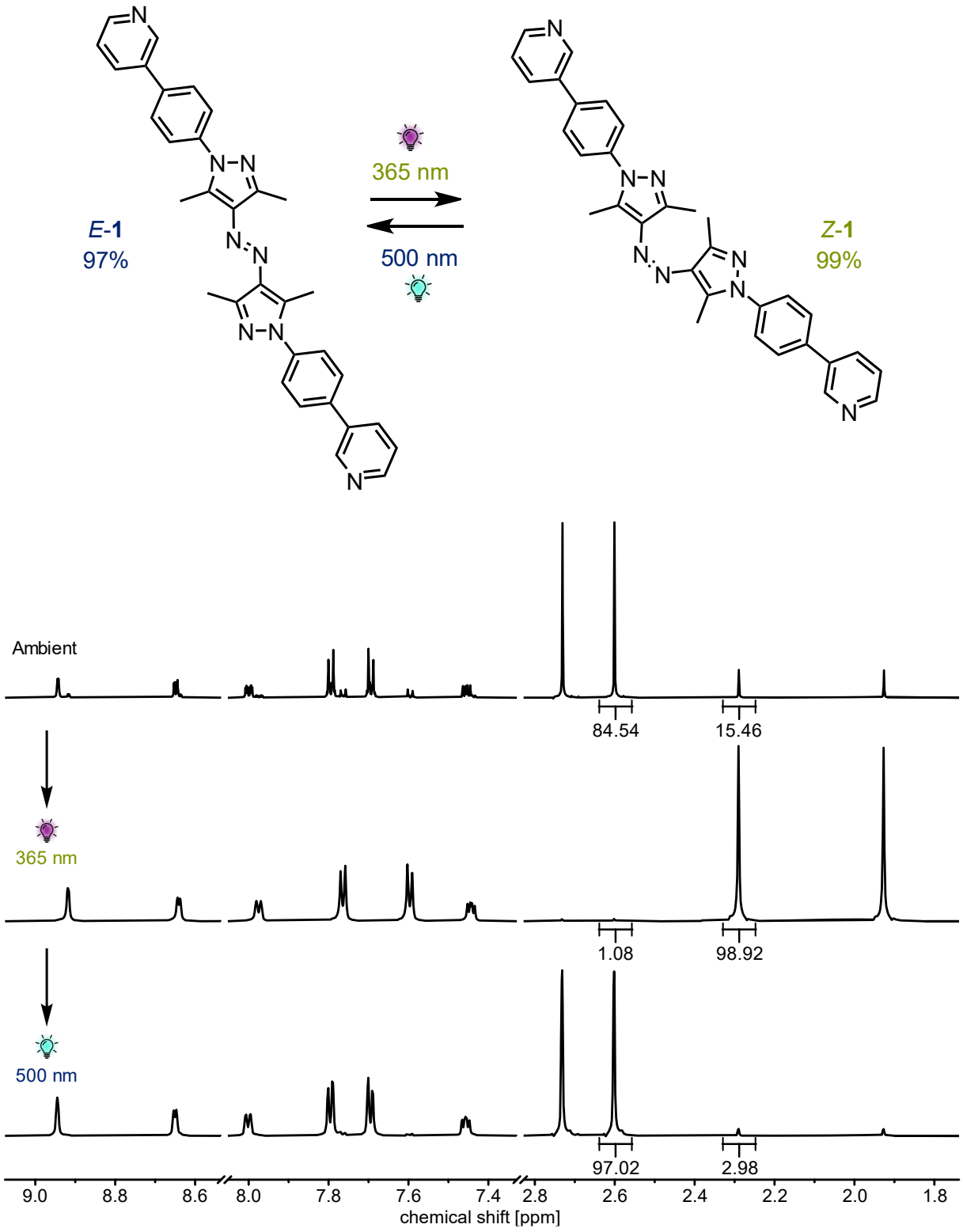

Figure S55. ^{1}H NMR (700 MHz, CD_2Cl_2, 298 K) spectra of **1** under ambient light, after *in-situ* irradiation with 365 nm light (20 min, PSS 99% *Z*-**1**), and after *in-situ* irradiation with 500 nm light (10 min, PSS 97% *E*-**1**).

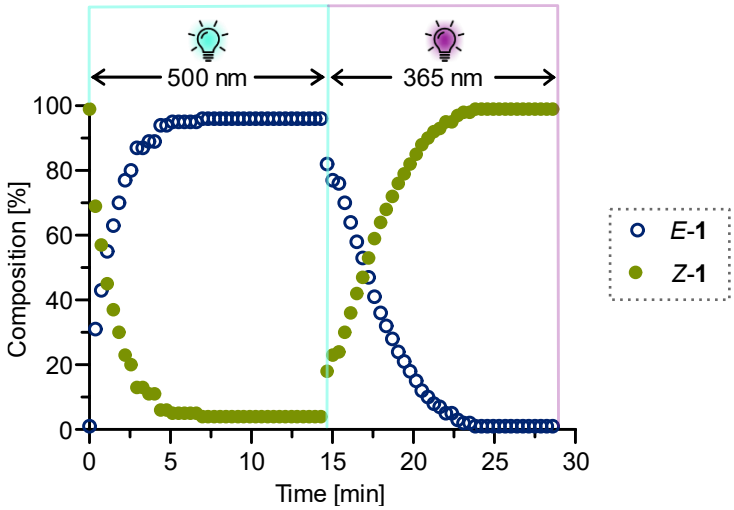

Figure S56. Changes in composition of *Z*-**1**/*E*-**1** measured by *in-situ* illumination ^{1}H NMR (700 MHz, CD_2Cl_2, 298 K). A sample of *Z*-**1** was irradiated with 500 nm light (LED power reduced to 2%) for approx. 15 min to induce the *Z*→*E* isomerisation, followed by illumination with 365 nm light (LED power reduced to 2%) for approx. 17 min to switch the ligand back to the *Z* configuration.

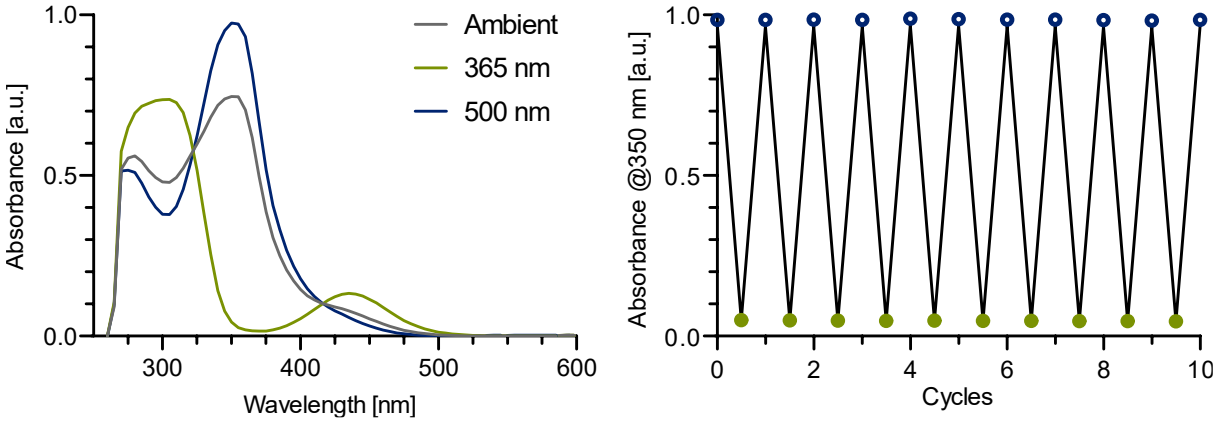

Figure S57. *Left*: UV-vis spectra of ligand **1** (24 µM, DMF, 25 °C) under ambient light and after irradiation with 365 and 500 nm for 1 min, respectively. *Right*: UV-vis switching reversibility experiment of **1** (24 µM, DMF, 25 °C) showing absorbance at 350 nm after alternating light irradiation with 365 nm (1 min) and 500 nm (1 min), respectively. No apparent photodegradation was observed over 10 switching cycles.

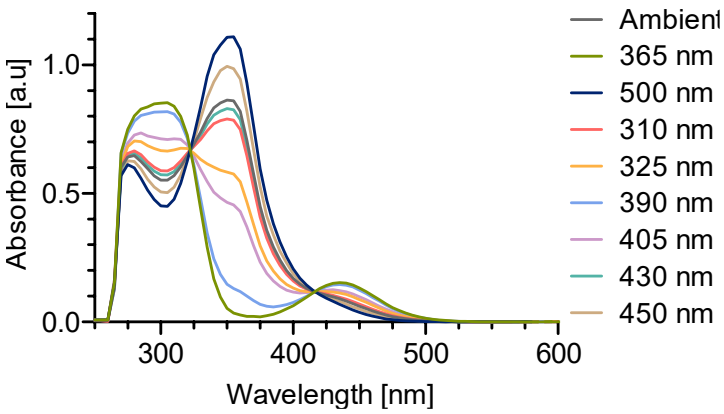

Figure S58. UV-vis spectra of ligand **1** (28 µM, DMF, 25 °C) before and after irradiation with different wavelengths of light for 1 min each.

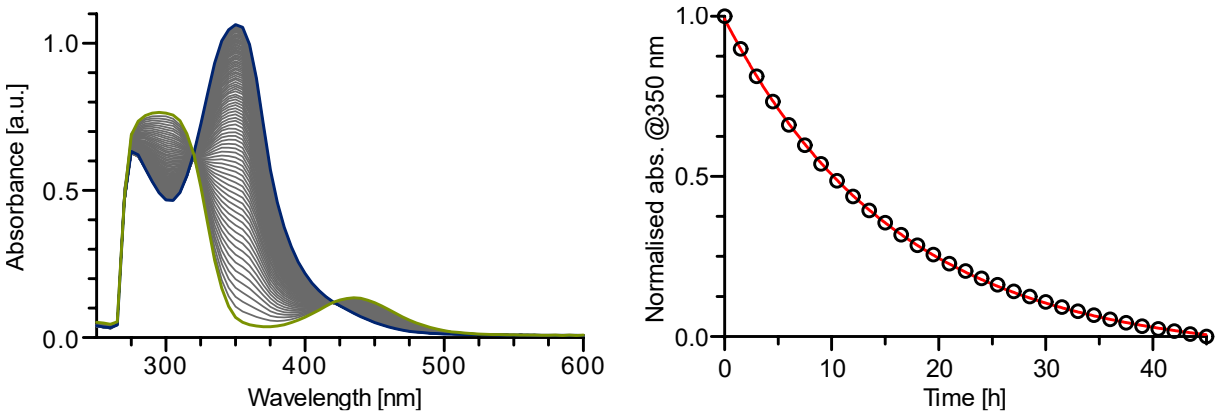

Figure S59. Thermal relaxation of ligand **1** (24 µM, DMF, 60 °C). *Left*: UV-vis spectra of **1** measured every 30 min in the dark after irradiating the sample with 365 nm light. *Right*: Change in absorption $(A_t - A_\infty) \cdot (A_0 - A_\infty)^{-1}$ plotted over time *t* following thermal relaxation of **1** to provide its half-life, $\tau_{½}$ = 10 h.

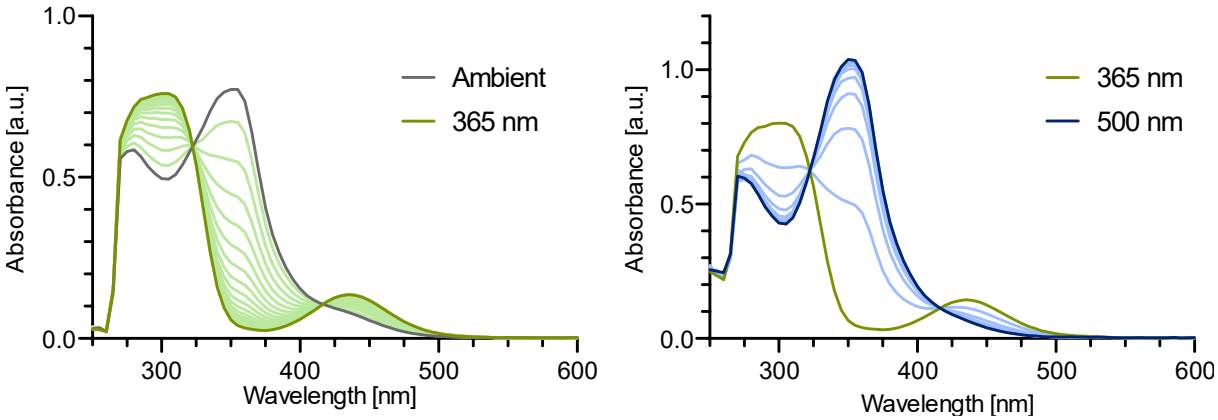

Figure S60. *Left*: UV-vis spectra of *E*-**1** (24 µM, DMF, 25 °C) under constant light irradiation with 365 nm light (2% LED power). A UV-vis spectrum was measured every 3 s for 1 min. Complete *E*→*Z* conversion was reached after 1 min. The power of the LED was reduced to 2% to observe the transition. *Right*: UV-vis spectra of *Z*-**1** (24 µM, DMF, 25 °C) under constant irradiation with 500 nm light. A UV-vis spectrum was measured every 3 s for 30 s. Complete *Z*→*E* conversion was reached after 30 s.

S4.3 Switching between Pd^{II} structures *E*-**T**, *E*-**L**, and *Z*-**L**

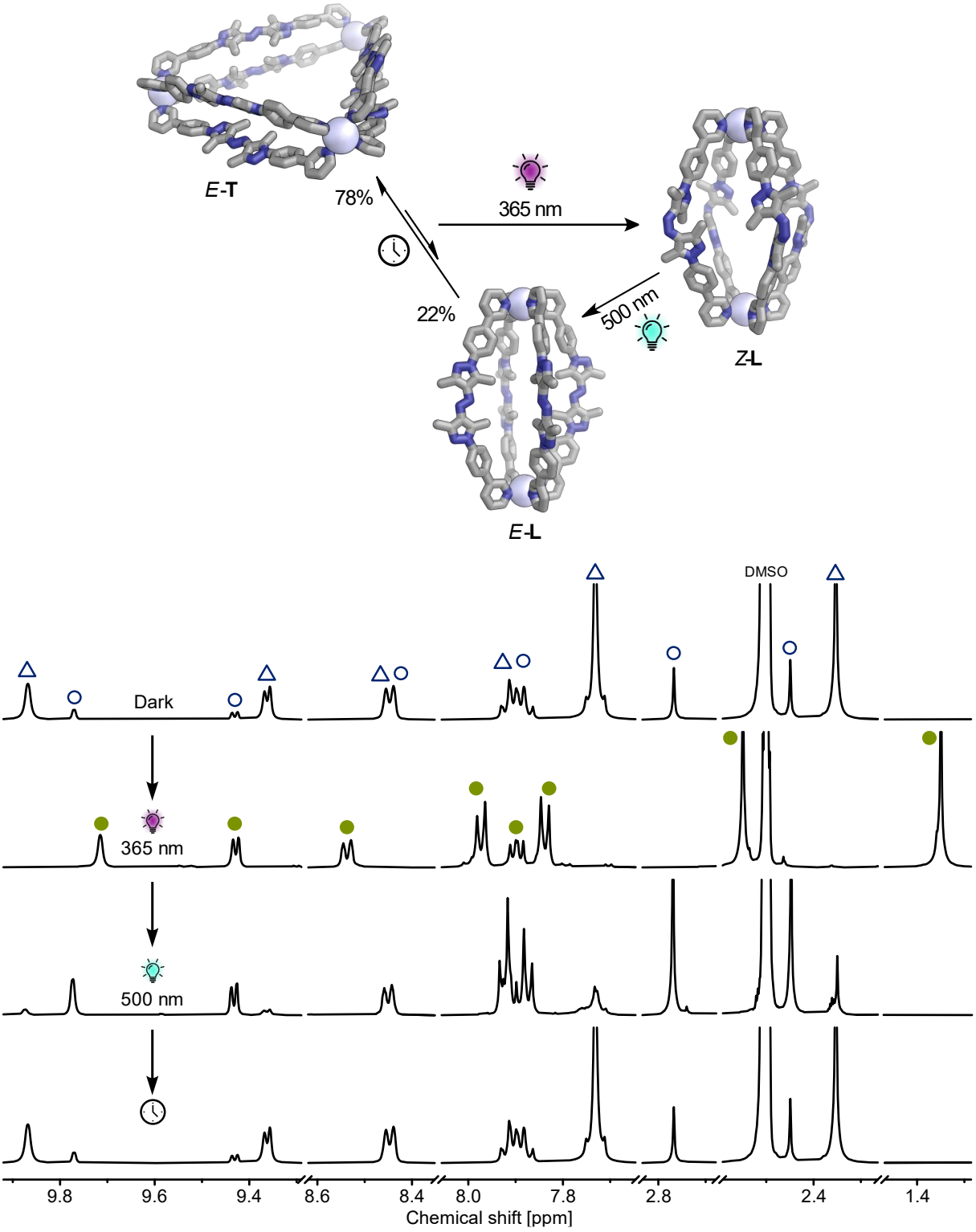

Figure S61. ^{1}H NMR (700 MHz, DMSO-d_6, 298 K) under light exclusion (*E*-**T**: *E*-**L**, 78:22), after *in-situ* irradiation with 365 nm light (14 min, 10% LED power) (*Z*-**L**), after *in-situ* irradiation with 500 nm light (6 min, 2% LED power) (*E*-**T**: *E*-**L**, 12:88), and after 22 h equilibrating in an amberised NMR tube wrapped in aluminium foil in an air-conditioned room (*E*-**T**: *E*-**L**, 78:22). *E*-**T** is denoted with **Δ**, *E*-**L** is denoted with **O**, and *Z*-**L** is denoted with ●.

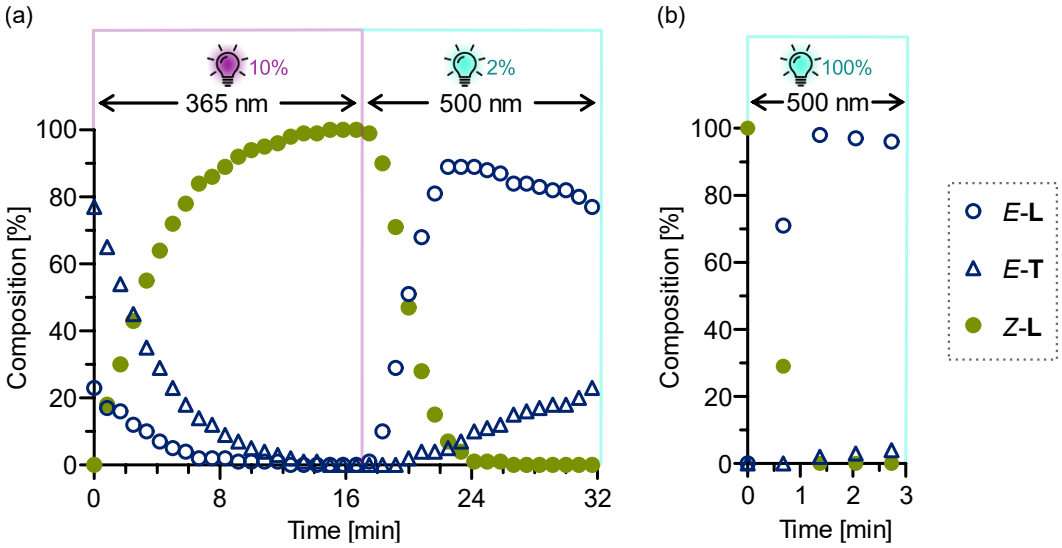

Figure S62. Changes in composition between *E*-**T**, *E*-**L**, and *Z*-**L** measured by *in-situ* illumination ^{1}H NMR (700 MHz, DMSO-d_6, 298 K) spectroscopy. (a) A sample of *E*-**T** / *E*-**L** (78:22, respectively) was irradiated with 365 nm light (LED power reduced to 10%) for approx. 17 min to induce *E*→*Z* isomerisation, followed by illumination with 500 nm light (LED power reduced to 2%) for approx. 16 min to induce *Z*→*E* isomerisation. The respective spectra are depicted in Figures S63 and S64, respectively. (b) A sample of *Z*-**L** was irradiated with 500 nm light (LED power 100%) for less than 3 min.

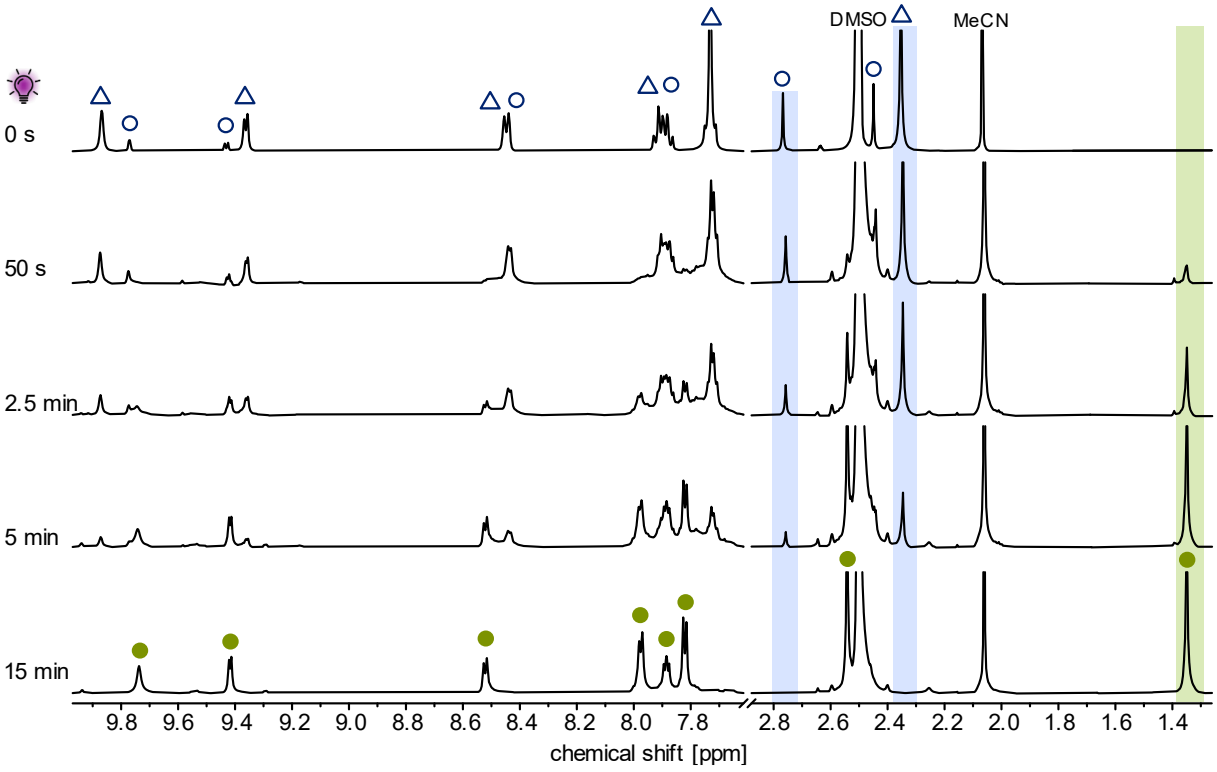

Figure S63. ^{1}H NMR (700 MHz, DMSO-d_6, 298 K) spectral changes during *in-situ* illumination with 365 nm light (10% LED power). The signals highlighted in blue and green were chosen to be line-fitted and plotted to display changes in composition between *E*-**T**, *E*-**L**, and *Z*-**L** (Figure S62). *E*-**T** is denoted with **Δ**, *E*-**L** is denoted with **O**, and *Z*-**L** is denoted with ●.

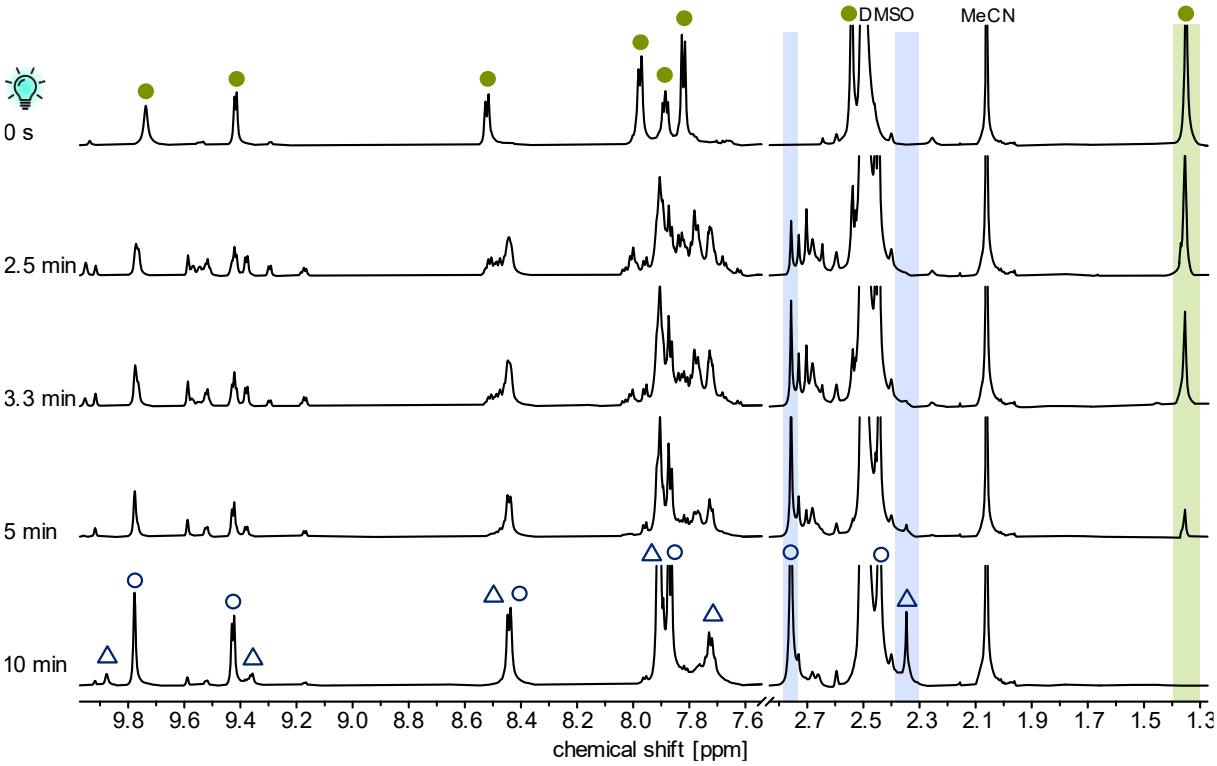

Figure S64. ^{1}H NMR (700 MHz, DMSO-d_6, 298 K) spectral changes during *in-situ* illumination with 500 nm light (2% LED power). The signals highlighted in blue and green were chosen to be line-fitted and plotted to display changes in composition between triangle *E*-**T**, *E*-**L**, and *Z*-**L** (Figure S62). *E*-**T** is denoted with **Δ**, *E*-**L** is denoted with **O**, and *Z*-**L** is denoted with ●.

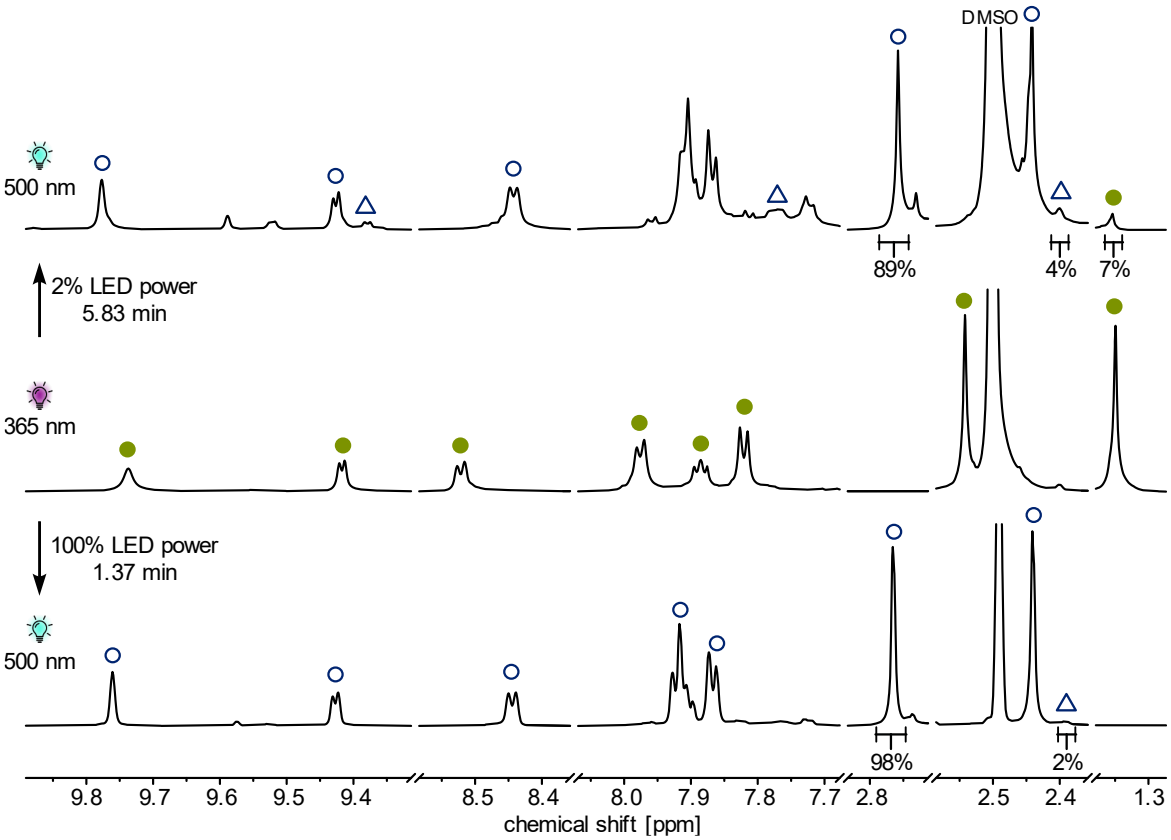

Figure S65. ^{1}H NMR (700 MHz, DMSO-d_6, 298 K) spectra of Z-L prior (middle) and after *in-situ* irradiation with 500 nm light with two different LED powers (2% LED power and 100% LED power, top and bottom, respectively). *Top*: When exposing *Z*-**L** to 500 nm light with a reduced 2% LED power, the maximum amount of *E*-**L** observed was 89% after 5.83 min of irradiation. *Bottom*: When exposing *Z*-**L** to 500 nm light with 100% LED power, the maximum amount of *E*-**L** observed was 98% after 1.37 min of irradiation. The spectra with the highest % of *E*-**L** were chosen to be displayed here, demonstrating the changes in composition when using different LED light powers. *E*-**T** is denoted with **Δ**, *E*-**L** is denoted with **O**, and *Z*-**L** is denoted with ●.

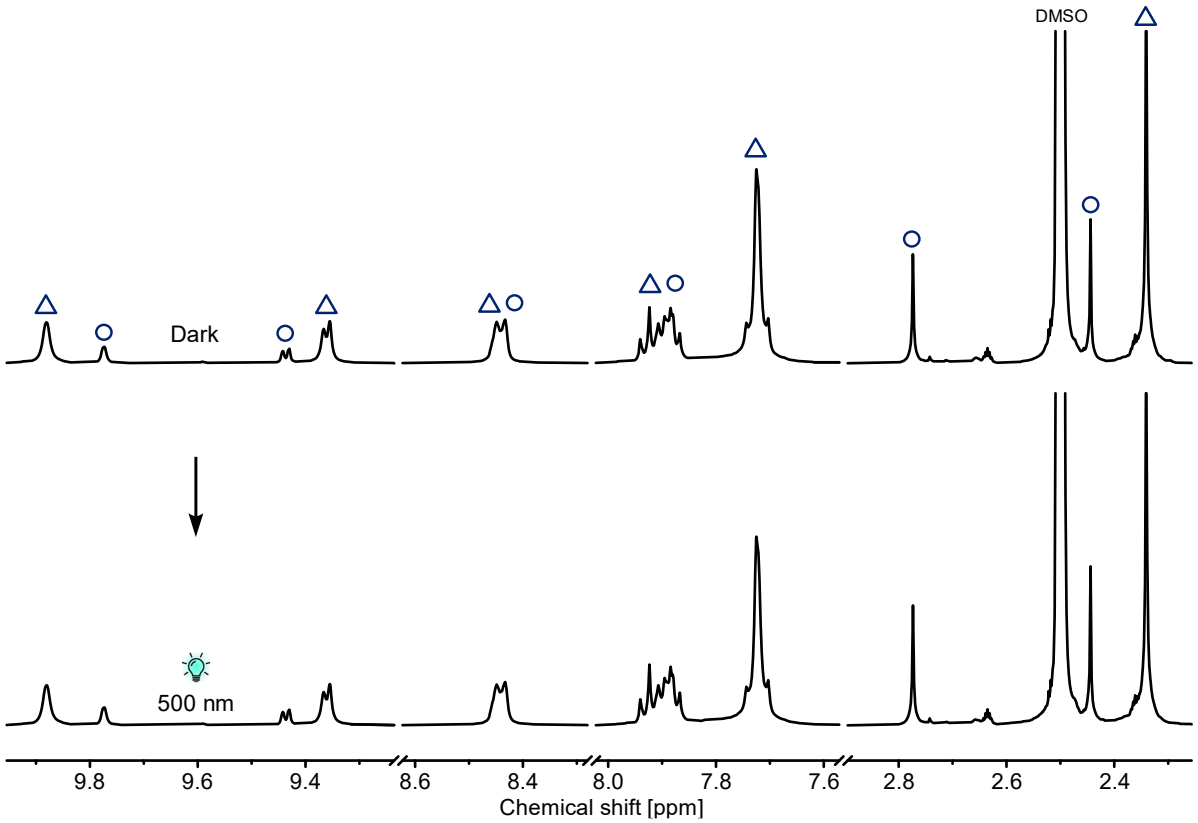

Figure S66. ^{1}H NMR (700 MHz, DMSO-d_6, 298 K) spectra under light exclusion (*E*-**T** / *E*-**L** 78:22; top) and after irradiation with 500 nm light (5 min; *E*-**T** / *E*-**L** 78:22; bottom). No change in cage composition was observed after irradiation with 500 nm light. *E*-**T** is denoted with **Δ**, *E*-**L** is denoted with **O**.

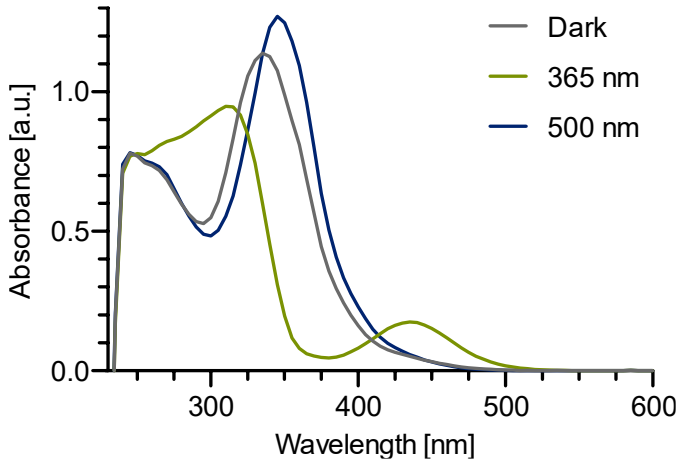

Figure S67. UV-vis (18 mM, DMSO, 298 K) spectra of *E*-**T** / *E*-**L** mixture under light exclusion and after light irradiation with 365 nm (i.e. *Z*-**L**) and 500 nm (i.e. *E*-**L**) for 1 min, respectively.

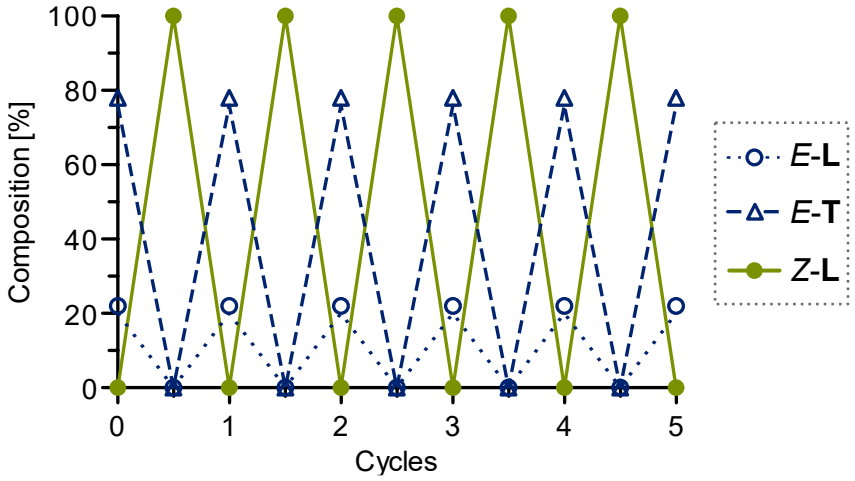

Figure S68. Investigation of switching reversibility by ^{1}H NMR (500 MHz, DMSO-d_6, 298 K) of *E*-**T**, *E*-**L**, and *Z*-**L**. A 78:22 *E*-**T** / *E*-**L** mixture was subjected to alternating light irradiation with 365 nm (5 min) and 500 nm (5 min), respectively. After irradiation with 500 nm light, the sample was left equilibrating for 22 h in an amberised NMR tube wrapped in aluminium foil in an air-conditioned room (22 °C) to allow for equilibration to the 78:22 *E*-**T** / *E*-**L** ratio. No apparent photodegradation was observed after five switching cycles.

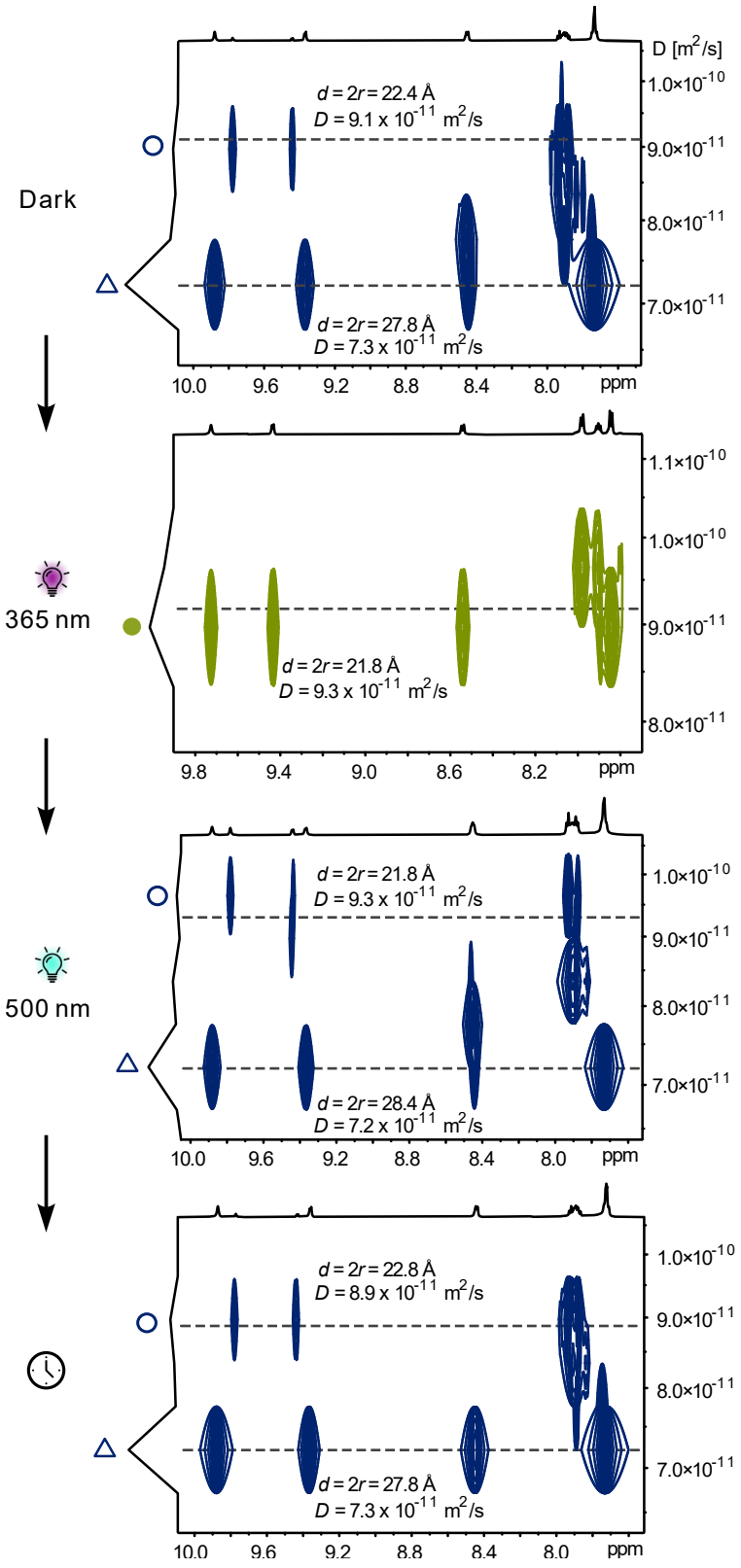

Figure S69. 2D-DOSY NMR (700 MHz, DMSO-d_6, 298 K, D20 = 0.35 s) spectra under light exclusion (*E*-**T** / *E*-**L** 78:22), after irradiation with 365 nm light (5 min) (*Z*-**L**), after irradiation with 500 nm light (5 min) (*E*-**T** / *E*-**L** 63:37), and after 22 h equilibrating in an amberised NMR tube wrapped in aluminium foil in an air-conditioned room (22 °C; *E*-**T** / *E*-**L** 78:22; top to bottom). *E*-**T** is denoted with **Δ**, *E*-**L** is denoted with **O**, and *Z*-**L** is denoted with ●. Calculated diffusion constants (*D*) and solvodynamic diameters (*d* = 2*r*) for each complex are depicted in the respective spectra.

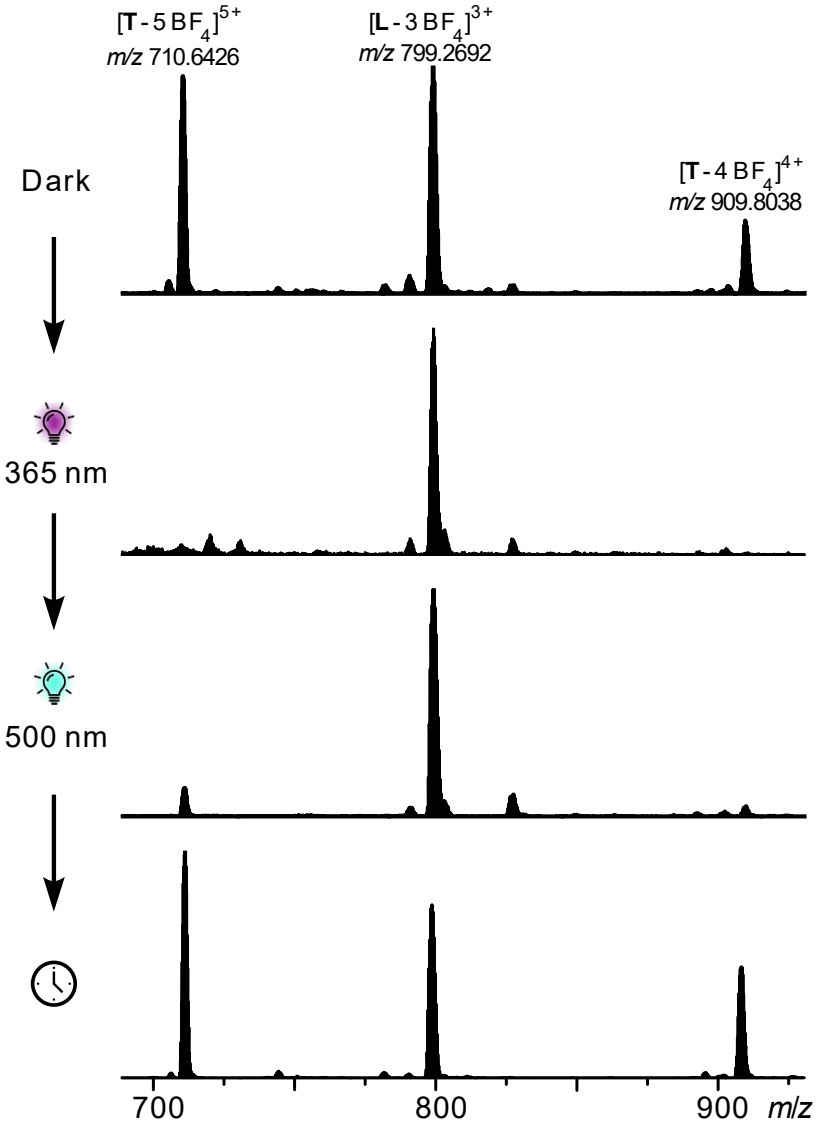

Figure S70. High-resolution ESI$^+$ mass spectra (DMSO/CH_3CN) of an *E*-**T** / *E*-**L** mixture under light exclusion, after irradiation with 365 nm light (5 min; i.e. *Z*-**L**), after irradiation with 500 nm light (5 min), and after 21 h equilibrating at 22 °C (top to bottom). *E*-**T** is denoted with **Δ**, *E*-**L** is denoted with **O**, and *Z*-**L** is denoted with ●.

S5 Kinetic studies

S5.1 Thermal relaxation of *Z*-**L**

To investigate the thermal stability of lantern *Z*-**L**, an NMR sample containing *E*-**T** / *E*-**L** mixture in a ratio of 78:22 was irradiated with 365 nm for 5 min to obtain lantern *Z*-**L**. ^{1}H NMR spectra were immediately measured over a period of 2 h at 75 °C (Figure S72) and the change in % of *Z*-**L** was plotted over time *t* (Figure S71). Non-linear curve fitting provided a half-life at 75 °C of $\tau_{½}$ = 21 min.

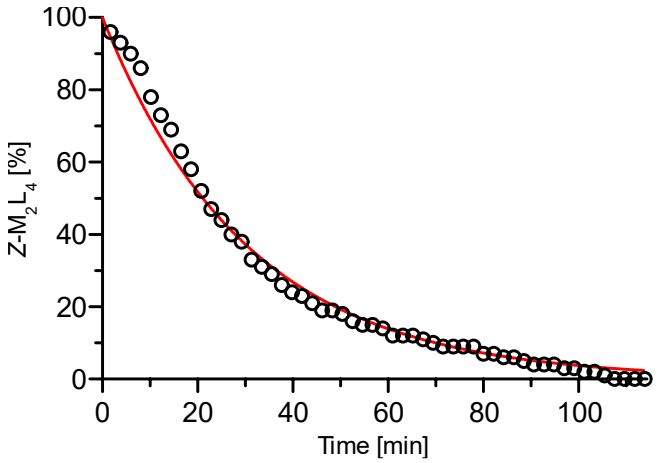

Figure S71. Thermal relaxation of *Z*-**L** (7.5 mM) investigated by ^{1}H NMR (500 MHz, DMSO-d_6, 348 K). Change in % of *Z*-**L** plotted over time *t* following thermal relaxation provides its half-life at 75 °C of $\tau_{½}$ = 21 min.

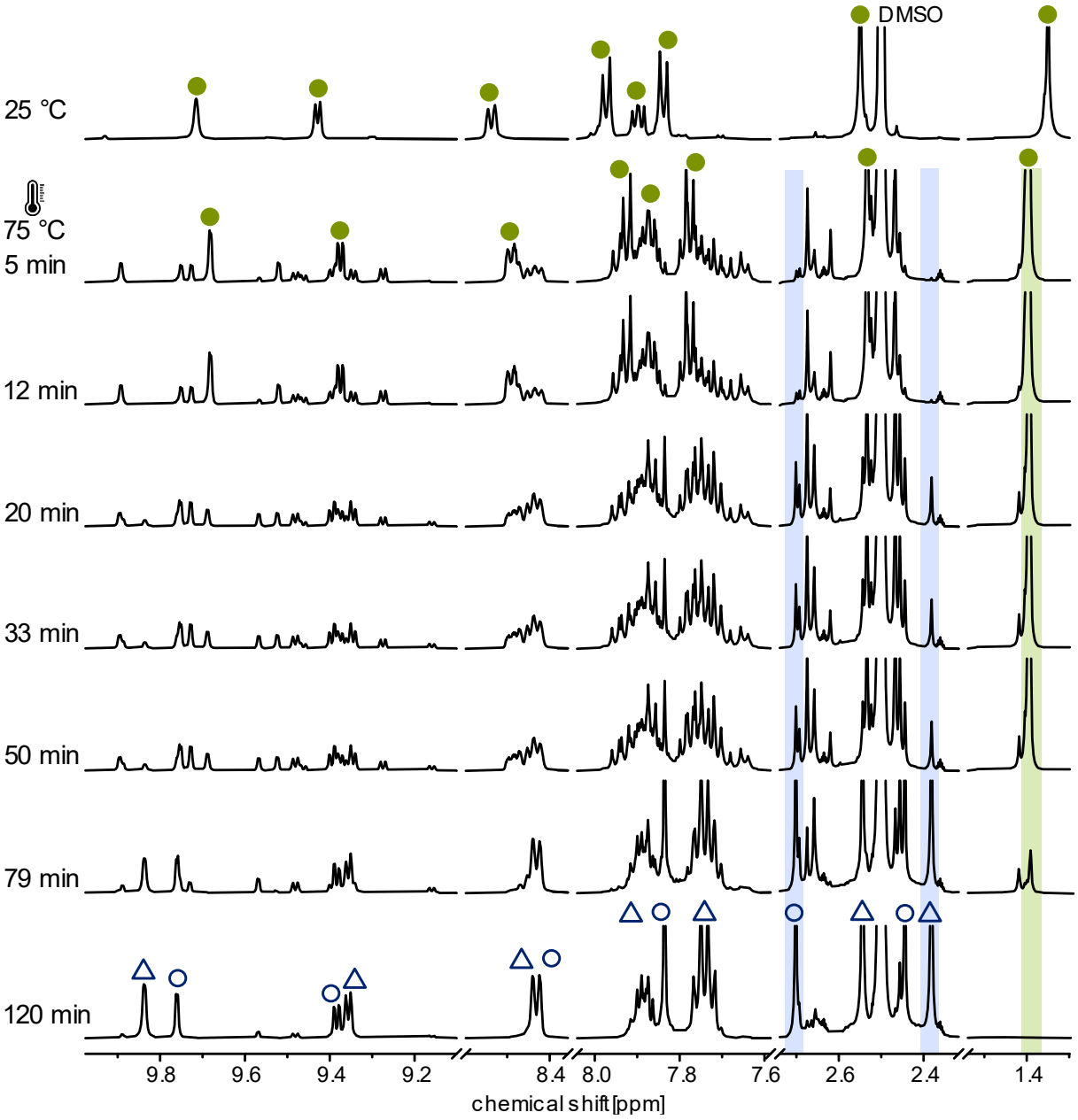

Figure S72. At the top ^{1}H NMR (500 MHz, DMSO-d_6, 298 K) spectrum of *Z*-**L** measured at 25 °C. The thermal relaxation of *Z*-**L** to *E*-**T** and *E*-**L** was then followed by ^{1}H NMR (500 MHz, DMSO-d_6, 348 K) at 75 °C under light exclusion over a period of 120 min. The signals highlighted in blue and green were chosen to be line-fitted and plotted to display changes in composition between triangle *E*-**T**, *E*-**L**, and *Z*-**L** (Figure S71). *E*-**T** is denoted with **Δ**, *E*-**L** is denoted with **O**, and *Z*-**L** is denoted with ●. The signals for *Z*-**L** have been assigned twice due to a signal shift at higher temperatures.

To investigate the thermal stability of *Z*-**L** at room temperature, an NMR sample containing *E*-**T** / *E*-**L** mixture in a ratio of 78:22 was irradiated with 365 nm for 5 min to obtain *Z*-**L**. The sample was then stored in an amberised NMR tube wrapped in aluminium foil in an air-conditioned room at 22 °C to prevent any disruption caused by either temperature or ambient light. ^{1}H NMR spectra were measured at irregular intervals over a period of more than one year (Figure S73).

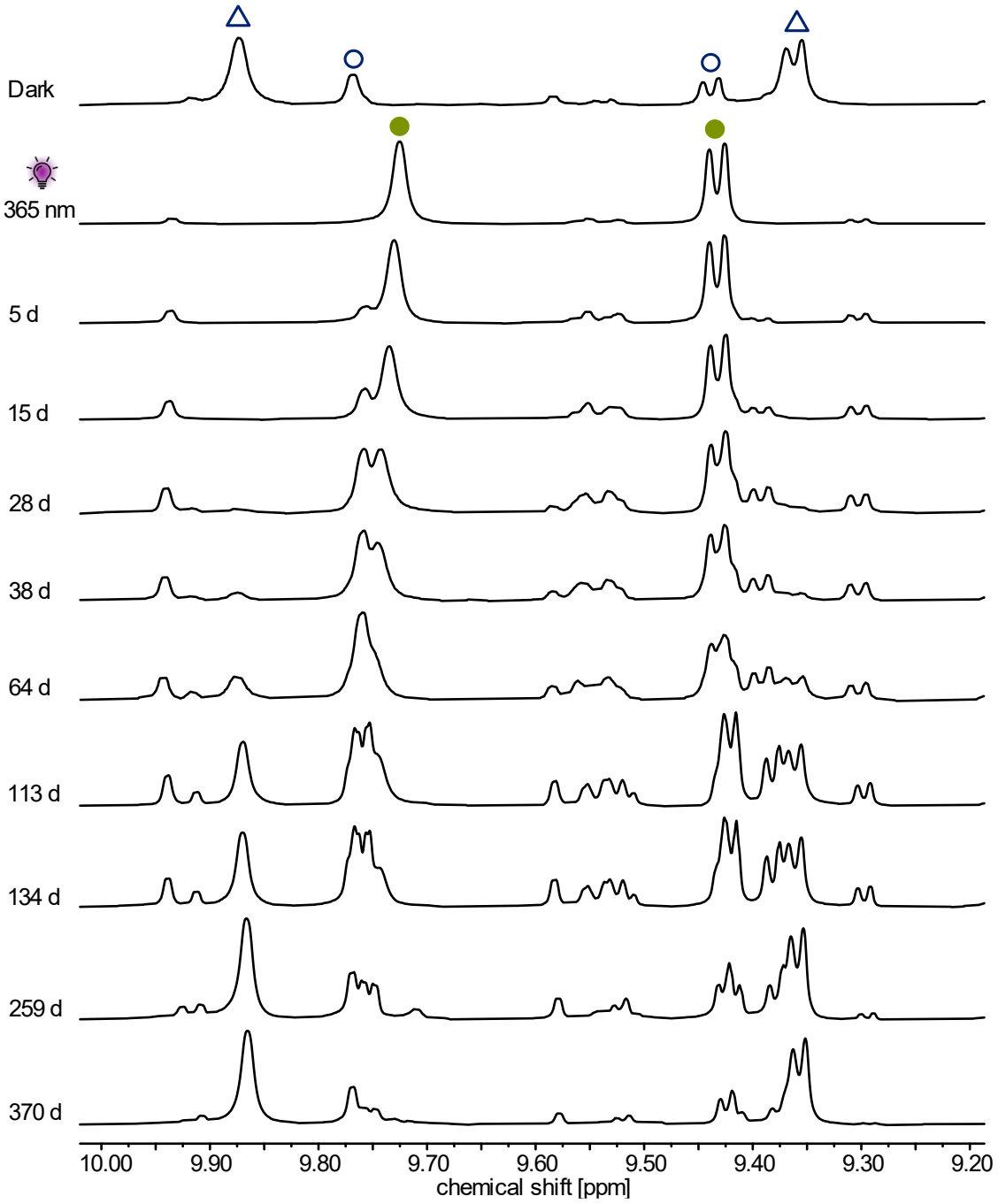

Figure S73. ^{1}H NMR (500 MHz, DMSO-d_6, 298 K) spectra under light exclusion (*E*-**T**: *E*-**L**, 78:22) following irradiation with 365 nm light (5 min; 0 d) to form *Z*-**L** and kept at 22 °C under light exclusion over a period of 370 d. *E*-**T** is denoted with **Δ**, *E*-**L** is denoted with **O**, and *Z*-**L** is denoted with ●.

Comparison of the lantern-scrambling experiments presented in Section S2.8 and the thermal relaxation of *Z*-**L** shown above (Figure S73) revealed some of the tentatively assigned signals for lanterns with mixed ligand configurations, namely *Z,E,E,E*-**L**, *cis*-*Z,Z,E,E*-**L**, *trans*-*Z,Z,E,E*-**L**, and *Z,Z,Z,E*-**L**, to be present as intermediates during thermal relaxation.

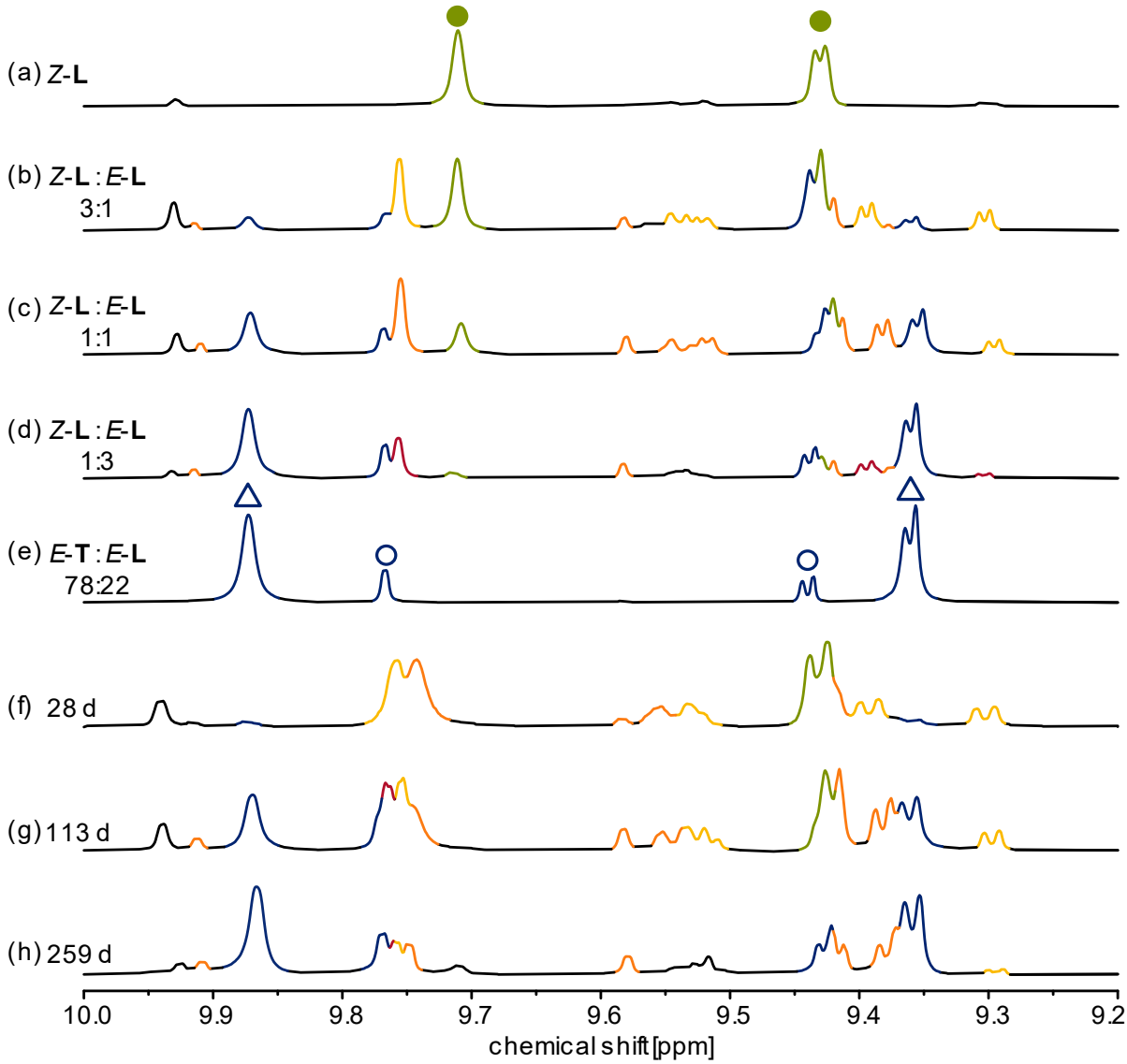

Figure S74. ^{1}H NMR (500/700 MHz, DMSO-d_6, 298 K) spectra of (a) *Z*-**L** and (e) *E*-**T** / *E*-**L** mixture under light exclusion (*E*-**T**: *E*-**L**, 78:22) for reference and of lantern-scrambling experiment after 13 h with *Z*-**L** / *E*-**L** ratios of (b) 3:1, (c) 1:1, and (d) 1:3; thermal relaxation of *Z*-**L** at 22 °C after (f) 28 d, (g) 113 d, and (h) 259 d. *E*-**T** is denoted with **Δ**, *E*-**L** is denoted with **O**, and *Z*-**L** is denoted with ●. Newly emerged signals are tentatively highlighted in yellow, orange, and red, respectively, depending on whether they were predominantly found in the 1:3, 1:1 or 3:1 *E*-**L** / *Z*-**L** mixtures.

S5.2 Kinetic investigation of the molecular ratchet

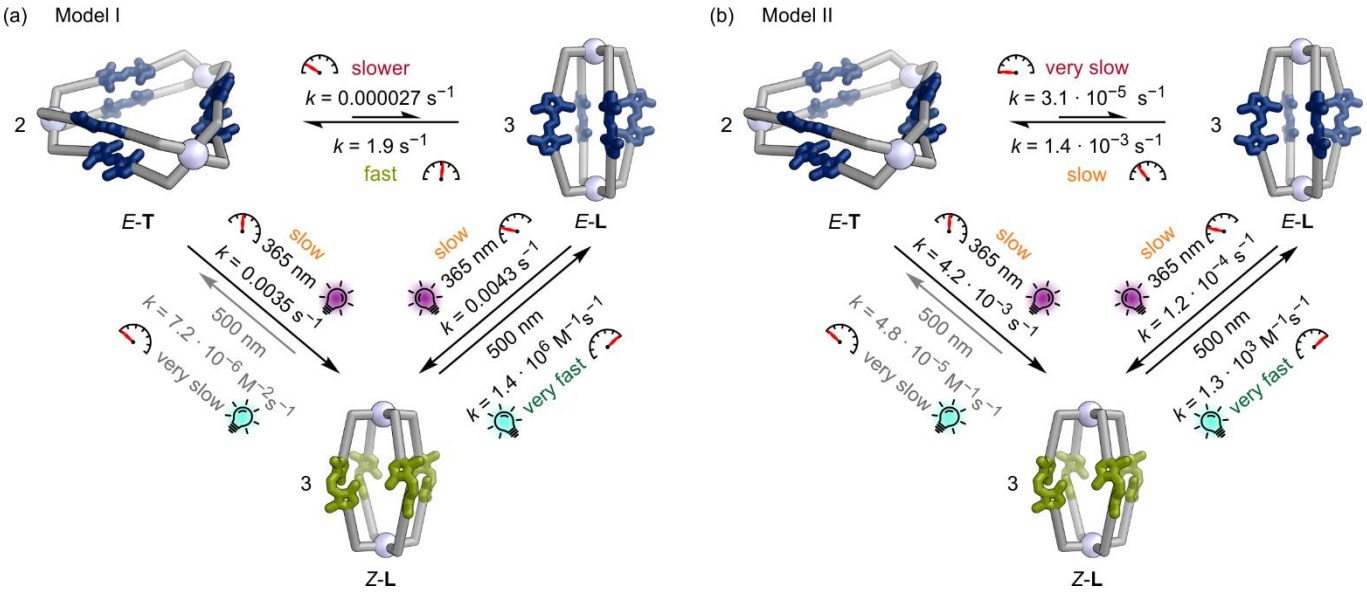

Figure S75. Schematic representation of the molecular ratchet governing the *E*-**T** / *E*-**L** → *Z*-**L** switching cycle, with the rate constants of the rate-determining steps indicated alongside the reaction arrows as determined by (a) Model I and (b) Model II.

Clearly distinguishable signals for each species — triangle *E*-**T**, lantern *E*-**L** and lantern *Z*-**L** — allowed the isomerisation kinetics of the complete photoisomerisation cycle (Figure S75) to be investigated using ^{1}H NMR spectroscopy (500 MHz or 700 MHz, DMSO-d_6, 298 K or 348 K):

i) The triangle *E*-**T** / lantern *E*-**L** equilibrium.

ii) The photoswitching of the triangle *E*-**T** / lantern *E*-**L** mixture to lantern *Z*-**L** under irradiation with 365 nm light.

iii) The photoswitching of lantern *Z*-**L** to lantern *E*-**L** under irradiation with 500 nm light and subsequent equilibration to the triangle *E*-**T** / lantern *E*-**L** mixture.

While some intermediates could be detected, which we tentatively assigned to be the partly switched lantern structures, i.e. *Z*,*Z*,*Z*,*E*-**L**, *Z*,*Z*,*E*,*E*-**L**, and *Z*,*E*,*E*,*E*-**L** (see Figure S74 and Section S8.2), these intermediates were minor and could not be clearly identified. Hence, we excluded them from the kinetic investigation of the switching cycle.

Prior to investigation, all samples were stored in the dark in an air-conditioned room at 22 °C to prevent any disruption caused by either temperature or ambient light, so that the absolute concentrations of the species could be calculated from the ^{1}H NMR integrals based on the initial amount of ligand in the NMR sample and the assumption that all species were visible in ^{1}H NMR. The resulting concentrations were plotted against time and fitted using the software COPASI (version 4.44).[9]

Kinetic investigation of these processes is non-trivial, and similar systems have rarely been investigated.[10–14] The kinetic data suggest that all transformations within the photoswitching cycle (Figure S71) follow (*pseudo*-) first-order kinetics. However, the transformation of triangle *E*-**T** to lantern *E*-**L**, for example, does formally require two molecules of triangle *E*-**T** that form three molecules of lantern *E*-**L**. This reaction would not follow first-order rate laws. Therefore, the apparent (*pseudo*-) first-order kinetics for all transformations indicate that their rate-determining steps depend solely on the concentrations of a single supramolecular species. We tentatively assume these rate-determining steps to be either (partial) capsule opening, in case of the equilibration between triangle *E*-**T** / lantern *E*-**L**, or photoswitch isomerisation (both photochemically or thermally), in case of the photoswitch isomerisation steps. All other processes involved in these transformations are not rate-limiting.

To account for these (*pseudo*-) first-order kinetics and fit the data to the correct stoichiometries, we developed two independent models to determine the rate-determining steps of the transformations:

(i) In Model I (Figure S75a), we deconstructed all triangle *E*-**T** to lantern *E*-**L** rearrangements into two-step processes with "Pd**1**$_2$ *pseudo*-intermediates" (Figure S76, Figure **S78**, Figure **S79**). We do not propose "Pd**1**$_2$" as an actual intermediate in the respective reaction mechanisms, which would be far more complex, but instead use this *pseudo*-intermediate "Pd**1**$_2$" to separate the rate-determining *pseudo*-first-order reaction step from the complex capsule rearrangement. We chose this model because it imposes the fewest restrictions on the potential reaction mechanism, which is too complex to resolve with the available data. However, this model results in second and third-order reaction kinetics for all rearrangement steps of triangle *E*-**T** and lanterns *E*-**L** and *Z*-**L**, respectively, which makes comparison of the rate constants within the reaction cycle of the molecular ratchet difficult.

(ii) In Model II (Figure S75b), we again made use of the "Pd**1**$_2$ *pseudo*-intermediates", however, for all transformations involving triangle *E*-**T**, we introduced lantern **L** as a second intermediate. Hiraoka and coworkers

previously demonstrated,[13,14] that smaller supramolecular assemblies are likely intermediates in the self-assembly of larger structures. Hence, we believe this to be a reasonable restriction on the reaction mechanism. Crucially, all transformation steps from triangle to lantern follow second-order rate laws and can therefore be compared.

We chose to present both models here because, most importantly, they produce similar results at a fundamental level.

S5.2.1 Model I

The necessary first step to investigate was the thermal interconversion of triangle *E*-**T** and lantern *E*-**L** at 298 K and 348 K. For this, an NMR sample containing 78:22 triangle *E*-**T** / lantern *E*-**L** mixture was irradiated with 365 nm light for 5 min to obtain *Z*-**L**. The sample was then immediately irradiated with 500 nm light for 5 min to obtain a sample that contains almost exclusively *E*-**L** lantern. The equilibration between triangle *E*-**T** and lantern *E*-**L** was followed over time by ^{1}H NMR spectroscopy (500 MHz, DMSO-d_6, 298 K or 348 K; Figure S77).

Fixing the formation of triangle *E*-**T** or lantern *E*-**L** from *pseudo*-intermediate "Pd**1**$_2$" as an arbitrarily fast reaction (k = 10^6 or 10^8, close to the diffusion limit in DMSO) allowed us to determine rate constants for the rate-determining steps that describe the triangle *E*-**T** / lantern *E*-**L** equilibrium at 298 K and 348 K, respectively (Figure S78 and Figure **S79**).

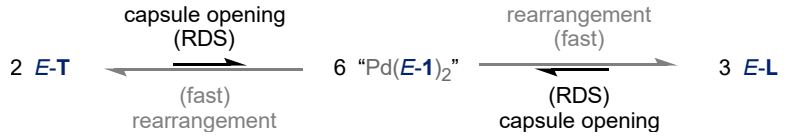

Figure S76. Schematic overview of the simplified kinetic model (within Model I) used for the interconversion between *E*-**T** and *E*-**L**. Note that the "Pd(*E*-**1**)$_2$" species is a *pseudo*-intermediate and not a real compound.

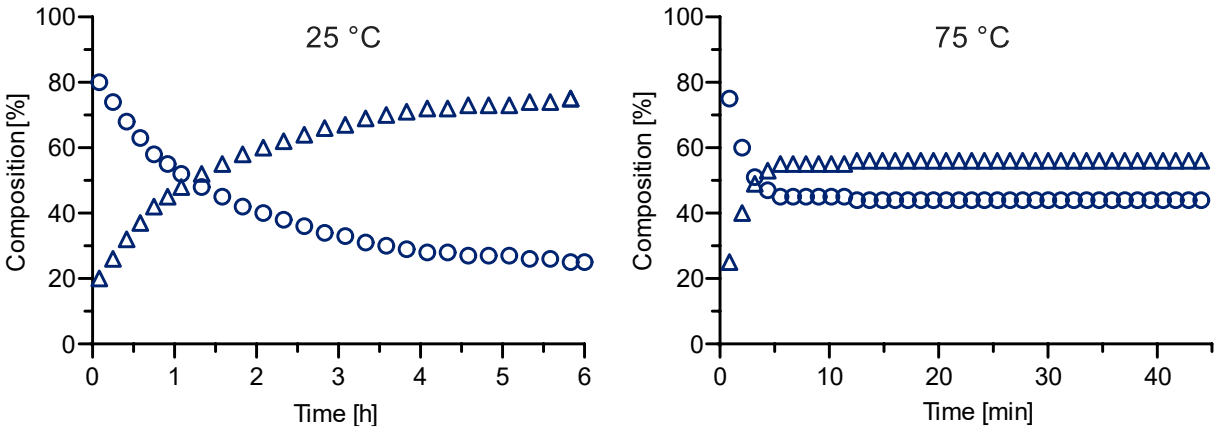

Figure S77. At room temperature, *Z*-**L** was irradiated with 500 nm for *ca*. 5 min to induce *Z*→*E* isomerisation. *Left*: ^{1}H NMR (500 MHz, DMSO-d_6, 298 K) was measured every 5 min for 6 h to monitor the equilibrium between *E*-**T** triangle and *E*-**L** at 298 K. Between 0 h and 1 h, every second data point was removed for clarity, between 1 h and 6 h, only every third data point was plotted (kinetic fitting in Figure S41). *Right*: ^{1}H NMR (500 MHz, DMSO-d_6, 348 K) was measured every 70 s for 45 min to monitor the equilibrium between *E*-**T** and *E*-**L** at 348 K (kinetic fitting in Figure S42). *E*-**T** is denoted with **Δ**, *E*-**L** is denoted with **O**.

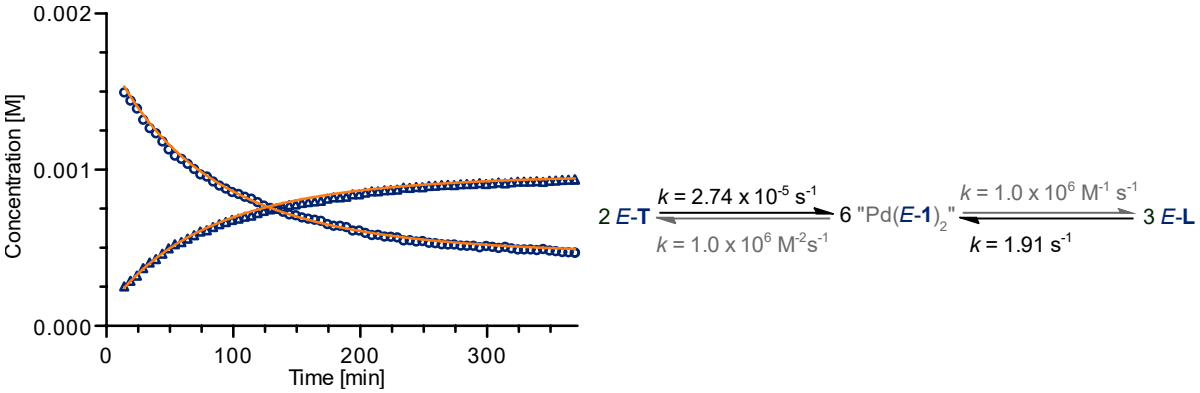

Figure S78. Kinetic plot of the equilibrium between *E*-**T** and *E*-**L** at 25 °C. *E*-**T** is denoted with **Δ** and *E*-**T** is denoted with **O**. The resulting reaction rates are provided within the reaction scheme on the right.

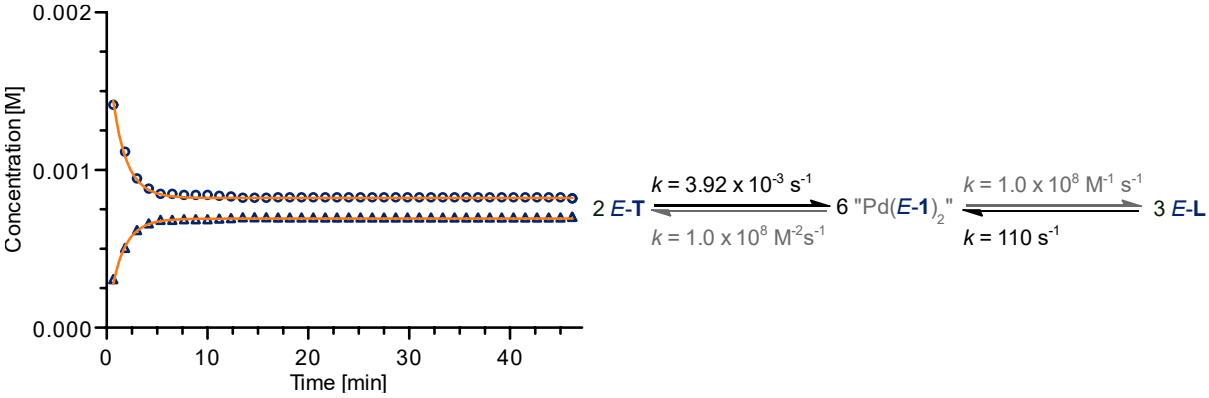

Figure S79. Kinetic plot of the equilibrium between *E*-**T** and *E*-**L** at 75 °C. *E*-**T** is denoted with **Δ** and *E*-**L** is denoted with **O**. The resulting reaction rates are provided within the reaction scheme on the right.

To investigate the *E*→*Z* and *Z*→*E* isomerisations of the capsules, a sample containing 78:22 triangle *E*-**T** / lantern *E*-**L** mixture was subjected to *in-situ* illuminated ^{1}H NMR spectroscopy (700 MHz, DMSO-d_6, 298 K), using 365 nm (10% LED power) and later 500 nm light (2% LED power). The power of the LEDs had to be turned to a lower setting to ensure enough data points could be measured (Figures S62–S64).

The data obtained from these experiments (Figure S62a) were fitted to a model using three different "Pd**1**$_2$" species ("Pd(*E*-**1**)$_2$", "Pd(*Z*-**1**)$_2$", and "Pd(*E*-**1**)$_2$*") with the kinetic data previously determined for the triangle *E*-**T** / lantern *E*-**L** equilibrium fixed within the model (Figure S80). Just like before, the capsule rearrangement was separated into two steps, in this case, a photoisomerisation (and capsule opening) step and a rearrangement step from the *pseudo*-intermediates "*Z*-Pd**1**$_2$" and "*E*-Pd**1**$_2$*", respectively.

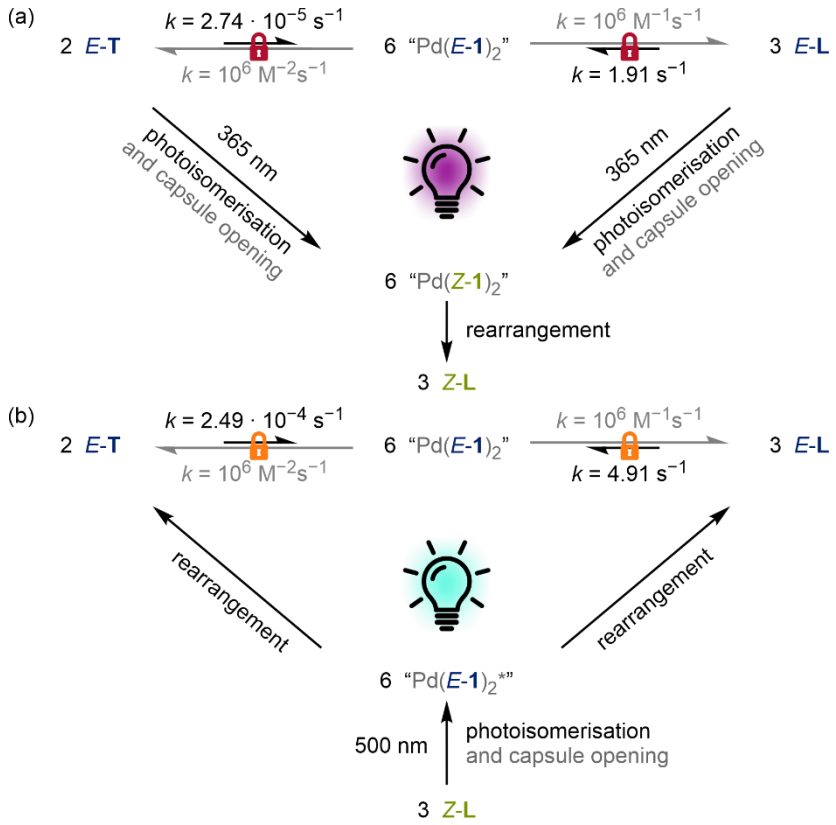

Figure S80. Kinetic models (within Model I) used for the fitting of the kinetic data of (a) *E*→*Z* photoisomerisation of triangle *E*-**T** / lantern *E*-**L** mixture under irradiation with 365 nm light and (b) *Z*→*E* photoisomerisation of lantern *Z*-**L** under irradiation with 500 nm light. Note that all "Pd**1**$_2$" species are *pseudo*-intermediates and not real compounds. The previously determined rate constants of the triangle *E*-**T** / lantern *E*-**L** equilibrium were fixed during fitting in (a), whereas irradiation likely elevated the sample temperature in (b), which is why the rate constants were changed by one order of magnitude to allow the fit to converge.

For the *in-situ* irradiation of the triangle *E*-**T** / lantern *E*-**L** mixture using 365 nm light, Model I suggests similar reaction rates for the photoswitching of triangle *E*-**T** and lantern *E*-**L**, indicating that both structures can photoswitch on a similar time scale to form the lantern *Z*-**L** (Figure S80a and Figure **S81**, also Section S4.3).

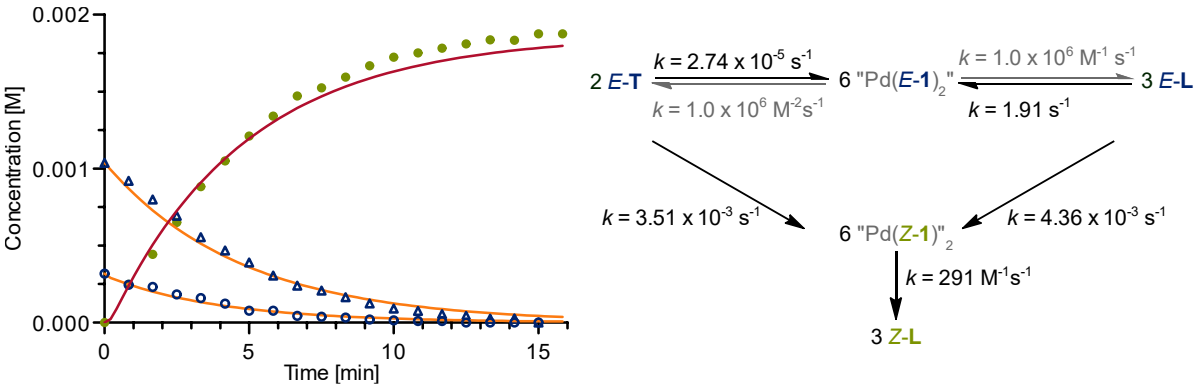

Figure S81. Kinetic plot of the formation of *Z*-**L** over time under *in-situ* illumination with 365 nm light (10% LED power) from a sample of *E*-**T**: *E*-**L** (78:22, respectively). *E*-**T** is denoted with **Δ**, *E*-**L** is denoted with **O**, and *Z*-**L** is denoted with ●. The resulting reaction rates are provided within the reaction scheme on the right.

The kinetic model for the irradiation of lantern *Z*-**L** with 500 nm light suggests that the formation of lantern *E*-**L** from lantern *Z*-**L** is significantly faster than the formation of triangle *E*-**T** from lantern *Z*-**L** (Figure S80b and Figure **S82**, also Section S4.3). The fastest reaction pathway to form triangle *E*-**T** is via photoisomerisation from lantern *Z*-**L** to lantern *E*-**L** and subsequent thermal equilibration from lantern *E*-**L** to triangle *E*-**T**, indicating that lantern *Z*-**L** will only slowly (or not at all) form the triangle *E*-**T** directly. For this fit to converge, it was necessary to give the model the freedom to slightly modify the rate constants of the thermal isomerisation between triangle *E*-**T** and lantern *E*-**L**. We assume that the irradiation needed to form lantern *Z*-**L** had heated the sample slightly, which in turn changed the equilibrium slightly and, hence, the corresponding rate constants.

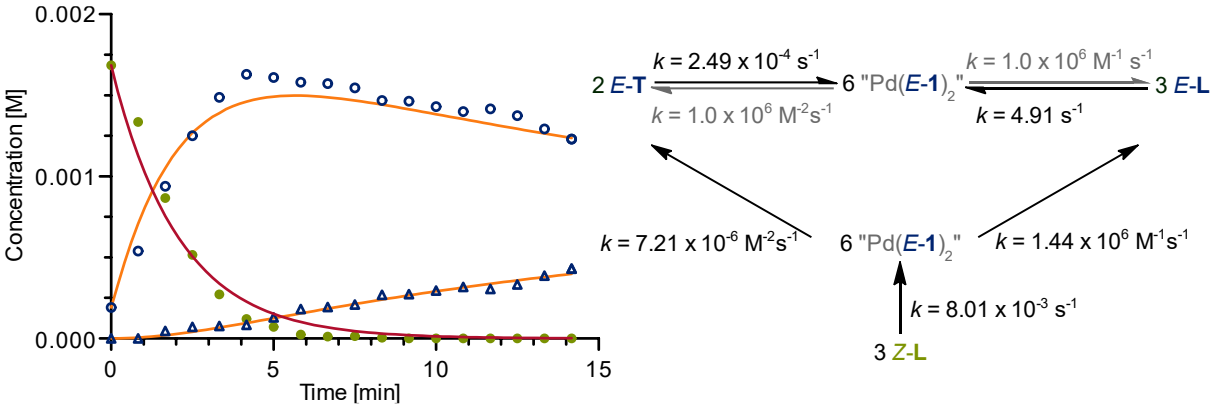

Figure S82. Kinetic plot of the formation of *E*-**T** and *E*-**L** over time under *in-situ* illumination with 500 nm light (2% LED power) from a sample of *Z*-**L**. *E*-**T** is denoted with **Δ**, *E*-**L** is denoted with **O**, and *Z*-**L** is denoted with ●. The resulting reaction rates are provided within the reaction scheme on the right.

The thermal relaxation of lantern *Z*-**L** to the triangle *E*-**T** / lantern *E*-**L** mixture was investigated by ^{1}H NMR spectroscopy (500 MHz, DMSO-d_6, 348 K). An NMR sample containing 78:22 triangle *E*-**T** / lantern *E*-**L** mixture was irradiated with 365 nm light for 5 min to obtain lantern *Z*-**L**. The sample was then immediately inserted into the NMR spectrometer at 348 K and a spectrum measured every 127 s (Figure S72).

The data obtained from these experiments were fitted to a model using two different "Pd**1**$_2$" species ("Pd(*E*-**1**)$_2$" and "Pd(*E*-**1**)$_2$*") with the kinetic data previously determined for the triangle *E*-**T** / lantern *E*-**L** equilibrium fixed within the model (Figure S83). Just like before, the capsule rearrangement was separated into two steps, in this case, a thermal relaxation (and capsule opening) step and a rearrangement step from the *pseudo*-intermediate "*E*-Pd**1**$_2$*".

Using the kinetic data of the *E*-**T** / *E*-**L** equilibrium at 348 K, which we fitted previously (Figure S79), the model determined the main pathway of the thermal relaxation of lantern *Z*-**L** to be the formation of the lantern *E*-**L** from lantern *Z*-**L** (Figure S84). The fastest reaction pathway that forms triangle *E*-**T** is again the isomerisation from lantern *E*-**L**, indicating that lantern *Z*-**L** will only slowly (or not at all) form triangle *E*-**T** by thermal relaxation.

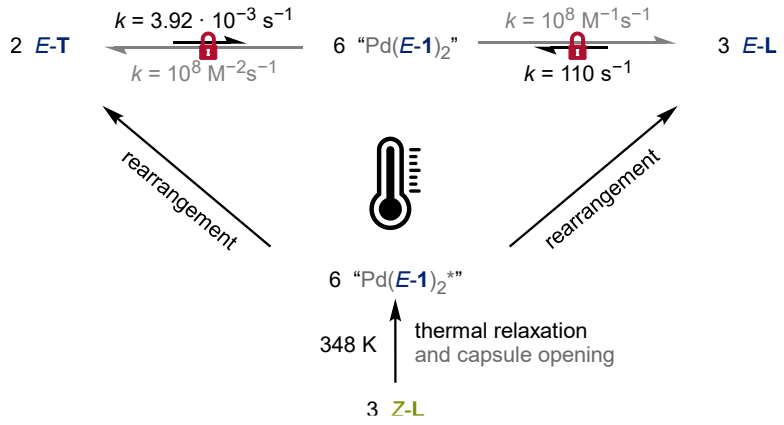

Figure S83. Kinetic model (within Model I) used for the fitting of the kinetic data of the thermal relaxation of lantern *Z*-**L** at 348 K. Note that all "Pd**1**$_2$" species are *pseudo*-intermediates and not real compounds. The previously determined rate constants of the triangle *E*-**T** / lantern *E*-**L** equilibrium were fixed during fitting.

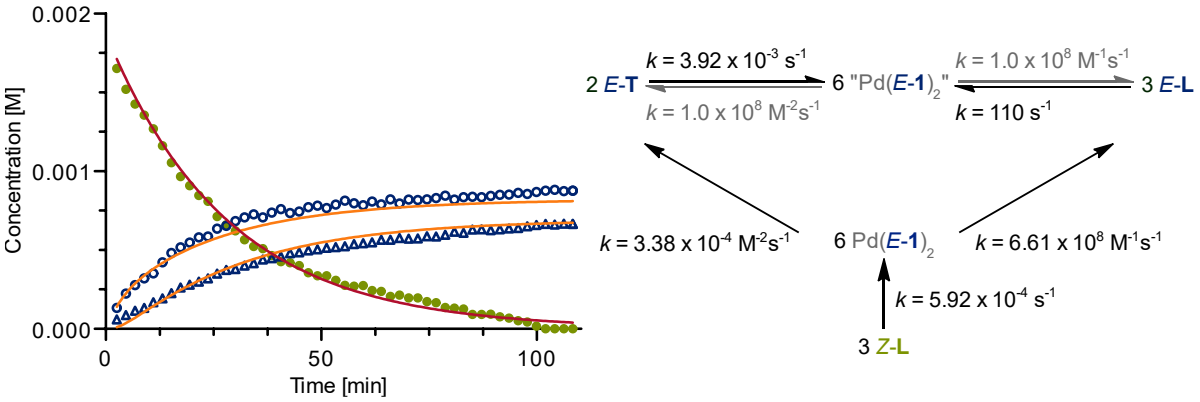

Figure S84. Kinetic plot of the thermal relaxation of *Z*-**L** at 348 K. *E*-**T** is denoted with **Δ**, *E*-**L** is denoted with **O**, and *Z*-**L** is denoted with ●. The resulting reaction rates are provided within the reaction scheme on the right.

S5.2.2 Model II

Model II was fitted to the same experimental data as Model I. The respective experiments are detailed in the previous section.

For the equilibration between triangle *E*-**T** or lantern *E*-**L**, Model II assumes triangle *E*-**T** to open into lantern *E*-**L** and *pseudo*-intermediate "Pd**1**$_2$". In contrast to Model I, all involved reaction steps could be fitted and allowed us to determine rate constants for the rate-determining steps that describe the triangle *E*-**T** / lantern *E*-**L** equilibrium at 298 K and 348 K, respectively (Figure S85–87).

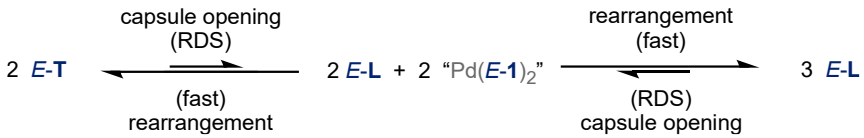

Figure S85. Schematic overview of the simplified kinetic model (within Model II) used for the interconversion between *E*-**T** and *E*-**L**. Note that the "Pd(*E*-**1**)$_2$" species is a *pseudo*-intermediate and not a real compound.

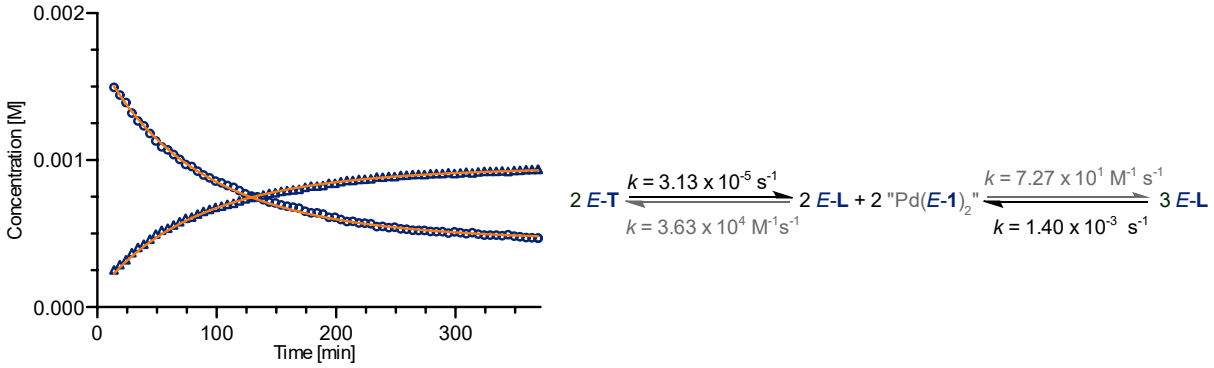

Figure S86. Kinetic plot of the equilibrium between *E*-**T** and *E*-**L** at 25 °C. *E*-**T** is denoted with **Δ** and *E*-**T** is denoted with **O**. The resulting reaction rates are provided within the reaction scheme on the right.

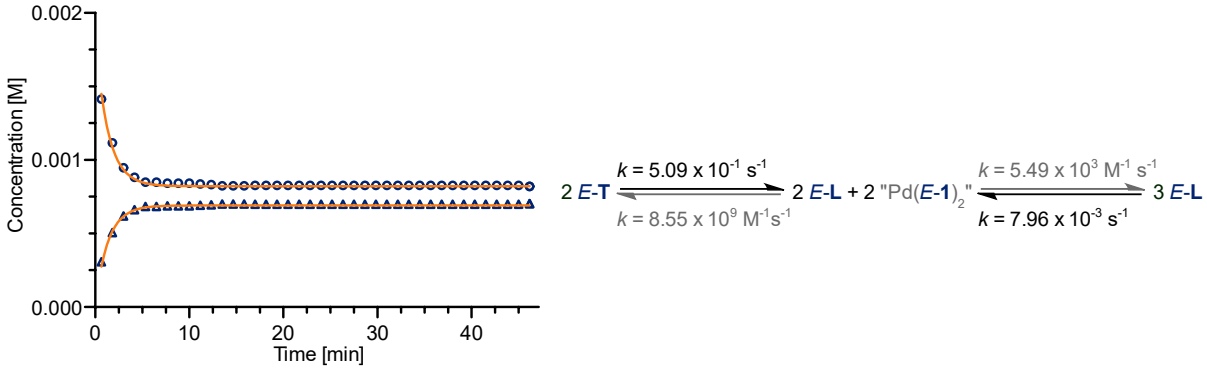

Figure S87. Kinetic plot of the equilibrium between *E*-**T** and *E*-**L** at 75 °C. *E*-**T** is denoted with **Δ** and *E*-**L** is denoted with **O**. The resulting reaction rates are provided within the reaction scheme on the right.

To investigate the *E*→*Z* and *Z*→*E* isomerisations, the data obtained from the illumination experiments (Figure S62a) were fitted to a model using three different "Pd**1**$_2$" species ("Pd(*E*-**1**)$_2$", "Pd(*Z*-**1**)$_2$", and "Pd(*E*-**1**)$_2$*") with the kinetic data previously determined for the triangle *E*-**T** / lantern *E*-**L** equilibrium fixed within the model (Figure S88). Just like before, the capsule rearrangement was separated into two steps, in this case, a photoisomerisation (and capsule opening) step and a rearrangement step from the *pseudo*-intermediates "*Z*-Pd**1**$_2$" and "*E*-Pd**1**$_2$*", respectively. Additionally, in Model II, *Z*-**L** and *E*-**L** act as further intermediates for all transformations involving triangle *E*-**T**.

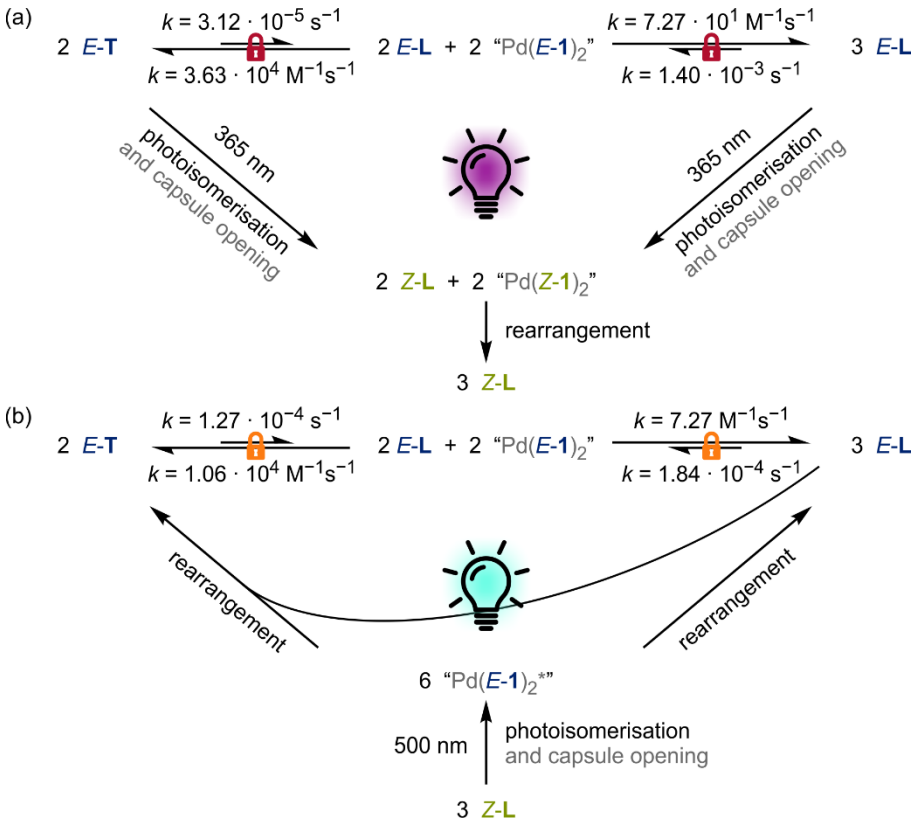

Figure S88. Kinetic models (within Model II) used for the fitting of the kinetic data of (a) *E*→*Z* photoisomerisation of triangle *E*-**T** / lantern *E*-**L** mixture under irradiation with 365 nm light and (b) *Z*→*E* photoisomerisation of lantern *Z*-**L** under irradiation with 500 nm light. Note that all "Pd**1**$_2$" species are *pseudo*-intermediates and not real compounds. Starting from *Z*-**L**, *E*-**T** would be formed from 2 "Pd(*E*-**1**)$_2$*" and 1 *E*-**L** via the direct reaction pathway. The previously determined rate constants of the triangle *E*-**T** / lantern *E*-**L** equilibrium were fixed during fitting in (a), whereas irradiation likely elevated the sample temperature in (b), which is why the rate constants were changed by one order of magnitude to allow the fit to converge.

For the *in-situ* irradiation of the triangle *E*-**T** / lantern *E*-**L** mixture using 365 nm light, similar to Model I, Model II suggests similar reaction rates (deviating by one order of magnitude) for the photoswitching of triangle *E*-**T** and lantern *E*-**L**, indicating that both structures can photoswitch on similar timescales to form the lantern *Z*-**L**, with *E*-**L** switching faster than *Z*-**L** by one order of magnitude (Figure S88a and Figure **S89**, also Section S4.3).

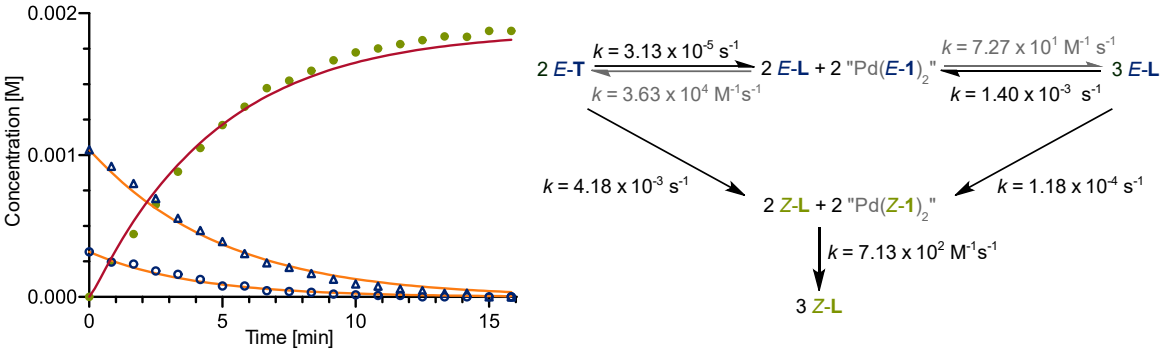

Figure S89. Kinetic plot of the formation of *Z*-**L** over time under *in-situ* illumination with 365 nm light (10% LED power) from a sample of *E*-**T**: *E*-**L** (78:22, respectively). *E*-**T** is denoted with **Δ**, *E*-**L** is denoted with **O**, and *Z*-**L** is denoted with ●. The resulting reaction rates are provided within the reaction scheme on the right.

As in Model I, Model II for the irradiation of lantern *Z*-**L** with 500 nm light suggests that the formation of lantern *E*-**L** from lantern *Z*-**L** is significantly faster than the formation of triangle *E*-**T** from lantern *Z*-**L** (Figure S88b and Figure **S90**, also Section S4.3). The fastest reaction pathway to form triangle *E*-**T** is via photoisomerisation from lantern *Z*-**L** to lantern *E*-**L** and subsequent thermal equilibration from lantern *E*-**L** to triangle *E*-**T**, indicating that lantern *Z*-**L** will only slowly (or not at all) form the triangle *E*-**T** directly. For this fit to converge, it was necessary to give the model the freedom to slightly modify the rate constants of the thermal isomerisation between triangle *E*-**T** and lantern *E*-**L**. We assume that the irradiation needed to form lantern *Z*-**L** had heated the sample slightly, which in turn changed the equilibrium slightly and, hence, the corresponding rate constants.

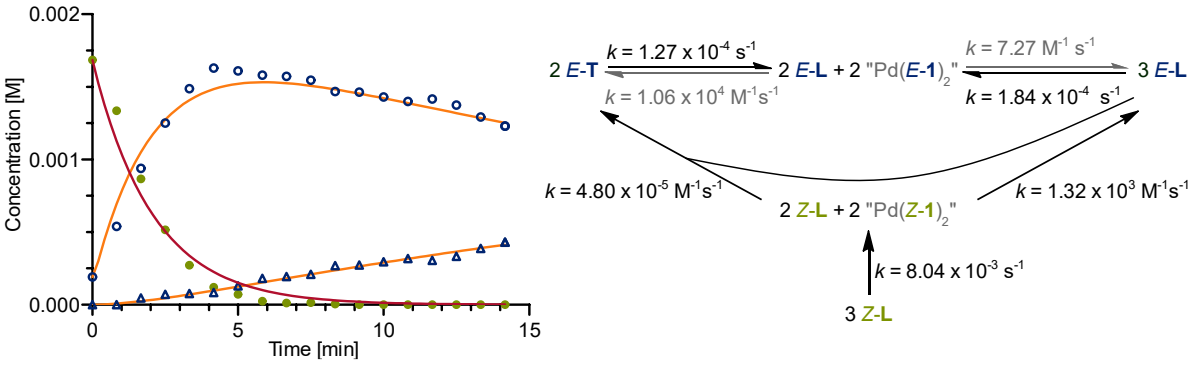

Figure S90. Kinetic plot of the formation of *E*-**T** and *E*-**L** over time under *in-situ* illumination with 500 nm light (2% LED power) from a sample of *Z*-**L**. *E*-**T** is denoted with Δ, *E*-**L** is denoted with O, and *Z*-**L** is denoted with ●. The resulting reaction rates are provided within the reaction scheme on the right.

For the thermal relaxation of lantern *Z*-**L** to the triangle *E*-**T** / lantern *E*-**L** mixture, the obtained data were fitted to a model using two different "Pd**1**$_2$" species ("Pd(*E*-**1**)$_2$" and "Pd(*E*-**1**)$_2$*") with the kinetic data previously determined for the triangle *E*-**T** / lantern *E*-**L** equilibrium fixed within the model (Figure S87). Just like before, the capsule rearrangement was separated into two steps, in this case, a thermal relaxation (and capsule opening) step and a rearrangement step from the *pseudo*-intermediate "*E*-Pd**1**$_2$*". Additionally, in Model II, *Z*-**L** and *E*-**L** act as further intermediates for all transformations involving triangle *E*-**T**.

Using the kinetic data of the *E*-**T** / *E*-**L** equilibrium at 348 K, which we previously fitted (Figure S83), Model II identified the main pathway of the thermal relaxation of lantern *Z*-**L** as the formation of lantern *E*-**L** from lantern *Z*-**L** (Figure S88), which was also observed for Model I. The fastest reaction pathway that forms triangle *E*-**T** is again the isomerisation from lantern *E*-**L**, indicating that lantern *Z*-**L** will only slowly (or not at all) form triangle *E*-**T** by thermal relaxation.

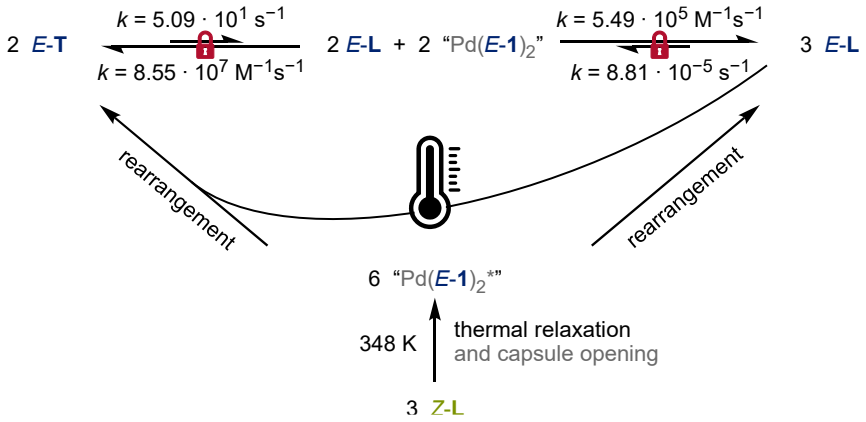

Figure S91. Kinetic model (within Model II) used for the fitting of the kinetic data of the thermal relaxation of lantern *Z*-**L** at 348 K. Note that both "Pd**1**$_2$" species are *pseudo*-intermediates and not real compounds. Starting from *Z*-**L**, *E*-**T** is formed from 2 "Pd(*E*-**1**)$_2$*" and 1 *E*-**L**. The previously determined rate constants of the triangle *E*-**T** / lantern *E*-**L** equilibrium were fixed during fitting.

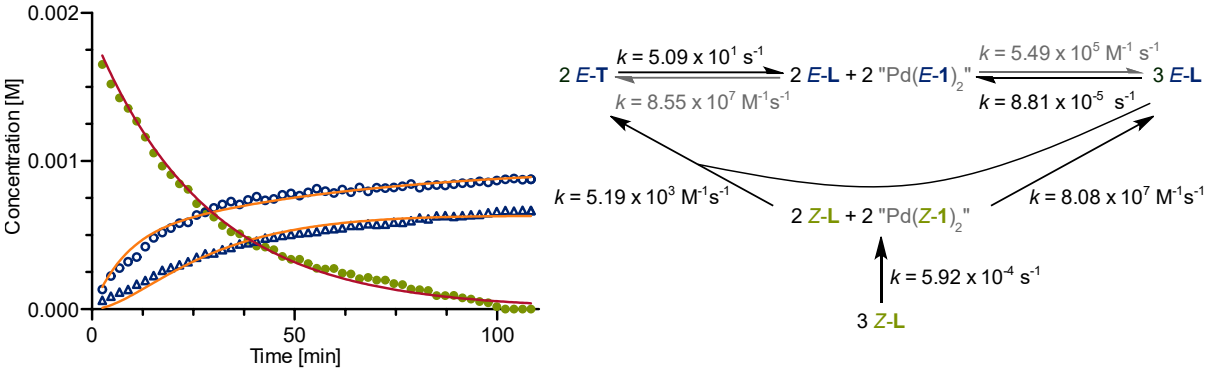

Figure S92. Kinetic plot of the thermal relaxation of *Z*-**L** at 348 K. *E*-**T** is denoted with **Δ**, *E*-**L** is denoted with **O**, and *Z*-**L** is denoted with ●. The resulting reaction rates are provided within the reaction scheme on the right.

S6 Autonomous energy ratchet

To investigate, whether the molecular ratchet could operate autonomously under white light irradiation, two different experiments were conducted (Figure S94). In the first experiment, an NMR sample of the 78:22 triangle *E*-**T** / lantern *E*-**L** mixture was left next to a window on a sunny spring day for 7 h (Figure S94d). The second experiment involved monitoring the changes in composition observed over time when an NMR sample of the 78:22 triangle *E*-**T** / lantern *E*-**L** mixture was irradiated *in situ* inside the NMR spectrometer with a white LED for 5.5 h (Figure S95 and Figure **S96**). Both experiments yielded a mixture enriched with lantern *E*-**L**.

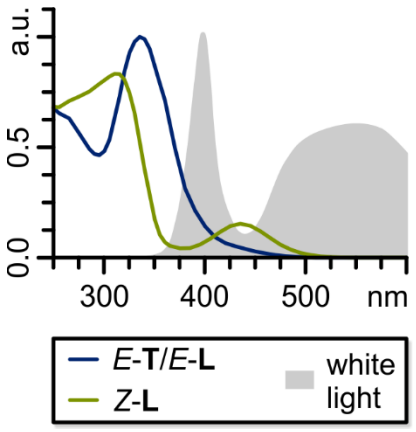

Figure S93. UV-vis spectrum of the *E*-**T** / *E*-**L** mixture after irradiation with 365 nm (green: *Z*-**L**) and 500 nm light (blue: *E*-**T**/*E*-**L**; 1 min each) with an overlay of the normalised emission spectrum of the white light LED (grey).

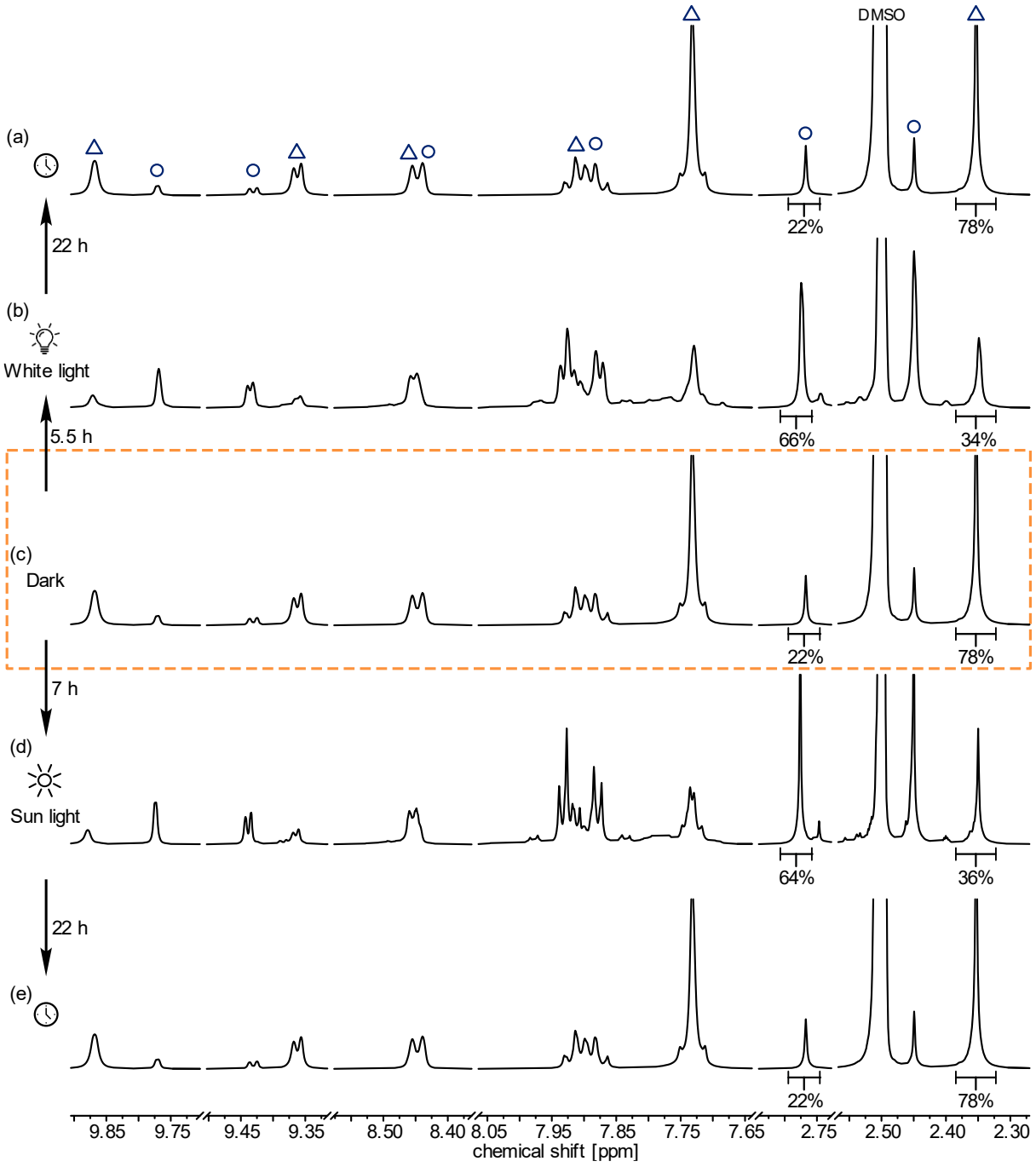

Figure S94. ^{1}H NMR (700 MHz, DMSO-d_6, 298 K) of (c) an *E*-**T**: *E*-**L** mixture under light exclusion (*E*-**T**: *E*-**L**, 78:22), (b) after *in-situ* irradiation with white light for 5.5 h (*E*-**T**: *E*-**L**, 34:66), (d) after leaving the initial NMR sample next to a window on a sunny spring day for 7 h (*E*-**T**: *E*-**L**, 36:64), and (a/e) after 22 h equilibrating in an amberised NMR tube wrapped in aluminium foil in an air-conditioned room (22 °C, *E*-**T**: *E*-**L**, 78:22). *E*-**T** is denoted with **Δ**, *E*-**L** is denoted with **O**.

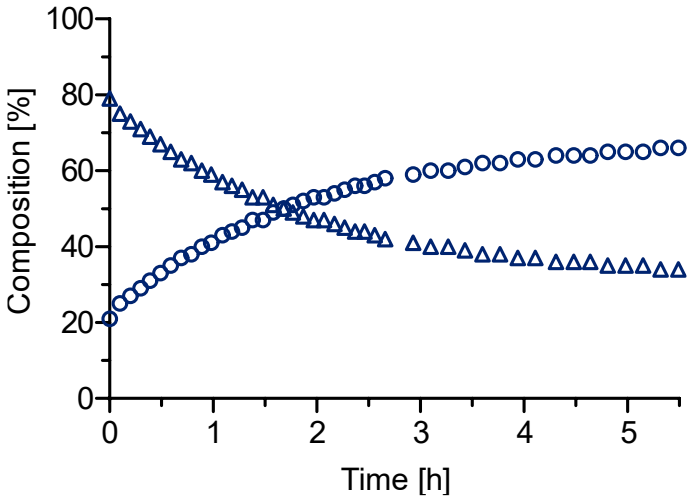

Figure S95. Changes in composition of *E*-**T** and *E*-**L** upon irradiation with white light, measured by *in-situ* illumination ^{1}H NMR (700 MHz, DMSO-d_6, 298 K) over 5.5 h (Figure S96). For the first 2.66 h a spectrum was recorded every 6 min. At 2.9 h, a gap of 18 min is observed due to changes made to the NMR time parameters; from 2.93 h onwards, a spectrum was measured every 10 min. *E*-**T** is denoted with **Δ**, *E*-**L** is denoted with **O**.

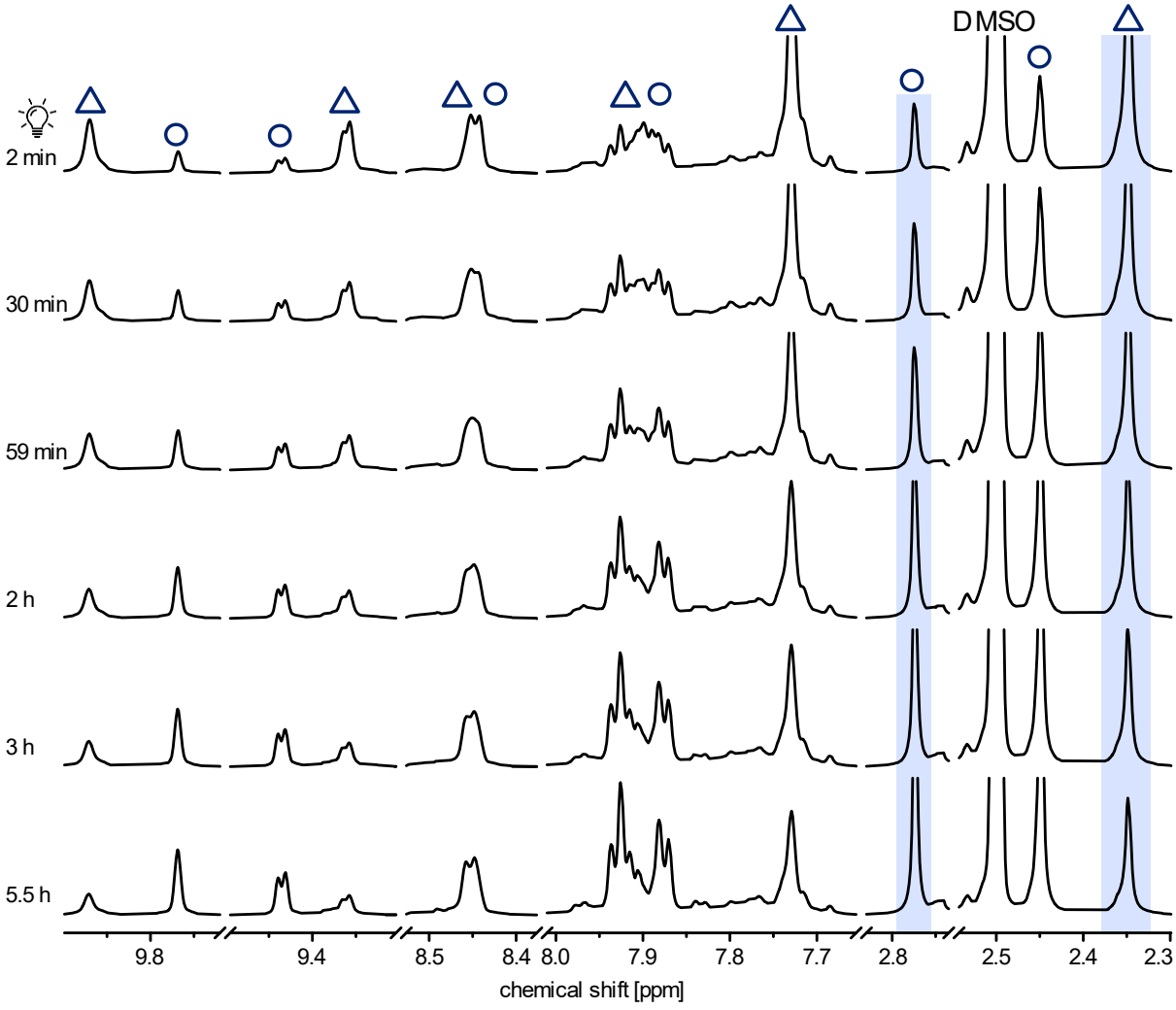

Figure S96. ^{1}H NMR (700 MHz, DMSO-d_6, 298 K) spectral changes during *in-situ* illumination with white light. The signals highlighted in blue were chosen to be line-fitted and plotted to display changes in composition between triangle *E*-**T** and lantern *E*-**L** (Figure S95). *E*-**T** is denoted with **Δ**, *E*-**L** is denoted with **O**.

S7 X-ray crystallography

Crystals of *E*-**1** were obtained by slow solvent evaporation of a saturated solution in dichloromethane at ambient temperature. Crystals of *E*-**L** were obtained by slow diffusion of ethyl acetate into a DMSO solution of the 78:22 triangle *E*-**T** / lantern *E*-**L** mixture.

A colourless plate-like specimen of *E*-**1** (0.18 x 0.08 x 0.02 mm and a clear yellow plate of *E*-**L** (0.16 x 0.03 x 0.02 mm were mounted on a Bruker D8 Venture 4-circle Kappa-diffractometer equipped with a low-temperature device (100(2) K, Oxford Cryostream 800er series, Oxford Cryosystems) by using Cu-K_α-radiation (λ = 1.54186 Å, Helios mirror optics, *E*-**1**) or Mo-K_α-radiation (λ = 0.71073 Å, Helios mirror optics, *E*-**1**) and a PHOTONIII/C14 CMOS detector system. Intensities were measured by fine-slicing φ- and ω-scans and corrected for background, polarisation and Lorentz effects. A semi-empirical absorption correction from equivalent reflections (multi-scan type) was performed using SADABS.[15]

Structure solution was done using intrinsic phasing methods included in the SHELXT program system[16] and refined by full matrix least-squares/difference Fourier synthesis with ShelXL-2019/3).[17] All non-hydrogen atoms were refined anisotropically; hydrogen atoms were placed in geometrically calculated positions and included using a riding model on the bound carbon atoms and relative isotropic displacement parameters. Olex2 was used for graphical representations of the molecular structures.[18]

CCDC numbers CCDC-2488074 (*E*-**1**), CCDC-2488075 (*E*-**L**) contain the supplementary crystallographic data for this paper, which can be obtained free of charge from the Cambridge Crystallographic Data Centre via http://www.ccdc.cam.ac.uk/data request/cif.

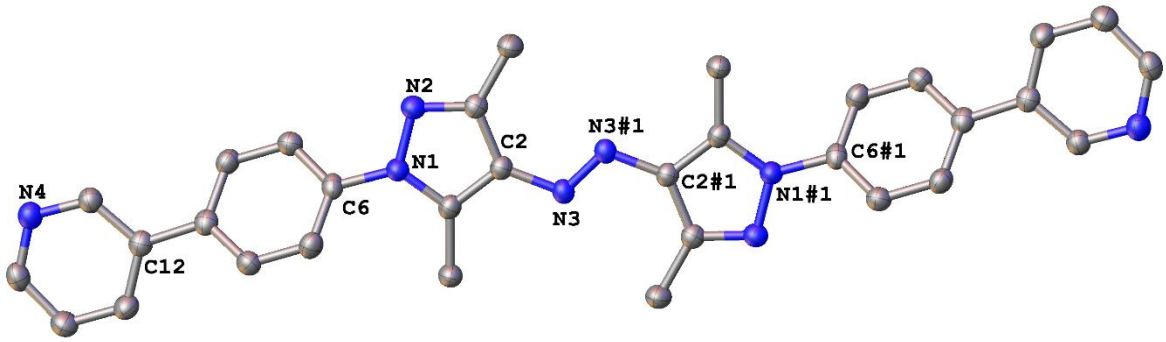

Figure S97. Solid-state structure of *E*-**1**. Hydrogen atoms are omitted for clarity. Thermal ellipsoids are set to 50% probability level. The crystallographic inversion centre is located at the midpoint of the N3 – N3#1 bond.

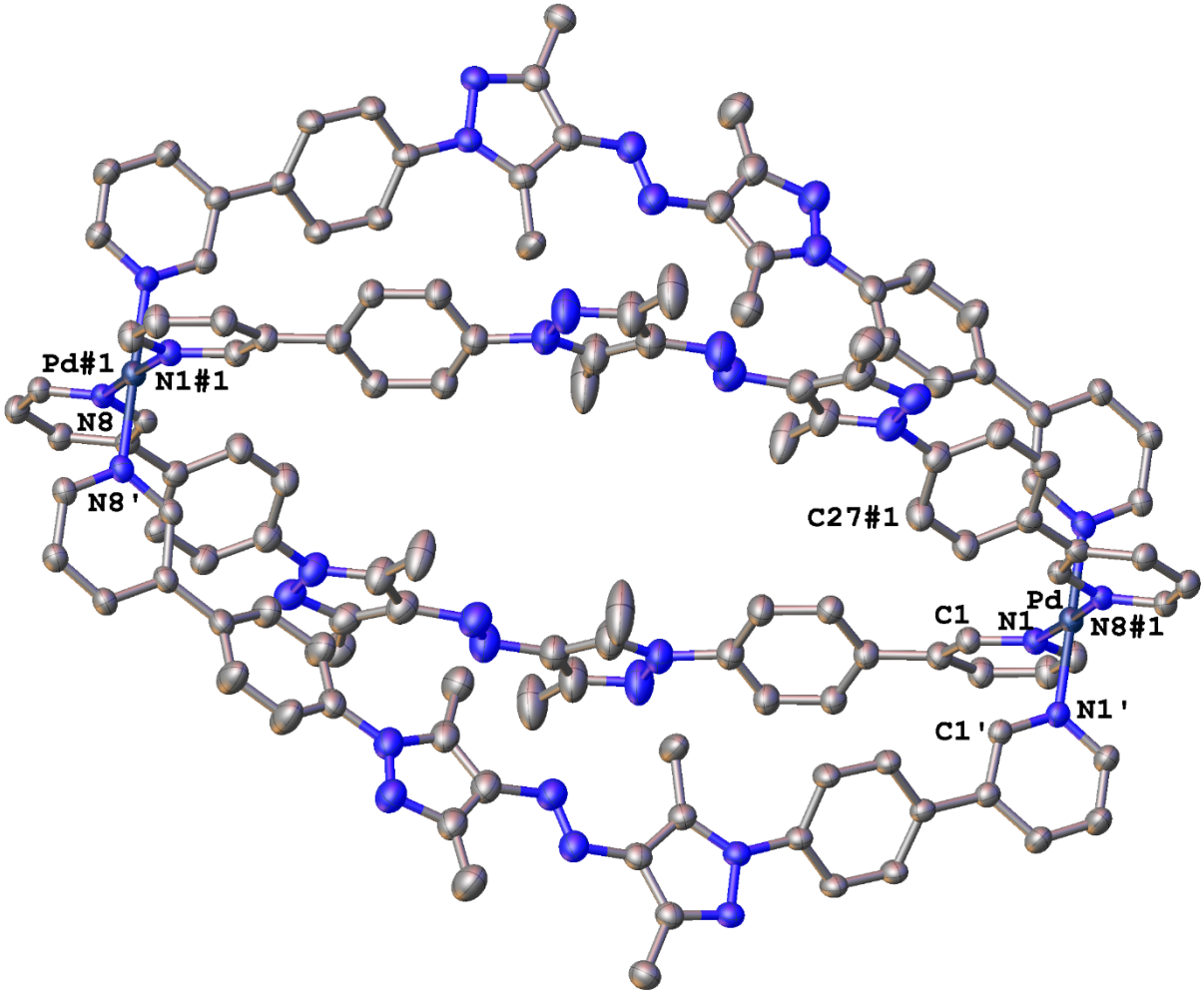

Figure S98. Solid-state structure of *E*-**L**. Hydrogen atoms, co-crystallised solvent molecules and anions are omitted for clarity. Thermal ellipsoids are set to 40% probability level. The crystallographic inversion centre is located at the midpoint of the Pd – Pd#1 vector. The contribution of some solvent molecules and anions in the cage to the overall scattering factor had to be modelled by using the squeezing methodology implemented in the Olex program system.[19]

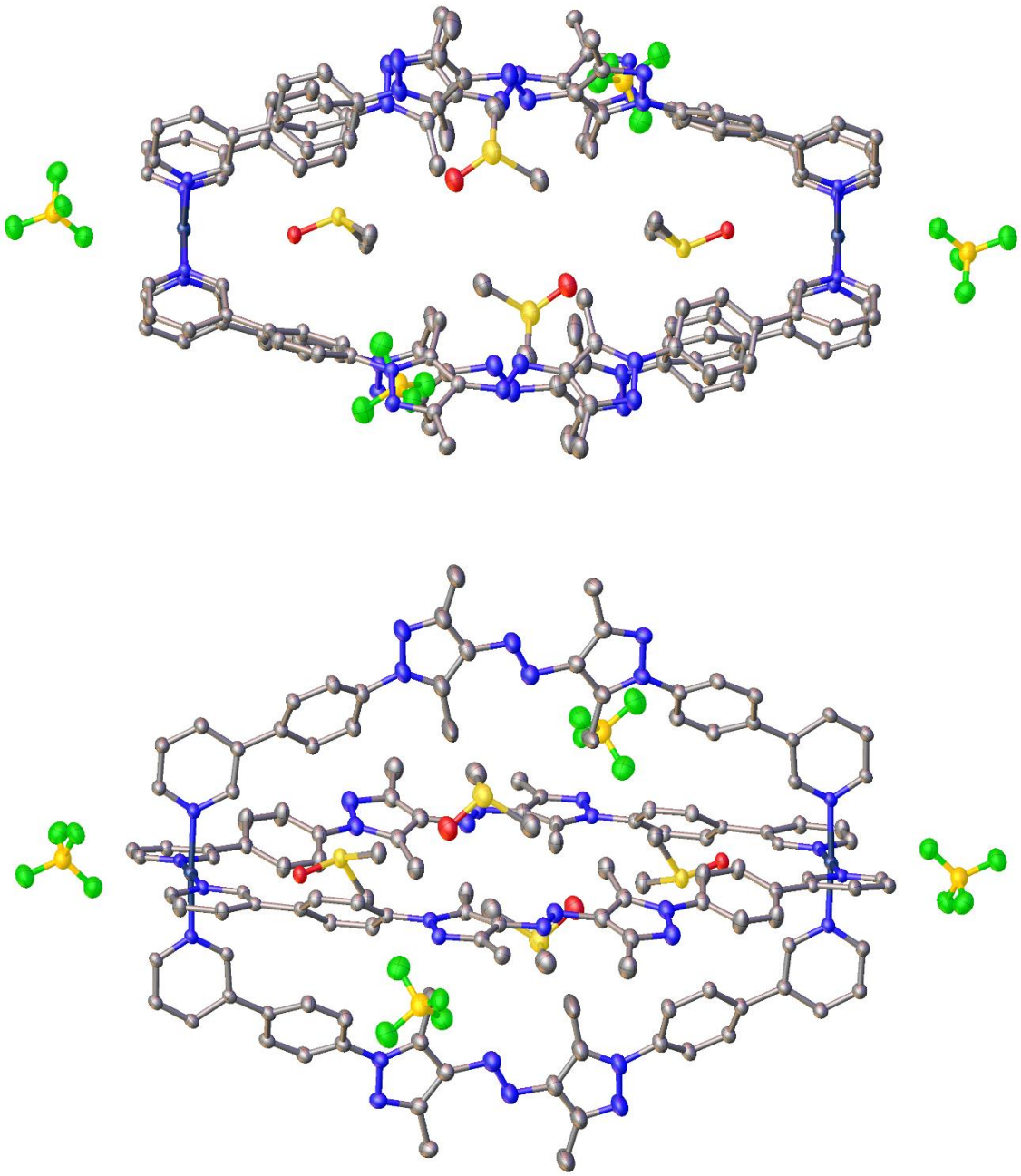

Figure S99. Solid-state structure of *E*-**L**, including four BF_4^- counterions and four DMSO solvent molecules located within the capsule cavity. Hydrogen atoms and additional co-crystallised solvent molecules are omitted for clarity. Thermal ellipsoids are set to 40% probability level. The crystallographic inversion centre is located at the midpoint of the Pd–Pd vector. The contribution of some solvent molecules and anions in the cage to the overall scattering factor had to be modelled by using the squeezing methodology implemented in the Olex program system.[19]

S8 Computational studies

S8.1 Computational Details

Due to the extended system size and flexibility of the investigated structures, solvent molecules and anions were not considered explicitly in the calculations unless stated otherwise. Thus, the lantern structures carry a formal charge of +4, while the triangle structures carry a charge of +6. These charges will not be indicated in subsequent figures or tables unless they differ from the values stated above.

For all computed structures, the energetically most favourable conformer was searched using meta-dynamics (MTD)-based[20] *C*onform-*R*otamer *E*nsemble *S*ampling *T*ool (CREST)[21] (v. 3.0.2), employing the semi-empirical quantum mechanical (SQM) method GFN2-xTB.[22,23] Solvation effects were accounted for using the implicit solvation model ALPB (DMSO).[24]

The respective lowest conformers found were then optimised using the ωB97X-3c[25] composite DFT method, while considering solvation effects using the CPCM implicit solvation model.[26] Final single-point calculations were performed using the ωB97X-3c method in combination with the more sophisticated SMD solvation model.[27] For all structures, thermal corrections were computed at a GFN2-xTB [APLB: DMSO] level of theory using the modified rigid-rotor-harmonic-oscillator approximation (mRRHO)[28] as implemented in the xTB software package (v. 6.6.1).[29]

Gibbs-free energies were then computed as follows:

$$G = E_{\mathrm{gas}} + G_{\mathrm{thermo}} + \delta G_{\mathrm{solv}}$$

With E_{gas} being the gas-phase electronic energy (using ωB97X-3c), G_{thermo} being the thermal corrections (using GFN2-xTB), and δG_{solv} being the solvation contributions (considered by SMD model).

All density functional calculations were performed using the ORCA[30] software package (v. 6.0.1). Model systems were constructed using the Avogadro program,[2] while the ChimeraX[31] software suite was used for the visualisation of structures in this section.

All structures discussed in the main manuscript and the supporting information can be found in the file “structures.zip”.

S8.2 Free Ligand & Lantern – *E*→*Z* Isomerisation

The free energy for the $E \rightarrow Z$ Isomerisation of the free ligand **1** (implicitly solvated by DMSO) was computed to be:

$\Delta G_{E\rightarrow Z} = G(\mathbf{1}_E) - G(\mathbf{1}_Z) = -47.4\ \text{kJ mol}^{-1} = -11.3\ \text{kcal mol}^{-1}$.

The respective structures are depicted in Figure S100.

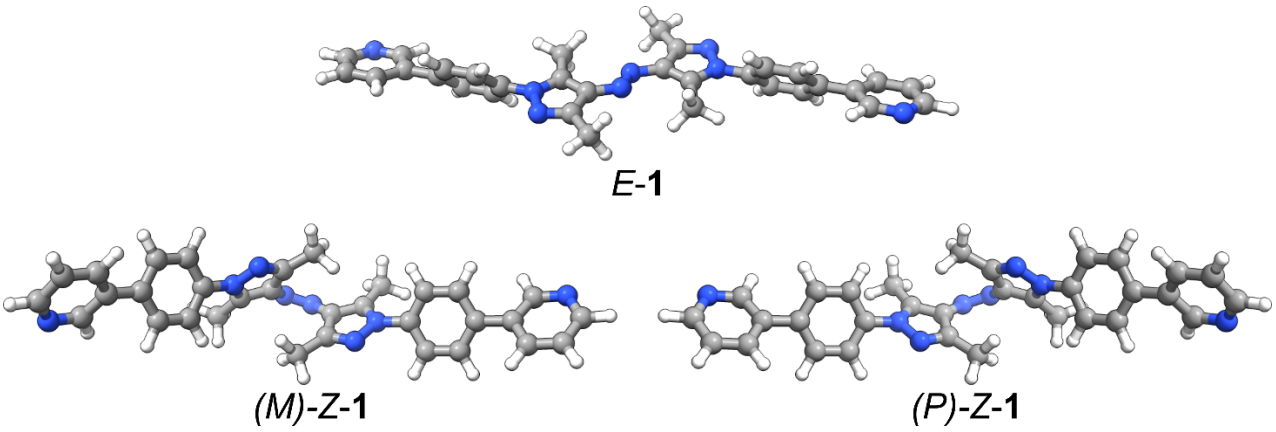

Figure S100. Lowest conformations found by CREST for the studied ligand **1** in *E* and *Z* (both enantiomers) configuration, respectively. Structures are optimised at the ωB97X-3c [CPCM: DMSO] level of theory. Atom colour code: H (white), C (grey), N (blue).

Note that *Z*-**1** is helically chiral. It can exist in either its *P* or *M* form.

Since each lantern structure contains four ligands, each of which can adopt either the *E*- or *Z*-configuration, *E*-**1** and *Z*-**1**, respectively, a total of six distinct lantern motifs can be constructed: *E,E,E,E*-**L** (or *E*-**L**), *Z,E,E,E*-**L**, *cis*-*Z,Z,E,E*-**L**, *trans*-*Z,Z,E,E*-**L**, *Z,Z,Z,E*-**L**, and *Z,Z,Z,Z*-**L** (or *Z*-**L**; Figure S101). All six motifs were investigated computationally. While only *E*-**L** and *Z*-**L** could be experimentally characterised in detail, tentative ^{1}H NMR evidence for the existence of *Z,E,E,E*-**L**, *cis*-*Z,Z,E,E*-**L**, *trans*-*Z,Z,E,E*-**L**, and *Z,Z,Z,E*-**L** in solution could be obtained by mixing *E*-**L** and *Z*-**L** in different ratios (Section S2.8) or during thermal relaxation of *Z*-**L** (Figure S74). The obtained structures are depicted in Table S4. The computed free energies relative to *E*-**L** reveal that each conversion of a ligand from the *E*- to the *Z*-configuration incurs an energetic penalty. Dividing the relative energy differences of each lantern by the number of ligands in *Z* configuration highlights this systematic trend, providing an average penalty of 47.8 kJ mol^{-1}. This value correlates closely with the computed free energy difference between free ligand **1** in its *E* and *Z* configurations (47.4 kJ mol^{-1}).

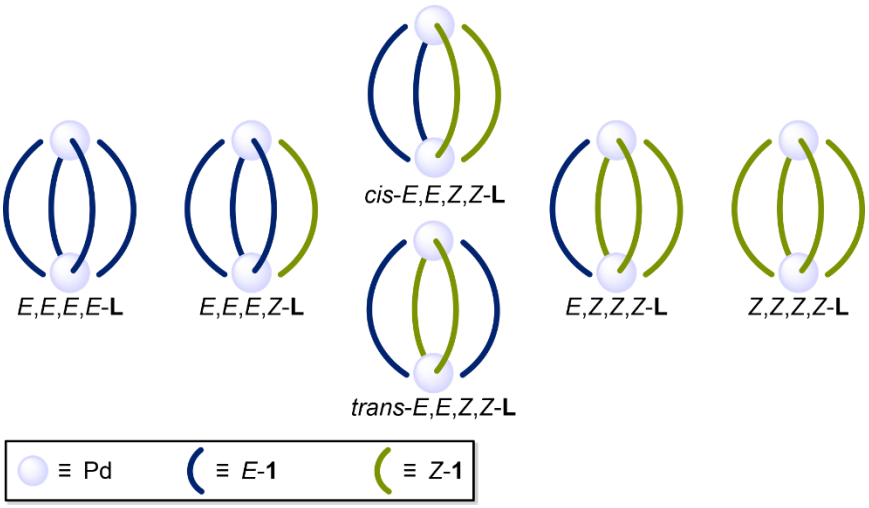

Figure S101. Cartoon representation of the six distinct lantern motifs derived from combining the two different ligand configurations, *E*-**1** and *Z*-**1**, within the same lantern structure: *E,E,E,E*-**L** (or *E*-**L**), *Z,E,E,E*-**L**, *cis*-*Z,Z,E,E*-**L**, *trans*-*Z,Z,E,E*-**L**, *Z,Z,Z,E*-**L**, and *Z,Z,Z,Z*-**L** (or *Z*-**L**).

Table S4. Side and top views of the lowest-energy conformers of all possible lantern motifs defined by the *E*/*Z* configurations of the four ligands. The motifs shown (top to bottom) are: *E*,*E*,*E*,*E*-**L** (or *E*-**L**), *Z*,*E*,*E*,*E*-**L**, *cis*-*Z*,*Z*,*E*,*E*-**L**, *trans*-*Z*,*Z*,*E*,*E*-**L**, *Z*,*Z*,*Z*,*E*-**L**, and *Z*,*Z*,*Z*,*Z*-**L** (or *Z*-**L**). Relative free energies with respect to *E*-**L** ($\Delta G_{\text{w.r.t. } E\text{-L}}$) along with values normalised by the number of ligands in the *Z*-configuration ($\Delta G_{\text{w.r.t. } E\text{-L}}$ / # of *Z*). Energies are given in kJ mol^{-1}. Structures are optimised at the ωB97X-3c [CPCM: DMSO] level of theory; free energies were computed at the ωB97X-3c [SMD: DMSO] level with thermal corrections obtained from GFN2-xTB [APLB: DMSO]. Atom colour code: H (white), C (grey), N (blue), Pd (teal).

Structure	Side View	Top View	$\Delta G_{\text{w.r.t. } E\text{-L}}$ [kJ mol^{-1}]	$\Delta G_{\text{w.r.t. } E\text{-L}}$ / # of *Z* [kJ mol^{-1}]
E,*E*,*E*,*E*-**L** (*E*-**L**)	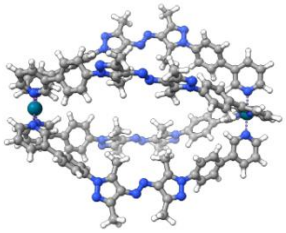	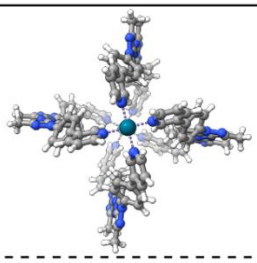	**0.0**	–
Z,*E*,*E*,*E*-**L**	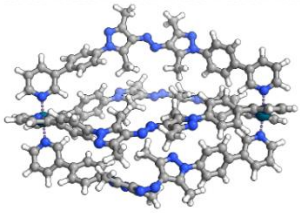	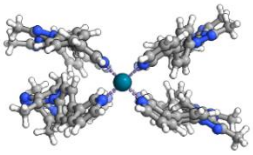	**39.6**	**39.6**
cis-*Z*,*Z*,*E*,*E*-**L**	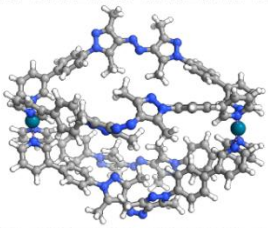	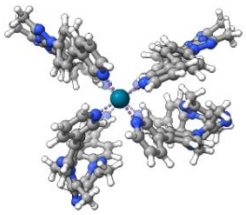	**97.0**	**48.5**
trans-*Z*,*Z*,*E*,*E*-**L**	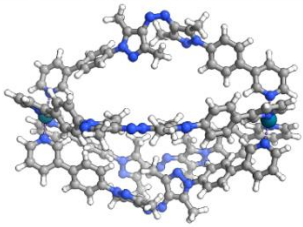	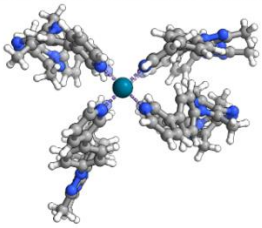	**99.8**	**49.9**
Z,*Z*,*Z*,*E*-**L**	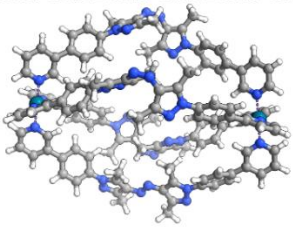	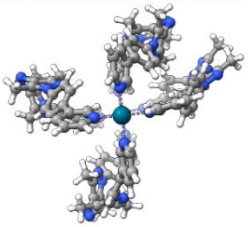	**146.1**	**48.7**
Z,*Z*,*Z*,*Z*-**L** (*Z*-**L**)	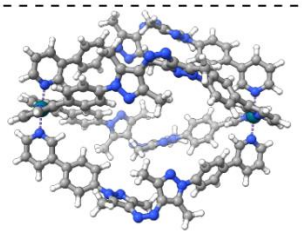	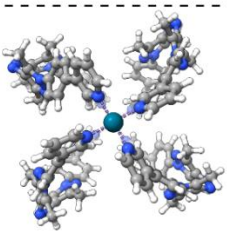	**209.3**	**52.3**

S8.3 Isomers of *Z*-**L**

Six diastereomers of *Z*-**L** exist, differing in the chirality of their ligands **1**, i.e. (*P*)-*Z*-**1** and (*M*)-*Z*-**1**, respectively: (*M*,*M*,*M*,*M*)-*Z*-**L** and its enantiomer (*P*,*P*,*P*,*P*)-*Z*-**L**, (*P*,*M*,*M*,*M*)-*Z*-**L** and its enantiomer (*P*,*P*,*P*,*M*)-*Z*-**L**, (*cis*-*P*,*P*,*M*,*M*)-*Z*-**L**, and (*trans*-*P*,*P*,*M*,*M*)-*Z*-**L** (Figure S102).

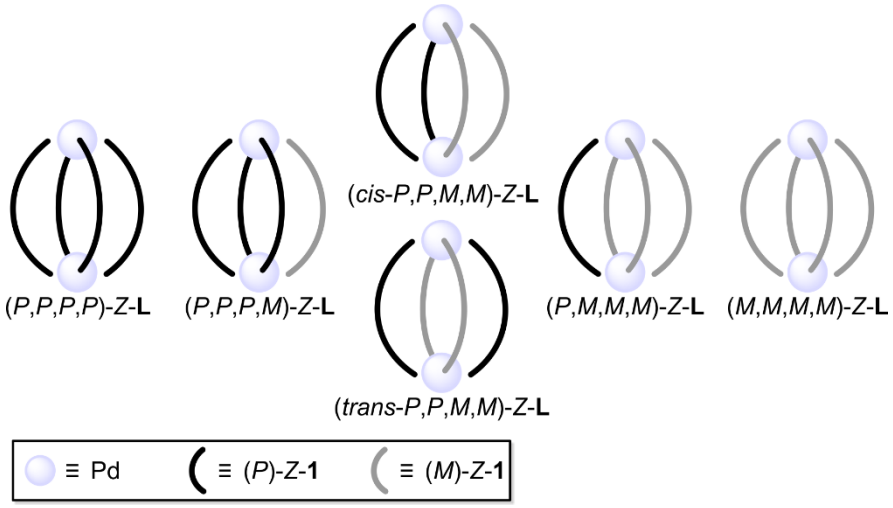

Figure S102. Cartoon representations of the six diastereomers of *Z*-**L**: (*M*,*M*,*M*,*M*)-*Z*-**L** and its enantiomer (*P*,*P*,*P*,*P*)-*Z*-**L**, (*P*,*M*,*M*,*M*)-*Z*-**L** and its enantiomer (*P*,*P*,*P*,*M*)-*Z*-**L**, (*cis*-*P*,*P*,*M*,*M*)-*Z*-**L**, and (*trans*-*P*,*P*,*M*,*M*)-*Z*-**L**.

To help visualise these isomers systematically, the cage is oriented such that the Pd atom with the lower index in the xyz file is placed at the bottom and the other at the top. If the upper methyl group adjacent to the azo bridge (tilted downwards) points to the left, the respective ligand is the M enantiomer (*M*)-*Z*-**1**; if it points to the right, it is the P isomer (*P*)-*Z*-**1**. This procedure is applied to all ligands in a structure to obtain an unambiguous classification of each isomer. An example of the procedure is shown in Figure S103. This convention is arbitrary and serves only to provide a consistent differentiation between isomers. Based on this scheme, the following *Z*-**L** configurations were constructed and investigated:

(*M*,*M*,*M*,*M*)-*Z*-**L** and its enantiomer (*P*,*P*,*P*,*P*)-*Z*-**L**, (*P*,*M*,*M*,*M*)-*Z*-**L** and its enantiomer (*P*,*P*,*P*,*M*)-*Z*-**L**, (*cis*-*P*,*P*,*M*,*M*)-*Z*-**L**, and (*trans*-*P*,*P*,*M*,*M*)-*Z*-**L**.

The xyz-files of all isomers can be found in the file “structures.zip

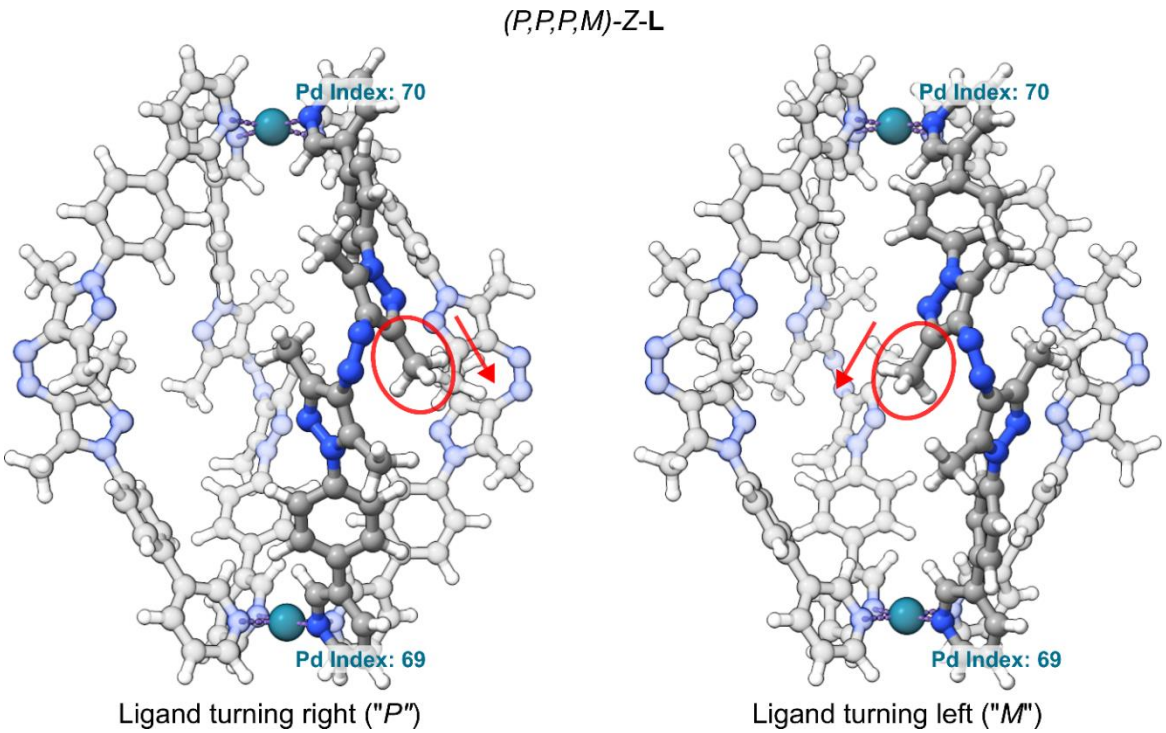

Figure S103. Illustration of the classification applied for (*P*)-*Z*-**1** and (*M*)-*Z*-**1** on two ligands within the structure of (*P,P,P,M*)-*Z*-**L**. The Pd atom with the lower index is positioned at the bottom of the lantern, and the defining upper methyl group adjacent to the azo bridge (tilted downwards, highlighted with a red circle) points either to the right (P isomer) or to the left (M isomer). Atom colour code: H (white), C (grey), N (blue), Pd (teal).

™

The computed relative free energies with respect to (*M*,*M*,*M*,*M*)-*Z*-**L** are summarised in Table S5. The largest absolute difference is 5.0 kJ mol^{-1}, which is likely within the error margin of the computational approach. One limitation of the method is evident in the energy differences between enantiomers, (*M*,*M*,*M*,*M*)-*Z*-**L** and its enantiomer (*P*,*P*,*P*,*P*)-*Z*-**L** as well as (*P*,*M*,*M*,*M*)-*Z*-**L** and its enantiomer (*P*,*P*,*P*,*M*)-*Z*-**L**, respectively, which ideally should be identical but deviate up to 1.0 kJ mol^{-1} for the considered pairs. Consequently, we focus on the general conclusion that all computed configurations are energetically similar, indicating that multiple isomers could coexist.

Table S5. Relative free energies of the investigated *Z*-**L** isomers with respect to (*M*,*M*,*M*,*M*)-*Z*-**L** ($\Delta G_{\text{w.r.t. (M,M,M,M)-Z-L}}$). Enantiomeric pairs are highlighted in blue or purple. Energies are computed at a ωB97X-3c [CPCM: DMSO] // ωB97X-3c [SMD: DMSO] level of theory with thermal corrections obtained at the GFN2-xTB [APLB: DMSO] level. Energies are given in kJ mol^{-1}. The corresponding structures can be found in the file "structures.zip".

***Z*-L Isomer**	$\Delta G_{\text{w.r.t (M,M,M,M)-Z-L}}$ [kJ mol^{-1}]
(*M*,*M*,*M*,*M*)-*Z*-**L**	0.0
(*P*,*M*,*M*,*M*)-*Z*-**L**	−0.6
(*cis*-*P*,*P*,*M*,*M*)-*Z*-**L**	−5.0
(*trans*-*P*,*P*,*M*,*M*)-*Z*-**L**	−2.7
(*P*,*P*,*P*,*M*)-*Z*-**L**	−0.1
(*P*,*P*,*P*,*P*)-*Z*-**L**	−1.0

S8.4 Isomers of *E*-**L**

As already mentioned in Section S2.6, lantern *E*-**L** can adopt six isomers, because ligand *E*-**1** is not C_2 symmetric (Figure S13 and Figure **S104**).

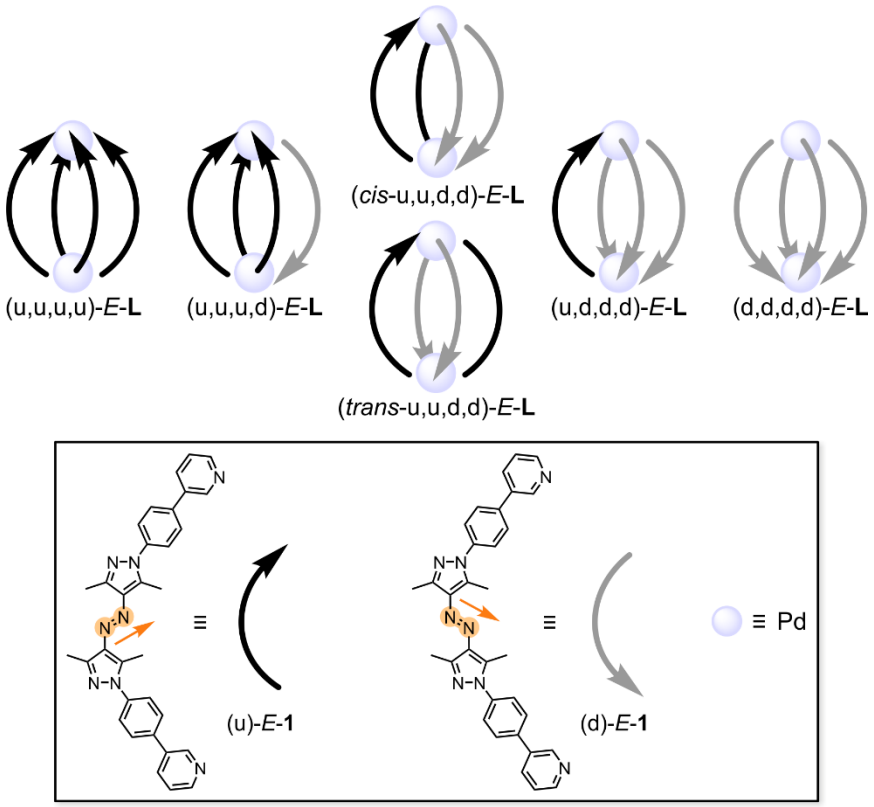

Figure S104. Cartoon representations of the different possible isomers of *E*-**L**. Ligand orientations are labelled "up" (u) and "down" (d), respectively, with respect to the orientations of the azo groups: If the N=N double bond of the azo bridge tilts slightly upward and into the concave side of the ligand (orange arrow), a ligand is assigned the "up" (u) orientation (black curved arrow); if it tilts slightly downward and into the concave side of the ligand (orange arrow), it is assigned the "down" (d) orientation (grey curved arrow). Note that the X-ray crystal structure showed the (*cis*-u,u,d,d)-*E*-**L** isomer (Section S7).

To systematically classify these isomers, the cage is oriented such that the Pd atom with the lower index in the xyz-file is at the bottom, with the other Pd atom on top. If the N=N double bond of the azo bridge points slightly upward and into the lantern, a given ligand is assigned the "up" (u) orientation; if it points slightly downward and into the lantern, it is assigned the "down" (d) orientation. This procedure is applied to all ligands in a structure to obtain an unambiguous classification of each isomer (Figure S105). These rules were arbitrarily chosen and serve solely to provide a

consistent differentiation between isomers. According to this nomenclature, the six possible isomers are:

(u,u,u,u)-*E*-**L** and its enantiomer (d,d,d,d)-*E*-**L**, (u,u,u,d)-*E*-**L** and its enantiomer (u,d,d,d)-*E*-**L**, (*cis*-u,u,d,d)-*E*-**L**, and (*trans*-u,u,d,d)-*E*-**L**.

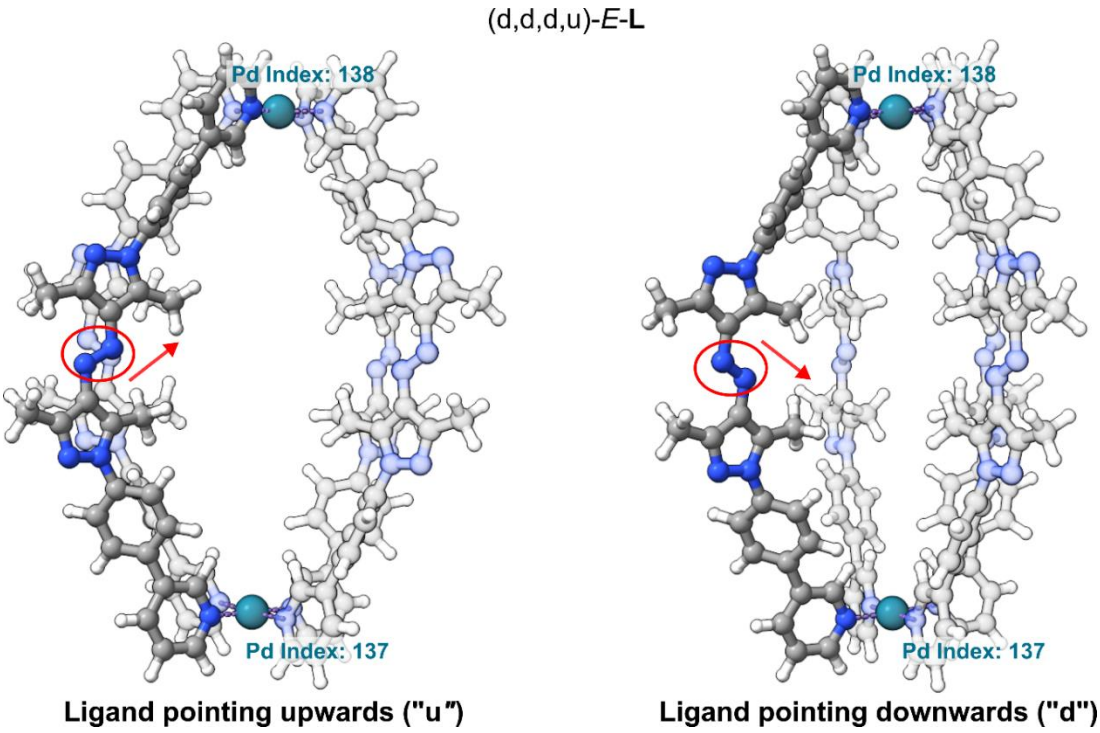

Figure S105. Illustration of the nomenclature scheme of *E*-**L** isomers for two ligands within the structure of (d,d,d,u)-*E*-**L**. The Pd atom with the lower index is positioned at the bottom of the lantern and the defining N=N double bond of the azo bridge (highlighted with a red circle) points into the lantern and either upwards or downwards, respectively. Atom colour code: H (white), C (grey), N (blue), Pd (teal).

The computed relative free energies with respect to (d,d,d,d)-*E*-**L** are summarised in Table S6. The results closely resemble those of the *Z*-**L** isomers. With absolute relative energy differences of up to 6.3 kJ mol^{-1}, all investigated isomers are predicted to be similarly stable. The computed energy difference of 4.2 kJ mol^{-1} between the enantiomers (d,d,d,d)-*E*-**L** and (u,u,u,u)-*E*-**L** further highlights the limitations of the applied workflow, indicating that conclusions should be considered qualitative rather than quantitative.

Table S6. Relative free energies of the investigated *E*-**L** isomers with respect to (d,d,d,d)-*E*-**L** ($\Delta G_{\text{w.r.t. (d,d,d,d)-}E\text{-L}}$). Enantiomeric pairs are coloured blue or purple, respectively. Energies are computed at the ωB97X-3c [CPCM: DMSO] // ωB97X-3c [SMD: DMSO] level of theory, with thermal corrections obtained at the GFN2-xTB [APLB: DMSO] level. Energies are given in kJ mol^{-1}. The corresponding structures can be found in the file "structures.zip".

***E*-L isomer**	$\Delta G_{\text{w.r.t (d,d,d,d)-}E\text{-L}}$ [kJ mol^{-1}]
(d,d,d,d)-*E*-**L**	0.0
(d,d,d,u)-*E*-**L**	−6.3
(*cis*-d,d,u,u)-*E*-**L**	0.9
(*trans*-d,d,u,u)-*E*-**L**	−6.2
(d,u,u,u)-*E*-**L**	−3.1
(u,u,u,u)-*E*-**L**	4.2

S8.5 Comparison to the crystal structure of *E*-**L**

The experimentally obtained crystal structure provides a means to validate the previously applied computational approach. In the crystal structure, all ligands adopt the *E*-configuration, corresponding to *E*-**L**. Using the nomenclature introduced in Section S8.4, the lantern is classified as the (*cis*-u,u,d,d)-*E*-**L** isomer. A comparison of the crystal structure with the computationally predicted structure is shown in Figure S106. Overall, good agreement can be observed between the two structures. The Pd–Pd distance in the crystal is 20.6 Å, which is slightly longer than the predicted distance of 19.9 Å, and some portions of the structure exhibit minor differences in ligand orientation. Notably, the benzene rings adjacent to the azo bridges seem to adopt two preferred orientations, rotated by approximately 60° relative to each other. This can also partially be seen in the measured crystal structure, in which they exhibit respective static site disorder. Cases where the predicted structure deviates by a comparable rotation are still considered good agreement with the experiment. Using a bleeding-edge version of the CREST program, a permutation-invariant root-mean-square deviation (iRMSD) of 1.1 Å was obtained between the two structures (for more information, see [32]).

We conclude that the comparison demonstrates the computational approach is sufficient to reliably predict lantern structures, despite the omission of explicit solvent molecules or anions. This observation provides validation for the previously presented data.

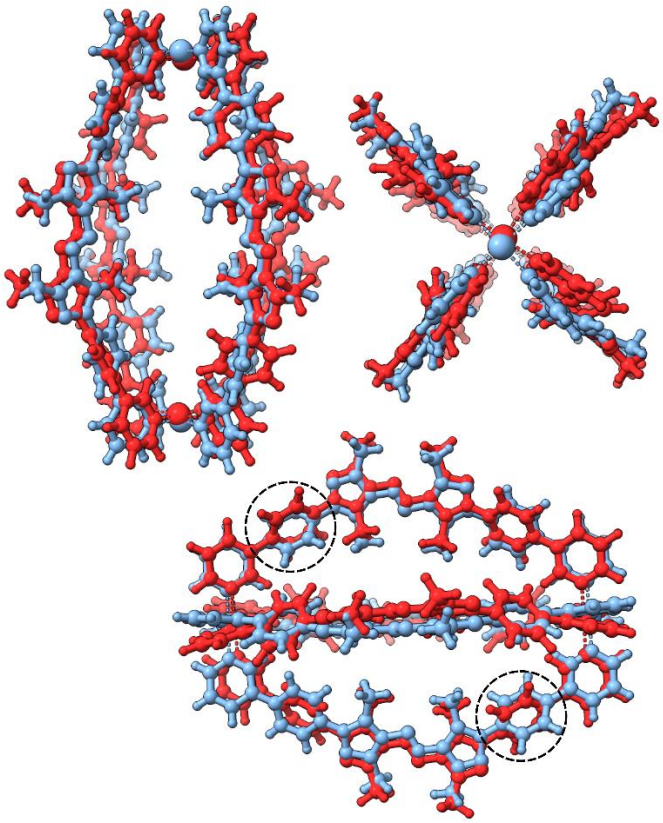

Figure S106. Overlay of the X-ray crystal structure of *E*-**L** (blue) with the computationally obtained structure (red) from CREST, reoptimized at the ωB97X-3c [CPCM: DMSO] level of theory. Following the nomenclature introduced in Section S8.4, the shown isomer is classified as (*cis*-u,u,d,d)-*E*-**L**. In the crystal structure, the benzene rings exhibit site disorder (main layer 55% occupancy), rotated by approximately 60°; black circles mark cases where the computed structure shows a similar rotation, which is therefore still considered good agreement. The structures have a permutation-invariant root-mean-square deviation (iRMSD) of 1.1 Å.

S8.6 Lantern models based on crystal structure

Analysis of the experimental crystal structure provided valuable information on the positions of solvent molecules and anions. A cutout of the crystal structure was used to construct a more sophisticated (but computationally more demanding) model, including four explicit DMSO molecules inside the lantern and two explicit BF_4^- anions coordinating the Pd^{II} cations in their octahedral positions outside the lantern. The cutout was relaxed at the r²SCAN-3c [CPCM: DMSO] level of theory.[33] The lower level of theory was necessary due to the extended system size to maintain feasible computation times; nonetheless, only negligible structural changes were observed upon relaxation.

Since no crystal structure could be obtained for *Z*-**L**, analogous model systems containing four DMSO and two BF_4^- anions in similar positions to those of *E*-**L** were constructed for all possible isomers.

CREST was then employed to identify the lowest-energy conformer of each system, utilising the "subrmsd" setting. Due to the increased model complexity, several distinct low-lying conformers were manually selected and reoptimized at the r²SCAN-3c [CPCM: DMSO] level of theory. The energetically most favourable conformer was found to be a (*M,M,M,M*)-*Z*-**L** isomer model system, which was subsequently used for further calculations. The resulting model systems for *E*-**L** and *Z*-**L** are shown in Figure S107.

Free energies were computed at the usual level of theory, yielding the following energy difference between *E*-**L** and *Z*-**L**:

$$\Delta G_{E\text{-}\mathbf{L}-Z\text{-}\mathbf{L}} = G(E\text{-}\mathbf{L}) - G(Z\text{-}\mathbf{L}) = 181.2\ \text{kJ mol}^{-1} = 43.3\ \text{kcal mol}^{-1}\ .$$

This value is 12% lower than the previously computed value of 209.3 kJ mol⁻¹ (compare Table S4), which was obtained without explicit solvent molecules or anions. This indicates that explicit interactions between the lantern and its environment have a non-negligible effect, highlighting the limitations of the previously applied approximate model system.

However, due to the larger system size, the computational cost for a geometry optimisation increased from approximately 1 day to about 7 days, even with the use of a more efficient composite DFT method for the structures.

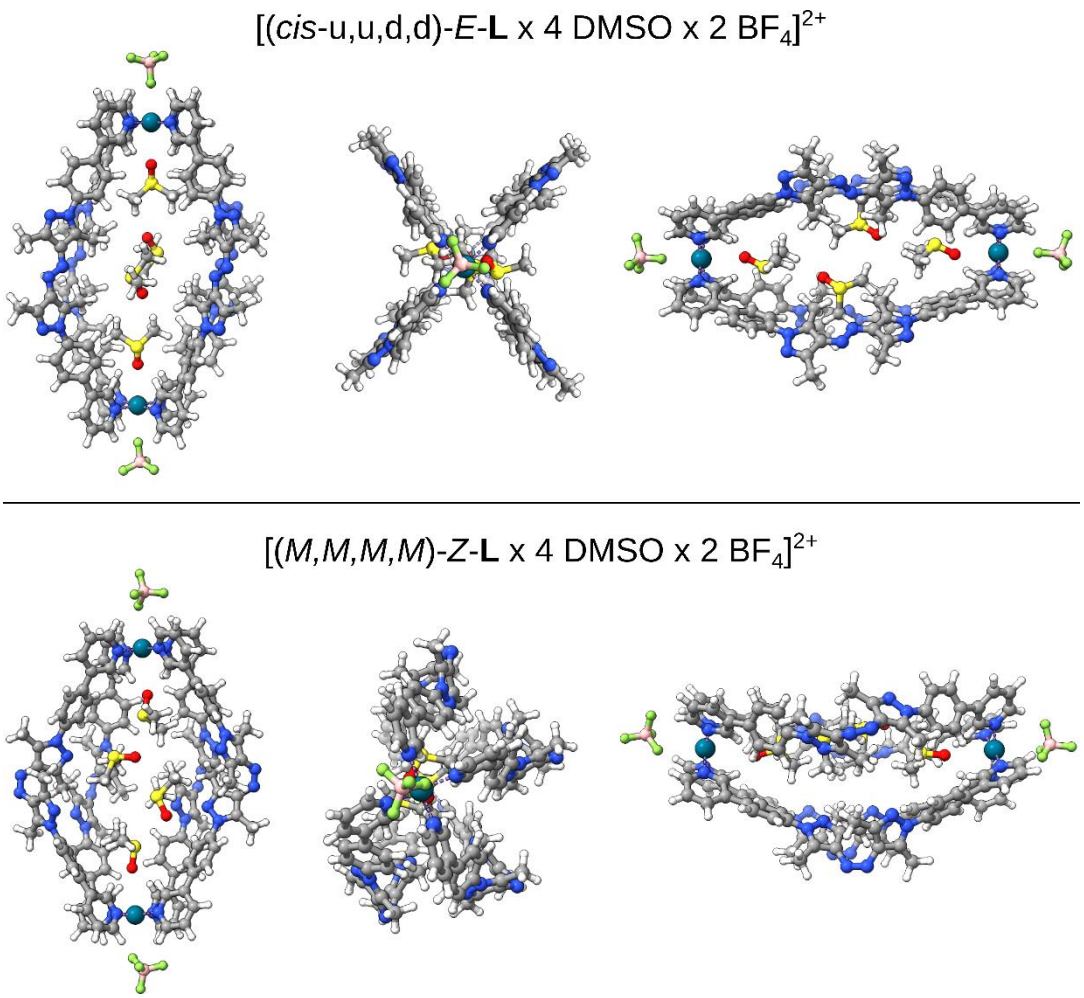

Figure S107. Model systems of *E*-**L** and *Z*-**L**, including four DMSO molecules and two BF_4^- anions. The *E*-**L** model was extracted from the experimental crystal structure and relaxed at the ωB97X-3c [CPCM: DMSO] level of theory. The given isomer is (*cis*-u,u,d,d)-*E*-**L**. The *Z*-**L** model was constructed analogously (for all isomers), and following conformational sampling, the lowest-energy conformer was relaxed at the same theory level. The given isomer is (*M*,*M*,*M*,*M*)-*Z*-**L.** Atom colour code: H (white), C (grey), N (blue), Pd (teal), O (red), S (yellow), F (green), B (pink).

S8.7 Investigation of *E*-**T** and *Z*-**T**

Model systems for the triangle complex with either all *E*-configured ligands (*E*-**T**) or all *Z*-configured ligands (*Z*-**T**) were constructed and conformationally sampled following the same procedure as for the lantern structures. However, technical difficulties arose, and the resulting low-lying conformers disagreed with the experimental NMR data presented in Section S2.6. This suggests that the combination of extended system size, flexibility, and high system charge (+6) renders the previously applied workflow unsuitable for obtaining reliable structures.

Based on the predicted lowest conformer of *E*-**T**, we attempted to reproduce the experimentally determined reaction energy for the transition of *E*-**L** to *E*-**T** (−27.8 kJ mol^{-1}) but obtained a qualitatively incorrect result. The inclusion of six explicit DMSO molecules and three BF_4^- anions in the model did not help to resolve this discrepancy.

Consequently, a model of *E*-**T** consistent with the experimental NMR data was constructed and optimised at the GFN2-xTB [ALPB: DMSO] level of theory, which was only used for visualisation of *E*-**T** in the figures of this study and to approximate dimensions for comparison with the solvodynamic diameters obtained via DOSY NMR (Figure S23).

References

[1] S. Millan, B. Gil-Hernández, E. Hastürk, A. Schmitz, C. Janiak, "A 2D Zinc Coordination Polymer Built from the Mono-deprotonated 4,4′-Azobis(3,5-dimethyl-1H-pyrazole) Ligand" *Z. für Anorg. Allg. Chem.* **2018**, *644*, 1311–1316.

[2] M. D. Hanwell, D. E. Curtis, D. C. Lonie, T. Vandermeersch, E. Zurek, G. R. Hutchison, "Avogadro: an advanced semantic chemical editor, visualization, and analysis platform" *J. Cheminformatics* **2012**, *4*, 17.

[3] M. J. Notheis, V. Sahiti, L. K. S. von Krbek, V. Prangenberg, J. S. Kruse, "2,8-Dihalogenated Diazocines: Versatile Reactants for Functionalized Photoswitches" *Synlett* **2025**, *36*, 1569–1573.

[4] M. J. Notheis, G. Schnakenburg, L. K. S. von Krbek, "Light-Driven Ratchet Mechanism Accelerates Regioselective Metal-Cation Exchange in a Heterobimetallic Helicate" *Angew. Chem. Int. Ed.* **2025**, e202508952.

[5] C. Feldmeier, H. Bartling, E. Riedle, R. M. Gschwind, "LED based NMR illumination device for mechanistic studies on photochemical reactions – Versatile and simple, yet surprisingly powerful" *J. Magn. Reson.* **2013**, *232*, 39–44.

[6] Y. Ji, D. A. DiRocco, J. Kind, C. M. Thiele, R. M. Gschwind, M. Reibarkh, "LED-Illuminated NMR Spectroscopy: A Practical Tool for Mechanistic Studies of Photochemical Reactions" *ChemPhotoChem* **2019**, *3*, 984–992.

[7] M. S. Maier, K. Hüll, M. Reynders, B. S. Matsuura, P. Leippe, T. Ko, L. Schäffer, D. Trauner, "Oxidative Approach Enables Efficient Access to Cyclic Azobenzenes" *J. Am. Chem. Soc.* **2019**, *141*, 17295–17304.

[8] S. Ghosh, C. Eschen, N. Eleya, A. Staubitz, "Synthesis of a Series of 12-Membered Azobenzene Macrocycles and Tuning of the Half-Life of the Thermal Z–E Isomerization" *J. Org. Chem.* **2023**, *88*, 3372–3377.

[9] S. Hoops, S. Sahle, R. Gauges, C. Lee, J. Pahle, N. Simus, M. Singhal, L. Xu, P. Mendes, U. Kummer, "COPASI—a COmplex PAthway SImulator" *Bioinformatics* **2006**, *22*, 3067–3074.

[10] S. Takahashi, Y. Sasaki, S. Hiraoka, H. Sato, "A stochastic model study on the self-assembly process of a Pd 2 L 4 cage consisting of rigid ditopic ligands" *Phys. Chem. Chem. Phys.* **2018**, *21*, 6341–6347.

[11] T. Tateishi, S. Takahashi, A. Okazawa, V. Martí-Centelles, J. Wang, T. Kojima, P. J. Lusby, H. Sato, S. Hiraoka, "Navigated Self-Assembly of a Pd2L4 Cage by Modulation of an Energy Landscape under Kinetic Control" *J. Am. Chem. Soc.* **2019**, *141*, 19669–19676.

[12] T. Tateishi, S. Kai, Y. Sasaki, T. Kojima, S. Takahashi, S. Hiraoka, "Two dominant self-assembly pathways to a Pd 3 L 6 double-walled triangle" *Chem. Commun.* **2018**, *54*, 7758–7761.

[13] S. Kai, T. Tateishi, T. Kojima, S. Takahashi, S. Hiraoka, "Self-Assembly of a Pd4L8 Double-Walled Square Takes Place through Two Kinds of Metastable Species" *Inorg. Chem.* **2018**, *57*, 13083–13086.

[14] T. Tateishi, T. Kojima, S. Hiraoka, "Multiple Pathways in the Self-Assembly Process of a Pd4L8 Coordination Tetrahedron" *Inorg. Chem.* **2018**, *57*, 2686–2694.

[15] B. A. Inc., *SADABS-2016/2*, Madison, Wisconsin, USA, **2016**.

[16] G. M. Sheldrick, "SHELXT– Integrated space-group and crystal-structure determination" *Acta Crystallogr. Sect. A* **2015**, *71*, 3–8.

[17] G. M. Sheldrick, "Crystal structure refinement with SHELXL" *Acta Crystallogr. Sect. C: Struct. Chem.* **2015**, *71*, 3–8.

[18] O. V. Dolomanov, L. J. Bourhis, R. J. Gildea, J. A. K. Howard, H. Puschmann, "OLEX2: a complete structure solution, refinement and analysis program" *J. Appl. Crystallogr.* **2009**, *42*, 339–341.

[19] P. V. D. Sluis, A. L. Spek, "BYPASS: an effective method for the refinement of crystal structures containing disordered solvent regions" *Acta Crystallogr. Sect. A* **1990**, *46*, 194–201.

[20] S. Grimme, "Exploration of Chemical Compound, Conformer, and Reaction Space with Meta-Dynamics Simulations Based on Tight-Binding Quantum Chemical Calculations" *J. Chem. Theory Comput.* **2019**, *15*, 2847–2862.

[21] P. Pracht, S. Grimme, C. Bannwarth, F. Bohle, S. Ehlert, G. Feldmann, J. Gorges, M. Müller, T. Neudecker, C. Plett, S. Spicher, P. Steinbach, P. A. Wesołowski, F. Zeller, "CREST—A program for the exploration of low-energy molecular chemical space" *J. Chem. Phys.* **2024**, *160*, 114110.

[22] C. Bannwarth, E. Caldeweyher, S. Ehlert, A. Hansen, P. Pracht, J. Seibert, S. Spicher, S. Grimme, "Extended tight-binding quantum chemistry methods" *Wiley Interdiscip. Rev.: Comput. Mol. Sci.* **2021**, *11*, DOI 10.1002/wcms.1493.

[23] C. Bannwarth, S. Ehlert, S. Grimme, "GFN2-xTB—An Accurate and Broadly Parametrized Self-Consistent Tight-Binding Quantum Chemical Method with Multipole Electrostatics and Density-Dependent Dispersion Contributions" *J. Chem. Theory Comput.* **2019**, *15*, 1652–1671.

[24] S. Ehlert, M. Stahn, S. Spicher, S. Grimme, "Robust and Efficient Implicit Solvation Model for Fast Semiempirical Methods" *J. Chem. Theory Comput.* **2021**, *17*, 4250–4261.

[25] M. Müller, A. Hansen, S. Grimme, "ωB97X-3c: A composite range-separated hybrid DFT method with a molecule-optimized polarized valence double-ζ basis set" *J. Chem. Phys.* **2023**, *158*, 014103.

[26] M. Cossi, N. Rega, G. Scalmani, V. Barone, "Energies, structures, and electronic properties of molecules in solution with the C-PCM solvation model" *J. Comput. Chem.* **2003**, *24*, 669–681.

[27] A. V. Marenich, C. J. Cramer, D. G. Truhlar, "Universal Solvation Model Based on Solute Electron Density and on a Continuum Model of the Solvent Defined by the Bulk Dielectric Constant and Atomic Surface Tensions" *J. Phys. Chem. B* **2009**, *113*, 6378–6396.

[28] S. Spicher, S. Grimme, "Single-Point Hessian Calculations for Improved Vibrational Frequencies and Rigid-Rotor-Harmonic-Oscillator Thermodynamics" *J. Chem. Theory Comput.* **2021**, *17*, 1701–1714.

[29], "GitHub - grimme-lab/xtb: Semiempirical Extended Tight-Binding Program Package," can be found under https://github.com/grimme-lab/xtb(accessed 12 August 2025), **n.d.**

[30] F. Neese, "Software update: The ORCA program system—Version 5.0" *Wiley Interdiscip. Rev.: Comput. Mol. Sci.* **2022**, *12*, DOI 10.1002/wcms.1606.

[31] E. F. Pettersen, T. D. Goddard, C. C. Huang, E. C. Meng, G. S. Couch, T. I. Croll, J. H. Morris, T. E. Ferrin, "UCSF ChimeraX: Structure visualization for researchers, educators, and developers" *Protein Sci.* **2021**, *30*, 70–82.

[32] P. Pracht, "Conformational Pruning via the Permutation Invariant Root-Mean-Square Deviation of Atomic Positions" *J. Chem. Inf. Model.* **2025**, *65*, 4501–4511.

[33] S. Grimme, A. Hansen, S. Ehlert, J.-M. Mewes, "r2SCAN-3c: A 'Swiss army knife' composite electronic-structure method" *J. Chem. Phys.* **2021**, *154*, 064103.